

# Characterization of a Reconstituted Low Plasticity Silt

by

**John Thomas Grennan**

National Certificate in Civil and Environmental Engineering  
Galway-Mayo Institute of Technology, Galway, Ireland (2004)

Bachelor of Engineering (Ord.) in Civil and Environmental Engineering  
Galway-Mayo Institute of Technology, Galway, Ireland (2005)

Bachelor of Engineering (Hon.) in Civil and Environmental Engineering  
National University of Ireland Galway, Galway, Ireland (2007)

Submitted to the Department of Civil and Environmental Engineering  
in Partial Fulfillment of the Requirements for the Degree of

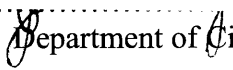
**Masters of Science in Civil and Environmental Engineering**

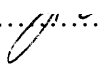
at the

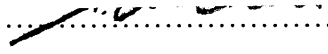
**MASSACHUSETTS INSTITUTE OF TECHNOLOGY**

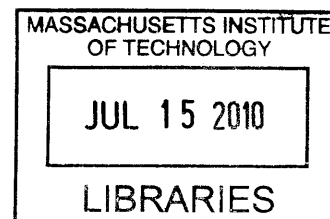
June 2010

© 2010 Massachusetts Institute of Technology. All rights reserved.

Signature of Author.....  
  
Department of Civil and Environmental Engineering  
May 7, 2010

Certified by.....  
  
John T. Germaine  
Senior Research Associate and Senior Lecturer of Civil and Environmental Engineering  
Thesis Supervisor

Accepted by.....  
  
Daniele Veneziano  
Chairman, Departmental Committee for Graduate Students



**ARCHIVES**



# Characterization of a Reconstituted Low Plasticity Silt

by

**John Thomas Grennan**

Submitted to the Department of Civil and Environmental Engineering on May 7, 2010  
in Partial Fulfillment of the Requirements for the Degree of  
Masters of Science in Civil and Environmental Engineering

## **ABSTRACT**

During a major upgrade of the wastewater infrastructure in Skibbereen, Co. Cork, Ireland, there were many challenges during construction. Many of these difficulties were associated with the soft silt ground conditions. Consequently, soil samples were sourced from the location and transported to MIT for the purposes of this research.

This thesis investigates the characteristics of the low plasticity silt encountered at Skibbereen to allow an understanding of the soil behavior and help explain some of the difficulties encountered during construction. The research program is divided up into two major components: 1) Index property testing; and 2) Engineering property testing. The index property testing defines the material as a well graded low plasticity silt with very low salt and organic contents.

An extensive testing program is undertaken using Constant Rate of Strain (CRS), Hydraulic Conductivity,  $K_0$ -Consolidated Direct Simple Shear ( $CK_0$ DSS), and Isotropic and  $K_0$ -consolidated undrained triaxial compression (CIUC and  $CK_0$ UC) tests to define the engineering properties of the material.

The experimental investigation finds that undercompaction is the best reconstitution technique for this material and it is almost impossible to test intact samples. The CRS tests demonstrate that the compression ratio increases with an increase in stress level but the recompression and swelling ratio are not significantly affected. The hydraulic conductivity results fit into the expected range for silt material and they are dependent on stress level. The DSS tests demonstrate that the undrained strength ratio ( $s_u/\sigma'_v$ ) increases with an increase in stress level. A similar trend is found for the peak arctan  $\tau_H/\sigma'_v$  ( $\psi'_p$ ) values. Overconsolidated tests prove that the SHANSEP framework can be successfully used for this material and the cyclic tests demonstrate that an increase in density through shearing will provide a dramatically higher  $s_u/\sigma'_v$  and greater ductility.

The triaxial compression tests indicate that  $s_u/\sigma'_v$  will increase with an increase in stress level. In the CIUC tests, ductility and the degree of dilation increase with an increase in stress level. However, the  $CK_0$ UC tests provide more consistent data at all stress levels and the  $s_u/\sigma'_v$ , friction angle, and modulus is lower than the CIUC counterpart.

Thesis Supervisor: John T. Germaine

Title: Senior Research Associate and Senior Lecturer of Civil and Environmental Engineering



## ACKNOWLEDGEMENTS

I would like to express my sincere gratitude to my thesis supervisor, research advisor, and academic advisor Dr. John T. Germaine. His never ending patience through the multitude of testing problems was amazing. His guidance and motivation throughout my time at MIT is greatly appreciated and will never be forgotten. Despite his extensive workload, the door was always open for questions. I owe all my laboratory skills to him and I have learned from the best in the business. I entered MIT with a research advisor and I leave with a good friend.

I would like to thank Ward and Burke Construction Ltd. for sponsoring this research and making my degree possible. In particular, I am indebted to Robert Ward (MIT SM 89'). His confidence in my ability, guidance through the application process, and encouragement through the early stages of life in MIT were invaluable.

My gratitude goes to the fantastic faculty at MIT that I have learned from and worked for. Professor Andrew J. Whittle, Professor Herbert H. Einstein, and Dr. Lucy Jen gave me knowledge and tools that I will use for the rest of my career. I would like to thank Dr. Jen for the advice she gave me on numerous occasions.

My gratitude also extends to all the staff of the CEE department for their assistance and friendship during my time in MIT.

For the multitude of friends I have made, I am not sure where to start. I moved to Boston knowing no one and I leave MIT with an endless list. I would first like to thank the geotechnical community of MIT. It is unfair to mention names from so many. However, extra thanks is needed for Naeem Abdulhadi for his help in the lab during my first few months at MIT, Brendan Casey for keeping the Irish contingent strong and the friendly banter on a daily basis, and Cullen Jones. Cullen and I started MIT together, worked together, and will graduate together. His help, friendship, and attitude to work were an inspiration. I wish him all the best in the future.

I would like to thank my many friends outside the geotechnical department, they have thought me to leave the pressures of work for a few hours and relax. Thanks to Francois O' Sulliivan for the many fitness and ensuing "hydration" sessions. My gratitude also goes to the Irish Association of MIT, the Unbelievable's soccer team, and the Kerry Boston Football club. I have made some lifelong friends.

I would also like to thank all my friends at home for their constant support.

My sincere gratitude to Sheena Dwyer for her friendship, the best memories of the last two years has been spent with her.

Finally I would like to thank all my family, especially my mother Ann and brother David, I sometimes take for granted their endless encouragement, consolation, and support. It is truly appreciated and loved.



To my father, the late John Francois Grennan, our short time together has given me the wisdom and courage to make the most out of life.

I dedicate this thesis to him.





## Table of Contents

<b>Abstract</b>	<b>3</b>
<b>Acknowledgements</b>	<b>5</b>
<b>Table of Contents</b>	<b>9</b>
<b>List of Tables</b>	<b>17</b>
<b>List of Figures</b>	<b>19</b>
<b>List of Symbols</b>	<b>31</b>
<b>1 INTRODUCTION</b>	<b>35</b>
1.1 BACKGROUND	35
1.2 RATIONALE FOR CHARACTERIZATION OF LOW PLASTICITY SILT FROM SKIBBEREEN	36
1.3 RESEARCH OBJECTIVES AND SCOPE	37
1.4 ORGANIZATION OF THE THESIS	39
<b>2 BACKGROUND</b>	<b>41</b>
2.1 INTRODUCTION	41
2.2 SKIBBEREEN	42
2.2.1 Introduction	42
2.2.1.1 River Ilen	43
2.2.1.2 Caol Stream	44
2.2.1.3 March Field	44
2.3 GEOLOGY	45
2.3.1 Introduction	45
2.3.2 Topography	45
2.3.3 Rock Types	45
2.3.3.1 Precambrian Rocks	46
2.3.3.2 The Lower Palaeozoic Rocks	46
2.3.3.3 Caledonian Movement	47
2.3.3.4 Devonian Rocks	48

2.3.3.5 Carboniferous Rocks	48
2.3.4 Geological Events after the Carboniferous Period	49
2.3.4.1 Variscan Deformation and Metamorphism	49
2.3.4.2 The Quaternary Period	50
2.3.4.3 The Holocene	51
2.3.5 Geology in Skibbereen today	52
2.3.5.1 Skibbereen town	52
2.3.5.2 Skibbereen Environs	52
2.3.5.3 Marsh Area	53
2.4 PROJECT DESCRIPTION	53
2.4.1 Introduction	53
2.4.2 Caisson Construction	54
2.4.3 Trenchless Technology	55
2.4.3.1 Horizontal Directional Drilling	55
2.4.3.2 Auger Boring	55
2.4.3.3 Microtunneling	56
2.4.4 Field Operation	57
2.4.4.1 Caissons	57
2.4.4.2 Earthworks	57
2.4.4.3 Pipe lines and tunnels	58
2.5 SITE INVESTIGATION AND LABORATORY TESTING	61
2.5.1. Original Testing Program	61
2.5.2. Further Investigation	63
<b>3 LITERATURE REVIEW</b>	<b>95</b>
3.1 INTRODUCTION	95
3.2 RECONSTITUTION	97
3.2.1 Introduction	97
3.2.2 Most Tamping (Undercompaction)	97
3.2.3 Slurry Sedimentation	100

3.2.4	Air and Water Pluviation	103
3.2.5	Fabric	104
3.3	SAMPLING	106
3.3.1	Introduction	106
3.3.2	Sampling Techniques	106
3.4	CONSOLIDATION PROPERTIES	109
3.5	STRESS-STRAIN-STRENGTH PROPERTIES	110
3.5.1	Introduction	110
3.5.2	Shear strength from triaxial tests – Failure criterion	111
3.5.3	Undrained Compression tests (UU)	112
3.5.4	Isotropically Consolidated Undrained triaxial tests	113
3.5.5	Anisotropically Consolidated Undrained triaxial tests	115
3.5.6	$K_0$ Consolidated Undrained triaxial tests	115
3.5.7	$K_0$ Consolidated Undrained Direct Simple Shear tests (CK <sub>0</sub> DSS)	116
3.5.8	Overconsolidation ratio and normalized behavior	116
3.6	LIQUEFACTION AND CYCLIC SHEAR RESISTANCE	118
<b>4</b>	<b>MATERIAL PROCESSING, RECONSTITUTION, EQUIPMENT, AND TESTING PROCEDURES</b>	<b>145</b>
4.1	INTRODUCTION	145
4.2	MATERIAL PROCESSING	146
4.2.1	Introduction	146
4.2.2	Samples for Laboratory Testing at MIT	147
4.2.3	Processing	148
4.3	RECONSTITUTION	150
4.3.1	Introduction	150
4.3.2	Resedimentation	150
4.3.2.1	Introduction	150
4.3.2.2	Resedimentation Procedure	152

4.3.2.3	Resedimentation Problems	153
4.3.2.4	Resedimentation Evaluation	154
4.3.3	Undercompaction	155
4.3.3.1	Introduction	155
4.3.3.2	Procedure	155
4.3.3.3	Undercompaction Problems	157
4.3.3.4	Undercompaction Evaluation	158
4.4	EQUIPMENT	158
4.4.1	Introduction	158
4.4.2	Measurement Instrumentation	158
4.4.2.1	Load Cells	159
4.4.2.2	Axial Displacement Transducers	159
4.4.2.3	Pressure Transducers	159
4.4.2.4	Volume Change Transducers	159
4.4.3	Data Acquisition System	160
4.4.4	Computer Control System	161
4.5	TESTING PROCEDURES	162
4.5.1	Introduction	162
4.5.2	Characterization	163
4.5.2.1	Introduction	163
4.5.2.2	Grain size analysis	163
4.5.2.3	Atterberg Limits	163
4.5.2.4	Specific Gravity	164
4.5.2.5	Salinity	164
4.5.2.6	Organic Content	165
4.5.3	Constant Rate of Strain (CRS) Tests	166
4.5.3.1	Introduction	166
4.5.3.2	Procedure	168
4.5.3.3	Problems	169
4.5.4	Hydraulic Conductivity Tests	170

4.5.4.1	Introduction	170
4.5.4.2	Procedure	171
4.5.4.3	Problems	172
4.5.5	Direct Simple Shear Tests	173
4.5.5.1	Introduction	173
4.5.5.2	Procedure	174
4.5.5.3	Problems	175
4.5.6	Triaxial Tests	175
4.5.6.1	Introduction	175
4.5.6.2	Procedure	176
4.5.6.3	Problems	179
<b>5</b>	<b>CHARACTERIZATION, CONSOLIDATION, AND HYDRAULIC CONDUCTIVITY</b>	<b>213</b>
5.1	INTRODUCTION	213
5.2	INDEX PROPERTIES	214
5.2.1	Introduction	214
5.2.2	Grain Size Distribution	214
5.2.3	Atterberg Limits	214
5.2.4	Specific Gravity, Organic Content, and Salt Concentration	215
5.2.5	Scanning Electron Microscope Images and Mineralogy	215
5.3	CONSOLIDATION BEHAVIOR	216
5.3.1	Introduction	216
5.3.2	Constant Rate of Strain Tests	217
5.3.3	Direct Simple Shear Tests	221
5.3.4	Triaxial Tests	223
5.3.4.1	Introduction	223
5.3.4.2	Series A tests – Isotropically consolidated	223
5.3.4.3	Series B tests – $K_0$ consolidated	225
5.3.5	Stiffness in Consolidation	227
5.4	HYDRAULIC CONDUCTIVITY	227

<b>6</b>	<b>DIRECT SIMPLE SHEAR AND UNDRAINED TRIAXIAL COMPRESSION BEHAVIOR</b>	<b>265</b>
6.1	INTRODUCTION	265
6.2	DIRECT SIMPLE SHEAR	266
6.2.1	Introduction	266
6.2.2	Normally Consolidated (NC) Behavior	267
6.2.2.1	Shear Stress-Strain Behavior	267
6.2.2.2	Effective Stress Behavior	268
6.2.2.3	Stiffness	269
6.2.2.4	Specimens with different initial densities	269
6.2.3	Overconsolidated (OC) Behavior	271
6.2.3.1	Shear Stress-Strain Behavior	271
6.2.3.2	Effective Stress Behavior	272
6.2.3.3	Stiffness	272
6.2.3.4	SHANSEP Equation for DSS	273
6.2.4	Cyclic Behavior	273
6.2.4.1	Introduction	273
6.2.4.2	Shear Stress-Strain Behavior	274
6.2.4.3	Effective Stress Behavior	275
6.2.4.4	Cyclic Behavior	276
6.3	ISOTROPICALLY CONSOLIDATED UNDRAINED TRIAXIAL COMPRESSION (CIUC) TESTS (SERIES A)	277
6.3.1	Introduction	277
6.3.2	Shear Stress-Strain Behavior	278
6.3.3	Effective Stress Behavior	279
6.3.4	Stiffness	281
6.3.5	Summary of behavior	282
6.4	$K_0$ - CONSOLIDATED UNDRAINED TRIAXIAL COMPRESSION ( $CK_0UC$ ) TESTS (SERIES B)	283
6.4.1	Introduction	283

6.4.2	Shear Stress-Strain Behavior	284
6.4.3	Effective Stress Behavior	285
6.4.4	Stiffness	286
6.4.5	Summary of behavior	286
6.5	<b>SHEAR BEHAVIOR SUMMARY</b>	288
6.5.1	Introduction	288
6.5.2	Triaxial comparison – CIUC versus $CK_0UC$	288
6.5.2.1	Shear Stress-Strain Behavior	288
6.5.2.2	Effective Stress Behavior	289
6.5.3	DSS - CIUC – $CK_0UC$ Summary	290
6.5.3.1	Undrained Strength Ratio	290
6.5.3.2	Friction Angle and $\text{Arctan } \tau_h/\sigma'_v$	290
6.5.3.3	Axial strain at failure	292
6.5.3.4	Stiffness	292
<b>7</b>	<b>SUMMARY, CONCLUSIONS, AND RECOMMENDATIONS</b>	<b>347</b>
7.1	OVERVIEW	347
7.2	SUMMARY OF WORK UNDERTAKEN AT MIT	348
7.3	RESULTS AND CONCLUSIONS	350
7.3.1	Feasibility of testing intact tube samples	350
7.3.2	Development of a successful reconstitution procedure for the material	351
7.3.3	Development of successful testing preparation procedures	352
7.3.4	Index properties	353
7.3.5	Engineering Properties	354
7.3.5.1	Introduction	354
7.3.5.2	Consolidation behavior	354
7.3.5.3	Hydraulic Conductivity	356
7.3.5.4	Direct Simple Shear Behavior	356
7.3.5.5	Undrained Triaxial Compression	358
7.3.5.6	Shear behavior	359

7.4	RECOMMENDATIONS FOR FUTURE RESEARCH	360
7.4.1	Triaxial Testing	360
7.4.2	Reconstitution Technique	361
7.4.3	Susceptibility to Liquefaction	361
7.4.4	Ground Treatment	362
	REFERENCES	363



## List of Tables

Table 2-1: Characterization results from Irish Drilling	65
Table 3-1: Parameters for triaxial specimens (Hoeg <i>et al.</i> 2000)	120
Table 3-2: Summary of dimensions and features of samplers (Long, 2007)	120
Table 3-3: Study of sampling induced desiccation effects on silts (Long, 2007)	120
Table 3-4: Summary of dimensions and features of 54 mm Norwegian samplers (Long <i>et al.</i> 2010)	121
Table 3-5: Su/p ratios for CIUC tests based on various failure criteria (Brandon <i>et al.</i> , 2006)	121
Table 3-6: Effective stress friction angles ( $\phi'$ ) and strain to failure ( $\epsilon_f$ ) from CIUC tests for various criteria for Yazoo and LMVD silt (Brandon <i>et al.</i> , 2006)	121
Table 3-7: Properties of samples of Arctic silt for shear test program (Ladd <i>et al.</i> , 1985)	122
Table 3-8: Values of $S_u/\sigma'_{1c}$ for Alaskan Silt (Fleming and Duncan, 1990)	122
Table 3-9: Normalized strength parameters for Normally consolidated Silts	122
Table 4-1: Characteristics of instrumentation used in CRS testing apparatus	182
Table 4-2: Characteristics of instrumentation used in Hydraulic Conductivity testing apparatus	182
Table 4-3: Characteristics of instrumentation used in DSS testing apparatus	183
Table 4-4: Characteristics of instrumentation used in manual control triaxial testing apparatus	183
Table 4-5: Characteristics of instrumentation used in automated triaxial testing apparatus	184
Table 5-1: Index Property results on Skibbreen Silt	229
Table 5-2: Summary of X Ray Diffraction giving the mineralogy breakdown of Skibbreen Silt	229
Table 5-3: Summary of CRS consolidation results	230
Table 5-4: Summary of consolidation results for DSS tests	231
Table 5-5: Summary of consolidation results from isotropically consolidated triaxial tests	232
Table 5-6: Summary of consolidation results from $K_0$ consolidated triaxial tests	233

Table 6-1: Summary of CK <sub>0</sub> DSS (NC) tests	294
Table 6-2: Summary of CK <sub>0</sub> DSS NC and cyclic tests	295
Table 6-3: Summary of CK <sub>0</sub> DSS OC tests	296
Table 6-4: Summary of CIUC triaxial tests	297
Table 6-5: Summary of CK <sub>0</sub> UC triaxial tests	298

## List of Figures

Figure 2-1: Skibbereen Location (Google Earth)	66
Figure 2-2: Skibbereen Location	66
Figure 2-3: Building use of town centre (not to scale) (Skibbereen Town Development Plan, 2009-2015)	67
Figure 2-4: Skibbereen town from the southwest (Skibbereen Circa 1900)	67
Figure 2-5: River Ilen (not to scale)	68
Figure 2-6: Tidal Influence on River Ilen: (a) Low Tide, (b) Low Tide, (c) High Tide and Heavy Rain, (d) High Tide and Heavy Rain	69
Figure 2-7: Caol Stream (not to scale)	70
Figure 2-8: Pollution along the Caol Stream in Skibbereen: (a) discharge pipe, (b) vertical discharge pipe, (c) polluted stream bed, (d) polluted stream bed (River Ilen and Caol Stream Redevelopment Project, 2007)	71
Figure 2-9: Marsh Field: (a) schematic (not to scale), (b) photograph	72
Figure 2-10: Topography of West Cork (Pracht & Sleeman, 2002)	73
Figure 2-11: (a) Geochronometric scale (Holland & Sanders, 2009), (b) county map of Ireland (Holland & Sanders, 2009)	73
Figure 2-12: Map showing the location of Precambrian rocks in Ireland (Holland and Sanders 2009)	74
Figure 2-13: Map showing distribution of land (dotted) and sea (white) in Lower Palaeozoic times (Charlesworth 1953)	75
Figure 2-14: Caledonian movement (Holland and Sanders, 2009)	75
Figure 2-15: Sea location during Devonian times (Dotted = land, Clear = water) (Charlesworth 1953)	76
Figure 2-16: Distribution of Old Red Sandstone rocks in Ireland today (Holland and Sanders, 2009)	76
Figure 2-17: Map showing the distribution of land during Carboniferous times, dotted is land, clear is water (Charlesworth, 1953)	76
Figure 2-18: Distribution of rock types around Skibbereen (Pracht & Sleeman, 2002)	77
Figure 2-19: Major structures in West Cork (Pracht & Sleeman, 2002)	77

Figure 2-20: The pattern of glaciation in Ireland during the last glaciation (Pracht & Sleeman, 2002)	78
Figure 2-21: Sinking of main pump station caisson using various excavators and hydraulic jacks	78
Figure 2-22: Schematic diagram of 6m internal diameter caisson (not to scale)	79
Figure 2-23: Directional Drilling equipment used in Skibbereen	80
Figure 2-24: Auger boring equipment used in Skibbereen; Launch shaft and jacking frame, augers, and clay pipes	80
Figure 2-25: Schematic diagram of the micro tunneling system used in Skibbereen	81
Figure 2-26: Pipe skin friction vs. distance for the micro tunneling in Skibbereen	81
Figure 2-27: Tunnel alignment: (a) schematic (blue line is tunnel), (b) photograph from launch shaft	82
Figure 2-28: Vertical tunnel alignment when TBM began to sink. (Zero in elevation indicates required grade, line with square data points is original TBM position, and line with circular data points is current pipe position)	83
Figure 2-29: Alignment of HDD grouting under tunnel (dimensions in m)	83
Figure 2-30: Crane attached to TBM: (a) At ground level, (b) inside TBM where crane is attached	84
Figure 2-31: Examples of structural damage as a result of tunneling; (a) Stone arch bridge cracked, (b) beginning of repair work on bridge, (c) retaining wall damaged where TBM exited stream (wall cracked and rotating towards river) (d) typical example of cracking in residential property	85
Figure 2-32: Vertical tunnel alignment after completion of tunnel (Zero in elevation indicates required grade, line with square data points is original TBM position, and line with circular data points is current pipe position)	86
Figure 2-33: Addition of kentledge over tunnel	86
Figure 2-34: Further site investigation in Skibbereen	87
Figure 2-35: Shell and auger for site investigation boreholes	87
Figure 2-36: Geonor field vane in use	88
Figure 2-37: Excavated silt from the shell and auger method	88

Figure 2-38: Field vane shear strength information: (a) Field data, (b) scatter plot for intact tests	89
Figure 2-39: Frequency versus intact undrained shear strength for field vane data	90
Figure 2-40: CPT output: Cone resistance, skin friction, friction ration, inclination, and interpreted soil profile	91
Figure 2-41: CPT output: Cone resistance, skin friction, pore pressure ratio, total pore pressure	92
Figure 2-42: CPT dissipation test in Skibbereen	93
Figure 3-1: Typical dry unit weight profiles obtained in triaxial silt specimens: (a) Block sample, (b) Undercompacted specimen (Baxter <i>et al.</i> , 2008)	123
Figure 3-2: Undrained triaxial results at $\sigma'_{ac} = 500$ kPa (Hoeg <i>et al.</i> 2000)	124
Figure 3-3: Undrained triaxial results at $\sigma'_{ac} = 250$ kPa (Hoeg <i>et al.</i> 2000)	125
Figure 3-4: Schematic diagram of sedimentation technique (Hyde <i>et al.</i> , 2006)	126
Figure 3-5: Comparison of results from undisturbed, slurry, and water pluviated specimens (Hoeg <i>et al.</i> , 2000)	127
Figure 3-6: One dimensional compressibility of Syncrude sand specimens reconstituted by different methods (Vaid and Sivathayalan, 1999)	128
Figure 3-7: Undrained simple shear response of specimens reconstituted by different techniques (Vaid and Sivathayalan, 1999)	128
Figure 3-8: Undrained triaxial compression response of reconstituted Fraser River Sand specimens (Vaid and Sivathayalan, 1999)	129
Figure 3-9: “Double” U 100 tubes (Standard Ireland-UK U100 or U4 sampling tubes. Crude cutting shoe shown on right hand side) (Long, 2007)	129
Figure 3-10: One dimensional behavior from oedometer tests, Sligo (Long, 2007)	130
Figure 3-11: One dimensional behavior from oedometer tests, Dunkettle (Long, 2007)	130
Figure 3-12: Consolidation test results for undisturbed samples of Yazoo Silt (Brandon <i>et al.</i> , 2006)	131
Figure 3-13: Compression curves for silt in Harrison Bay area (Ladd <i>et al.</i> , 1986)	131
Figure 3-14: Compression test results, Sligo (Long, 2007)	132

Figure 3-15: Typical oedometer test results (a) Norwegian upper Os silt, (b) lower OS clayey silt, and (c) Norwegian E39 silt (Long <i>et al.</i> 2010)	133
Figure 3-16: Idealized stress path showing stresses at failure for different failure criteria (Brandon <i>et al.</i> , 2006)	134
Figure 3-17: Deviator stress-strain curves from UU triaxial tests of undisturbed specimens of Yazoo silt (Brandon <i>et al.</i> , 2006)	134
Figure 3-18: Deviator stress-strain curves for reconstituted specimens of Yazoo and LMVD silt; (a) Yazoo silt, (b) LMVD silt (Brandon <i>et al.</i> , 2006)	135
Figure 3-19: Stress-strain relationship for UU tests at confining pressure ( $\sigma_{con}$ ) = 1.5 ksc ( $\approx 147$ kPa) on Alaskan Silt (Fleming and Duncan, 1990)	135
Figure 3-20: CIUC tests on undisturbed specimens of Yazoo silt; (a) Deviator stress strain curve, (b) stress paths (Brandon <i>et al.</i> , 2006)	136
Figure 3-21: Deviator stress versus axial strain for reconstituted low plasticity silt (Hyde <i>et al.</i> , 2006)	137
Figure 3-22: Stress path for reconstituted low plasticity silt (Hyde <i>et al.</i> , 2006)	137
Figure 3-23: Comparison of deviator stress and pore pressure behavior for undisturbed and remolded samples isotropically consolidated to 1.5 ksc ( $\approx 150$ kPa) (Fleming and Duncan, 1990)	138
Figure 3-24: Effective stress path for triaxial tests on natural silt; intact and reconstituted specimen data above stress path (Hoeg <i>et al.</i> , 2000)	138
Figure 3-25: CAUC results on Norwegian glaciomarine silt; (a) upper silt, (b) lower clayey silt 7m and 9m samples, and (c) lower clayey silt 8m and 10m samples (Long <i>et al.</i> , 2010)	139
Figure 3-26: Normalized stress strain data from CU triaxial tests on OCR = 1 Harrison Bay Arctic Silt (Ladd <i>et al.</i> , 1985)	140
Figure 3-27: Normalized stress strain data from CU Direct Simple Shear tests on OCR = 1 Harrison Bay Arctic Silt (Ladd <i>et al.</i> , 1985)	140
Figure 3-28: Intact and reconstituted specimens of NC Fraser River silt during constant volume DSS shear; (a) stress strain and (b) stress path response (Wijewickreme and Sanin, 2008)	141
Figure 3-29: Deviator stress and effective stress ratio versus axial strain curves in CIUC tests; (a) deviator stress-axial curve and (b) effective stress ratio-axial strain (Yasuhara <i>et al.</i> , 2003)	142

Figure 3-30: Effective stress paths in CIUC tests; (a) deviator stress path and (b) normalized effective stress path (Yasuhara <i>et al.</i> , 2003)	142
Figure 3-31: Normalized undrained shear strength versus OCR for Alaskan Silt (Fleming and Duncan, 1990)	143
Figure 3-32: Normalized cyclic stress ratio versus plasticity index on undisturbed samples (Prakash and Puri, 2003)	143
Figure 4-1: Typical MOSTAP Sampler (Lankelma, 2008)	185
Figure 4-2: Extruded tube sample	186
Figure 4-3: Bulk Samples Air Drying	186
Figure 4-4: Schematic of the blending procedure for large samples (Germaine & Germaine, 2009)	187
Figure 4-5: Blending in Buckets	187
Figure 4-6: Vacuum setup to de air the RBBC slurry (Abdulhadi, 2009)	188
Figure 4-7: Pouring of RBBC into Consolidometer (Abdulhadi, 2009)	188
Figure 4-8: Consolidometer with internal diameter of 7.62 cm: (a) schematic, (b) photograph (Abdulhadi, 2009)	189
Figure 4-9: Uniform sedimentation with various salt concentrations	190
Figure 4-10: Typical deformation vs. Time Plot during resedimentation	190
Figure 4-11: Specimen “flow” during and after extrusion from consolidometer	191
Figure 4-12: Cut through dense material with razor blade after extrusion flow	191
Figure 4-13: “Jelly donut” behavior of material: (a) extrusion of material, (b) Just after extrusion (the ring in the cross section shows the start of the soft “jelly” material), (c) touching of sample causing disturbance	192
Figure 4-14: The trimming process: (a) partially saturated specimen after extrusion, (b) placement of specimen in the CRS trimming rig, (c) beginning of trimming when the specimen appears dry, (d) water drawn to trimming location, preventing further trimming and causing collapse of the specimen structure	193
Figure 4-15: Schematic of reconstituting specimens using the undercompaction procedure (Germaine & Germaine, 2009)	194
Figure 4-16: Schematic diagram of a centralized data acquisition system (Germaine & Germaine, 2009)	194

Figure 4-17: Schematic diagram of the control system hardware components	195
Figure 4-18: Original CRS device developed by Smith and Wahls (1969)	196
Figure 4-19: MIT CRS device (Wissa et al., 1971)	196
Figure 4-20: Oedometer configuration for CRS testing: (a) schematic, (b) photograph	197
Figure 4-21: CRS Test setup: (a) schematic, (b) photograph	198
Figure 4-22: Dead load configuration for CRS saturation: (a) successful, (b) unsuccessful	199
Figure 4-23: “Blow holes” resulting from a high water head	200
Figure 4-24: Undercompaction in CRS specimen ring from top to bottom using recess tool underneath the specimen ring	200
Figure 4-25: Schematic Diagram of Geonor Model 4 DSS Apparatus (Ortega, 1992)	201
Figure 4-26: The DSS device with reservoir and ancillary plumbing	201
Figure 4-27: DSS setup: (a) specimen mold and Geonor membrane, (b) membrane placed in mold, (c) vacuum applied to membrane and specimen ring lower onto pedestal in trimming apparatus, (d) positioning of mold using calipers	202
Figure 4-28: Compaction procedure: (a) schematic diagram showing how specimen is compacted in layers, (b) scarifying between layers, (c) final specimen after compaction	203
Figure 4-29: Connection of the drainage lines for saturation: (a) schematic, (b) photograph	204
Figure 4-30: Manual triaxial apparatus used for CIUC tests (modified from Sheahan, 1991)	205
Figure 4-31: Schematic of MIT automated stress path triaxial cell (Santagata, 1998)	206
Figure 4-32: Schematic of automated triaxial cell (Santagata, 1998)	207
Figure 4-33: Compaction configuration: (a) schematic, (b) photograph	208
Figure 4-34: Triaxial setup procedure: (a) placing porous stone on specimen, (b) placing top cap on specimen and folding membrane around top cap, (c) fixing o-rings and applying vacuum, (d) removing expander/former , rolling up thin membrane, and fixing final o-ring	209
Figure 4-35: Uneven cross sectional area after backpressure saturation and consolidation	210



Figure 4-36: Unstable structure causing the specimen to lean to one side during saturation when there is a top cap with no recess for lateral stability	211
Figure 5-1: Grain Size Distribution Curves for Skibbereen Silt from hydrometer tests	234
Figure 5-2: Surface curvature around fall cone during liquid limit testing on Skibbereen Silt: (a) Extended view, (b) close up	235
Figure 5-3: Classification of Skibbereen Silt on Casagrande Plasticity Chart	236
Figure 5-4: SEM image on Skibbereen Silt, magnified to 2000 times the actual size	236
Figure 5-5: X Ray Diffraction analysis for Skibbereen Silt: Intensity versus Degrees Two Theta for Cu Ka Radiation (5-39)	237
Figure 5-6: X Ray Diffraction analysis for Skibbereen Silt: Intensity versus Degrees Two Theta for Cu Ka Radiation (39-65)	238
Figure 5-7: Compression behavior in $\epsilon_a$ - $\log\sigma'_v$ space from CRS 976	239
Figure 5-8: Compression behavior in $e$ - $\log\sigma'_v$ space from CRS 976	240
Figure 5-9: Axial strain versus $\sigma'_v/\sigma'_{vm}$ ( $OCR^{-1}$ ) from the unload phases of a typical CRS test	241
Figure 5-10: Axial strain-time behavior with different initial densities from CRS tests	242
Figure 5-11: Axial strain-log time behavior with different initial densities from CRS tests	242
Figure 5-12: Axial strain-time (close up view) behavior with different initial densities from CRS tests	243
Figure 5-13: Axial strain post saturation versus initial setup dry density from CRS tests	243
Figure 5-14: Void ratio post saturation versus initial setup dry density from CRS tests	244
Figure 5-15: Compression behavior in $\epsilon_a$ - $\log\sigma'_v$ space from CRS tests	245
Figure 5-16: Compression behavior in $e$ - $\log\sigma'_v$ space from CRS tests	246
Figure 5-17: Virgin Compression behavior in $e$ - $\log\sigma'_v$ space from CRS tests	247
Figure 5-18: Post consolidation behavior; a) CRS specimen extrusion into evaporating dish, b) material behavior after one blow to evaporating dish, c) material behavior after 5 blows to evaporating dish	248
Figure 5-19: Compression behavior in $\epsilon_a$ - $\log\sigma'_v$ space from DSS 800	249

Figure 5-20: Axial strain-time behavior during inundation using different confining stresses from CRS tests	250
Figure 5-21: Axial strain-log time behavior during inundation using different confining stresses from CRS tests	250
Figure 5-22: Void ratio post saturation versus initial setup dry density from CRS and DSS tests	251
Figure 5-23: Axial strain post saturation versus initial setup dry density from CRS and DSS tests	251
Figure 5-24: Compression behavior in $\epsilon_a$ - $\log\sigma'_v$ space from DSS tests	252
Figure 5-25: Compression behavior in $e$ - $\log\sigma'_v$ space from DSS tests (CRS range included)	253
Figure 5-26: Compression behavior in $\epsilon_v$ - $\log\sigma'_v$ space from CIUC tests	254
Figure 5-27: Compression behavior in $e$ - $\log\sigma'_v$ space from CIUC tests	255
Figure 5-28: Compression behavior in $e$ - $\log\sigma'_v$ space from CIUC tests compared with the CRS test range	256
Figure 5-29: Post saturation void ratio versus initial setup dry density for CRS, DSS, and CIUC triaxial tests	257
Figure 5-30: Compression behavior in $\epsilon_a$ - $\log\sigma'_v$ space from $CK_0$ UC tests	258
Figure 5-31: Compression behavior in $e$ - $\log\sigma'_v$ space from $CK_0$ UC tests	259
Figure 5-32: Post saturation void ratio versus initial setup dry density for CRS, DSS, CIUC, $CK_0$ UC tests	260
Figure 5-33: Compression and swelling ratios versus stress level from all consolidation tests	261
Figure 5-34: Lateral stress ratio versus stress level from $CK_0$ UC tests	262
Figure 5-35: Effective Stress path during consolidation from $CK_0$ UC tests	262
Figure 5-36: Compression behavior in $e$ - $\log\sigma'_v$ space from $CK_0$ UC tests compared with the CRS range and a CIUC test	263
Figure 5-37: Hydraulic conductivity versus void ratio and hydraulic conductivity versus vertical effective stress for Skibbereen Silt	264
Figure 6-1: Stress-Strain curves from NC $CK_0$ DSS tests	299

Figure 6-2: Normalized stress-strain curves from NC $CK_0$ DSS tests	299
Figure 6-3: Normalized undrained shear strength versus stress level from NC $CK_0$ DSS tests	300
Figure 6-4: Strain at failure versus stress level from NC $CK_0$ DSS tests	300
Figure 6-5: Effective stress paths from NC $CK_0$ DSS tests	301
Figure 6-6: Normalized effective stress paths from NC $CK_0$ DSS tests	301
Figure 6-7: Normalized effective stress paths (close up view) from NC $CK_0$ DSS tests	302
Figure 6-8: Friction angle at peak and end of shear strain versus stress level from NC $CK_0$ DSS tests	302
Figure 6-9: Normalized undrained secant modulus versus shear strain from NC $CK_0$ DSS tests	303
Figure 6-10: Normalized undrained secant modulus versus stress level from NC $CK_0$ DSS tests	303
Figure 6-11: Normalized stress-strain curves from NC $CK_0$ DSS tests of different initial density	304
Figure 6-12: Normalized effective stress paths from NC $CK_0$ DSS tests of different initial density	304
Figure 6-13: Normalized undrained shear strength versus stress level from NC $CK_0$ DSS tests with different initial setup densities	305
Figure 6-14: Strain at failure versus stress level from NC $CK_0$ DSS tests with different initial setup densities	305
Figure 6-15: Normalized effective stress paths (close up view) from NC $CK_0$ DSS tests of different initial density	306
Figure 6-16: Effective stress paths for NC $CK_0$ DSS tests of different initial density	306
Figure 6-17: Normalized undrained secant modulus versus shear strain from NC $CK_0$ DSS tests of different initial density	307
Figure 6-18: Normalized stress-strain curves from OCR=1, 2, 3, and 4 $CK_0$ DSS tests (normalized to the vertical consolidation stress, $\sigma'_{vc}$ )	308
Figure 6-19: Normalized stress-strain curves from OCR=1, 2, 3, and 4 $CK_0$ DSS tests (normalized to the maximum vertical consolidation stress, $\sigma'_{vm}$ )	308

Figure 6-20: Normalized Undrained Shear strength variations with OCR from CK <sub>0</sub> DSS tests	309
Figure 6-21: Normalized effective stress paths from OCR = 1, 2, 3, and 4 CK <sub>0</sub> DSS tests (normalized to the maximum vertical consolidation stress, $\sigma'_{vm}$ )	310
Figure 6-22: Normalized effective stress paths from OCR = 1, 2, 3, and 4 CK <sub>0</sub> DSS tests (normalized to the vertical consolidation stress, $\sigma'_{vc}$ )	310
Figure 6-23: Friction angle versus vertical consolidation effective stress from OCR = 1, 2, 3, and 4 CK <sub>0</sub> DSS tests	311
Figure 6-24: Normalized undrained secant modulus ( $E_u/\sigma'_{vc}$ ) versus shear strain from OCR = 1, 2, 3, and 4 CK <sub>0</sub> DSS tests	312
Figure 6-25: Normalized undrained strength versus OCR from CK <sub>0</sub> DSS tests	312
Figure 6-26: Shear stress versus strain from a typical cyclic CK <sub>0</sub> DSS test	313
Figure 6-27: Effective stress path from a typical cyclic CK <sub>0</sub> DSS test	313
Figure 6-28: Stress-Strain curves from Cyclic CK <sub>0</sub> DSS tests (standard NC CK <sub>0</sub> DSS included for comparison)	314
Figure 6-29: Normalized Stress-Strain curves from Cyclic CK <sub>0</sub> DSS tests (standard NC CK <sub>0</sub> DSS included for comparison)	314
Figure 6-30: Effective stress paths from cyclic CK <sub>0</sub> DSS tests	315
Figure 6-31: Normalized effective stress paths from cyclic CK <sub>0</sub> DSS tests	315
Figure 6-32: Compression behavior in $e$ - $\log\sigma'_v$ space from cyclic CK <sub>0</sub> DSS tests	316
Figure 6-33: Normalized shear strength versus total density from NC and cyclic CK <sub>0</sub> DSS tests	317
Figure 6-34: Shear strain at failure versus total density from all NC and cyclic CK <sub>0</sub> DSS tests	317
Figure 6-35: Undrained strength ratio versus vertical consolidation stress for NC and cyclic CK <sub>0</sub> DSS tests	318
Figure 6-36: Stress-strain curves from CIUC triaxial tests	319
Figure 6-37: Normalized stress-strain curves from CIUC triaxial tests	320
Figure 6-38: Normalized stress-strain curves (small strains) from CIUC triaxial tests	321
Figure 6-39: Normalized stress- (log) strain curves from CIUC triaxial tests	321

Figure 6-40: Effective stress paths from CIUC triaxial tests showing the failure criteria used this research	322
Figure 6-41: Effective stress paths from CIUC triaxial tests	323
Figure 6-42: Normalized effective stress paths from CIUC triaxial tests	324
Figure 6-43: Principle stress ratio versus axial strain from CIUC triaxial tests	325
Figure 6-44: Friction angle versus axial strain from CIUC triaxial tests	325
Figure 6-45: Normalized excess pore pressure versus strain from CIUC triaxial tests	326
Figure 6-46: Normalized shear induced pore pressure versus strain from CIUC triaxial tests	326
Figure 6-47: Skempton A parameter versus strain from CIUC triaxial tests	327
Figure 6-48: Normalized undrained secant modulus versus axial strain from CIUC triaxial tests	328
Figure 6-49: Normalized undrained secant modulus versus stress level from CIUC triaxial tests	328
Figure 6-50: Normalized undrained shear strength versus stress level from CIUC triaxial tests	329
Figure 6-51: Friction angle versus stress level from CIUC triaxial tests	329
Figure 6-52: Strain at failure versus stress level from CIUC triaxial tests	330
Figure 6-53: Stress-strain curves from $CK_0UC$ triaxial tests	331
Figure 6-54: Normalized stress-strain curves from $CK_0UC$ triaxial tests	331
Figure 6-55: Normalized stress-strain curves (small strain) from $CK_0UC$ triaxial tests	332
Figure 6-56: Normalized stress (log) - strain curve from $CK_0UC$ triaxial tests	332
Figure 6-57: Effective stress paths from $CK_0UC$ triaxial tests	333
Figure 6-58: Normalized effective stress paths from $CK_0UC$ triaxial tests	333
Figure 6-59: Principle stress ratio versus axial strain from $CK_0UC$ triaxial tests	334
Figure 6-60: Friction angle versus axial strain from $CK_0UC$ triaxial tests	334

Figure 6-61: Normalized excess pore pressures versus strain from $CK_0UC$ triaxial tests	335
Figure 6-62: Normalized shear induced pore pressures versus strain from $CK_0UC$ triaxial tests	335
Figure 6-63: Normalized undrained secant modulus versus axial strain from $CK_0UC$ triaxial tests	336
Figure 6-64: Normalized undrained secant modulus versus stress level from $CK_0UC$ triaxial tests	336
Figure 6-65: Normalized undrained strength versus stress level from $CK_0UC$ triaxial tests	337
Figure 6-66: Friction angle versus stress level from $CK_0UC$ triaxial tests	337
Figure 6-67: Axial strain at failure versus stress level from $CK_0UC$ triaxial test	338
Figure 6-68: Stress-strain curves from CIUC and $CK_0UC$ triaxial tests	339
Figure 6-69: Normalized stress-strain curves from CIUC and $CK_0UC$ triaxial tests	340
Figure 6-70: Normalized stress-strain curves from CIUC and $CK_0UC$ triaxial tests (Normalized by mean consolidation effective stress)	341
Figure 6-71: Effective stress paths from CIUC and $CK_0UC$ triaxial tests	342
Figure 6-72: Normalized effective stress paths from CIUC and $CK_0UC$ triaxial tests	343
Figure 6-73: Normalized undrained strength versus stress level from DSS, CIUC, and $CK_0UC$ tests	344
Figure 6-74: Peak friction angle versus stress level from DSS, CIUC, and $CK_0UC$ tests	344
Figure 6-75: Friction angle versus consolidation stress level for DSS, CIUC, and $CK_0UC$ tests	345
Figure 6-76: Friction angle versus mean effective stress for DSS, CIUC, and $CK_0UC$ tests	345
Figure 6-77: Axial strain at failure versus stress level for DSS, CIUC, and $CK_0UC$ tests	346
Figure 6-78: Normalized undrained secant modulus versus stress level from DSS, CIUC, and $CK_0UC$ tests	346

## List of Symbols

AC	Alternating Current
A/D	Analog-to-Digital Converter
BASIC	Beginner's All-purpose Symbolic Instruction Code
BBC	Boston Blue Clay
CF	Clay Fraction
CHL	Chlorite
CID	Isotropically Consolidated Drained Shear Test
CIU	Isotropically Consolidated Undrained Shear Test
CIUC	Isotropically Consolidated Undrained Shear Compression Test
CK <sub>0</sub> U	K <sub>0</sub> -Consolidated Undrained Shear Test
CK <sub>0</sub> UC	K <sub>0</sub> -Consolidated Undrained Compression Test
CK <sub>0</sub> UDSS	K <sub>0</sub> -Consolidated Undrained Direct Simple Shear Test
CK <sub>0</sub> UE	K <sub>0</sub> -Consolidated Undrained Extension Test
CL	Low Plasticity Clay
CR	Virgin Compression Ratio
CRS	Constant Rate of Strain
CU	Consolidated Undrained Test
D/A	Digital-to-Analog Converter
DC	Direct Current
DCDT	Direct Current Displacement Transducer
DSS	Direct Simple Shear Test
ESE	Effective Stress Envelope
ESP	Effective Stress Path
F	Feldspar
HC	Hydraulic Conductivity
LVDT	Linear Variable Differential Transformer
MADC	Multi-Channel Analog to Digital Converter
MIT	Massachusetts Institute of Technology
ML	Low Plasticity Silt
NC	Normally Consolidated
OC	Overconsolidated
OCR	Overconsolidation Ratio
PC	Personal Computer
PID	Proportional-Integral-Derivative
PSD	Particle size distribution curve
PVA	Pressure Volume Actuator
PVC	Pressure-Volume Controller

Q	Quartz
RBBC	Resedimented Boston Blue Clay
RR	Recompression Ratio
SD	Standard deviation
SR	Swelling Ratio
TC	Triaxial Compression Shear Test
TE	Triaxial Extension Shear Test
TX	Triaxial
USR	Undrained Strength Ratio ( $s_u/\sigma'_{vc}$ )
UU	Unconsolidated Undrained Compression Test
SHANSEP	Stress History and Normalized Soil Engineering Properties
VCL	Virgin Compression Line
A ( $A_f$ )	Skempton's pore pressure parameter (at failure)
b	Skempton's pore pressure parameter
$C_c$	Coefficient of curvature, Compression index
$C_k$	Permeability change index
$C_s$	Swelling index
$C_u$	Coefficient of uniformity
$c_v$	Coefficient of consolidation
$c'$	Cohesion intercept
$D_{10}$	Grain size with 10% passing particle size distribution curve
$D_{30}$	Grain size with 30% passing particle size distribution curve
$D_{60}$	Grain size with 60% passing particle size distribution curve
E	Young's modulus
$E_u$	Undrained secant Young's modulus
$E_{uMAX}$	Undrained secant Young's modulus (maximum)
e	Void ratio
$e_c$	Void ratio at end of consolidation
$e_i$	Initial setup void ratio
$G_s, SG$	Specific gravity
G	Shear Modulus
$G_i$	Initial shear modulus
H	Height
$I_p$	Plasticity index
K	Lateral coefficient of earth pressure
$K_0$	Coefficient of lateral earth pressure at rest
$K_{0(NC)}$	Normally consolidated coefficient of lateral earth pressure at rest
$K_c$	Lateral coefficient of earth pressure at end of consolidation



k	Hydraulic conductivity
$k_v$	Vertical hydraulic conductivity
L	Length
m	OCR exponent in SHANSEP equation for undrained strength ratio
$m_v$	Coefficient of volume change
p, p'	Average effective stress, $(\sigma_1 + \sigma_3) / 2$ , $(\sigma'_1 + \sigma'_3) / 2$
q	Shear stress, $(\sigma_1 - \sigma_3) / 2$
$q_f$	Shear stress at failure
$r^2$	Coefficient of determination
S	Undrained strength ratio for NC soil in SHANSEP equation
$S_i$	Initial setup saturation
$s_u$	Undrained shear strength
t	Time
$t_p$	Time to end of primary
u, $\Delta u$	Pore pressure, change in pore pressure
$u_e$	Excess pore pressure
$u_s$	Shear induced pore pressure
$u_i$	Pore (back) pressure at start of shearing
V, $\Delta V$	Current volume, change in volume
$V_i$	Initial volume
w, $w_c$	Water content
$w_i$	Initial setup water content
$w_L$ , LL	Liquid limit
$w_n$	Natural water content
$w_p$ , PL	Plastic limit
$\varepsilon$	Strain
$\varepsilon_a$	Axial strain
$\varepsilon_f$	Strain at peak shear stress
$\varepsilon_v$	Specimen volume strain
$\varepsilon^\circ$ , $\delta\varepsilon/\delta t$	Strain rate
$\phi$ , $\phi'$	Friction angle, effective friction angle
$\phi'_p$	Effective friction angle at peak
$\gamma$	Shear strain
$\gamma^\circ$ , $\delta\gamma/\delta t$	Shear strain rate
$\gamma_d$	Dry Unit Weight
$\gamma_t$	Total Unit weight
$\gamma_w$	Unit weight of water
v	Poisson's ratio

$\rho$	Density
$\sigma_v, \sigma'_v$	Vertical stress, vertical effective stress
$\sigma_h, \sigma'_h$	Horizontal stress, horizontal effective stress
$\sigma_p$	Preconsolidation pressure
$\sigma'_v$	Vertical effective stress
$\sigma'_{vc}$	Vertical consolidation effective stress
$\sigma'_{vm}$	Maximum vertical consolidation effective stress
$\sigma_1, \sigma_2, \sigma_3$	Principal stresses
$\sigma_{oct}$	Mean octahedral stress
$\tau$	Shear stress
$\tau_h$	Horizontal shear stress
$\psi$	Arctan $\tau_h/\sigma'_v$ for direct simple shear
$\psi'$	Effective arctan $\tau_h/\sigma'_v$ for direct simple shear
$\psi'_p$	Peak effective arctan $\tau_h/\sigma'_v$ for direct simple shear

# 1 INTRODUCTION

## 1.1 BACKGROUND

In contrast to the extensive geotechnical research that exists on clay and sand soils, little information exists on the engineering properties of low plasticity silts. There are many reasons for this trend. The material is not very common and it is generally avoided in construction due to the poor site conditions. Disturbance during sampling and the subsequent preparation and testing in the laboratory also pose significant difficulties and problems. As a consequence, industry relies more on field testing from methods such as the standard penetration test, field vane test, and cone penetration test. However, many of the empirical methods that transform field results into engineering parameters were originally developed from laboratory data. Therefore, the need for accurate laboratory information still exists.

The difficulty in obtaining intact samples has resulted in laboratory research concentrating more on reconstituted specimens to obtain the engineering parameters. Several reconstitution techniques have been used on silts, some to a greater degree of success than others. They have generally been modified from techniques used in reconstituting clays and sands. However, the exact details of a successful reconstitution procedure have still to be defined.

The material source for this study comes from Skibbereen, Co. Cork, Ireland. The town is located in Southwest Ireland approximately 85km south west of Cork City and 32 km from the town of Clonakilty. It is situated on the N71, the primary Cork to Killarney road. The southwest area is deeply penetrated by the sea in a series of long coastal inlets whose depth and width gradually diminish inland. Skibbereen is located in a valley close to the sea on the banks of the River Illen. The river is tidally influenced causing a fluctuation in ground water levels in the town on a daily basis.

The town is home to an interesting and intricate geology. Various rock types outcrop the Southwest Irish area while the town itself is built on a limestone bed overlain by alluvial deposits from glacier melt-water and river deposits. The properties of the overlying deposits are the focus of this thesis.

The material was obtained during a major upgrade of the wastewater infrastructure in Skibbereen. The project was needed to stop the discharge of raw sewerage into water courses and to increase the capacity of the system for the increasing population. The project involved the construction of many deep pumping stations and new sewerage pipelines. To minimize the risks of ground settlement and structural damage to existing developments, many innovative and technically challenging construction techniques were utilized. Caisson construction and the most recent trenchless technologies were used continuously throughout the project.

Despite the efforts to prevent damage to existing structures in the town, some serious problems did occur. Structural damage together with other construction difficulties soon made it apparent that a greater understanding of the soil properties and behavior was required. The realization of the difficulty to obtain this information ultimately resulted in the transportation of both intact and disturbed samples to the MIT geotechnical laboratory.

## **1.2 RATIONALE FOR CHARACTERIZATION OF LOW PLASTICITY SILT FROM SKIBBEREEN**

The rationale behind the need to characterize the low plasticity silt found in Skibbereen is extremely simple. The original site investigation and laboratory testing program undertaken at Skibbereen was extremely limited and can be described as “poor” quality. The original site investigation produced standard penetration test values less than 10, some cone penetrometer data, and some index testing information. However, there was a large deviation in the results obtained from this program. Furthermore, no laboratory tests were conducted to provide the engineering properties of the material, i.e. such as oedometer tests for the consolidation properties or simple triaxial tests to provide stress-strain-strength information. Therefore, it can be stated that up until the arrival of the material at the MIT geotechnical laboratory relatively nothing was known about its properties and behavior.

Reliable testing information was needed to understand the behavior seen in the field and to help explain some of the problems encountered during the construction. The silt deposits found in Skibbereen are not localized to that area only. Throughout the south and west coast of

Ireland, low plasticity silts are reported in many locations. However, the properties and testing techniques are relatively unknown. For future construction projects it is imperative that an understanding of the behavior and properties are known before construction work commences to limit the possibility of construction problems and structural damage like that encountered in Skibbereen.

Besides the need to characterize the material at the Skibbereen site and Irish locations, at present there is a shortage of information for low plasticity silts. It is known that the behavior of silts are somewhere between the behavior of clay and sand. However, silt properties cannot be interpolated from clay and sand results. Of those who have studied the properties of low plasticity silts, there are many contrasting views, opinions, and results. Various sampling, testing, and reconstitution procedures have been documented with no one preferred method emerging. The results and behavior found among researchers also show a large deviation.

It can be concluded that low plasticity silts are difficult to test and characterize. There is a shortage of information about the material and the properties can change significantly with location. Therefore, the need for further research exists.

### **1.3 RESEARCH OBJECTIVES AND SCOPE**

The objectives and corresponding scope of the research can be divided into the following components.

- 1) Conduct a detailed literature review of low plasticity silt properties and behavior.
- 2) Process the bulk material transported to the MIT geotechnical laboratory to ensure that the engineering tests will be run on material that is homogeneous and of high quality.
- 3) Characterize the material by the use of index property tests. Methods utilized will include grain size distribution analysis, specific gravity tests, Atterberg limits, organic content evaluation, salt concentration testing, scanning electron microscope images, and X-ray diffraction.
- 4) Develop a successful reconstitution procedure for the material.

- 5) Determine the feasibility of testing tube samples without disturbance.
- 6) Develop successful testing preparation procedures for tests such as constant rate of strain tests, hydraulic conductivity tests, direct simple shear tests, and isotropically and  $K_0$  consolidated triaxial tests.
- 7) Characterize the engineering properties of Skibbereen silt. This objective will be accomplished through a combination of sophisticated laboratory tests run on the processed material. The program can be broken into the following components:-
  - a) The use of constant rate of strain (CRS) tests on material with different initial densities to stresses up to 15 MPa.
  - b) The use of hydraulic conductivity testing using a modified CRS device with automated control.
  - c) The use of the automated direct simple shear (DSS) device to provide consolidation and stress-strain-strength information on normally consolidated and overconsolidated specimens. The overconsolidated specimens will make use of the SHANSEP theory. The DSS device will finally be used for cyclic shear testing.
  - d) The use of isotropically consolidated undrained triaxial compression tests to develop stress-strain-strength properties over a range of consolidation stresses for normally consolidated specimens
  - e) The use of automated triaxial equipment to conduct  $K_0$ -consolidated undrained compression tests. The tests will provide good one-dimensional compression curves, measurements of the coefficient of earth pressure at rest ( $K_0$ ), plus the stress-strain-strength properties over a range of consolidation stresses.
- 8) Develop a recommended set of properties for the low plasticity silt in Skibbereen. This portion of the research will make a detailed analysis of the results from the laboratory consolidation and strength testing. The collective evaluation will lead to a set of

engineering properties that can be used with confidence for the geotechnical design of future construction in this soil type. The research will include:

- a) Typical consolidation properties at various stress levels, along with representative hydraulic conductivity properties.
- b) A set of normalized soil properties correlated to stress level dependence, such as undrained shear strength and undrained modulus. Other critical parameters such as the friction angle and strains at failure will also be included.

## **1.4 ORGANIZATION OF THE THESIS**

This thesis is organized into seven chapters, with the aim of presenting the reader with a logical picture of the problem investigated.

Chapter 2 provides the background information related to this research project. The town of Skibbereen is first discussed with its location and features presented in detail. The geologic history of the soil underlying the town is then reviewed. The area has a very interesting and intricate geology. A summary of the south Ireland geology is first discussed and then a correlation is made for Skibbereen. The rest of the chapter focuses on information specific to the construction of the new waste water infrastructure in the town. First, an overview of the project is presented, followed by some of the construction techniques used during the project. Some of the major construction difficulties are then discussed. The chapter ends with details of the original site investigation and the secondary investigation where the material for this thesis was sourced.

Chapter 3 presents a literature review of low plasticity silt properties and behavior. The chapter summarizes existing reconstitution procedures to prepare test specimens, test preparation methods for various test types, sampling, and sampling disturbance. Typical index and engineering properties are provided. In particular, the current knowledge on the consolidation and undrained shear strength is reviewed in great detail. The various testing conditions and failure criteria for shear strength testing are finally presented. The main aim of this chapter is to provide a good database to analyze the results found in this research.

Chapter 4 provides a complete description of the experimental procedures and equipment used to perform the tests presented in this thesis. The chapter includes the successful and unsuccessful reconstitution procedures, the test preparation methods undertaken for all devices, and the modifications to existing testing procedures. The control system hardware, software, measurement instrumentation, and data acquisition system are all described.

Chapter 5 presents the consolidation results from constant rate of strain (CRS) tests, direct simple shear (DSS) tests, and isotropically and  $K_0$  consolidated triaxial tests. The initial conditions were varied for the CRS tests and specimens were consolidated to stresses up to 15 MPa. The DSS and triaxial tests were consolidated prior to shear. The chapter also includes hydraulic conductivity results from three tests in a modified CRS device.

The DSS and triaxial shear results are presented and analyzed in Chapter 6. The chapter first reviews the DSS results. Both normally and overconsolidated behavior is analyzed, the SHANSEP framework for the material is presented, followed by cyclic DSS test results. The second part of the chapter focuses on the isotropically consolidated behavior before a similar analysis is presented for the  $K_0$  consolidated results. The final section of the chapter summarizes all DSS and triaxial test findings.

Chapter 7 summarizes the most important results from the research, presents the best estimates of properties and other correlations for low plasticity silt from Skibbreen, and recommends guidelines for future research.



## **2 BACKGROUND**

### **2.1 INTRODUCTION**

This chapter provides the background information about Skibbereen and the reasons behind the testing program at the MIT Geotechnical laboratory. The town of Skibbereen is located in Southwest Ireland and serves as an administrative, employment, commercial, health, recreational, and educational centre for a large hinterland area. The town is also a very popular destination for many tourists and tourism is now one of its main industries. Skibbereen has many key geological features such as the River Ilen, Caol stream, and the Marsh area. All relevant features of the town are presented including the sewerage system before the new upgrade.

Section 2.3 discusses in detail the geology of Skibbereen. The town is located on low lying ground in a valley floored by sandstones and mudstones of the Carboniferous age. The overlying sediments are as a result of glaciation and they have accumulated to great depths. The geology of Skibbereen has been interpreted from information found on the West Cork area and general Irish geology. The rock developments are first discussed in detail followed by the overlying sediment formations. Finally, the existing geologic conditions are presented.

Section 2.4 describes the new sewerage scheme construction. It presents a brief overview of the overall contract and the various construction techniques. The project relied heavily on caisson and trenchless technology construction to overcome the poor ground conditions. However, numerous construction difficulties occurred despite these measures.

The final section of the chapter covers the site investigation for the project. The original site investigation is first described. An extensive field testing program was undertaken. Standard penetration tests, in situ falling head tests, and groundwater observations provide important information about the ground conditions. However, the original testing program was not backed with a good laboratory investigation. During construction of the project a second site investigation was undertaken to provide additional information. Field vane tests and cone penetration tests were conducted to give strength properties for the soil. Both intact and disturbed samples were taken for laboratory testing. Results from index tests on the disturbed material are also presented.

## **2.2 SKIBBEREEN**

### **2.2.1 Introduction**

Skibbereen is located in Southwest Ireland. The southwest area is deeply penetrated by the sea in a series of long coastal inlets whose depth and width gradually diminish inland. The southwest encompasses Kerry and West Cork and is generally divided up into four regions; the lowlands of Kerry, the uplands of north and central Kerry, the six peninsulas, and the lowlands forming the extreme southwest of Cork.

Skibbereen falls into the extreme southwest category. The town is approximately 85km south west of Cork City and 32 km from the town of Clonakilty. It is situated on the N71, the primary Cork to Killarney road. Figure 2-1 and 2-2 show Skibbereen on the south west Ireland map.

Skibbereen has an interesting history from its establishment in the early 1600's. The town is located on the banks of the River Ilen. The river was the primary transport route for people, goods, and services. During the Irish Potato Famine (1845-1849), an estimated 8,000 – 10,000 victims died in Skibbereen from starvation. Emigration continued in Skibbereen extensively after the famine and the population was halved due to the decline in the fishing industry. Today, Skibbereen Urban District has a population of 2,338, which accounts for a 16.9% population increase from 2002 (Skibbereen town development plan, 2009-2015). It serves as an administrative, employment, commercial, health, recreational, and educational centre for a large hinterland area. The town has a limited manufacturing base consisting of light engineering, food, and dairy products. Apart from functioning as an important employment and service centre, the town has increased its tourism potential and it is now a popular destination for many visitors. A building use survey of the town center can be seen in Figure 2-3. The figure shows a plan of the town center and commercial buildings in use.

Skibbereen is located in a valley. Skibbereen Heights lies to the west of the town and The Rock to the east. The town has expanded in a north south direction as a result. Skibbereen Heights comprises an area of very elevated land dominated by sheer rock. The Rock consists of an elevated area to the east of the town but unlike the Heights, it is easily accessible via

pathways and laneways. Figure 2-4 shows a picture taken from an elevated area at the south west of the town.

Besides the residential, industrial, and commercial development in the town, there are three other significant features located in the heart of the town. The River Ilen, Caol Stream, and Marsh field provide both character and service to the town.

#### 2.2.1.1 River Ilen

The river originates approximately 30 km from the town in the hills north of Drimoleague. The river is a depositing lowland river and it flows into Roaringwater Bay approximately 3 km downstream of Skibbereen. It cuts transversely across the country gathering longitudinal tributaries before turning sharply west at Skibbereen. At the turning point, it is approximately 40m in width and it carves a large meander through the town forming the floodplain know as the Marsh along the northern and western bank. The Ilen is highlighted at the heart of Skibbereen in Figure 2-5.

The river is subject to tidal influences due to its close proximity to the bay. A tidal pulse extends upstream to Skibbereen. The water remains fresh during high tide; however, water levels rise by approximately 1m and the shallow fast waters during low tide in some locations are replaced by water that backs up and slackens. During very high tides and heavy rain the tidal pulse has flooded the town on many occasions. Figure 2-6 shows the Marsh area before and during these extreme conditions.

Up until the recent sewerage scheme works, the river Ilen had a number of waste water and surface water discharge points along its route. The waste water discharged was untreated sewage and the river was moderately to slightly polluted as a consequence.

### 2.2.1.2 Caol Stream

The Caol stream is a major water course artery. Originating in Lough (Lake) Abisdealy it runs in a south to north direction through the center of the town until it joins the Ilen at the Marsh field. The stream is confined through the town by private properties. Upstream the banks are generally constructed of soft mud reinforced with stones/boulders while through the town vertical stone walls and concrete retaining walls provide support for the structures built in close proximity to the stream.

The stream passes under transport and pedestrian crossings at many locations in the town. However, a twin arch stone masonry bridge located on Bridge Street is of great historic significance. The location of the Caol Stream in the town can be seen in Figure 2-7.

Before the construction of the sewerage system, the Caol Stream was used extensively for collection and transportation of raw untreated sewerage from residential, retail, and commercial developments. The water quality before the stream reached the town was moderate to fair. However, at the town the water quality deteriorated rapidly. The stream is approximately 9m in width in the heart of the town and the flow through the stream is slow and low during times of dry weather. The large number of discharge outlets resulted in extremely poor water quality. Extensive mats of sewage fungus and soft sediments accumulated downstream. The stream was scarce of life and a foul smell emanated in many locations. Figure 2-8 shows some of the pollution along the Caol Stream.

### 2.2.1.3 Marsh Field

The Marsh field is a floodplain located to the north of the town. The area is not designated for conservation but due to its low lying nature and susceptibility to flooding, the area has seen no development. Dumped spoil has overgrown into grassland vegetation. The land has been neglected and is used for pasture during summer months. The area enclosed by the new N71 bypass and the River Ilen can be seen in Figure 2-9.

Recent development in the Marsh field includes the construction of a foot bridge from the town over the River Ilen. The footbridge will provide access for a proposed car park in the field.

Section 2.4 will discuss in detail the project information regarding the new waste water sewerage system. However, the main collection pump station and ancillary pipes, shafts, and manholes were constructed in the marsh field.

## **2.3 GEOLOGY**

### **2.3.1 Introduction**

The topography of West Cork has a pronounced grain with ridges and valleys that elongate east-north-east to west-south-west. The valley base rock consists of sandstones and mudstones of Carboniferous age while the ridges are made up of older Devonian sandstones and mudstones. The valleys have been drowned due to sea-level rise following the melting of the glaciers which covered most of the area during the ice age. No detailed description of the geology of Skibbereen has ever been published. Pracht and Sleeman (2002) published a report on the geology of west cork and other authors such as Holland and Sanders (2009), Charlesworth (1953), and Woodlock and Strachan (2000) have produced geological information for the island of Ireland. The following information presented is an interpretation of the above work.

### **2.3.2 Topography**

Figure 2-10 shows the topography of West Cork. Skibbereen lies between sea level and 60m (≈200ft) in elevation. From the experience of the authors work, the town elevations are approximately 2-3 m above sea level in the low lying areas. Due to the low altitude many areas are susceptible to flooding during periods of high spring tides and heavy rain (as shown in Figure 2-6):

### **2.3.3 Rock Types**

All the rocks exposed around Skibbereen are sedimentary and were deposited during the Devonian and Carboniferous periods, between about 370 and 310 million years ago (Ma). In

order to understand the rock formation the following sections will describe the development of each rock type. The geochronometric scale and the map of Ireland are presented in Figure 2-11. The figure translates geological terms into times, which is useful when discussing the geology of a location.

#### 2.3.3.1 Precambrian Rocks

Precambrian rocks are the oldest in Ireland and lie below all other rocks. The rock makes up about ten percent of the surface area of Ireland, as shown in Figure 2-12. Almost all of the Precambrian rocks belong to the Dalradian Super group, a thick succession of rocks which accumulated between 1000 and 542 Ma. The Dalradian sediments were spread out on the floor of a shallow sea which deepened gradually from a shore that probably ran, in general, north of the present Ireland (Charlesworth 1953). The original Dalradian sediments were soft and incoherent but they suffered an intense regional metamorphism, owing to later movements. These movements have bent rocks into great folds. The metamorphism varied according to stress, temperature, and the chemical composition of the individual rock. The muds were metamorphosed into schists, the sandstones into quartzites and the clear water limestones into crystalline marble (Charlesworth, 1953). While the Dalradians were being deposited, magmas from subterranean reservoirs erupted as lavas. The metamorphism that changed the sediments into schists also altered the basalts and dolerites into dark greenstones. The Precambrian rocks of Ireland have all been affected by Caledonian events between 369 and 542 Ma. The Caledonian cycle refers to the sum of the tectonic activities surrounding the closing Iapetus Ocean that once divided Ireland in two, as shown in Figure 2-14.

#### 2.3.3.2 The Lower Palaeozoic Rocks

By superposition (the lower layer is older than the upper layer) the Devonian and Carboniferous rocks in the Skibbereen area are underlain by rocks of Lower Palaeozoic age. The Lower Palaeozoic period occurred between 542 and 416 Ma. A trough like sea, shallow to the northwest and off the present coast to the south east crossed Ireland obliquely (Charlesworth,

1953). Figure 2-13 shows the distribution of land and sea in Lower Palaeozoic times. The Cambrian rocks consist of a great series of alternating purple and green sandstones, highly cleaved and crushed slates, quartz and quartzites, together with conglomerates or breccias (Charlesworth 1953). Ordovician rocks display a complex interplay of volcanic activity, sedimentation, and tectonics that were associated with the margin of the Iapetus Ocean. The Ordovician and Silurian strata have sharp folds which strike with remarkable persistence from the north east. The dip varies considerably but is generally high and often vertical (Charlesworth 1953). The rocks are thoroughly compacted, so that they have been widely used in buildings of ancient monuments. The rocks mainly consist of dark shales. Banded slates have also been found and they are associated with light colored, purplish or greenish sandstones which, being tough and hard, have been extensively quarried (Holland 1981).

#### 2.3.3.3 Caledonian Movement

As mentioned previously, during the Precambrian a wide ocean, termed the Iapetus Ocean, separated two continents. The Laurentian continent included northwest Ireland while the Avalonian microcontinent included south east Ireland (Holland and Sanders 2009). During the Cambrian, this ocean started to close. A series of tectonic events, ranging in time from the Cambrian to Devonian were associated with the ocean's closure. Combined, this series of tectonic events have been termed the Caledonian Orogeny.

The Iapetus Ocean was characterized by shallow water sands, muds and coarse materials (Charlesworth 1953). The sediments, many thousands of feet thick, were deposited in a shallow depth of water. This indicates that the floor of the sea was sinking step by step with accumulating sediment (Holland 1981). The cause of this sagging is still not exactly understood and there are many contrasting views on this development. During the Ordovician, the two continents began to move towards each other and by the late Silurian a continent – continent collision occurred. Figure 2-14 best describes this collision.

The Caledonian movement resulted in the sediments being compressed and uplift in the ground which formed mountains. This movement was associated with intense metamorphism and igneous activity (Charlesworth 1953). The lateral pressure converted the sandstones in places into quartzites. It crumpled, crushed, shattered, bent, and faulted the rocks. The advancing

earth wave broke up the resistant Dalradians, remolded them, and worked them upwards. This produced great dislocations and thrust planes (Holland and Sanders 2009). These movements elevated the Lower Palaeozoic into a mountain system thousands of feet high. The compressive earth movements were associated in some way with the formation of granites.

#### 2.3.3.4 Devonian Rocks

The oldest rocks exposed in Skibbereen are Devonian age, 416 to 359 Ma. They make up the ridges and hills around the town. The turmoil of the Caledonian movement left behind a continental climate of high relief (Charlesworth, 1953). The continental sea beds of the Irish basin formed the Old Red Sandstone. The vertical movements which brought the Caledonian disturbance to a close initiated broad downfolds upon which the Old Red Sandstone accumulated. The floors continued to sink and the intervening ridges of the corresponding upfolds to rise (Holland and Sanders 2009). A sea which covered much of Europe at this time lay to the south of the country, as shown in Figure 2-15. The Old Red Sandstone was widely distributed by this sea but today its outcrops are chiefly two, a southern one which constitutes the highest ground in Co. Kerry and Co. Cork and a northern one which is entrenched between Dalradian rocks in Donegal (Charlesworth 1953). The locations of Old Red Sandstone in Ireland today can be seen in Figure 2-16.

The sediments that formed the Old Red Sandstone were deposited from rivers, whose flow was dominated by flash floods fed by episodic rainfall, which originated predominantly from the mountainous area lying to the north. In Cork, the sediments accumulated to one of the thickest Old Red Sandstone formations in the world with a depth of over 6 km. The Devonian rocks around Skibbereen are mostly red and green sandstones, siltstones, and mudstones which were deposited on a continental landmass in a low altitude desert or semiarid environment.

#### 2.3.3.5 Carboniferous Rocks

Rocks of the Carboniferous age occur at the surface or beneath the Quaternary deposits. They cover nearly half the land area of Ireland (Holland and Sanders 2009). They are still of



great economic importance and are quarried extensively for aggregates and industrial minerals, host major base metal deposits, contain coal, and influence water supply and agriculture.

During the Devonian times the Caledonian mountains were subjected to atmospheric attack. The hills and mountains were reduced to gentle uplands and the hollows filled with the deposition (Charlesworth 1953). The dawn of the Carboniferous era brought a slow incoming tide transforming the world greatly from the Devonian time. The world in the Carboniferous times can be seen in Figure 2-17.

As the sea deepened and the shore advanced, the irregularities of the sea bottom were filled in by a buildup of dead organisms. Early shingle conglomerates became buried beneath off shore deposits. Pale yellow sandstones, sandy flagstones and grey and black limestone shale were produced. These sandy and muddy deposits gave place in turn to clear and tranquil waters of moderate depth in which countless organisms lived and died. The buildup of organisms led to the development of limestones which locally gave way to shales in many locations.

The limestone produced by this era are generally bluish or grey compact limestone of almost pure calcium carbonate. It is well bedded, usually horizontal or only slightly inclined. The limestone is traversed by innumerable well defined joints and in places by veins of calcite.

Skibbereen lies in a valley floored by limestones, sandstones, and mudstones of the Carboniferous age. The distribution of rock types around Skibbereen can be seen in Figure 2-18.

## **2.3.4 Geological Events after the Carboniferous Period**

### **2.3.4.1 Variscan Deformation and Metamorphism**

The Variscan orogenic belt can be traced from Russia through Western Europe and across the Atlantic to the eastern seaboard of the United States (Holland and Sanders, 2009). It resulted from the collision of a large southern continent known as Gondwana with the combined northern landmasses of Laurentia and Baltica. It is difficult to state the timing of the Variscan deformation in Ireland with any great precision. However, latest evidence by Holland and

Sanders (2009) suggests most of the movement occurred between 299 and 200 Ma at the end of the Carboniferous era to the beginning of the Jurassic.

Near the end of the Carboniferous Period, the rocks of West Cork were uplifted, cleaved, folded, and faulted by the Variscan Orogeny. Tight folds in the south gave way to broad gentle folds and existing fault movement in the north (Chareswroth 1953). A large number of new faults were produced. Displacement of these faults is often difficult to determine due to the overlying material that is now present. The main fault trends recorded from field observations are near strike faults and east-west and south east – north west faults (Holland and Sanders, 2009). Figure 2-19 shows the synclines, anticlines, and faults produced as a result of Variscan deformation in the Skibbereen area. As a result of the movement, the sedimentary sandstones and mudstones have been weakly metamorphosed, producing finer grained rocks most noticeably slates. There is very little evidence of what happened in Skibbereen following the Variscan Orogeny until the Quaternary period. It is therefore concluded that this time period had little impact on the geology.

#### 2.3.4.2 The Quaternary Period

The Quaternary Period which occurred from about 2.65 Ma to 11,000 years ago is famous for the great ice age. During most of the geological history, Ireland was favored by the warm climates. The Tertiary era had a climate which gradually worsened. The seas became cooler and the winters sharper and longer (Holland and Sanders 2009). The exact cause of this occurrence is still unknown. However, this age of snow, ice, glaciers, and ice sheets had a profound effect on the soils, agriculture, and its animals and plants.

Frost acted upon the cliffs around the coasts. The higher mountains acted as gathering grounds for the accumulating snows. Small glaciers, fed by snow travelled down the mountains (Charlesworth 1953). Finally, they coalesced upon the plains.

The evidence for all these movements is extremely clear. The ice, enriched with sand, mud and boulders held firmly in its sole, rasped the solid rock over which it passed engraving ice scratches in the direction of flow (Holland and Sanders 2009). Material gathered by the glaciers

in this way were deposited as glacial drift. This drift is also known as till or boulder clay. It floors the valleys and plains of most areas in Ireland. It is typically stiff, tenacious and unstratified and contains boulders of all sizes, often without any arrangement.

In southwest Ireland there is evidence for two glaciations. The earlier, the Greater Cork-Kerry glaciation, left a featureless drift that covers much of the southwest. The later glaciation was not as extensive. Ice was centered to the south of the Macgillycuddy Reeks, extending radially to form an ice dome that covered the central and southern midlands. The ice of the main dome flowed southwestwards into the Atlantic, eastwards into Co.Cork, and northward, overtopping mountains up to 700 m above sea-level. Figure 2-20 shows the southern ice dome and the direction of ice flow. The rock that was picked up by the ice and partly ground down was later deposited either directly from the base or margin of the ice, or by melt water flowing from the ice. In the former case it became boulder till or boulder clay and in the latter case it was sorted and deposited separately as gravel, sand, silt, or clay. The composition of these sediments reflects the sandstones and limestones over which the ice flowed (Pracht & Sleeman, 2002).

#### 2.3.4.3 The Holocene

The Holocene extends from the present day back to approximately 11000 years ago. About 2500 years ago, a rise in sea level occurred from melting ice masses in polar latitudes, producing the Irish Sea as we know it today. The higher water levels drowned the long parallel inlets of Kerry and Cork.

The steep sloped hills and mountains were flattened by weathering action. Atmospheric disintegration decomposed the surface rocks into soils. The newly formed lakes and rivers that emerged after the ice age cut through moraines and boulder strewn gorges. The rivers transported the newly formed soil to the coastline where it was deposited in saline conditions. Overtime, the shorelines moved further out from the buildup of deposition. The depths of the deposition increased with time producing extremely deep deposits, greater than 100m in some locations.

In Skibbereen, the river deposition in marine conditions accounts for the research material in this thesis. The deposition has produced a fine grained material with an Old Red Sandstone, limestone, shale, and slate background. Extremely thick deposits exist, up to a depth

of 40m in many locations. Generally, the soil deposits overly the limestone base formed by the Carboniferous period and there is little evidence of any other geologic action in the area.

### **2.3.5 Geology in Skibbereen today**

The overlying sediments across the area vary dramatically in nature and thickness. It generally comprises of topsoil (weathered sandy silt with rootlets) to a maximum depth of 0.8m, gravelly fine to coarse sands to a maximum depth of 1.5m. fine to coarse gravels with cobbles to a maximum depth of 6.2m and soft silt to a maximum depth of 32.5m. The bedrock is predominantly moderately weak to moderately strong shale of Carboniferous age, occasionally inter-bedded with moderately weak to very strong siltstones.

#### **2.3.5.1 Skibbereen town**

The town is constructed on made ground, considered to be generally imported and reworked natural material used as backfill and landscaping from previous road construction projects. The depth of the made ground is variable, ranging from 0.1m to a maximum depth of 3.2m. The made ground generally comprises a crushed rock sub-base. The underlying material is natural silty sands to a maximum depth of 2m, followed by medium dense to dense sandy gravels to a maximum depth of 4m, followed by very soft to soft bluish grey silt to a maximum depth of 13m.

#### **2.3.5.2 Skibbereen Environs**

The area of Skibbereen is generally underlain by silty sandy topsoil to a maximum depth of 0.62m on top of gravelly fine to coarse sands to a maximum depth of 3.2m. Underlain by very loose to very dense silty sandy fine to coarse gravels with cobbles to a maximum depth of 6.2m, and very soft to soft silt to a maximum depth of 13m. Bedrock of moderately weak to moderately strong, thinly laminated, weathered grey shale with occasional interbeds of siltstone underlies these sediments.

### 2.3.5.3 Marsh Area

The geology of this area generally comprises of weathered topsoil to a maximum depth of 0.8m, underlain by fine to medium sands to a maximum depth of 1.7m, underlain by loose to dense sandy fine to coarse gravels to a maximum depth of 4.7m and very soft to soft light bluish grey silt to a maximum depth of 32.5m. Bedrock of moderately weak to occasionally strong, thinly laminated, weathered shale is encountered at depths between 31.6m and 35.7m.

## 2.4 PROJECT DESCRIPTION

### 2.4.1 Introduction

A major upgrade of the wastewater infrastructure was needed in Skibbereen to stop the discharge of raw sewerage into water courses and to increase the capacity of the system for the increasing population. RPS Consulting Engineers prepared the Preliminary report, Preliminary design, Contract documents, Foreshore License, Planning Permission and Wayleave Acquisitions for the client, Cork County Council. The new system included the construction of five pumping stations and approximately 18 km of pipework (150mm to 1200mm internal diameter (ID)) to meet the needs of up to 9,400 people. The construction of the project was awarded to Ward and Burke Construction Ltd for a value of €11,600,000. The contract was divided up into 14 km of 150mm to 1200mm diameter precast concrete storm, foul, and combined sewers, 2km of 100mm to 1000mm ductile iron rising mains, and construction of pumping stations and storm water holding tanks.

Poor ground conditions consisting of low plasticity silts with standard penetration test (SPT) values less than 10 and a high water table, approximately 1.5m below ground level, presented construction challenges to the scheme. Also, the existing structures in the town were seen as a major construction risk. They are founded on shallow foundations, bearing in the imported fill or sandy upper layer. The construction of the pipelines was below these foundations and therefore the possibility of damaging existing structures was great.

Innovative construction techniques for both pipelines and structures were required to permit efficient and effective construction progress, minimize the effects of vibration, stop

groundwater loss, prevent settlement, and reduce ground movement. To achieve these goals, a large amount of the scheme was redesigned by Ward and Burke Construction Ltd.

During construction many difficulties were associated with the soft silt ground conditions. The soil produced poor bearing conditions for pipes and structures causing significant settlement in many locations. There were also many other challenges during construction due to the poor ground conditions. The following sections describe some of the construction techniques used and the observations associated with different construction aspects.

#### **2.4.2 Caisson Construction**

Originally all structures were to be constructed using the traditional approach of excavation using temporary support. However, the difficulty associated with dewatering silts and the possibility of the formation becoming “quick” inevitably led to the use of another technique. Pumping stations, shafts, and manholes were re-designed using the caisson construction method. The sewerage scheme was simplified and many unnecessary deep manholes were removed from the original design.

All caissons were constructed underwater. The caissons are sunk by removing material underwater from inside the caisson. The caisson sinks from its own self weight or by the aid of hydraulically powered jacks. The concrete base or plug of the caisson is poured underwater with a tremie pipe. Once the concrete base has set, the caisson can be dewatered. In areas of particularly bad ground or where the weight of the caisson was large, steel H-Piles were driven to the bearing bedrock around the structures perimeter. The piles were tied to the structure with an overhanging cast in situ top ring. The largest structure constructed using the caisson method was the main pumpstation, 16 x 16m in plan area, 17m deep, and weighing 40,000 tonnes. Figure 2-21 shows the sinking of the main pumpstation. Two CAT 328 excavators fixed with hydraulic clam shells and an 80 tonne crawler crane fixed with clam shell were used to sink this caisson. The hydraulic jacks on each corner guide the caisson and ensure it sinks vertically. Figure 2-22 shows a schematic diagram of a 6m internal diameter caisson fixed with supporting H-Piles, top ring and cover slab.

### **2.4.3 Trenchless Technology**

Trenchless technologies were extensively used for pipeline construction instead of the open cut method. In some situations, trenchless technology was the only possible solution for items such as deep pipelines (> 6m deep) and river crossings. However, some of the pipelines in residential and commercial areas that were originally designated for open cut were changed to trenchless technologies. The risk of damage to nearby structures is greatly reduced using this method because there is minimal ground disturbance and there is no requirement for dewatering of the ground. Three different trenchless methods were used in Skibbereen; Horizontal Directional Drilling (HDD), auger boring and micro tunneling.

#### **2.4.3.1 Horizontal Directional Drilling**

The horizontal directional drilling equipment used in the project can be seen in Figure 2-23. The machine bores a small pilot drive through the ground with drilling rods. The drive is controlled for line and grade by a tracker at ground level and a receiver in the drilling head. Once the pilot drive reaches the reception shaft, a reamer is placed on the rods at the reception end and it is pulled back through the ground, enlarging the diameter of the tunnel. Reaming can be repeated many times until the desired tunnel diameter is reached. Finally, a polyethylene pipe is attached to the rods at the reception end and pulled through the ground, thereby, creating the permanent pipeline. Horizontal directional drilling up to 450mm internal diameter with lengths over 100m were successfully carried out in Skibbereen.

#### **2.4.3.2 Auger Boring**

Some of the auger boring equipment can be seen in Figure 2-24. A jacking frame is placed in a 2.4m internal diameter concrete launch shaft. First, a pilot pipeline with steel casings is driven out of the shaft. The drive is guided with a theodolite and continues until it reaches the reception shaft. The wedge shaped cutting head is pushed through the ground; however, if steering correction is needed during the pilot drive, the cutting head can be rotated to compensate for any deviation in direction. Once the pilot drive is complete, a cutting head is fitted in the

launch shaft to accommodate the size of the permanent pipeline. The cutting head advances forward by use of the jacking frame. There is rotation at the cutting head and the excavated material is transported through the permanent pipeline into the launch shaft through the use of augers. Clay pipes with augers fitted inside are continuously jacked out of the launch shaft until the clay pipes reach the reception shaft. Pipes with a diameter from 200 to 450 mm were successfully driven to maximum lengths of about 50m in Skibbereen using the auger boring system.

#### 2.4.3.3 Microtunneling

The microtunneling system is the most complicated of all trenchless systems used in Skibbereen but because of the larger pipe diameters required it was used the most extensively. Five 600mm ID tunnels with a total length of 366m, six 900mm ID tunnels with a total length of 500m, and two 1200 mm ID tunnels with a total length of 360m were successfully constructed using the microtunneling system. All jacking pipes used were reinforced concrete. Figure 2-25 shows the microtunneling operation. The system has three main components. The tunnel boring machine (TBM) excavates the ground and provides steering and pipe direction. All TBM's used in Skibbereen were the slurry shield type (AVN range) and were manufactured by Herrenknecht. The AVN 1200, 900, and 600 (1200, 900, and 600 refer to internal diameter of the tunnel in mm) TBM's reduce the risk of over excavation at the tunneling face because a pressure slightly greater than the in situ effective stress can be applied by use of a slurry fluid. The control unit provides hydraulic power for the tunnel boring machine (TBM) and jacking frame while also providing a remote steering location for the TBM driver. The slurry separation system is an integral part of the slurry shield TBM. The slurry fluid transports the excavated material from the TBM out the shaft. The separation system cleans this slurry so it can be continually recycled. In terms of location, the microtunnel drives in Skibbereen were the most hazardous. There were four river crossings with the AVN 900 TBM and one with the AVN 1200 TBM. The 1200mm ID tunnel crossed the River Ilen, went parallel under the middle of the Caol stream, under the existing stone arch bridge in the town before taking a 300m radius horizontal curve left to avoid existing structures before reaching the reception shaft. The 1200mm ID tunnel will be discussed in further detail later in this chapter.



#### **2.4.4 Field Operation**

There were many challenges during construction. The difficulties were associated with the soft silt ground conditions. The soil was sensitive and highly susceptible to liquefaction, producing poor ground bearing situations for pipes and structures. The silt was very difficult to dewater and “quick” conditions could easily occur. The material also appeared to densify through vibration or after liquefaction, creating ground settlement. The following sections describe some of the observations associated with different construction aspects.

##### **2.4.4.1 Caissons**

Few problems occurred during the sinking of the caissons. However, the ground disturbed around the perimeter of the shafts during sinking produced problems during the subsequent tunnel process. As the TBM’s exited the launch shaft they had a tendency to nose dive in the soft material and therefore go off the required alignment for the gravity sewers. To overcome this problem, vertical and horizontal grouting with a cement based grout was used. Vertical ground mixing with a cement based grout was also implemented. The effectiveness of these techniques to stabilize the ground is not specifically quantified. However, where grouting did occur, the TBM exit and entry into shafts was found to be less problematic.

The soft material around the caissons also caused bearing difficulties during the jacking of the tunnel pipes. The 3.2m ID concrete caissons used for the AVN 600 TBM were found to move on many occasions when jacking forces greater than 120 tonnes were applied. On one occasion concrete punching failure occurred in the shaft at the back of the jacking frame. The low passive resistance on the wall at that location was the main factor behind the failure.

##### **2.4.4.2 Earthworks**

Vibrations from excavation equipment were found to transmit large distances. Excavation of ground or even movement of “tracked” equipment produced vibrations through the ground which travelled into nearby structures. At least one commercial development was structurally

damaged by the movement of a tracked excavator 10 meters from the property. Residents reported vibrations in their homes with work taking place over 30m away. The ground behavior associated with the damage is unknown. However, the vibrations from the moving excavator most likely increased the pore pressure and caused the ground to liquefy slightly. Densification and settlement that followed the pore pressure dissipation could be attributed to the damage.

#### 2.4.4.3 Pipe lines and tunnels

Several problems were associated with the pipeline and tunnel construction. Pipes were found to settle in the ground in many locations after backfilling of the trench. The cause of the problem is unknown and there are only a few possible explanations. The formation level of the trenches appeared dry because sump pumps were in use. When backfilling took place the added weight caused settlement of the pipe. The cycle of drying and wetting the formation could have contributed to the settlement in some way. In most cases, “sheep’s foot” compactors were used on the backfill. However, the use of vibration based backfill compactors may have initiated excess pore pressures and liquefied the ground under the pipe causing settlement.

All trenchless technologies experienced high soil-pipe interface friction and jacking forces were high in all trenchless methods. The high jacking forces may be associated with the ground swelling around the pipes during jacking. Bentonite was pumped where possible to reduce interface friction. The jacking force was also found to be up to 30% greater after the resumption of tunneling from an overnight stoppage. The increase in jacking forces after an overnight stoppage might be from the excavation overcut closing around the pipe or the bentonite dissipating into the soil over time. Figure 2-26 shows the skin friction against tunnel distance for some of the drives in Skibbereen. All drives shown were with the AVN 900, except tunnel 10, which was constructed with the AVN 600. The 600mm ID jacking pipes have fewer bentonite outlets when compared with the 900mm ID pipes. The higher skin friction associated with this pipe can be seen in the Figure. Tunnel 10 has a constant skin friction approximately equal to  $10 \text{ kN/m}^2$ , which is high for microtunneling applications.

Steering and alignment of the TBM was occasionally a problem. The machine tended to drift out of control on several occasions despite full steering corrections. Steel shims were often

used between joints in the TBM to increase its turning potential and correct drift problems. The majority of drift problems were in the horizontal plane, i.e., the machine wanted to go left or right. However, severe vertical alignment problems occurred during a long 220m drive underneath the Caol stream.

The alignment of the 220m, 1200mm ID tunnel can be seen in Figure 2-27. The AVN 1200 TBM launched from a 6m ID caisson in the Marsh field, it then passed the abutment of the new pedestrian bridge and went underneath the River Ilen before going under the bed of the Caol stream. The tunnel then continued up the Caol stream and passed under the left arch of the town bridge. Once the tunnel past the bridge, it took a 300m horizontal curve left under the Caol stream retaining wall, it then followed this curve past many nearby structures. Before entering the reception shaft in the shopping center car park, the tunnel went under the Coal stream for a second time. The tunnel was a critical component of the scheme because it was the only route to convey the town center sewage to the new pumping station. It was always expected that this tunnel would be the most hazardous and challenging part of the project.

Tunneling continued without any major problem until the TBM entered the Coal Stream section. The machine then began to lose vertical alignment and sink in the soft ground. Figure 2-28 shows the vertical alignment of the tunnel at 66 m into the drive. The machine had sunk 400mm off the intended grade in a 15 m distance. When all TBM steering attempts failed ground treatment techniques were considered. Due to the location and alignment of the tunnel, ground treatment techniques vertically would have been almost impossible. As a solution to the problem, the horizontal directional drilling (HDD) machine was used to grout the ground under the tunnel alignment. The head of the HDD machine mixed the ground with cement grout pumped from its the control container. The layout of the ground treatment can be seen in Figure 2-29. Four HDD grouting cylinders were installed under the invert. The cement-soil mixture was allowed to set for three days before tunneling recommenced. However, at this particular location the ground treatment did not work and the machine continued to sink once it was advanced. Due to the low cover (only 2.4m) and the very soft ground conditions in the stream, it was decided that a crane could be attached to the TBM to help with the vertical alignment. Figure 2-30 shows such a configuration. The crane put an upward force of up to 10 tonnes on the TBM and the steel rope from the crane cut through the ground as the TBM advanced. The vertical alignment was

recovered just before the TBM came to the bridge. At this point the crane was unattached and the TBM continued unassisted to the reception shaft. There are no documented cases of a crane used with a TBM in this way. Therefore, it can be said, this was the first in the world.

During the driving of this tunnel, many settlement problems occurred in the developed area of the town. The bridge which the tunneling machine passed under suffered significant structural damage with a longitudinal crack forming in the right arch caused from settlement in the middle abutment. The masonry retaining wall of the Caol Stream suffered damaged where the TBM exited the stream. The wall cracked and the top of the wall rotated towards the stream. Three other residential structures showed signs of settlement through cracking. Figure 2-31 shows some of the damage as a result of the tunnel construction. There are some explanations to cause of the damage. However, the possibility of over excavation at the face cannot be considered as the reason for damage. There was never a drop in slurry face pressure and the volume of excavation was constantly monitored. After completion of the tunnel, information withheld from the contractor during tendering and construction stage emerged. An excavator had dredged the Caol Stream 30 years previously. At the location where the TBM exited the Caol Stream, a house had collapsed into the stream during the dredging. The dredging had also removed the majority of the “flag stone” mat foundations under the retaining walls and under the bridge. The road section of the bridge was micro piled after the damage occurred. However, the pedestrian section of the bridge which cracked during tunneling was left untreated. The extremely poor soil conditions in the stream can therefore be attributed to disturbed ground rather than intact and the susceptibility of structures to damage was increased because their foundations were damaged previously.

Further problems were noticed after completion of the tunnel. A survey of alignment showed that the section of tunnel once 400mm low was now 170mm high. The profile generated from the survey can be seen in Figure 2-32. The line with square data points indicates the original tunnel position and the line with circular data points shows the current position. The ground above the tunnel had insufficient strength to hold the buoyant pipeline in place and it was floating out of the ground. Kentledge in the form of concrete slabs were placed on the stream bed over the tunnel alignment, as shown in Figure 2-33. The additional weight and confinement on the ground stopped further pipe movement.

## **2.5 SITE INVESTIGATION AND LABORATORY TESTING**

### **2.5.1. Original Testing Program**

In April 2004, Skibbereen Town Council accepted the tender of Marine Geotechnical Ireland (MGI) to carry out the Skibbereen Sewerage Scheme Geotechnical Ground Investigation Contact under the instruction of RPS Consulting Engineers.

The aim of the site investigation was to provide factual geotechnical information on the existing ground conditions to facilitate the design of the sewerage collection pipelines throughout the town and the proposed pumping station in the Marsh field.

The three main areas of investigation were Skibbereen Town, its local environs and the Marsh Field. The program comprised of the following:

- 23 no. cable percussion boreholes drilled to final depths of between 0.7m and 25m with 108 no. standard penetration tests (SPT) and 13 no. falling head tests. Boreholes were generally terminated when bedrock was encountered or at their scheduled depths, unless otherwise directed by the resident engineer.
- 80 no. sealed intact samples of material were taken for moisture content evaluation. 111 no. bulk disturbed samples at locations of non recovery of attempted intact samples. 13 no. water samples were collected.
- 17 no. rotary boreholes drilled to recover rock core from a maximum depth of 41.2m. The boreholes were drilled using non-coring drilling techniques through the overburden materials with 78 no. SPT's. Coring recovered 61mm and 47.5mm diameter cores.
- Groundwater monitoring wells were installed in 19 no. cable percussion and 3 no. rotary boreholes.
- 44 no. trial pits machine excavated to a maximum depth of 4.5m. The trial pits were excavated without supports or shoring and were terminated upon collapse of the sidewalls or at the excavator limits. 70 no. sealed samples were recovered from the trial pits. In areas of groundwater, 22 no. sealed water samples were taken for laboratory analysis.

- 55 no. slit trenches were excavated by hand and machine to determine locations of services. 45 no. bulk samples, 47 no. disturbed samples, and 2 no. water samples were recovered.

Despite the extensive testing program that was undertaken, in general, the results of the site investigation were poor. The site investigation failed to identify the major engineering properties of the material. SPT values for the silt range from 11 to 0 with a mean value of 6.2. The values are consistent with depth in most cases but decrease with depth in some boreholes. The hydraulic conductivity information from falling head tests appears to be very repeatable. The tests in silt range in depth from 2.5 to 9.2 m. The hydraulic conductivity varies between  $4.23 \times 10^{-5}$  and  $1.23 \times 10^{-5}$  m/sec with no trend found between depth and hydraulic conductivity. From the observation well data, the ground water level was found to range between 1.07 and 2.14 m below ground level. The PH of the water was found to average at 6.7.

The laboratory testing was sub contracted to TESTCONSULT IRELAND LIMITED. The quality of results are extremely poor and therefore the information cannot be considered as trustworthy. Typical examples of poor results are as follows:

Moisture contents range from 5.8% to 72.5% for silt. The problem associated with water content tests on disturbed granular material is highlighted here, the structure segregates during transport and the results are practically worthless. The particle size distribution (PSD) curves are also of extremely poor quality. No hydrometer tests were conducted on the silt and clay size material. All PSD curves were generated using mechanical sieving. The description of the material does not match the PSD curves, i.e., materials are described as sandy silt but they have 60% gravel in their PSD curve. The PSD curves do not match the Atterberg limits. Up to 35% clay content is shown in some PSD figures but the corresponding Atterberg limit test states that the material is non plastic. More serious problems appear when the Atterberg limits are analyzed. In nearly all boreholes the silt is described as non plastic and no Atterberg limits could be established, then in others the liquid limit is determined but not the plastic limit. Where the plastic limit result is not present the material is then said to be non plastic, despite some specimens having liquid limit information. Liquid limits for the silt range between 20 and 114%, which is also a disturbing range. The laboratory testing also made no attempt to define the compression or shear strength properties of the material.

### 2.5.2. Further Investigation

It became obvious during construction that further site investigation was needed to assess the problems encountered. The additional information could also be used on the remaining technical aspects of the construction. Irish Drilling Limited were appointed by Ward and Burke Construction Ltd. to conduct testing at eight strategic testing locations around the Skibbereen area. The various locations can be seen in Figure 2-34. The borehole locations coincided with the remaining pipeline and tunnel construction in the project. 11 boreholes were constructed using the shell and auger system shown in Figure 2-35. Once the borehole advanced through the overlying fill and sand deposits, a Geonor field vane was used to determine the shear strength properties of the material at 1m intervals. The remolded shear strength was also checked at each interval to provide sensitivity data. The Geonor field used in Skibbereen can be seen in Figure 2-36. Figure 2-37 shows the excavated material from the shell and auger system. The excavated material was placed in plastic bags and sealed for later laboratory testing.

The results of the undrained shear vane testing for the intact ground can be seen in Figure 2-38. The average intact shear strength is 25.3 kPa and the remolded shear strength is 6.3 kPa, producing a sensitivity of 4.0. However, there is large scatter with a standard deviation of 14.6 kPa found in the intact results and 5.0 kPa in the remolded findings. It can be seen in the figure that there is no relationship between depth and undrained shear strength. Figure 2-39 presents the frequency versus undrained shear strength. Similar to Figure 2-28, there is no well defined undrained shear strength value.

Cone penetration tests (CPT's) were also conducted at the eight locations. They were performed by Lankelma with an 8.5 tonne crawler mounted CPT unit equipped with a 20 Tonne Capacity Hydraulic ram set.

A single electric piezocone (S10-CFIP.272) of a type conforming to the requirements of clause 3.1 of BS1377:1990: Part 9 was used on this project.

The cone was manufactured by Geopoint systems B.V of the Netherlands and measures the cone end resistance ( $q_c$ ), the local side friction ( $f_s$ ), and porewater pressure ( $u$ ). The cone resistance and local side friction are measured by load cells housed in the cone while pore water is measured by a pressure transducer that is also housed in the cone. The recorded data is

transmitted through the hollow push rods by an umbilical cable that is attached to a computerized data acquisition system. The rate of penetration is kept constant at  $20\text{mm} \pm 5\text{mm}$  per second except where penetrating very dense or hard strata. The system gives instantaneous and continuous graphical records of the cone resistance, local side friction and porewater pressure with depth. Simultaneously, the results are recorded on the computer hard disc at 10mm depth intervals and this facility enables automatic controlled processing and plotting of the data.

Nine CPT tests in total were performed at the testing locations. Dissipation tests were performed in situations where excess pore pressures were generated as the cone pushed through the ground. For these tests the cone penetration is stopped and the excess pore pressure is allowed to dissipate. The horizontal coefficient of hydraulic conductivity can then be derived from their data. The output from one of the CPT tests can be seen in Figure 2-40, 2-41, and 2-42. The cone resistance, sleeve friction, friction ratio, inclination, pore pressure ratio, total porewater pressure, and pore pressure dissipation at 6.41m are shown in the figures. It can be seen that the piezocone produces good data. However, without accurate shear strength information the piezocone data cannot be calibrated to the site conditions and therefore, the data is very limited.

In addition to the CPT tests, MOSTAP samples were taken at each location. The MOSTAP utilizes the hydraulic jacking frame from the CPT equipment to push the sampler into the ground. The sampling technique is appropriate to all soils and provides a high quality sample. The sampling technique is discussed in detail in Chapter 4. Mostap samples up to 12.5m deep were taken using this technique.

Irish Drilling Limited performed moisture content and Atterberg limit tests on the bulk material excavated by the shell and auger method. The findings are presented in Table 2-1. The tests were carried out in accordance with BS1377: Part 2:1990. The minimum water content was found to be 13.7% with a max of 28.7%. The average water content was 22% producing a standard deviation of 4.2%. The atterberg limit tests produced an average liquid limit of 29.19% with a standard deviation of 3.3%. A high plastic limit of 25.5% was found for the material with a 2.95% standard deviation. These results produce a plasticity index of 3.64%. The results put the material in the low plasticity range. The bulk material used in this classification was later transported to MIT for detailed testing.



<b>Borehole/ Trialpit</b>	<b>Depth m</b>	<b>Moisture Content %</b>	<b>Liquid Limit %</b>	<b>Plastic Limit %</b>	<b>Plasticity Index %</b>	<b>% passing 425 micron %</b>	<b>Description of fraction passing 425 micron sieve</b>
TP 01	2	13.7					
TP 01	4	24	28.8	25.4	3.4	99.5	Silt- Low Plasticity
TP 01	6	21.8					
TP 02	1	28.7					
TP 02	2	24.8					
TP 02	3	21.1					
TP 02	4	19.9	28.7	25.8	2.9	99.8	Silt- Low Plasticity
TP 02	5	18.9					
TP 04	3	21					
TP 04	4	24.6	26.5	23.7	2.8	97	Silt- Low Plasticity
TP 04	5	19.5					
TP 04A	3	21.3					
TP 04A	4	14.6	26.1	22.1	4	96.7	Silt- Low Plasticity
TP 04A	5	20.2					
TP 07	2	20.3					
TP 07	3	26.7					
TP 07	4	27.2	35.4	31.2	4.2	100	Silt- Low Plasticity
TP 07	5	22.9					
TP 11	3	22.7					
TP 11	4	24.9	31.6	26.8	4.8	99	Silt- Low Plasticity
TP 11	5	26.8					
TP 12	4	22.9	27.2	23.8	3.4	94.5	Silt- Low Plasticity
TP 12	5	18					

Table 2-1: Characterization results from Irish Drilling



Figure 2-1: Skibbereen Location (Google Earth)



Figure 2-2: Skibbereen Location

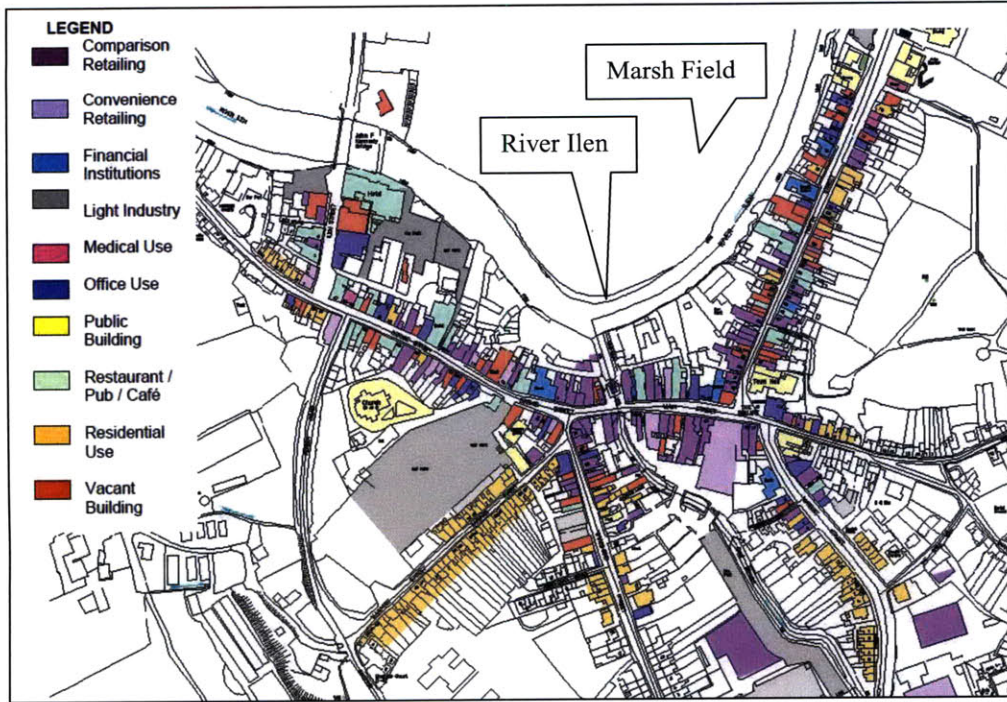


Figure 2-3: Building use of town centre (not to scale) (Skibbereen Town Development Plan, 2009-2015)



Figure 2-4: Skibbereen town from the southwest (Skibbereen Circa 1900)

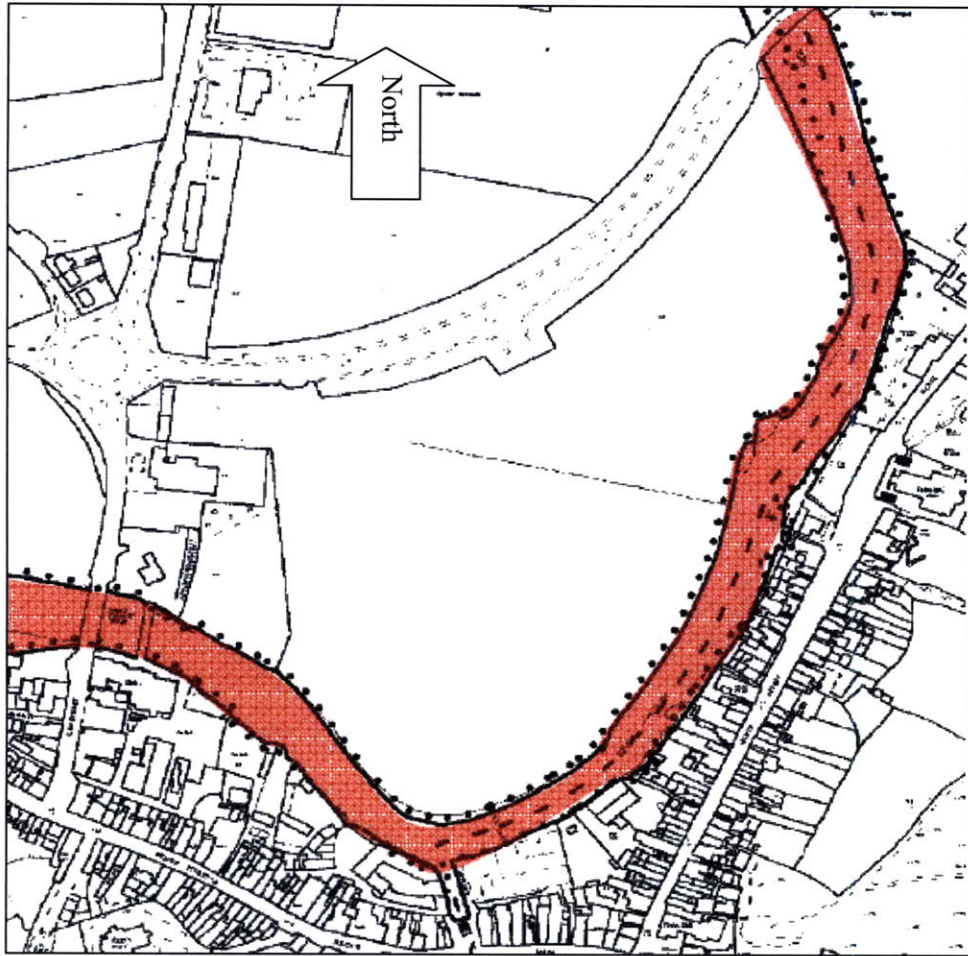


Figure 2-5: River Ilen (not to scale)



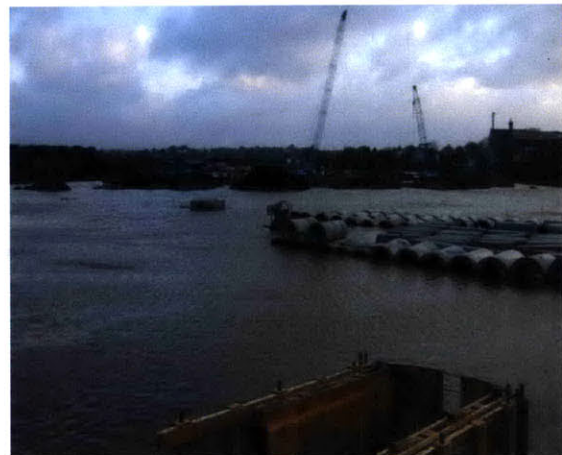
(a)



(b)



(c)



(d)

Figure 2-6: Tidal Influence on River Ilen: (a) Low Tide, (b) Low Tide, (c) High Tide and Heavy Rain, (d) High Tide and Heavy Rain

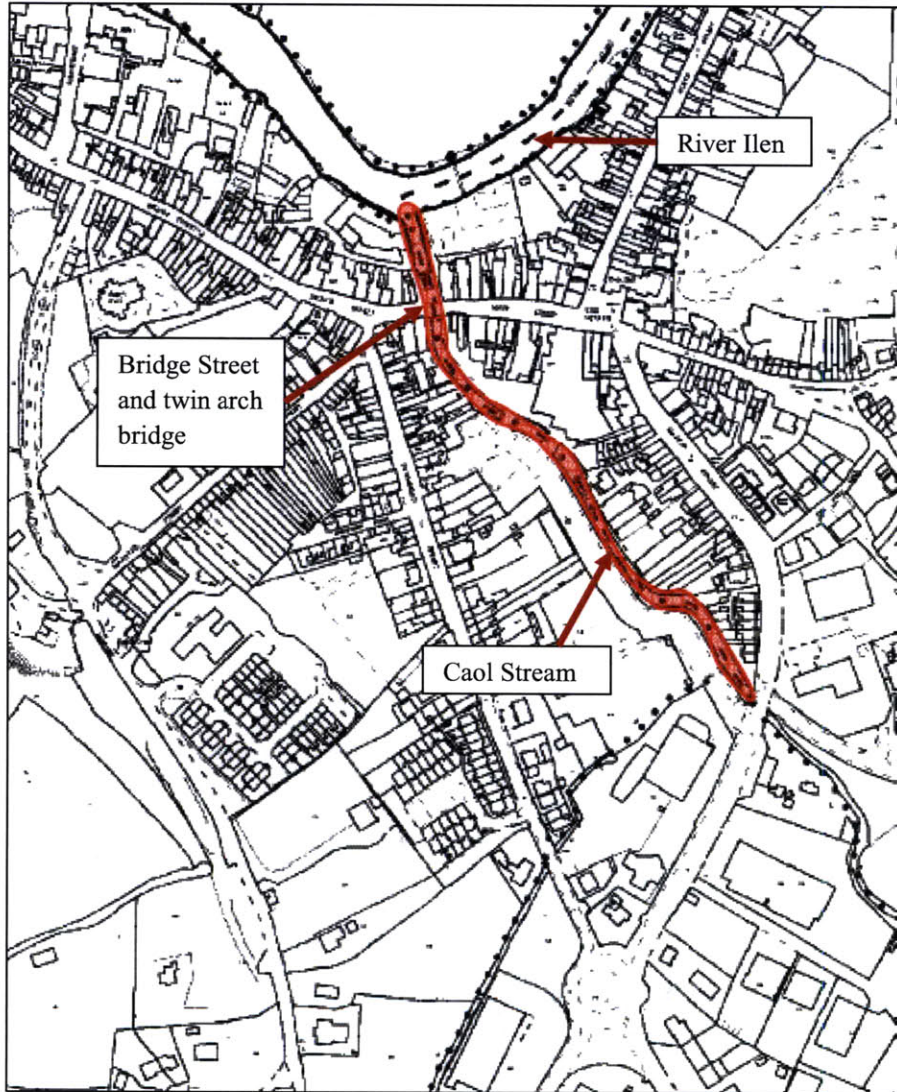


Figure 2-7: Caol Stream (not to scale)



(a)



(b)



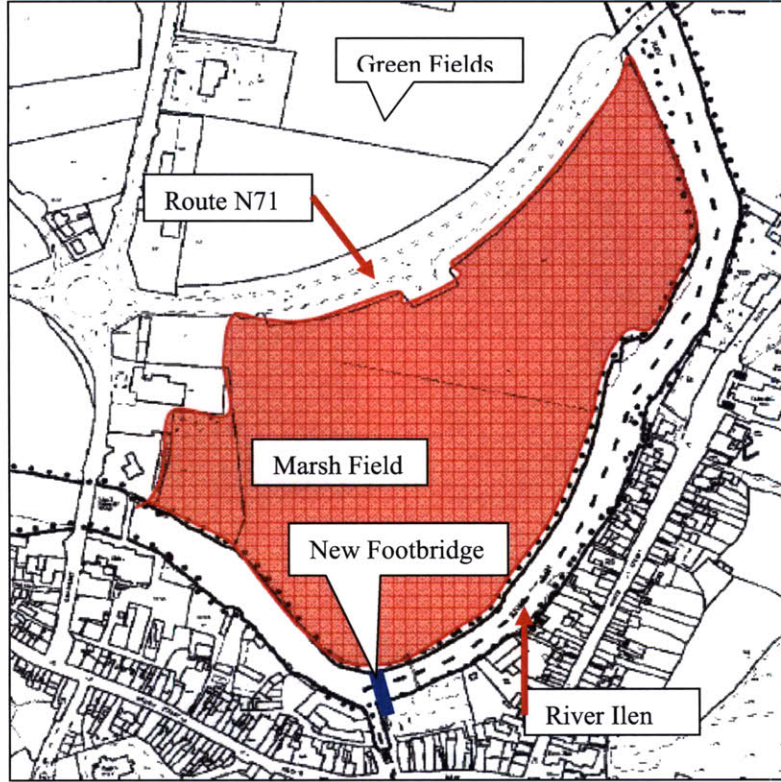
(c)



(d)

Figure 2-8: Pollution along the Caol Stream in Skibbereen: (a) discharge pipe, (b) vertical discharge pipe, (c) polluted stream bed, (d) polluted stream bed (River Ilen and Caol Stream Redevelopment Project, 2007)

(a)



(b)



Figure 2-9: Marsh Field: (a) schematic (not to scale), (b) photograph



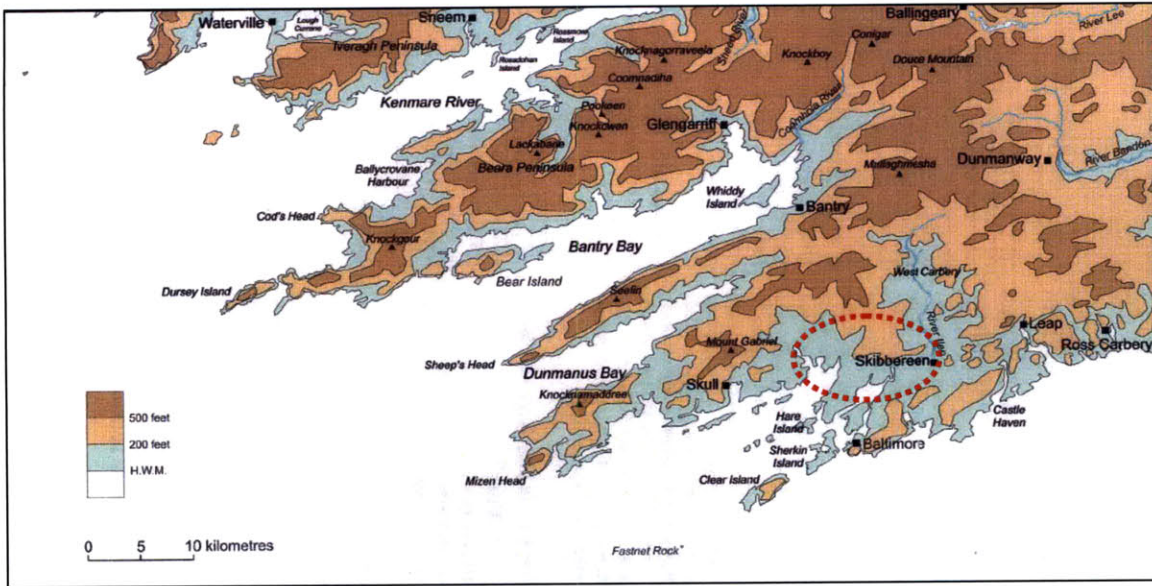
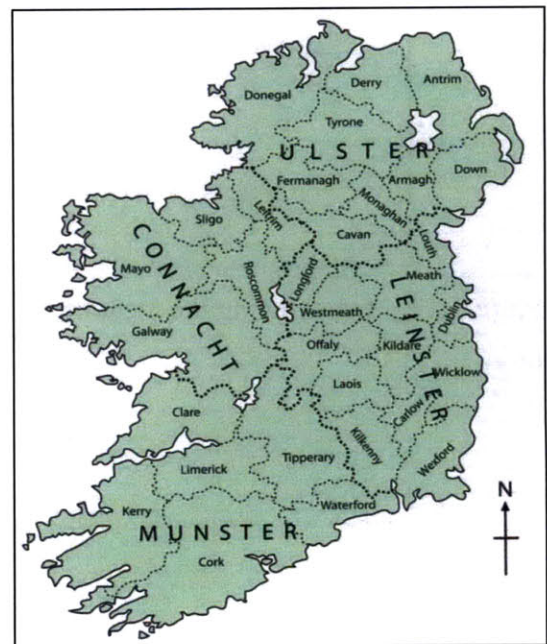


Figure 2-10: Topography of West Cork (Pracht & Sleeman, 2002)

Eras	Periods	Approximate age in millions of years (Ma)	
Cenozoic	Quaternary		
	Tertiary	Neogene	2.65
		Pliocene	5.3
		Miocene	23
		Oligocene	34
		Eocene	56
Mesozoic	Palaeocene	65	
	Cretaceous	146	
	Jurassic	200	
	Triassic	251	
	Permian	299	
Palaeozoic	Upper	Carboniferous	359
	Lower	Devonian	416
		Silurian	444
		Ordovician	488
		Cambrian	542
Precambrian eras	Proterozoic		
	Archaean	2,500	
— origin of the Earth —		4,567	

(a)



(b)

Figure 2-11: (a) Geochronometric scale (Holland & Sanders, 2009), (b) county map of Ireland (Holland & Sanders, 2009)

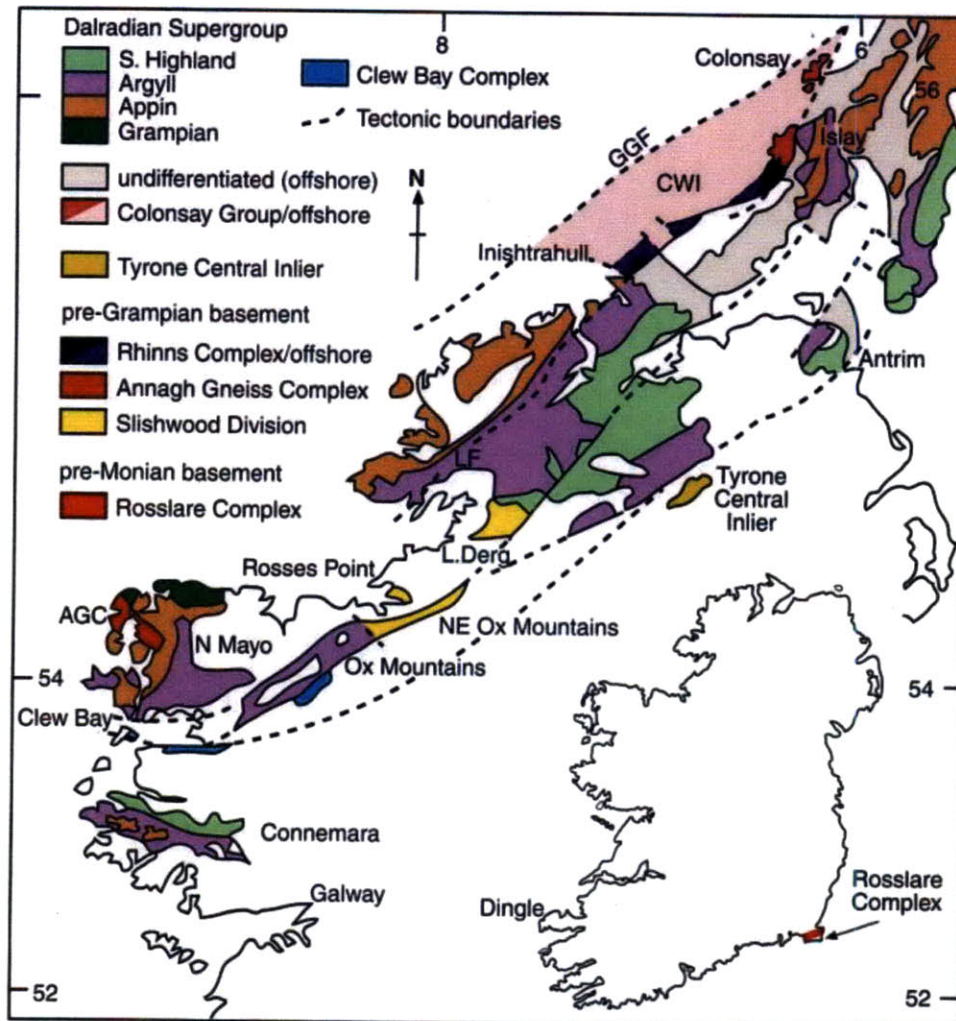


Figure 2-12: Map showing the location of Precambrian rocks in Ireland (Holland and Sanders 2009)

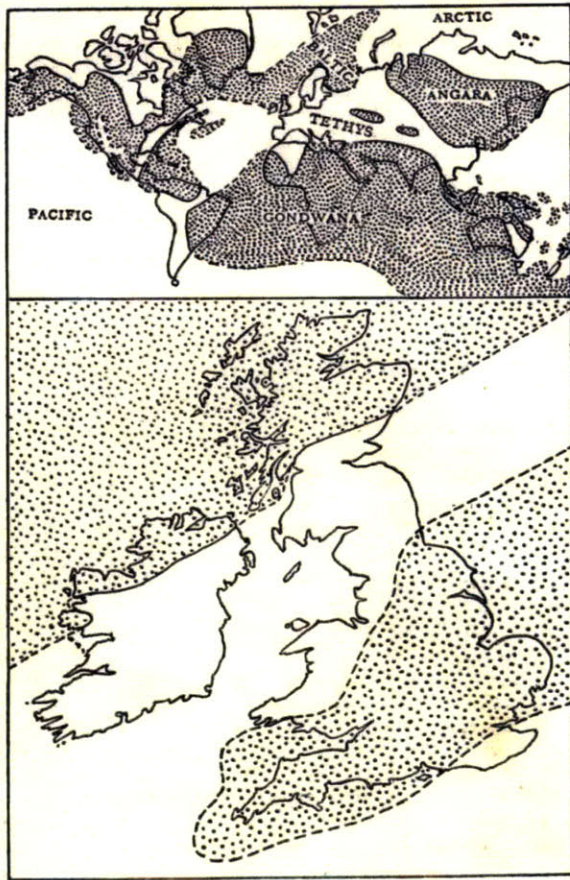


Figure 2-13: Map showing distribution of land (dotted) and sea (white) in Lower Palaeozoic times (Charlesworth 1953)

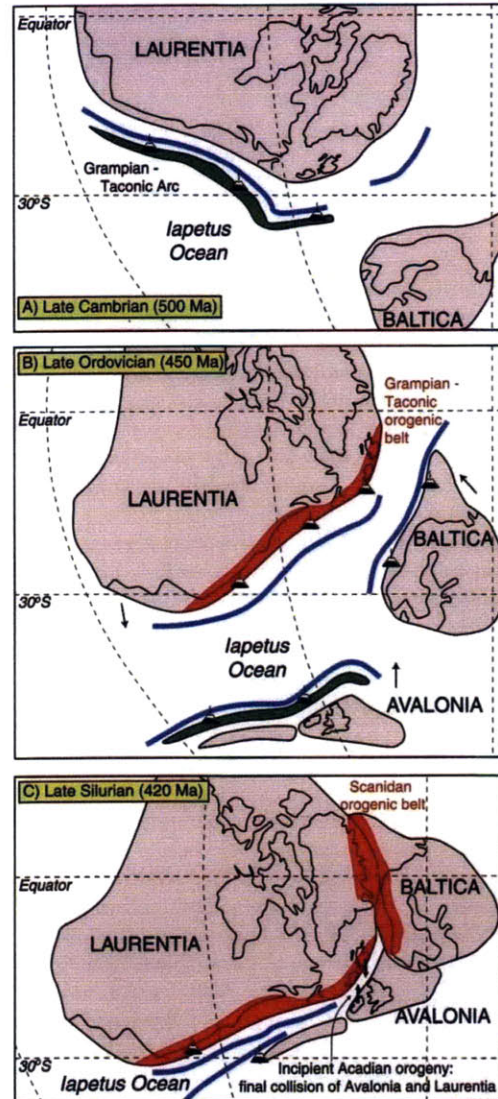


Figure 2-14: Caledonian movement (Holland and Sanders, 2009)

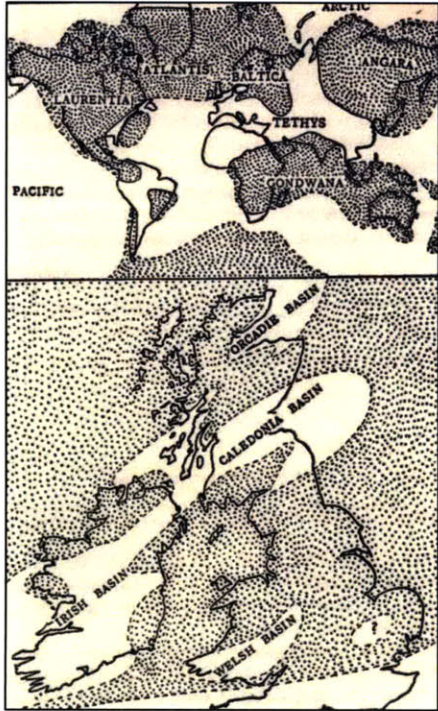


Figure 2-15: Sea location during Devonian times (Dotted = land, Clear = water) (Charlesworth 1953)

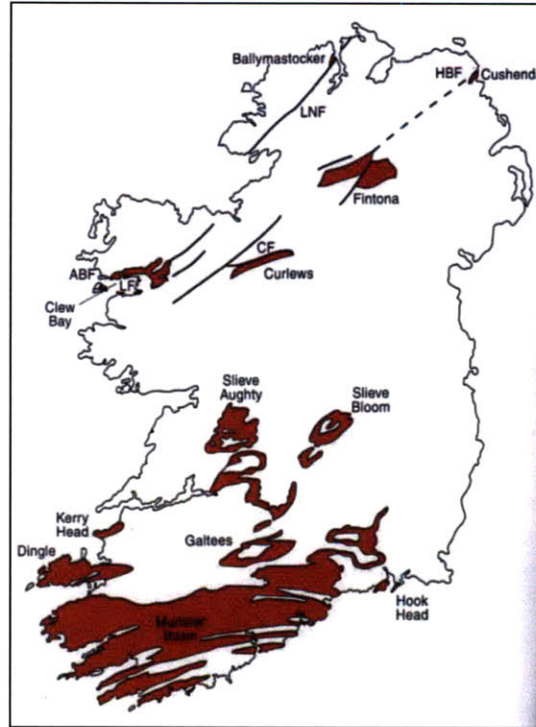


Figure 2-16: Distribution of Old Red Sandstone rocks in Ireland today (Holland and Sanders, 2009)

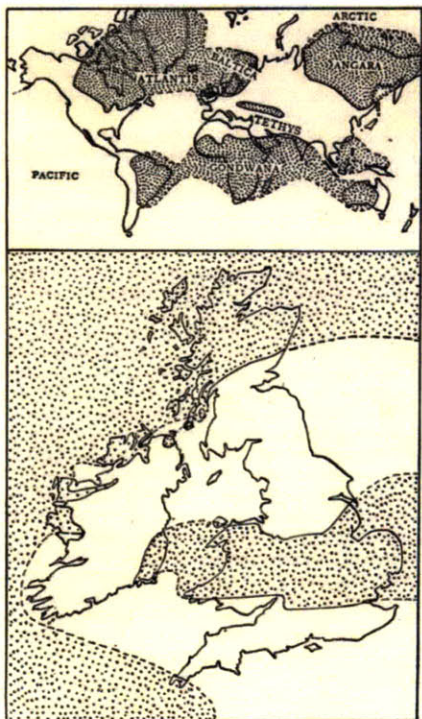


Figure 2-17: Map showing the distribution of land during Carboniferous times, dotted is land, clear is water (Charlesworth, 1953)

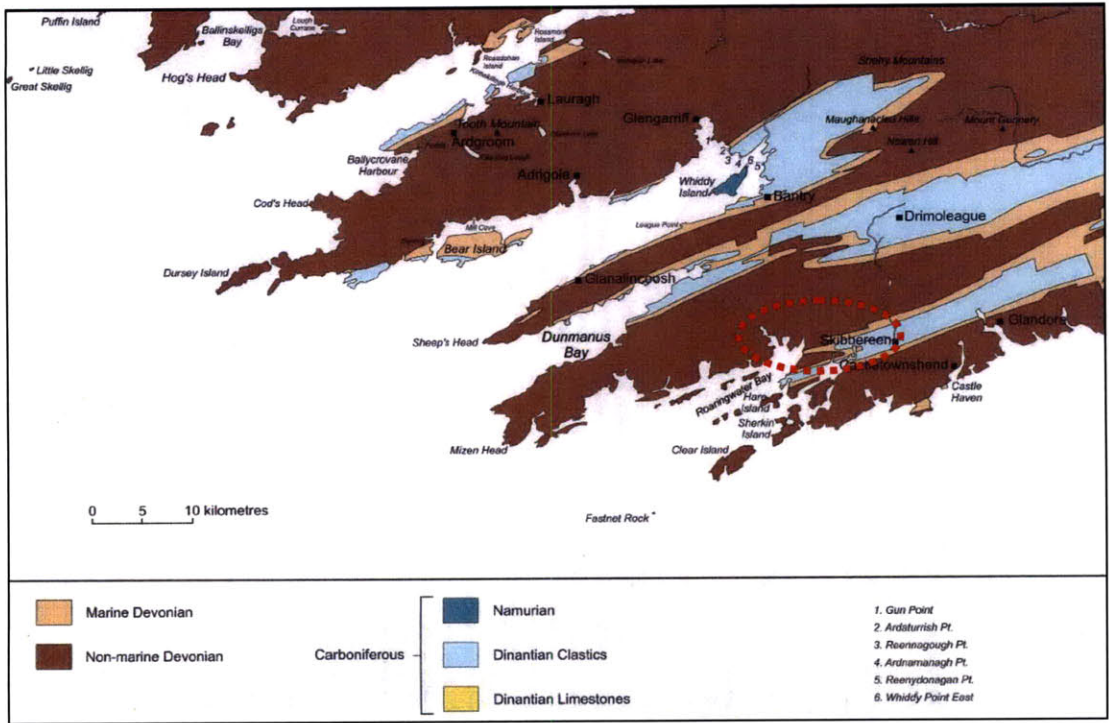


Figure 2-18: Distribution of rock types around Skibbereen (Pracht & Sleeman, 2002)

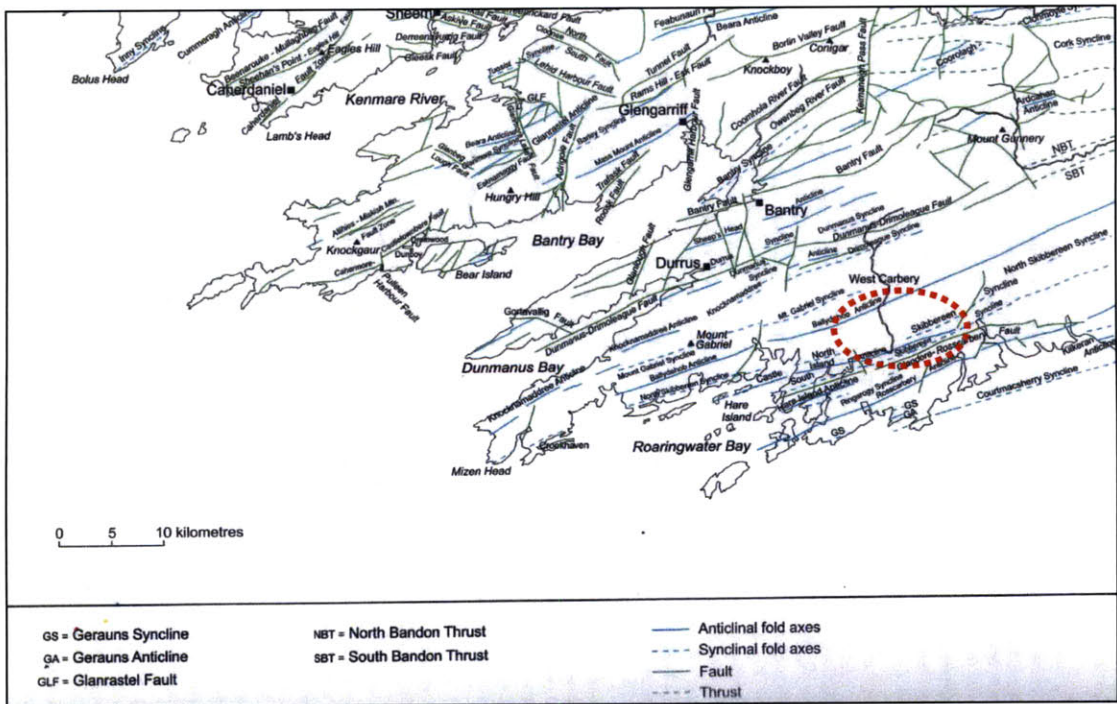


Figure 2-19: Major structures in West Cork (Pracht & Sleeman, 2002)

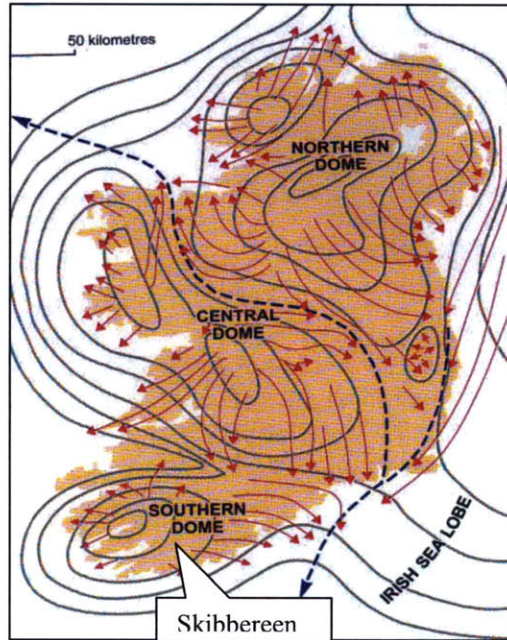


Figure 2-20: The pattern of glaciation in Ireland during the last glaciation (Pracht & Sleeman, 2002)



Figure 2-21: Sinking of main pump station caisson using various excavators and hydraulic jacks

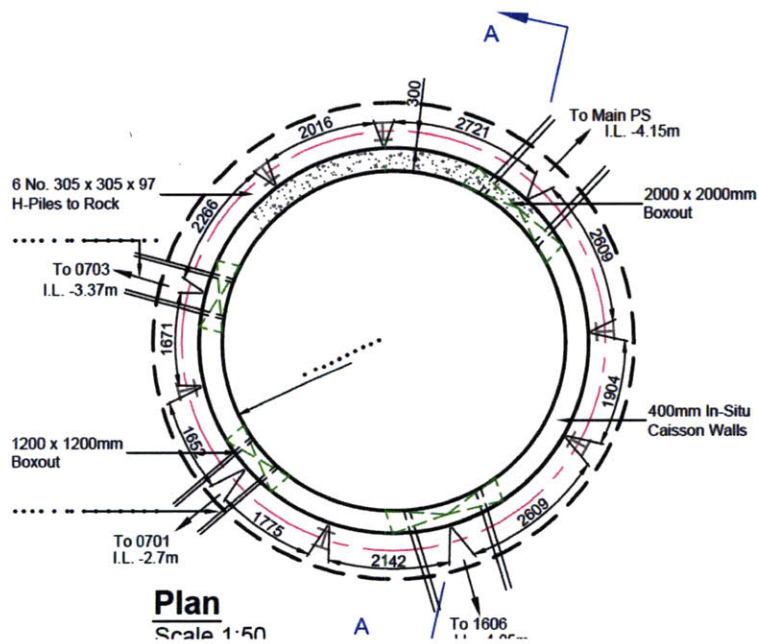
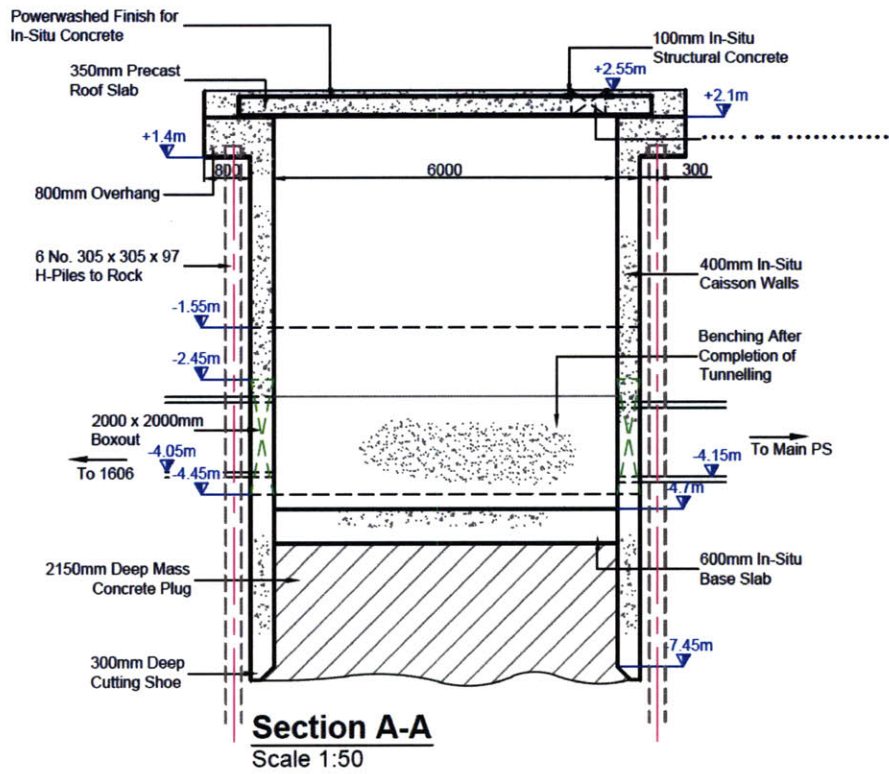


Figure 2-22: Schematic diagram of 6m internal diameter caisson (not to scale)



Figure 2-23: Directional Drilling equipment used in Skibbereen

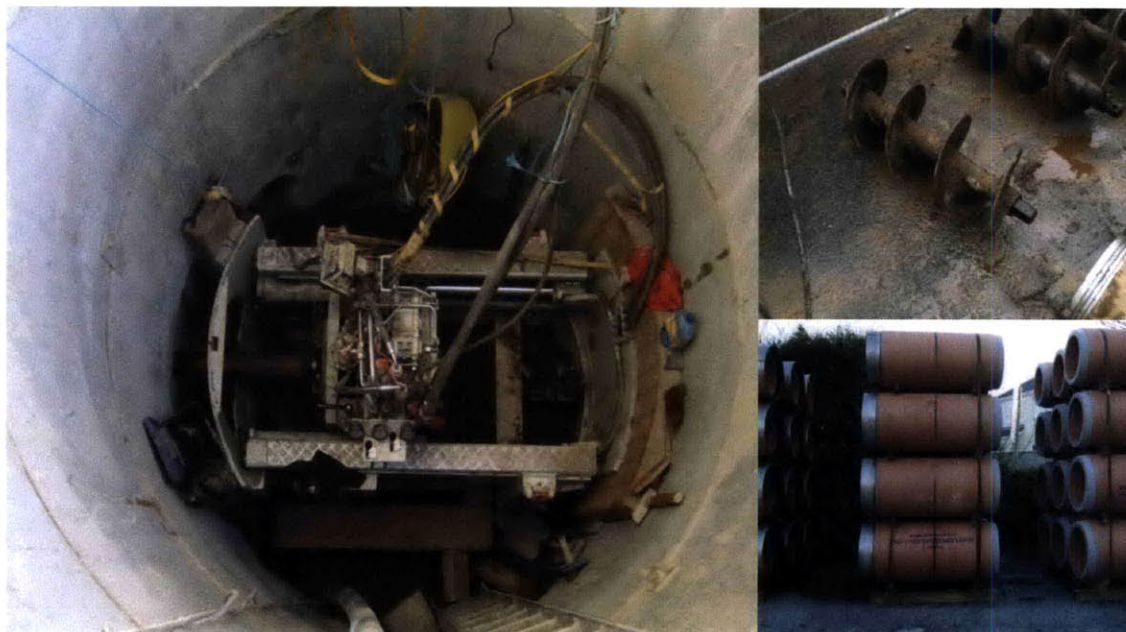


Figure 2-24: Auger boring equipment used in Skibbereen; Launch shaft and jacking frame, augers, and clay pipes.



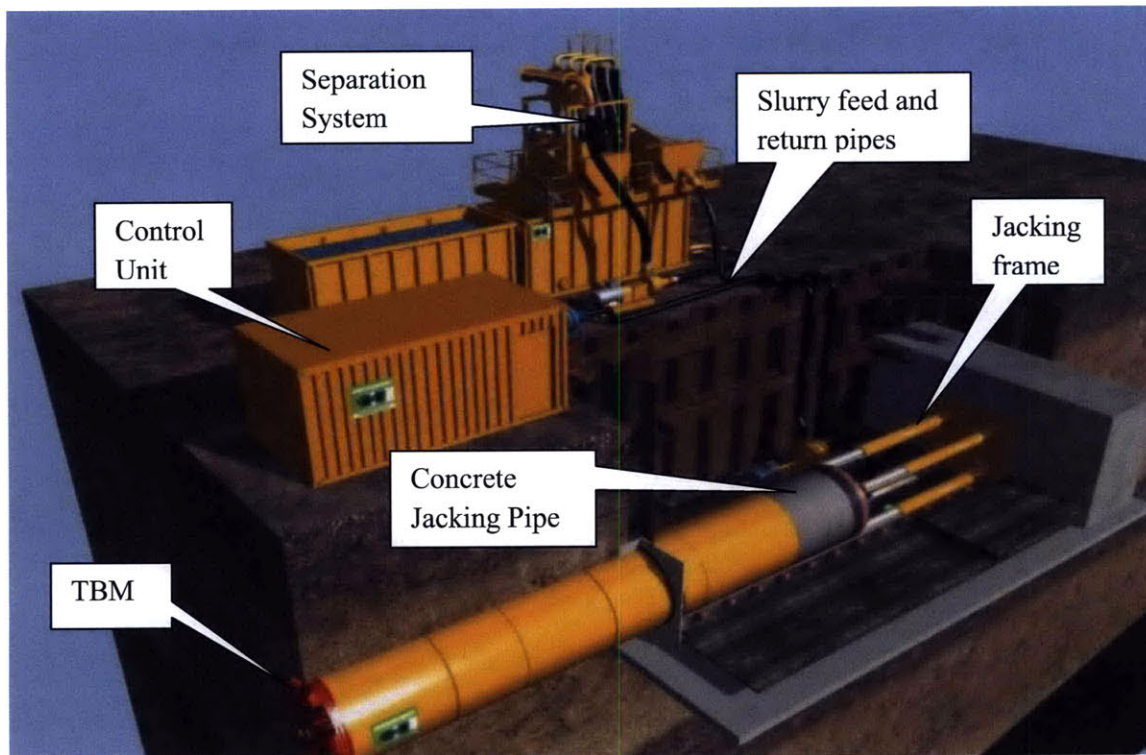


Figure 2-25: Schematic diagram of the micro tunneling system used in Skibberen

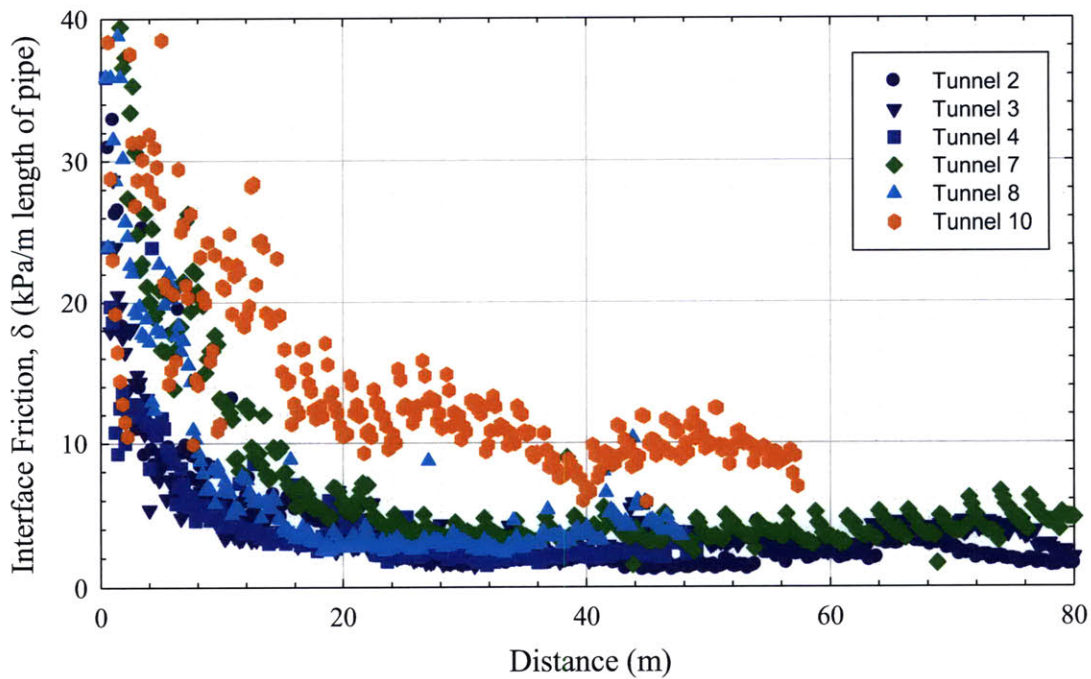
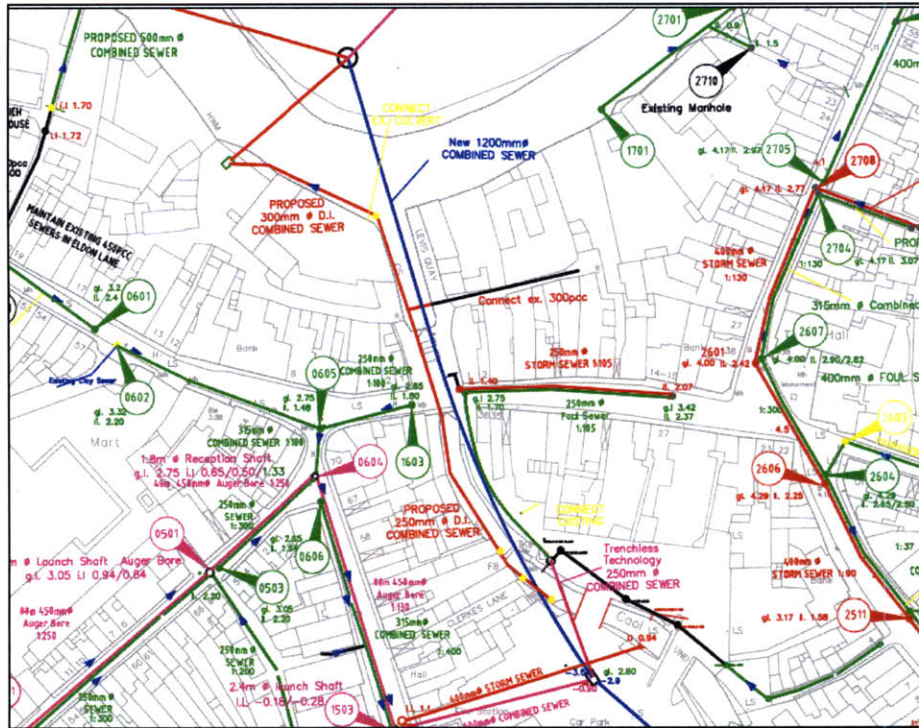


Figure 2-26: Pipe skin friction vs. distance for the micro tunneling in Skibberen

(a)



(b)



Figure 2-27: Tunnel alignment: (a) schematic (blue line is tunnel), (b) photograph from launch shaft

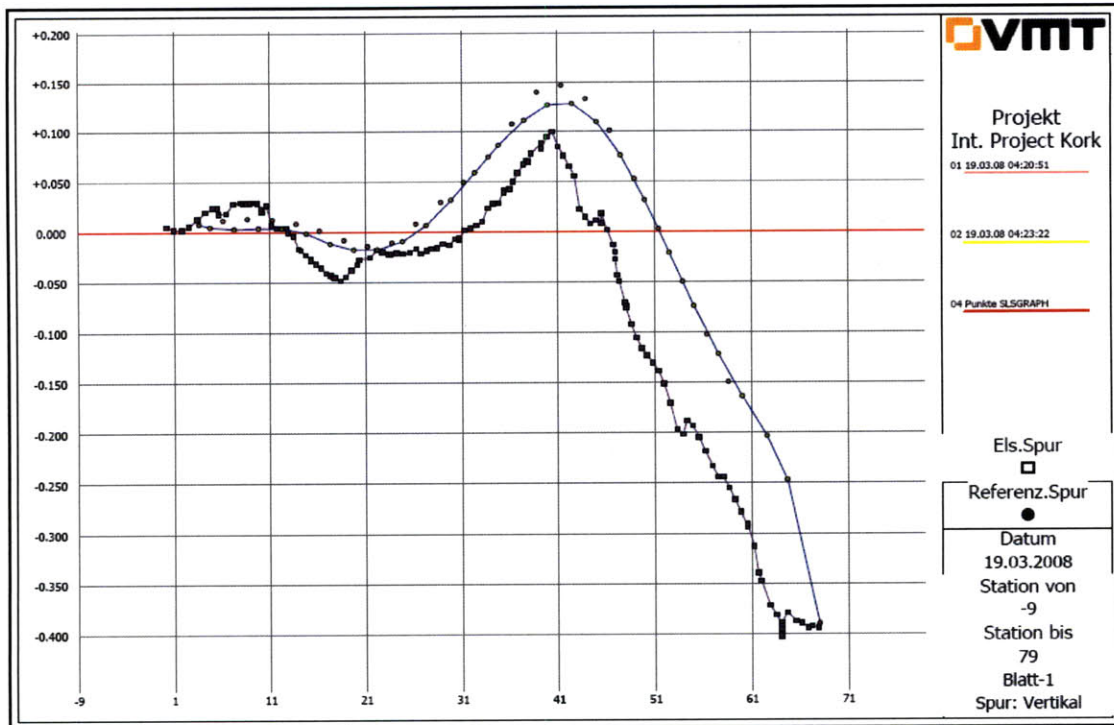


Figure 2-28: Vertical tunnel alignment when TBM began to sink. (Zero in elevation indicates required grade, line with square data points is original TBM position, and line with circular data points is current pipe position)

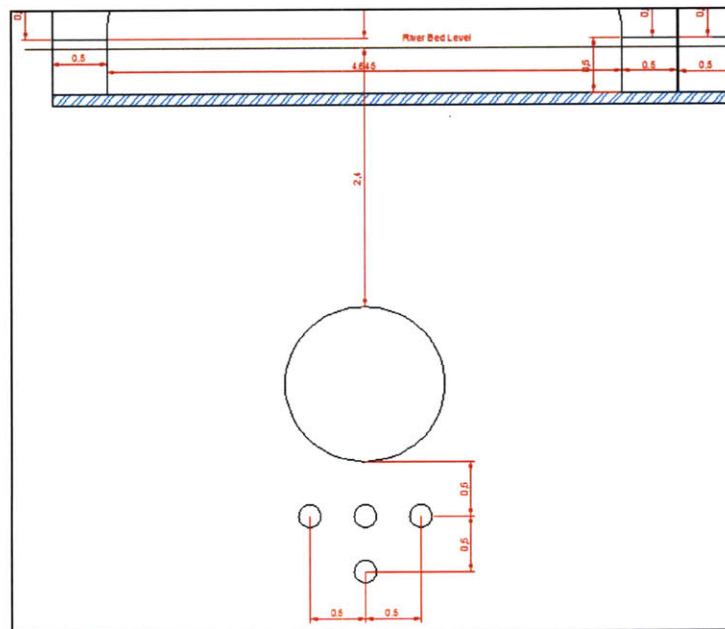


Figure 2-29: Alignment of HDD grouting under tunnel (dimensions in m)

(a)



(b)



Figure 2-30: Crane attached to TBM: (a) At ground level, (b) inside TBM where crane is attached



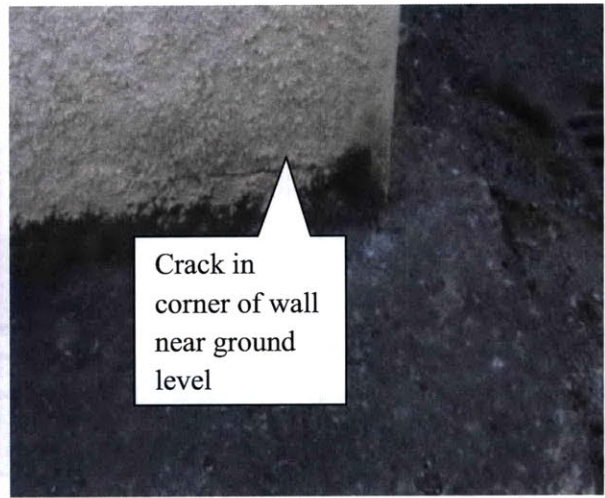
(a)



(b)



(c)



(d)

Figure 2-31: Examples of structural damage as a result of tunneling; (a) Stone arch bridge cracked, (b) beginning of repair work on bridge, (c) retaining wall damaged where TBM exited stream (wall cracked and rotating towards river) (d) typical example of cracking in residential property

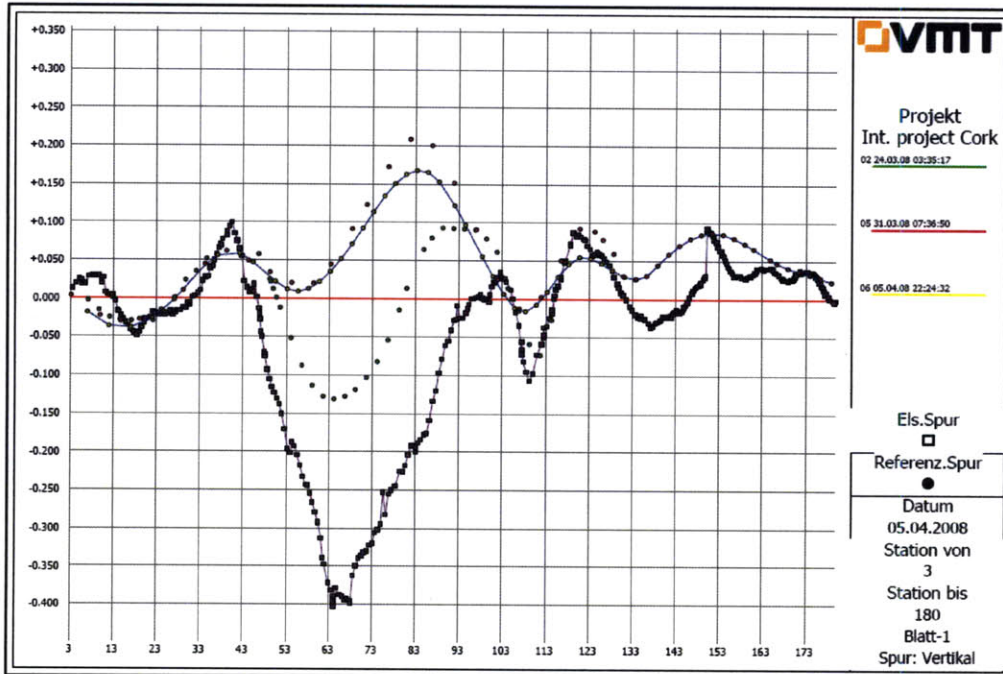


Figure 2-32: Vertical tunnel alignment after completion of tunnel (Zero in elevation indicates required grade, line with square data points is original TBM position, and line with circular data points is current pipe position)



Figure 2-33: Addition of kentledge over tunnel

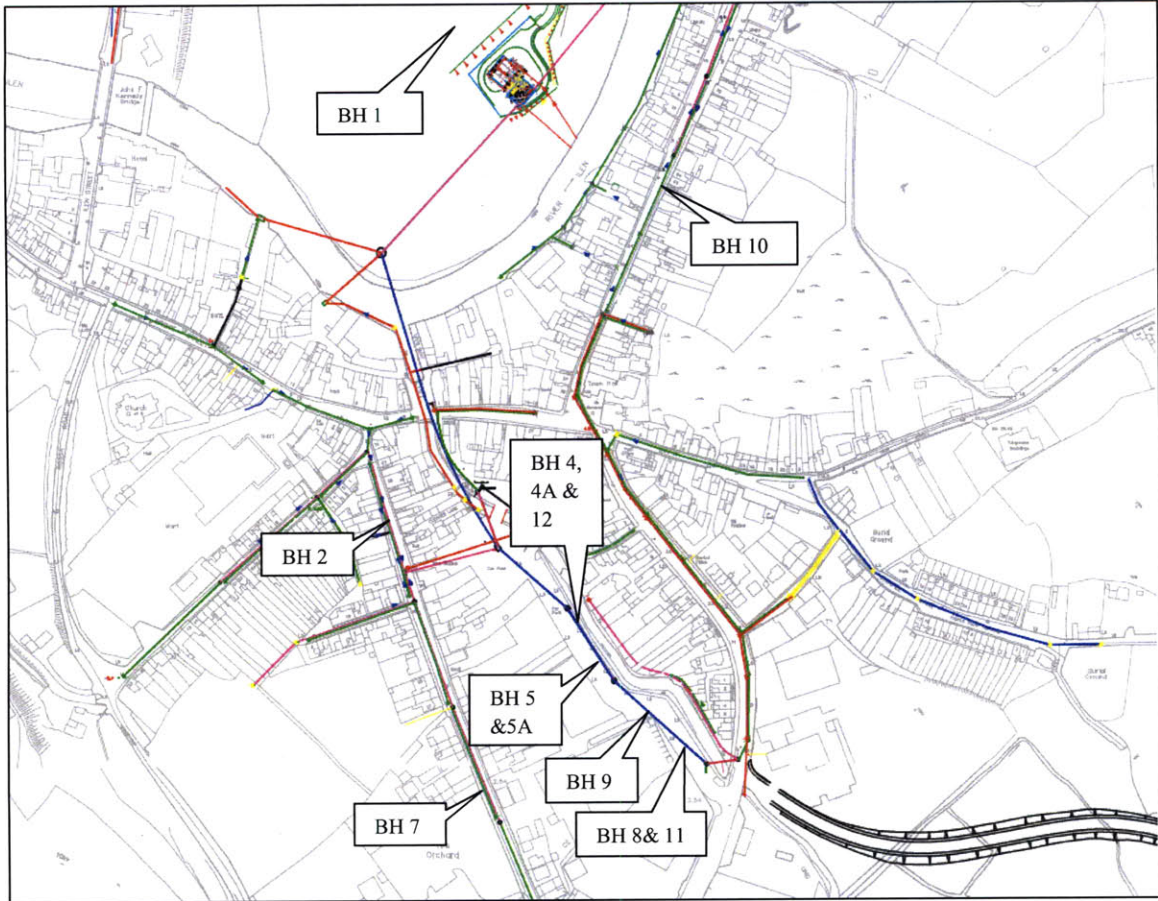


Figure 2-34: Further site investigation in Skibbereen



Figure 2-35: Shell and auger for site investigation boreholes

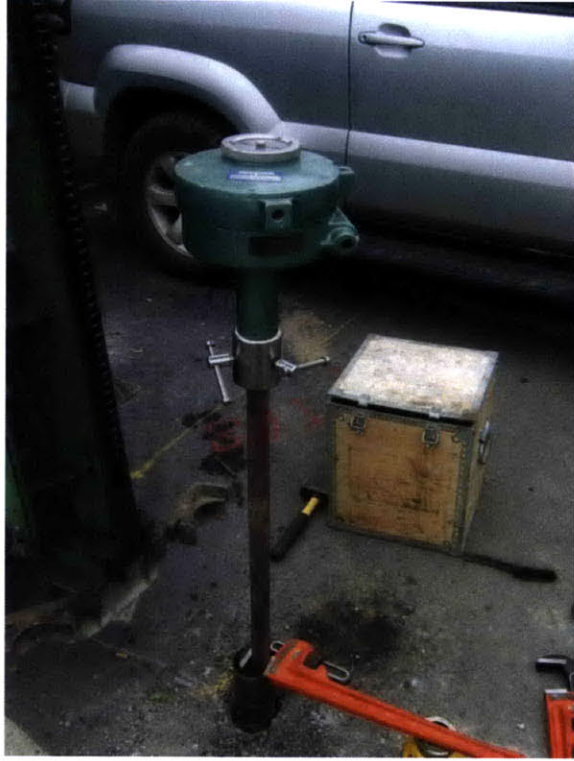


Figure 2-36: Geonor field vane in use

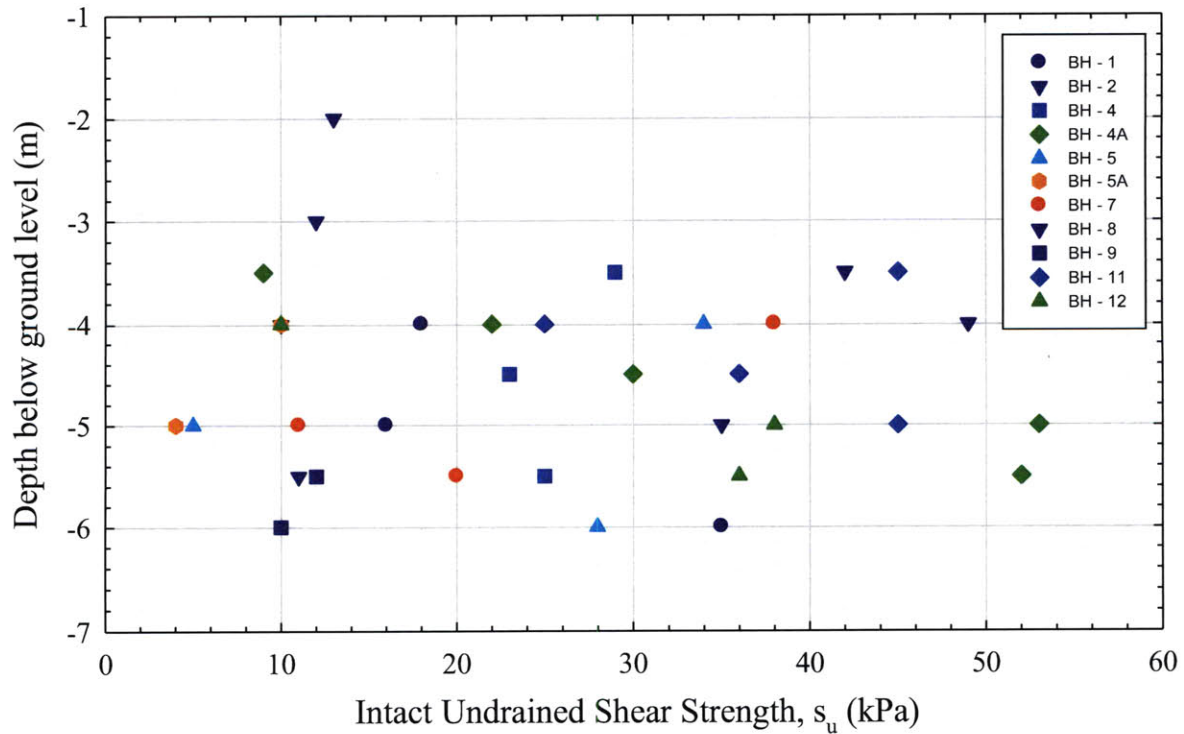


Figure 2-37: Excavated silt from the shell and auger method.



	BH-1	BH-2	BH-4	BH-4A	BH-5	BH-5A	BH-7	BH-8	BH-9	BH-11	BH-12	Average	Std Dev.
<b>Depth (m)</b>	<b>Su Intact</b>												
	<b>kN/m<sup>2</sup></b>												
-2		13										13.00	0.00
-3		12										12.00	0.00
-3.5			29	9				42		45		31.25	16.38
-4	18	10		22	34	10	38	49		25	10	24.00	13.92
-4.5			23	30						36		29.67	6.51
-5	16	35		53	5	4	11			45	38	25.88	19.14
-5.5		11	25	52			20		12		36	26.00	15.71
-6	35				28				10			24.33	12.90
												<b>25.46</b>	<b>14.47</b>
<b>Depth (m)</b>	<b>Su Remoulded</b>												
	<b>kN/m<sup>2</sup></b>												
-2		6										6.00	0
-3		4										4.00	0
-3.5			6	5				6		26		10.75	10.18
-4	2	5		6	12	1	18			14	3	7.63	6.25
-4.5			5	4						6		5.00	1.00
-5	2	3		6	4	3	7			8	5	4.75	2.12
-5.5		3	2	5			9		4			4.60	2.70
-6	4				5				2		8	4.75	2.50
												<b>6.15</b>	<b>4.96</b>

(a)



(b)

Figure 2-38: Field vane shear strength information: (a) Field data, (b) scatter plot for intact tests

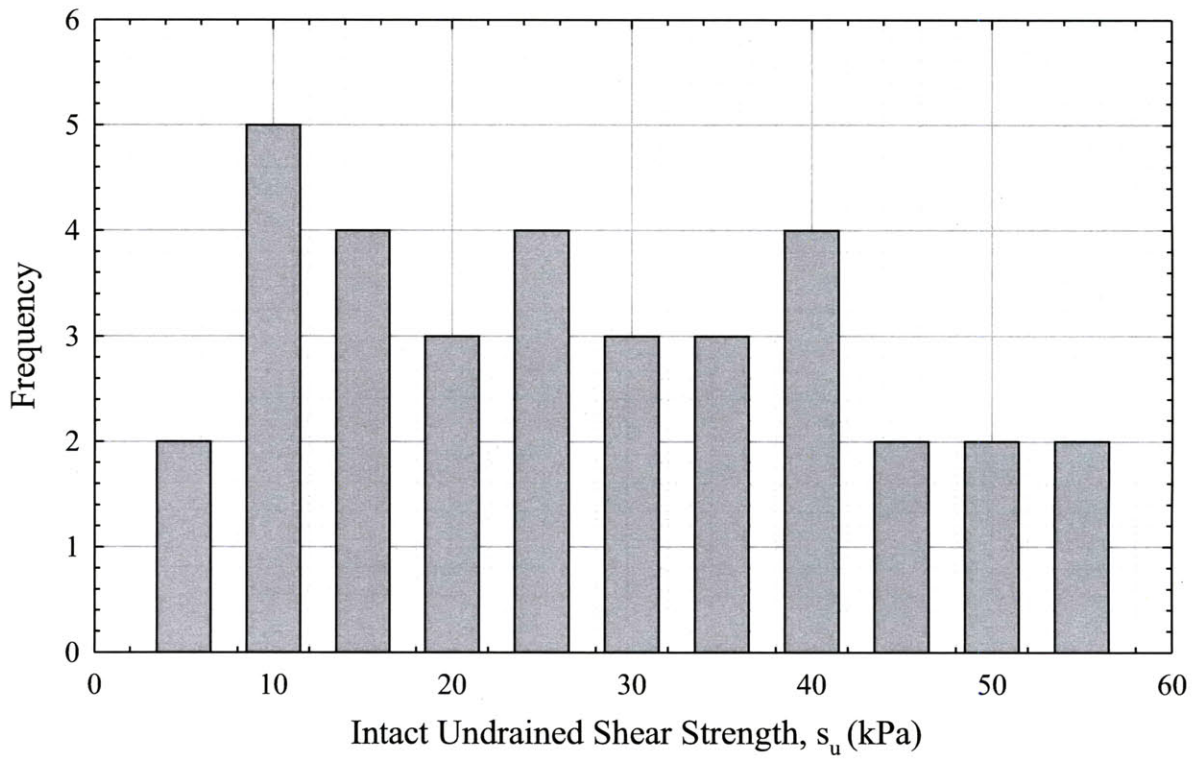


Figure 2-39: Frequency versus intact undrained shear strength for field vane data

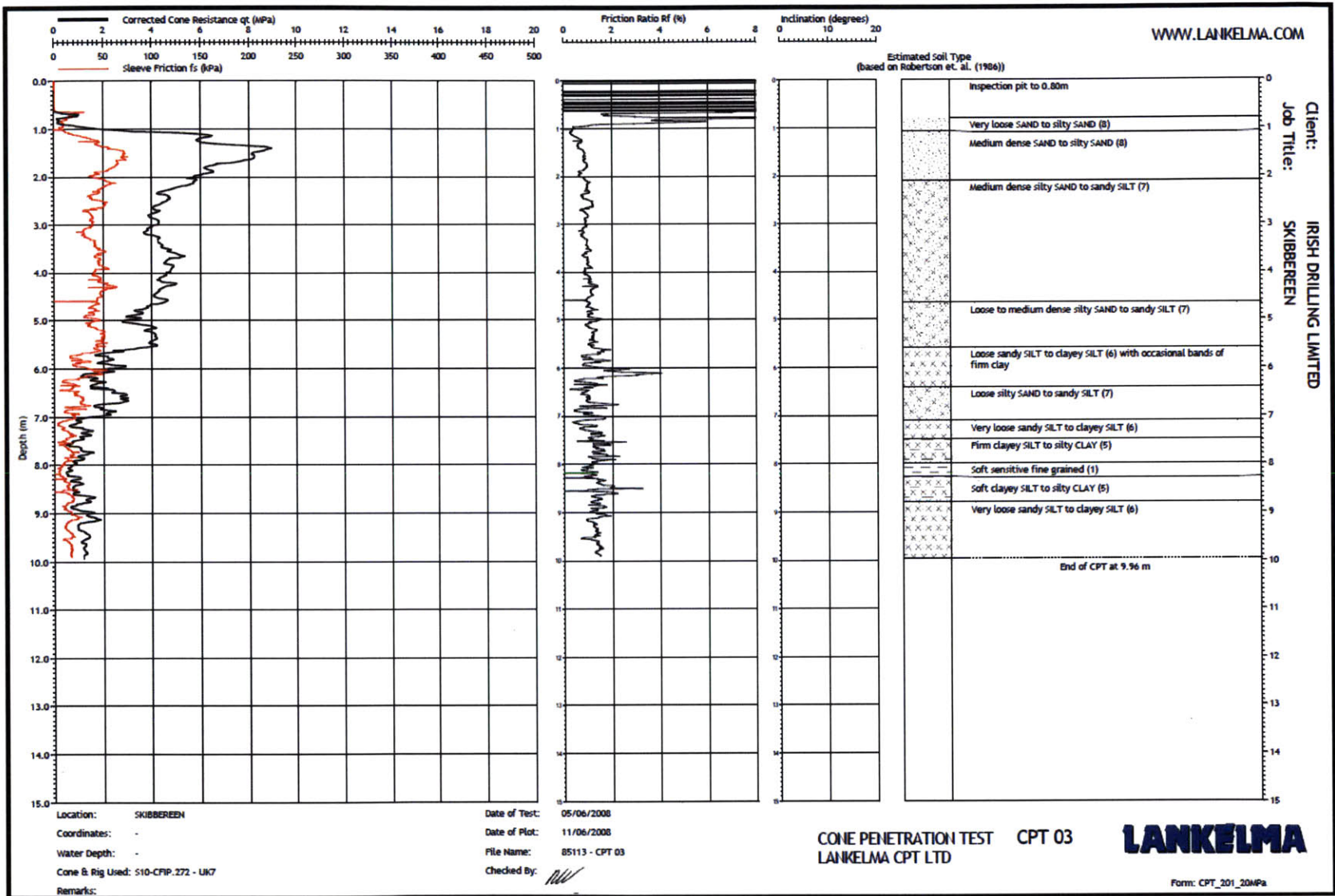


Figure 2-40: CPT output: Cone resistance, skin friction, friction ratio, inclination, and interpreted soil profile

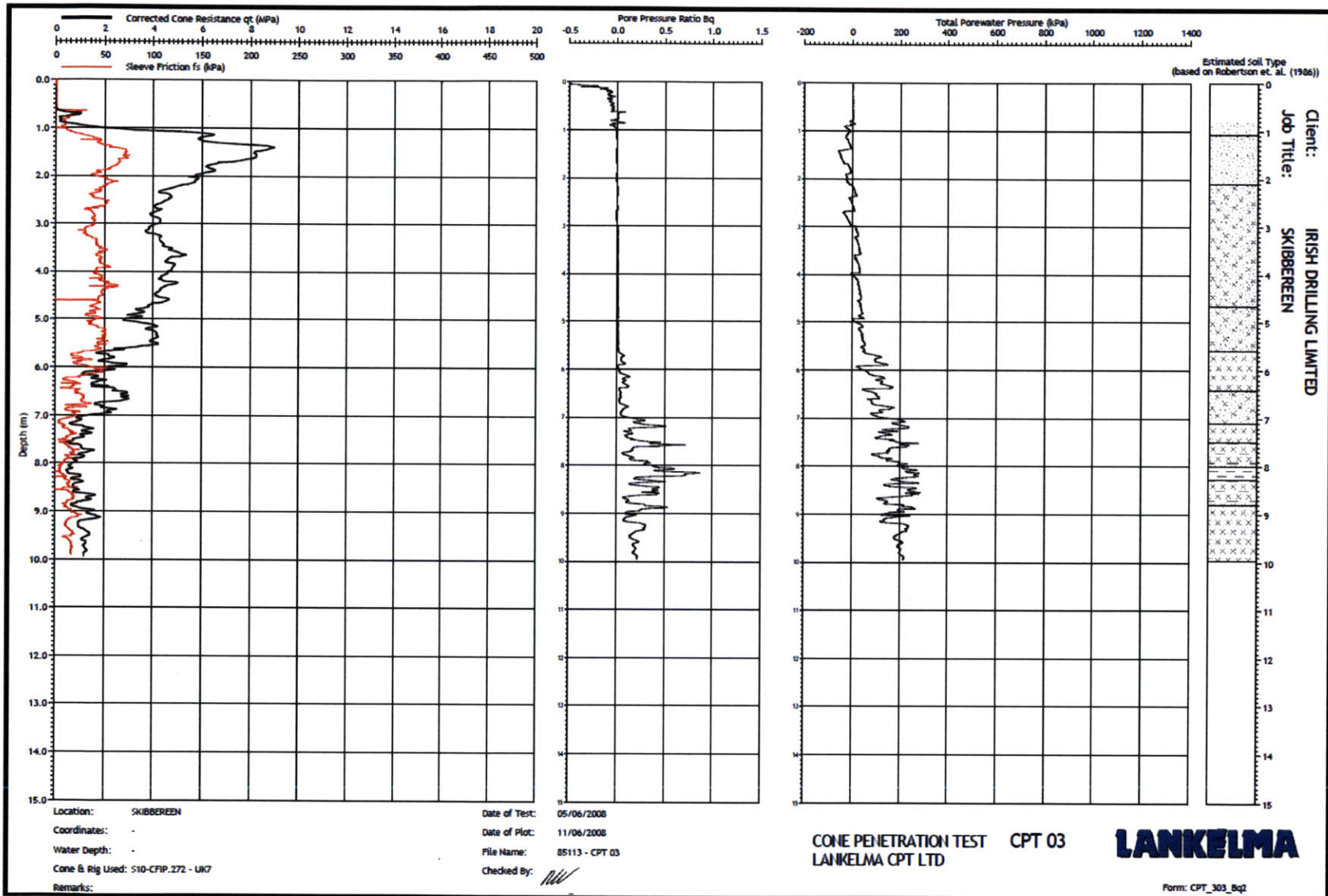


Figure 2-41: CPT output: Cone resistance, skin friction, pore pressure ratio, total pore pressure

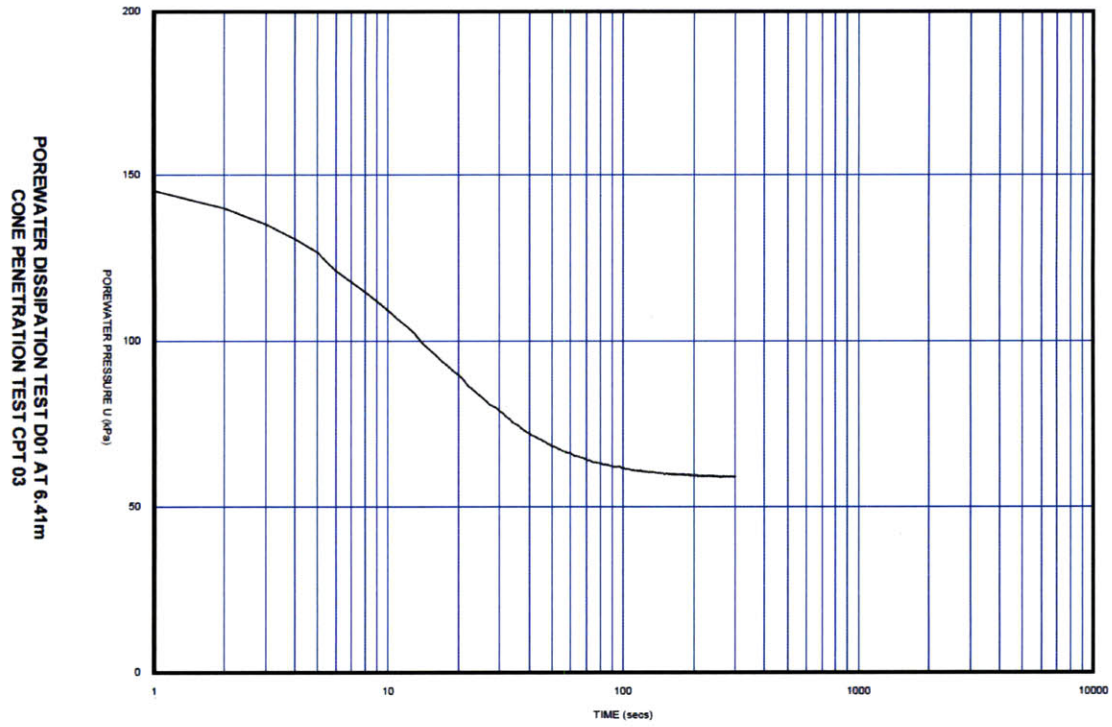


Figure 2-42: CPT dissipation test in Skibberen



## 3 LITERATURE REVIEW

### 3.1 INTRODUCTION

Extensive geotechnical research has been conducted on clay and sand soils. In contrast, very little information exists on the engineering properties of silts. There are several reasons for this trend and they are primarily related to the end conditions. Generally, sands exhibit fully drained behavior and clays are undrained, while silts can be either of the two. Difficulties in sampling and subsequent test preparation in the laboratory have contributed to the shortage of information (Long, 2000). Low plasticity silts are very easily disturbed during sampling and preparing silt specimens for strength testing without disturbance is difficult. Due to these problems, research has concentrated on reconstituted material.

Several reconstitution techniques have been used to study silt behavior. They have generally been modified from techniques used in reconstituting clays and sands. Some researchers have analyzed differences in undrained stress-strain-strength behavior between intact and reconstituted silt specimens at the same void ratio and effective stress. Contrasting views exist, with some researchers stating dramatic differences and others claiming they are similar. However, all researchers note that the reconstitution technique used is important when assessing silt behavior.

Many geotechnical engineers consider the behavior of silts as being somewhere between the behavior of clay and sand (Brandon *et al.*, 2006). However, due to the vast differences in behavior, silt properties cannot be interpolated from clay and sand results. Brandon *et al.* (2006) say that low plastic or non plastic silts have characteristics in common with both sands and clays. They are more subject to compression by static pressures than sands and they are more subject to densification by vibrations than clays. They tend to dilate during shear and changes in pore pressure can become negative as strains increase.

Due to the unknown behavior during earthquake conditions, the liquefaction potential of silt has received research in recent times. The behavior of saturated sands subjected to cyclic loading has been extensively studied, mainly in connection with earthquake loading and offshore

machine foundations. However, when it comes to predicting the behavior of silts there are still significant uncertainties.

This chapter reviews existing research on silts. The first section presents specimen reconstitution techniques. Various methods are available, with undercompaction, resedimentation, and pluviation being the most popular. The techniques are discussed in detail and the advantages and disadvantages are highlighted. Reconstituted specimen behavior is compared to intact behavior and it can be seen that soil fabric of a specimen is very important.

Section 3.3 reviews existing sampling techniques on silts. Many different samplers have been used to various degrees of success. The most effective samplers have a thin wall, sharp cutting shoe, no inside clearance ratio, and an internal diameter of approximately 75mm. The positives and negatives of intact sampling on silts are covered in detail.

Section 3.4 covers the consolidation behavior and properties of silt. Little information exists, most likely due to the use of in situ tests, such as the standard penetration test, to derive the settlement characteristics.

Section 3.5, describes the stress-strain-strength properties of low plasticity silt. A detailed review is given of different testing techniques used to produce strength information. They are derived from two devices; the triaxial apparatus and the direct simple shear apparatus. Due to the dilative nature of most silts, assessing the strength is a very difficult task. As a result, various failure criteria for triaxial tests exist. A summary of the available criteria is given along with the corresponding test information. The section concludes by describing normalized behavior and the effects of overconsolidation.

Finally, Section 3.6 gives a brief account of the liquefaction potential and cyclic shear resistance of silt. Research has primarily concentrated on the liquefaction potential of sands. However, due to recent evidence of liquefaction in finer grained material, research is now focusing more on silt and clay material.



## **3.2 RECONSTITUTION**

### **3.2.1 Introduction**

Obtaining intact samples of silts and sands is difficult, time consuming, and costly. Therefore, the fundamental understanding of silt behavior is primarily based on laboratory research on reconstituted specimens. Reconstitution allows a systematic study of the behavior as a function of material density, void ratio, fines content, grain size distribution, and other factors. However, predicting in situ behavior based on reconstituted specimens is uncertain. Therefore, in practice, the engineering properties have been derived from cone penetration resistance and standard penetration data. These derivations have empirical correlations that are partly based on the behavior of reconstituted laboratory test specimens (Hoeg *et al.*, 2000). The importance for good reconstituted test specimens then exists.

Several reconstituting techniques have been developed to prepare specimens for laboratory testing. Moist tamping (undercompaction) and slurry sedimentation are the most used reconstitution techniques. However, other methods such as air pluviation, wet pluviation, vibration, and proctor compaction are gaining popularity.

The most appropriate method of reconstitution has proven to be controversial. The argument is associated around the soil fabric produced by the various techniques. It can vary significantly between methods. In a few cases, where intact samples have been tested, the results have shown that there can be behavior differences between intact and reconstituted specimens. As a result, work has been conducted on the properties produced by different reconstitution techniques in comparison with intact information. Some of this information will be presented in this section.

### **3.2.2 Most Tamping (Undercompaction)**

For sands and silts with fines, segregation during specimen preparation using the resedimentation or slurry technique becomes a problem. The coarse grains will have a tendency to settle to the bottom and the fines will be at the top. Therefore, the procedure of moist tamping in layers, using the method of undercompaction, developed by Ladd (1977), can achieve a

homogeneous specimen of uniform density over its height. The method allows for quick specimen preparation of prescribed void ratio, grain size distribution, and fines content. A typical density profile in silts produced by undercompaction can be seen in Figure 3-1. The density was obtained in a triaxial specimen using a multisensor core logger. The consistent density using undercompaction is compared against the deviations in a block sample in the figure.

Hoeg *et al.* (2000) produced undercompacted silt triaxial specimens (5-10% clay, PI = 5%). Dry silt material was mixed with a small amount of water and stored overnight before being tamped into the equipment mold. The specimens were prepared in six separate equal volume lifts. The lower layers were undercompacted such that the compaction from successive layers would produce a specimen of approximately uniform density throughout when the preparation was finished. After the specimen was mounted in the triaxial cell, an internal underpressure of 10 kPa was applied, and the dimensions of the specimen were carefully measured. To ensure saturation, a back pressure of 980 kPa was applied prior to consolidation in all tests. The reconstituted samples were first flushed with CO<sub>2</sub> to facilitate saturation. The B value measured was 0.98 or higher in all cases. All reconstituted specimens had a void ratio around 0.73 after consolidation to an effective stress of 50 kPa.

Baxter *et al.* (2008) also reconstituted silt samples using the undercompacted moist tamping method. The material in the study was Providence silt with 6% clay and 5% sand. The method developed by Bradshaw and Baxter (2007) was repeated. The triaxial specimens are compacted in layers, while systematically increasing the compaction effort in each layer. They note that the molding water content used during tamping has a significant influence on the cyclic resistance. The strengths of samples tamped at an initial saturation (S) of about 55% matched strengths of both normally consolidated samples prepared from a slurry, as well as overconsolidated specimens trimmed from the block sample. At lower molding water contents, the cyclic resistance was higher due to a difference in fabric.

Some researchers have highlighted problems with the undercompaction technique. After reconstitution, carbon dioxide is percolated through the pore space. The saturation process that follows causes unknown volume change because the structure of the specimen tends to collapse. Freezing of the specimen may be required at the conclusion of the test in order to confidently measure void ratio prior to shear (Vaid & Sivathayalan, 1999). Vaid & Sivathayalan (1999)

conducted their study on sand but they state that specimen density can vary by as much as 10% over the length of the specimen. The specimen density is usually greatest at the bottom. Therefore, the selection of the correct undercompaction percentage is a critical component in the moist tamping method. The authors also state during saturation the specimen density can increase by up to 25 % under a confinement pressure of 20 kPa. The compressibility can be high in loose specimens due to the potentially collapsible fabric that is created using undercompaction.

There is agreement among researchers and geotechnical engineers that intact samples provide greater shear strengths than undercompacted samples. Hoeg *et al.* (2000) published a detailed review of this topic. The undercompacted triaxial specimens were made from the soil of the intact specimen just tested. They were prepared to give the same void ratio after consolidation as the accompanying intact specimen. The specimens were consolidated with  $K_o = 0.5$  to axial effective stresses of 50, 250, and 500 kPa. Table 3-1 and Figures 3-2 and 3-3 present the results of the tests. Table 3-1 provides the parameters for the triaxial specimens needed for interpretation of the figures. The results from the highest consolidation stresses are shown Figure 3-2. The intact specimens dilated and reached undrained strength values 2-3 times greater than the companion reconstituted specimens at high strains. This was primarily due to the reconstituted specimens contracting. The reconstituted specimens all showed peak strengths at very low strains and strain softening. Only one test regained strength at large strains. Figure 3-3 shows the results from the intermediate level of consolidation stress ( $\sigma'_{ac} = \sigma'_1 = 250$  kPa). The intact samples dilated strongly, while the reconstituted ones at the same void ratio contracted and showed very brittle behavior except for one test that dilated. For the lowest level of consolidation stress, both intact and reconstituted specimens showed dilative behavior. However, the pore pressure response and the stress strain curves are different. For Tests 7 and 8 the reconstituted specimen was stronger than the intact. However, in general, a clear pattern emerges with the intact specimens having greater strength than the companion reconstituted ones. The authors note a possible explanation could be due to the existence of layering in the intact specimens, which was clearly evident. The layering may have caused the increase in strength. However, the difference in stress strain response is likely due to a different soil fabric.

However, Fourie and Papageorgiou (2003) make a strong argument for the use of the undercompaction technique. The extensive flow failures witnessed in silts cannot occur unless the material that flows is predominantly contractive in nature. Undercompaction produces a structure that is susceptible to strain softening during undrained loading which shows that such behavior is possible.

### 3.2.3 Slurry Sedimentation

The method generally involves 1-D consolidation of soil slurry to a stress that is representative of its in situ state. The specimen produced can then be tested like an intact one. The technique has been used in two ways with silts. Some researchers prepare a specimen in a consolidation device or consolidometer. A predetermined mass of thoroughly mixed slurry is carefully spooned, poured or tremied into the consolidation device. The specimen is incrementally loaded to the desired stress, extruded, trimmed if required, and finally placed in the testing device. However, a major disadvantage with this technique is that the specimen can slump while it is being transferred from the consolidometer to the testing device. This is because the material does not have sufficient surface tension at the boundary to maintain the structure and shape. To overcome this problem, other researches prepare the specimen in a mold in the testing device, eliminating the transfer process. The slurry is carefully spooned into the specimen mold and consolidated to the desired volume. The later method was adopted by Hoeg *et al.* (2000) in their examination of different reconstitution techniques. The specimen was vertically compressed over a period of time until the desired specimen height was reached to produce a relative density of about 70%. The amount of water content in the slurry is very important and has a considerable influence on the uniformity of the samples (Izadi *et al.* (2008)). If the water content is too low, air voids can form within the specimen. If the water content is too high, stratification within the silt can be a problem.

Izadi *et al.* (2008) successfully reconstituted low plasticity silt with a liquid limit of 28%, plasticity index (PI) of 6%, and a clay fraction of 16.5% using the slurry technique. All samples were prepared from silt slurry with a water content of 44%. Initially a specimen was prepared in a large diameter consolidometer using radial consolidation and later triaxial specimens were

created using penetration of thin walled tubes. In addition, a series of specimens were prepared in a two inch diameter split mold using top loading only. The uniformity of the specimens were assessed by examination of the change in water contents along its length. It was observed that when specimens were consolidated using only top loading, a significant change in water content (approximately 3.5%) was found from top to bottom. The friction between the silt and the membrane causes a non uniform density distribution with the specimen being denser at the top. In order to solve this problem a vacuum pressure equal to the top consolidation pressure was applied to the bottom of the specimen. The method reduced the difference in water content throughout the sample to 1.4%.

A similar problem and solution was adopted by Hyde *et al.* (2006). The properties of the material were as follows: specific gravity  $G_s = 2.71$ ;  $LL = 24\%$ ;  $PL = 18\%$ ;  $PI = 6\%$  with 69.2% silt sized particles, 19% clay, and 11.8% sand. The properties classify the material as ML, low plasticity silt in the Unified Soil Classification System. Three different sample preparation methods were attempted in the process of seeking an ideal sample reconstitution technique to produce triaxial specimens. One dimensional consolidation was conducted by consolidating a slurry, mixed to twice the liquid limit, to a vertical stress of 80 kPa using a piston in a steel cylinder of a 105 mm internal diameter. Samples with an average moisture content of 21% were then extruded and sealed in three 38 mm diameter, 100 mm long thin walled sample tubes for later assembly in the triaxial cell. The silt prepared using the 1-D pre consolidation method had dilative shear characteristics similar to dense sand with a high compressive stiffness. The stiff response is thought to be due to the high 80 kPa 1-D consolidation pressure required to produce a sample that could be handled. The samples were found to be highly variable due to the friction in the consolidation tubes and sample disturbance during test setup. They were easily damaged by the top platen and membrane. It was felt that this method was not successful. A simple sedimentation technique was therefore developed for the preparation of looser liquefiable samples. In the sedimentation technique a membrane was fitted to the triaxial cell base supported by a split former. A de-aired slurry with a water content equal to 48% was poured into the mold and water was drawn through a porous disc at the base of the sample using a negative head of water of either 1m (10 kPa) or 4 m (40 kPa). The configuration of the system can be seen in Figure 3-4. The amount of slurry used depended on the negative head of water. Therefore, the height and initial void ratio of samples were easily controlled. The average moisture content was

found to be 24% for the 40 kPa samples and 26% for the 10 kPa ones, providing looser samples than the 1-D technique. However, it is unknown if the specimens remained saturated during this process.

Many other researchers have successfully re-sedimented silt slurry with no documented problems. Boulanger and Idriss (2006) reconstituted silt slurry using initial water contents of 2.1 to 2.3 times the liquid limit. The material was classified as low plasticity silt with LL equal to 26%, PI equal to 1%, having 19% sand and 5% clay. Fleming and Duncan (1990) reconstituted silt slurry in a one dimensional consolidometer with a 127mm internal diameter. The material was all less than 75  $\mu\text{m}$  with an average clay content of 23%. The samples were successfully extruded and trimmed to 35mm diameter triaxial specimens. Brandon *et al.* (2006) reconstituted low plasticity silt from a slurry in a batch consolidometer to vertical stresses of 159 kPa producing void ratio of approximately 0.73 to 0.77. They found scatter in the undrained unconsolidated triaxial tests even though the specimens were prepared very carefully, using identical procedures. They associated the errors to disturbance effects in transferring the material to the testing device and stated that disturbance is virtually impossible to avoid with low plasticity silts. DSS specimens were prepared by Wijewickreme and Sanin (2008) by placing Fraser River silt in the form of thick slurry in a specimen mold containing the reinforced rubber DSS membrane. Care was taken to reconstitute the specimens in several loading stages to avoid loss of material due to squeezing. The silt was low plastic with 10% sand, 10% clay, LL 31%, and PI 4%. The researchers found lower strengths in the reconstituted specimens when compared against intact specimens, despite a slightly lower void ratio in the reconstituted specimens. Yasuhara *et al.* (2003) reconstituted low plasticity silt with an initial water content of 200% in a large consolidation vessel 20cm in diameter and 30cm in height to a pressure of 68.6 kPa. Triaxial specimens with a diameter of 5 cm were later trimmed from the samples successfully.

Similar to their findings for undercompacted specimens versus intact ones, Dyvik and Hoeg (1999) found that re-sedimented slurry reconstitution produced specimens which yielded contractive stress strain behavior, very different in character from that of dilating intact specimens with a similar density.

### 3.2.4 Air and Water Pluviation

Air and water pluviation techniques are rarely used for reconstituting silts. The techniques have been developed on sands. Specimen preparation by air pluviation (AR) is carried out using a known mass of dry material that is poured from a minimum height into the specimen cavity with the aid of a funnel. Water pluviation (WP) is done in a very similar manner but the soil particles are deposited into water.

Hoeg *et al.* (2000) indicate in silts that water pluviation with some form of vibration is promising and should be studied further. They state the technique is likely to best represent the initial in situ sedimentation and produce a specimen similar to an undisturbed one. The stress-strain-strength results from slurry and water pluviated specimens in their study are shown with an undisturbed specimen in Figure 3-5. The void ratio  $e_c$  after consolidation to  $\sigma'_{ac}$  ( $\sigma'_1$ ) = 500 kPa and  $\sigma'_{rc}$  ( $\sigma'_3$ ) = 250 kPa are shown for each specimen. The slurry specimen gave a peak strength of 155 kPa at 0.1% axial strain; it strain weakened to a quasi steady state strength of 130 kPa and then climbed to a steady state strength of approximately 230 kPa. The water pluviated specimen showed a peak strength of 175 kPa at 0.3% axial strain, insignificant strain weakening, and then strain hardening toward steady state strength of approximately 320 kPa.

Similar to undercompaction and slurry sedimentation, there are problems documented with the water pluviation technique. The method can result in segregation when used with silty or well graded sands and as a result laboratory studies using the water pluviation technique have been confined to mainly clean sands (Kuerbis *et al.*, 1988). Chillarige *et al.* (1997) prepared soil specimens using undercompaction and water pluviation techniques. They observed that water pluviation inhibited the formation of a loose structure by maintaining fine particles in suspension that resulted in slightly denser specimens. The water pluviation method develops upward turbulence of water that inhibits the formation of a metastable structure. The fine particles tend to form thin lenses in the water pluviated specimens, resulting in non uniform specimens. Vaughan (1997) provided an investigation on silty fine sand that was pluviated into water containing various amounts of colloidal clay particles. The amount of colloidal clay varied from 0 to 0.4% of the dry solids. The void ratio achieved in these tests varied from a value consistent with a relative density of about 50% with initially clear water to a value significantly less than 0%

relative density for 0.4% fine particles in the water. The study highlights some of the problems that could occur when water pluviating silts with a clay content.

### 3.2.5 Fabric

A difference between the intact and reconstituted specimens can be attributed to many of the following properties:

- The level of initial confining and shear stresses.
- Inclination of the principal stresses in relation to the deposition direction prior to undrained shear.
- Rotation of principle stress directions.
- The magnitude of  $\sigma_2$  relative to  $\sigma_1$  and  $\sigma_3$ .

Abundant experimental evidence of these properties has been reported by Vaid and Sivathayalan (1999). The difference in the shear response between intact and reconstituted specimens can also be attributed to other considerations such as aging effects or cementation. This structure cannot be recreated using reconstitution. If testing were undertaken at consolidation stresses significantly higher than the in situ preconsolidation stress,  $\sigma'_p$ , the shear response difference between the specimens will be less (Wijewickreme and Sanin, 2008). This is possibly due to the higher consolidation stresses destroying some of the cementation and aging effects.

However, despite these explanations, the primary reason for the differences in stress strain behavior is most probably due to the differences in soil fabric between the intact and reconstituted specimens. The fabric of the field specimens is determined by the deposition process as well as creep effects in situ (Hoeg *et al.* 2000). The soil fabric is characterized by the orientation and arrangement of the individual soil grains and the contact planes between the grains. Although, the total void ratio is the same, the structural configuration of particle assembly and the sizes and shapes of the individual voids may well be different in the intact and reconstituted specimens (Hoeg *et al.*, 2000).



There is no best reconstitution technique for representing the field conditions. Hoeg *et al.* (2000) favor the wet pluviation technique but state that more work is required to determine its appropriateness for silts. Their view is supported by Vaid and Sivathayalan (1999) when they conducted a similar analysis on sands. Figure 3-6 shows the one dimensional compressibility of the loosest sand deposited by moist tamping and pluviation from their study. The compressibility of the moist tamped sand is very high compared with that of air and water pluviated sand. This could be attributed to the potentially collapsible fabric that ensues upon moist tamping. The undrained stress strain response under a confining stress  $\sigma'_{vc} = 200$  kPa is show in Figure 3-7. The moist tamped sand was noted to be very contractive compared to the air pluviated sand which also contracted but showed only a marginal drop in shear strength beyond peak. The wet pluviated sand, in contrast, does not even exhibit any strain softening and behaves dilative. Figure 3-8 shows the stress path difference between moist tamped and water pluviated sand at the same consolidation stress with a similar void ratio. The difference between contractive and dilative behavior is highlighted. However, it should be again noted that this behavior is for sand.

However, there are still uncertainties with the wet pluviation method and many authors (Kuerbis *et al.*, 1988, Chillarige *et al.*, 1997, Fourie and Papageorgiou, 2003) believe that it is not superior to undercompaction or resedimentation. In cyclic triaxial tests for three different sands, Ladd (1977) found that soil samples prepared by wet tamping could have a cyclic strength as much as 100% greater than those prepared by dry deposition. Mulilis *et al.*, (1977) noted that samples prepared by pluviation through water had a cyclic strength 10% greater than samples prepared by pluviation through air. However, they demonstrated that each preparation method produced a sample with a slightly different soil fabric.

Undercompacted specimens produce very similar behavior to resedimented specimens. Therefore, no apparent superiority exists between the two. In all techniques, reconstituted specimens will give lower strength values than intact counterparts, making the techniques conservative for design. However, the difference in stress strain strength behavior between reconstituted and intact specimens should be emphasized and difficulties could occur in modeling in situ behavior based on reconstituted specimens. Due to the costs and difficulties associated with field “intact sampling” there is still a tendency to use reconstituted specimens for assessing the shear response in silts.

## **3.3 SAMPLING**

### **3.3.1 Introduction**

Obtaining intact samples of non plastic silts for triaxial and consolidation testing is very difficult. Unlike clays, strong cohesive bonds do not hold the sample together as it is being transferred to a laboratory. The sampling device is also known to cause significant disturbance as it is cutting the material in the ground. The disturbance of silt samples highly influences their shear strength and behavior. Like sands, it is therefore common to rely on reconstituted laboratory specimens or field techniques such as the standard penetration test or cone penetration test to provide material properties. Some researchers state that it is impossible to obtain undisturbed samples of loose, non plastic silt using conventional thin walled piston samplers. This view is taken by Baxter *et al.* (2008), stating only block samples can be used for undisturbed testing. However, many researchers have performed laboratory tests on undisturbed tube samples. This section of the chapter will give a brief review of some sampling techniques used by researchers on silts. The benefits and disadvantages of various samplers will be discussed.

### **3.3.2 Sampling Techniques**

Long (2007) conducted a detailed investigation of various sampling techniques on Irish estuarine silts. Two different sites were used in the study, one in Sligo, and the other in Dunkettle, Co. Cork (70 km east of Skibbereen). The Sligo material is low plastic with average clay, silt, and sand contents of 6, 38, and 56%. The Dunkettle site has a silt content much higher than the sand, being on average 65 to 30%. Original site investigation for intact samples were mostly by means of conventional open drive U100 tubes (U4 tubes), as shown in Figure 3-9. Frequently the samples were lost during retrieval from the borehole. Efforts were subsequently made to retrieve samples by screwing two U100 tubes together to retrieve “double U 100 samples”. Finally it was decided to investigate the effects of sampling on silt by several techniques. To provide baseline data, samples were taken at both sites using the ELE 100mm diameter fixed piston sampler. The device is commonly used in Ireland and the UK to obtain high quality samples of soft compressible material. The tubes had a standard cutting edge angle

of  $30^\circ$  at the Sligo site. This angle was sharpened to  $5^\circ$  for the Dunkettle site. In addition, sampling was carried out using the Norwegian Geotechnical Institute (NGI) 95mm diameter sampler, which is known to yield high quality samples of soft clays. Finally, at Sligo, samples were obtained using the “double U100” technique described above and at Dunkettle continuous samples were recorded using the MOSTAP process.

With the exception of the continuous samples, all of the samples were recovered by the same drilling crew from the base of a borehole, which was 200mm in diameter. The borehole was advanced using shell and auger drilling and was maintained full of water. A summary of the dimensions and features of samplers is given in Table 3-2. Table 3-3 provides a comparison of average densities ( $\rho$ ) and water contents ( $w$ ) for each sampler type. For Sligo, values for the NGI 95mm, double U100 and U100 samples are similar. The ELE  $30^\circ$  sampler gives  $\rho$  values on average 3% lower and  $w$  on average 7% higher than those of the other samplers. For Dunkettle, the MOSTAP data show a clear difference from the others. Density and water contents are on average 25% higher and 4% lower. The poor area ratio of the MOSTAP sampler is said to have induced significant densification. Figure 3-10 shows a stress strain plot from an incremental oedometer test at the Sligo site. It is difficult to determine the preconsolidation stress based on the results. However, the curve from the NGI 95mm sampler is particularly flat, indicating a higher stiffness than the other samples, suggesting that sampling densified the material. However, the method of testing the 9.66cm diameter intact sample in the 10cm diameter oedometer ring is not stated and there were no similar deviations in the compressibility tests at the Dunkettle site, as shown in Figure 3-11. The paper concludes that sampling, by all techniques used, densified the material, resulting in measured effective shear strength values larger than would be encountered in situ. The results support the necessity to apply a generous safety factor when using triaxial effective strength parameters in design.

Long *et al.* (2010) produced similar results from a study on the engineering characterization of Norwegian glaciomarine silt. Sampling was conducted by means of standard Norwegian 54 mm steel and 54 mm composite samplers. The dimensions and features of the samplers can be seen in Table 3-4. For an exact description of their use, see Long *et al.* (2010). In order to prevent slumping and handling during the triaxial setup, the specimens were extruded directly into a rubber membrane/membrane stretcher in the triaxial device. An examination of  $\rho$ ,

and  $w$ , found that the composite liner had a lower  $w$  and higher  $\rho$  indicating that the less favorable dimensions of the composite sampler produced more densification. The authors state that block sampling would produce high quality samples which would truly indicate the properties of the material. However, extraction is problematic and very expensive. They recommend larger sample tubes, approximately 75mm in diameter, with a very sharp cutting edge for silt sampling.

Such a sampler was used by Wijewickreme and Sanin (2008). Samples of upper natural silt from Fraser River Delta, Canada were obtained using fixed piston tube sampling. The sampler was a specially fabricated stainless steel, thin walled tube with no inside clearance. It had a 75 mm internal diameter, a  $5^\circ$  cutting shoe and a wall thickness of 1.5mm. They indicate the use of these thin, sharp edged tubes offers an acceptable method to obtain good quality specimens of low plasticity silt for laboratory testing. No disturbance problems are indicated in their work.

Similarly, Fleming and Duncan (1988) used a thin walled sampler to recover 70mm diameter undisturbed samples from an offshore site in Alaska. They refer to the material as intact samples. They conducted a series of tests on the intact material before reconstituting and testing it again.

Hoeg *et al.* (2000) obtained samples from a Swedish site by the Swedish Geotechnical Institute piston sampler with an interior plastic lining and inner diameter of 50mm. Most of the sampling attempts were successful with generally full recovery when avoiding all forms of vibration. However, subsequent attempts to take 95 mm diameter NGI piston samples were not successful. The Swedish piston samples were subjected to some disturbance due to the material displacement at the cutting edge during sampling tube penetration. The void ratio of the samples are said to have decreased somewhat during sampling, transportation, and subsequent extrusion.

Despite the failure of the 95 mm NGI sampler in Sweden, Brandon *et al.*, (2006) successfully used a larger diameter 127 mm diameter Shelby tube from depths of 13.7m to 15.2m for sampling low plasticity Yazoo silt from the lower Mississippi valley. The silt had a clay content ranging between 13 and 16% and a sand content between 3 and 18%.

Ladd *et al.* (1986) used 75mm pushed tube sampling, 63.5mm pushed tube sampling, and 75mm special continuous fixed piston sampling adjacent to Mukluk Island in Arctic silt. Fixed piston sampling yielded about 95% recovery versus only about 50% for the pushed samples.

### 3.4 CONSOLIDATION PROPERTIES

In comparison to other engineering properties, very little consolidation information exists on silts. The exact reason for this is unknown, but it is likely due to geotechnical engineers relying heavily on empirical interpretations from in situ tests such as the standard penetration test to give guidance on the ground conditions. However, a few researchers have published data on consolidation. This section will present the information that is available.

Brandon *et al.*, (2006) conducted two consolidation tests on samples of intact silt from approximately the same depth (14m deep). Silt 1 had a clay, silt, sand composition of 16, 82, and 3%, while silt 2 had a makeup of 13, 70, and 18%. Both had a specific gravity of 2.655 and were classified as low plasticity silt. The consolidation curves are shown in Figure 3-12. Neither curve shows a definite break at the maximum past preconsolidation pressure,  $\sigma'_p$ . A best estimate of 250 kPa was applied by the authors. The compression index,  $C_c$ , was found to range between 0.12 to 0.19, ( $CR_{ave} \approx 0.09$ ) and the recompression index between 0.012 and 0.021 ( $RR_{ave} \approx 0.009$ ). The in situ vertical stress was estimated at about 138 kPa. Therefore it was concluded that the soil was overconsolidated in situ, with an overconsolidation ratio OCR in the range of 1.5-2.0.

Figure 3-13 shows two compression curves: one is typical of a soft high natural water content layer that has a well defined  $\sigma'_p$  and virgin compression ratio ( $CR = C_c/(1+e_o)$ ); the other is more representative of a low plasticity silt where it is difficult to define these parameters. For this particular area in Harrison Bay, CR was found to range between 0.14 and 0.15 and the coefficient of consolidation,  $c_v$ , was between 0.03 and 0.11 m<sup>2</sup>/day (Ladd *et al.* 1985). The soft high natural water content specimen was tested at various temperatures using unload reload cycles. The properties of the specimens are given on the right hand side of the figure. The low plasticity silt is in the left column and the soft high natural water content layer is in the right column.

The incremental oedometer compression curves from Long (2007) on Irish estuarine silts have already been presented in Figure 3-10 and 3-11. In addition to these, the results of constant rate of strain (CRS) tests are shown in Figure 3-14. The CRS tests compare well with the incremental oedometer test (test MSLS5) shown in the figure. The compression CRS curves show that strain rate had no effect on the stress strain response, with good repeatability regardless of strain rate. However, the stress strain curves produced in this study appear to be much steeper than that produced by other researchers. Greater strain and deformation is apparent at comparable stresses ( $CR > 0.21$  in the silt from Sligo). It also appears that the preconsolidation pressure could easily be determined by the Casagrande or strain energy method, which is unusual for sands and silts. The author does not give a possible explanation for this trend.

Typical incremental oedometer curves in low plasticity silt are shown in Figure 3-15. They are produced by Long *et al.* (2010) in their study of Norwegian glaciomarine silt. The three graphs present three different locations in Western Norway. Figure 3-15 (a) presents the findings from Norwegian upper Os silt using three different samplers, Figure 3-15 (b) shows lower OS clayey silt results using different samplers, and Figure 3-15 (c) presents the Norwegian E39 silt results from three different depths. All compression curves are very flat with little strain or change in void ratio. They do not show a clear  $\sigma'_p$  and they are generally non linear throughout loading. Despite stress levels up to almost 2000 kPa the stress strain curves show no sign of convergence and this indicates that extremely large stresses would be required to bring the curves together.

## **3.5 STRESS-STRAIN-STRENGTH PROPERTIES**

### **3.5.1 Introduction**

This section of the chapter will review existing stress-strain-strength information on both intact and reconstituted silt material. The properties have been derived from undrained unconsolidated (UU) triaxial compression tests, isotropically consolidated undrained triaxial compression and extension tests (CIUC and CIUE), anisotropically consolidated undrained triaxial compression and extension tests (CAUC and CAUE),  $K_0$  consolidated undrained triaxial

compression and extension tests (CK<sub>0</sub>UC and CK<sub>0</sub>UE) , and K<sub>0</sub> consolidated direct simple shear tests (CK<sub>0</sub>DSS).

### 3.5.2 Shear strength from triaxial tests – Failure criterion

The shear strength determination from triaxial tests on silts can be very difficult due to their tendency to dilate during shear. The topic has been studied extensively by Brandon *et al.* (2006) for silts from the Lower Mississippi valley. The type of failure criteria appropriate for a given case depends on: (1) the type of triaxial test (e.g. UU, CIUC, CK<sub>0</sub>UC, CIDC); (2) the strength parameters to be determined (effective stress or total stress); and (3) the stress-strain-volume change behavior of the soil. Some possibilities for the determination of undrained shear strength,  $S_u$ , for silt are as follows:

- Peak deviator stress regardless of strain,  $(\sigma_1 - \sigma_3)_{\max}$
- Shear stress at some limiting strain
- Peak principle stress ratio,  $(\sigma'_1 / \sigma'_3)_{\max}$
- Peak pore pressure,  $u_{\max}$
- Reaching Mohr-Coulomb line (or also known as  $K_f$  line, referred to by Brandon *et al.*, 2006)
- Pore pressure parameter  $A = 0$  or  $\Delta u = 0$

Figure 3-16 shows how the different failure criteria apply to a triaxial test. Peak deviator stress and limiting strain are applicable to any type of triaxial test. However, their use as failure criterion in dilative silts results in wide scatter and therefore does not provide useful guidance. The other criteria apply to only consolidated drained or undrained tests, where pore pressures and effective stresses are known.

The use of peak principle stress ratio as a failure criteria also results in wide scatter because the stress path tracks very closely along the effective stress failure envelope and the exact value of deviator stress at which the principle stress is largest is nearly a random result, i.e., the value of principle stress ratio is essentially constant over a wide range of deviator stresses

(Brandon *et al.*, 2006). Reaching the Mohr-Coulomb line ( $K_f$  line) has similar disadvantages because the stress path follows the failure line over such a wide range of deviator stresses.

Figure 3-16 shows that the peak pore pressure is very conservative. The effective stresses have not reached the effective stress strength line at a pore pressure maximum.

Use of  $A = 0$  or  $\Delta u = 0$  as a failure criterion ensures that reliance is not placed on strength that results from negative changes in pore pressure (Brandon *et al.*, 2006). Brandon *et al.*, 2006 showed that it results in undrained shear strengths with little scatter. However, for silts that do not dilate as strongly as the Mississippi Valley low plasticity silts, values of  $A = 0$  and  $\Delta u = 0$  will not be reached. In such a case, the maximum deviator stress criterion is the most appropriate. If the  $A$  parameter or  $\Delta u$  criteria are used, higher values will need to be selected as an appropriate failure point.

### 3.5.3 Undrained Compression tests (UU)

Triaxial tests are widely used to determine the stress-strain characteristics of soils. The versatility of the test allows for soil samples to be subjected to a wide variety of stress conditions. The unconsolidated undrained triaxial test (UU test) is widely used as a quick, economical means of obtaining a measure of the undrained shear strength of soils. In clays, UU tests can measure of the shear strength of the soils in the field. However, sample disturbance can cause a significant distortion of the results. The dilatant nature of silt can also cause resulting cavitation and the degree of saturation can drop below 100% (Brandon *et al.*, 2006). However, more importantly, the stress path cannot climb up the failure envelope.

Three UU tests on intact Yazoo silt (properties given in Section 3.4) showing the deviator stress strain curves are presented in Figure 3-17. Applying the maximum deviator stress criteria produces undrained shear strengths that range from 25 to 55 kPa (Brandon *et al.* 2006). Based on the best estimate of in situ effective stress at 138 kPa, the values of  $S_u/p = S_u/\sigma'_v$  range from 0.18 to 0.4, with an average of about 0.25.

Brandon *et al.* (2006) also conducted five UU tests on reconstituted specimens of Yazoo silt consolidated from slurry to a vertical effective stress of 159 kPa in a batch consolidometer. In



addition, four UU tests were performed on LMVD silt consolidated from slurry to a vertical effective stress of 172 kPa in the batch consolidometer. The LMVD silt has very similar properties to the Yazoo silt. Figure 3-18 shows the stress strain response from the tests. The scatter is associated with disturbance effects. The maximum deviator stress occurs between 15 and 21% strain. Values of  $S_u/p$  for the tests vary from 0.3 to 0.7 if the maximum deviator stress is used and 0.2 to 0.4 if limiting strain equal to 10% is used as the failure criteria. The higher strengths for reconstituted specimens are thought to be due to the lower void ratio compared with the intact specimen (reconstituted  $e = 0.73-0.77$  against intact  $e = 0.86-0.95$ )

Similar behavior is shown in Figure 3-19 from a UU test on reconstituted Alaskan silt. The specimen was consolidated in a mold and then carefully trimmed and prepared for triaxial testing. The silt exhibits dilative behavior throughout undrained shear and therefore no unique undrained shear strength exists. A stress at 15% strain was defined as its strength (Fleming and Duncan, 1990). At an overconsolidation ratio of 1,  $S_u/\sigma'_{1c}$  ranges from 0.25-0.3 (Fleming and Duncan, 1990).

#### **3.5.4 Isotropically Consolidated Undrained triaxial tests**

CIUC tests were conducted on intact and reconstituted specimens of Yazoo silt and on remolded specimens of LMVD silt by Brandon *et al.* (2006). Tests were conducted in accordance with ASTM D4767. Both normally consolidated (NC) and overconsolidated (OC) tests were conducted. All specimens were back pressure saturated to a minimum pressure of 550 kPa. The specimens were sheared at strain rates from 0.05 to 0.1%/min. The stress strain curves and stress paths for six tests on intact Yazoo silt are presented in Figure 3-20. Many tests were terminated at small strains due to the specimens dilating very strongly, resulting in large reductions in pore pressures and increases in deviator stresses that threatened to exceed the capacity of the load cell. The behavior is characteristic of low plasticity silts that dilate strongly but do not cavitate. Values of  $S_u/p$  from the CIUC tests are summarized in Table 3-5. It can be seen that the results for the maximum deviator stress, maximum principle stress ratio, reaching the Mohr Coulomb line, and reaching 10% strain vary over a wide range. Values of  $S_u/p$  determined using the maximum pore pressure are very consistent. However, as mentioned in Section 3.5.2, they are

considered conservative. Brandon *et al.* (2006) have highlighted the A parameter = 0 as the best failure criteria. Although they note that the results are very high compared to most clays.

Table 3-6 displays friction angle,  $\phi'$ , and the average strain at failure,  $\epsilon_f$ , from the tests. All the failure criteria except maximum pore pressure result in values of  $\phi'$  from 34 to 39°, producing an average  $\phi'$  of about 36°.

A series of CIUC and CIUE tests were conducted on reconstituted samples of low plasticity silt by Hyde *et al.* (2006). The samples were consolidated to effective confining pressures of 100, 300, and 600 kPa, and sheared at an axial strain rate of 0.1% per minute. Stress strain curves are presented in Figure 3-21. There is a point of flexure in compression followed by hardening and then strain softening. An initial peak in extension at very low strains (0.2-0.5%) is followed by hardening behavior. Failure in extension and compression is defined by a peak deviator stress at strains of 8.7 to 11%. Then there is a decrease in deviator stress after the failure with a tendency to approach a constant critical state value at large strains.

The corresponding stress plot is shown in Figure 3-22. Initial phase transformation points (IPT) are indicated where the beginning of contractive behavior occurs. These points are related to the initial peak points in the stress strain curve. Contractive behavior changes to dilative at the phase transformation (PT) point. The dilative behavior continues until an ultimate peak deviator stress was reached. The pore pressures then increase again and  $q$  and  $p'$  decrease.

The effect of disturbance on CIUC silt test specimens is shown in Figure 3-23. Some specimens were intentionally remolded and the stress strain and pore pressure behavior are different as a result. The study used a shear stress at a limiting strain of 15% as the failure criteria and found a 25 to 40% decrease in strength in the remolded specimens (Fleming and Duncan, 1990).  $S_u/\sigma'_1$  values were found to range between 0.85 and 1 for normally consolidated specimens (Fleming and Duncan, 1990).

### 3.5.5 Anisotropically Consolidated Undrained triaxial tests

Anisotropic consolidation has been used by a few researchers to describe the behavior of low plasticity silt. Hoeg *et al.* (2000), Fleming and Duncan (1990), and Long *et al.* (2007) have all used  $K_0 = 0.5$  for anisotropic consolidation.

Some of the results from Hoeg *et al.* (2000) have already been discussed in Section 3.2.2 and were presented in Figure 3-2 and 3-3. All triaxial tests were sheared at a strain rate of 2% per hour to a strain limit of approximately 20%. In addition, the stress paths for three undisturbed and five reconstituted CAUC tests are presented in Figure 3-24. The Figure also provides supporting information on each test. The reconstituted specimens had a tendency to contract while the intact specimens all dilated.

The stress strain and stress path characteristics of intact Norwegian glaciomarine silt are shown in Figure 3-25. In contrast to the very dilative nature of intact silt from Hoeg *et al.* (2000), the Norwegian silt shows contraction and strain softening in some cases. Therefore, the highly dilative behavior could be associated with densification during sampling and if careful sampling takes place contractive behavior can also occur. Fleming and Duncan (1990) found  $S_u/\sigma'_1 = 0.78$  for normally consolidated material. However, similar to their CIUC tests, they used the 15% strain value as the criterion, which provides very high values.

### 3.5.6 $K_0$ Consolidated Undrained triaxial tests

Almost no information exists on  $K_0$  consolidation triaxial testing. The sophisticated equipment required for testing may be one of the reasons for the shortage of information. Ladd *et al.* (1985) performed  $CK_0UC$  and  $CK_0UE$  tests on arctic silt in addition to CIUC and  $CK_0DSS$  tests. The samples used in the tests had significantly different properties due to natural variability. Table 3-7 provides the properties for the material and Figure 3-26 shows normalized stress strain data from the CIUC and  $CK_0U$  triaxial tests, where  $q = 0.5(\sigma_v - \sigma_h)$  and  $p' = 0.5(\sigma'_v + \sigma'_h)$ . Only slightly dilative behavior is shown in the CIUC tests. The low water content  $CK_0UE$  tests exhibit greater dilatancy. Little difference was found between CIUC and  $CK_0U$  triaxial compression tests with  $q_p/\sigma'_{vc}$  ranging from 0.32 to 0.39 and  $\phi' = 33 \pm 3^\circ$ .  $K_0$  was found to vary

between 0.84 and 0.59, which is unexpectedly high and this might explain the small deviation in strength results between consolidation techniques.

### 3.5.7 $K_o$ Consolidated Undrained Direct Simple Shear tests ( $CK_o$ DSS)

The direct simple shear apparatus provides an easy method for measuring the shear strength of the material. However, little information exists on its use with silts. Figure 3-27 presents plots from a  $CK_o$ DSS testing program, where  $\tau_h$  = applied horizontal shear stress and  $\sigma'_v$  = vertical effective stress that was varied to maintain constant volume throughout the test. Tests 1, 2, 3, and 4 show very different behaviors compared to CIUC test data. In general, the behavior can be normalized with  $\epsilon_f = 11.8\% \pm 1.3$  SD,  $\tau_h/\sigma'_{vc} = 0.245 \pm 0.01$  SD, and  $\sigma'_v/\sigma'_{vc} = 0.64 \pm 0.05$  SD. Effective stress always decreases during shear and there is very significant strain softening with  $\tau_h/\sigma'_{vc} = 0.13$  at  $\epsilon = 30\%$ . The two CAUDSS tests can be ignored for the purposes of this chapter.

In contrast a more dilative response for  $CK_o$ DSS tests is shown in Figure 3-28. The stress path and stress strain response from intact and reconstituted specimens of Fraser River silt are presented. The intact specimen initially deforms in a contractive manner followed by a dilative response that commences at around 5% shear strain. The specimen exhibits increasing shear resistance with increasing strain. Initially the behavior of the intact and reconstituted specimens is almost identical. However, the reconstituted specimen then exhibits a more contractive response than that observed for the intact specimen. The reconstituted specimen experiences a mild strain softening response before regaining its shear resistance and in general the weaker stress strain response is shown by the reconstituted specimen. Using a limiting strain of 15% failure criteria, the intact  $\tau_h/\sigma'_{vc}$  is approximately equal to 0.29 and the reconstituted  $\tau_h/\sigma'_{vc}$  is approximately equal to 0.2.

### 3.5.8 Overconsolidation ratio and normalized behavior

Clay samples with the same overconsolidation ratio but different consolidation stress, exhibit very similar stress strain characteristics when normalized with respect to the vertical

consolidation stress (Ladd and Foot, 1974). These clays are said to exhibit normalized behavior. Once its established that normalized behavior occurs, a testing program can be developed to determine the relationship between the normalized stress  $S_u/\sigma'_{1c}$  and the overconsolidation ratio (OCR). The relationship can be used to calculate strengths at any location in the ground based on the knowledge of the overburden stress and preconsolidation pressure (Fleming and Duncan, 1990). However, the applicability of this concept to silt is not as well known.

Yasuhara *et al.* (2003) performed CIUC triaxial tests on normally consolidated (OCR = 1:  $p'_c = 196$  and  $392$  kPa) and overconsolidated silt specimens (OCR = 2, 4, 10:  $p'_c = 196, 98,$  and  $39.2$  kPa). The deviator stress and stress ratio versus axial strain relations, and the effective stress path in  $p'$ -  $q$  space are shown in Figure 3-29 and 3-30. The results in Figure 3-29 (b) and 3-30 (b) demonstrate that the boundary between the contractive and dilative behavior is around OCR = 4 and that normalizing the results provides an adequate means of evaluating in situ strength.

Table 3-8 shows measured normalized shear strengths at various overconsolidation ratios for UU, CIUC, and CAUC tests. Fleming and Duncan (1990) found that the normalized strength varied with consolidation pressure. The higher the consolidation pressure, the lower was the normalized strength. However, the variations are relatively small and they are believed to be due to sample preparation and reconsolidation effects. Similar to Yasuhara *et al.* (2003), they found normalizing test results would provide a fully adequate means of evaluating in situ strength. Using this assumption, the relationship between the normalized strength ( $S_u/\sigma'_{1c}$ ) and the overconsolidation ratio (OCR) for the Alaskan silt specimens can be seen in Figure 3-31. The figure shows an increasing  $S_u/\sigma'_{vc}$  with a higher OCR.

Data from Fleming and Duncan (1990) are compared with Ladd *et al.* (1985) and Wang *et al.* (1982) in Table 3-9. It can be seen that there is a considerable variation among the measured values of normalized strength. Fleming and Duncan (1990) conclude that values of normalized strength vary considerably from one silt to another, and would need to be evaluated specifically for each new silt deposit.

### 3.6 LIQUEFACTION AND CYCLIC SHEAR RESISTANCE

The determination of the liquefaction potential of low plasticity silts has been a challenge in geotechnical engineering. Liquefaction is generally associated with sands, loss of strength, and large deformations (Izadi *et al.*, 2008). Recent evidence of ground failure during strong earthquakes has indicated that certain saturated fine grained soils can be susceptible to earthquake induced softening and strength reduction as much as clean sands (Wijewickreme and Sanin, 2008).

Prakash and Puri (2003) describe the cyclic shear stresses that develop in a soil deposit as a result of the passage of seismic waves. They describe the process as follows: The cyclic stresses may result in progressive build up of pore water in certain types of soils in a saturated state. Cohesionless soils of loose and medium density have a tendency to compact under vibrations leading to decrease in inter granular space. This tendency for volume decrease gives rise to increase in pore water pressure. The progressive build up of pore water pressure may eventually become large enough to cause complete loss of shear resistance accompanied by large deformations and failure. The evaluation of liquefaction potential of soils at any site requires the combination and interaction of two sets of parameters; namely the cyclic loads due to vibration and soil properties which describe the soil resistance under these loads.

Earlier studies on the liquefaction phenomenon were on sands and cohesionless material. They were extensively studied under seismic loading conditions. However, increasing reports of liquefaction in fine material with clay fractions has redirected some of the latest research. Liquefaction is now known to occur in both non plastic and plastic fine grained material.

Several criteria have been suggested to assess the liquefaction potential of silts. One of the first of these was the Chinese Criteria (Wijewickreme and Sanin, 2008), which has been modified several times. However, the ground motion characteristics triggering liquefaction are not specified in this criteria and any soil will be considered susceptible to liquefaction irrespective of the level of ground shaking. It has also been recognized that the plasticity of soil plays an important role in its liquefaction potential. Figure 3-32 shows a typical example of this study. The cyclic stress ratio ( $CSR = \tau_{av}/S_u$ ) is lowest at a plasticity index (PI) of 5%. "N" in the figure corresponds to the number of loading cycles until failure. Many more failure criteria have

been developed based on the grain size distribution and Atterberg limits. In recent times, researchers have focused more heavily on the dynamic properties of silts. The CSR versus the number of loading cycles to failure and the CSR versus the shear wave velocity are being studied extensively. Wijewickreme and Sanin (2008), Izadi *et al.* (2008), Prakash and Puri (2003), Baxter *et al.* (2008), Boulanger and Idriss (2006), Hyde *et al.*, (2006), and Hyde *et al.* (2007) have all produced recent information on the liquefaction potential and cyclic shear resistance of silts.

Test Pair (1)	Test (2)	Distance from crest (m) (3)	Sample preparation (4)	Initial Parameters			After Consolidation						
				Water content (%) (5)	Dry density (kN/m <sup>3</sup> ) (6)	Void ratio (7)	$\sigma'_{ac}$ (kPa) (8)	$\sigma'_{re}$ (kPa) (9)	$\epsilon_{vol}$ (%) (10)	Dry density (kN/m <sup>3</sup> ) (11)	Void ratio (12)	$G_{max}$ (MPa) (13)	$\frac{G_{max,rec}}{G_{max,und}}$ (14)
I	1	40	U	28.5	15.03	0.78	50.0	25.0	0.14	15.05	0.77	36.3	1.07
	2	40	MT	27.6	15.25	0.75	50.0	25.0	0.16	15.27	0.75	38.8	
II	3	40	U	26.8	15.44	0.73	250.1	125.0	0.81	15.57	0.72	126.4	0.75
	4	40	MT	27.2	15.35	0.74	250.3	125.1	0.57	15.44	0.73	95.2	
III	5	40	U	28.2	15.10	0.77	500.0	250.0	1.51	15.33	0.74	162.5	0.79
	6	40	MT	28.6	15.01	0.78	500.0	250.0	2.73	15.43	0.73	128.2	
IV	7	120	U	26.4	15.54	0.72	50.0	25.0	0.17	15.57	0.72	41.4	1.00
	8	120	MT	26.3	15.56	0.72	50.1	25.0	0.04	15.57	0.72	41.2	
V	9	120	U	27.6	15.24	0.75	249.9	125.1	1.15	15.42	0.73	120.1	0.71
	10	120	MT	28.3	15.09	0.77	249.9	125.0	2.05	15.41	0.73	84.7	
VI	11	120	U	29.9	14.72	0.81	500.3	250.0	2.49	15.10	0.77	164.4	0.83
	12	120	MT	30.1	14.68	0.82	499.2	249.8	2.81	15.10	0.77	136.9	
VII	13	200	U	27.4	15.33	0.75	50.0	25.0	0.55	15.41	0.74	(74.3)	(0.55)
	14	200	MT	27.5	15.31	0.75	49.9	25.0	0.18	15.34	0.75	40.6	
VIII	15	200	U	28.5	15.06	0.78	249.9	125.0	2.30	15.41	0.74	99.2	0.81
	16	200	MT	28.5	15.06	0.78	249.7	125.0	3.25	15.57	0.72	79.9	
IX	17	200	U	27.7	15.25	0.76	499.6	250.0	3.38	15.78	0.70	172.3	0.77
	18	200	MT	27.7	15.25	0.76	499.6	250.1	5.11	16.07	0.67	133.1	

Note: Values in parentheses represent uncertain reading. Each moist tamped (MT) specimen was reconstituted with material from undisturbed (U) specimen directly above it in this table.  $G_c = 2.72$  for material 40 m and 120 m from crest,  $G_c = 2.73$  for material 200 m from crest.

Table 3-1: Parameters for triaxial specimens (Hoeg *et al.* 2000)

Sampler	Length (cm)	$D_c$ (cm)	$D_w$ (cm)	$D_s$ (cm)	Area ratio (%)	Cutting edge angle (deg)	Inside clearance (%)
ELE 100	100	10.14	10.48	10.14	6.8	30 (Sligo) 5 (Dunkettle)	0
NGI 95	100	9.63	10.16	9.66	11	9	0.3
Double U100	90	10.14	11.44	10.14	27	60 and 15 (Fig. 2b)	0
MOSTAP <sup>u</sup>	200	6.5	9.3	6.5	105	15	0

$D_c$ , inside diameter of cutting shoe;  $D_w$ , outside diameter of cutting shoe;  $D_s$ , inside diameter of sampling tube; area ratio =  $(D_w^2 - D_c^2)/D_c^2$ ; inside clearance =  $(D_s - D_c)/D_c$ .

Table 3-2: Summary of dimensions and features of samplers (Long, 2007)

	ELE 30°	ELE 5°	NGI 95	Double U100	U100	MOSTAP <sup>u</sup>
Sligo $\rho$ (Mg m <sup>-3</sup> )	1.627	n.a.	1.695	1.683	1.648 <sup>a</sup>	n.a.
w (%)	63.1	n.a.	58.8	59.5	56.9 <sup>a</sup>	n.a.
Dunkettle $\rho$ (Mg m <sup>-3</sup> )	50.6 <sup>a</sup>	48.9	47.5	n.a.	49.1 <sup>a</sup>	36.9
w (%)	1.748 <sup>a</sup>	1.772	1.777	n.a.	1.735 <sup>a</sup>	1.823

n.a., not applicable.  
<sup>a</sup>Not UCD but is from original site investigation.

Table 3-3: Study of sampling induced desiccation effects on silts (Long, 2007)



Sampler	L (mm)	D <sub>w</sub> (mm)	t (mm)	C <sub>a</sub> (%)	D <sub>w</sub> /t	C <sub>i</sub> (%)	α (deg.)
54 mm composite	800	65	5.5	44	12	0.6	5
54 mm steel	800	56.5	1.25	9.5	45	0.9	14.3 <sup>a</sup>

L = length, D<sub>w</sub> = outside diameter, D<sub>c</sub> = inside diameter of cutting shoe, D<sub>s</sub> = inside diameter of sampling tube, t = wall thickness, C<sub>a</sub> = area ratio = (D<sub>w</sub><sup>2</sup> - D<sub>c</sub><sup>2</sup>)/D<sub>s</sub><sup>2</sup>, C<sub>i</sub> = inside clearance ratio clearance = (D<sub>s</sub> - D<sub>c</sub>)/D<sub>c</sub>, α = cutting edge angle.  
<sup>a</sup> For 54 mm steel sampler α varied between 13° and 16° with an average of about 14.3°.

Table 3-4: Summary of dimensions and features of 54 mm Norwegian samplers (Long *et al.* 2010)

Failure criterion	Undisturbed	Remolded OC	Remolded NC	Remolded OC
	Yazoo silt $S_u/p$	Yazoo silt $S_u/p$	Yazoo silt $S_u/p$	LMVD silt $S_u/p$
Maximum $\sigma_1 - \sigma_3$	1.0	1.6	1.39	>4.5 <sup>a</sup>
Maximum $\sigma'_1 / \sigma'_3$	0.88	1.00	0.96	1.90
$\bar{A}=0$	1.58	1.43	1.47	1.38
$K_f$ line	0.88	1.00	0.96	1.90
10% strain	1.40	1.26	1.24	3.50
$u_{max}$	0.49	0.49	0.48	0.49

<sup>a</sup>The maximum deviator stress was never achieved. The last data points were used for calculation of  $S_u/p$ .

Table 3-5:  $S_u/p$  ratios for CIUC tests based on various failure criteria (Brandon *et al.*, 2006)

Failure criterion	Yazoo silt undisturbed		Yazoo silt remolded OC		Yazoo silt remolded NC		LMVD silt remolded NC	
	$\phi'$ (degrees)	$\epsilon_f$ (%)	$\phi'$ (degrees)	$\epsilon_f$ (%)	$\phi'$ (degrees)	$\epsilon_f$ (%)	$\phi'$ (degrees)	$\epsilon_f$ (%)
Maximum $\sigma_1 - \sigma_3$	37	13	34	21	35	13	N/A	N/A
Maximum $\sigma'_1 / \sigma'_3$	39	6	36	8	36	7	36	7
$\bar{A}=0$	38	5	36	10	37	10	35	4
$K_f$ line	39	6	36	8	36	7	36	7
Limiting strain	39	7	36	10	36	10	36	10
$u_{max}$	33	2	32	2	33	2	28	1

Table 3-6: Effective stress friction angles ( $\phi'$ ) and strain to failure ( $\epsilon_f$ ) from CIUC tests for various criteria for Yazoo and LMVD silt (Brandon *et al.*, 2006)

Test	Tube*	w <sub>N</sub> (%)	I <sub>p</sub> (%)	I <sub>L</sub>	Clay Size(%)	Macrofabric
CIUC - 1	a	50	11.5	1.05	40	Uniform
- 2	b	38	14	0.35	15	Stratified
CK <sub>0</sub> UC - 1	a	42	17	0.25	15	Stratified
- 2	b	38	14	0.35	15	Stratified
CK <sub>0</sub> UE - 1	c	29.5	16.5	0.1	40	Uniform
- 2	b	37	14	0.35	15	Stratified
CK <sub>0</sub> UDSS - 1	d	32.5	17	0	50	Uniform
to - 3		± 1				
- 4	b	39.5	14	0.35	15	Stratified
CAUDSS	d	33	17	0	50	Uniform

- \* a: z = 12.4 ft. from high w<sub>N</sub> layer beneath Mukluk Island  
b: z = 9 ft. from low w<sub>N</sub> layer adjacent to Mukluk Island  
c: z = 12.5 ft. from M-EBA boring 4  
d: z = 16 ft. from M-EBA boring 3

Table 3-7: Properties of samples of Arctic silt for shear test program (Ladd *et al.*, 1985)

Type of test (1)	Overconsolidation Ratio			
	1 (2)	2 (3)	3 (4)	8 (5)
UU	0.25-0.30	0.60-0.64	—	1.55-1.60
IC-U	0.85-1.00	1.70-1.85	—	2.85-3.00
AC-U	0.78	—	1.28	2.37

Table 3-8: Values of  $S_u/\sigma'_{1c}$  for Alaskan Silt (Fleming and Duncan, 1990)

Strength Test	$S_u/\sigma'_{1c}$	K <sub>0</sub>	Reference
UU	0.25-0.30	-----	Fleming and Duncan (1990)
UU	0.185	-----	Ladd <i>et al.</i> (1985)
IC-U	0.25	-----	Ladd <i>et al.</i> (1985)
IC-U	0.3	-----	Ladd <i>et al.</i> (1985)
IC-U	0.85-1.0	-----	Fleming and Duncan (1990)
IC-U	0.30-0.65	-----	Wang <i>et al.</i> (1982)
AC-U	0.32-0.39	0.84; 0.59	Ladd <i>et al.</i> (1985)
AC-U	0.26	0.59	Ladd <i>et al.</i> (1985)
AC-U	0.75	0.5	Fleming and Duncan (1990)

Table 3-9: Normalized strength parameters for Normally consolidated Silts

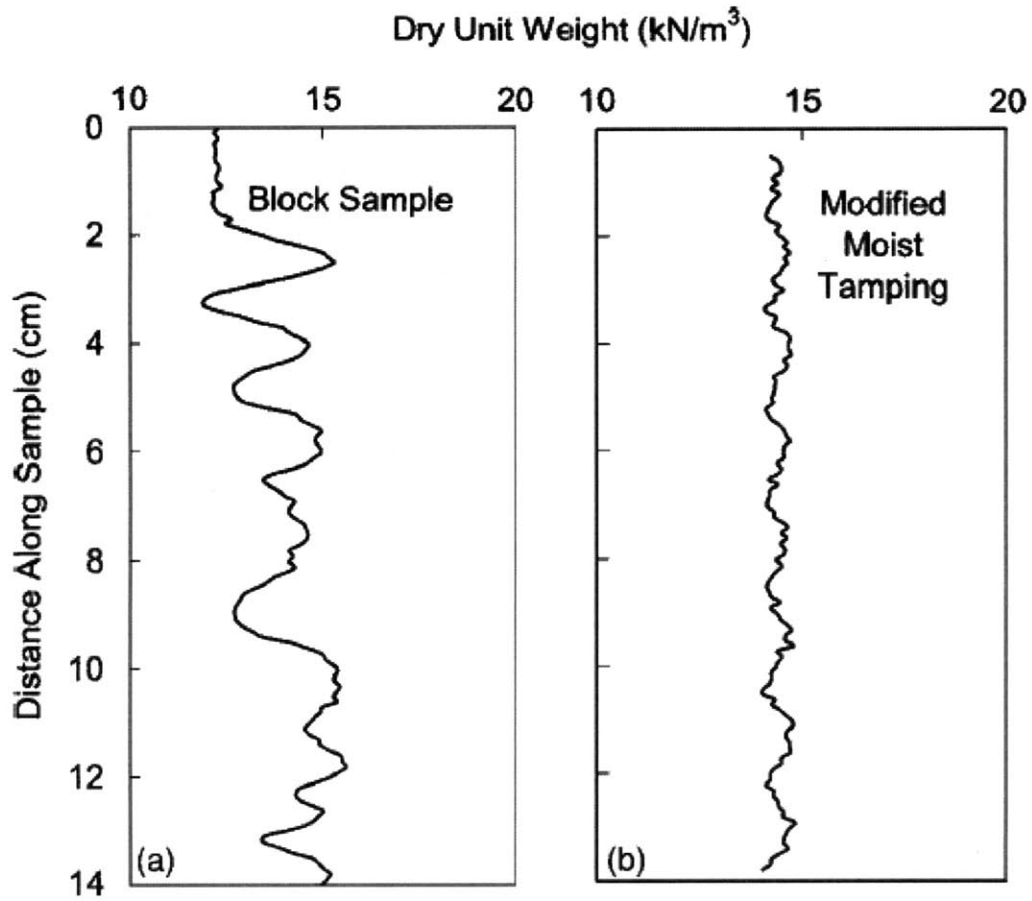


Figure 3-1: Typical dry unit weight profiles obtained in triaxial silt specimens: (a) Block sample, (b) Undercompacted specimen (Baxter *et al.*, 2008)

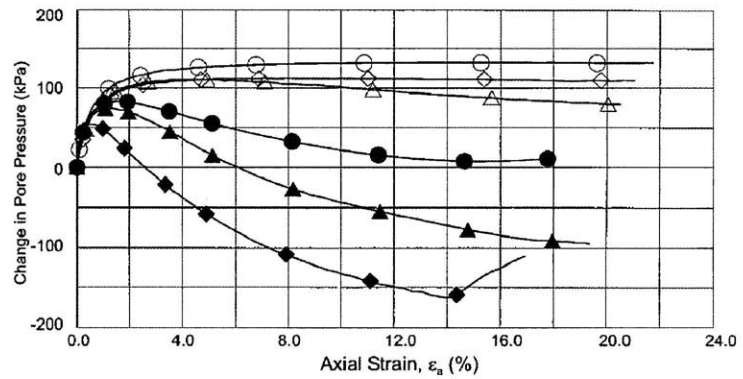
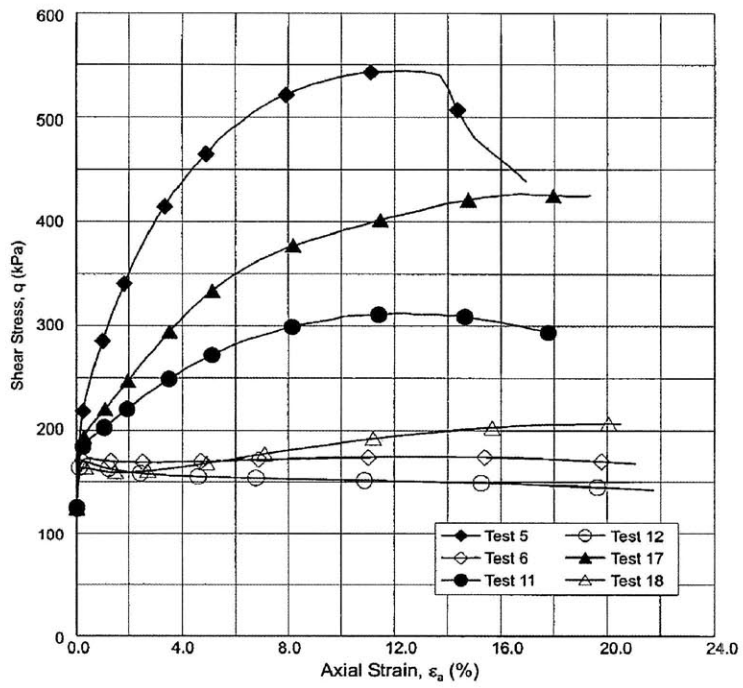
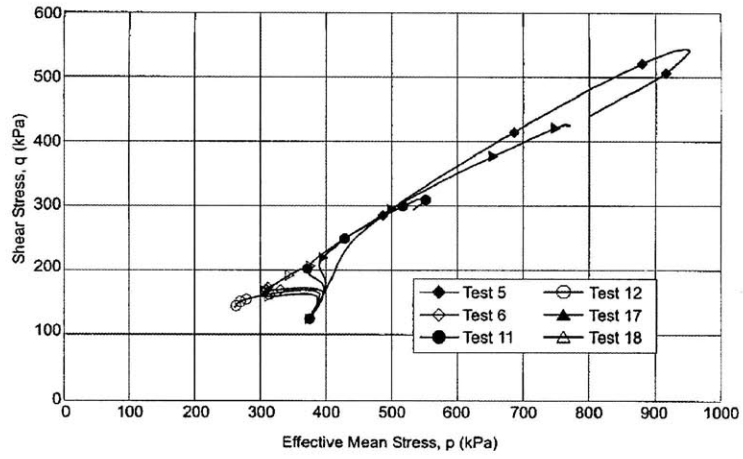


Figure 3-2: Undrained triaxial results at  $\sigma'_{ac} = 500$  kPa (Hoeg *et al.* 2000)

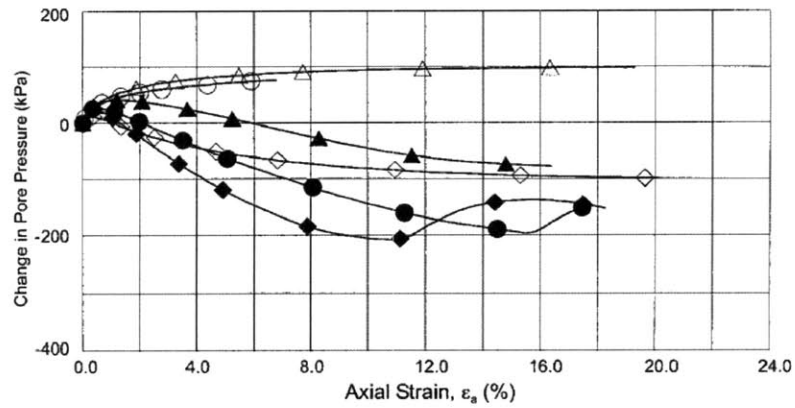
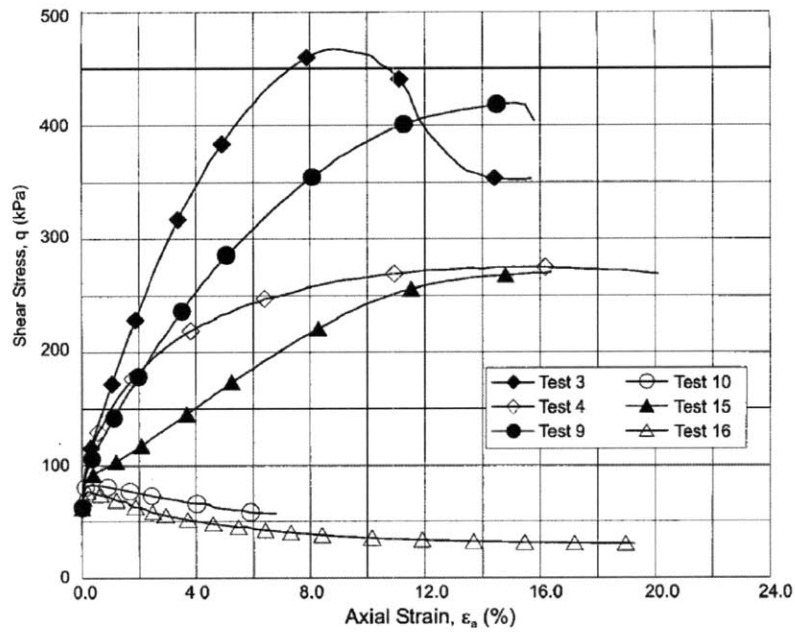
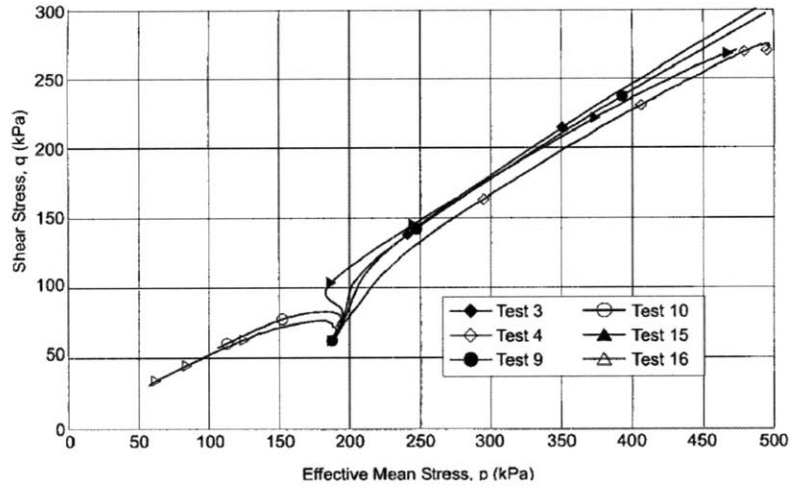


Figure 3-3: Undrained triaxial results at  $\sigma'_{ac} = 250$  kPa (Hoeg *et al.* 2000)

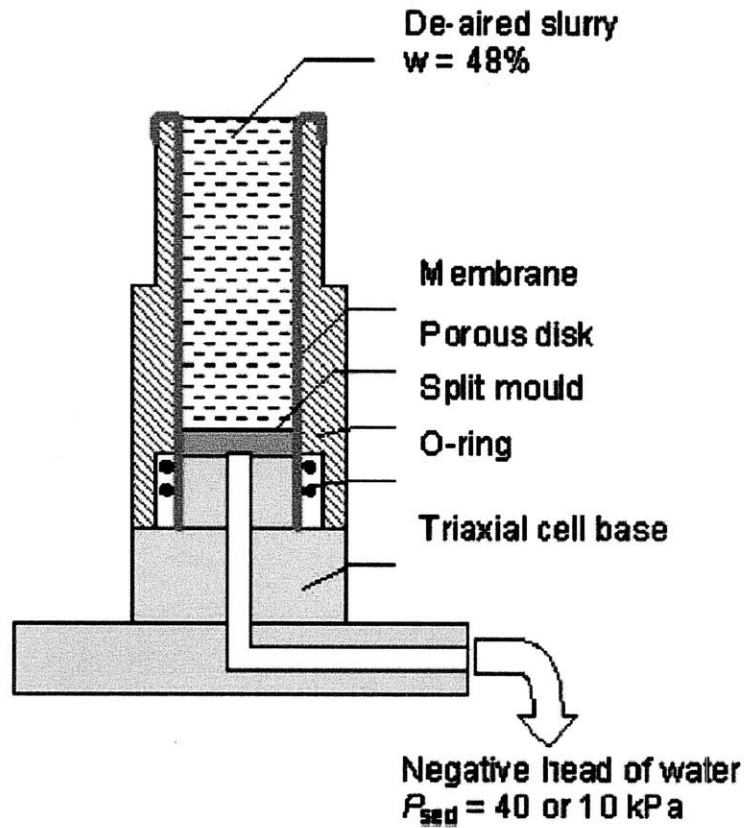


Figure 3-4: Schematic diagram of sedimentation technique (Hyde *et al.*, 2006)

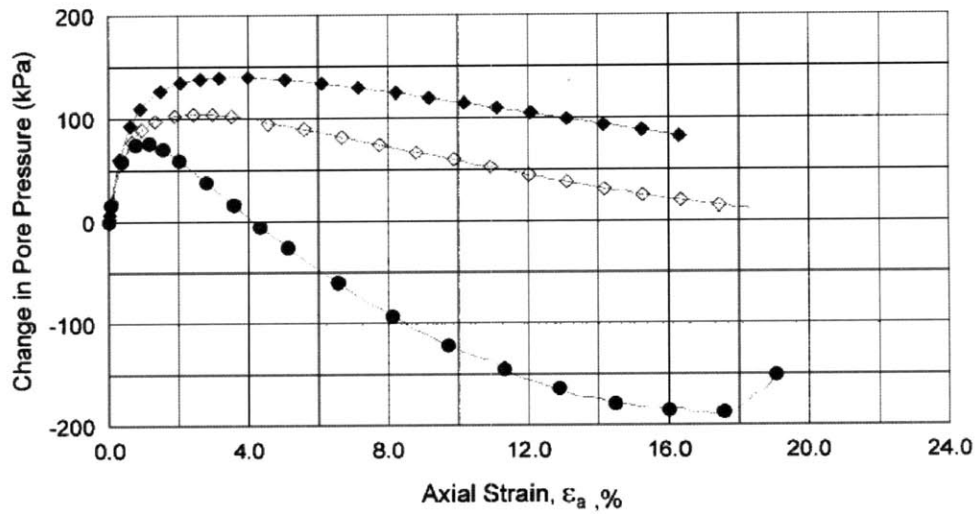
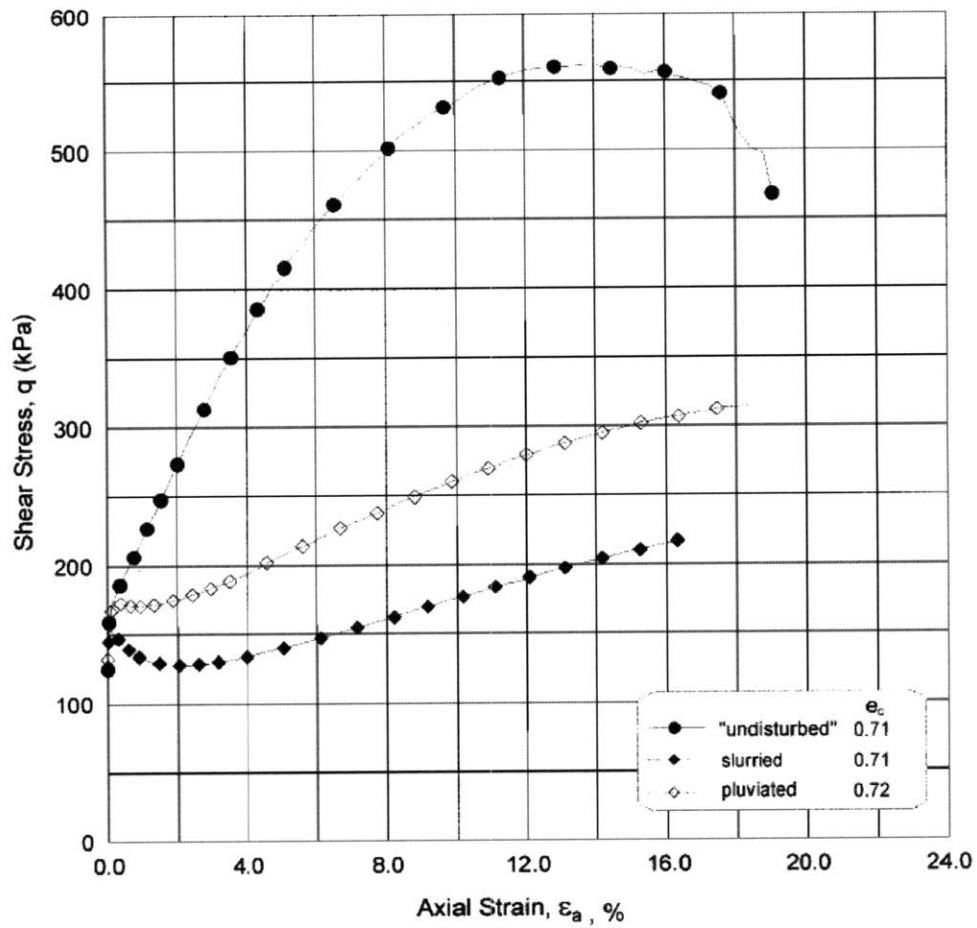


Figure 3-5: Comparison of results from undisturbed, slurry, and water pluviated specimens (Hoeg *et al.*, 2000)

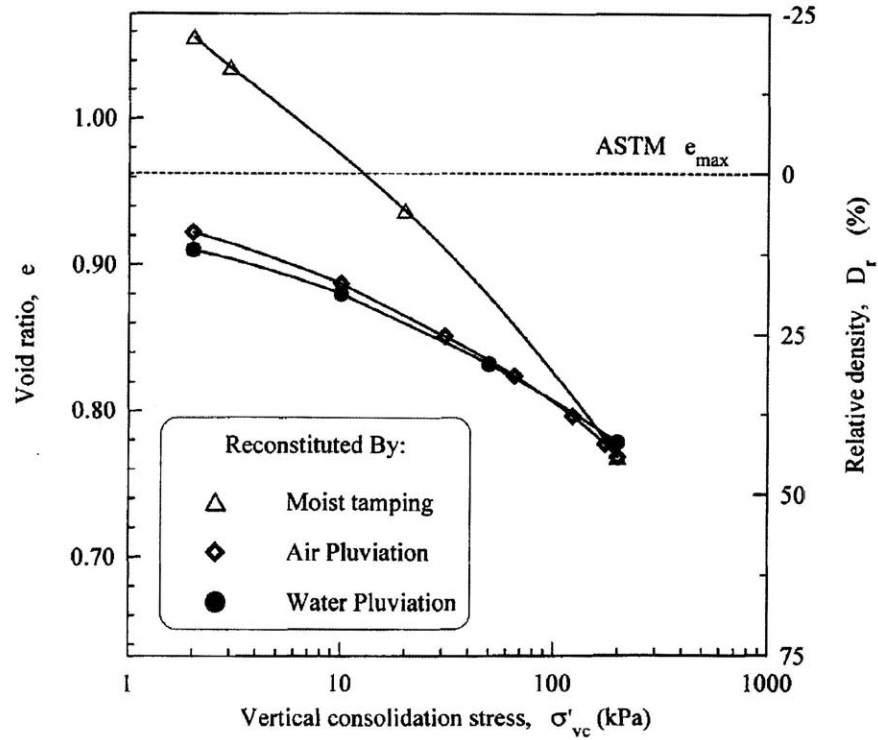


Figure 3-6: One dimensional compressibility of Syncrude sand specimens reconstituted by different methods (Vaid and Sivathayalan, 1999)

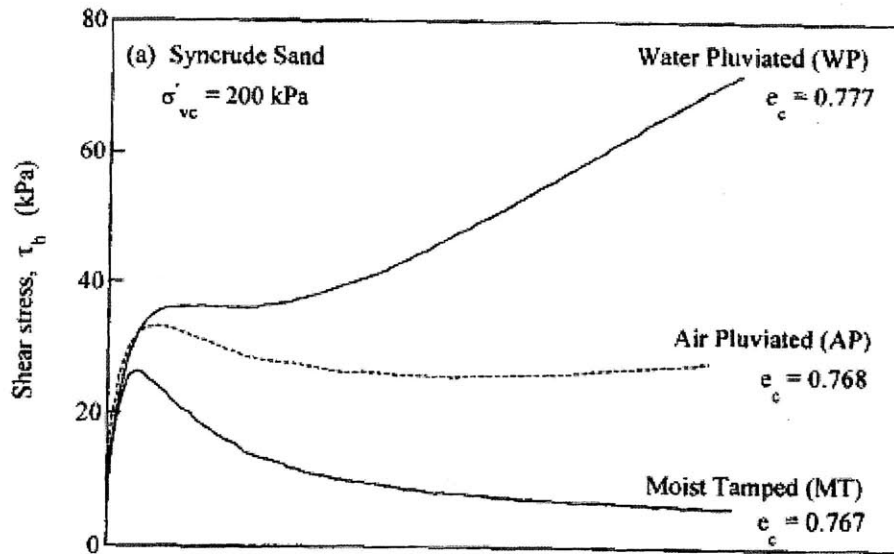


Figure 3-7: Undrained simple shear response of specimens reconstituted by different techniques (Vaid and Sivathayalan, 1999)



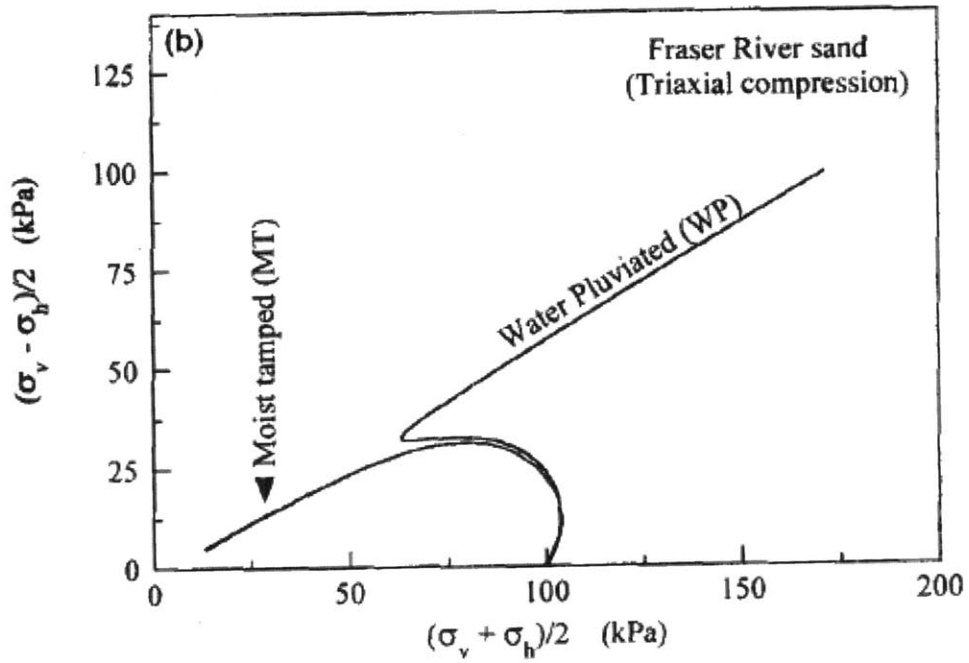


Figure 3-8: Undrained triaxial compression response of reconstituted Fraser River Sand specimens (Vaid and Sivathayalan, 1999)



Figure 3-9: “Double” U 100 tubes (Standard Ireland-UK U100 or U4 sampling tubes. Crude cutting shoe shown on right hand side) (Long, 2007).

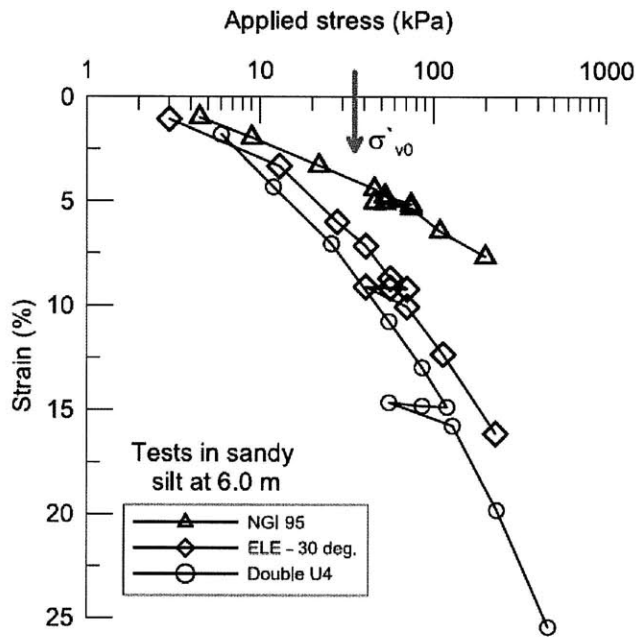


Figure 3-10: One dimensional behavior from oedometer tests, Sligo (Long, 2007)

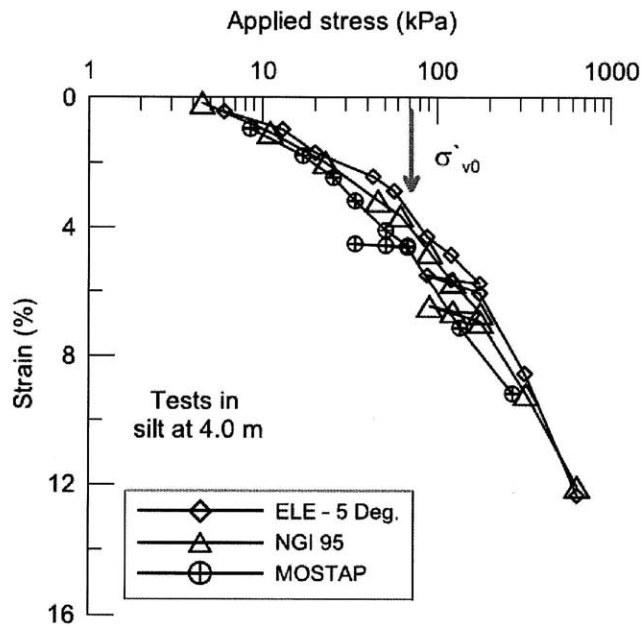


Figure 3-11: One dimensional behavior from oedometer tests, Dunkettle (Long, 2007)

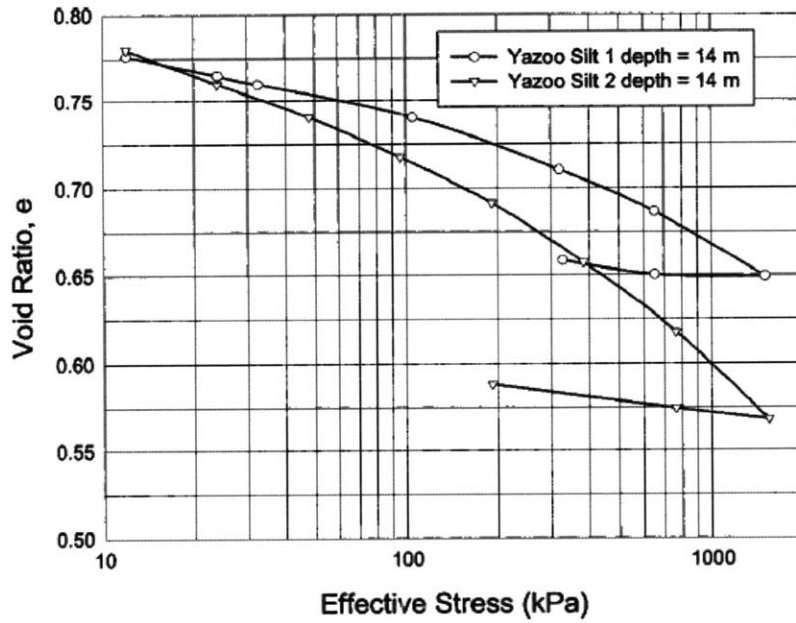


Figure 3-12: Consolidation test results for undisturbed samples of Yazoo Silt (Brandon *et al.*, 2006)

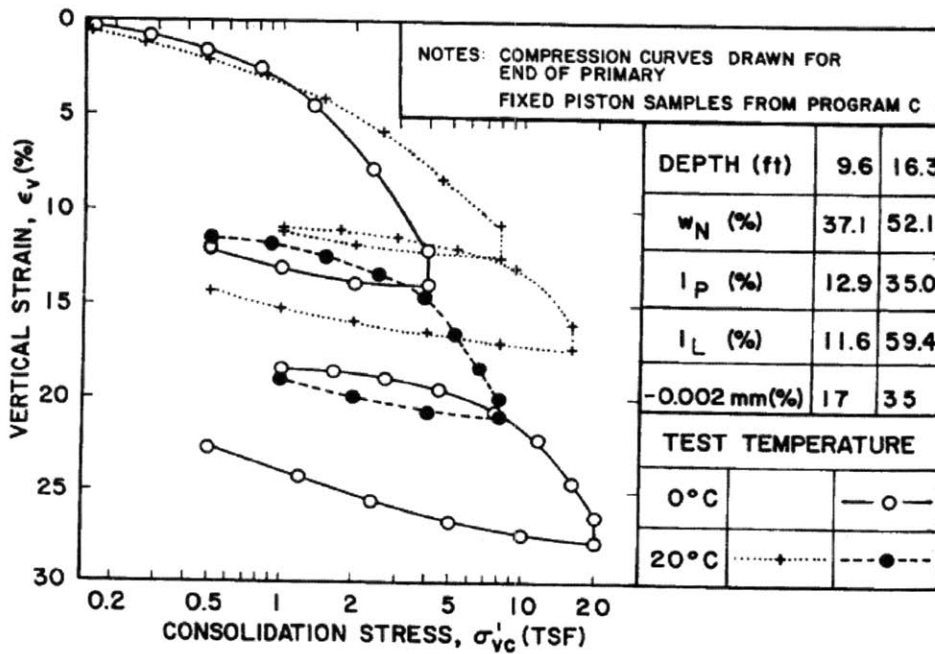


Figure 3-13: Compression curves for silt in Harrison Bay area (Ladd *et al.*, 1986)

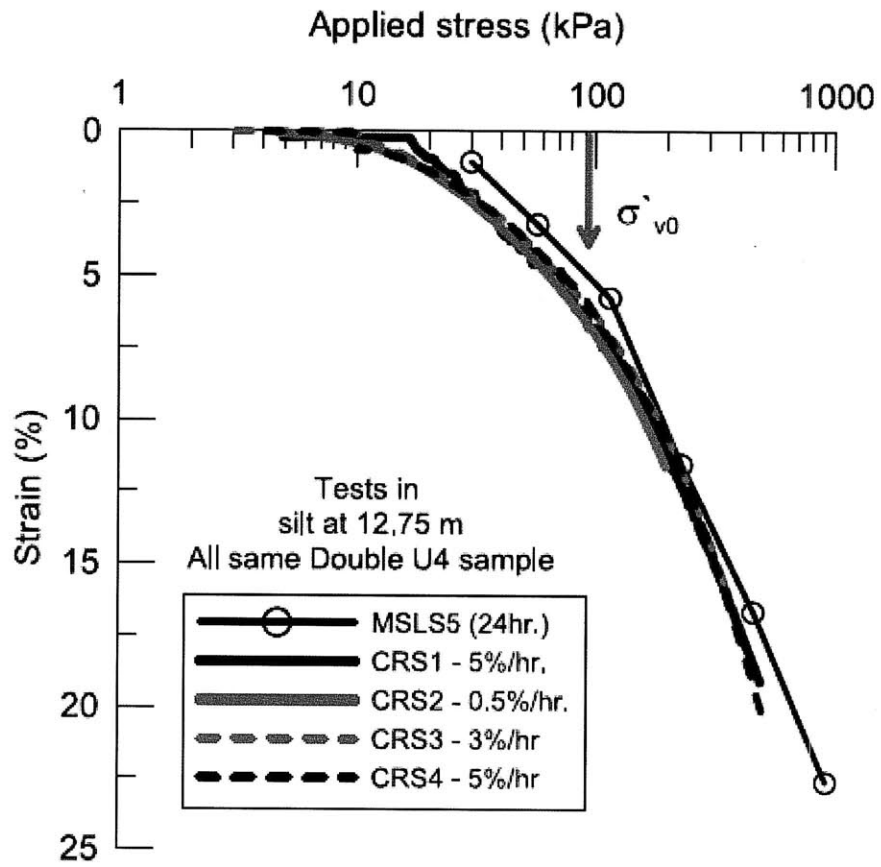


Figure 3-14: Compression test results, Sligo (Long, 2007)

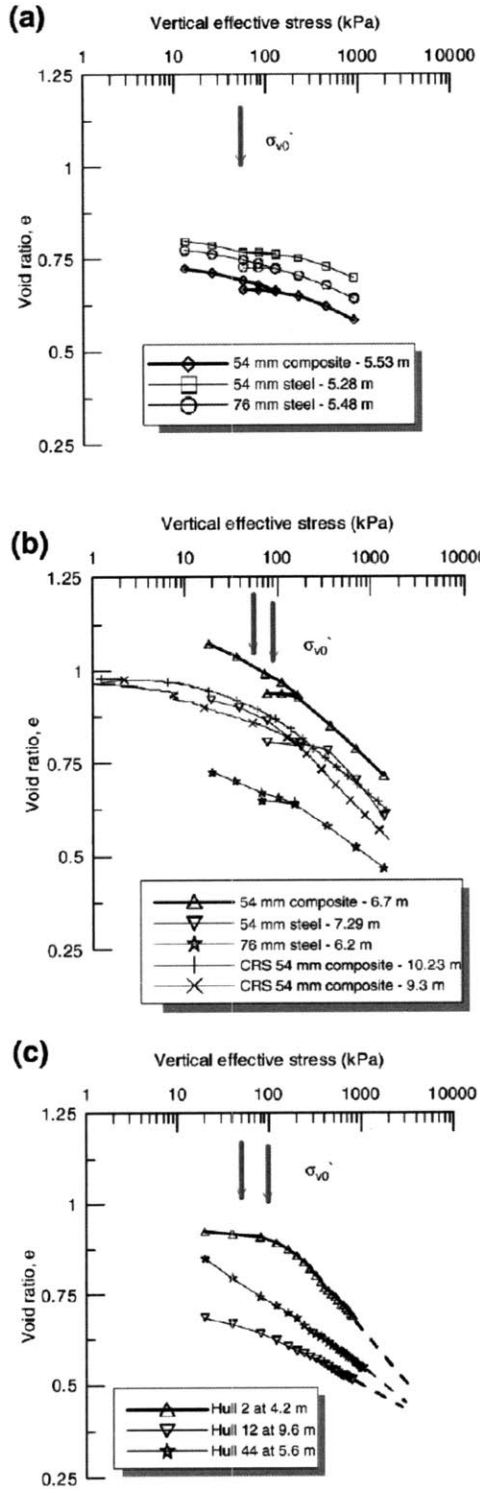


Figure 3-15: Typical oedometer test results (a) Norwegian upper Os silt, (b) lower OS clayey silt, and (c) Norwegian E39 silt (Long *et al.* 2010)

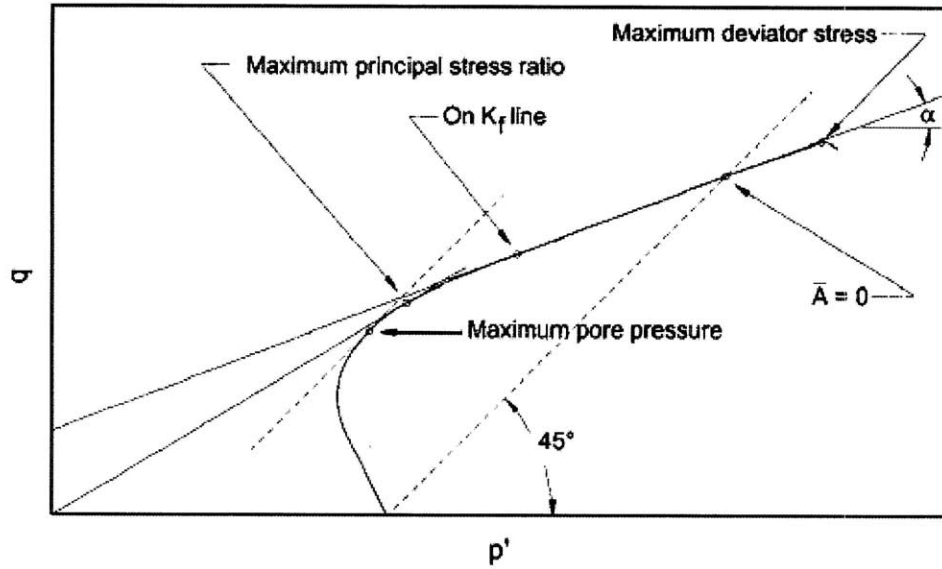


Figure 3-16: Idealized stress path showing stresses at failure for different failure criteria (Brandon *et al.*, 2006)

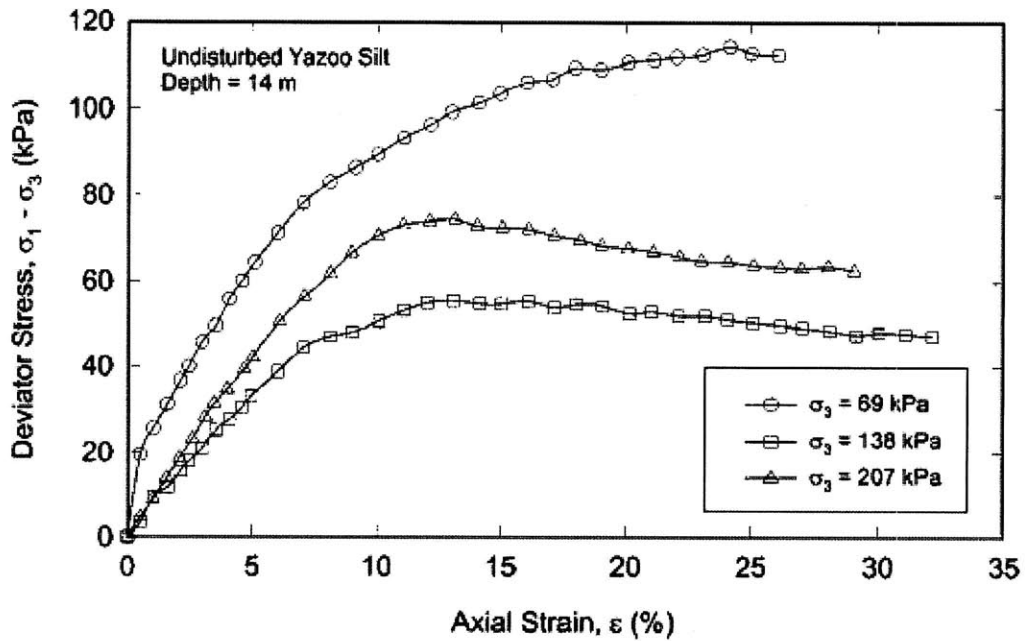


Figure 3-17: Deviator stress-strain curves from UU triaxial tests of undisturbed specimens of Yazoo silt (Brandon *et al.*, 2006)

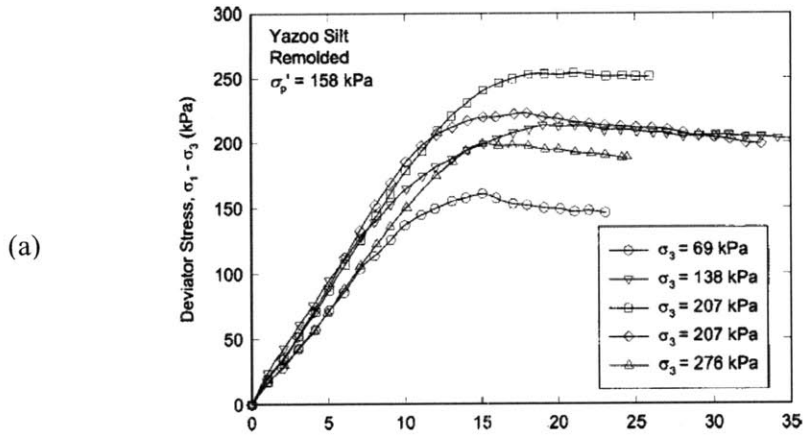


Fig. 6. Deviator stress-strain curves for remolded Yazoo silt

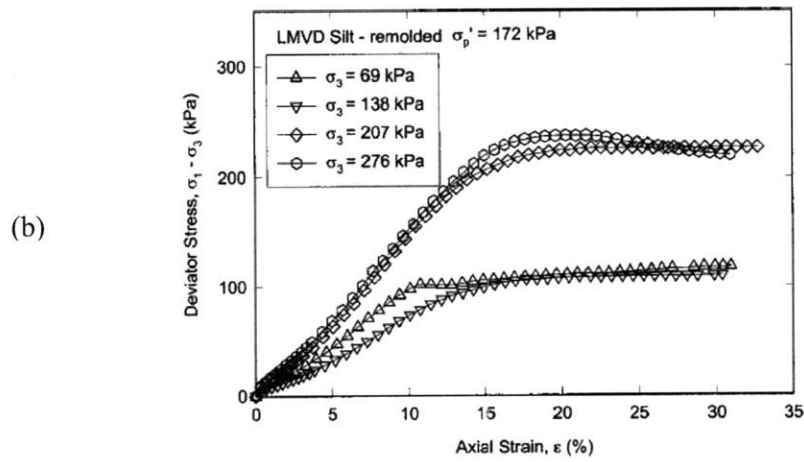


Figure 3-18: Deviator stress-strain curves for reconstituted specimens of Yazoo and LMVD silt; (a) Yazoo silt, (b) LMVD silt (Brandon *et al.*, 2006)

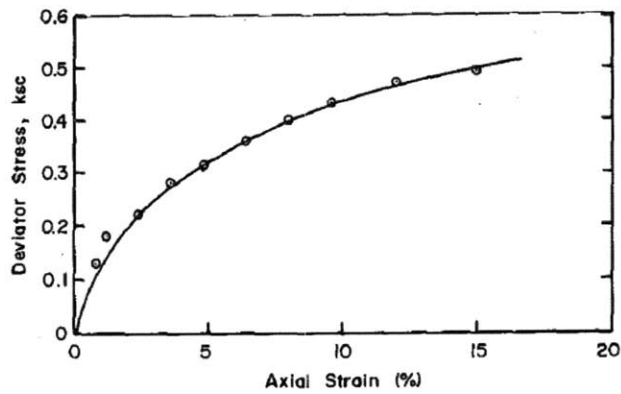


Figure 3-19: Stress-strain relationship for UU tests at confining pressure ( $\sigma_{con}$ ) = 1.5 ksc ( $\approx 147$  kPa) on Alaskan Silt (Fleming and Duncan, 1990)

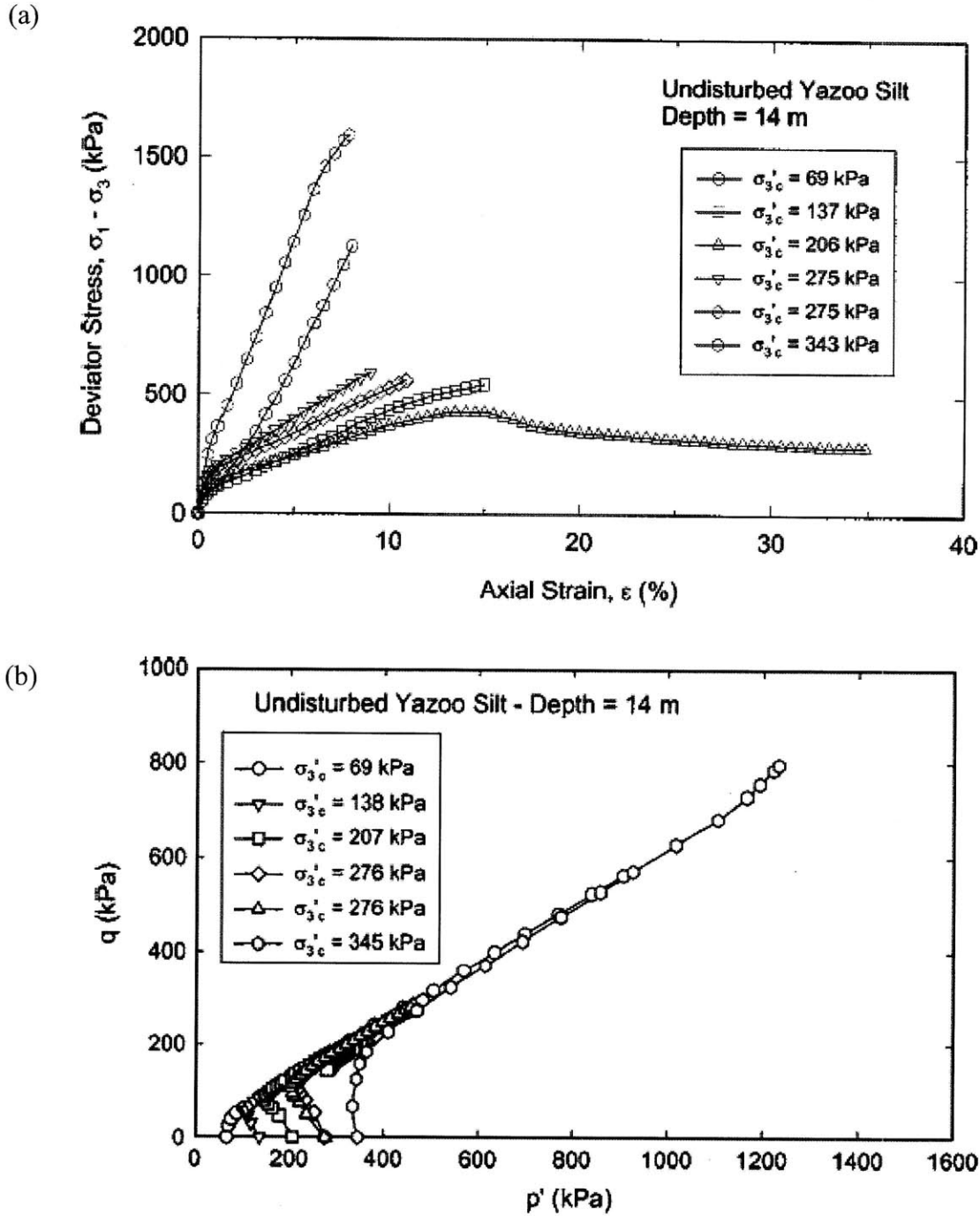


Figure 3-20: CIUC tests on undisturbed specimens of Yazoo silt; (a) Deviator stress strain curve, (b) stress paths (Brandon *et al.*, 2006)



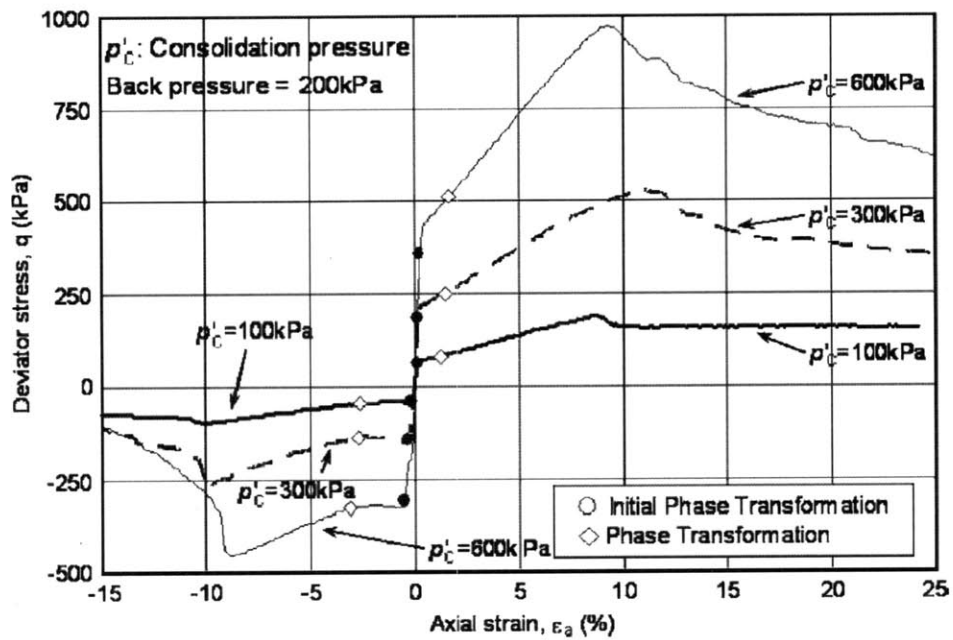


Figure 3-21: Deviator stress versus axial strain for reconstituted low plasticity silt (Hyde *et al.*, 2006)

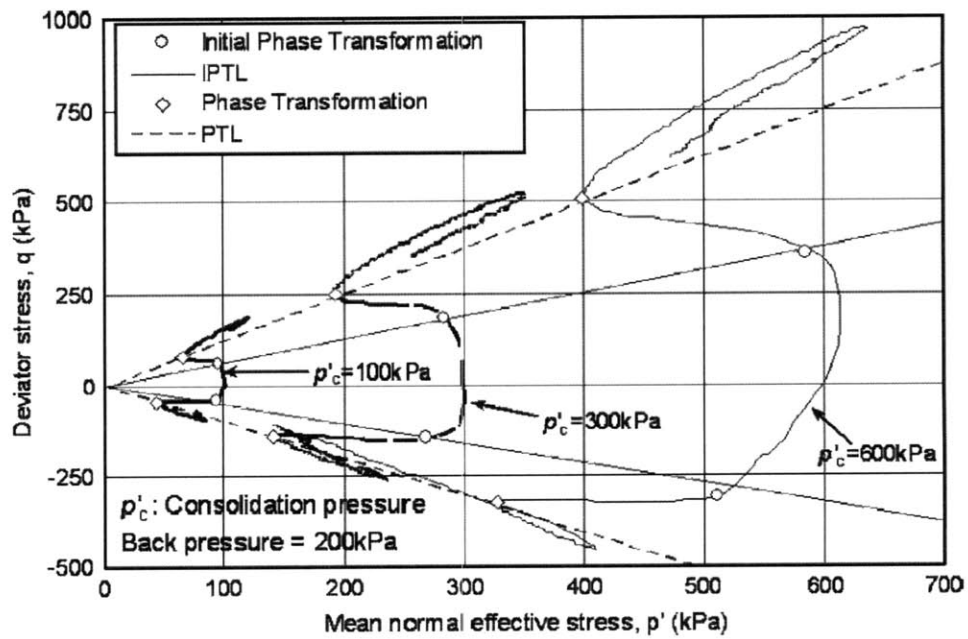


Figure 3-22: Stress path for reconstituted low plasticity silt (Hyde *et al.*, 2006)

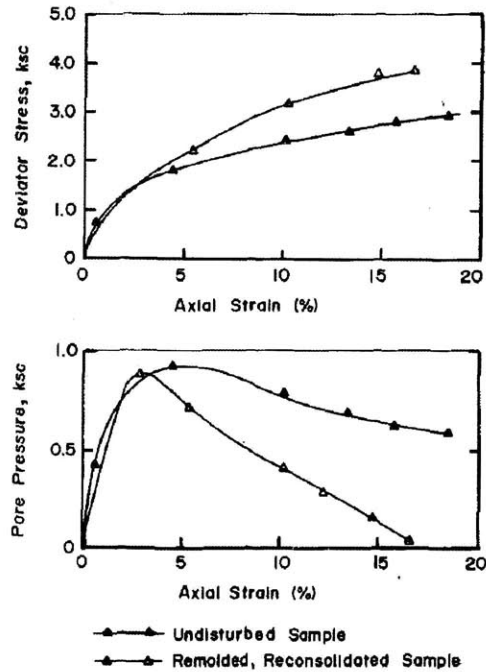


Figure 3-23: Comparison of deviator stress and pore pressure behavior for undisturbed and remolded samples isotropically consolidated to 1.5 ksc ( $\approx 150$  kPa) (Fleming and Duncan, 1990)

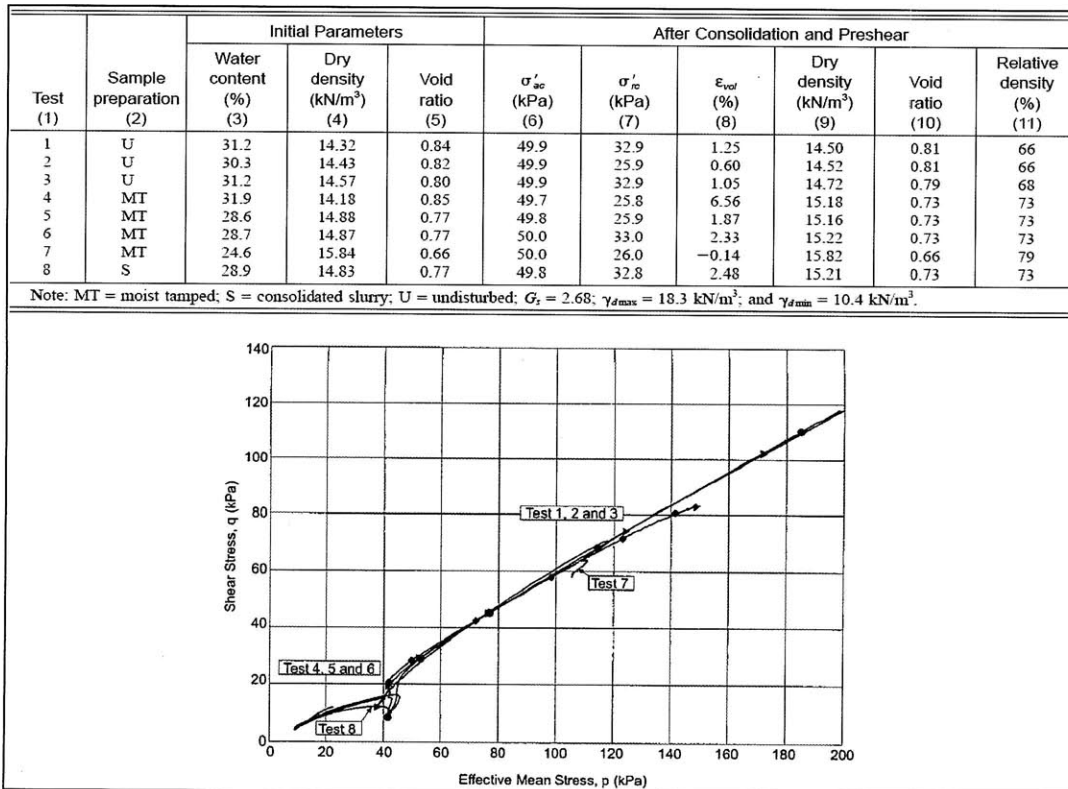


Figure 3-24: Effective stress path for triaxial tests on natural silt; intact and reconstituted specimen data above stress path (Hoeg *et al.*, 2000)

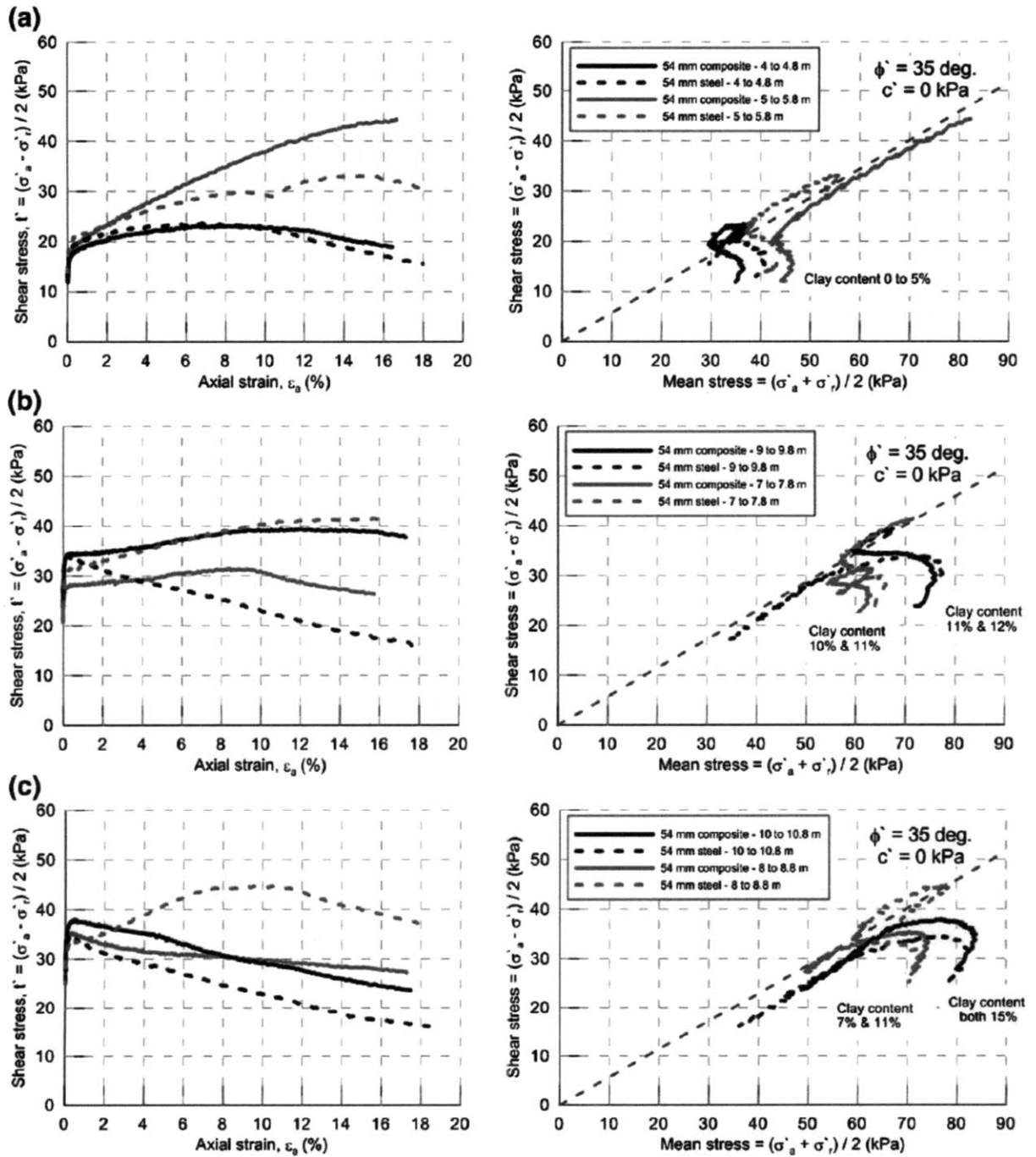


Figure 3-25: CAUC results on Norwegian glaciomarine silt; (a) upper silt, (b) lower clayey silt 7m and 9m samples, and (c) lower clayey silt 8m and 10m samples (Long *et al.*, 2010)

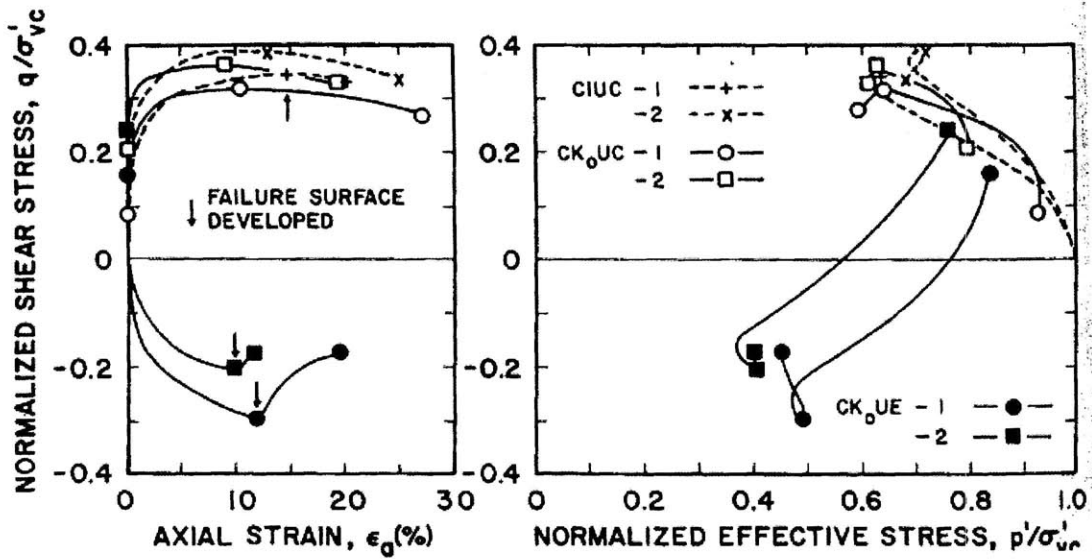


Figure 3-26: Normalized stress strain data from CU triaxial tests on OCR = 1 Harrison Bay Arctic Silt (Ladd *et al.*, 1985)

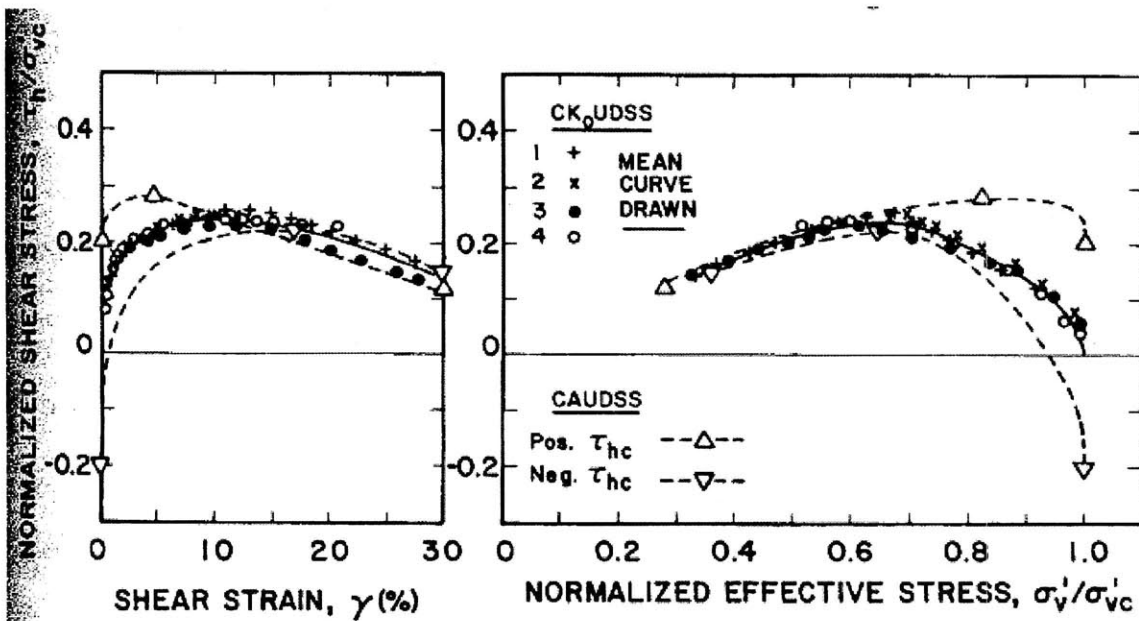


Figure 3-27: Normalized stress strain data from CU Direct Simple Shear tests on OCR = 1 Harrison Bay Arctic Silt (Ladd *et al.*, 1985)

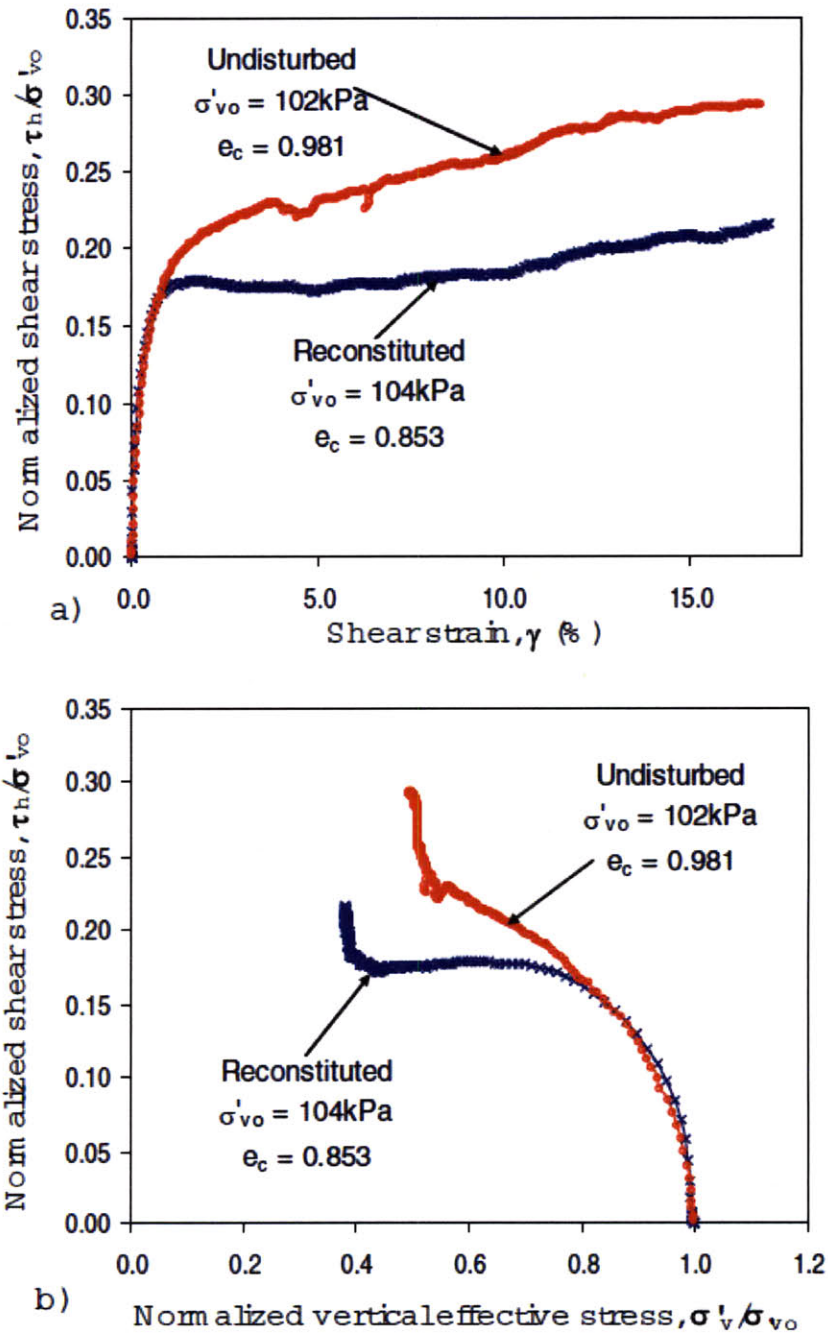


Figure 3-28: Intact and reconstituted specimens of NC Fraser River silt during constant volume DSS shear; (a) stress strain and (b) stress path response (Wijewickreme and Sanin, 2008)

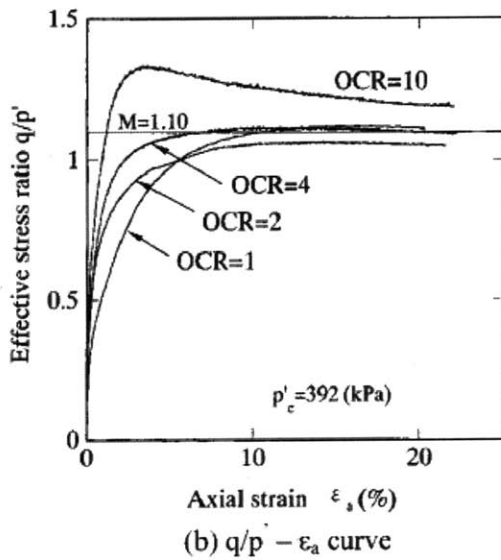
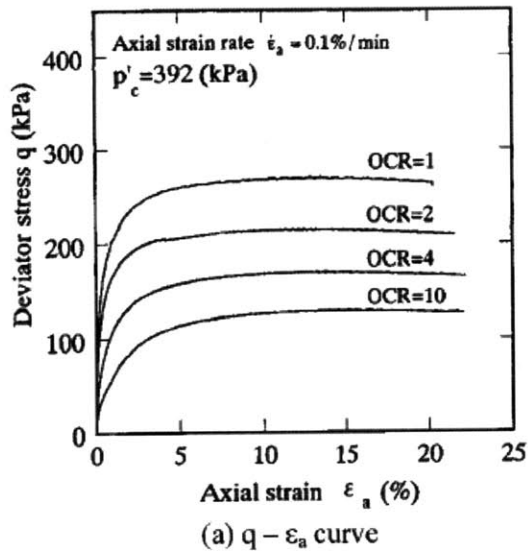


Figure 3-29: Deviator stress and effective stress ratio versus axial strain curves in CIUC tests; (a) deviator stress-axial curve and (b) effective stress ratio-axial strain (Yasuhara *et al.*, 2003)

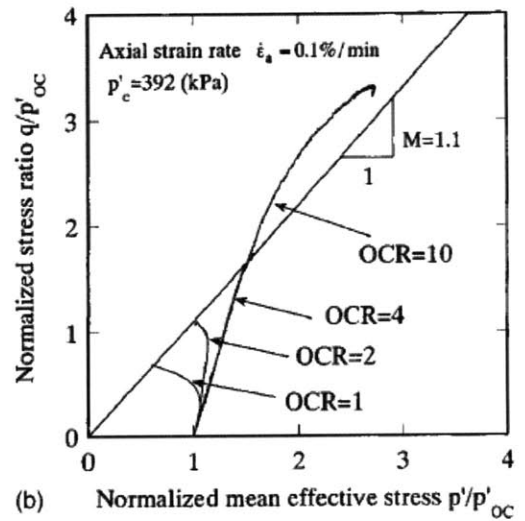
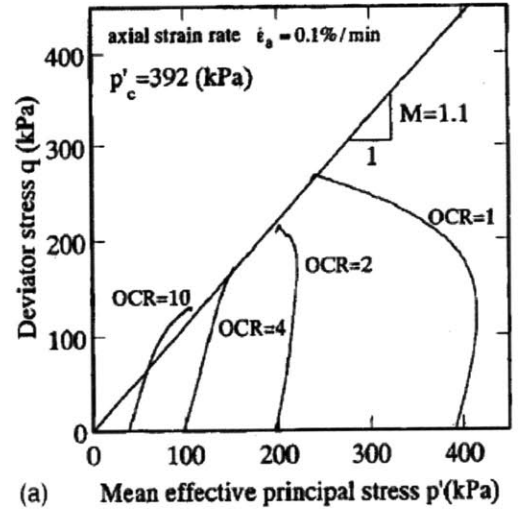


Figure 3-30: Effective stress paths in CIUC tests; (a) deviator stress path and (b) normalized effective stress path (Yasuhara *et al.*, 2003)

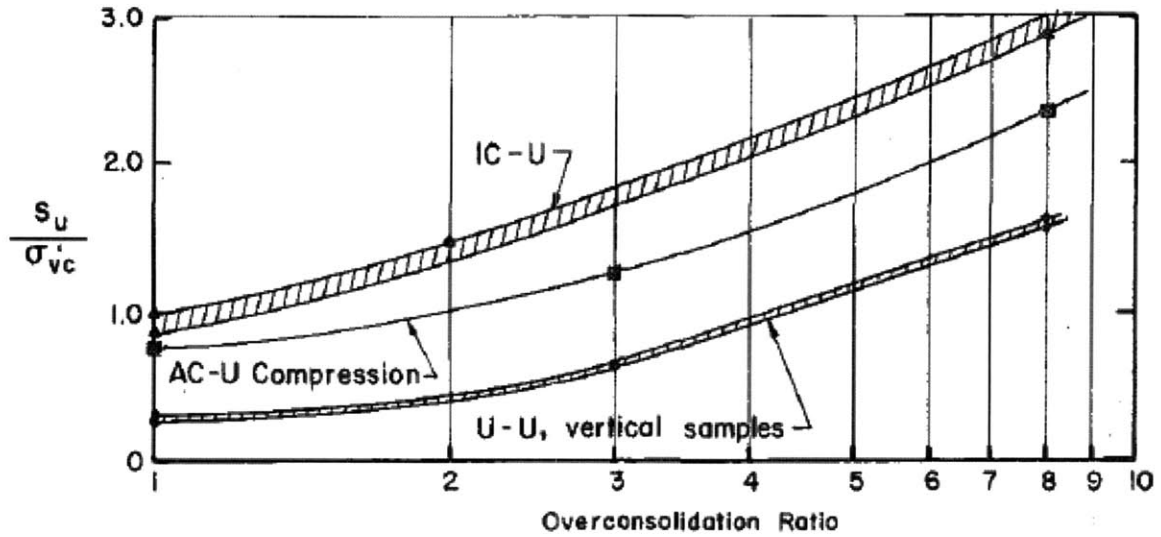


Figure 3-31: Normalized undrained shear strength versus OCR for Alaskan Silt (Fleming and Duncan, 1990)

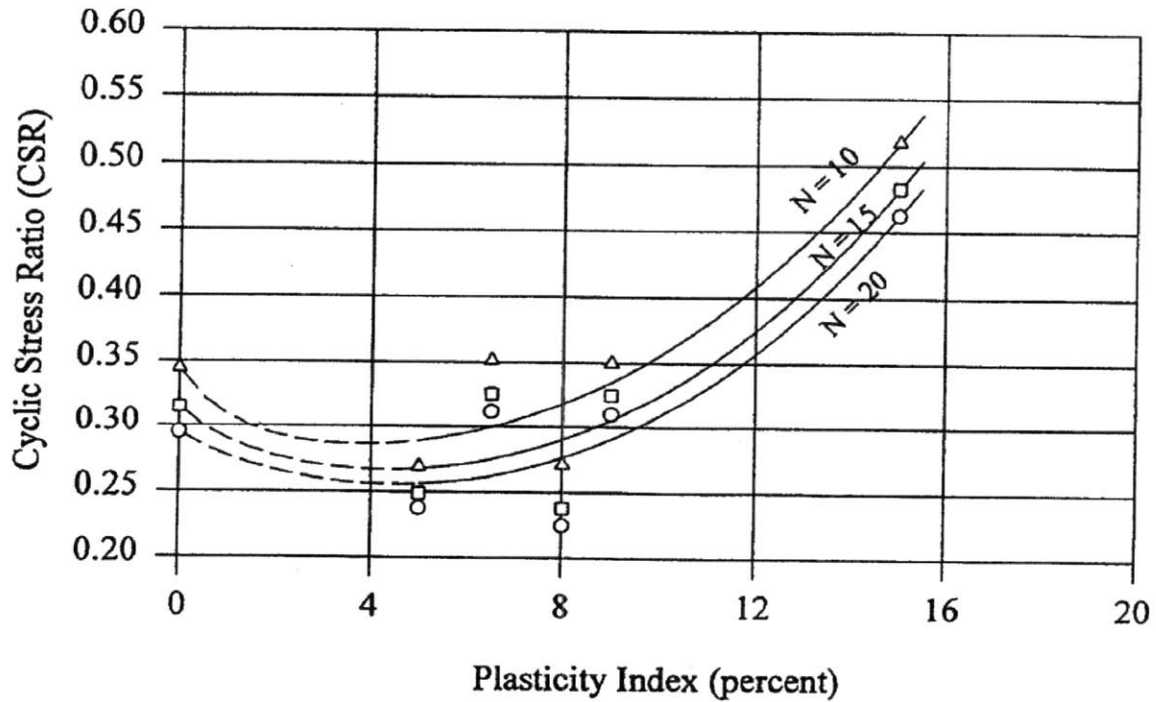


Figure 3-32: Normalized cyclic stress ratio versus plasticity index on undisturbed samples (Prakash and Puri, 2003)





# **4 MATERIAL PROCESSING, RECONSTITUTION, EQUIPMENT, AND TESTING PROCEDURES**

## **4.1 INTRODUCTION**

This chapter describes the material, equipment, and testing procedures used in the testing program. The chapter is divided into four sections. The first, Section 4.2, presents the samples that were taken from the field and the processing of the material at MIT Geotechnical laboratory. A significant intact and disturbed sampling program was undertaken at Skibbereen with a large quantity of the samples transported to MIT for testing. A procedure for processing the material is presented together with transportation disturbance effects and the observations.

Section 4.3, covers in detail the reconstitution methods that were undertaken for this material. The section is essentially broken into two methods; resedimentation and undercompaction. The resedimentation procedure is well established at MIT with Abdulhadi (2009) the latest to successfully re-sediment and test. The possibility of being able to re-sediment this type of material was unknown before this work. The procedure, problems, and evaluation are presented in this section. The undercompaction method developed by Ladd (1977) has long been established at MIT. The applicability of this material to undercompaction is assessed. A successful procedure is defined. However, some of the problems with undercompaction, particularly saturation difficulties, are discussed.

Section 4.4 describes the equipment used in the majority of the devices. The section first deals with measurement devices. The principles of the various transducers are reviewed. The section then discusses the data acquisition system and the automated testing equipment that is in use today.

The final section describes the equipment and procedures used to perform the experimental program. The characterization procedures are briefly stated. The CRS consolidation tests were performed on small diameter specimens to vertical consolidation stresses of 15,000 kPa using an oedometer cell. The successful testing procedure, rational behind selecting an

oedometer cell and the problems are reviewed. The hydraulic conductivity tests were performed in a modified Trautwein CRS cell. The equipment was recently developed at MIT and it is successful at giving accurate hydraulic conductivity information. The procedure and problems of the device are discussed in detail.

The DSS device was used extensively to provide the shear properties of the material. The device was modified for the testing of this material. Finally, two types of triaxial cells were used in testing: 1) a manual device for isotropically consolidated undrained compression tests, and 2) a automated stress path device for  $K_0$  consolidated undrained compression tests. The manual device was first used to develop a successful testing method which provides repeatable results. Isotropically consolidated testing is most common for sands. Once complete, the  $K_0$  tests provide results which are closer to stress conditions in the field.

## **4.2 MATERIAL PROCESSING**

### **4.2.1 Introduction**

As indicated in Section 2.5.2, field sampling in Skibbereen consisted of material removed from the ground by shell and auger and a tube sampler. Field sampling can generally be divided into two categories, disturbed methods and intact methods. Disturbed methods are used to collect a quantity of material without care for its condition. Intact methods are designed to collect a quantity of material while maintaining its in situ properties. Changes to the in situ condition known as disturbance will always occur. However, minimizing the magnitude of the disturbance depends on soil condition, sampling methods, and expertise (Germaine & Germaine, 2009).

Both intact and disturbed samples were sent to MIT in August 2008 for laboratory testing. However, due to transportation vibrations, the intact samples were found to be worthless when they arrived at MIT. A system of processing the disturbed material into a homogenous testing material was then undertaken. The following two sections give a review of the work that was conducted.

#### 4.2.2 Samples for Laboratory Testing at MIT

Intact sampling can be very expensive due to the low quantities of material that are recovered, specialized equipment, and the greater time that is required. In Skibbereen, a MOSTAP sampler was used to obtain the intact samples. The MOSTAP soil samplers obtain as nearly "undisturbed" samples as possible through the use of a porous nylon stocking that minimizes friction during sampling. The thin-wall sampling tube (or liner) acts as a guide for the piston during sampling and distributes the stocking uniformly around the soil sample. The stocking and tube also serves effectively to transport and store the sample. After Cone Penetration Test's (CPT's) or other methods have provided soil stratigraphy, the sampling depths are chosen. The MOSTAP is attached to the CPT rods and is pushed to the top of the desired sampling depth interval. Next a wire-line latching tool that fits in the CPT rods or casing is lowered and latched into the cone point mechanism to unlock it. Subsequently, the CPT rods are pushed down until the MOSTAP cutting mouth reaches the limit of its sampling length. Then the latch mechanism inside the MOSTAP opens and the operator can pull out the wire-line latching tool. Next the CPT rods or casing with the sampler attached can be pulled up to remove the MOSTAP sample tube. The samples obtained are appropriate for most soils; alluvial and consolidated cohesive soils, peats, sands, and gravels. The samples obtained in Skibbereen were 65mm in diameter and 1.2m in length. Figure 4-1 shows a schematic diagram and a picture of a typical MOSTAP sampler. Table 2-1 in the previous Chapter shows the locations and depths of the samples taken. In total, 8 tube samples from the 8 testing locations were transported to MIT via road and air in August 2008.

Disturbed sampling is very common when evaluating materials for various post-processing operations with little concern for in situ conditions (Germaine & Germaine, 2009). Samples can be obtained from methods such as trial pitting, mechanical auguring, and hand augers. As illustrated in Section 2.5.2, a shell and auger technique was used in Skibbereen. This method is very common in the United Kingdom for site investigation work. The samples recovered ranged from 2.5m to 5.5m in depth. They were stored in plastic bags that were sealed by tying. Due to the vast amounts of material that was collected and the availability of more in the location, not all of material was transported to MIT. Bags were selected ensuring that the testing range in depth would be incorporated. In total, 9 bags were transported, each weighing between 2 and 15 kg.

### 4.2.3 Processing

All samples were checked and logged when they arrived at MIT. The tube samples were opened to check their integrity. It was found that the samples had become very disturbed during transport. The samples appeared to have liquefied and segregated. This was apparent due to the water at the top of each tube. An extruded sample from a piece of the tubes can be seen in Figure 4-2. The slumped shape and water separation indicate that the material is extremely disturbed. It was therefore decided that the tube samples would not be suitable for testing and the research would focus on the disturbed samples.

The disturbed material had to be processed before testing could begin. Bulk material is considered any sample that arrives at the laboratory as a disturbed sample or portions of intact samples that will be used for testing (Germaine & Germaine, 2009). Three processing methods are available to manipulate the material. They are blending, splitting, and separating. Each has well defined objectives and can be performed using a variety of techniques and devices. Blending is the process of making a sample homogenous by mixing in a controlled manner. V-blenders, tumble mixers, and hand mixing are all forms of blending. The disturbed material at MIT was processed and blended so a uniform homogenous material could be used for testing.

First, a criterion was established to assess the bulk samples sent to MIT. Color, moisture content, unusual material in sample, maximum particle size, and particle size range were all considered. General comments about the material were as follows:-

Color:	Grey
Moisture Content:	Moist. It was obvious the material had dried significantly during storage and transportation.
Unusual Material:	Nothing unusual was found in the majority of the samples.
Maximum Particle Size:	Silt size (<75 $\mu\text{m}$ ). Not able to feel grains between fingers but possible between teeth.
Particle Size range:	Silt to Clay

In addition to the above criterion a slake test was conducted for each of the bags. A small representative sample was allowed to soak in a container of distilled water overnight. It was

found that material did not disperse; showing that the material has true cohesion properties from an initial moist state.

Two of the bags were eliminated from the blending process due to abnormalities from the general trend. Their material was found to have a brownish color, larger particle size with sand evident, high quantities of contaminants most likely from the overlying ground fill, and they dispersed during the slake test. The remaining material was then removed from the 7 bags and laid out to air dry as shown in Figure 4-3. It was decided to blend all the material together. Therefore, the 2.5m to 5.5 m depth range was eliminated. Once the material was dry, it was pulverized to powder by hand and Batch 1 was created.

To ensure homogenous properties throughout the entirety of the powder sample, an extensive blending process took place. Blending is relatively easy when working with small quantities. However, for large quantities, based on the largest quantity that fits in the mixer, the material must be mixed in portions and in sequential blending operations. Figure 4-4 provides a schematic for a sample that is four times larger than the available blender. The material is first divided into 4 portions labeled 1,2,3, and 4. Each of these portions is blended using the appropriate process. Each blended portion is then carefully split into equal quarters labeled a,b,c and d. The four “a” portions are then combined together and blended in a second operation. Each of the four second blends will now be uniform and equal.

Due to the large quantity of material, buckets having a capacity of 5 gallons were selected to blend the material (Figure 4-5). Lids were fixed on the buckets and the material was blended by hand. The above procedure was then implemented to insure uniform testing material. The material was sieved through a No. 40 US sieve before it was stored in a sealed 40 gallon container. The purpose of sieving is to insure no particles from the overlying fill in Skibbereen are in the testing material. Approximately, 50 kg of dry testing powder were processed for research.

## **4.3 RECONSTITUTION**

### **4.3.1 Introduction**

Reconstitution is the formation of soil in a laboratory to particular conditions. The primary aim of reconstitution is to recreate the field conditions of the material. It is now common practice to reconstitute free draining coarse grained soils, thereby, avoiding the problems associated with sample disturbance. Reconstitution generally occurs from a bulk source using a controlled process. Water content and density are key components when reconstituting material. A number of techniques are used for reconstitution. They vary depending on the soil characteristics. Dynamic compaction, kneading compaction, static compaction, vibratory compaction, and pluviation techniques are all used to reconstitute material. However, two popular techniques for reconstitution in MIT are resedimentation and undercompaction. The two techniques were performed on the processed material in an aim to successfully reconstitute it to field conditions. The background of the processes, procedures, problems, and evaluations are presented in the following sections.

### **4.3.2 Resedimentation**

#### **4.3.2.1 Introduction**

Resedimentation involves consolidating a dilute slurry one dimensionally in a cylindrical container known as a consolidometer. The process goes back to Ladd & Varallyay in 1965 when they produced partially saturated samples that were subsequently saturated using a 200 kPa back pressure. Germaine (1982) refined this technique to produce fully saturated, uniform samples of Reconstituted Boston Blue Clay (RBBC) with a salt concentration of 16 g/l. Further modifications were introduced by Seah (1990) to increase productivity, improve sample uniformity, and to allow continuous monitoring of the consolidation process. All these techniques produced a large soil cake that was trimmed into smaller pieces and stored for use in a number of tests.

Abdulhadi (2009) developed a new resedimentation procedure for Boston Blue Clay (BBC) in order to produce test specimens. Dry powder is thoroughly mixed with deaired water

to achieve a water content of 100% in order to produce homogeneous soil slurry without lumps. This water content is about double the liquid limit (43 – 47%). Sodium chloride is added to slurry to achieve a concentration of 16 g/l. The sodium chloride produces a flocculated particle structure and prevents segregation of soil particles during sedimentation. The slurry is then vacuumed to get rid of the entrapped air bubbles using the setup shown in Figure 4-6. The slurry is de-aired as it drops into the vacuum flask. A funnel with a long tube is used to place the slurry into the consolidometer to ensure no air is introduced back into the slurry as shown in Figure 4-7. The consolidation of the slurry takes place in a rigid wall consolidometer. Figure 4-8 shows the general setup of the consolidometer. A tube sits on a porous stone base in a bath of water. A smaller porous stone topped with filter paper is located inside the tube and separates the soil slurry from the base stone to prevent extrusion of the slurry. Another porous stone and filter paper lay on top of the slurry and a top cap is placed over the stone. The soil consolidates by applying load at the top through a piston. The soil slurry is loaded incrementally, with a load increment ratio,  $\Delta\sigma_v/\Delta\sigma_v = 1$ , to a prescribed maximum vertical effective stress then unloaded to overconsolidation ratio (OCR) of 4. At OCR = 4 the soil is close to hydrostatic effective stress conditions (i.e.,  $K_0 = \sigma'_h/\sigma'_v \approx 1$ ) and therefore, the shear strains due to sample extrusion from the consolidometer are minimal (Abdulhadi, 2009). After consolidation is complete, the soil is removed from the consolidometer by extrusion and prepared for testing.

Other soils that have been successfully resedimented include Kaolinite, Ugnu clay, Gulf of Mexico Clay, and San Francisco bay mud. However, the property requirements for successful resedimentation are not known. Cohesion characteristics and clay content can be generally regarded as important attributes. The minimum levels of cohesion and clay content required have not been developed to date. Before work began to reconstitute this material, it was believed that the true cohesion displayed in the slake test and the 10% clay content in the silt would allow successful resedimentation. The following sections discuss the procedure, problems and evaluation of resedimentation.

#### 4.3.2.2 Resedimentation Procedure

Before attempting to prepare a sample for resedimentation, sedimentation quick tests were performed with various salt quantities. The aim of the tests was to establish the salt and water content combination that resulted in a stable slurry. Uniform sedimentation of the material is a key characteristic in determining if salt has an effect, i.e., if the coarse grains fall to the bottom first where there is no salt and they don't if there is a salt content. The exact conditions during sedimentation in Skibbereen are unknown. However, based on an understanding of the geology (Section 2.4), a good assumption is that the material was deposited in a marine environment. This indicates that the salt content at the time of deposition would have been 35 grams per liter of pore fluid (g/l) (sea water conditions). The results of salinity tests will be presented in detail in Chapter 5, however, it was found that the salt content has been leached. The cause of this is most likely due to the fresh water river running through the town, artesian pressure from surrounding hills, and diffusion.

Four test tubes were filled with 5 grams of material. Water was then added to each test tube so the specimens would have a water content equal to 200%. Finally the tubes were modified for salt content. One test tube had no salt added and it was the control tube. The other three test tubes were adjusted by adding natural sea salt, leaving the salt content in the pore fluid equal to 10, 20, and 30 g/l, respectively. A natural water content of 25% was selected for these calculations. This value is approximately equal to the liquid limit. The test tubes were then shaken for 10 minutes, ensuring that the salt dissolved. They were then placed in a test tube holder and monitored. The sedimentation speeds appeared to be the same for all four tubes. After two hours the material had completely settled and the pore fluid was almost clear at the top of each tube. Figure 4-9 shows uniform sedimentation was found in each tube when the sedimentation profile was analyzed. Due to equal sedimentation speeds and uniform profiles, it can be concluded that salt has a negligible impact on the resedimentation process. However, due to the known marine environment in which the material was originally deposited a slurry containing 10 grams of salt per liter of pore fluid was selected.

After the salt concentration was selected, the water content to prepare the slurry at was investigated. As mentioned previously, Abdulhadi (2009) used approximately twice the liquid limit for RBBC. This approach was selected as a good starting point for resedimentation of this



material. Chapter 5 will present the characterization results in detail. However, the liquid limit was found to be 25.77%. Using this information, a water content of 50% was first selected. A small batch was created; however, it was found that the slurry was very “watery”. The slurry was found to be segregating, where the particles were found to settle to the bottom and the water was coming to the top of the slurry. Further trials were then conducted, reducing the water content in each. A final water content of 35% was selected, producing a slurry that was workable for vacuuming and placement in the consolidometer with enough viscosity to hold its integrity throughout the re-sedimentation process.

A consolidometer with the same diameter to the one shown in Figure 4-8 was used (7.62 cm). The height of the consolidometer was reduced to 20 cm because the reconstituted material was to be first used for Constant Rate of Strain (CRS) tests. The first batch filled the tube with 10.2 cm of slurry. Using the same technique as Abdulhadi (2009), the slurry was incrementally loaded. Strain was measured using an axial displacement transducer. The slurry was loaded to a vertical effective stress of 100 kPa and unloaded to an OCR of 4. The total deformation during loading was found to be 1.8cm producing a strain of 18% for the batch. A typical time strain deformation plot can be seen in Figure 4-10. It can be noted in the figure that the end of primary consolidation occurs at 7 minutes for the 4 kg load added in this increment.

#### 4.3.2.3 Resedimentation Problems

There were significant problems associated with the resedimentation procedure. They were all associated around extruding the specimen from the consolidometer and trimming it for testing.

The difficulties of the material became apparent during the extrusion of the first specimen. Figure 4-11 shows the material after it was extruded. The material “flowed” like a viscous fluid as it was being extruded from the consolidometer. Its maximum height was approximately 0.5cm, it displayed no structural shape, and it looked like a fluid after it stopped “flowing”. However, Figure 4-12 shows some of the observations after the flow. The material generated a very dense state and it was difficult to cut and remove from the glass plate. The exact cause this behavior is unknown. However, the behavior could be attributed to the material not

having enough cohesion to generate negative pore pressures and induce effective stresses while it is being extruded. Once a situation occurs where zero effective stresses are present the material begins to flow. The flow then accelerates until it finds a stable position and stress state. The flow rearranges the particles into a very dense state, i.e., a parallel plate like structure is formed, where it was difficult to cut and remove.

After the failure of the first batch, modifications were made to the extrusion process. The material was allowed to dry in the consolidometer after the consolidation process providing a partially saturated material to extrude. The decrease in water content increased the stability of the material during extrusion. However, in the second batch a “jelly donut” effect was observed. The outside of the sample had a stable structure but the internal section was “liquid like” displaying very soft unstable properties. Figure 4-13 shows some examples of the behavior observed. Allowing the material to dry further increased the stability, enabling the material to be trimmed.

Further problems were encountered during the trimming process. Despite the partially saturation conditions and the material appearing dry enough to work, trimming the material attracted moisture to the locations where the trimming knife was being used. This caused the material to become “sticky” and difficult to cut, which further exacerbated the excess water problem further. Eventually the specimen became unstable and disturbed as shown in Figure 4-14. Successful trimming was conducted over an eight hour period. The excess water attracted to the trimming locations was allowed to dry and then trimming would recommence. The procedure was repeated until the specimen was trimmed to the desired dimensions.

#### 4.3.2.4 Resedimentation Evaluation

After four batches it was decided to abandon resedimentation as a method of reconstituting the material. Poor repeatability in the CRS testing results, the extremely difficult process of extruding and trimming, and the realization that it would not be possible to trim a free standing sample for a triaxial test were the principle reasons for this decision. It was also obvious from the observations that trimming was causing disturbance.

### **4.3.3 Undercompaction**

#### 4.3.3.1 Introduction

When it became apparent that resedimentation was not an option for this material, another method of reconstituting the material had to be considered. The undercompaction procedure is a method that combines kneading compaction with density control (Germaine & Germaine, 2009). The method was first developed by Ladd (1977) for specimen preparation and cyclic stability testing of sands. The procedure is applicable to any material and density. It is mainly used on sands due to the difficulty in fully saturating samples with smaller grain sizes when the undercompaction procedure is complete. The undercompaction method was considered the only alternative to reconstitute this material. However, before attempting to use undercompaction it was still uncertain if it would be successful. This was due to the difficulty associated with saturating silt and clay size particles in the various testing devices.

#### 4.3.3.2 Procedure

The specimen is compacted by tamping the surface with a rod to a specific height. The specimen is constructed in layers. The height and number of each layer is dependent on the required specimen height. Typically, 3 layers are used for the CRS and one dimensional oedometer tests, while 5 layers are normal for a triaxial specimen. The aim of undercompaction is to achieve a specimen with uniform density by adjusting for the fact that compaction of the upper layers induce additional compaction of the layers below (Germaine & Germaine, 2009). The number of layers, the molding water content, the target density, and the undercompaction of the bottom layer all effect the uniformity of the specimen. Initial molding water contents can be almost any value, but must have continuous air voids in the compacted condition. For coarse grained materials such as sand, low water content in the region of 2% is typically used to bulk up the material.

Specimens are formed in a rigid mold. The total specimen mass is computed based on the mold dimensions. This mass is divided up into equal portions based on the number of layers. The

percent of undercompaction in the bottom layer is determined experimentally and varies linearly with each layer. The compaction control height for each layer is calculated with Equation 4.1:

$$h_n = \frac{h}{m} [(n-1) + (1 + u_n)] \quad (4.1)$$

Where:

$h_n$  = height to top of layer n (mm)

$m$  = total number of layers

$h$  = total height of specimen (mm)

$n$  = layer number

$u_n$  = undercompaction for layer m

The percentage of undercompaction for each layer is calculated using Equation 4.2:

$$u_n = u_1 - \left( \frac{u_1}{m-1} \right) (n-1) = u_1 \left( \frac{m-n}{m-1} \right) \quad (4.2)$$

Where:

$u_1$  = the first layer, which is the bottom layer.

A schematic diagram showing the notations used in Equations 4.1 and 4.2 can be seen in Figure 4-15.

The required water content to bulk up the material was first investigated. Batches of the dry powder material were prepared and sprayed with water to various degrees of saturation, as shown in Figure 4-16. It was found that a minimum water content of 3% is required to allow the material to be compacted and the material bulks up well at a water content of 7%. After a water content of 9% the material becomes too cohesive and tends to stick to the bowl and compaction devices. An original water content of 7% was selected for undercompaction. This value was later modified to 3% for the purposes of the triaxial tests. The reasons for this change will be discussed in Section 4.5.5.3.

When the water content was decided, trials for the percent of undercompaction to use were conducted. In general, 4% is used in the bottom layer for sands, while clays can be as low

as 0%. Due to the low clay content (11%), 4% of undercompaction was first selected. However, it was found that the top layer was difficult to compact and appeared much denser than the layers beneath. Another trial was conducted at 2% undercompaction, producing similar results. Finally, a trial using undercompaction at 0% in the bottom layer worked best for this material. It was observed that densification tends to occur close to the tamping rod; therefore, the material does not distribute the impact throughout the depth of the material.

Once the specimens were prepared, various saturation techniques for the different devices were generated. A detailed description of the saturation process for each device can be found in Section 4.5.

#### 4.3.3.3 Undercompaction Problems

The undercompaction procedure is a very simple and effective method for producing silt specimens. However, the saturation process which follows specimen preparation is problematic.

Saturation is required to remove air from the specimens and allow uniform starting conditions for testing. Undercompacted specimens of Skibbereen Silt deform during this saturation process. Significant strains are sometimes recorded. The magnitude of strain is dependent on the initial specimen density and the confining pressure during saturation. A high density will produce lower strains, i.e., a dry density of  $1.45 \text{ g/cm}^3$  or greater will minimize strain. However, dry densities of  $1.35 \text{ g/cm}^3$  or lower can produce strains of up to 20% during saturation. The confining stress is required to keep the specimen stable during saturation. The larger the confining stress the greater the strain during saturation. The problem is highlighted in the next chapter when the consolidation results are presented. Different confining stresses produce different strains and void ratios. The problem is magnified because the compression curves do not converge easily at higher stresses.

Non uniform density throughout the undercompacted specimens is also an issue. As mentioned in the previous section the force of the tamper tends to produce localized increases in density, i.e., the top of each individual layer has a higher density than the bottom of it. The problem became particularly evident during triaxial testing. The radial cell pressure reduced the

cross section area more in the bottom of each layer. A solution to this problem will be discussed in section 4.5.5.3.

#### 4.3.3.4 Undercompaction Evaluation

Undercompaction provides a very simple and repeatable way for producing specimens. Despite the problems outlined above, at present there is not a better method for reconstituting this type of material. Care must be taken during the saturation phase. However, the positives of this technique far outweigh the negatives and undercompaction produces repeatable results which was critical in the testing program.

## 4.4 EQUIPMENT

### 4.4.1 Introduction

The various testing devices will be reviewed with the relevant testing procedures in the final section of this chapter. This section will focus on the common elements used to successfully run a test, namely, measurement instrumentation, data acquisition, and computer control software.

### 4.4.2 Measurement Instrumentation

Tests require simultaneous readings of time, deformation, and force. These measurements can be made by manual devices, such as stopwatches, dial gages, and proving rings. However, as the frequency, need for greater resolution, and testing time increase, the manual devices are limited and electronic instrumentation prevails. Transducers are used to measure physical quantities during a test. The transducers can be logged by a central data acquisition system, reducing man hours required to run a test and the possibility of recording errors. Transducers can be broken down into the following categories: load cells, axial displacement transducers, pressure transducers, and volume change transducers. They require a common input voltage of approximately 5.5 volts Direct Current (DC) to operate efficiently. The measurements obtained together with the devices, calibration factors, resolution, and transducer stability can be seen in

Table 4-1, 4-2, 4-3, 4-4, and 4-5. The following sections present the different transducer categories.

#### 4.4.2.1 Load Cells

The load cells used in the various testing equipment are Data Instruments JP type shear beam load cells with an exception of a 10,000 lb (44.5 kN) load cell from Toledo Transducers Inc. used in CRS tests. All load cells use an S-shaped steel section instrumented with strain gages. The triaxial devices use a 500 lb (2.2 kN) load cell, the DSS device uses a 1000 lb (4.45 kN) load cell to measure vertical stress and a 500 lb (2.2 kN) load cell to measure horizontal stress, the hydraulic conductivity apparatus uses a 2000 lb (8.9 kN) load cell, and finally the CRS equipment uses a 500 lb (2.2 kN) load cell for low stresses and a 10,000 lb (44.5 kN) one for high stresses.

#### 4.4.2.2 Axial Displacement Transducers

The specimen's axial displacement is measured using a Linear Variable Differential Transformer (LVDT) manufactured by Trans-Tek inc. (Series 240). These transducers have a linear range of approximately 2.5 cm. The LVDT casing is a faraday cage and generates a magnetic field through which the ferromagnetic core moves. When the core moves through the casing it produces an output voltage change directly proportional to the displacement.

#### 4.4.2.3 Pressure Transducers

Pressure transducers are used in tests such as the Trautwein CRS and triaxial device, where accurate measurement of cell and back (pore water) pressures is required. Data Instruments AB/HP type pressure transducers measure absolute pressures by the deflection of a steel diaphragm instrumented with strain gages. Both the CRS and triaxial device use 200 psi (1.4 MPa) pressure transducers.

#### 4.4.2.4 Volume Change Transducers

Volume change of the specimen during a triaxial test or hydraulic conductivity measurements are determined by measuring the displacement of the piston in the Pressure Volume Controller (PVC) cylinder (known as Pressure Volume Actuator (PVA) in computer

control) using either an LVDT or a string pot. The area of the piston is known and remains constant; therefore, volume change equals displacement multiplied by the calibrated piston area. The LVDT used in standard PVC's is a Trans-Tek Series 240 displacement transducer with a linear range of 10 cm. The string pot (linear position transducer) is manufactured by Celesco (SP1 type). They work under the principle that when movement occurs the wire rope rotates an internal capstan and sensing device (precision potentiometer) to produce an electrical output signal proportional to the wire rope extension. The string pot is now favored over the LVDT because its range is 30 cm, it has a very high output, and there is no A/C noise.

#### **4.4.3 Data Acquisition System**

The MIT Geotechnical laboratory utilizes a computer based central data acquisition system for the majority of its tests. This provides a single repository for all transducer measurements. The computer based system is flexible, allowing setup of complicated recording schedules. It is also a very cost effective method of recording data in larger laboratories.

A schematic diagram of the centralized data acquisition system can be seen in Figure 4-16. The data acquisition can be broken down into the following basic components:

- The laboratory device, which contains the transducers, power supply, junction box, voltmeter, and ground.
- A switching mechanism which allows the data acquisition computer to select a particular transducer to measure.
- A Analog to Digital (A/D) converter then changes the voltages from each transducer and the power supply to digital word. This device is critical to the precision of the final measurement.
- A computer which orchestrates the components and performs the administrative and computational tasks.

The MIT Geotechnical data acquisition system is based on an Intel 486 microprocessor PC driven by Windows based software interfaced with an expanded channel Hewlett Packard HP3497A data acquisition unit which uses very low noise integrating analog to digital converter.



The system has a 5.5 digit integrating analog to digital converter with auto-ranging amplification to four voltage scales (0.1, 1, 10, 100V). The system is configured to monitor 140 channels simultaneously while providing analog to digital conversion and data storage at rates up to 1 Hz.

#### **4.4.4 Computer Control System**

The modification of existing manual system components to permit automation was first conducted in the MIT Geotechnical laboratory in the early 90's. Sheahan (1991) developed an automated stress path triaxial cell for testing. The addition of innovative new components to complete the system automation, increase flexibility, and quality control has continued ever since. Automation of other laboratory devices has followed such as the high pressure triaxial cell (Anderson, 1991), the direct simple shear device (Ortega, 1992) and a special Caisson Element Test (CET) cell (Cauble, 1996). The main advantages of automation are the huge reduction in labor requirements. Automation also reduces the chances of human error in a test.

Automation is controlled by a closed feedback loop for the driving systems of the apparatus. It works under the following principles:

- The transducers measure the actual specimen stress-strain state.
- The transducer signals are sent to the computer and converted to engineering units.
- Software compares these engineering units with a prescheduled time history of specimen state.
- A control algorithm computes what action needs to be taken by the electric motors to keep the stress-strain state on schedule.
- Signals are then sent to the electric motors carry out the action required.

Sheahan et al., (1990) describes closed loop feedback control as direct measurements in an iterative system to maintain specific time histories of the parameters being measured.

The hardware to convey electronic information along the digital feedback control loop is presented in Figure 4-17. The output from the transducers is sent to an analog to digital (A/D) converter which translates the analog signal in volts to digital signal in bit counts. Multichannel analog to digital converter devices (MADC) are used. They provide high precision with a

minimum 18 bit resolution. The key component of the MADC is the Analog Devices AD 1170 analog to digital convertor. A computer processes the incoming signals and determines the new command signal to be sent to the testing device. The command signal generated is then converted back into an analog signal through a digital to analog (D/A) converter board that is located within the computer. The D/A converters are a commercial board manufactured by Strawberry Tree Inc. with a 12 bit resolution and a  $\pm 5$  volt range. The analog signals are sent via a motor driver from the D/A converter to the electric motor. The electric motor then drives the required components such as the piston in the PVA to adjust pressures or the piston of the load frame to adjust axial load. Electro-craft motors Model E286 are used in the majority of MIT load frames, while Electro-craft motors Model E372/352 drive 0.5 Tonne actuators in the PVA's.

Automated control is carried out using a control program written in the QBASIC programming language. The program allows the user to set up the system for testing and also allow for test control. The software was originally developed for automated triaxial tests but has been constantly updated since. It is now task specific, allowing functions such as initial pressure up, saturation, consolidation, and shear phases. However, even with local computer control the central data acquisition system is used for recording data.

## **4.5 TESTING PROCEDURES**

### **4.5.1 Introduction**

This section will cover procedures for the various tests conducted in this research. The first section will identify the methods used to characterize the material. Then the section will move on to the more complicated testing procedures used in constant rate of strain (CRS), hydraulic conductivity, direct simple shear (DSS), and triaxial testing. The problems encountered will also be stated where applicable and what methods were deployed to overcome these difficulties.

## 4.5.2 Characterization

### 4.5.2.1 Introduction

After processing the material into a dry powder an extensive characterization program was undertaken to identify the physical properties. The grain size distribution, atterberg limits, salinity, specific gravity, organic content, and mineralogy were established. The procedures employed are briefly presented here. This section does not include the procedures for mineralogy identification. Scanning electron microscope (SEM) technology and X-ray diffraction were utilized for the mineralogy. The work and evaluation was conducted by Robert Martin

### 4.5.2.2 Grain size analysis

The sedimentation method was used for determining the grain size distribution. Hydrometer tests were conducted in accordance with ASTM D422 Particle-Size Analysis of Soils. The concept is that the smaller particles take longer to drop out of solution. Determination of the particle size during sedimentation is based on Stoke's Law. A full description of the procedure and the calculations involved can be found in the ASTM standard.

### 4.5.2.3 Atterberg Limits

Atterberg limits are determined for fine grained soil material. Atterberg limits are conceptual boundaries between various states of material behavior involving mixes of soil and water. The liquid limit tests were first run in accordance with ASTM D4318. The method uses the Casagrande cup and measures the number of drops or "blows" required to close a groove for a length of 13mm. However, this method was unsuitable for the material. The material is difficult to groove at any water content and liquefies at small vibrations. Therefore, it was extremely difficult to get satisfactory results. The method was abandoned for the BS 1377 Fall Cone Method for determining the liquid limit. Germaine & Germaine (2009) states that the fall cone method provides more consistent results since it is subject to fewer experimental and operational errors. The plastic limit was established by rolling as directed in ASTM D4318.

#### 4.5.2.4 Specific Gravity

Specific gravity is defined as the ratio of the mass of a given volume of soil particles to the mass of an equal volume of distilled water at 4<sup>0</sup>C. The specific gravity analysis was performed in general accordance with ASTM Standard Test Method D854.

#### 4.5.2.5 Salinity

The chemical composition of the pore fluid is important to the behavior of fine grained soils. As indicated in Section 4.3.2, salt concentration can have an effect on resedimentation characteristics. High soil sensitivities are also noted in places where salt is leached from clay deposits. This is particularly prominent in fine grained soils where the thickness of the double layer around clay particles and consequent interaction between particles is influenced by salt concentration.

Salinity is the term used for the amount of salt that is dissolved in the pore fluid. Salinity is expressed in terms of grams per liter. The measurement system must be calibrated to obtain the relationship between salt concentration and electrical conductivity. A traceable portable conductivity meter, model 23226-505 from VWR International was used for the measurements. The meter was calibrated using various concentrations of sea salt while recording the electrical conductivity.

There is currently no standard test method for salinity analysis. The following procedure is based a protocol used at MIT (Martin, 1982).

- Record the mass of a centrifuge tube with cap.
- Add soil to the tube (approximately 15g dry mass).
- Record the mass of centrifuge tube, cap, and soil.
- Add distilled water and record mass of centrifuge tube, cap, soil and water.
- Add a few glass beads and shake vigorously for 30 seconds.
- Allow 20-30 minutes for equilibration and repeat 30 seconds of shaking.
- Place tubes in centrifuge and run at approximately 5000 rpm for 10-20 minutes.  
A Damon/IEC Division, IEC HT Centrifuge was used for these samples.
- Decant the supernatant liquid from each tube into a 10ml glass beaker.

- Clean the probe with distilled water and dry.
- Measure the conductance of the reference salt solution.
- Clean the probe with distilled water and dry.
- Measure the conductance of distilled water.
- Dry the probe.
- Measure the conductance of the clear supernatant liquid from the sample.
- Clean and store the probe.

The conversion factor generated from the calibration can be used to determine the salinity of the supernatant. The salinity of the test specimen can be then calculated by multiplying this figure by the testing water content and dividing it by the natural water content, as shown in Equation 4.3:

$$RSS = SS \times \frac{w_c}{w_n} \quad (4.3)$$

Where:

RSS = salinity of the test specimen (g/L)

SS = Salinity of the liquid supernatant (g/L)

$w_c$  = water content of soil specimen (%)

$w_n$  = natural water content of the specimen (%)

#### 4.5.2.6 Organic Content

Organic content by loss on ignition is typically determined on sandy soils as well as organic clay, organic silt, and mucks for geotechnical purposes. The organic content analysis was performed in accordance with ASTM Standard Test Method D2974. The material was placed in an oven at 400<sup>0</sup>C overnight.

### 4.5.3 Constant Rate of Strain (CRS) Tests

#### 4.5.3.1 Introduction

The Constant Rate of Strain Consolidation test was first developed by Smith and Whals (1969). It was similar to the one shown in Figure 4-18 with the intended purpose of performing quicker consolidation tests. Soon afterwards, Wissa et al. (1971) developed the MIT CRS device we are familiar with today. It incorporates a cell which allows for back pressure saturation before consolidation (Figure 4-19). In comparison with the conventional oedometer test, the CRS device produces better defined compression curves and the tests are performed more quickly. Data are also easily collected with a basic data acquisition system and little labor is needed.

CRS tests for this research were performed in a fixed ring oedometer with top and bottom drainage capacity. Figure 4-20 shows the oedometer used. There were many reasons why this apparatus was selected instead of the conventional CRS device. The principle reasons are presented here:

- a) The strain rate must be selected in advance in anticipation of the drainage properties of the soil. Hazen's formula (Equation 4.4) was used to estimate the expected hydraulic conductivity. Based on this estimated hydraulic conductivity, Equation 4.5 was then applied to calculate the strain rate required to generate excess pore pressures. It was found that the strain rate required was very high (>10%/hour) and it would cause stability problems with the automated control of the test. Therefore, it was decided that the rate of consolidation and hydraulic conductivity properties of the material could not be measured using the CRS method. A slower strain rate (6%/hour) generating no excess pore water pressures was used.

$$k = 0.01D_{10}^2 \text{ (m/s)} \quad (4.4)$$

$$k = \frac{1}{2} \frac{\varepsilon^o H^2 \gamma_w}{u_h} \quad (4.5)$$

Where:

$k$  = hydraulic conductivity in meters/second

$D_{10}$	=	the grain size in millimeters corresponding to 10 % passing on the particle size distribution curve.
$\epsilon^{\circ}$	=	strain rate
H	=	height to drainage
$\gamma_w$	=	unit weight of water
$u_h$	=	measure pore pressure

- b) Saturation of the material from a moist undercompacted state also was a major issue. The drainage lines in the base of the oedometer can easily be connected to a water reservoir. The reservoir can be used to apply a constant head of water to the specimen, thereby, saturating it through upward water flow. Upward flow is particularly important in saturation because it minimizes the possibility of trapped air. Germaine (1985) also states that back pressure saturation has little to no effect on the compression curve but does generally increase the rate of consolidation. Because rate effects were no longer an issue, this saturation procedure was adopted.
- c) The load frames for the conventional CRS apparatus are 1 Tonne (9.8 kN) capacity bench top Wykeham Farrance screw driven load frames with adjustable gear ratios. The oedometer cell is much more robust, therefore, a Wykeham Farrance Model T-57, screw-driven loading frame with a 10,000 lb (44.4 kN) capacity and 30 displacement rates ranging from 0.0037 to 46 cm/hour was used. The increase in load frame capacity allowed the oedometer CRS setup to go to stresses of approximately 15 MPa.

Strain was measured using a specifically designed system. A stainless steel top cap was fitted with an LVDT holding plate. The plate had an opening in its center to allow for direct contact between the load cell and the top cap. This prevented distortion of the plate at high stresses and allowed for accurate strain measurement. The plate had two LVDT's attached so an average value could be used in the event that there may not be uniform deformation in all areas.

#### 4.5.3.2 Procedure

- 150 grams of dry powder is placed in a bowl and “bulked up” to a moist state with the addition of 7% water. The sample is stirred continuously and then covered with a plastic wrap to prevent moisture loss.
- The mass required for the testing density is then divided equally into 3 tares. Each tare represents a layer that will be compacted in the oedometer ring. The tares are also covered with plastic wrap until they are required.
- The oedometer cell is assembled and the specimen layers are compacted into place by a tamping rod. The rod has a locking ring on it which controls layer depth and a compaction collar sits over the oedometer ring which provides a stable platform for using the rod. Figure 4-21 shows the devices used and the standard configuration for the test setup. Undercompaction at 0% is used in all tests.
- Once the material is compacted, 10 micron nylon filter screen, a porous stone, a standard oedometer top cap, and the fabricated top cap with the LVDT holder are placed on the specimen and the oedometer is aligned into position in the load frame.
- The reservoir is connected to the oedometer and filled with water. A hose clamp is used to prevent flow to the oedometer until required.
- Dead weights are placed on the top cap. A hanger system with two loading points at each end of a crossbar was used. The purpose of the dead weights is to apply a vertical stress to the specimen and ensure “quick” conditions will not occur during the saturation process. i.e., the material will not have zero effective stress and turn to a fluid from the upward flow of water. A vertical stress of 3.6 kPa is applied to the specimen.
- Water is then allowed to flow through the specimen for a 12 hour period to saturate it. Once the saturation process is complete, the reservoir and dead weights are removed from the system.
- A 500 lb (2.2 kN) load cell is first used to measure the force during the first phase of constant state of strain. Once its maximum capacity is reached, the specimen is unloaded. The load cell is then replaced with a 10,000 lb (44.5 kN) load cell and the specimen is loaded again, producing a unload reload curve. At the desired stress, a second unload reload curve is usually incorporated before the stress applied reaches the



maximum capacity of the load frame and load cell. When maximum capacity is reached, loading is stopped for 3 hours to allow secondary compression take place, then the specimen is unloaded to an over consolidation ratio (OCR) greater than 4, thereby, completing the test. The lower capacity load cell at the beginning of the test gives greater resolution at low initial stresses. This is important when calculating the preconsolidation stress,  $\sigma'_p$ . When the initial portion of the stress-strain curve is well defined the load cell can be changed to allow for higher stresses.

As mentioned previously, strain is measured from the initial dead loading stage to the end of the test using two LVDT's. The readings are also corrected for apparatus compressibility.

Two CRS tests were also performed with the material starting from a slurry state. These tests were run in order to establish if a lower void ratio could be developed during consolidation if the starting conditions were different. Slurry with a 35% water content was prepared and poured into the specimen ring. The oedometer was then placed in the loading frame. Dead weights, starting with the porous stone were then incrementally applied to the slurry. Strain was recorded during every increment with a LVDT. When the slurry was "stiff", constant strain loading then began and the test was run as presented above.

#### 4.5.3.3 Problems

The CRS testing program was relatively successful. Few problems were encountered during loading cycles and the interchange between load cells worked well. The majority of problems were associated with the saturation process before loading. The first tests were failures because of the way the material behaves when it comes in contact with water. As mentioned in Section 4.3.3.3, the structure of the specimen created by undercompaction collapses with the addition of water. This caused problems for the testing configuration. The top caps sitting on the porous stones became unstable and any slight eccentricity caused them to lean to one side, preventing the test from continuing. The addition of axial stress before saturation is the only way to ensure stability. Figure 4-22 shows the successful and unsuccessful loading configuration. The stress is best applied by a crossbar configuration with a loading point at each end. This configuration was found to be much more stable than loading axially through center of the

specimen. Loading axially through the center produced uneven strains during the saturation process.

The correct head of water to apply for saturation was another issue. Calculations were performed to determine a maximum head which could be applied without producing “quick” conditions. However, a head much lower than the maximum limit was used because “blow holes” were found to form around the edges of the specimen ring. The blow holes forced material out of the ring and around the top porous stone, as shown in Figure 4-23. The figure gives a plan view of the specimen ring with the top porous stone in place. The water turned the soil into a slurry and it flowed out the gap between the stone and the specimen ring. A low head results in a very long saturation process. By trial and error a head of approximately 30 cm was used.

#### **4.5.4 Hydraulic Conductivity Tests**

##### **4.5.4.1 Introduction**

Hydraulic conductivity ( $k$ ) is defined as the flow rate through a cross section of soil. As described in the previous section, hydraulic conductivity can be determined by the excess pore pressure generated in a standard CRS test. However, this method was not possible because the hydraulic conductivity of the material was not low enough. Alternatives considered were the standard falling head and constant head hydraulic conductivity tests. However, a new method recently developed at MIT was utilized. It uses a modified CRS device very similar to the one shown in Figure 4-19. The standard CRS device employs one PVA to increase the cell and pore pressure simultaneously during back pressure saturation. The same PVA then holds the cell pressure constant during consolidation while a pressure transducer measures excess pore pressure in the bottom drainage line. The modified setup uses two PVA's. Back pressure saturation and consolidation still occurs in the same manner. However, consolidation can be stopped at any point in the test and a hydraulic gradient can be created across the specimen by setting the pore pressure greater than the cell pressure. The pore pressure PVA will then pump water through the bottom drainage line up through the specimen and the cell PVA will collect the water being driven through the system. The system utilizes Darcy's Law, as shown in Equation

4.6. The head is calculated based on the different stresses recorded by the cell and pore pressure transducers. The volume of flow is simply measured by the LVDT's on the PVA's. The volumes recorded in the cell and pore PVA should be equal. Time is automatically recorded in the data acquisition system. Finally, the height of the specimen can be easily calculated from the strain measurements. The advantage of using this device is that hydraulic conductivity can be checked at different stresses, strains, and void ratios.

$$k = \frac{q}{iA} \tag{4.6}$$

Where:

k = hydraulic conductivity (m/s)

q = volume of flow per unit time (m<sup>3</sup>/s)

A = cross-section area (m<sup>2</sup>)

i = hydraulic gradient (dimensionless) ( $i = \frac{h}{L}$ , where: h = total head dissipation across specimen (m) and L = length of flow path (m))

#### 4.5.4.2 Procedure

- The same procedure to bulk up the material is applied to this test setup. Compaction into the specimen ring is more difficult due to the confinements of the apparatus. A successful approach was found where the specimen ring is taken out of the device and inverted with the recess tool placed under the ring. Figure 4-24 shows the ring being filled from top to bottom with the described configuration. The ring is inverted so the compaction equipment will not damage the cutting edge used in the conventional trimming setup. The method also provides a standard recess for testing.
- Once the specimen is prepared, it is placed in the CRS device. The piston of the CRS device applies a uniform stress across the area of the specimen. The weight of the piston alone is considered adequate stress to allow for saturation.
- The flow for saturation is controlled by manually adjusting the PVA motor. One motor revolution per minute is regarded as slow enough to prevent quick conditions and “blow outs”.

- Once the saturation process is complete, back pressure saturation can occur in the conventional fashion. When complete, consolidation to the desired stress is achieved. The stress is applied through use of a 1 Tonne (9.8 kN) capacity bench top Wykeham Farrance screw driven load frame. The load is monitored through a 2000 lb (8.9 kN) capacity load cell.
- At the selected axial stress, the hydraulic conductivity measurement can take place. The consolidation process is stopped and the piston is locked in place. New target top and bottom pore pressures are inputted, creating a gradient across the specimen. The flow is recorded over the desired period of time. A differential between cell and pore pressure of 10 and 20 kPa is used to create the gradient. The flow is recorded for 6 hours or until the LVDT's run out of range. When the hydraulic conductivity test is complete, consolidation to a new axial stress level can then continue.

#### 4.5.4.3 Problems

Similar to the CRS tests run in the oedometer cell, saturation is a problem. The water reservoir on top of the PVC was first used as a means of saturating the material. However, the head was found to be too high and it produced the “blow hole” problem that was found in the CRS tests. Manual control of the water supply through the PVC was used as a method to overcome this problem.

Selecting the correct gradient for the hydraulic conductivity testing is also another issue. A high gradient was found to wash the material out of the specimen ring and a low gradient does not create enough of a differential pressure to accurately calculate hydraulic conductivity. As indicated in the procedures section, a differential of 10 and 20 kPa was found to work best.

The selection of filter screen was also found to be a problem. MIT uses a synthetic based material for all its CRS tests. A screen with a 10 micron ( $\mu\text{m}$ ) aperture covering the entire area of the specimen was used in the first hydraulic conductivity tests. The continuous screen was then replaced with a “donut shaped” layout, i.e., the screen only covered the circumference for a thickness of 5mm and the internal part had no filter screen. A significant difference was found in

the plot of void ratio vs. hydraulic conductivity, indicating that filter screen selection plays an important role in CRS testing and the resistance of the screen is significant.

#### **4.5.5 Direct Simple Shear Tests**

##### 4.5.5.1 Introduction

The MIT Automated Direct Simple Shear (DSS) apparatus consists of a standard Geonor Model 4 DSS device, modified for automatic testing. The device used is shown in Figure 4-25. The apparatus features load cells for measuring vertical and horizontal force and LVDT's for measuring vertical and horizontal displacements. Vertical and horizontal displacement motors allow for application of stresses to the specimen. The full automation allows for consolidation under constant rate of strain (CRS) loading and maintains constant height during shear. The test specimens are approximately 35 cm<sup>2</sup> in area and 2.1 cm in height. They are enclosed in a Geonor wire reinforced rubber membrane. The membrane is assumed to have negligible lateral deformation and therefore specimens are consolidated under  $K_0$  conditions. The trimming apparatus is specially designed to trim specimens with minimum disturbance.

A procedure was developed to setup and saturate the specimens. First, the brass pedestal (which the specimen sits on) was modified and a water feed system was created which allowed for saturation. Six drainage holes in groups of three usually exist in a pedestal. They are located just below the porous stone and allow for free drainage during consolidation. Two of these holes and the internal drainage lines in the pedestal were enlarged to accommodate water flow during saturation. The enlarged openings were required to fit water lines to the pedestal. A reservoir was setup underneath the vertical loading arm of the DSS device. Pipes were fitted to form a flow path from the reservoir to the pedestal. A "T" section was incorporated so the flow would be divided to the two drainage holes. The DSS device and reservoir with the accompanying plumbing can be seen in Figure 4-26. Once the hardware was modified, tests were conducted using the procedure presented here.

#### 4.5.5.2 Procedure

- 150 g of dry powder is “bulked up” in the same manner as the CRS tests.
- The mass required for the testing density is divided into 3 tares. Each tare corresponds to a layer that will be compacted in the specimen ring.
- The wire reinforced Geonor membrane is placed in the membrane stretcher and a vacuum is applied to keep the membrane tight to the ring.
- The ring is then lowered down over the pedestal in the trimming rig and clamped in place at the desired position to allow placement and compaction of the material. A height of 2.77 cm is measured down from the top of the ring to the porous stone with a caliper then the ring is clamped. Figure 4-27 shows the membrane, specimen ring, applied vacuum, and trimming device.
- The material is compacted in 3 layers using the same method as the CRS test, producing a final specimen height of 2.13 cm. The material is scarified between each layer to ensure no weak shear planes are present. The compaction sequence is shown in Figure 4-28.
- Once the specimen is prepared, the top cap is lowered down and the membrane is folded around the base pedestal and top cap. The specimen is now enclosed, the vacuum is turned off, and the specimen is ready for testing.
- The reservoir is filled with water and a hose clamp is used to prevent flow through the saturation lines. The saturation lines are then connected to the pedestal as shown in Figure 4-29 and the specimen is placed in the device like a conventional DSS setup. Zero values from the various transducers are recorded at this point. Before saturation begins, the vertical load hanger is disconnected from the loading motor and 2 lb (8.9 N) of dead weight is added to the hanger. This load translates to a vertical stress of 20 kPa (lever arm on device multiplies force applied).
- The hose clamp is removed and water flows up through the specimen and out the drainage holes in the top cap. Saturation occurs over a 12 hour period. Then the vertical load hanger is reconnected to the axial motor and constant rate of strain consolidation begins. The specimen is consolidated at a rate of 1%/hour.

- At the desired axial stress, undrained shear occurs. The specimen is sheared at constant volume, i.e., the computer control maintains constant height throughout the shearing phase while also compensating for apparatus compressibility. Shearing occurs at a rate of 4%/hour until a prescribed strain limit of 30% is reached.
- When shearing ends the sample is removed from the device and its water content is determined.

#### 4.5.5.3 Problems

No significant problems were encountered during the DSS tests. However, care is needed during the compaction process because it is easy to damage the rubber Geonor membranes. These membranes are very expensive and to avoid damage during compaction, a plexiglas compaction collar was manufactured, enabling the material to be viewed during compaction.

The axial strains recorded during consolidation are larger than that recorded in the CRS device at the same stress level. The CRS specimen ring is more rigid than the Geonor wire reinforced membrane and the cause of the greater axial strains is most likely due to the membrane elastically straining in a horizontal direction.

### 4.5.6 Triaxial Tests

#### 4.5.6.1 Introduction

A series of Consolidated-Undrained triaxial tests were performed on the research material. They can be broken down into two groups; Series A and Series B. Series A consisted of Isotropically Consolidated Undrained Compression (CICU) tests, while Series B consisted of  $K_0$  Consolidated Undrained Compression ( $CK_0UC$ ) tests.

Series A tests were carried out in a manually controlled triaxial apparatus. There were many reasons why this system was selected over the automated system typically used at MIT. A considerable “learning curve” was needed to develop a successful and repeatable way of setting up and testing this material. The “less complicated” manual system allows for better access when

preparing the specimens, straightforward methods of applying vacuums and saturating the material, and fingertip controls for cell and back pressures. It is also considerably less expensive than automated machinery for trial and error purposes. Figure 4-30 shows the cell used for testing. These cells were originally manufactured by Wykeham-Farrance and modified in MIT. The cell's loading piston runs through a double linear ball bearing. A Bellofram seal allows low friction movement of the piston while sealing the bearings from the cell fluid. However, cell fluid pressure acting on the seal imparts a large upward force on the piston, and this must be accurately accounted for when computing the axial load on the specimen. A calibration of cell pressure against uplift force was conducted for this calculation.

Series B tests were carried out using the existing automated triaxial apparatus at MIT Geotechnical Laboratory. The significant advantage of automated testing is the ability to perform  $K_0$  consolidated tests, which provide a stress state similar to field conditions. Sheahan (1991), Sheahan & Germaine (1992) and Santagata (1998) give detailed descriptions of the automated stress path triaxial cells. However, a brief overview is presented in this section.

Figure 4-31 shows a schematic of a computer controlled triaxial testing apparatus. The triaxial cell, load frame, PVC's, motor control box, PC, power supply, and data acquisition system are all the basic components required to run an automated test. The triaxial cell shown in Figure 4-32 contains the specimen and sets the boundary conditions. It incorporates internal posts, top and bottom drainage, a fixed top cap and a compact load cell (500 lb (2.2 kN) capacity) located within a Plexiglas chamber for direct measurement of the axial deviator stress. The internal load cell eliminates the effects of friction between the piston and the rubber O-ring seals in the load measurements. The chamber is filled with Dow-Corning "200 fluid", 20 centistokes silicone oil. The oil limits the membrane leakage over time, but more importantly it is not conductive which is essential when locating electronic devices such as the load cell within the triaxial chamber.

#### 4.5.6.2 Procedure

A typical triaxial test can be broken into four stages; 1) cell and specimen preparation, 2) specimen saturation, 3) consolidation and 4) shear of the specimen. The consolidation and shear



procedure for this material are not different from a standard test. However, the methods to prepare and saturation the specimen were unknown before this work. A description of the successful testing procedure for Series A tests will first be presented. The modifications to this procedure for Series B tests will then be discussed. The procedure developed is very similar to that presented by Swan (1994) in his work on Unfrozen Manchester Fine Sand.

#### Series A

- Prior to preparing a specimen, the cell base and the external drainage lines are flushed with water and then pressurized air. A thick membrane (thickness  $\approx 0.3$  mm from Humboldt MFG. Co.) is placed around the pedestal and two o-rings are fitted. A thin membrane (unlubricated latex Trojan brand condom) is then placed around the pedestal and over the O-rings. A third o-ring is placed between the two o-rings covered by the thin membrane. The sealed pedestal is then encased in a split mold, called the membrane expander/specimen former. The expander/former is clamped to the base pedestal by semi circular clamps. The thick membrane passes through the cylinder opening of the expander/former and is folded over the top of it. A vacuum ( $\approx 50$  kpa) is then placed to the space between the inner wall of the expander/former and the thick membrane creating a cylindrical space to create the specimen. The expander/former produces specimens with typical dimensions of 3.54 cm in diameter and 7.46 cm in height.
- The preparation of the material for compaction is very similar to that presented in previous sections. 150 grams of the dry material is placed in a bowl. The material is bulked up with a 3% moisture content. A dry density of  $1.5 \text{ g/cm}^3$  with seven layers of compaction is optimum for triaxial setup. The material is divided by mass equally into tares and covered with plastic wrap until they are required.
- A plastic collar is placed on top of the expander/former to protect the membrane from damage during compaction. Zero percent undercompaction works best for this material. The layers are compacted using a tamping rod with a depth gage to control the height in each layer. Similar to the DSS setup, the specimen is scarified between each layer to ensure no localized weak planes. The compaction configuration can be seen in Figure 4-33.

- Once the specimen is prepared, the porous stone and top cap are placed on top of the specimen. The thick membrane is then folded off the expander/former and placed around the top cap and sealed with two o-rings. The top drainage line is connected to the cell base. The specimen is now completely sealed and a 40 kPa vacuum is applied to the specimen through the top and bottom drainage lines creating an effective stress and a stable specimen. The expander/former is then removed and initial specimen dimensions are measured with a caliper. The thin membrane is then rolled up from the base pedestal, over the specimen and onto the top cap. A final o-ring is fitted to seal the thin membrane against the top cap. Figure 4-34 shows the final stages of the setup.
- The upper frame of the triaxial cell is lowered over the cell base and bolted down. The piston of the cell is then lowered into the recessed hole in the top cap until contact occurs. The recessed hole provides lateral stability. The cell is then filled with water and an initial cell pressure, equal to the applied vacuum, is applied while the vacuum is removed. Dead weights are added to the piston to counteract the uplift forces from the cell pressure on the Bellofram seal.
- Once open to the atmosphere, the specimen is flushed with carbon dioxide, CO<sub>2</sub>, for approximately 20 minutes, and then saturation begins. A reservoir of water with a head of approximately 80 cm is used to saturate the specimen. Flow occurs through the bottom drainage line and out the top line for a 12 hour period. The reservoir is then disconnected and the specimen is back pressure saturated in 25 kPa increments until the cell pressure reaches 350 kPa and the pore pressure reaches 300 kPa.
- A B-value evaluation is followed by isotropic consolidation in 50 kPa increments to the desired stress level. Like the saturation process dead weights are added to the piston to counteract uplift forces from the cell pressure. The specimen is allowed to rest for a 24 hour period at the end of consolidation and then it is sheared undrained at a rate of 10%/hour. After shear, the cell is dismantled, the final dimensions are recorded, the specimen is removed from the cell base and placed in an oven to obtain its dry mass.

## Series B

The procedure outlined above was broadly applied to the Series B tests. However, some modifications were made due to the lower flexibility and confinements of the device. There are no changes to the procedure until the placement of the top cap, application of the vacuum, and saturation of the specimen. The top cap is fixed to the piston in this device and the drainage lines are plumbed directly to the PVA's making the setup more difficult.

- Once the specimen is prepared, the upper frame is lowered over the cell base and bolted down. The piston is then released until contact occurs between the top cap and the porous stone. The piston is clamped in this position and the membrane is folded up around the top cap and sealed with two o-rings. Then the top drainage line is connected to the cell base and a 40 kPa vacuum is applied to the specimen by attaching a vacuum pump to the pore pressure PVA reservoir. As before, the specimen is now stable and the expander/former can be removed. The thin membrane is rolled up and sealed with the final o-ring.
- After assembly of the remaining cell components, the cell is filled with silicone oil and pressurized to 40 kPa (equal the applied vacuum). The vacuum can then be removed, exposing the specimen to the atmosphere. The pore pressure PVA reservoir is also used to feed CO<sub>2</sub> through the drainage lines and flush the specimen. Following 20 minutes of CO<sub>2</sub> saturation, the pore PVA and reservoir are replenished with water. The reservoir is located approximately 40cm above the specimen and this head is sufficient for flow through saturation purposes.
- Saturation occurs over a 12 hour period. Once the saturation phase is complete, back pressure saturation, B-value check, K<sub>0</sub> consolidation, and undrained shear can occur in the conventional automated manner. A strain rate of 0.2%/ hour is used to consolidate the specimen, while a rate of 2% per hour is used in undrained shear.

### 4.5.6.3 Problems

Several mechanical and procedural problems occurred during the triaxial testing program. Most of the difficulties were rectified by experience or by trial and error.

The number of layers to form the specimen, the optimum water content to “bulk” the material, and the percentage of undercompaction were some of the unknowns before testing. A dry density of  $1.45 \text{ g/cm}^3$  with a water content of 7% was first selected. These figures were based on a successful series of DSS tests. Five layers with 2% undercompaction was initially selected as compaction criteria. During back pressure saturation and consolidation significant deviations in the cross sectional area appeared, as shown in Figure 4-35. As mentioned in Section 4.3.3.3, the material consolidated more at the bottom of each layer, indicating that the density of the specimen was not uniform. The force applied by the tamping rod is not transmitted down through the sample but instead it is adsorbed very close to the point of contact. The undercompaction percentage was changed to 0%, the dry density was increased to  $1.5 \text{ g/cm}^3$ , and the bulking water content was reduced to 3%. There was a considerable improvement in the cross section area uniformity; however, the evidence of layers was still present. The number of layers was then increased to 7. The 30% reduction in layer height was found to produce cross sections that looked uniform after consolidation. All successful tests were produced using  $1.5 \text{ g/cm}^3$  dry density with a 3% water content using 7 layers with 0% undercompaction.

The structural collapse of the material during saturation caused problems during Series A tests. The top cap is not connected to the piston in this cell, which allows for isotropic consolidation without the need for piston movement. Initially, the piston was clamped in place so the uplift forces from the cell pressure on the rolling diaphragm could not push it up during back pressure saturation and consolidation. No dead weights are used in this method and when the material collapsed during saturation the piston and top cap are no longer in contact with each other. As indicated in the testing procedure, the top cap has a recess for the piston which allows for lateral stability of the top cap. However, this recess produced a friction problem between the two. During undrained shear, the piston had to slide back down the hole until it re-established the point of contact. The friction forces during this phase generated excess pore pressures, which distorted the results. The first solution to overcome the problem was a top cap with no recess. However, Figure 4-36 shows the results of that method. The lack of structural stability during the early stages of saturation caused the specimen to fall to one side. A further attempt was made using a vacuum saturating technique but it also was a failure. Finally, the only other solution available was to load the piston incrementally with dead weights to counteract the increase in cell pressure. The method keeps the piston in contact with the top cap at all times; however, it is

very laborious and care must be taken that you do not overload the piston at any point, which would change the isotropic stress conditions. In the Series B tests, the piston is fixed to the top cap; however, the triaxial cell has a different design. The Series B triaxial cell had O-ring seals around the piston instead of the rolling diaphragm seal that was used in Series A tests. The O-ring seals increase the friction between the piston and triaxial frame but the internal load cell removes this piston friction measurement. A major advantage of this system is that there is no upward force acting on the piston. During saturation, the piston was free from loading and therefore, it could follow the deformation of the material.

The final and most significant problem that comes from testing this material in a triaxial device is computational based. The sudden collapse of the material during saturation produces high strains and leaves the exact volume of the specimen at the end of the saturation stage unknown. If the volume is unknown, the cross sectional area during shearing cannot be confidently calculated and therefore, the shear strengths are affected. Two methods were employed to mitigate this problem. Both use the final sheared specimen for the calculations. Method one measures the dimensions of the failed specimen thoroughly at the end of the test. The final volume can then be calculated, and the height and area can then be back calculated. Method two uses the final water content to calculate the void ratio and then the final volume. Again, once the volume is determined the heights and areas can be back calculated. Method two has been found to be much more successful. The void ratios fit in much better with the consolidation properties found in the CRS tests. Method one tends to produce low void ratios that are unrealistic for the stress level that was applied.

Measurement	Device	Calibration Factor	Range	Resolution	Stability
Axial Deformation	External LVDT	2.118 cm/v/v	2.5 cm	±0.0003% (0.1 mV)	±0.003% (1 mV)
Axial Deformation	External LVDT	2.079 cm/v/v	2.5 cm	±0.0003% (0.1 mV)	±0.003% (1 mV)
Axial Force	External Load Cell	68.944 kN/v/v	2.2 kN	0.01 N (0.001 mv)	0.1 N (0.01 mV)
Axial Force	External Load Cell	14803.224 kN/v/v	44.5 kN	0.26 N (0.001 mv)	2.6 N (0.01 mv)

Table 4-1: Characteristics of instrumentation used in CRS testing apparatus

Note: Resolution and stability based on central data acquisition system, calculations based on specific dimensions

Measurement	Device	Calibration Factor	Range	Resolution	Stability
Axial Deformation	External LVDT	2.068 cm/v/v	2.5 cm	±0.0007% (0.1 mV)	±0.007% (1 mV)
Axial Force	External Load Cell	357.792 kN/v/v	8.9 kN	0.05 N (0.001 mV)	0.5 N (0.01 mV)
Cell Pressure	Pressure Transducer	68568 kPa/v/v	1400 kPa	0.01 kPa (0.001 mV)	0.1 kPa (0.01 mV)
Pore Pressure	Pressure Transducer	68734 kPa/v/v	1400 kPa	0.01 kPa (0.001 mV)	0.1 kPa (0.01 mV)
Cell Volume	Volume Strain LVDT	21.997 cm <sup>3</sup> /v/v	45 cm <sup>3</sup>	±0.0005% (0.1 mV)	±0.005% (1 mV)
Specimen Volume	Volume Strain LVDT	22.923 cm <sup>3</sup> /v/v	45 cm <sup>3</sup>	±0.0005% (0.1 mV)	±0.005% (1 mV)

Table 4-2: Characteristics of instrumentation used in Hydraulic Conductivity testing apparatus

Note: Resolution and stability based on central data acquisition system, calculations based on specific dimensions.

Measurement	Device	Calibration Factor	Range	Resolution	Stability
Axial Deformation	External LVDT	2.467 cm/v/v	2.5cm	±0.0006% (0.1 mV)	±0.006% (1 mV)
Horizontal Deformation	External LVDT	2.426 cm/v/v	2.5cm	±0.0006% (0.1 mV)	±0.0006% (0.1 mV)
Axial Force	External Load Cell	130.536 kN/v/v	4.45 kN	0.02 N (0.001 mV)	0.2 N (0.01 mV)
Horizontal Force	External Load Cell	67.177 kN/v/v	2.2 kN	0.01 N (0.001 mv)	0.1 N (0.01 mV)

Table 4-3: Characteristics of instrumentation used in DSS testing apparatus

Note: Resolution and stability based on central data acquisition system, calculations based on specific dimensions.

Measurement	Device	Calibration Factor	Range	Resolution	Stability
Axial Deformation	External LVDT	2.614 cm/v/v	2.5cm	±0.0006% (0.1 mV)	±0.006% (1 mV)
Axial Force	External Load Cell	65.356 kN/v/v	2.2 kN	0.01 N (0.001 mv)	0.1 N (0.01 mV)
Cell Pressure	Pressure Transducer	69237 kPa/v/v	1400 kPa	0.01 kPa (0.001 mV)	0.1 kPa (0.01 mV)
Pore Pressure	Pressure Transducer	68638 kPa/v/v	1400 kPa	0.01 kPa (0.001 mV)	0.1 kPa (0.01 mV)
Specimen Volume	Volume Strain LVDT	75.045 cm <sup>3</sup> /v/v	70 cm <sup>3</sup>	±0.0005% (0.1 mV)	±0.005% (1 mV)

Table 4-4: Characteristics of instrumentation used in manual control triaxial testing apparatus

Note: Resolution and stability based on central data acquisition system, calculations based on specific dimensions.

Measurement	Device	Calibration Factor	Range	Resolution	Stability
Axial Deformation	External LVDT	2.084 cm/v/v	2.5cm	±0.0006% (0.1 mV)	±0.006% (1 mV)
Axial Force	External Load Cell	68.625 kN/v/v	2.2 kN	0.01 N (0.001 mv)	0.1 N (0.01 mV)
Cell Pressure	Pressure Transducer	68735 kPa/v/v	1400 kPa	0.01 kPa (0.001 mV)	0.1 kPa (0.01 mV)
Pore Pressure	Pressure Transducer	68671 kPa/v/v	1400 kPa	0.01 kPa (0.001 mV)	0.1 kPa (0.01 mV)
Specimen Volume	Pressure Volume Actuator	96.262 cm <sup>3</sup> /v/v	45 cm <sup>3</sup>	±0.0005% (0.1 mV)	±0.005% (1 mV)

Table 4-5: Characteristics of instrumentation used in automated triaxial testing apparatus

Note: Resolution and stability based on central data acquisition system, calculations based on specific dimensions.



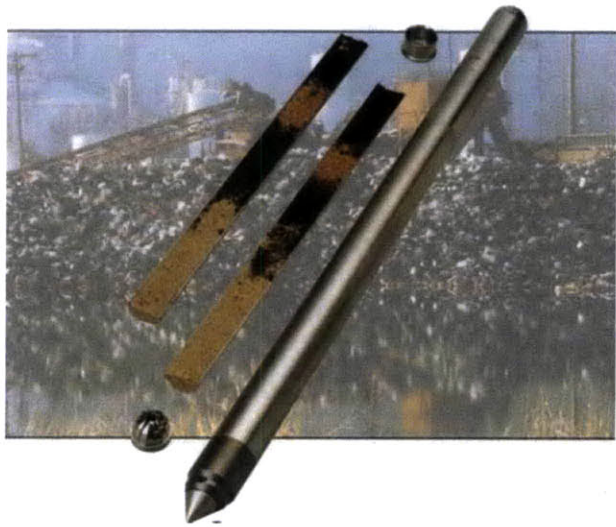
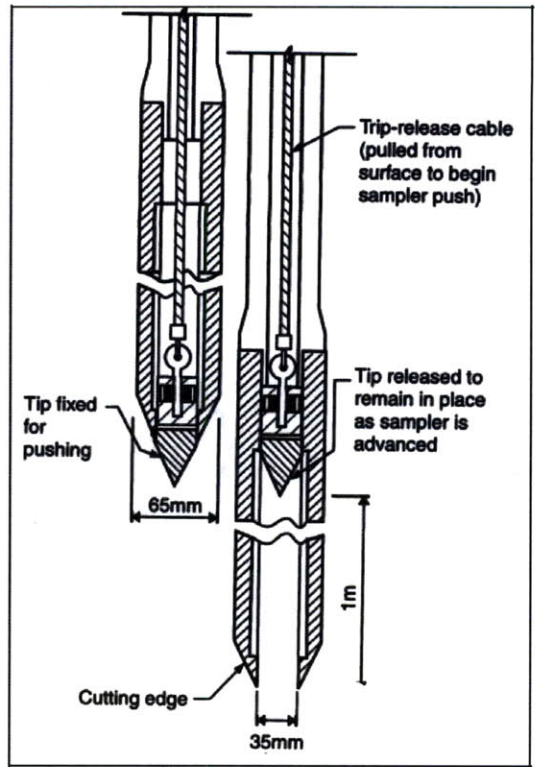


Figure 4-1: Typical MOSTAP Sampler (Lankelma, 2008)



Figure 4-2: Extruded tube sample



Figure 4-3: Bulk Samples Air Drying

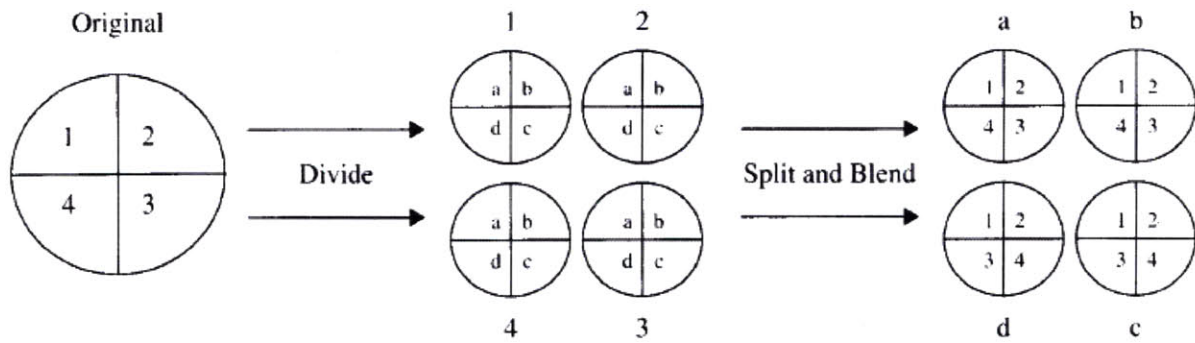


Figure 4-4: Schematic of the blending procedure for large samples (Germaine & Germaine, 2009)



Figure 4-5: Blending in Buckets



Figure 4-6: Vacuum setup to de air the RBBC slurry (Abdulhadi, 2009)

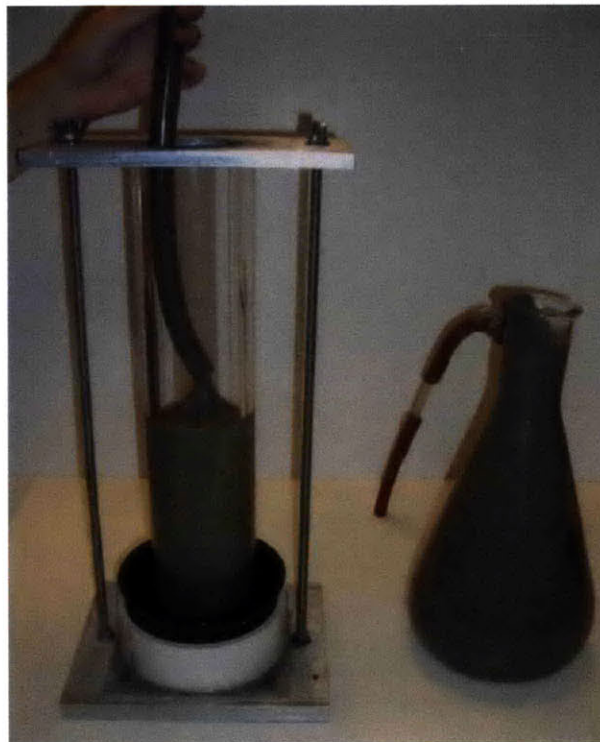
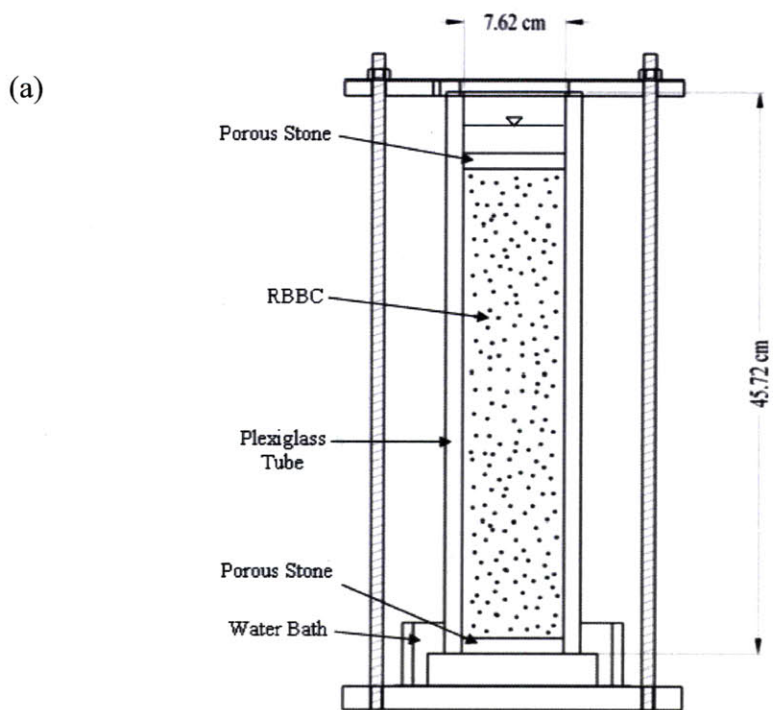


Figure 4-7: Pouring of RBBC into Consolidometer (Abdulhadi, 2009)



(b)

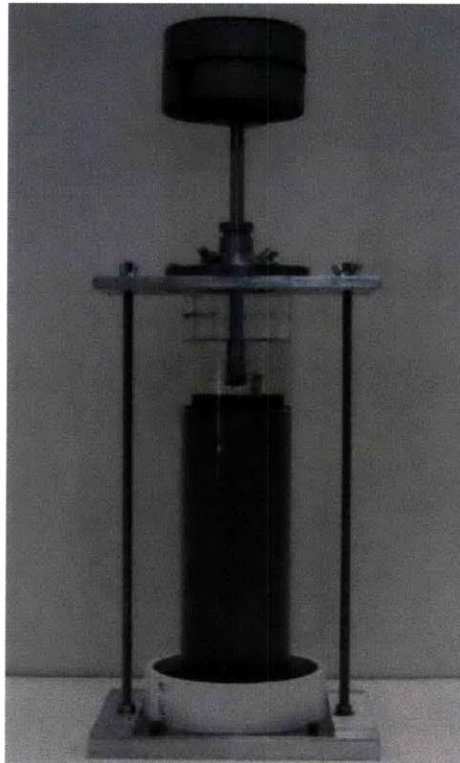


Figure 4-8: Consolidometer with internal diameter of 7.62 cm: (a) schematic, (b) photograph (Abdulhadi, 2009)

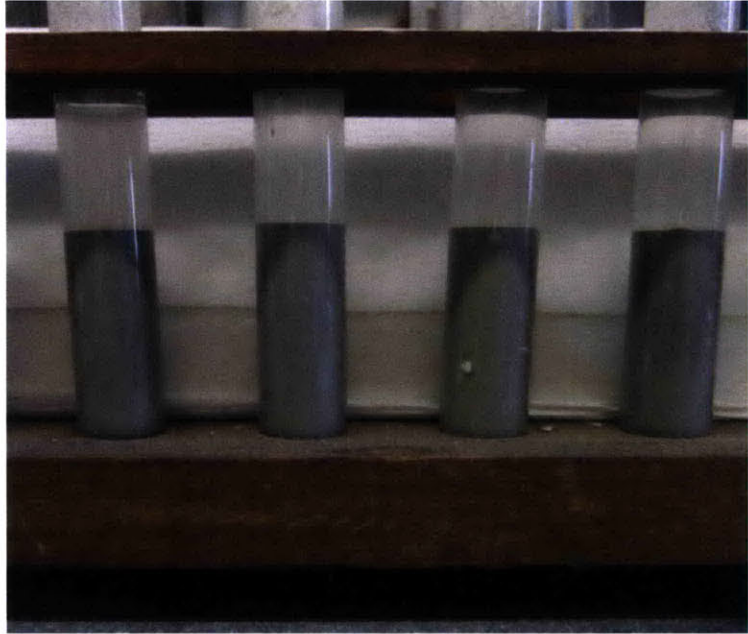


Figure 4-9: Uniform sedimentation with various salt concentrations

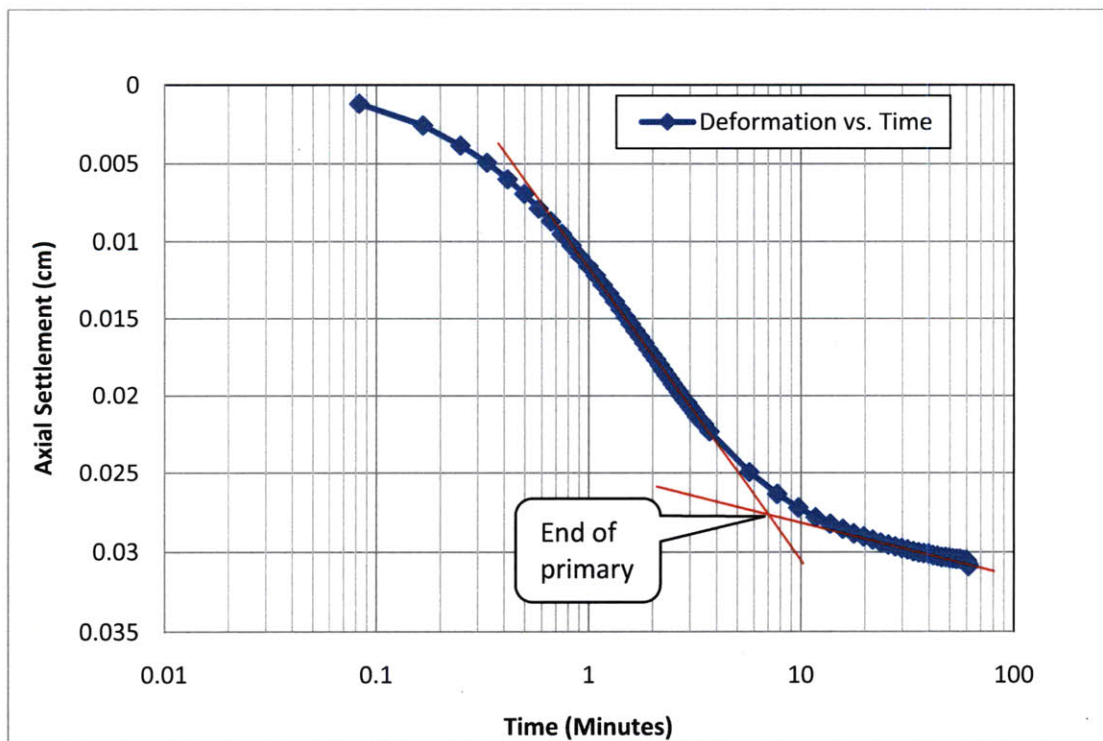


Figure 4-10: Typical deformation vs. Time Plot during resedimentation



Figure 4-11: Specimen “flow” during and after extrusion from consolidometer



Figure 4-12: Cut through dense material with razor blade after extrusion flow



(a)



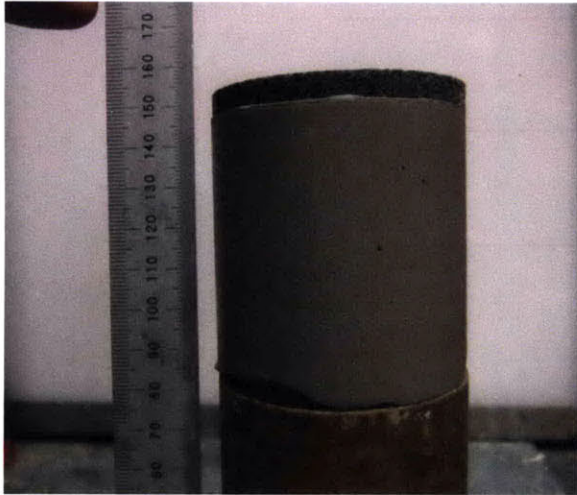
(b)



(c)

Figure 4-13: “Jelly donut” behavior of material: (a) extrusion of material, (b) Just after extrusion (the ring in the cross section shows the start of the soft “jelly” material), (c) touching of sample causing disturbance





(a)



(b)



(c)



(d)

Figure 4-14: The trimming process: (a) partially saturated specimen after extrusion, (b) placement of specimen in the CRS trimming rig, (c) beginning of trimming when the specimen appears dry, (d) water drawn to trimming location, preventing further trimming and causing collapse of the specimen structure

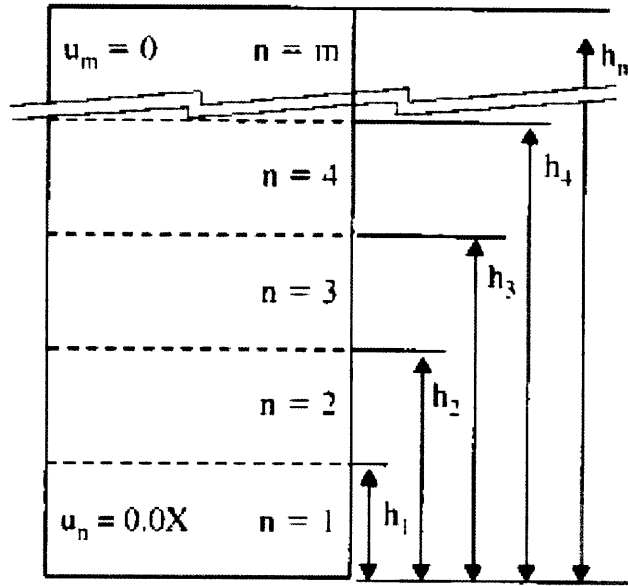


Figure 4-15: Schematic of reconstituting specimens using the undercompaction procedure (Germaine & Germaine, 2009)

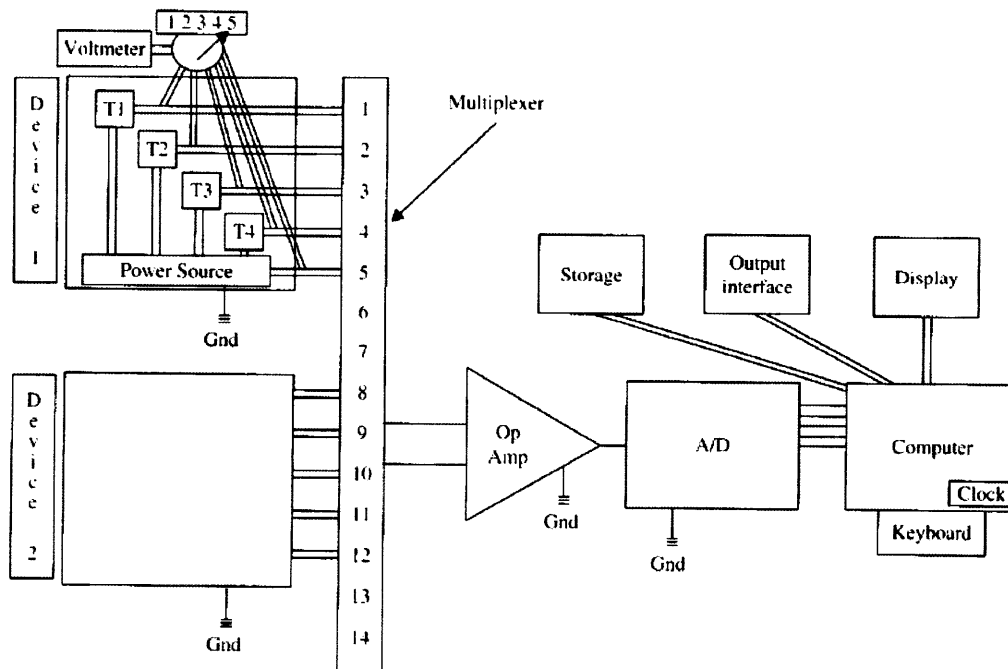


Figure 4-16: Schematic diagram of a centralized data acquisition system (Germaine & Germaine, 2009)

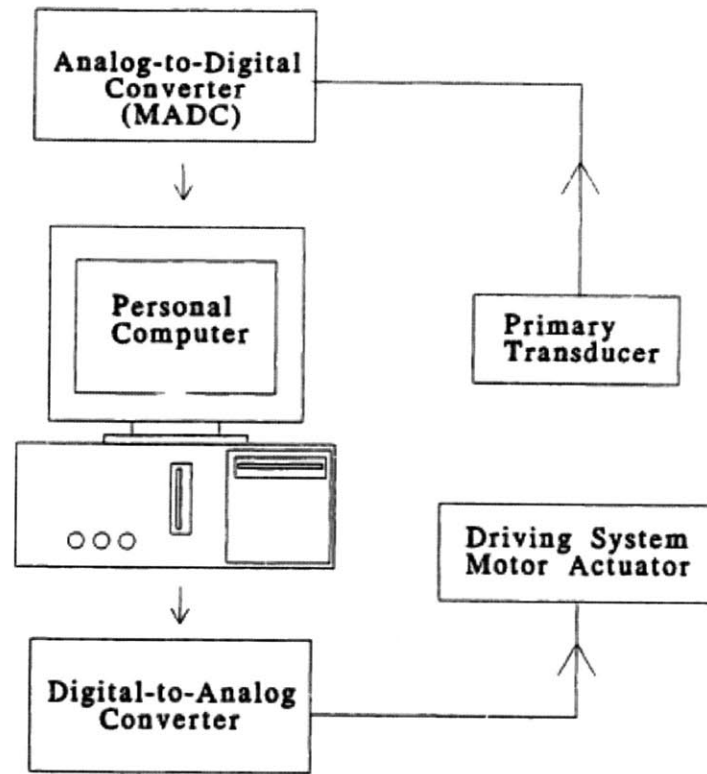


Figure 4-17: Schematic diagram of the control system hardware components

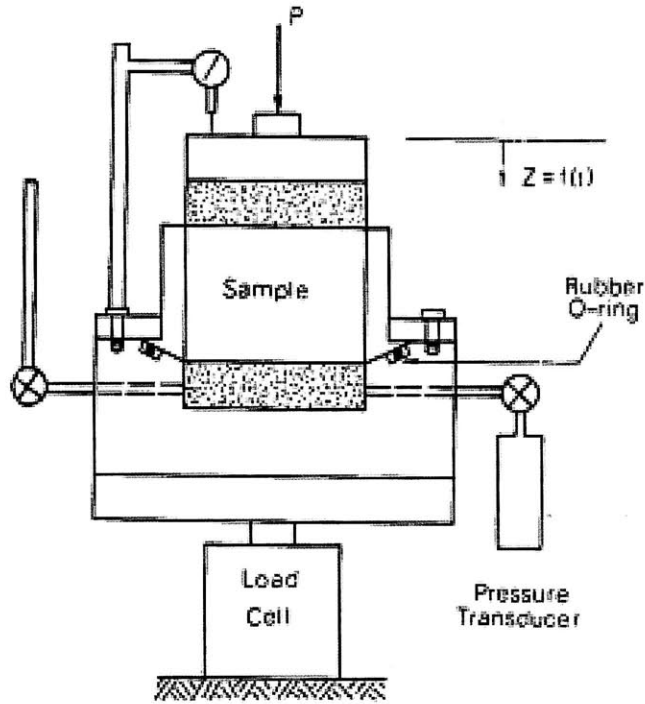


Figure 4-18: Original CRS device developed by Smith and Wahls (1969)

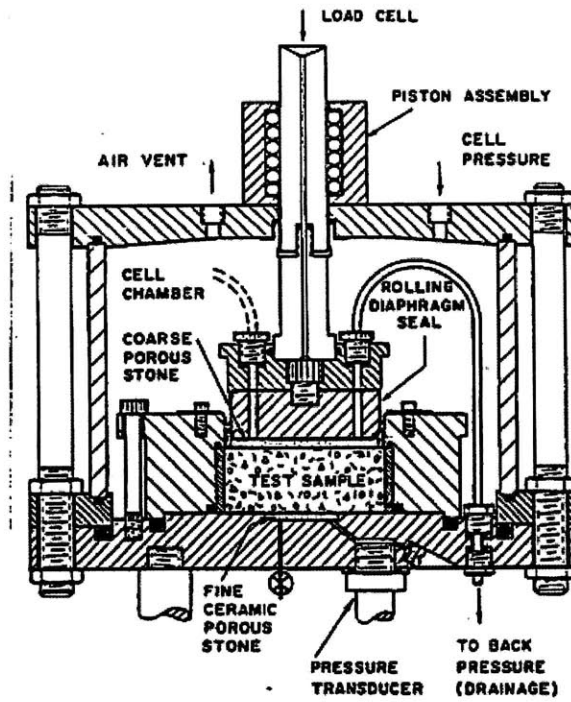
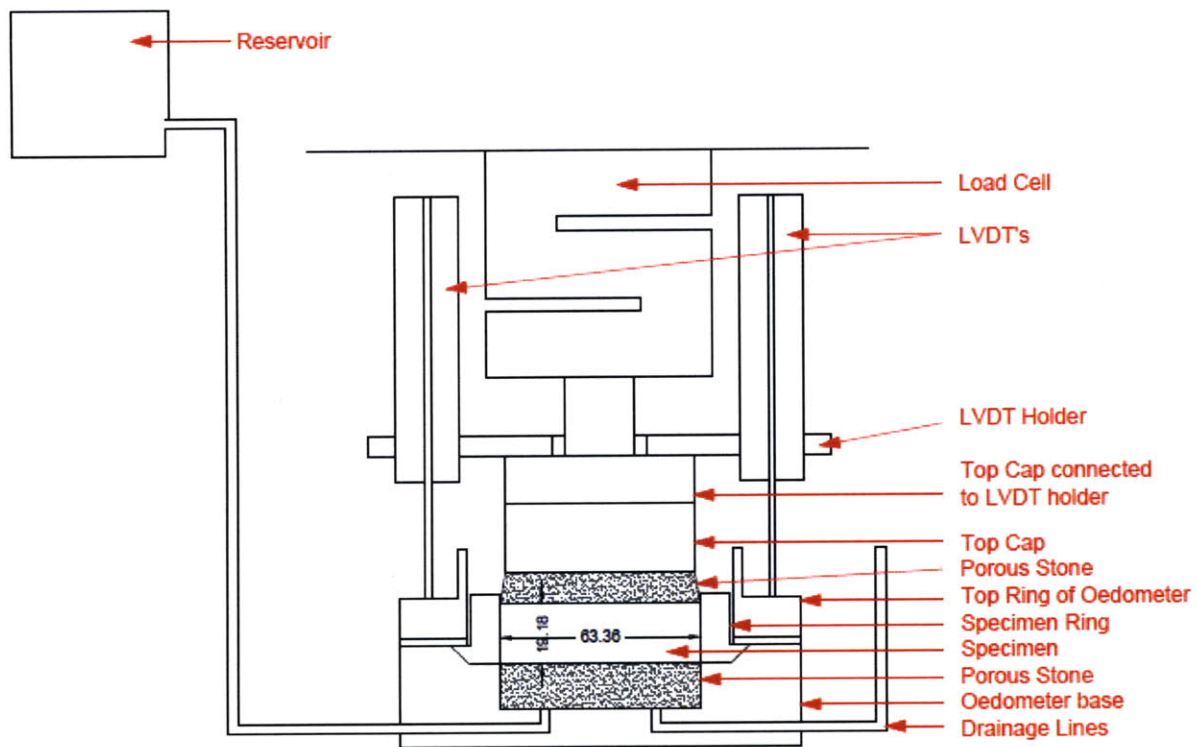
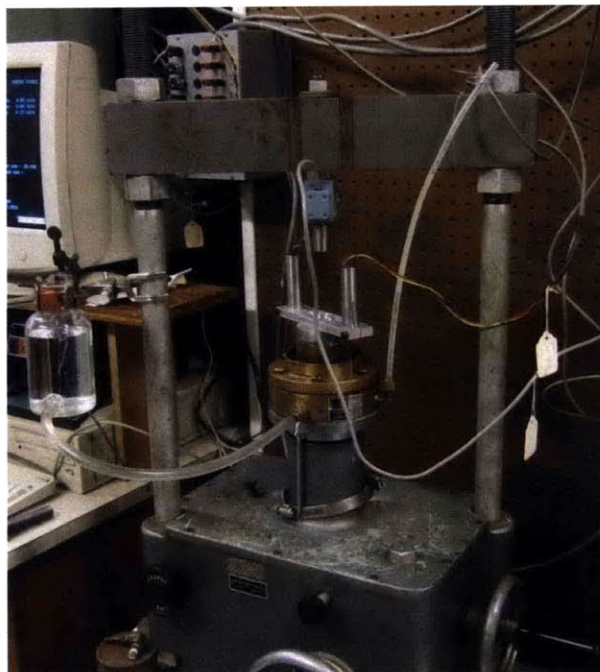


Figure 4-19: MIT CRS device (Wissa et al., 1971)



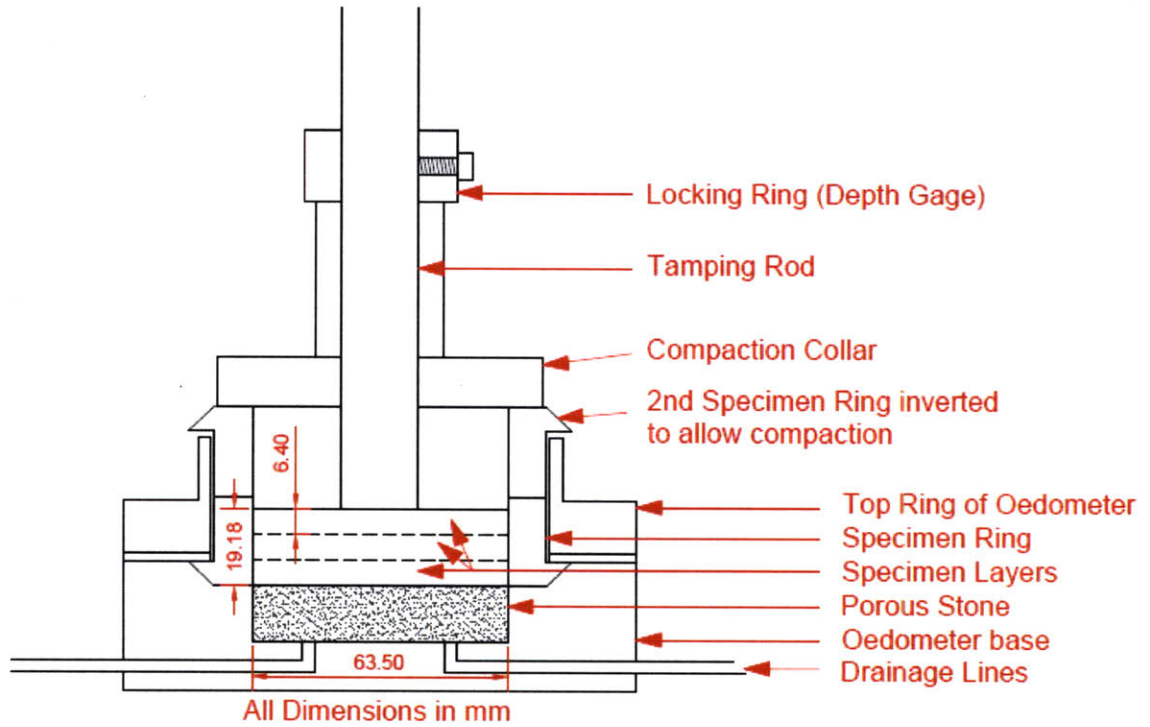
(a) (Dimensions in mm)



(b)

Figure 4-20: Oedometer configuration for CRS testing: (a) schematic, (b) photograph

(a)



(b)



Figure 4-21: CRS Test setup: (a) schematic, (b) photograph

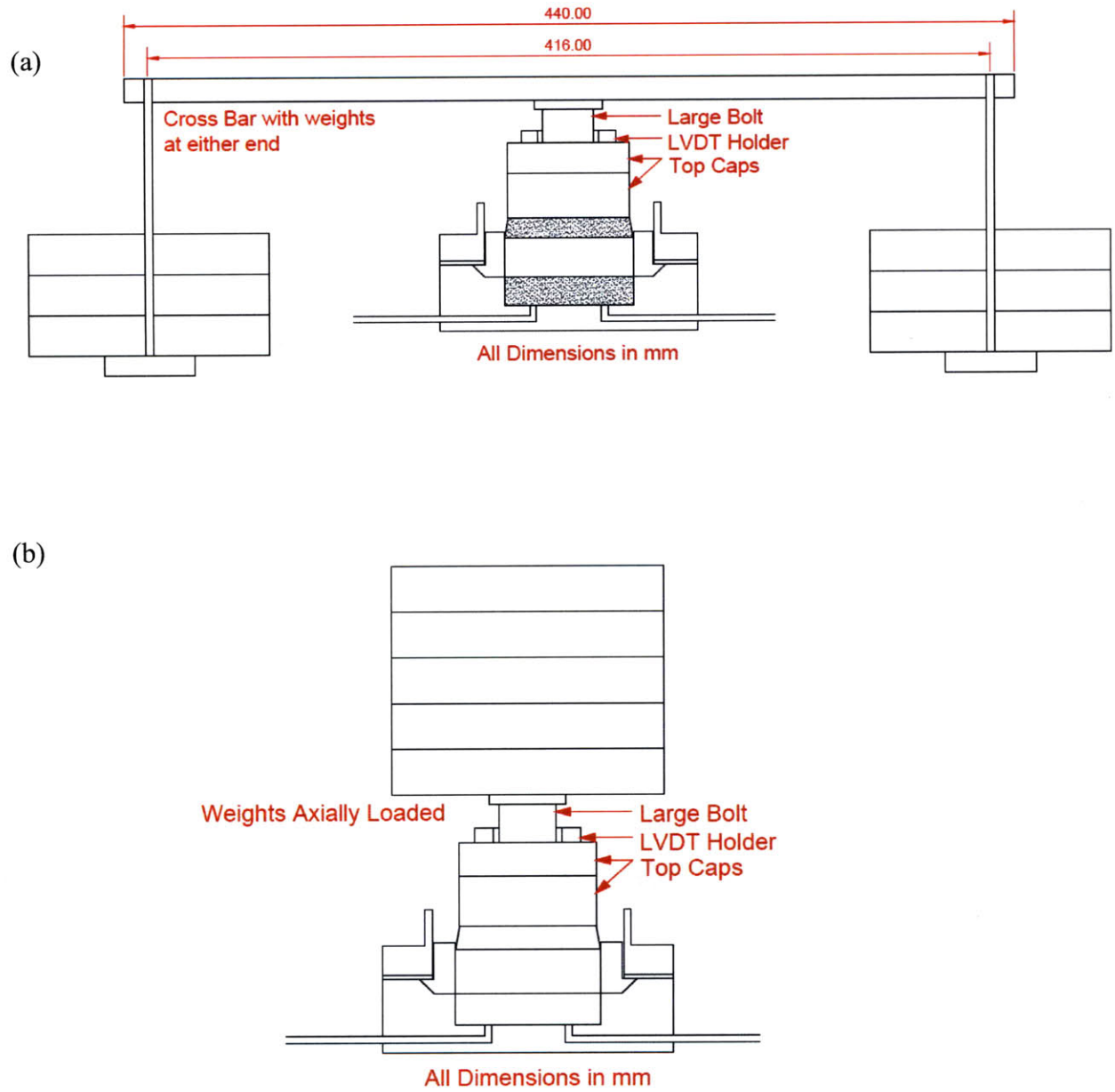


Figure 4-22: Dead load configuration for CRS saturation: (a) successful, (b) unsuccessful



Figure 4-23: “Blow holes” resulting from a high water head



Figure 4-24: Undercompaction in CRS specimen ring from top to bottom using recess tool underneath the specimen ring



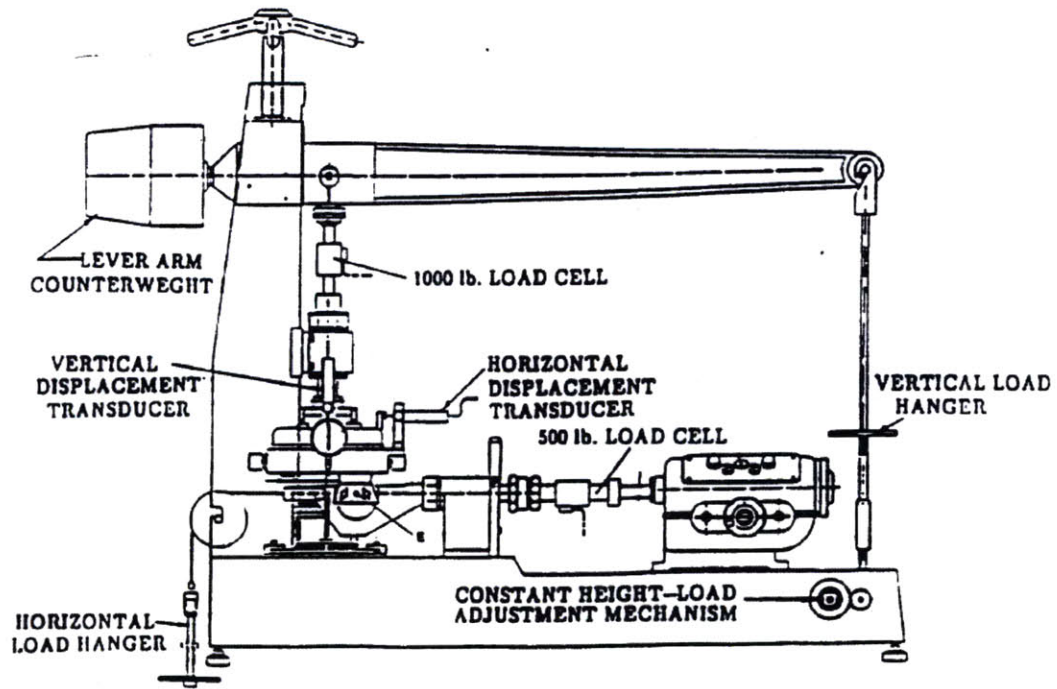


Figure 4-25: Schematic Diagram of Geonor Model 4 DSS Apparatus (Ortega, 1992)

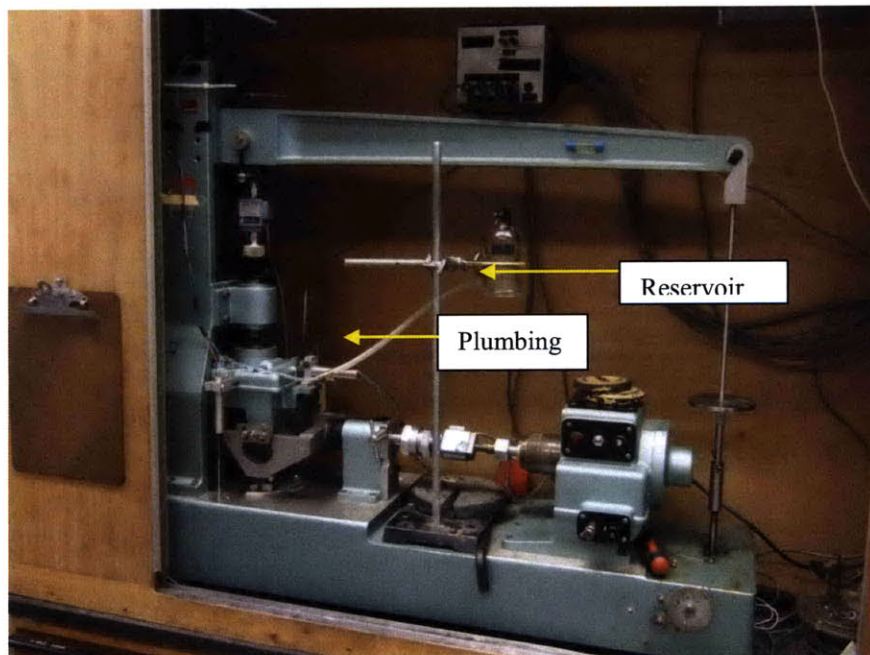


Figure 4-26: The DSS device with reservoir and ancillary plumbing



(a)



(b)



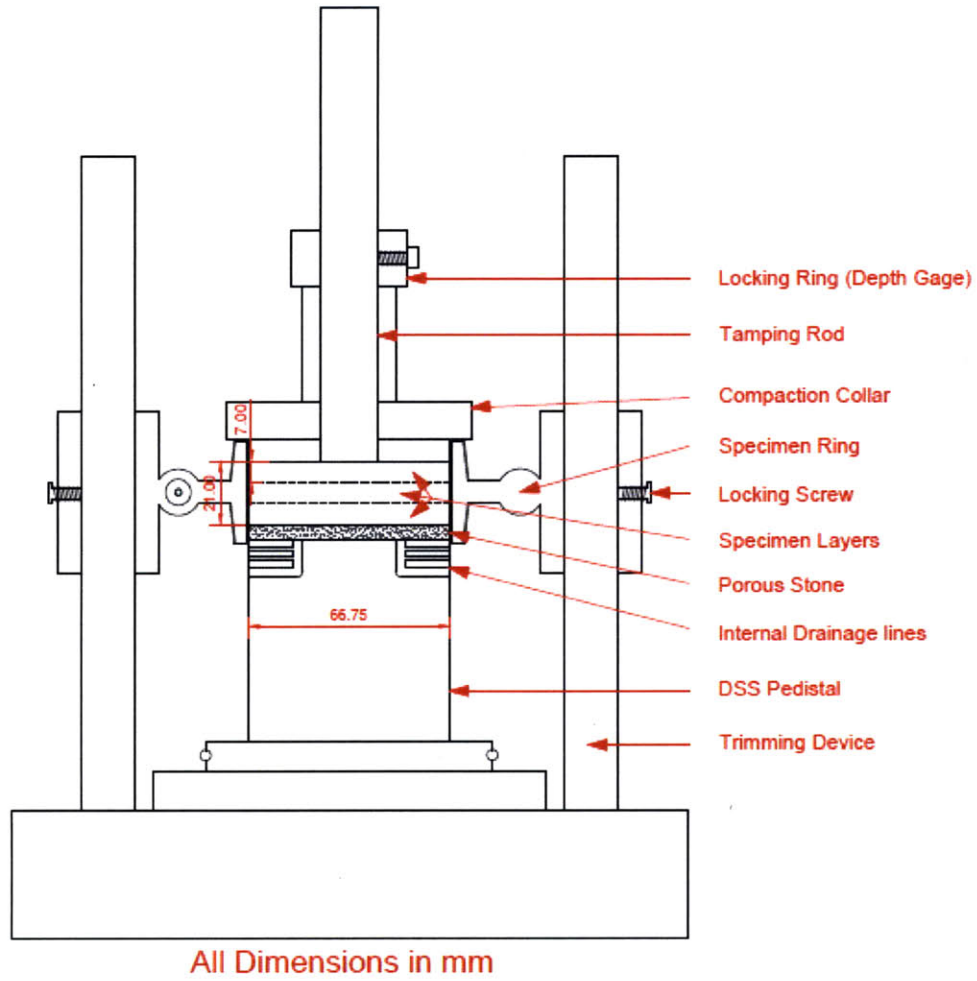
(c)



(d)

Figure 4-27: DSS setup: (a) specimen mold and Geonor membrane, (b) membrane placed in mold, (c) vacuum applied to membrane and specimen ring lower onto pedestal in trimming apparatus, (d) positioning of mold using calipers

(a)



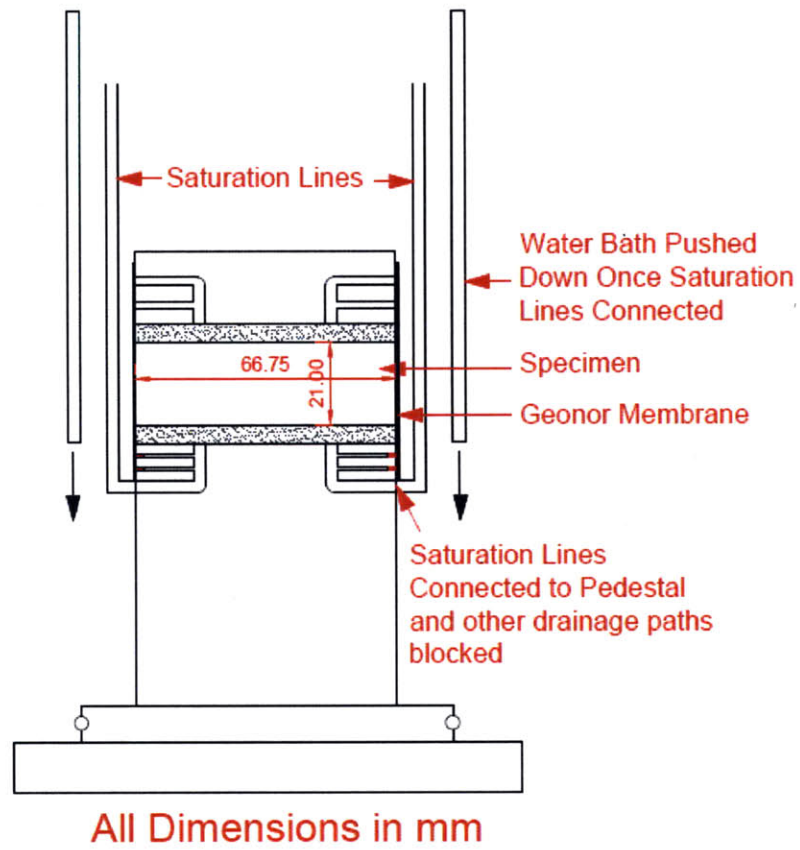
(b)



(c)

Figure 4-28: Compaction procedure: (a) schematic diagram showing how specimen is compacted in layers, (b) scarifying between layers, (c) final specimen after compaction

(a)



(b)



Figure 4-29: Connection of the drainage lines for saturation: (a) schematic, (b) photograph

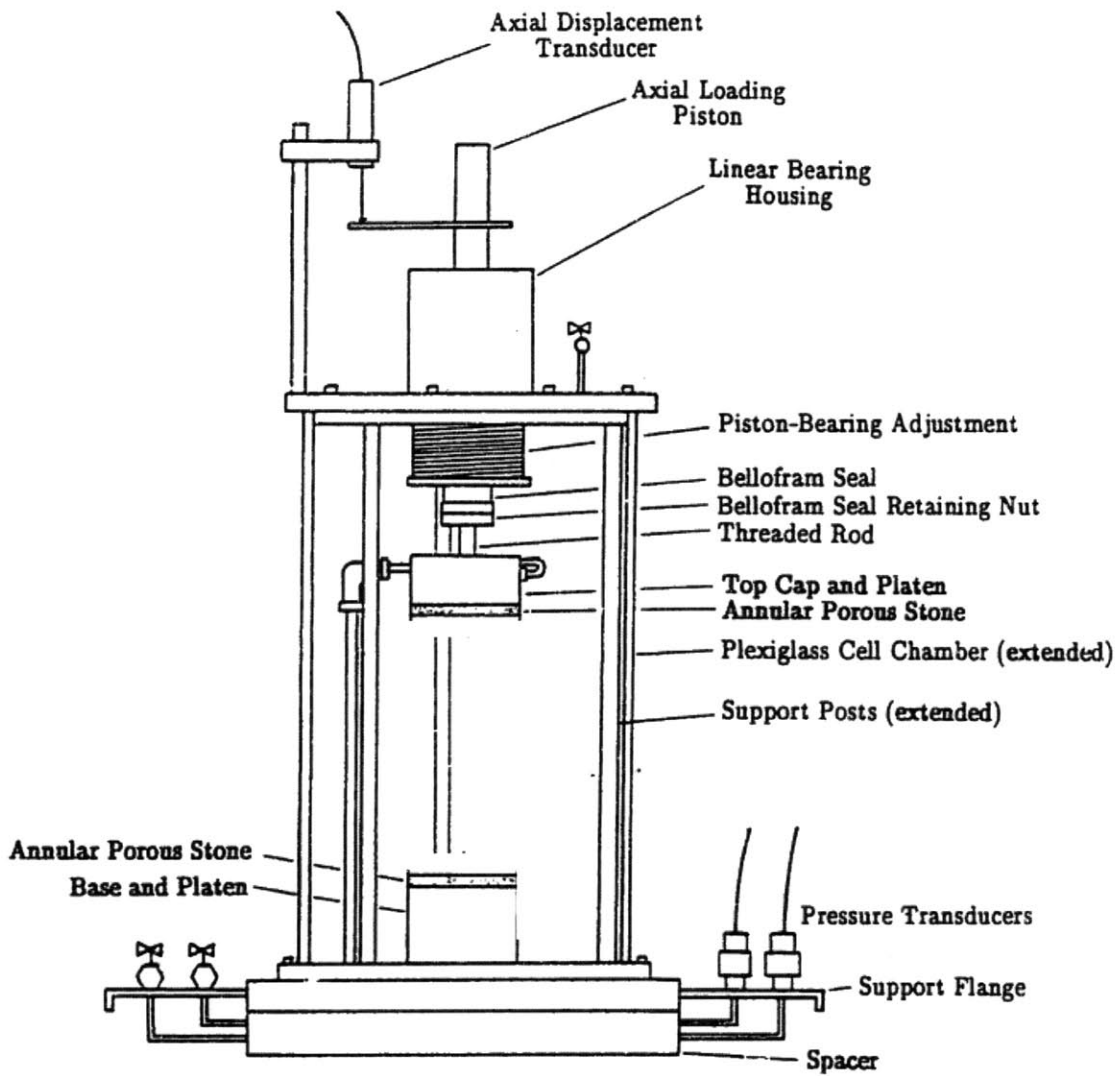
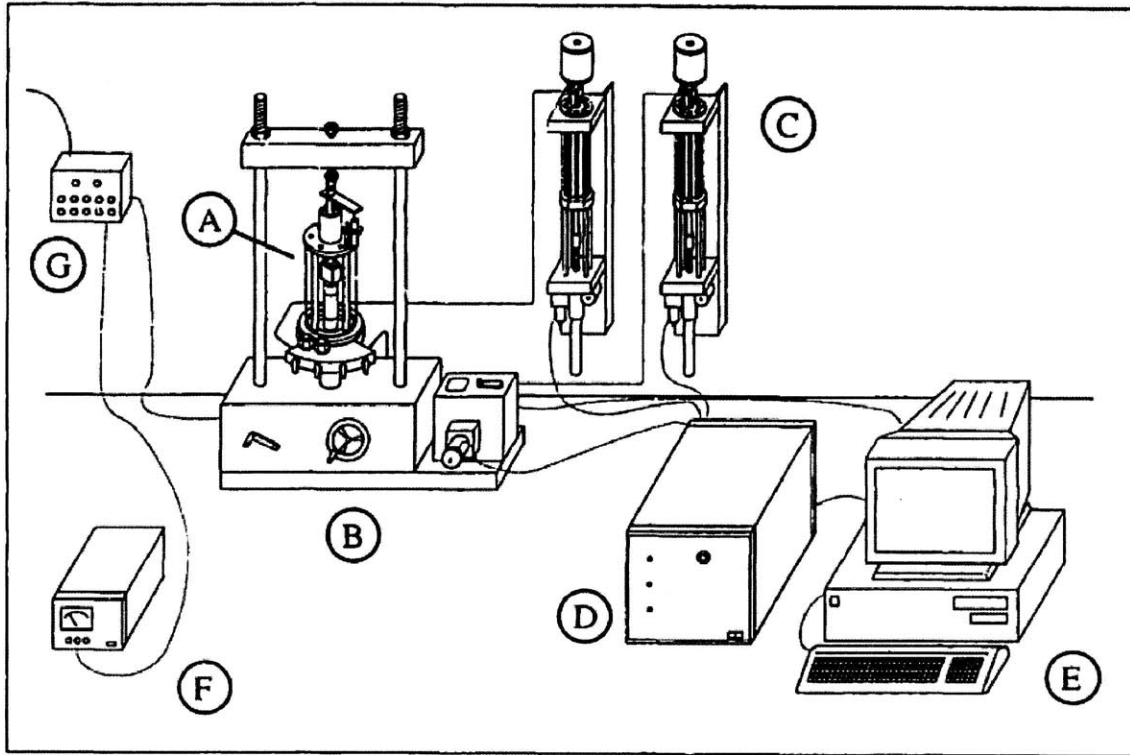


Figure 4-30: Manual triaxial apparatus used for CIUC tests (modified from Sheahan, 1991)



- A - Triaxial Cell
- B - Load Frame
- C - Pressure/Volume Controllers
- D - Motor Control Box
- E - Personal Computer
- F - DC Power Supply
- G - Data Acquisition Channels

Figure 4-31: Schematic of MIT automated stress path triaxial cell (Santagata, 1998)

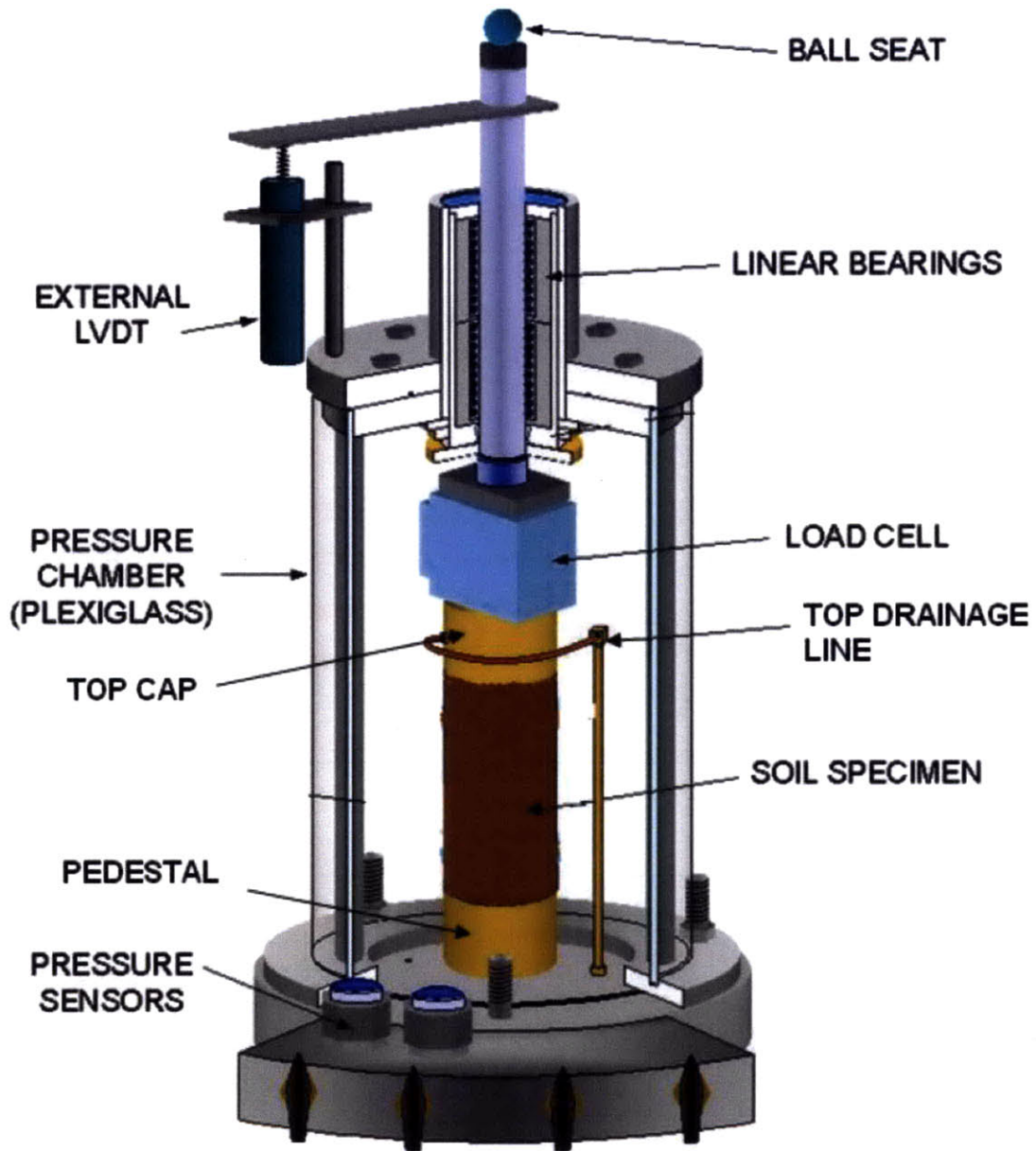
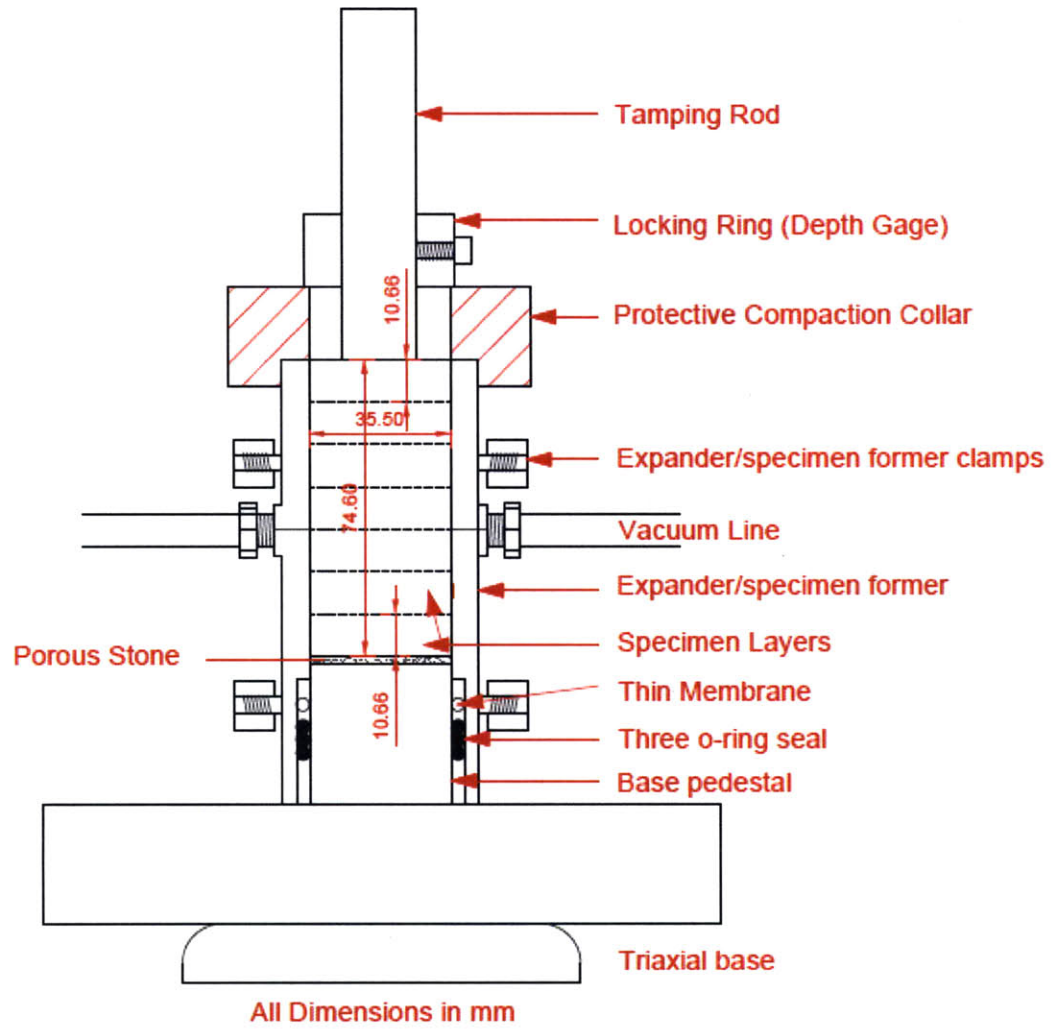


Figure 4-32: Schematic of automated triaxial cell (Santagata, 1998)

(a)



(b)

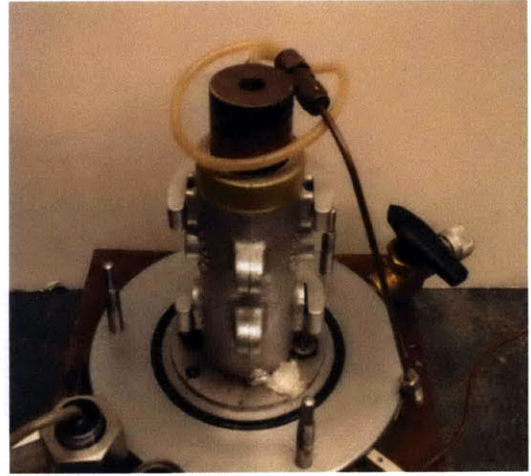


Figure 4-33: Compaction configuration: (a) schematic, (b) photograph

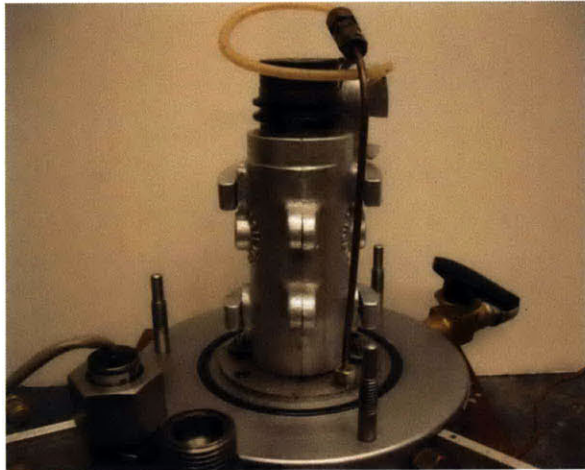




(a)



(b)



(c)



(d)

Figure 4-34: Triaxial setup procedure: (a) placing porous stone on specimen, (b) placing top cap on specimen and folding membrane around top cap, (c) fixing o-rings and applying vacuum, (d) removing expander/former , rolling up thin membrane, and fixing final o-ring



Figure 4-35: Uneven cross sectional area after backpressure saturation and consolidation



Figure 4-36: Unstable structure causing the specimen to lean to one side during saturation when there is a top cap with no recess for lateral stability



# **5 CHARACTERIZATION, CONSOLIDATION, AND HYDRAULIC CONDUCTIVITY**

## **5.1 INTRODUCTION**

Due to the limited information available on Skibbereen Silt, an extensive index testing program was first conducted. The grain size distribution, atterberg limits, specific gravity, organic content, salt content, and mineralogy were all investigated as part of this study. Following index testing, the mechanical properties of the material were evaluated using constant rate of strain (CRS) tests, hydraulic conductivity tests, direct simple shear (DSS) tests, isotropically consolidated undrained triaxial compression (CIUC) tests, and  $K_0$  consolidated undrained triaxial compression tests (CK<sub>0</sub>UC) on lab found specimens. This chapter presents the index property results, the results from a series of CRS tests, the consolidation properties produced by DSS and triaxial tests, and the hydraulic conductivity properties at different void ratios.

First, Section 5.2 provides the index property information for Skibbereen Silt. Three random samples were taken from the processed batch and were tested for the various index properties. A fourth sample was taken for salt concentration and organic content testing. Only “Sample A” was used for scanning electron microscope images and the mineralogy evaluation.

Section 5.3 presents all the consolidation behavior from CRS, DSS, and triaxial tests. The results from 1-D consolidation CRS tests are first presented. A series of specimens at various starting densities were consolidated to stresses of approximately 15 MPa. Most tests have an unload-reload cycle to provide swelling and recompression information. Two re-sedimented slurry based specimens are compared against undercompacted tests. The DSS compression behavior is then presented. The section includes a comparison between the DSS and CRS compression behavior. Finally, the triaxial results are summarized and compared with the CRS consolidation behavior.

The final section presents the hydraulic conductivity results obtained from a modified Trautwein consolidometer device. A constant head hydraulic conductivity test was used, where

the flow of water through the specimen is recorded over a period of time at a specified gradient, thereby, allowing calculation of the hydraulic conductivity. Hydraulic conductivity is presented against void ratio and vertical effective stress in the section.

## **5.2 INDEX PROPERTIES**

### **5.2.1 Introduction**

An extensive testing program was undertaken to determine the index properties of the material. Three samples were selected at random from the processed batch. The grain size distribution, specific gravity, atterberg limits were first determined. An additional sample was then selected for evaluation of the organic content and salt concentration. Finally, mineralogy evaluation using X-ray diffraction was conducted on one of the samples.

### **5.2.2 Grain Size Distribution**

The grain size distribution curves from three hydrometer tests are shown in Figure 5-1. One hydrometer test was conducted on each sample. It can be seen by the shape of the curves that there is excellent repeatability indicating a well blended batch. The curves show that the material is predominantly silt with a 2% sand fraction and a 10% clay content. The  $D_{10}$ ,  $D_{30}$ , and  $D_{60}$  values were found to equal 0.002, 0.009, and 0.028 mm. They produce a coefficient of uniformity ( $C_u$ ) equal to 14 and a coefficient of curvature ( $C_c$ ) equal to 1.446. Therefore, the material can be classified as a well graded silt.

### **5.2.3 Atterberg Limits**

As indicated in Chapter 4, due to the difficulties in testing the material in the Casagrande cap, the liquid limit was determined with the fall cone. The fall cone produced good repeatability and consistent results. However, on many occasions it was noticed that the cone penetrated the material to a certain point and then the surface of the material in the cup arched downwards

around the cone. Figure 5-2 shows a typical example of this behavior. The line in the figure represents the material surface profile around the cone.

The Atterberg limits together with the specific gravity, organic content, and salt concentration are presented in Table 5-1. The liquid limit was found to be equal to  $25.77 \pm 0.21\%$  and the plastic limit was equal to  $18.24 \pm 0.94\%$ . The results produce a plasticity index of 7.53%. Figure 5-3 shows the findings on the Casagrande Plasticity Chart. The material falls into the low plasticity clay (CL) – low plasticity silt (ML) box on the Casagrande Plasticity Chart.

#### **5.2.4 Specific Gravity, Organic Content, and Salt Concentration**

As mentioned in the previous section, the results from specific gravity, organic content, and salt concentration analysis are presented in Table 5-1. Three specific gravity tests were conducted, one on each sample. The specific gravity flasks were first calibrated for volume and then the soil was tested. A specific gravity of 2.724 was found with a standard deviation between the tests of only 0.002.

The organic content found in the samples is very low with an average value of 0.44%. The material can be classified as non organic.

The salt concentration analysis found a low salt concentration in the pore fluid. The average value is 0.459 grams of salt per 1000cc of pore fluid. A natural water content of 25% was selected for this calculation. Due to the marine environment in which the material was deposited, a higher salt concentration was expected. The low salt concentration is likely due to leaching by ground water flow over time.

#### **5.2.5 Scanning Electron Microscope Images and Mineralogy**

A scanning electric microscope (SEM) was used for the imaging analysis and X ray diffraction was utilized for mineralogy evaluation. The X ray diffraction interpreted was conducted by Dr. Robert T. Martin.

Figure 5-4 shows an example of the images taken by the SEM equipment. The image is magnified to 2000 times its actual size. It can be seen that the particle shapes are angular. They are also very jagged and plate like in shape.

The X-ray diffraction results can be seen in Figure 5-5 and 5-6. The figures show intensity versus degrees two theta for Cu Ka Radiation from 5 to 65. The peaks represent the various mineral elements. In the figures, Q is quartz, F is feldspar, CHL is chlorite, and "CLAY" is illite. A complete breakdown of the Skibbereen Silt mineralogy is presented in Table 5-2. The predominant mineral is quartz, having 76% of the total composition. Feldspar is another predominant mineral with a 7.6% component. Clay content was found to be 15.6%, which is 5.6% greater than that found in the hydrometer analysis. The clay content is made up of two minerals; illite and chlorite, with the breakdown between the two being 6.8 and 8.8% of the total composition. The material was found to have no sulfides and there was 0.8% of the material that could not be identified.

## **5.3 CONSOLIDATION BEHAVIOR**

### **5.3.1 Introduction**

To evaluate the mechanical properties of Skibbereen Silt, the initial phase of testing involved 1-D consolidation in an oedometer ring at constant rates of strain. The initial specimen density was varied to evaluate the possibility of curve convergence at higher stresses. The majority of specimens were reconstituted using undercompaction. However, two specimens were prepared using resedimentation from a slurry to investigate differences in behavior as a result of a variation in preparation method.

Prior to undrained shear, all Direct Simple Shear (DSS) tests were  $K_0$  consolidated in the automated Geonor Model 4 DSS device. Similarly, prior to undrained shear in the triaxial apparatus, all specimens were either isotropically consolidated or  $K_0$  consolidated. Manual consolidation control was used in the isotropic case while an automated stress path triaxial cell was used for  $K_0$  consolidation.



This section presents the consolidation results from all tests. Table 5-3 summarizes the phase relations and consolidation characteristics for the CRS tests. Table 5-4 lists for each DSS test, the phase relations and the consolidation properties. Finally, Table 5-5 and 5-6 presents the test type, the phase relations, the applied  $K_0$  consolidation stress history, and consolidation properties from all the triaxial tests.

Section 5.3.2 describes the results from the CRS tests and Section 5.3.3 presents the results from the DSS tests performed in this research. The triaxial information is broken into two sections. Section 5.3.4 and 5.3.5 present the isotropic and  $K_0$  consolidated triaxial compression test information.

### **5.3.2 Constant Rate of Strain Tests**

In total, 17 CRS tests were performed on Skibbereen silt specimens. The first four tests were performed on resedimented material. The tests showed little repeatability and the poor quality results can most likely be associated with the unstable nature of the sample during trimming.

Eleven tests were conducted on undercompacted specimens. Of these, 3 tests experienced experimental problems and hence, are not reported. The tests were found to be unsatisfactory due to saturation problems and specimen stability issues during saturation. In the successful tests, the initial setup density and void ratio was varied to investigate the consolidation behavior from different starting conditions. Initial setup dry density varied between 1.09 and 1.59 g/cm<sup>3</sup>, corresponding to an initial void ratio range of 1.5 to 0.71.

In order to evaluate the effects of different reconstitution methods, a further two CRS specimens were reconstituted by placing a soil slurry into the CRS cell and incrementally loading it until it was stable enough to test. Once the specimen was stable, the test was run identically to the undercompacted specimens.

All specimens were consolidated at a strain rate of 6%/hour to a maximum consolidation effective stress,  $\sigma'_{vm} \approx 15$  MPa. The majority of the tests have two unload reload cycles. At a vertical effective stress of approximately 750 kPa the load cell capacity is exceeded and

unloading is required. The load cells were changed at the end of the first unload curve. During loading with the higher capacity load cell a second unload reload cycle was incorporated to estimate the swelling and reload effects at higher stresses. At the maximum capacity of the second load cell ( $\sigma'_v \approx 15$  MPa), the specimen was finally unloaded to an OCR greater than 4.

Figure 5-7 shows a typical compression curve in a conventional  $\epsilon_a$ - $\log\sigma'_v$  space for one of the tests. The specimen was prepared by undercompaction with an initial setup dry density of  $1.44 \text{ g/cm}^3$  and a void ratio equal to 0.89. Figure 5-8 shows the corresponding compression curve in  $e$ - $\log\sigma'_v$  space. It can be seen that there is no apparent preconsolidation pressure. The curve is very flat with no well defined yield point. The virgin consolidation line is not perfectly linear but rather slightly rounded. The slope of the virgin compression line increases with stress and a maximum compression ratio can be found at the greatest stress level. The unload-reload cycles separate more at lower stresses. Figure 5-9 shows axial strain increment versus vertical effective stress normalized by the maximum vertical consolidation effective stress ( $\epsilon_a$  increment versus  $\sigma'_v/\sigma'_{vm}$  or  $\text{OCR}^{-1}$ ) for the three unload phases in a typical CRS test. The axial strain has been set to zero for the three phases to illustrate the deviation in behavior. The results show that the unload curve is stress level dependent and hence, the swelling ratio is stress level dependent. A higher vertical effective stress will provide a slightly greater swelling ratio at a corresponding OCR.

The initial part of the curves shows the effects of saturation. Despite a small confinement stress on the specimen, it dilated slightly during inundation of water. Dilation was followed by relaxation back towards its initial height. This behavior was typical for specimens with this initial setup density. Figure 5-10, 5-11, and 5-12 show the saturation effects over time for specimens with different starting densities in axial strain-time, axial strain-log time, and axial strain-time (early time) space. Specimens created with an initial setup dry density greater than  $1.44 \text{ g/cm}^3$  produce very stable behavior during saturation with only small contractions or dilations. It should be noted that specimens tend to dilate first followed by continuous contraction over time. The figures show that specimens with a dry density of  $1.34 \text{ g/cm}^3$  or less produce very contractive behavior during saturation. CRS 985 was reconstituted to an initial dry density of  $1.19 \text{ g/cm}^3$  and it produced strains during saturation greater than 15%. The maximum strains during saturation were recorded at 20% for a specimen with an initial dry density of 1.09

$\text{g/cm}^3$ . It should be noted that a vertical stress of 3.6 kPa was placed on the specimens during this inundation and saturation process. Figure 5-13 presents the axial strain recorded at the end of saturation versus initial setup dry density. The results show that initial dry densities greater than  $1.4 \text{ g/cm}^3$  produce axial strains close to zero during saturation. However, for initial dry densities less than  $1.4 \text{ g/cm}^3$ , significant contraction will occur. It can be seen that the axial strains during saturation will increase with a decrease in the initial setup density. Figure 5-14 shows the corresponding void ratio versus initial setup dry density. The results are more consistent with changing density. However, an initial setup dry density greater than  $1.5 \text{ g/cm}^3$  will produce lower void ratios during the saturation process.

In the case of Figures 5-7 and 5-8, a strain of 20.4% corresponds to a void ratio of 0.50 at the maximum stress of 14.23 MPa. A comparison between tests using  $\epsilon_a\text{-log}\sigma'_v$  space is very difficult because large contraction was experienced in specimens with lower densities. Figure 5-15 demonstrates the problems associated with this space for specimens with different starting densities. The saturation phase of the tests has been removed for clarity but the post saturation strain is included. It can be seen that much larger strains occur in specimens with a lower starting density. A typical example is between test CRS987 and CRS1002. The first test was prepared with a initial setup density of  $1.09 \text{ g/cm}^3$ . It strained to approximately 40% at the maximum stress compared with test CRS1002 which was prepared with a dry density of  $1.59 \text{ g/cm}^3$  and only strained to 12.42% at maximum stress.

The  $e\text{-log}\sigma'_v$  space is a much better way to analyze behavior between specimens of this type. Figure 5-16 presents the results of CRS testing in this space. Once again the saturation phase of the tests has been removed for clarity. The figure includes two specimens reconstituted from slurry (CRS993 and CRS1001). In the undercompacted specimens, it can be seen that despite a different initial starting density the curves converge at higher stresses. At stresses greater than 5500 kPa (5.5 MPa) and void ratios lower than 0.58, there is good repeatability in the behavior. The compression curves almost become linear and the final unload cycles are very close to each other with most unloading occurring at a void ratio of about 0.50.

Figure 5-17 presents the  $e\text{-log}\sigma'_v$  space for virgin consolidation in the undercompacted and resedimented specimens. Only the extremities of the range in behavior are shown to increase clarity. The figure identifies some problems with the selection of a reconstitution technique. The

two re-sedimented slurry specimens have much lower void ratios at the maximum stress despite having an identical loading sequence to their undercompacted counterparts. The void ratio is also much lower at the beginning of tests when compared with the majority of undercompacted specimens. Only one undercompacted specimen with an initial dry density of  $1.59 \text{ g/cm}^3$  had a similar starting void ratio of about 0.70. However, despite a similar starting void ratio, the undercompacted specimen does not follow the same consolidation curve. The undercompacted specimen achieved a void ratio of 0.5 at maximum stress but the re-sedimented specimens produced void ratios of 0.42 and 0.40 at the same stress level.

The compression ratio (CR), swelling ratio (SR), and recompression ratio (RR) also vary between undercompacted and re-sedimented specimens. Table 5-3 shows the CR, SR, and RR values for the tests. The values of CR for undercompacted specimens range from 0.077 to 0.104 at a stress level of 14 MPa. However, the re-sedimented specimen values are much higher with a range from 0.145 to 0.157 at the same stress level. A similar trend is observed with the swelling ratio, SR. The SR values for undercompacted specimens are very repeatable with a range from 0.007 to 0.010 at an  $\text{OCR} = 4$  from the maximum vertical consolidation effective stress. The re-sedimented SR values are almost double, ranging from 0.015 to 0.018. However, there is no difference between undercompacted and re-sedimented values of RR for the first unload reload cycle. All RR values are between 0.006 and 0.011. For the second unload reload curve, RR is slightly greater for the re-sedimented specimens but the difference is not significant.

The difference in behavior between undercompacted and re-sedimented specimens could be due to a different soil fabric. The re-sedimented specimens are more likely to have a parallel plate like structure because they are prepared from a slurry with a water content much greater than the liquid limit ( $w_c=35\%$ ,  $\text{LL}=25.77$ ) while the undercompacted specimen structure will be randomly oriented because they are formed in moist conditions. Figure 5-17 gives little indication if the compression curves for the two different reconstitution methods would converge at higher stresses. It is possible that another order of magnitude in stress level would be required to crush the soil particles and bring them together. However, it is also possible that they will never converge.

Some interesting observations in the post consolidation material behavior can be seen in Figure 5-18. The figure shows a specimen extruded from the CRS cell into an evaporating dish

after consolidation to a vertical effective stress of 15 MPa. The specimen first experiences a stable structure. However, after 5 blows to the evaporating dish, the structure completely collapses into a fluid like substance. The figure identifies the impossibility of testing intact samples and resedimentation in a consolidometer as a reconstitution technique. The structure of the material will collapse if it is unsupported for even a short length of time.

### 5.3.3 Direct Simple Shear Tests

In total, 24 DSS tests were performed to evaluate the consolidation and shear properties of Skibbereen silt. Of those, 5 tests experienced experimental problems and hence, are not reported. The unknown method to prepare and test the material in the DSS device, mechanical issues, and human errors are reasons for test losses.

As mentioned in Chapter 4, the DSS device uses a Geonor wire reinforced rubber membrane to confine the material. The membrane assumes that there is no lateral deformation and therefore, the specimen is consolidated under  $K_0$  conditions. All specimens, except two, were prepared to an initial setup dry density of  $1.45 \text{ g/cm}^3$ , corresponding to an initial void ratio of 0.88. The two other specimens were prepared to an initial setup dry density of  $1.50 \text{ g/cm}^3$  to estimate the effects of a different starting density on the shear properties. Six tests were unloaded to an overconsolidation ratio of 2, 3, and 4 to provide information on the impact of a different stress history on the shear properties. The specimens were  $K_0$  consolidated at a constant strain rate of 1%/hour to stress levels of approximately 200, 600, 1200, and 1800 kPa.

Figure 5-19 shows the compression data from a DSS test in  $\epsilon_a\text{-log}\sigma'_v$  space. The compression behavior is typical of all tests. Similar to the CRS tests, the curve is slightly rounded for the entire loading period. The initial portion of the plot shows the effects of saturation. The first point is the seating load at approximately 5 kPa. A dead weight was then placed on the loading arm of the DSS device increasing the vertical stress to about 20 kPa. Then water was allowed to flow through the specimen to saturate it. For this test, the axial strain was found to be 3.6% after saturation. However, the test is at the low end of the range and axial strains up to 7.7% were found in some specimens during saturation. The large range in strain is caused by the target initial dry density of  $1.45 \text{ g/cm}^3$  not being achieved in some situations with many specimens having an initial dry density of only approximately  $1.35 \text{ g/cm}^3$ . As

demonstrated in the CRS tests, a lower initial density causes a significant increase in strain during saturation. However, the strains during saturation are greater in the DSS apparatus when compared with specimens of the same initial setup density in the CRS tests. There are two possible explanations for this:-

- 1) The stress applied during saturation was greater in the DSS device, approximately 20 kPa was applied in the DSS tests while only 4 kPa was added in the CRS tests. The extra vertical stress was a requirement to keep the system stable during saturation.
- 2) It is very likely that the Geonor membrane stretches laterally during the addition of stress. Small lateral deformations will increase the strain magnitude significantly.

A subsequent investigation into stress level effects during saturation was undertaken to determine if the greater strain experienced in the DSS device could be replicated in the CRS device. A CRS specimen was prepared to an initial dry density of  $1.45 \text{ g/cm}^3$ . A vertical effective stress of 20 kPa was applied to the specimen before saturation. Figure 5-20 and 5-21 show the axial strain-time and axial strain-log time behavior for all CRS specimens with an initial setup dry density of  $1.45 \text{ g/cm}^3$  using different vertical stresses during saturation. The results show that greater strains are experienced during saturation with an increase in vertical stress. An axial strain of about 4% was found in the specimen with a confinement stress of 20 kPa compared to about 0.25% axial strain in the specimens using a 4 kPa stress level. The post saturation void ratio versus initial setup dry density for all CRS and DSS undercompacted specimens are shown in Figure 5-22. The results show that if the confinement stress is the same, the CRS and DSS device will produce similar void ratios. Figure 5-23 presents the corresponding post saturation axial strain versus initial setup dry density. Again, the results show that the CRS and DSS will have similar strains during saturation if the same confinement stress is used.

A summary of the DSS compression curves in  $\epsilon_a\text{-log}\sigma'_v$  space are presented in Figure 5-24. The saturation sections of the compression curves have been removed to improve clarity. The corresponding  $e\text{-log}\sigma'_v$  space together with the CRS undercompacted results are presented in Figure 5-25. Figure 5-25 shows the difference in void ratio between DSS and CRS tests at the post saturation or beginning of CRS consolidation phase. The higher confinement stress during saturation in the DSS device ( $\sigma'_v = 20 \text{ kPa}$  for DSS versus  $\sigma'_v = 4 \text{ kPa}$  for CRS) has produced greater axial strains and lower void ratios in specimens with a similar initial setup dry density.

The slope of the compression curve is greater in the early stages of a DSS test as a result. However, the compression ratios become equal at higher stresses. It can be seen in the figure that the DSS compression curves will not converge with the CRS compression curves at any stress level. This trend and behavior is expected. The walls of the Geonor reinforced membrane are not as rigid as the CRS ring. Lateral deformations increase with an increase in stress in the Geonor membrane, producing larger strains and possibly a steeper compression curve.

Figures 5-22, 5-23, 5-24, and 5-25 also show scatter in the post saturation void ratio and strain in the DSS tests. The sensitivity of the material to the initial setup density and the placement of the specimens in the DSS device is most likely the cause of this deviation.

### **5.3.4 Triaxial Tests**

#### 5.3.4.1 Introduction

This section presents triaxial consolidation behavior from two series of triaxial tests. Series A tests were isotropically consolidated and Series B tests were  $K_0$  consolidated. All triaxial tests are normally consolidated in this investigation. Therefore, the effective vertical consolidation stress ( $\sigma'_{vc}$ ) is equal to the maximum vertical stress ( $\sigma'_{vm}$ ).

#### 5.3.4.2 Series A tests – Isotropically consolidated

A total of 17 isotropically consolidated tests were performed manually using a pneumatic system before shearing. Of those, only 11 tests produced satisfactory results. The high failure rate was due to many factors. The unknown specimen preparation method before testing, the unknown initial density and water content for undercompaction, piston friction problems with the top cap, rolling diaphragm leaks, top drainage line leaks, and membrane leaks were some of the reasons for test losses. The specimens were manually consolidated in 50 or 100 kPa increments. Due to the large consolidation increments, the compression plots are not perfect. There are no flowing curves and the results are of limited quality at lower effective vertical consolidation stresses ( $\sigma'_{vc}$ ). The piston was not fixed to the top cap during the CIUC tests and it created a tendency for a gap to form between the two. Therefore, the measurements of axial strain during consolidation are not accurate. However, the volumetric strain measurements can be used to analyze the consolidation behavior.

Figure 5-26 shows the compression curves in  $\varepsilon_v$ - $\log\sigma'_v$  space for all CIUC triaxial tests. The specimens were consolidated to a maximum vertical effective consolidation stresses,  $\sigma'_{vm} = 100 - 900$  kPa from an initial setup dry density of  $1.5 \text{ g/cm}^3$ . Volumetric strain has been set at zero for the start of consolidation in all tests. Therefore, volumetric changes during inundation and back pressure saturation have been ignored for the purposes of this figure. Before consolidation, the specimens were backpressure saturated to a pore pressure,  $u$ , equal to 300 kPa with an effective stress equal to 50 kPa. Despite the stepped incremental loading, the figure shows good agreement and repeatability.

The virgin consolidation ratio (CR) was determined for each test and the results are presented in Table 5-5. The table illustrates that CR values range from 0.036 to 0.047.

The  $e$ - $\log\sigma'_v$  space for the CIUC tests are presented in Figure 5-27. The figure shows some scatter in the data. The post saturation void ratio ranges from 0.64 to 0.69. The range is not large, however, there was difficulty determining void ratios for the CIUC tests. The unknown axial and volumetric strain during saturation makes it difficult to determine the void ratio after this phase of the test. Two methods were investigated to evaluate the void ratios. Method 1 used the final specimen dimensions after shearing to calculate the void ratio. Once the final void ratio was calculated, the void ratios during consolidation were back calculated. The method found void ratios that were unrealistically low. Therefore, Method 2 was utilized for all tests. The method uses the final water content to determine the final void ratio. Similar to Method 1, the void ratios during consolidation can then be back calculated. The method produced void ratios in the expected range. However, it is obvious that the method is not perfect and the volumetric collapse of triaxial specimens during saturation is a problem when using the undercompaction technique.

Figure 5-28 shows the compression behavior in  $e$ - $\log\sigma'_v$  space for the CIUC tests compared with the CRS range. It can be seen that there is a large deviation between void ratios at the same stress level between CRS and CIUC tests. The variation could be attributed to the higher effective confinement stresses during saturation. A confining stress of 40 kPa was applied to the specimens to keep them stable during saturation. The stress level is significantly higher than the 4 kPa applied to the CRS specimens during saturation. However, the lower void ratios are more likely to be a result of the isotropic confinement conditions. Figure 5-29 shows the post



saturation void ratio versus initial setup dry density for CRS, DSS, and isotropically consolidated triaxial tests. The results show that the lower void ratios in the isotropically consolidated tests are most likely due to a higher initial dry density, a greater confinement stress during saturation, and isotropic stress conditions.

#### 5.3.4.3 Series B tests – $K_0$ consolidated

Six specimens were  $K_0$  consolidated to vertical effective consolidation stresses,  $\sigma'_{vm} = 100$  to 900 kPa. Of those, two specimens experienced experimental problems and hence, are not included. The triaxial tests were  $K_0$  consolidated at a constant strain rate of about 0.2%/hour to the desired stress level and then left for 24 hours of aging. The slow consolidation rate ensured that the  $K_0$  consolidated algorithm maintained equal axial and volumetric strains during the consolidation process.

Figure 5-30 shows the compression curves in  $\epsilon_a$ - $\log\sigma'_v$  space for all  $K_0$  consolidated triaxial tests. Similar to the DSS tests, there is a deviation in the magnitude of strain at the beginning of consolidation. The strain ranges from 0.67 to 2.26% at the end of back pressure saturation/beginning of consolidation. An isotropic stress of 40 kPa was applied to the specimen to keep it stable during inundation. The deviation in strain can be attributed to the sensitivity of the material to the setup conditions and the difficulty of producing repeatable specimens in the automated triaxial device. Like the DSS compression curves, if the initial strain at the start of consolidation is different, the compression curves will not converge at higher stresses.

The compression behavior in  $e$ - $\log\sigma'_v$  space is presented in Figure 5-31. The strain deviation at the beginning of the tests translates to a void ratio range from 0.68 to 0.71. The range is not large; however, the figure shows that the compression curves will not converge with different starting void ratios. The post saturation void ratio versus initial setup dry density for CRS, DSS, CIUC, and  $CK_0UC$  tests are shown in Figure 5-32. As expected, the CIUC and  $CK_0UC$  triaxial tests produce similar values because both were isotropically confined to 40 kPa during the inundation process.

The compression curves are characteristic of all the consolidation results. They are very rounded with no linear trend. The virgin compression ratio (CR) was determined for all tests and the results are presented in Table 5-6. The table illustrates that CR values range from 0.030 at low pressures to 0.046 at higher pressures. CR increases with an increase in stress and they are generally in good agreement with the CIUC tests. The CR and SR results from all the consolidation data (CRS, DSS, CIUC, and  $CK_0UC$ ) are presented in Figure 5-33. It can be seen with a greater vertical consolidation stress, CR increases. However, there is no similar trend between stress and SR.

The feedback-controlled consolidation in the automated triaxial cell allows the coefficient of earth pressure at rest ( $K_0$ ) to be obtained. Figure 5-34 shows the variation in  $K_0$  with vertical stress during consolidation for the  $CK_0UC$  triaxial tests. The results show that  $K_0$  decreases rapidly during initial loading and then the rate of  $K_0$  decrease slows with a further increase in stress. However, there is no plateau or constant value. It is obvious that higher stresses would produce lower  $K_0$  results. This trend is not common in testing and generally there is a plateau in  $K_0$  with an increase in stress. Table 5-6 shows that the values of  $K_0$  at maximum stress range from 0.55 to 0.64. The deviation is a result of different maximum stresses. Figure 5-34 is presented with Figure 5-35, the effective stress path during consolidation. The figure shows good agreement and repeatability between tests. It can also be seen that the stress path is linear from the initial consolidation point to the final loading conditions. The linear stress path is very unusual. Generally, there is curvature, particularly at the beginning of consolidation.

A possible explanation for the unusual  $K_0$  and stress path behavior is the volumetric strain assumptions at the beginning of  $K_0$ -consolidation. Similar to the CIUC triaxial tests, the final void ratios in the  $CK_0UC$  triaxial tests were determined using the final specimen water content and a back calculation process. However, during testing, the void ratios and volumetric strains are unknown and can only be estimated. Standard practice sets the volumetric strain equal to the measured axial strain after the saturation process. This method is normal for clays because they experience very small strains during saturation. The  $K_0$ -consolidation control program then keeps the volumetric strain equal to the axial strain during loading. This method was adopted for the purposes of this research. However, the final void ratios calculated from the specimen water content suggest that the volumetric strain is greater than the axial strain at the end of the

saturation process. When the volumetric strain is equal to the axial strain during saturation, the radial strain is assumed to be zero. For this material, the radial strain is not zero due to the larger volumetric strains. The deviation in the actual volumetric strain from the assumed one is almost 3% in some cases. The discrepancy in the volumetric strain estimation before  $K_0$ -consolidation has likely produced  $K_0$  and stress path behavior that deviates from the true behavior. However, it is expected that this deviation is not large.

Figure 5-36 shows the  $CK_0UC$  triaxial tests compared with the CRS test range and a CIUC test. The  $CK_0UC$  and CIUC triaxial compression behavior shows good agreement and repeatability. Generally, the curves start at the same void ratio and follow a similar path. Again, there is a large deviation between  $CK_0UC$  and CRS behavior. The higher isotropic confinement stress during inundation is the likely cause for this deviation.

### **5.3.5 Stiffness in Consolidation**

A comprehensive analysis of the compression behavior from CRS, DSS, CIUC, and  $CK_0UC$  tests was presented in the previous sections. However, it should be noted, for all testing devices, the deviations in post saturation void ratios are not large when compared against typical clay behavior such as that found in Boston Blue Clay. Generally, in clays, much greater strains are recorded during consolidation. As a result, high resolution void ratios are not needed because the void ratio is recorded over a much greater range.

The compression behavior found in this study is extremely stiff. After, the initial inundation and saturation process low strains are recorded during consolidation. The low strains magnify any deviation in void ratio at the beginning of the consolidation process and the change in void ratio during consolidation is small in comparison with a typical clay.

## **5.4 HYDRAULIC CONDUCTIVITY**

As stated in Chapter 4, it was not possible to generate excess pore pressures during consolidation in the CRS equipment. Therefore, no hydraulic conductivity estimation could be made from the CRS test data. To overcome this problem, nine hydraulic conductivity tests were conducted on three specimens in a modified CRS device. The modified setup uses two pressure

volume actuators (PVA's) to vary cell and pore pressures and thereby, introduce a gradient across the specimen. Volume of flow is recorded by the PVA's, gradient is recorded by the pressure transducers, the height of the specimen can be calculated from strain data, and therefore, Darcy's equation can be used to calculate hydraulic conductivity. For each specimen, three hydraulic conductivity tests were conducted at different vertical effective stresses. One specimen had filter screens, while the other two had a "donut" filter screen (a filter screen that only went around the perimeter of the specimen). The results from the specimen with full filter screens deviated slightly from the two specimens with "donut" filter screens and therefore, it is not reported in this section.

Figure 5-37 presents the hydraulic conductivity results versus void ratio and vertical effective stress. It can be seen that the hydraulic conductivity ranges from 1.03 to  $1.18 \times 10^{-5}$  cm/sec at a void ratio of about 0.67. At the lower end of the scale it ranges from 3.41 to  $3.77 \times 10^{-6}$  cm/sec at a void ratio of approximately 0.56. The results in k-e space show good agreement and repeatability. The results in  $k\text{-}\log\sigma'_v$  space show slightly more scatter, however, the trend is the same with hydraulic conductivity decreasing with an increase in vertical effective stress. The hydraulic conductivity ranges between 3.41 to  $3.77 \times 10^{-6}$  cm/sec at  $\sigma'_v$  equal to 2500 kPa. The results also show linear behavior between hydraulic conductivity and void ratio and hydraulic conductivity and the log of vertical effective stress.

Using the coefficient of volume change in the vertical direction,  $m_v$ , from the CRS tests and hydraulic conductivity,  $k$ , at the corresponding void ratio, the vertical coefficient of consolidation ( $c_v$ ) can be computed. The resulting vertical coefficient of consolidation ( $c_v$ ) ranges from 0.106 to 0.198 cm<sup>2</sup>/sec. Hazen's formula (equation 4.4) was applied to check the hydraulic results. The formula produces a hydraulic conductivity equal to  $4 \times 10^{-6}$  cm/sec which corresponds very well to the values obtained in this study.

	Specific Gravity	Liquid Limit (%)	Plastic Limit (%)	Plasticity Index (%)	Salt Concentration at 25% w <sub>c</sub> g/1000cc pore fluid	Organic Content (%)
Sample A	2.724	25.91	18.92	6.99	0.501	0.50
Sample B	2.726	25.53	18.62	6.91	0.462	0.39
Sample C	2.723	25.86	17.17	8.69	0.441	0.46
Sample D					0.433	0.40
Mean values	<b>2.724</b>	<b>25.77</b>	<b>18.24</b>	<b>7.53</b>	<b>0.459</b>	<b>0.44</b>
St. Dev.	<b>0.002</b>	<b>0.21</b>	<b>0.94</b>	<b>1.01</b>	<b>0.030</b>	<b>0.05</b>

Table 5-1: Index Property results on Skibbereen Silt

Mineral	Proportion (%)	Cumulative Proportion (%)
Quartz	76	76
Feldspar	7.6	83.6
Carbonates	0	
Dolomite	0	
Calcite	0	
Clay:	15.6	99.2
Illite	6.8	
Chlorite	8.8	
Sulfides:	0	
Pyrite	0	
Marcasite	0	
Unknown:	0.8	100

Table 5-2: Summary of X Ray Diffraction giving the mineralogy breakdown of Skibbereen Silt

Test No.	Type	Setup Conditions					Post Saturation			Max Stress				Final w <sub>c</sub> (%)	CR @ (15 MPa)	SR OCR = 4	RR (OCR = 4) (Stress Range Mpa)	
		w <sub>i</sub> (%)	e <sub>i</sub>	S <sub>i</sub> (%)	γ <sub>d</sub> (g/cm <sup>3</sup> )	γ <sub>t</sub> (g/cm <sup>3</sup> )	ε <sub>a</sub> (%)	e <sub>s</sub>	γ <sub>t</sub> (g/cm <sup>3</sup> )	σ' <sub>vm</sub> (MPa)	ε <sub>a</sub> (%)	e <sub>c</sub>	γ <sub>t</sub> (g/cm <sup>3</sup> )				0.1 -1.0	1.0 - 3.0
CRS968	U	8.13	0.89	24.89	1.442	1.559	---	---	---	14.212	20.05	0.51	2.141	19.88	0.104	0.010	N/A	N/A
CRS971	U	7.75	0.88	23.93	1.447	1.559	0.55	0.87	1.922	14.177	20.23	0.50	2.148	21.00	0.099	0.009	N/A	N/A
CRS976	U	8.19	0.89	25.05	1.441	1.559	0.28	0.89	1.912	14.229	20.40	0.50	2.146	20.70	0.098	0.009	0.008	0.005
CRS982	U	8.13	0.89	24.89	1.442	1.559	0.12	0.88	1.917	14.828	19.80	0.51	2.140	20.08	0.094	0.009	0.011	N/A
CRS983	U	7.96	1.03	21.04	1.342	1.449	5.18	0.92	1.898	14.204	25.84	0.50	2.147	20.94	0.098	0.008	0.011	0.006
CRS985	U	5.12	1.29	10.82	1.190	1.251	15.92	0.92	1.898	14.284	34.35	0.50	2.149	21.55	0.093	0.008	0.008	0.006
CRS987	U	8.11	1.50	14.78	1.092	1.092	24.13	0.89	1.912	14.819	40.03	0.49	2.155	20.60	0.077	0.007	0.008	N/A
CRS993	S	35.00	0.84	100.00	1.488	2.009	N/A	N/A	N/A	14.663	27.15	0.42	2.213	20.40	0.145	0.015	0.010	0.009
CRS1001	S	35.00	0.94	100.00	1.411	1.905	N/A	N/A	N/A	16.705	35.66	0.40	2.229	20.15	0.157	0.018	0.011	0.013
CRS1002	U	7.93	0.71	30.45	1.594	1.720	0.60	0.70	2.014	14.580	12.42	0.49	2.160	20.18	0.100	0.009	0.006	0.007
CRS1091	U	7.84	0.89	24.05	1.440	1.560	3.98	0.81	1.952	15.010	21.31	0.48	2.165	21.03	0.101	0.008	N/A	N/A

Table 5-3: Summary of CRS consolidation results

U = Undercompacted specimen

S = Slurry sedimented specimen

Test No.	Setup Conditions					Post Saturation			At Max. Stress				Preshear					CR Range Mpa 0.6-1.8	SR (OCR =4)	
	w <sub>i</sub> (%)	e <sub>i</sub>	S <sub>i</sub> (%)	γ <sub>d</sub> (g/cm <sup>3</sup> )	γ <sub>t</sub> (g/cm <sup>3</sup> )	ε <sub>a</sub> (%)	e <sub>s</sub>	γ <sub>t</sub> (g/cm <sup>3</sup> )	σ' <sub>vm</sub> (kPa)	ε <sub>a</sub> (%)	e <sub>c</sub>	γ <sub>t</sub> (g/cm <sup>3</sup> )	σ' <sub>ve</sub> (kPa)	ε <sub>a</sub> (%)	e <sub>c</sub>	γ <sub>t</sub> (g/cm <sup>3</sup> )	OCR			w <sub>c</sub> (%)
DSS788	8.33	1.02	22.23	1.348	1.461	7.19	0.88	1.919	593	15.20	0.71	2.006	593	15.20	0.71	2.006	1	23.99	0.059	N/A
DSS790	8.01	0.99	22.16	1.372	1.482	7.06	0.84	1.935	1182	17.24	0.64	2.050	1182	17.24	0.64	2.050	1	23.66	0.070	N/A
DSS791	8.65	0.97	24.33	1.384	1.502	6.66	0.84	1.938	1177	17.49	0.62	2.061	1177	17.49	0.62	2.061	1	22.45	0.070	N/A
DSS792	8.52	0.97	23.86	1.381	1.499	7.08	0.83	1.941	197	12.13	0.73	1.995	197	12.13	0.73	1.995	1	22.53	0.053	N/A
DSS793	8.36	0.94	24.15	1.402	1.519	7.27	0.80	1.957	197	12.65	0.70	2.016	197	12.65	0.70	2.016	1	22.73	0.051	N/A
DSS794	7.85	0.94	22.79	1.406	1.516	5.96	0.82	1.946	628	14.58	0.66	2.041	628	14.58	0.66	2.041	1	23.28	0.062	N/A
DSS795	7.99	0.92	23.73	1.421	1.534	5.88	0.80	1.955	1765	18.02	0.57	2.097	1765	18.02	0.57	2.097	1	22.67	0.084	N/A
DSS796	7.77	0.92	22.99	1.418	1.529	4.87	0.83	1.944	1765	17.13	0.59	2.083	1765	17.13	0.59	2.083	1	23.40	0.083	N/A
DSS807	3.40	0.82	11.32	1.498	1.549	3.21	0.76	1.980	592	9.22	0.65	2.044	592	9.22	0.65	2.044	1	24.21	0.050	N/A
DSS809	5.06	0.86	16.07	1.467	1.541	6.69	0.73	1.995	593	15.39	0.57	2.097	593	15.39	0.57	2.097	1	23.86	0.057	N/A
DSS810	8.83	1.04	23.19	1.337	1.455	7.02	0.72	2.002	597	15.30	0.73	1.999	597	15.30	0.73	1.999	1	22.66	0.057	N/A
DSS811	9.66	1.04	25.21	1.333	1.462	8.97	0.69	2.020	591	17.47	0.69	2.022	591	17.47	0.69	2.022	1	---	0.060	N/A
DSS815	7.84	0.95	22.47	1.397	1.506	4.99	0.69	2.020	590	13.41	0.69	2.021	590	13.41	0.69	2.021	1	23.03	0.064	N/A
DSS798	8.15	0.92	24.14	1.419	1.534	5.23	0.82	1.948	1188	15.97	0.61	2.069	595	15.76	0.62	2.066	2	23.32	0.074	0.008
DSS799	8.06	0.93	23.63	1.412	1.526	5.85	0.82	1.949	1178	16.62	0.61	2.072	591	16.36	0.61	2.068	2	24.10	0.078	0.008
DSS800	7.94	0.90	24.11	1.436	1.550	3.71	0.83	1.944	1766	15.80	0.90	1.909	591	15.30	0.61	2.073	3	23.20	0.087	0.010
DSS801	9.97	0.94	29.02	1.407	1.547	5.11	0.84	1.938	1766	17.64	0.59	2.081	591	17.18	0.60	2.075	3	23.22	0.085	0.010
DSS806	7.88	0.91	23.73	1.430	1.543	4.24	0.82	1.945	1770	15.72	0.61	2.074	444	15.15	0.62	2.067	4	21.95	0.083	0.009
DSS808	7.80	0.90	23.50	1.431	1.542	4.77	0.81	1.951	1771	16.45	0.59	2.084	446	15.92	0.60	2.077	4	22.89	0.082	0.009

Table 5-4: Summary of consolidation results for DSS tests

Test No.	Test Type	Setup Conditions					Post Saturation		At Max. Stress				Preshear				CR	
		w <sub>i</sub> (%)	e <sub>i</sub>	S <sub>i</sub> (%)	γ <sub>a</sub> (g/cm <sup>3</sup> )	γ <sub>t</sub> (g/cm <sup>3</sup> )	e <sub>s</sub>	γ <sub>t</sub> (g/cm <sup>3</sup> )	σ' <sub>vm</sub> (kPa)	e <sub>c</sub>	γ <sub>t</sub> (g/cm <sup>3</sup> )	K <sub>θ(NC)</sub>	σ' <sub>vc</sub> (kPa)	e <sub>c</sub>	γ <sub>t</sub> (g/cm <sup>3</sup> )	K <sub>c</sub>		w <sub>c</sub> (%)
TX920	CIUC	8.18	0.89	25.02	1.441	1.559	0.66	2.040	97	0.64	2.050	1	97	0.64	2.050	1	23.59	---
TX921	CIUC	8.32	0.83	27.30	1.489	1.612	0.66	2.037	98	0.64	2.049	1	98	0.64	2.049	1	23.64	---
TX922	CIUC	5.90	0.82	19.51	1.494	1.582	0.64	2.049	98	0.63	2.061	1	98	0.63	2.061	1	22.96	---
TX945	CIUC	3.77	0.83	12.37	1.489	1.545	0.65	2.045	198	0.62	2.067	1	198	0.62	2.067	1	22.61	0.036
TX970	CIUC	3.46	0.82	11.44	1.493	1.545	0.67	2.034	399	0.62	2.067	1	399	0.62	2.067	1	22.60	0.042
TX972	CIUC	3.17	0.82	10.53	1.497	1.545	0.69	2.023	589	0.62	2.063	1	589	0.62	2.063	1	22.84	0.038
TX989	CIUC	3.05	0.82	10.16	1.498	1.544	0.65	2.043	198	0.62	2.067	1	198	0.62	2.067	1	22.60	0.041
TX994	CIUC	3.44	0.81	11.55	1.504	1.556	0.68	2.027	391	0.62	2.062	1	391	0.62	2.062	1	22.88	0.041
TX997	CIUC	3.36	0.81	11.33	1.507	1.557	0.68	2.025	590	0.61	2.070	1	590	0.61	2.070	1	22.44	0.044
TX1000	CIUC	3.35	0.81	11.29	1.506	1.556	0.67	2.030	886	0.59	2.083	1	886	0.59	2.083	1	21.73	0.045
TX1003	CIUC	3.28	0.81	11.02	1.505	1.554	0.69	2.020	893	0.60	2.074	1	893	0.60	2.074	1	22.20	0.047

Table 5-5: Summary of consolidation results from isotropically consolidated triaxial tests



Test No.	Test Type	Setup Conditions					Post Saturation		At Max. Stress				Preshear					CR
		w <sub>i</sub> (%)	e <sub>i</sub>	S <sub>i</sub> (%)	γ <sub>d</sub> (g/cm <sup>3</sup> )	γ <sub>t</sub> (g/cm <sup>3</sup> )	e <sub>s</sub>	γ <sub>t</sub> (g/cm <sup>3</sup> )	σ' <sub>vm</sub> (kPa)	e <sub>c</sub>	γ <sub>t</sub> (g/cm <sup>3</sup> )	K <sub>0(NC)</sub>	σ' <sub>vc</sub> (kPa)	e <sub>c</sub>	γ <sub>t</sub> (g/cm <sup>3</sup> )	K <sub>c</sub>	w <sub>c</sub> (%)	
TX1013	CKoUC	3.00	0.79	10.32	1.521	1.567	0.70	2.017	557	0.62	2.066	0.59	557	0.62	2.066	0.59	27.42	0.040
TX1018	CKoUC	2.82	0.79	9.743	1.524	1.567	0.70	2.011	363	0.63	2.056	0.56	363	0.63	2.056	0.56	23.25	0.042
TX1019	CKoUC	3.03	0.79	10.43	1.520	1.567	0.68	2.024	186	0.64	2.052	0.64	186	0.64	2.052	0.64	23.50	0.030
TX1021	CKoUC	3.13	0.79	10.75	1.519	1.567	0.71	2.007	830	0.62	2.065	0.57	830	0.62	2.065	0.57	22.70	0.046

Table 5-6: Summary of consolidation results from K<sub>0</sub> consolidated triaxial tests

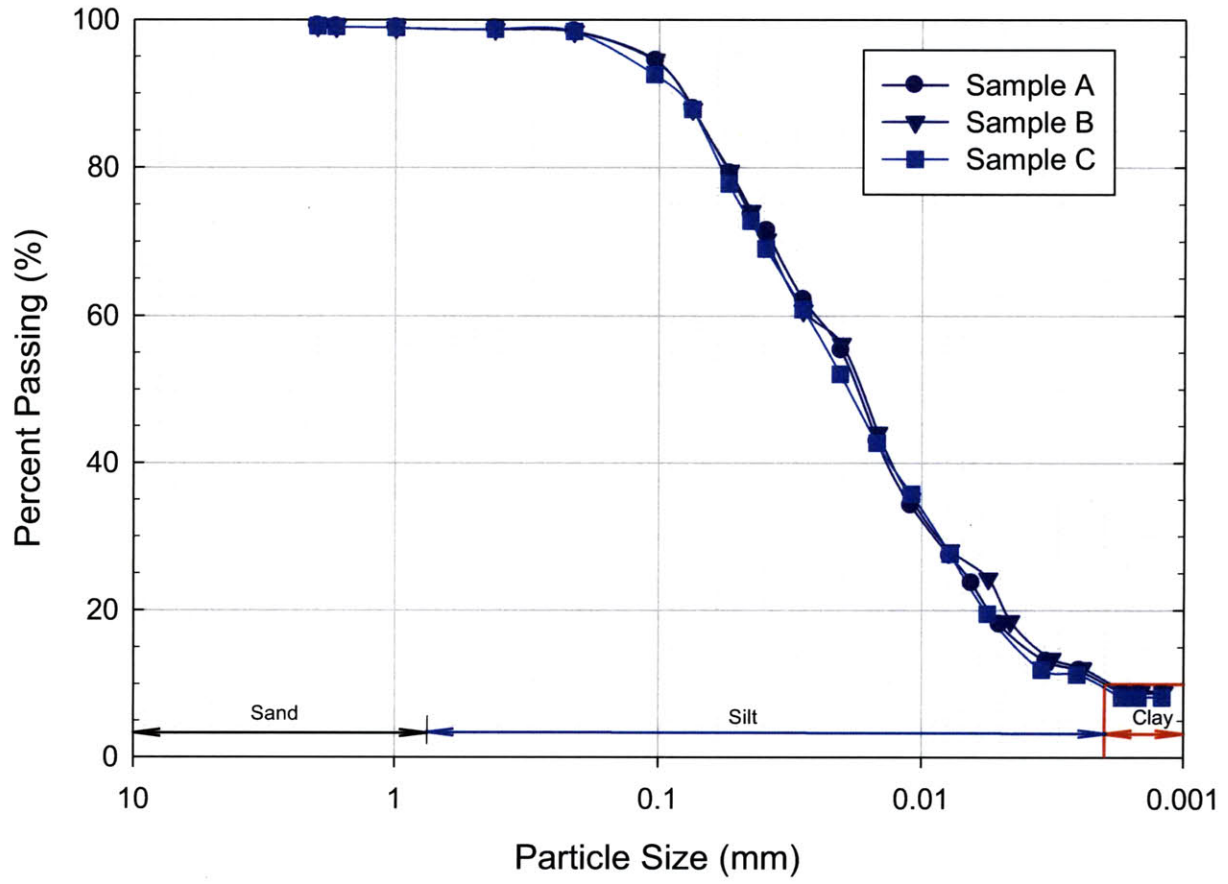
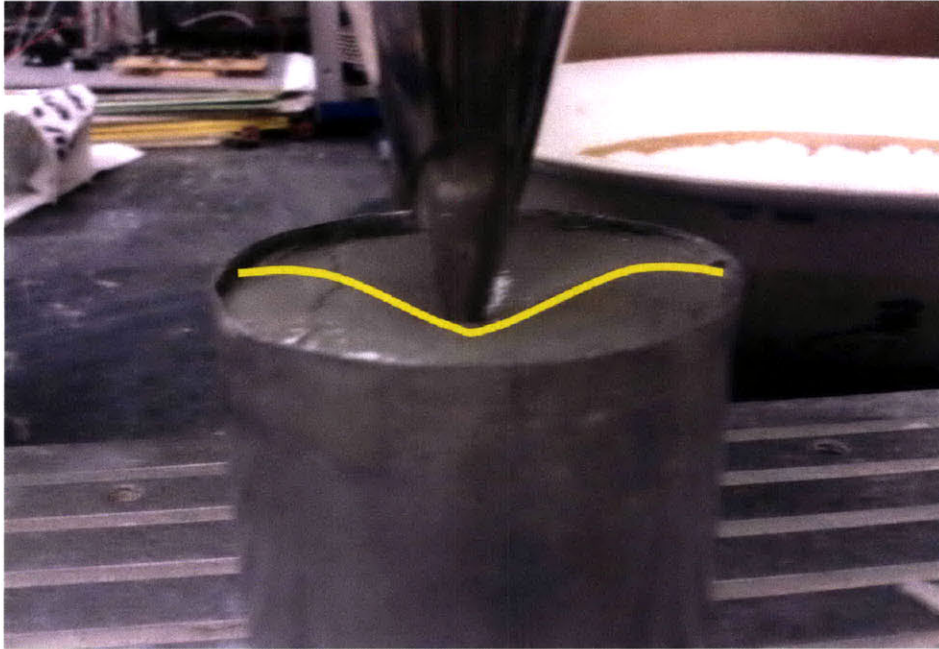


Figure 5-1: Grain Size Distribution Curves for Skibbereen Silt from hydrometer tests

(a)



(b)

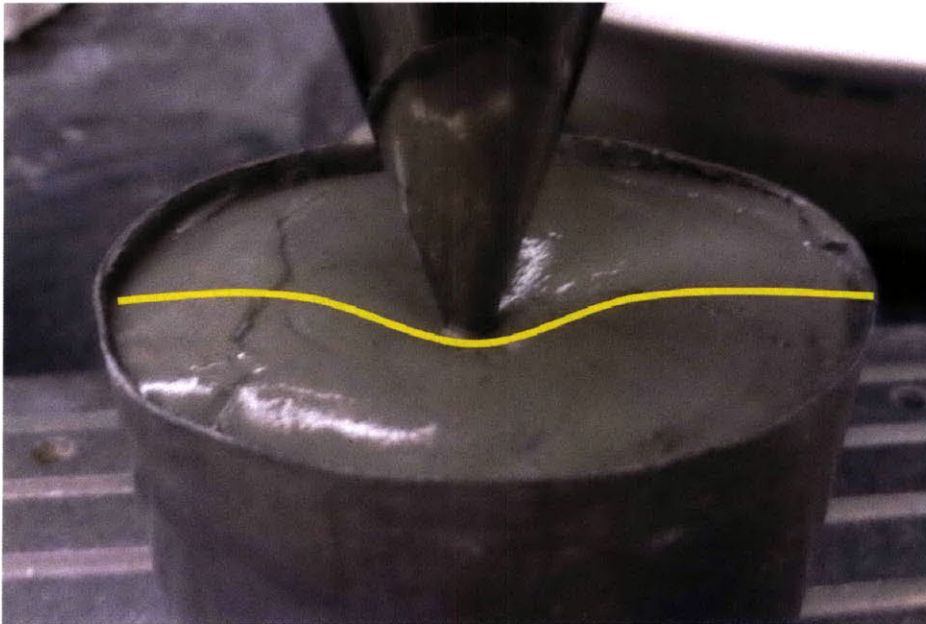


Figure 5-2: Surface curvature around fall cone during liquid limit testing on Skibbereen Silt: (a) Extended view, (b) close up

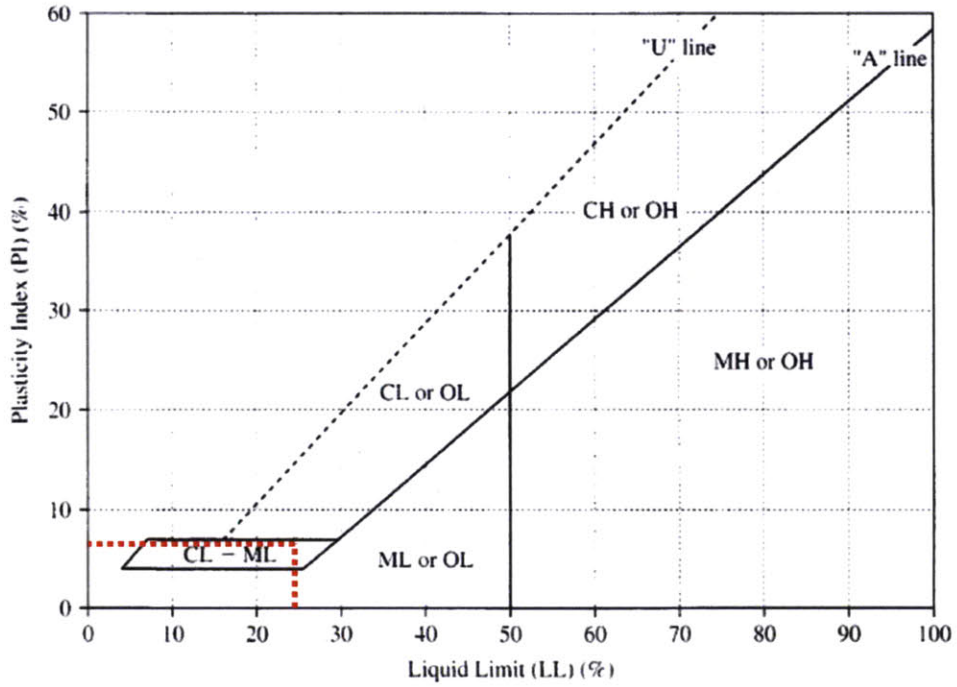


Figure 5-3: Classification of Skibbereen Silt on Casagrande Plasticity Chart

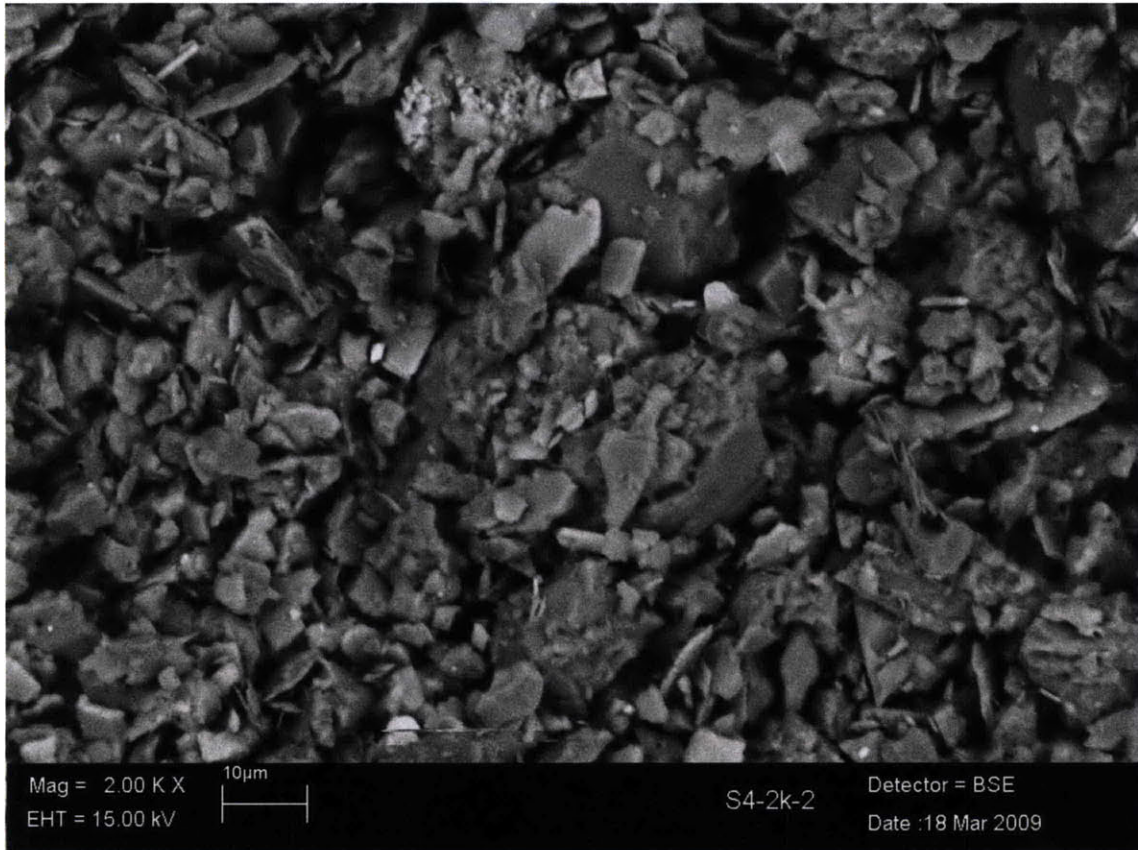


Figure 5-4: SEM image on Skibbereen Silt, magnified to 2000 times the actual size

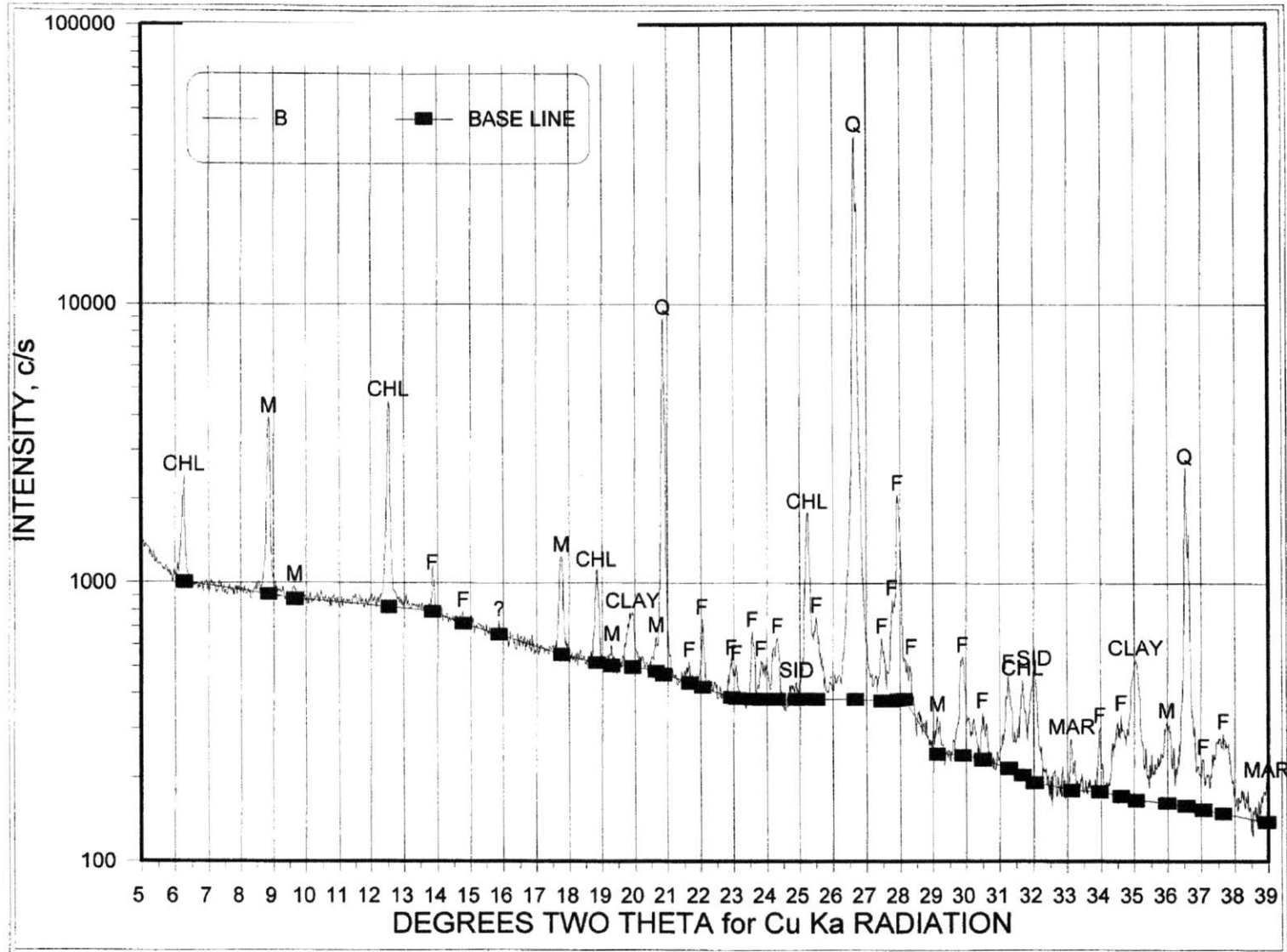


Figure 5-5: X Ray Diffraction analysis for Skibberreen Silt: Intensity versus Degrees Two Theta for Cu Ka Radiation (5-39)

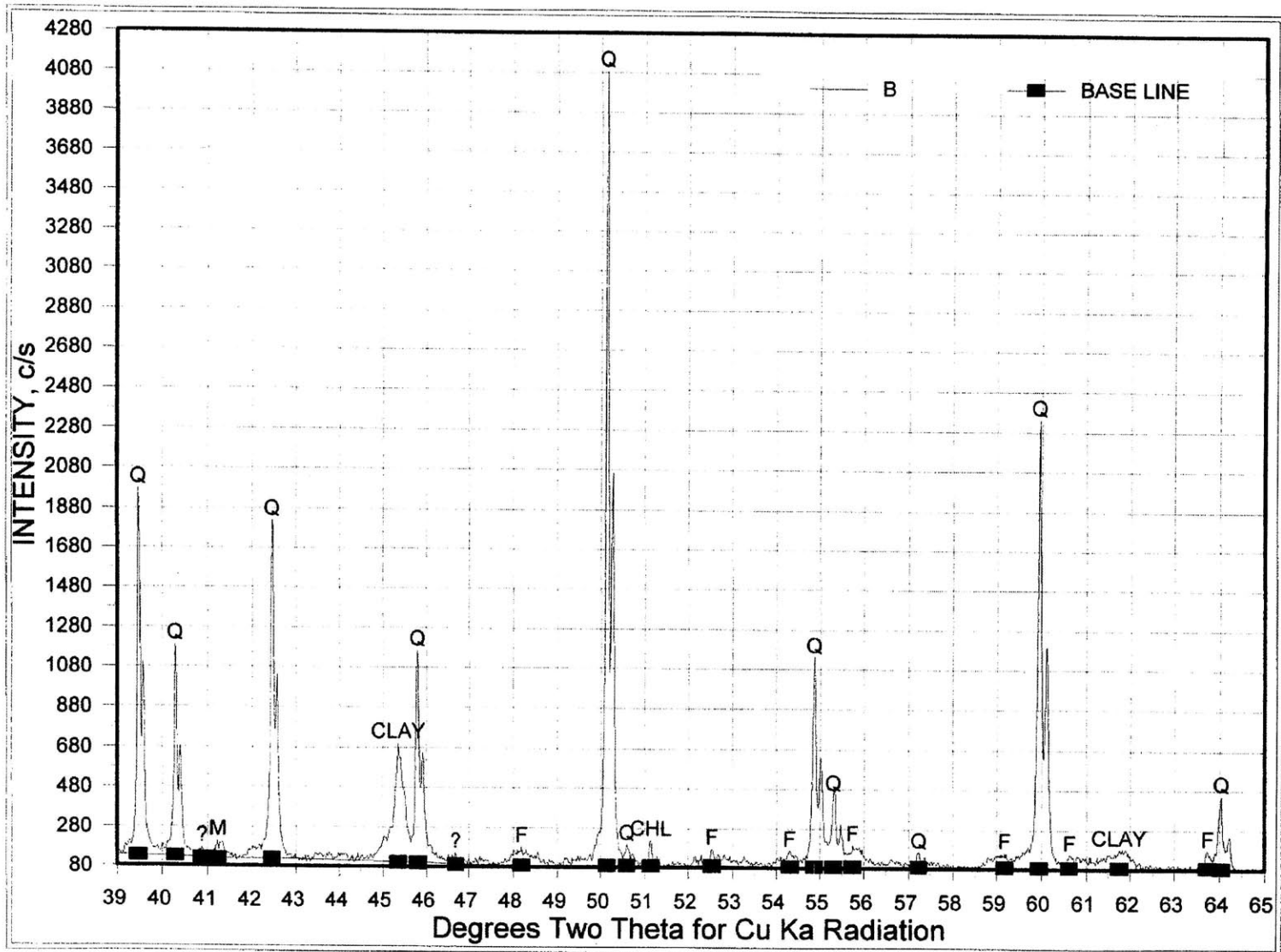


Figure 5-6: X Ray Diffraction analysis for Skibbereen Silt: Intensity versus Degrees Two Theta for Cu Ka Radiation (39-65)

CRS 976

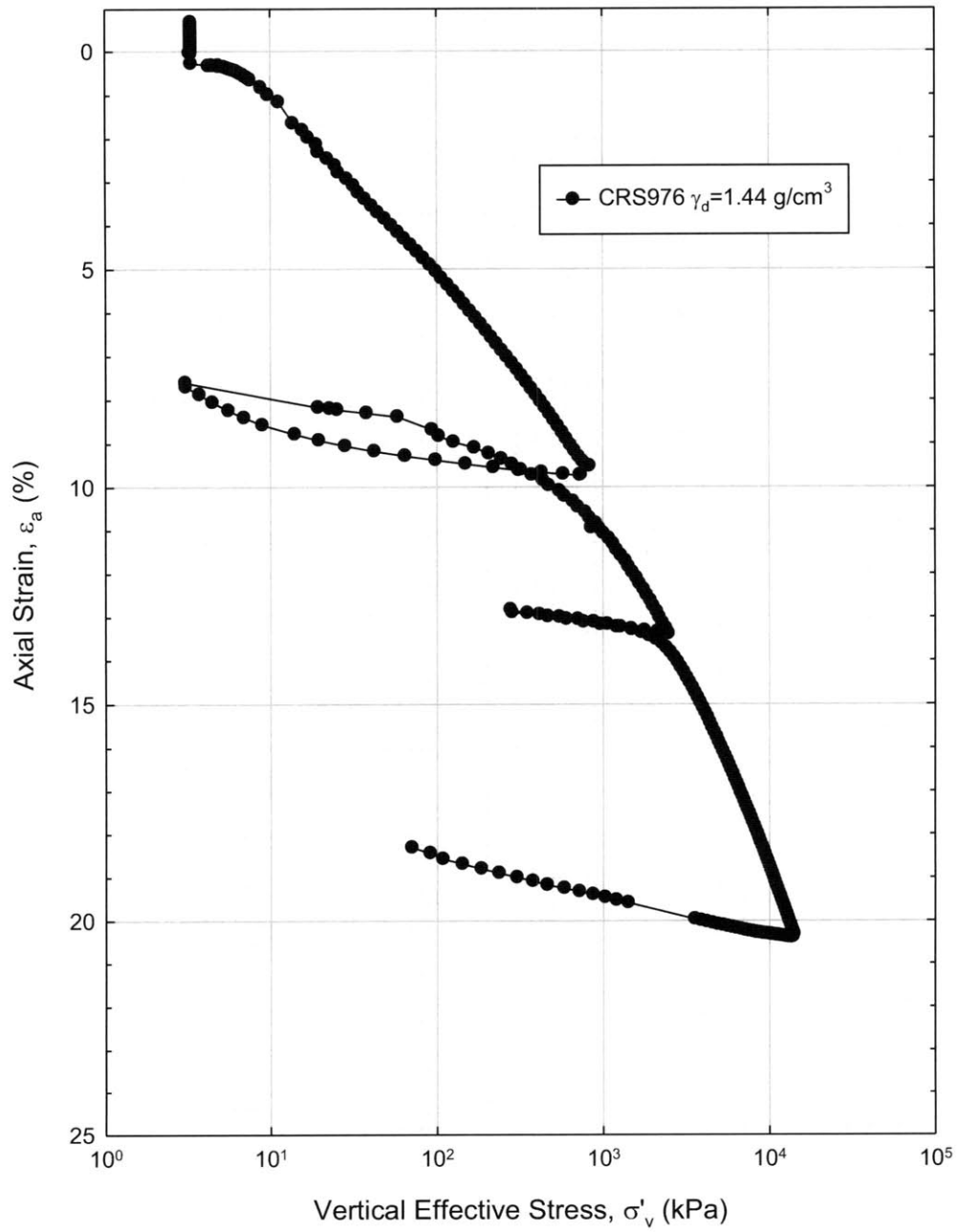


Figure 5-7: Compression behavior in  $\epsilon_a$ - $\log \sigma'_v$  space from CRS 976

CRS 976

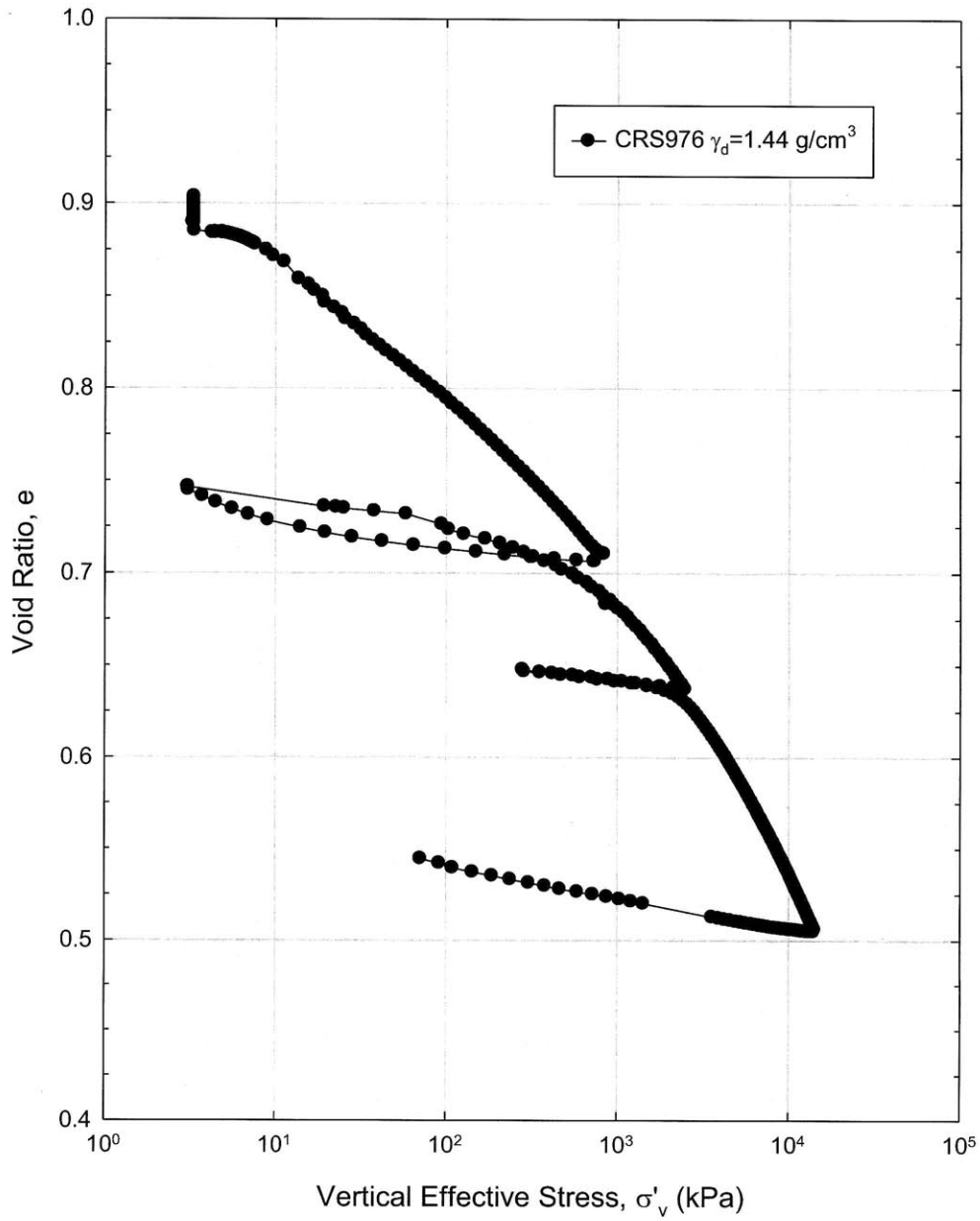


Figure 5-8: Compression behavior in  $e$ - $\log \sigma'_v$  space from CRS 976



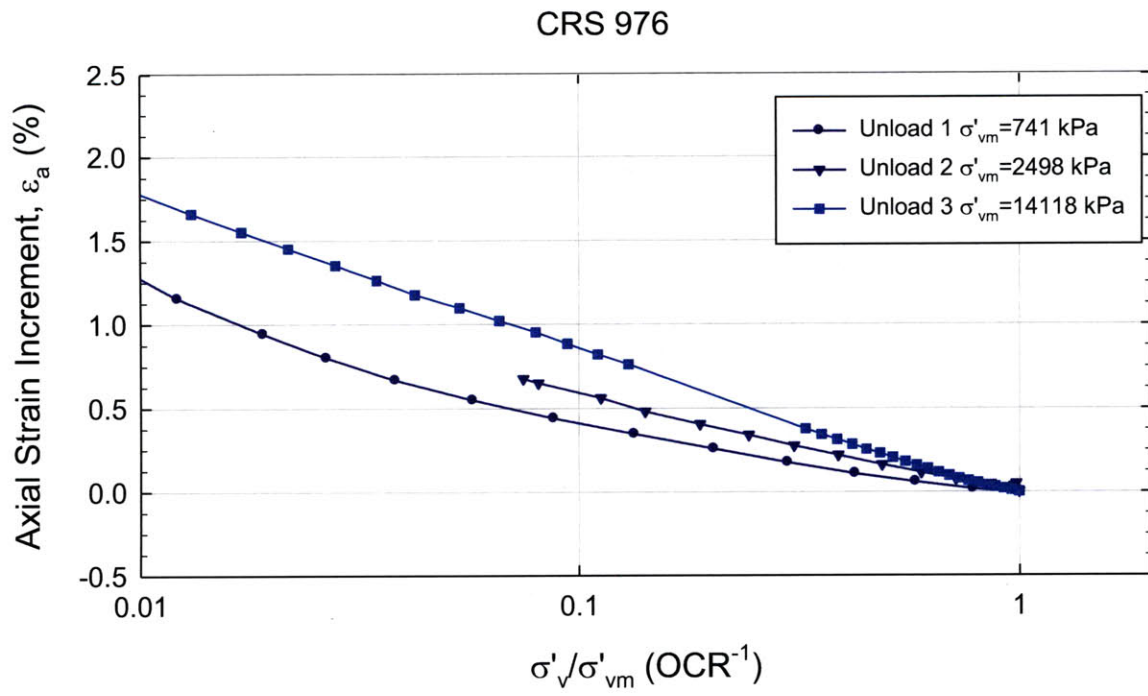


Figure 5-9: Axial strain versus  $\sigma'_v/\sigma'_{vm}$  ( $\text{OCR}^{-1}$ ) from the unload phases of a typical CRS test

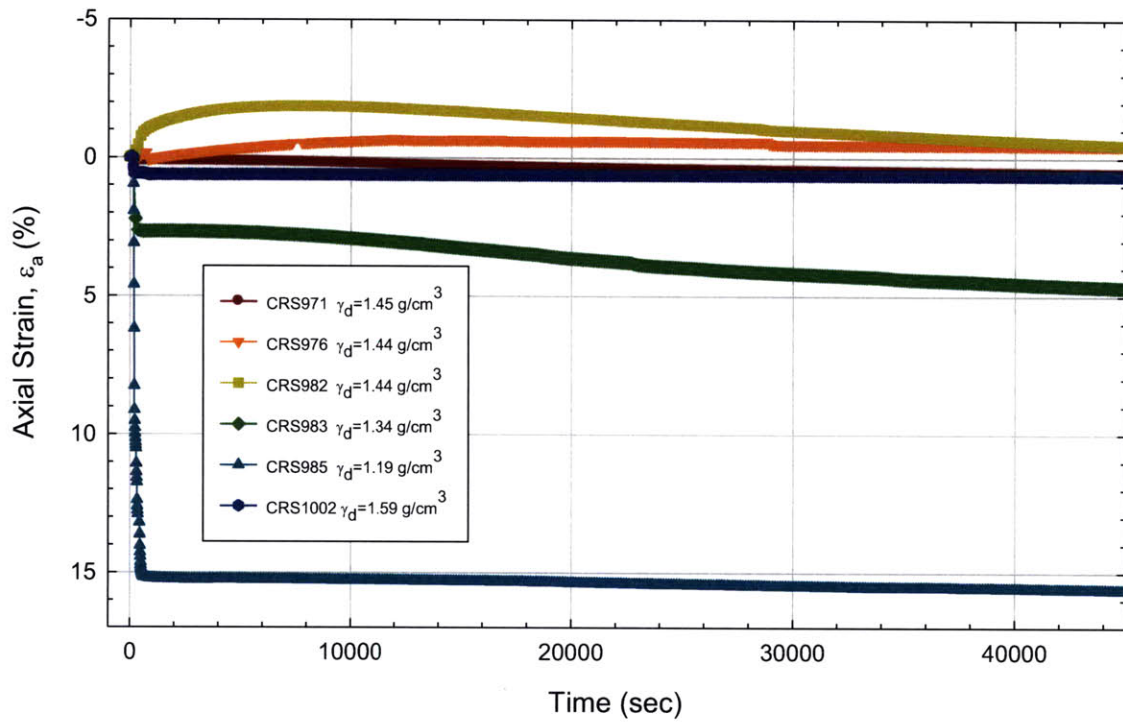


Figure 5-10: Axial strain-time behavior with different initial densities from CRS tests

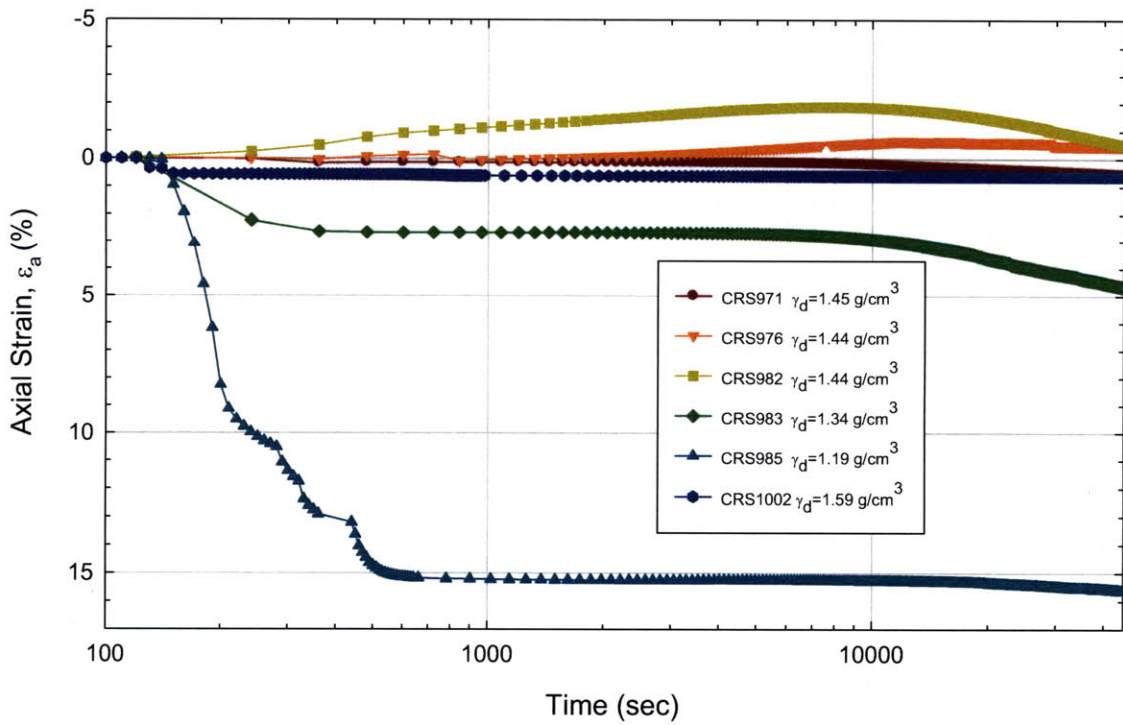


Figure 5-11: Axial strain-log time behavior with different initial densities from CRS tests

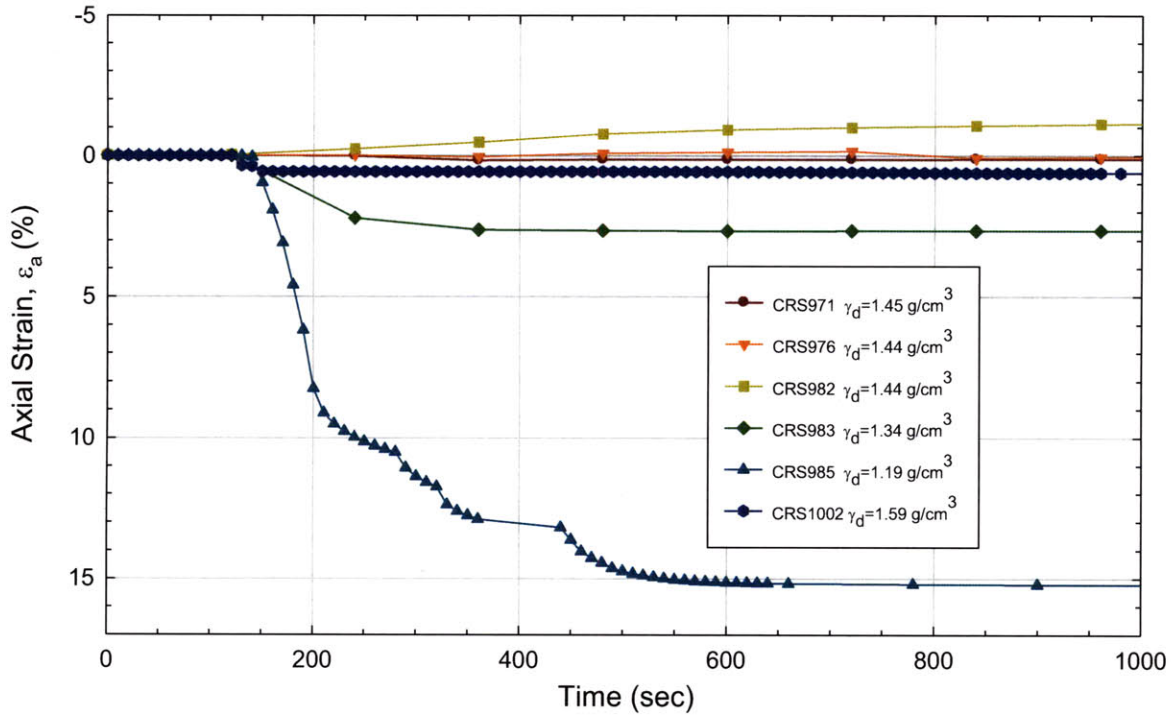


Figure 5-12: Axial strain-time (close up view) behavior with different initial densities from CRS tests

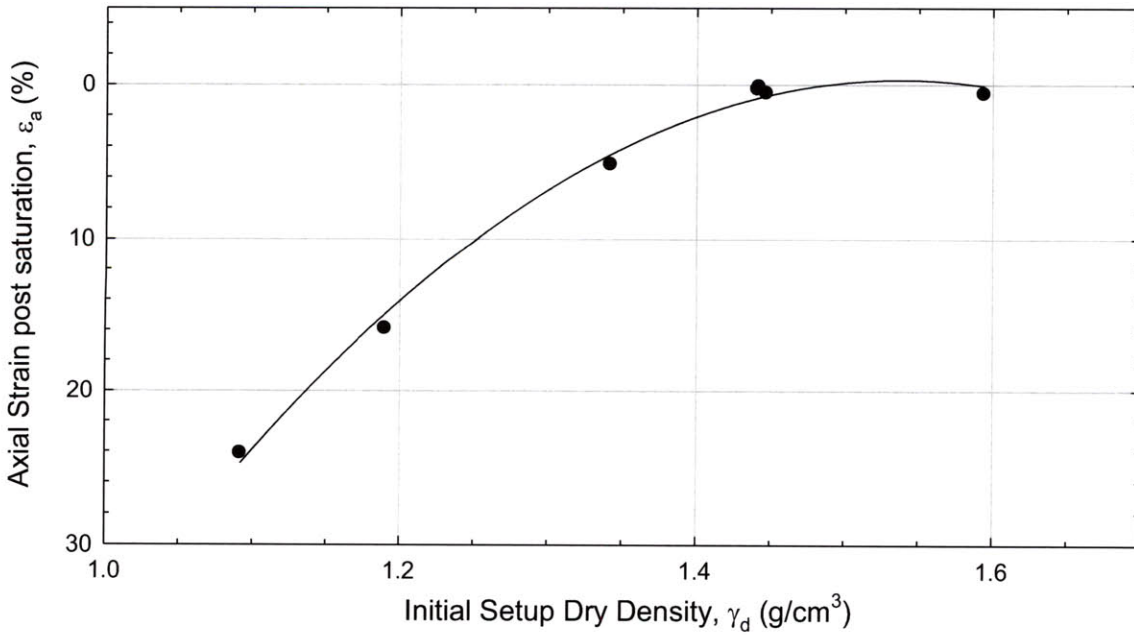


Figure 5-13: Axial strain post saturation versus initial setup dry density from CRS tests

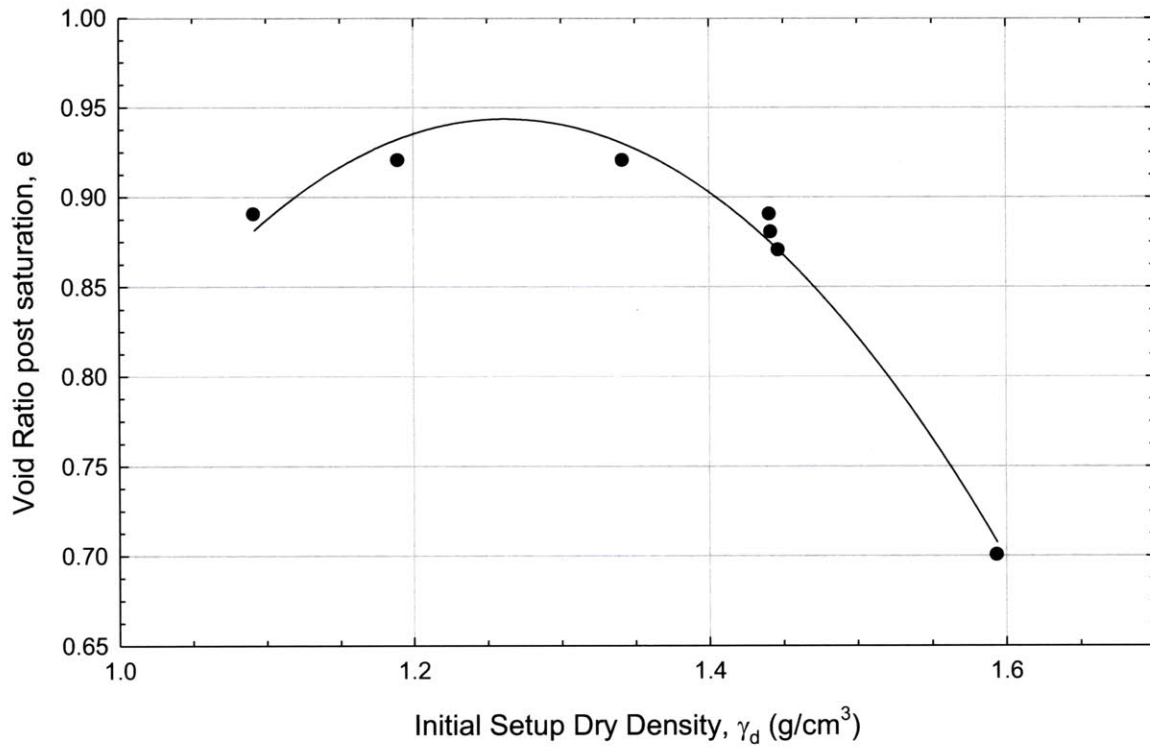


Figure 5-14: Void ratio post saturation versus initial setup dry density from CRS tests

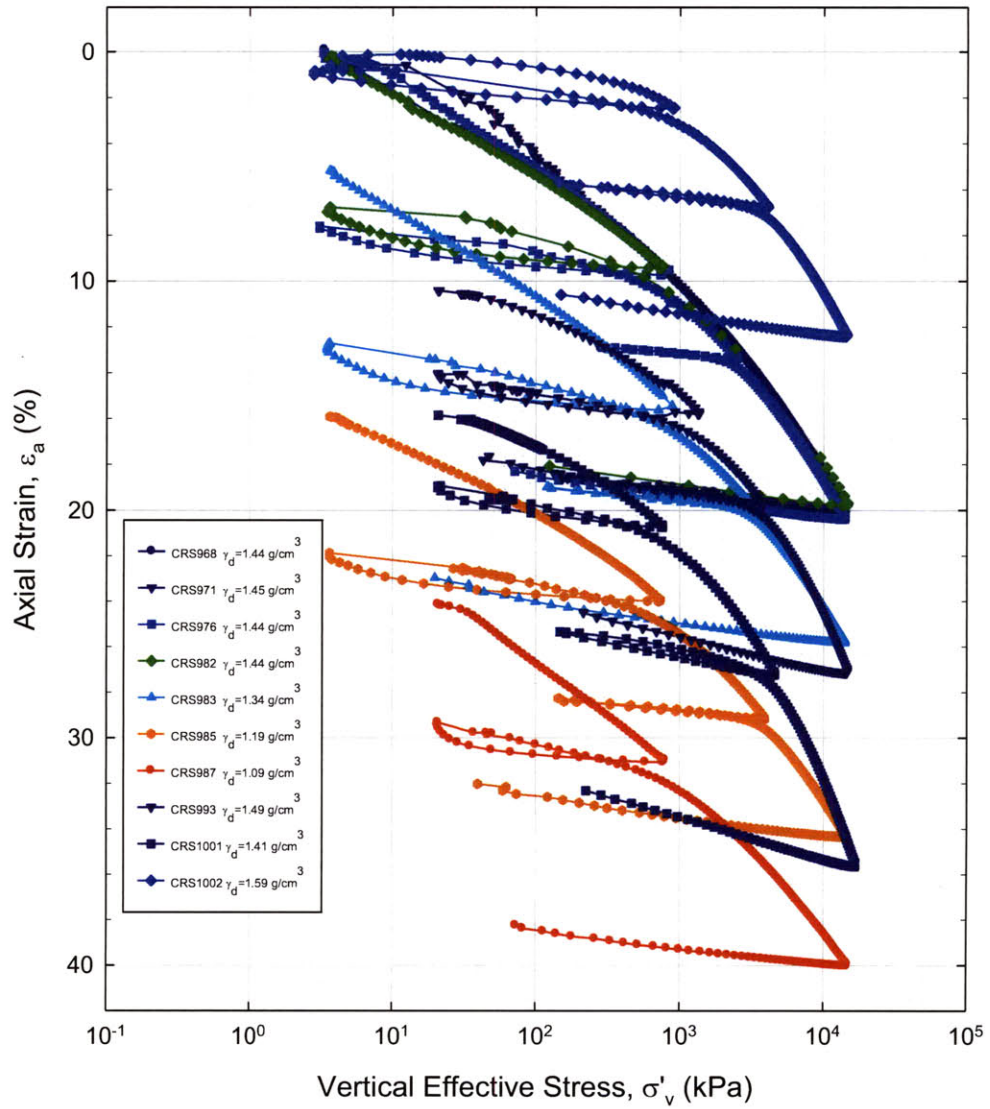


Figure 5-15: Compression behavior in  $\varepsilon_a$ - $\log \sigma'_v$  space from CRS tests

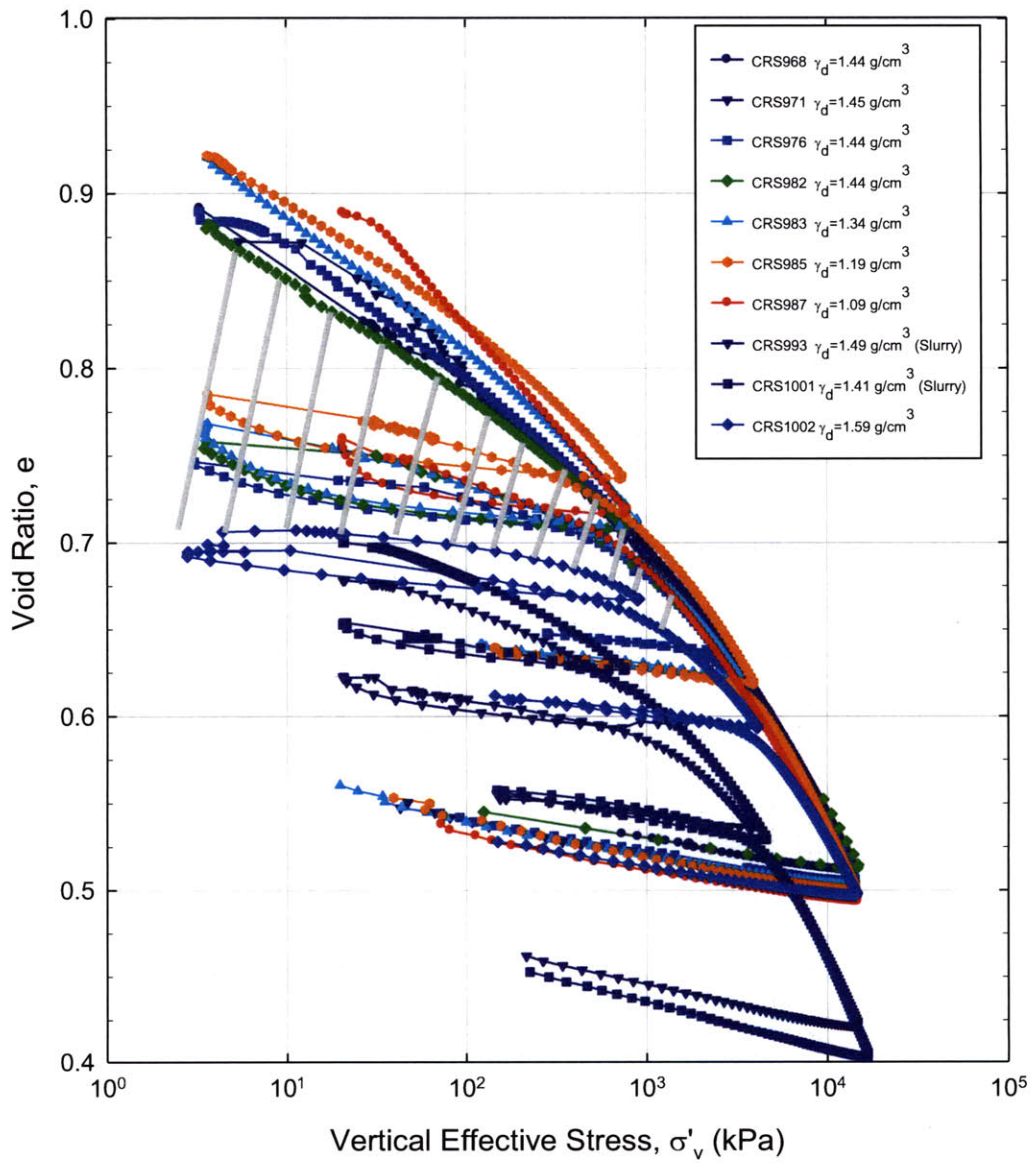


Figure 5-16: Compression behavior in  $e$ - $\log \sigma'_v$  space from CRS tests

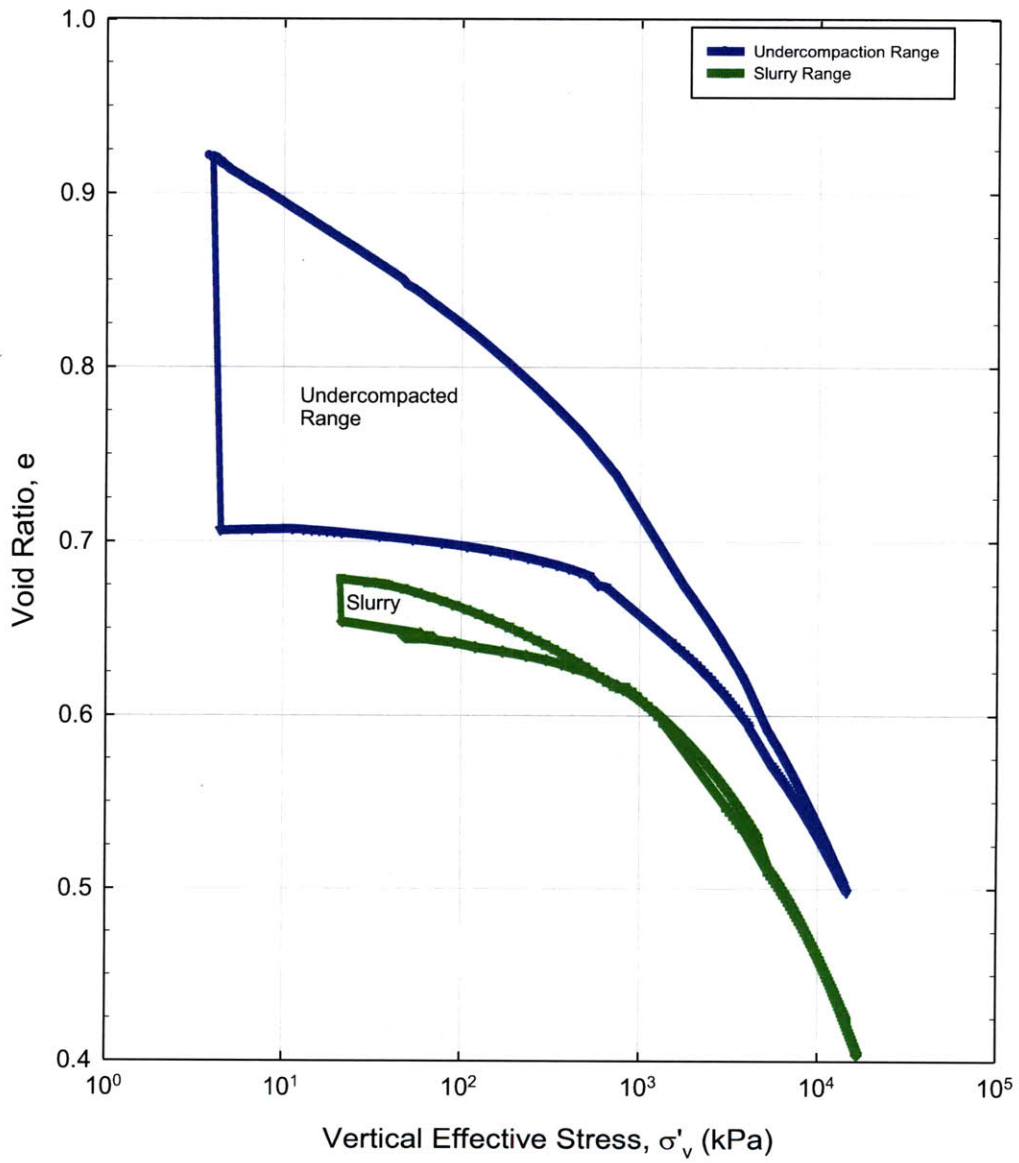


Figure 5-17: Virgin Compression behavior in  $e$ - $\log \sigma'_v$  space from CRS tests

a)



b)



c)



Figure 5-18: Post consolidation behavior; a) CRS specimen extrusion into evaporating dish, b) material behavior after one blow to evaporating dish, c) material behavior after 5 blows to evaporating dish



### DSS 800

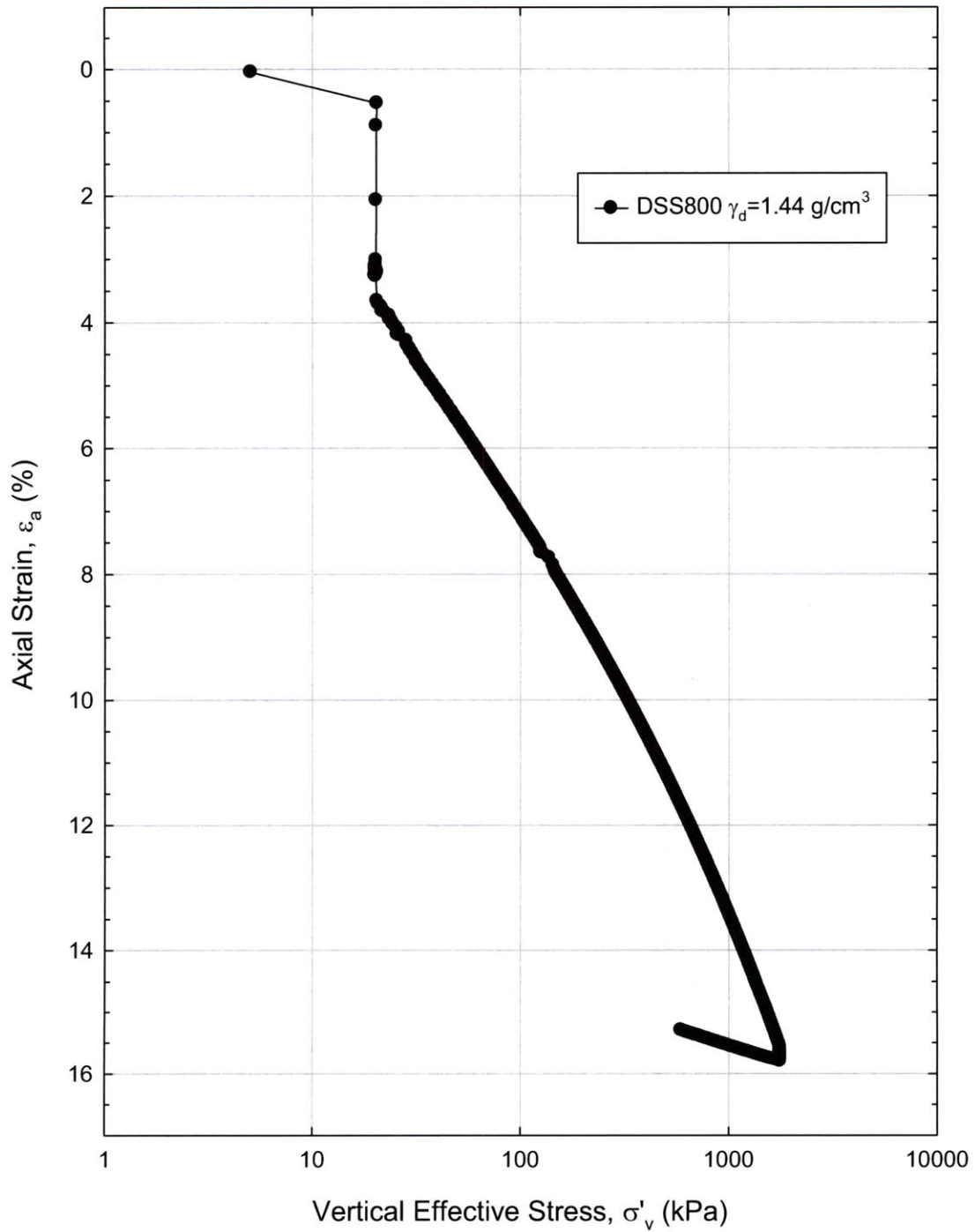


Figure 5-19: Compression behavior in  $\epsilon_a$ - $\log\sigma'_v$  space from DSS 800

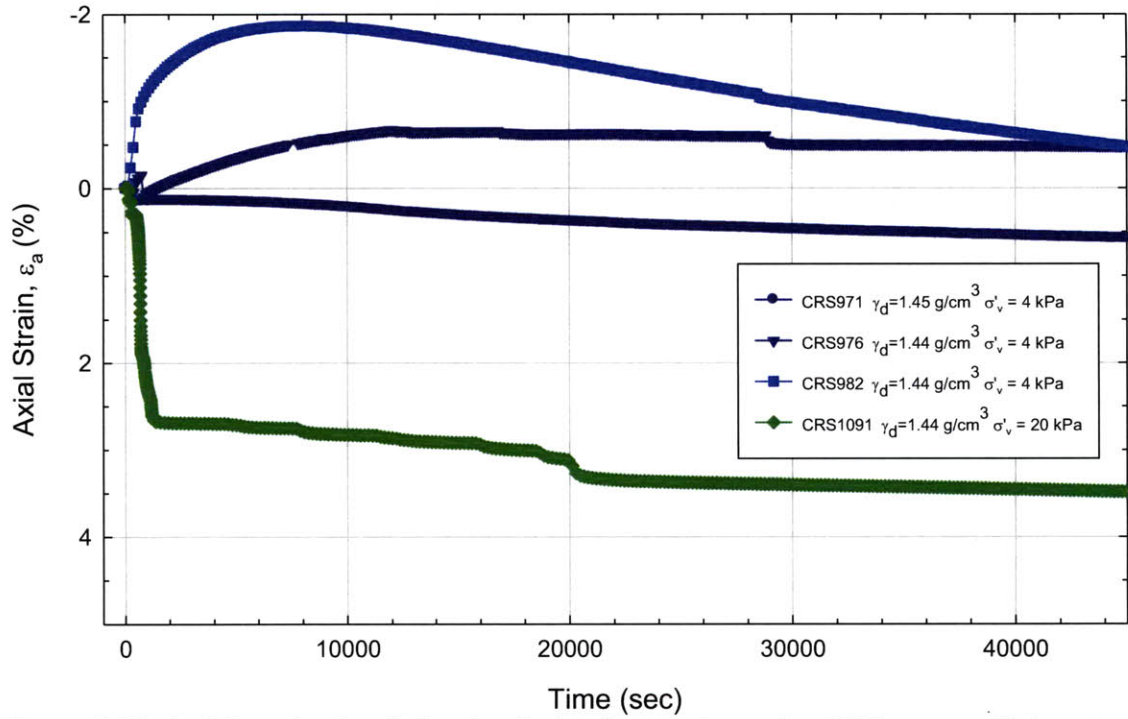


Figure 5-20: Axial strain-time behavior during inundation using different confining stresses from CRS tests

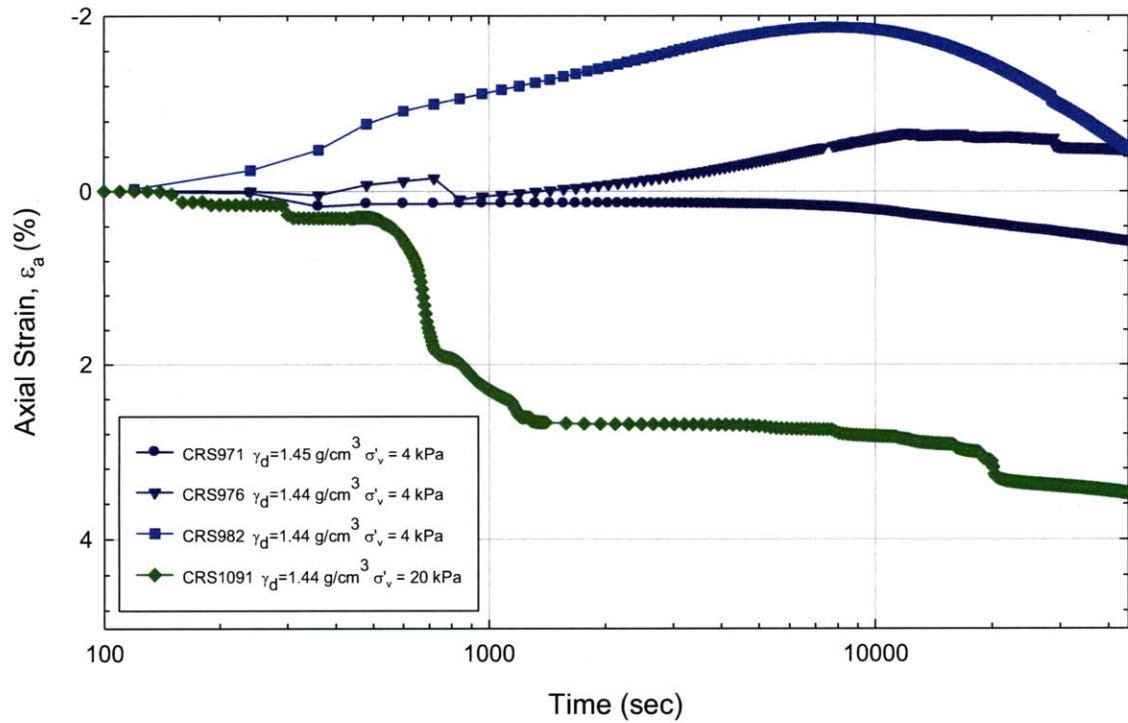


Figure 5-21: Axial strain-log time behavior during inundation using different confining stresses from CRS tests

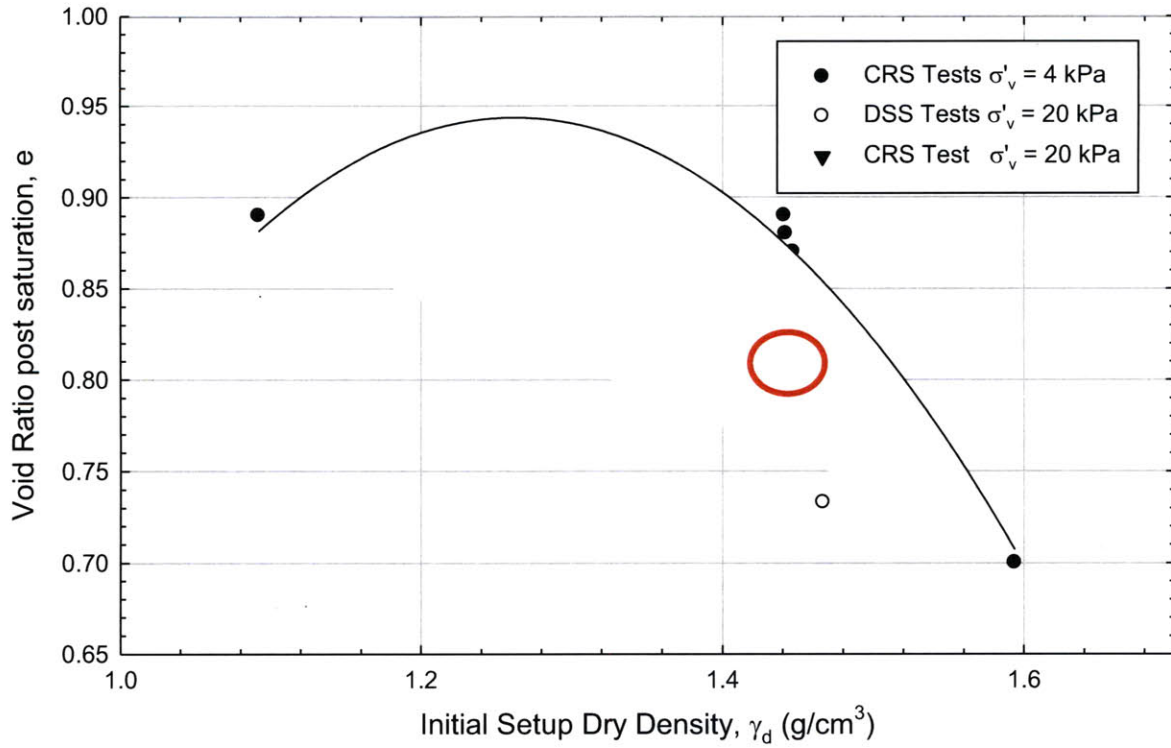


Figure 5-22: Void ratio post saturation versus initial setup dry density from CRS and DSS tests

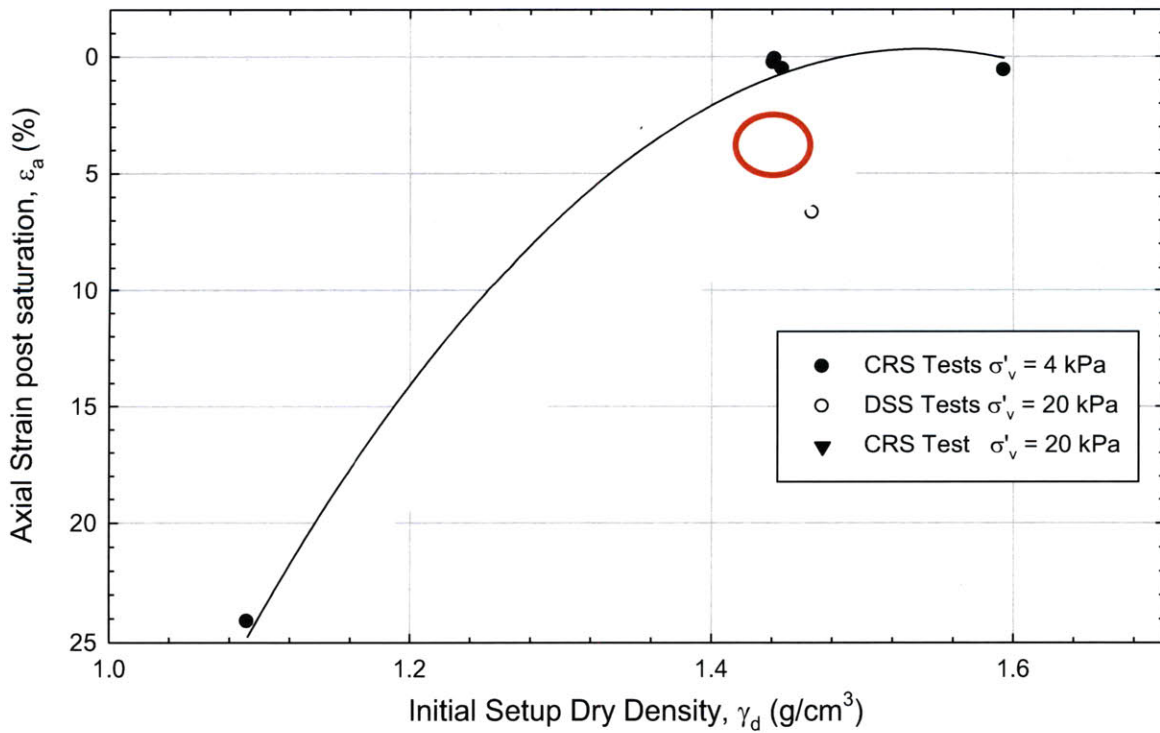


Figure 5-23: Axial strain post saturation versus initial setup dry density from CRS and DSS tests

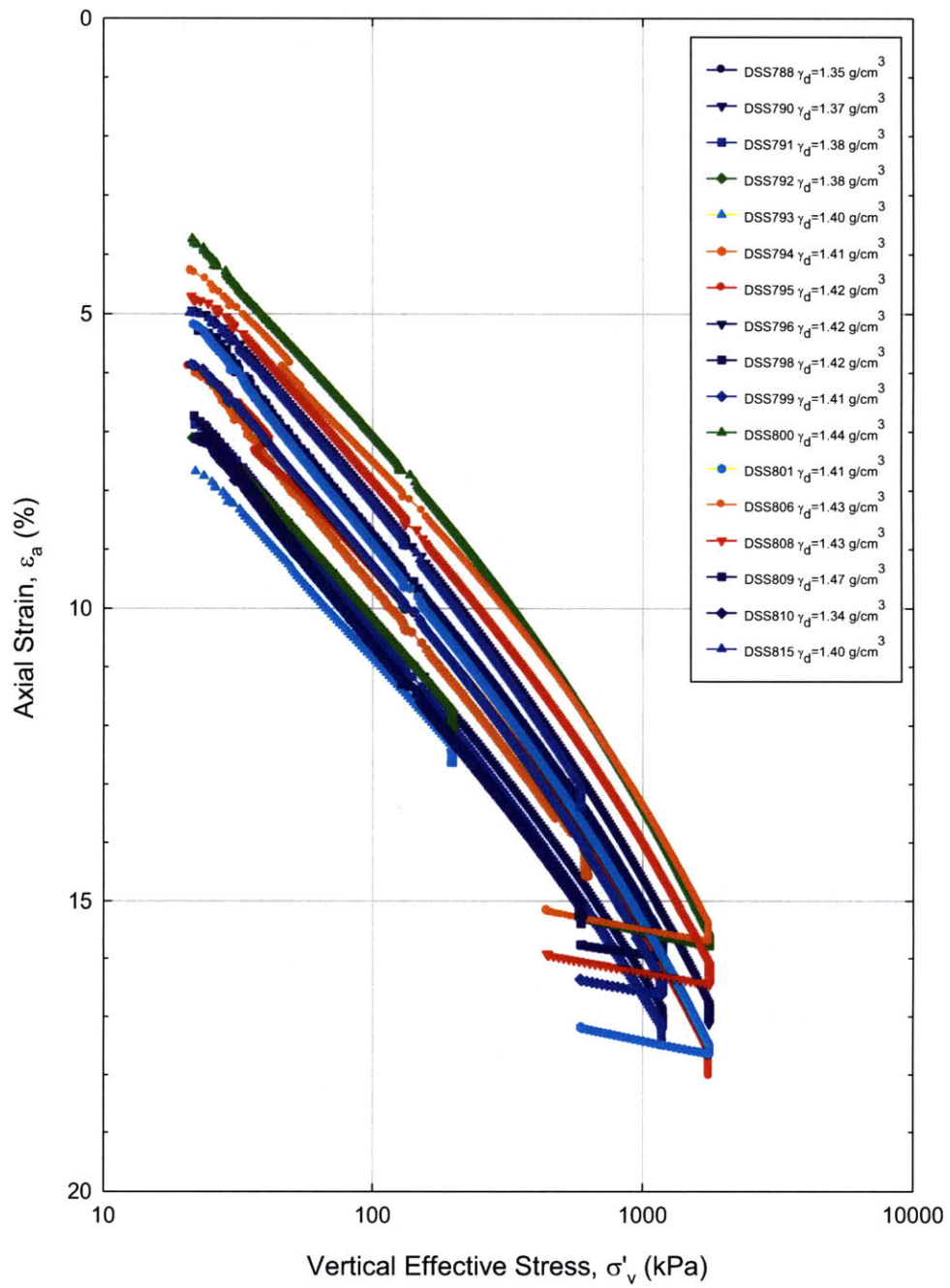


Figure 5-24: Compression behavior in  $\epsilon_a$ - $\log \sigma'_v$  space from DSS tests

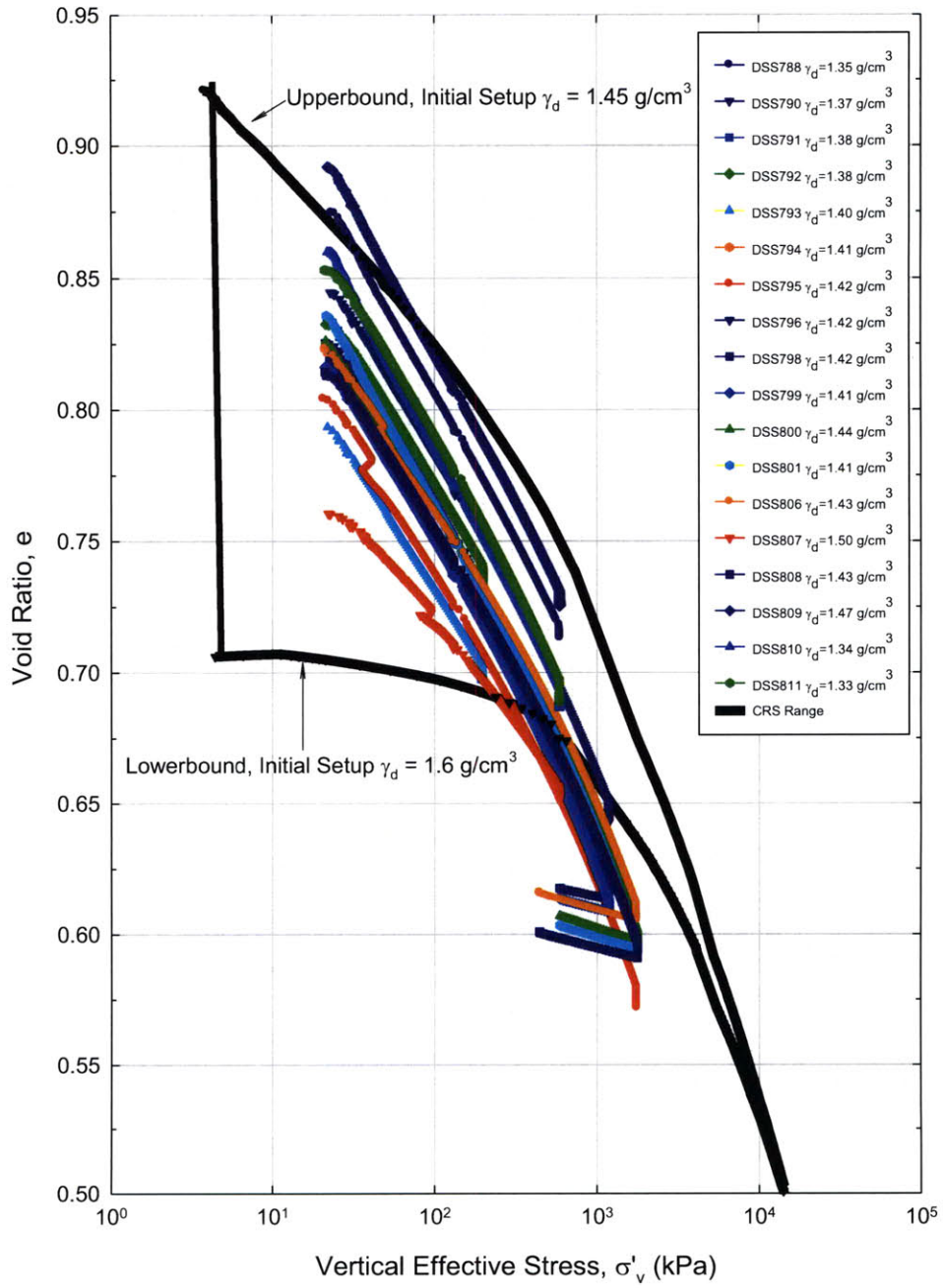


Figure 5-25: Compression behavior in  $e$ - $\log \sigma'_v$  space from DSS tests (CRS range included)

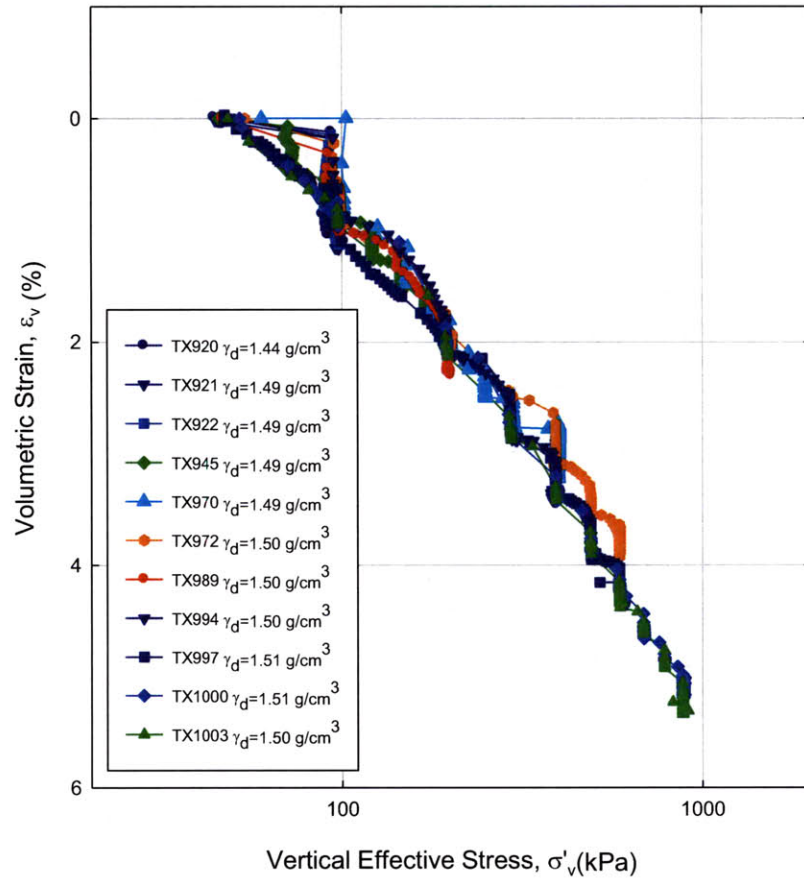


Figure 5-26: Compression behavior in  $\epsilon_v$ - $\log \sigma'_v$  space from CIUC test

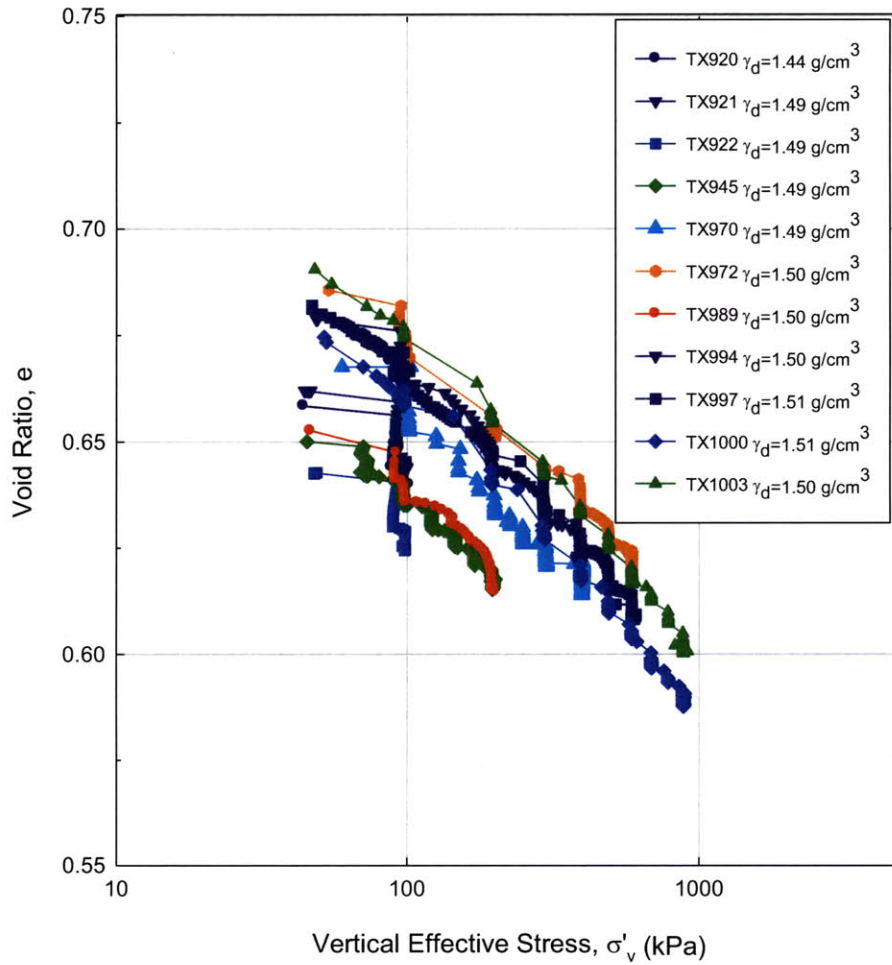


Figure 5-27: Compression behavior in  $e$ - $\log \sigma'_v$  space from CIUC tests

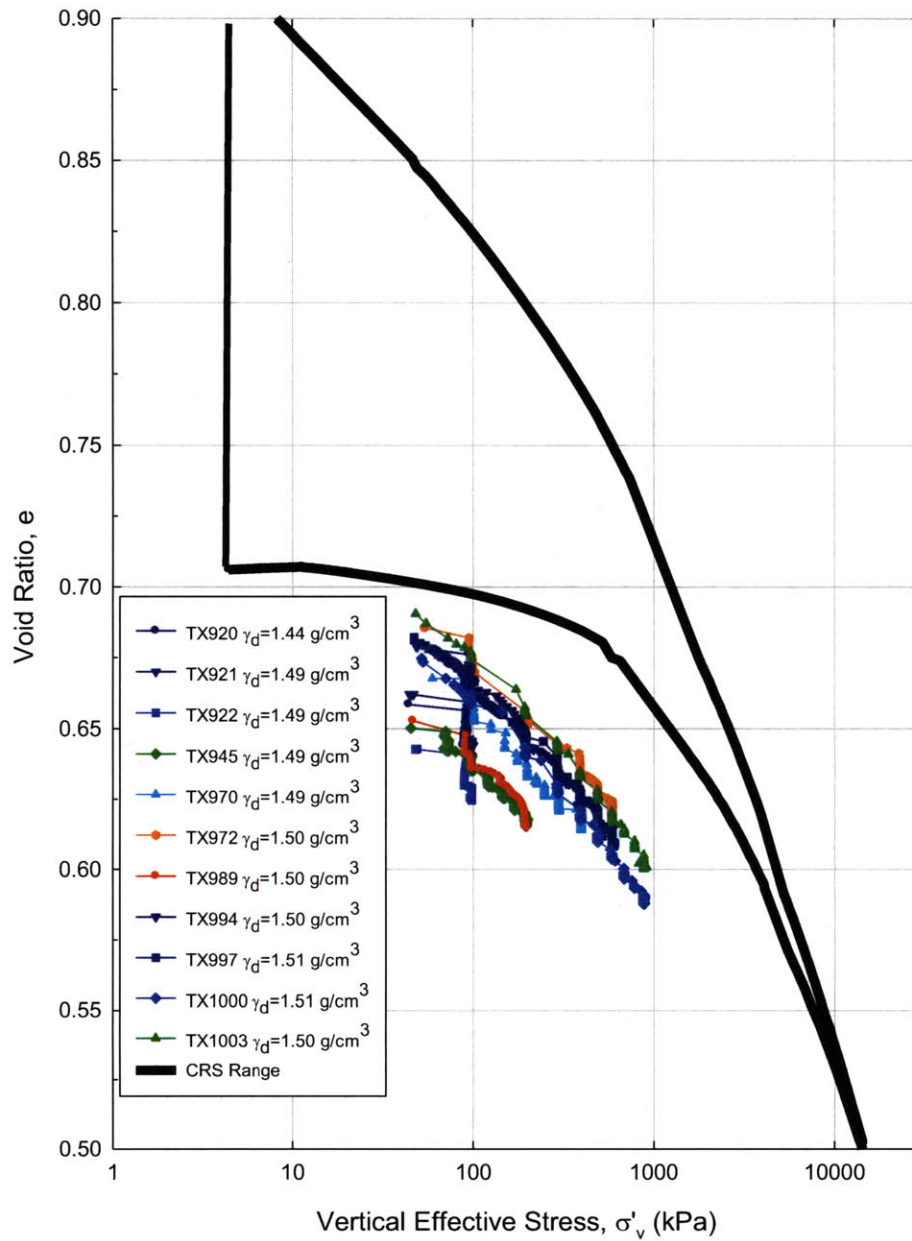


Figure 5-28: Compression behavior in  $e$ - $\log \sigma'_v$  space from CIUC tests compared with the CRS test range



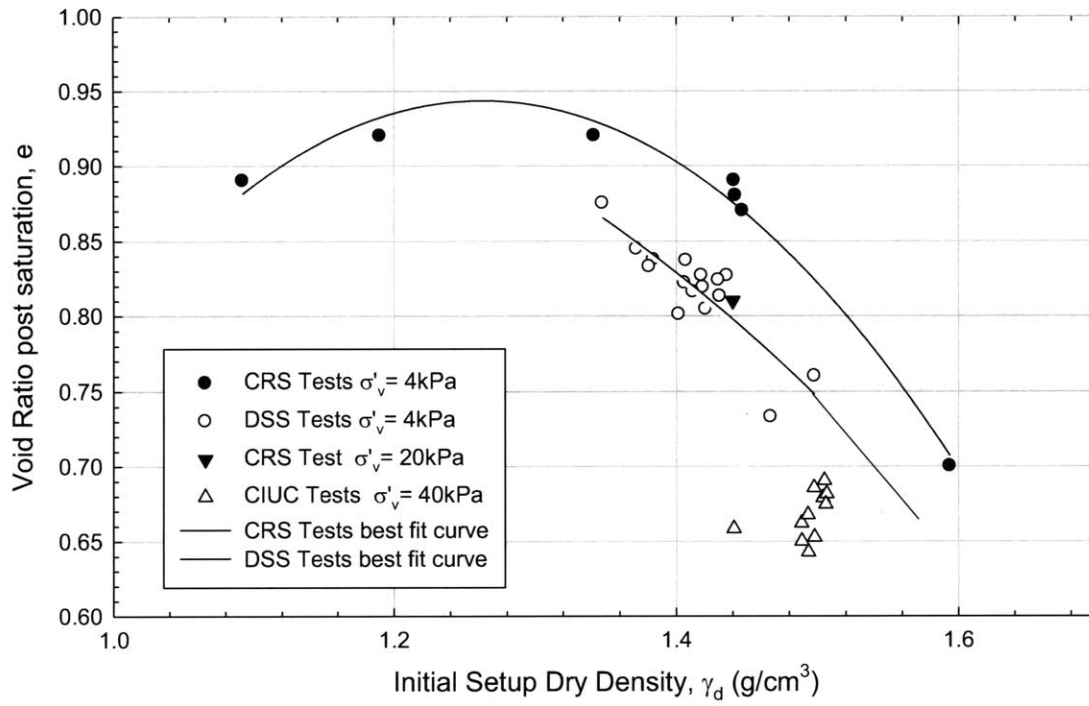


Figure 5-29: Post saturation void ratio versus initial setup dry density for CRS, DSS, and CIUC triaxial tests

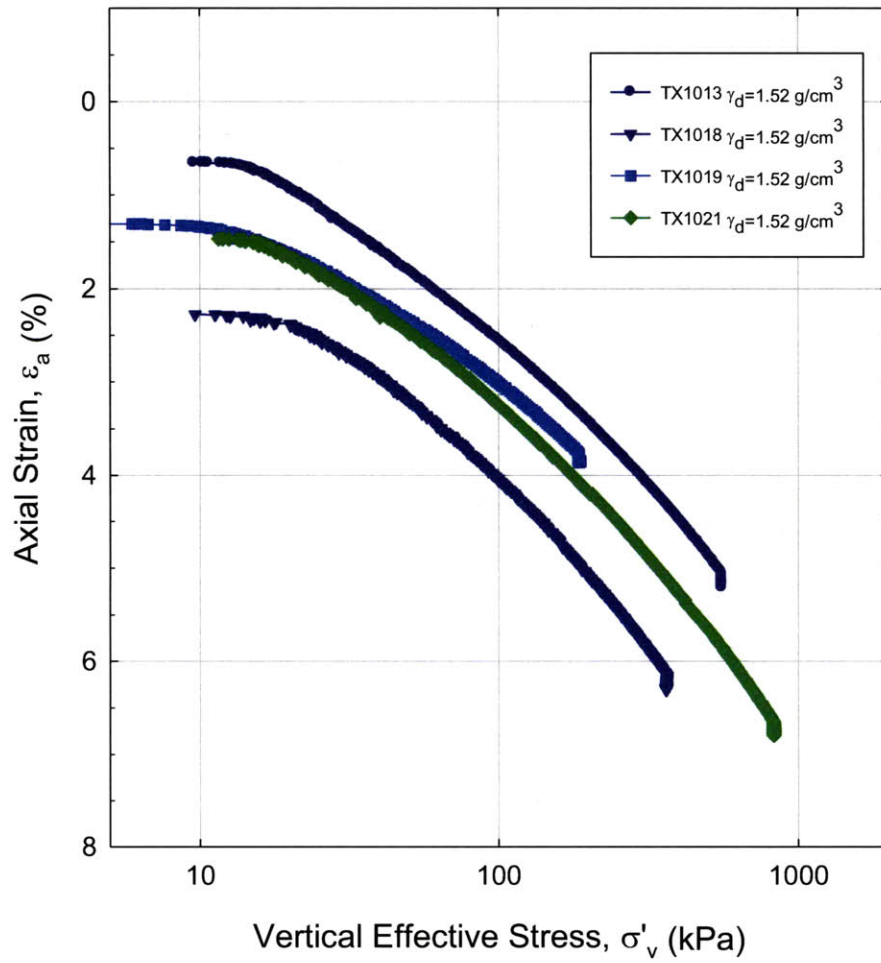


Figure 5-30: Compression behavior in  $\epsilon_a$ - $\log\sigma'_v$  space from  $CK_0UC$  tests

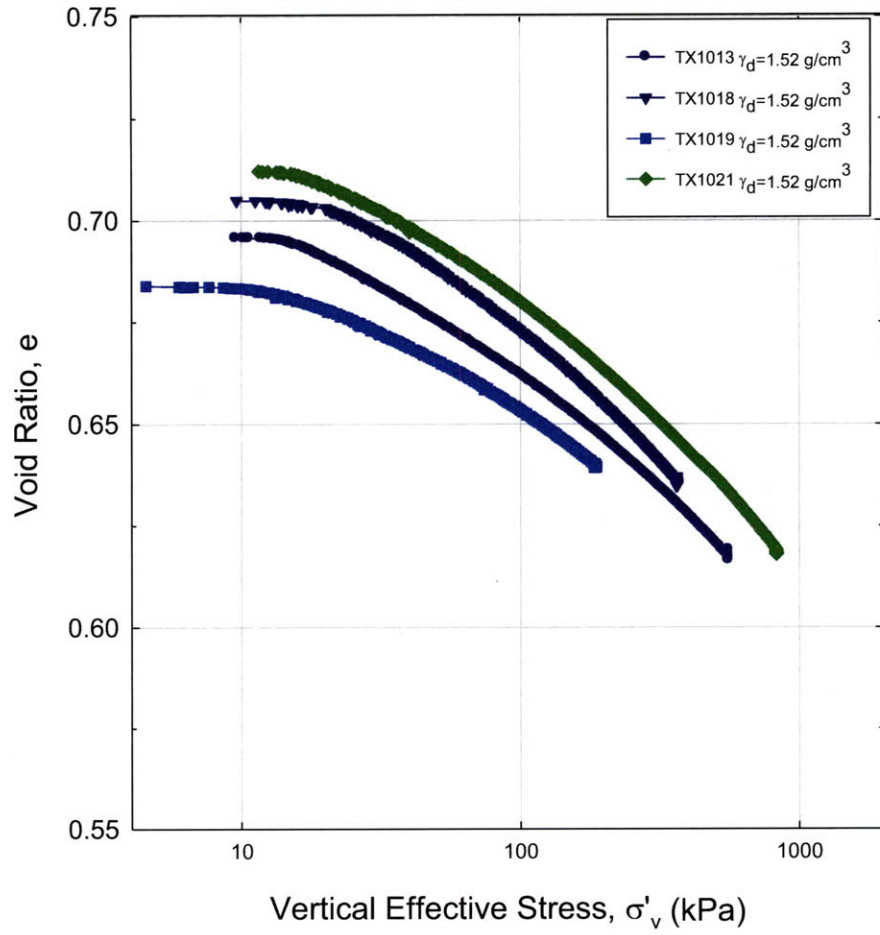


Figure 5-31: Compression behavior in  $e$ - $\log \sigma'_v$  space from  $CK_0$ UC tests

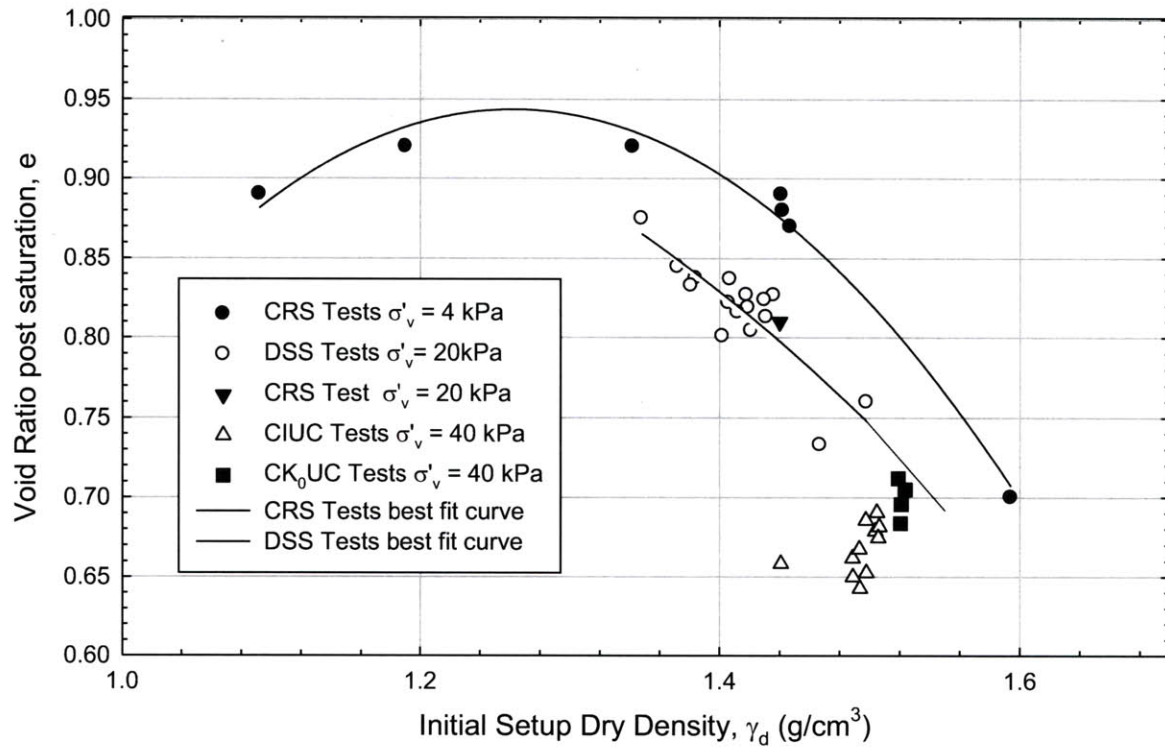


Figure 5-32: Post saturation void ratio versus initial setup dry density for CRS, DSS, CIUC, CK<sub>0</sub>UC tests

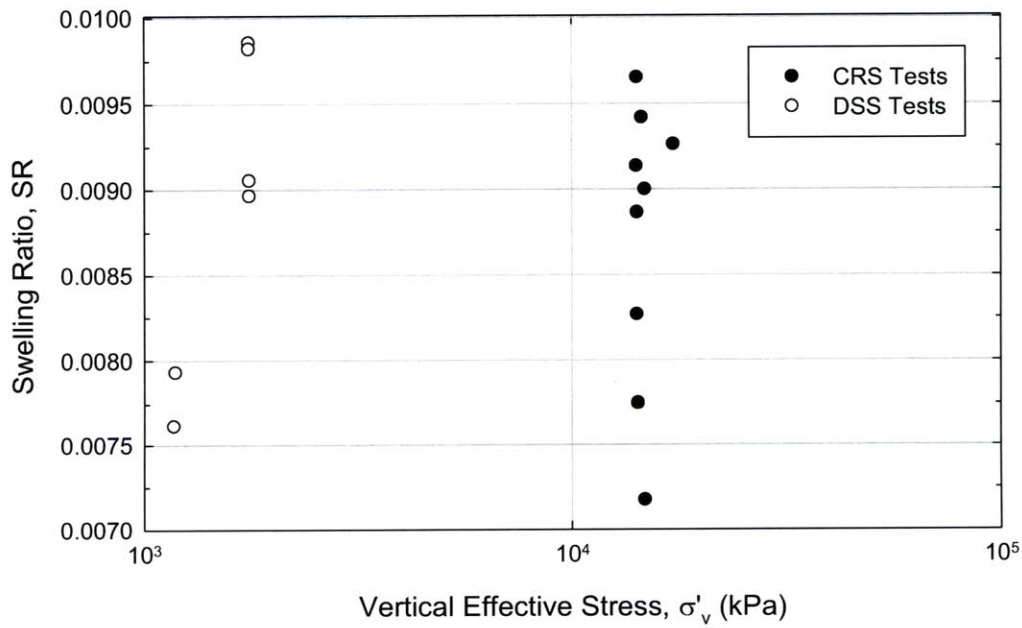
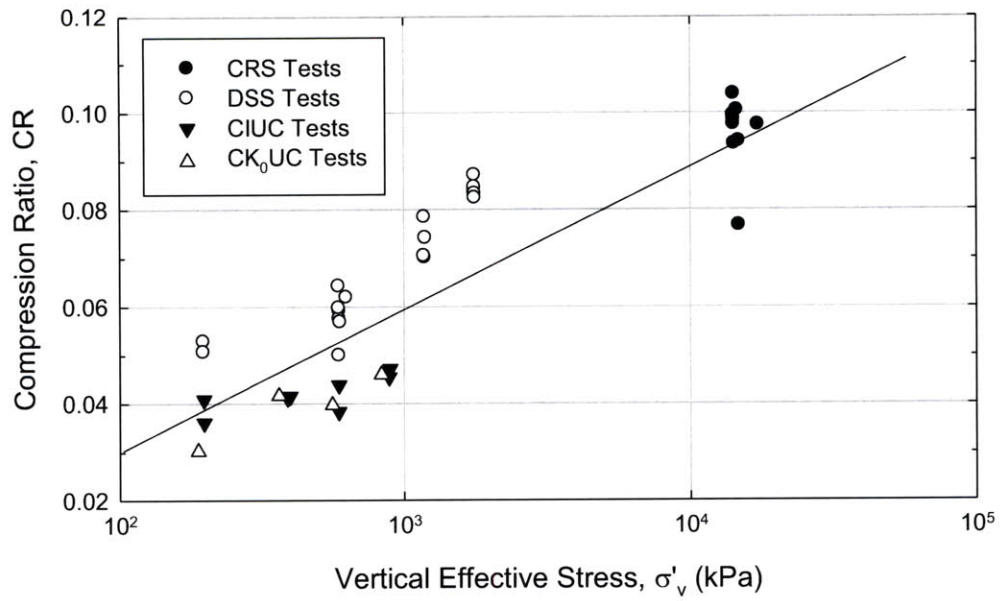


Figure 5-33: Compression and swelling ratios versus stress level from all consolidation tests

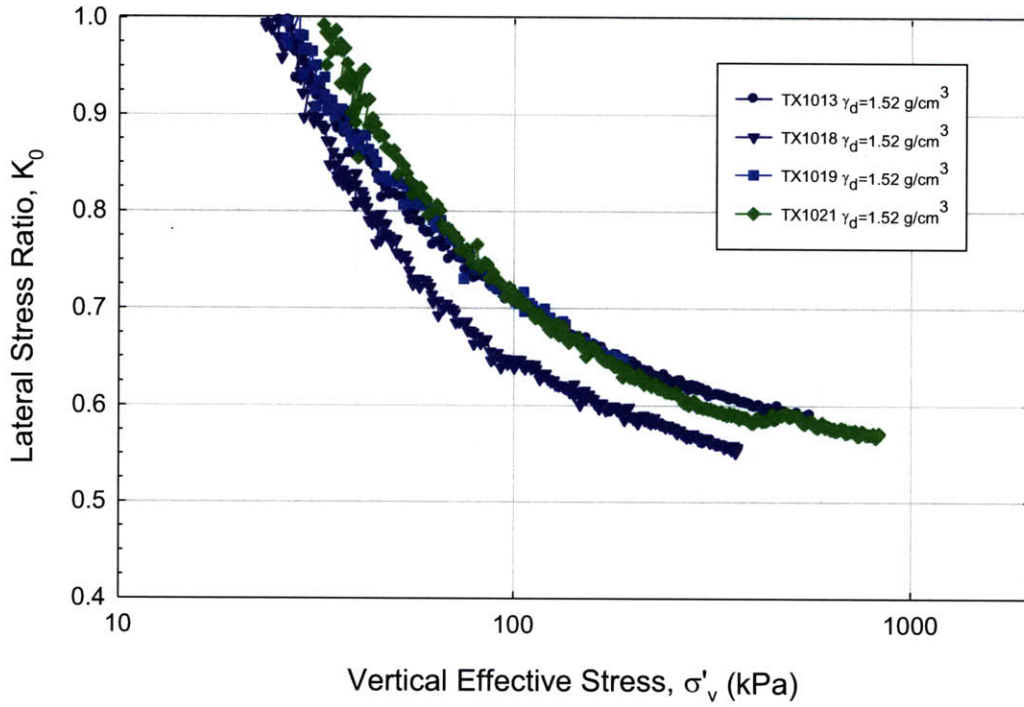


Figure 5-34: Lateral stress ratio versus stress level from CK<sub>0</sub>UC tests

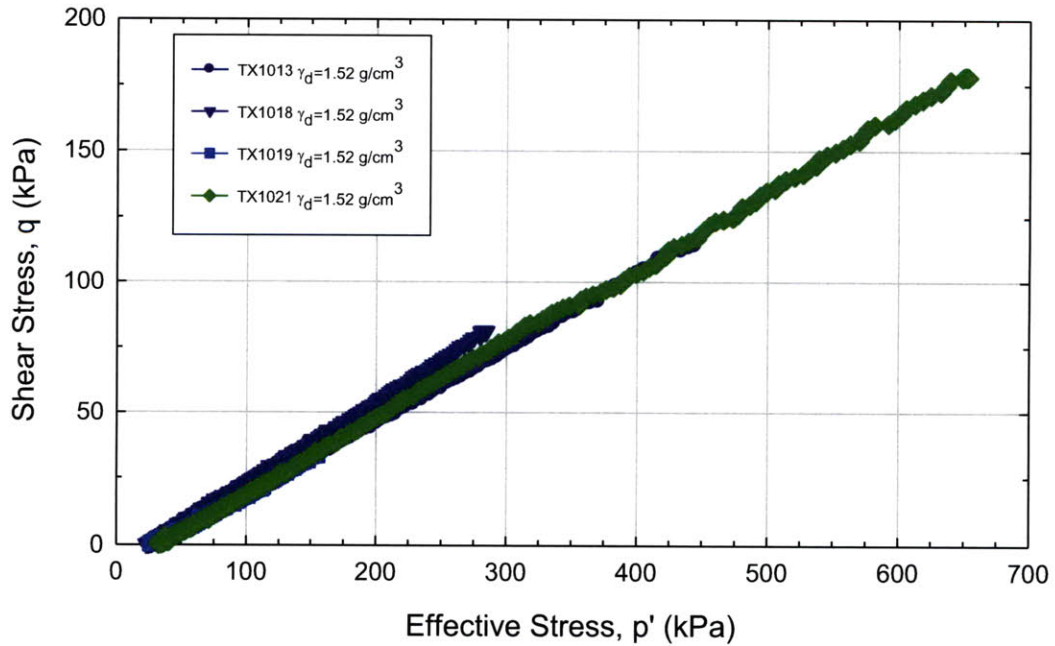


Figure 5-35: Effective Stress path during consolidation from CK<sub>0</sub>UC tests

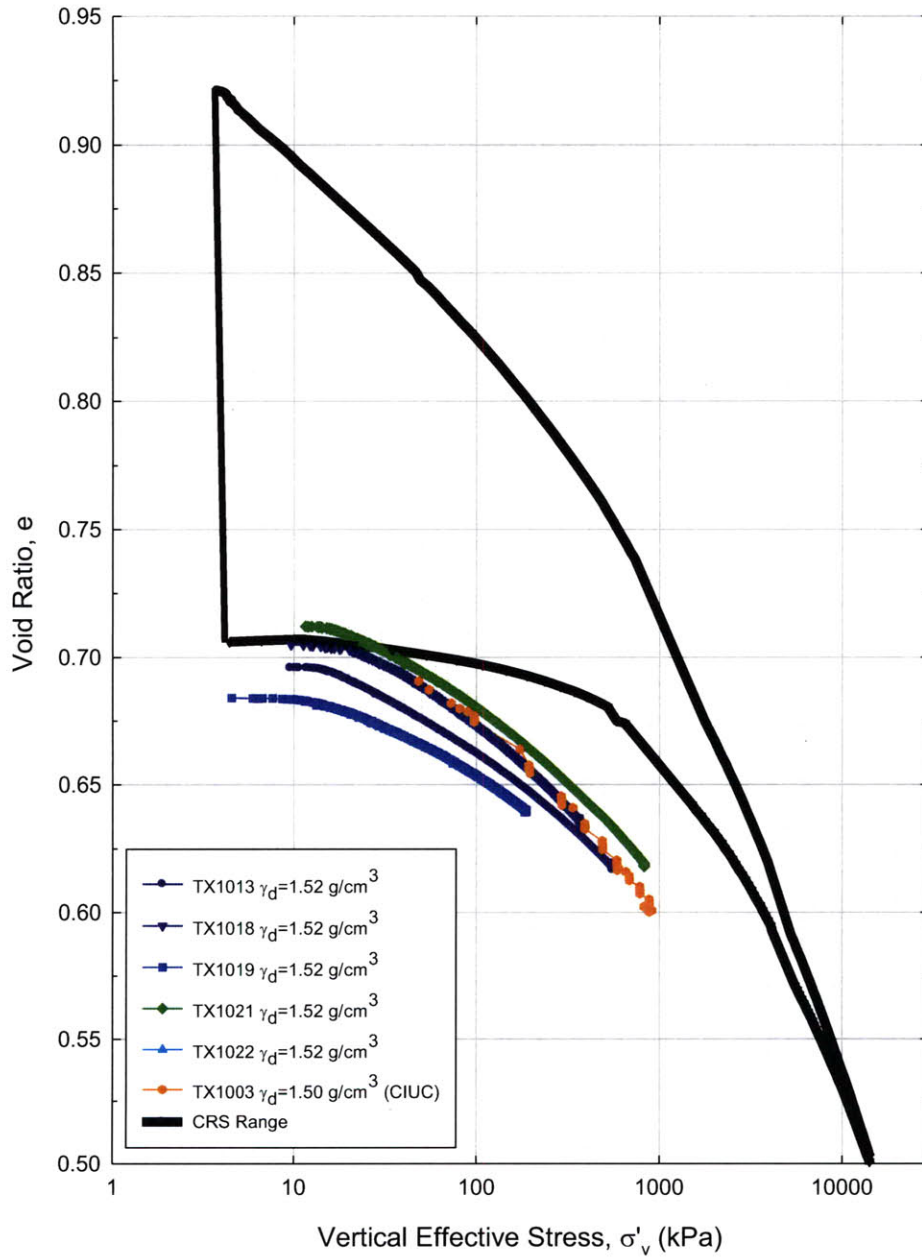


Figure 5-36: Compression behavior in  $e$ - $\log \sigma'_v$  space from CK<sub>0</sub>UC tests compared with the CRS range and a CIUC test

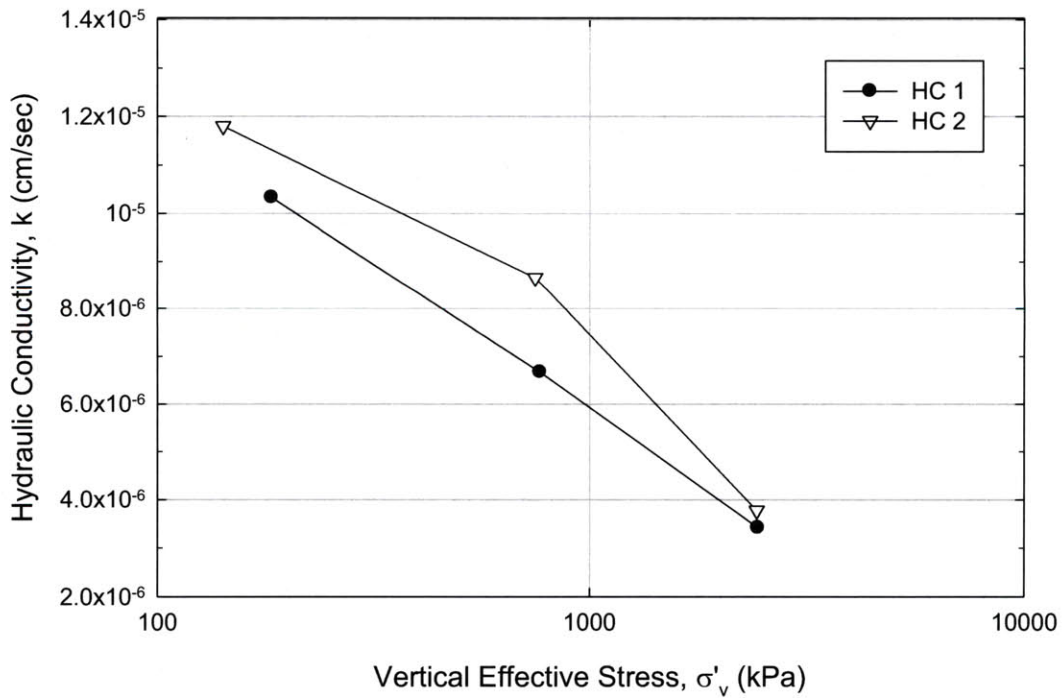
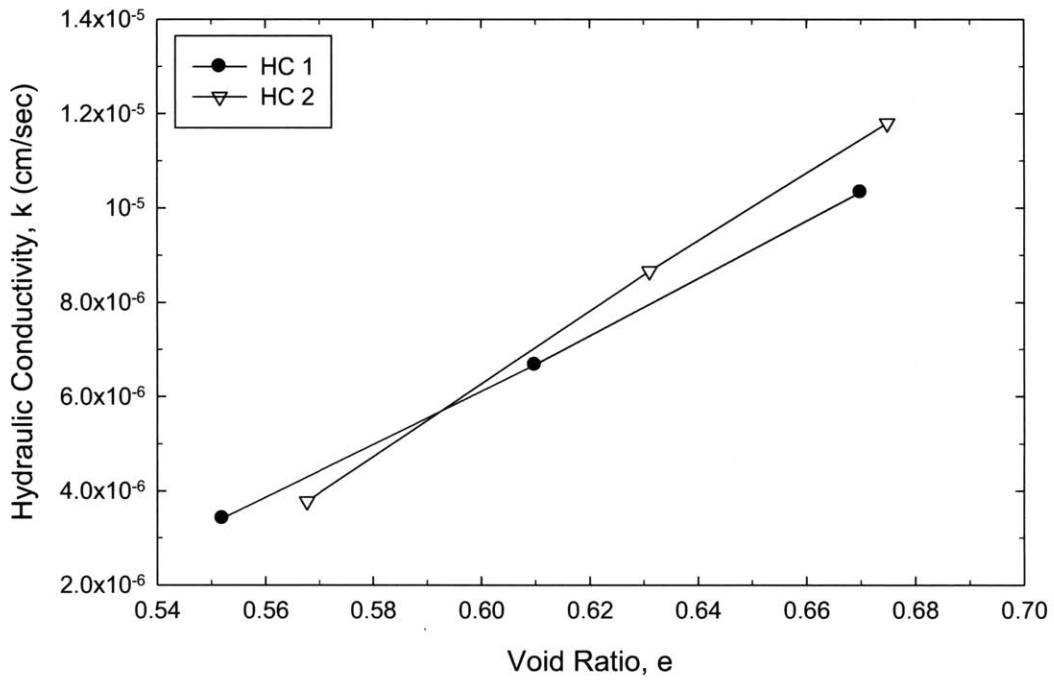


Figure 5-37: Hydraulic conductivity versus void ratio and hydraulic conductivity versus vertical effective stress for Skibbereen Silt



# **6 DIRECT SIMPLE SHEAR AND UNDRAINED TRIAXIAL COMPRESSION BEHAVIOR**

## **6.1 INTRODUCTION**

An experimental testing program was conducted on Skibbereen Silt to investigate its shear properties and behavior. The program was broken down into two different sections. The first section consisted of  $K_0$ -consolidated direct simple shear ( $CK_0$ DSS) tests on both normally consolidated and overconsolidated specimens. The DSS testing program was followed by an extensive undrained triaxial testing program using both isotropic and  $K_0$  consolidation techniques. As denoted in Chapter 4 and 5, the isotropically consolidated undrained compression (CIUC) tests are referred to as Series A tests and the  $K_0$ -consolidated undrained compression ( $CK_0$ UC) tests are referred to as Series B tests.

Section 6.2 presents the shear behavior from the  $CK_0$ DSS tests. The normally consolidated results are first presented and analyzed. This review is followed by an investigation into the effects of the overconsolidation ratio (OCR) on the shear properties. The section summarizes the shear stress-strain and effective stress behavior, and provides values for the SHANSEP parameters in direct simple shear. The effects of cyclic shearing are then presented in the final part of this section.

The results from CIUC tests are presented in Section 6.3. A total of 17 specimens were isotropically consolidated. Of these, only 11 tests will be presented due to experimental problems. The section will present the stress-strain and effective stress behavior. Other parameters such as the modulus, friction angle,  $A$  parameter, and excess pore pressure are also reviewed. The last part of this section analyzes the undrained shear strength, friction angle, and axial strain at failure against vertical consolidation stress.

Section 6.4 summarizes the results for the normally consolidated  $CK_0$ UC tests. Four tests are presented across a range in vertical consolidation effective stresses from 180 to 880 kPa. Similar to the CIUC tests, the stress-strain and effective stress behavior are analyzed together

with other testing parameters. The undrained shear strength, friction angle, and axial strain at failure are reviewed against vertical consolidation stress in the final part of this section.

The behavior from CIUC and  $CK_0UC$  are compared and analyzed in the final section. The variation in stress-strain-strength properties are presented in detail. The final part of this section will include the DSS normally consolidated results. The shear strengths, friction angles, and axial strains at failure will be presented together for the various test types.

## 6.2 DIRECT SIMPLE SHEAR

### 6.2.1 Introduction

This section presents results from DSS tests in which normally consolidated (NC) and overconsolidated (OC) specimens were sheared at a constant strain rate of about 5%/hour after  $K_0$ -consolidation to vertical consolidation effective stresses,  $\sigma'_{vc} = 200$  to 1800 kPa. In total 19 tests are analyzed, 10 of which are attributed to NC tests. As mentioned in Section 5.3.3, all NC specimens, except two, were prepared to an initial dry density of 1.45 g/cm<sup>3</sup>. The two other specimens were prepared to an initial dry density of 1.5 g/cm<sup>3</sup> to estimate the effects of a different starting density on the shear properties. The next section will present the NC results and behavior. Following this section, six tests on overconsolidated specimens will be presented to evaluate the effect of stress history on undrained stress level effects. Two of the tests were performed at nominal OCR = 2, two more at OCR = 3, and finally, a further two at OCR = 4. The final phase of the DSS testing program involved cyclically shearing three specimens. The tests were prepared and consolidated in the same manner as the NC specimens. However, the cyclic specimens were sheared three times with vertical consolidation back to the original value between each phase of shearing. A full description of the process together with the results and behavior are presented in Section 6.2.4.

Table 6-1, 6-2, and 6-3 show for each specimen, the test number, the index testing information, the preshear consolidation conditions, the stress-strain-strength parameters at peak shear stress and at the final point, and the normalized undrained modulus values at various stages of shear strain and strength. The tables also include friction angle ( $\phi'$ ) values at the peak and end of test conditions. All DSS tests were terminated a shear strain ( $\gamma$ ) of 30%. Table 6-1 presents the information for the NC tests at the initial dry density of 1.45g/cm<sup>3</sup>. This information is followed

by Table 6-2 which provides the testing results for specimens at an initial dry density of 1.5 g/cm<sup>3</sup> and for specimens that were cyclically sheared. Table 6-3 shows all the overconsolidated testing properties.

## 6.2.2 Normally Consolidated (NC) Behavior

### 6.2.2.1 Shear Stress-Strain Behavior

Figure 6-1 shows the shear stress-shear strain behavior ( $\tau_h$  versus  $\gamma$ ) for the NC CK<sub>0</sub>UC tests with an initial undercompacted dry density of 1.45 g/cm<sup>3</sup>. It can be seen that there is excellent agreement and repeatability between tests at the same stress level. The results show that the peak undrained shear strength ( $s_u$ ) is mobilized at low strains with all specimens reaching failure at less than 3.71% shear strain. The peak shear strength is followed by strain softening. The magnitude of the softening increases with an increase in vertical consolidation effective stress. The specimens consolidated to 200 kPa exhibit almost steady state shear strength at high strains while the specimens that were consolidated to higher stresses show a much greater reduction in shear strength with an increase in strain. The figure shows that the undrained shear strength ( $s_u$ ) increases significantly with an increase in vertical consolidation stress. This trend is seen more clearly in Figure 6-2 where the normalized shear stress-strain behavior ( $\tau_h/\sigma'_{vc}$  versus  $\gamma$ ) is presented. The figure shows that the preshear consolidation stress level has a significant impact on the normalized strength. The peak undrained strength ratio (USR =  $s_u/\sigma'_{vc}$ ) increases with increasing consolidation effective stress. The undrained strength ratio increases from 0.130 at a vertical consolidation effective stress ( $\sigma'_{vc}$ ) of 200 kPa to 0.182 at  $\sigma'_{vc} \approx 1800$  kPa. The increase in the undrained strength ratio with an increase in vertical consolidation effective stress can be clearly seen in Figure 6-3. The figure shows good agreement between tests at the same stress level. It can be seen that the USR increases with an increase in vertical consolidation stress. However, the figure indicates that the magnitude of this increase will slow with greater vertical effective stresses.

Figure 6-2 also shows that the behavior becomes more ductile with an increase in stress level. Larger strains are required to mobilize the peak shear strength with increasing vertical consolidation stress. Figure 6-4 shows the strain at failure against vertical consolidation effective

stress. It can be seen that there is a linear trend between the two. The strain at failure increases from about 0.98% at low stresses ( $\sigma'_{vc} = 200$  kPa) to 3.67% at high stresses ( $\sigma'_{vc} = 1800$  kPa).

The stress-strain behavior shows that large shear strains are required to get to the critical state value. In the case of these tests, the shear strain was terminated at 30%. As shown in Figure 6-2, the shear stress is still reducing at this strain level and the stress-strain curves have not converged.

#### 6.2.2.2 Effective Stress Behavior

Figure 6-5 shows the effective stress paths using shear stress,  $\tau_h$ , versus vertical effective stress,  $\sigma'_v$ , space for the normally consolidated DSS tests. The results show excellent repeatability between tests at the same vertical consolidation effective stress. All specimens show contractive behavior with no increase in shear strength after the peak shear strength is mobilized.

Figure 6-6 shows the corresponding normalized effective stress path ( $\tau_h/\sigma'_{vc}$  versus  $\sigma'_v/\sigma'_{vc}$ ). The increase in the undrained strength ratio with vertical consolidation effective stress is more obvious in the close up view of this space as shown in Figure 6-7. It can be seen that all tests start at the same point, they deviate during loading with higher strength ratios for specimens with higher consolidation stresses, and then the curves begin to converge at the end of the tests.

Table 6-1 presents the corresponding  $\arctan \tau_h/\sigma'_v$  ( $\psi$ ) angles at peak strength and the end of shear strain (30%). The friction angles versus vertical consolidation effective stress are presented in Figure 6-8. The figure shows for both peak shear stress and end of shear strain conditions, the friction angle increases with an increase in vertical consolidation effective stress. The friction angle at peak shear strength ( $\phi'_p$ ) increases from  $\phi'_p = 13^\circ$  at  $\sigma'_{vc} = 200$  kPa to  $\phi'_p = 20^\circ$  at  $\sigma'_{vc} = 1800$  kPa. The friction angle increase is directly related to the increase in the peak shear strength as the stress level increases. A similar assumption can be made for the friction angle at the end of shear strain. The stress-strain curves (presented in Figure 6-2) do not converge and therefore, the friction angles are greater with an increase in vertical consolidation effective stress. Friction angles increase from  $\phi' = 23^\circ$  at low stresses to  $\phi' = 36^\circ$  at high stresses. It should

be noted that the friction angles obtained from the DSS apparatus are not as reliable as other devices such as the triaxial device. The values presented here are probably approximate estimations of the materials friction angle with stress.

### 6.2.2.3 Stiffness

Figure 6-9 shows the undrained secant Young's modulus normalized to the vertical consolidation stress ( $E_u/\sigma'_{vc}$ ) versus axial strain in a log-log scale for the NC specimens. The figure shows good agreement and repeatability between tests. The behavior is non linear with well rounded curves displaying no well defined yielding point. The decrease in stiffness with an increase in shear strain is relatively slow. There appears to be little vertical consolidation stress dependence. However, the two specimens consolidated to a vertical effective stress of 1800 kPa (tests DSS795 and DSS796) display lower starting normalized modulus values. Table 6-1 best represents this difference. The normalized modulus for the high pressure tests at 0.02% shear strain are 104 and 114 while other tests have normalized modulus values greater than 200 for the same shear strain.

The normalized undrained modulus versus stress level at shear strains,  $\gamma$ , of 0.02, 0.1, and 1% are presented in Figure 6-10. It can be seen that there is very consistent behavior at a shear strain of 1% with normalized modulus values of approximately 42. However, at shear strains of 0.02 and 0.1%, there is a trend that normalized undrained modulus decreases with increasing vertical consolidation effective stress.

### 6.2.2.4 Specimens with different initial densities

As indicated in the introduction, most specimens were prepared to an initial dry density of 1.45 g/cm<sup>3</sup> with a 7.5% moisture content. During the subsequent triaxial testing program, it was found that an initial dry density of 1.5 g/cm<sup>3</sup> with a 3% water content worked better for undercompaction (the specimens appeared to be much more uniform using these values). Two DSS specimens were prepared using the triaxial initial conditions to investigate if the change would have an impact on the results and behavior.

Figure 6-11 shows the normalized shear stress-strain behavior for the two tests plotted with two of the original DSS tests. All specimens were consolidated to a vertical effective stress of approximately 600 kPa. The figure shows good repeatability between the tests. The stress strain behavior is identical before and after the peak shear strength is mobilized. However, the specimens with a higher initial density produced an undrained strength ratio slightly greater. The undrained strength ratio is 0.153 at the peak for the standard DSS setup while the modified one produces an undrained strength ratio of about 0.163 at the peak. The shear strain at failure is similar for all tests, averaging at approximately 1.74%.

The normalized effective stress path is shown in Figure 6-12. Once again, the figure shows excellent repeatability with all tests displaying identical behavior. Figure 6-15 shows the close up view of this space. It can be seen that the behavior is similar. However, the greater undrained strength ratio for specimens with a higher initial density is evident. The corresponding effective stress space (not normalized) is presented in Figure 6-16. Like figure 6-12, there is no difference in behavior in this figure.

The undrained strength ratio and axial strain at failure are plotted against vertical consolidation effective stress in Figure 6-13 and 6-14. The results confirm that a higher initial setup density will produce higher strengths but a change in initial density will have no effects on the strain at failure.

Finally, to complete the analysis between the different preparation conditions, Figure 6-17 presents the undrained secant Young's modulus normalized to the vertical consolidation stress versus axial strain. The figure shows good repeatability in behavior and there is no evidence that the different initial conditions have an effect on the modulus properties.

In summary, the density and initial water content for undercompaction have an impact on the properties of the material. The stress-strain, effective stress path, and modulus behavior are almost identical in this study. However, there is a trend that a higher initial setup density will produce a greater undrained strength ratio.

## 6.2.3 Overconsolidated (OC) Behavior

### 6.2.3.1 Shear Stress-Strain Behavior

Figure 6-18 shows the normalized stress-strain behavior for the CK<sub>0</sub>DSS tests performed on specimens with an OCR = 1, 2, 3, and 4. In this figure, the shear stress is normalized with the vertical consolidation effective stress,  $\sigma'_{vc}$ . Similar to the normally consolidated specimens, the curves are characterized by a peak followed by post peak softening. The strain softening increases with an increase in OCR. The softening is almost linear after the peak strength is mobilized and the curves do not converge at high strains. The results show that as OCR increases, the peak value of strength normalized to the vertical consolidation stress increases. The undrained strength ratio ranges from 0.18 at OCR = 1 to 0.51 at OCR = 4. In contrast, Figure 6-19 shows the normalized shear stress-strain behavior with the shear stress normalized to  $\sigma'_{vm}$ , the maximum vertical consolidation stress. The results show that as OCR increases, the peak value of strength normalized to the maximum vertical stress decreases. However, the rate of the post peak strain softening is very similar.

Figure 6-20 shows the undrained strength normalized by both the vertical consolidation stress ( $\sigma'_{vc}$ ) and the maximum vertical consolidation stress ( $\sigma'_{vm}$ ) versus OCR. The consistent trend of decreasing  $s_u/\sigma'_{vm}$  with increasing OCR is clearly evident for the values normalized by the maximum consolidation stress. The undrained strength ratio values decrease from  $s_u/\sigma'_{vm} = 0.18$  at an OCR = 1 to  $s_u/\sigma'_{vm} = 0.125$  at an OCR = 4 with a linear trend over the OCR range. The trend of the peak shear strength normalized to the vertical consolidation stress increasing with an increase in OCR will be discussed later in this section when the SHANSEP parameters are presented.

The results show that the strain at peak shear stress ( $\epsilon_f$ ) is unaffected by OCR. The stress-strain curves before the peak stress is mobilized show good agreement and repeatability. All specimens fail at approximately 3% shear strain. The OCR specimens normalized by the maximum consolidation stress show excellent repeatability after the peak stress is obtained. The curves begin to converge at shear strains greater than 25%.

### 6.2.3.2 Effective Stress Behavior

Figure 6-21 shows the effective stress paths normalized to the maximum vertical consolidation stress ( $\sigma'_{vm}$ ) for OCR = 1, 2, 3 and 4 CK<sub>0</sub>DSS tests. The figure shows a large deviation in behavior between NC and OC specimens. The NC specimens show contractive behavior throughout the loading cycle. However, all OC specimens display dilative behavior during the initial phase of testing. The dilative behavior continues until the peak shear stress is mobilized and then the behavior becomes contractive. The dilation is more pronounced in specimens with a higher OCR. The behavior between specimens consolidated to the same vertical stress is excellent with duplicate results at each OCR level. The results show that all stress paths converge at large strains.

The dilative behavior before peak stress mobilization is more apparent in Figure 6-22. The effective stress paths are presented normalized by the vertical consolidation stress and the maximum vertical consolidation stress. The stress paths normalized by the vertical consolidation stress show significant dilative behavior before the peak stress is mobilized. The OCR = 3 and 4 specimens display dilative behavior that becomes more prominent towards the peak. The post peak strain softening is very uniform and the curves all converge to produce a linear trend with one post peak failure envelope.

Figure 6-23 shows the arctan  $\tau_h/\sigma'_v$ ,  $\psi$ , angles obtained at the peak shear stress and at 30% shear strain versus vertical consolidation effective stress,  $\sigma'_{vc}$ . It can be seen that the overconsolidated specimens produce slightly higher arctan  $\tau_h/\sigma'_v$  angles than the normally consolidated specimens. The arctan  $\tau_h/\sigma'_v$  at peak shear stress ( $\psi'_p$ ) ranges between 20 and 25° and the arctan  $\tau_h/\sigma'_v$  angle at 30% shear strain ranges from 31 to 37°. At a 30% shear strain the average  $\psi$  is 35°, indicating that there could have been a problem with the test that produced the 31° value.

### 6.2.3.3 Stiffness

Figure 6-24 shows the undrained secant Young's modulus normalized to the vertical consolidation stress,  $\sigma'_{vc}$ , versus axial strain in log-log space for OCR = 1, 2, 3 and 4 specimens.



It can be seen that there is no correlation between OCR and the normalized modulus. The curves show excellent agreement and repeatability. One test at an OCR = 4 has a lower starting modulus than the others. However, this deviation is most likely due to an experimental issue rather than a behavioral one. It can be concluded that OC specimens will produce modulus values similar to NC specimens.

#### 6.2.3.4 SHANSEP Equation for DSS

Ladd and Foot (1974) developed the SHANSEP (Stress History and Normalized Soil Engineering Properties) design method. The technique takes the assumption that the in situ stress history can be simulated in the laboratory and it will provide accurate predictions of in situ soil behavior at various OCRs. The technique can be represented by the equation:

$$\frac{S_u}{\sigma'_{vc}} = S \cdot (OCR)^m \quad (6.1)$$

Where S is the undrained strength ratio for the normally consolidated material, and m is the slope of the regression line.

Figure 6-25 shows the undrained strength ratio ( $S_u/\sigma'_{vc}$ ) versus OCR for the CK<sub>0</sub>DSS tests performed in the study. The figure shows that the SHANSEP parameters S and m are equal to 0.180 and 0.761 respectively. The regression through the data is very good;  $r^2$  is equal to 0.997, indicating good conformity to the technique.

### 6.2.4 Cyclic Behavior

#### 6.2.4.1 Introduction

As mentioned in the opening to this section, three tests were performed to evaluate changes in shear strength and density as a result of cyclic shearing. Figure 6-26 and 6-27 show the stress-strain and effective stress path behavior of a typical cyclic DSS test. The figures are presented to describe the various steps during the cyclic shearing process.

All specimens for cyclic testing were consolidated to a vertical effective stress ( $\sigma'_{vc}$ ) of 600 kPa. The undrained shearing process was started identically to the conventional DSS tests. However, once the peak shear stress was mobilized, the shearing process was stopped and the shear strain was manually returned to the starting position ( $\gamma = 0\%$ ). This phase of the test is denoted in the figures as “Shear Phase 1”. The specimens were then consolidated back to the original vertical effective stress. The original vertical effective stress was maintained for one hour before the next phase of shearing. “Shear Phase 2” is a repeat of phase 1. The undrained shearing process is started again and it continues until a shear strain of at least 5%. Again, the shearing process is stopped at this point, the shear strain is manually returned to the starting value, and the specimen is consolidated back to the original vertical consolidation stress. The final phase of the test (Shear Phase 3) involves shearing the specimen in the conventional manner to a limiting shear strain of 30% and hence, completing the test.

The negative shear stress shown in the figures is a result of the pulling action on the load cell when the specimen is being returned to 0% shear strain. It takes a small percentage of positive strain to return to positive shear stress conditions. Therefore, the vertical stress ( $\sigma'_v$ ) is less than the vertical consolidation stress ( $\sigma'_{vc}$ ) at zero shear stress in phases 2 and 3.

#### 6.2.4.2 Shear Stress-Strain Behavior

Figure 6-28 shows the shear stress-strain behavior of the cyclic  $CK_0$ DSS tests together with a typical NC  $CK_0$ DSS test. The manual change of shear strain after each shear phase and the consolidation back to the vertical effective stress has been removed for greater clarity. The results show that during the first shearing phase (marked in blue) the behavior is identical to the standard NC specimen. However, after the first phase of shearing the behavior changes dramatically. The second shear phase (marked in green) shows that the peak undrained shear strength ( $S_u$ ) increases significantly after shearing and consolidation back to the original vertical effective stresses. The material also becomes much more ductile. All specimens were sheared past 5% strain during the second phase but it can be seen that the peak strength was only mobilized in one of the tests. The deviation in behavior is even more pronounced when the third and first phase of shearing are compared. The peak shear strength during the third phase is

almost double the peak shear strength during phase 1. The ductility also increases from that observed during shear phase one and two. The strain at failure ( $\epsilon_f$ ) increases from about 1.5% during the first phase to 10% during the third phase, identifying a significant change in the materials properties.

Figure 6-29 shows the corresponding normalized shear stress-strain behavior. Again, the figure shows that cyclic shearing has a pronounced effect on the normalized strength and shape of the stress-strain curves. The peak undrained strength ratio ( $S_u/\sigma'_{vc}$ ) increases from 0.158 at shear phase 1 to 0.191 at shear phase 2 to about 0.28 at shear phase 3. Possible explanations for this increase will be discussed in detail later in Section 6.2.4.4. However, the material becomes denser during each shearing and consolidation cycle, contributing to the increase in strength. The post peak strain softening in shear phase 3 is more pronounced than the typical DSS test. The cyclic tests show good agreement during strain softening; however, it can be seen that cyclic stress strain curves do not converge with the standard DSS test at high shear strains.

#### 6.2.4.3 Effective Stress Behavior

Figure 6-30 shows the effective stress paths for the cyclic  $CK_0$ DSS tests. Again, a typical DSS test and only the shearing phases of the cyclic tests have been included for clarity. The corresponding normalized effective stress paths are shown in Figure 6-31. There is pronounced difference in behavior with increasing shear phases. Shear phase 1 shows contractive behavior, the vertical stress decreases steadily during the shearing process. Shear phase 2 also shows contractive behavior; however, it is not as pronounced as shear phase 1. The largest deviation in behavior occurs during shear phase 3. The stress path first follows a contractive alignment very similar to shear phase 2 but then it develops an inflection point and the behavior becomes dilative with an increase in vertical stress during shearing. The dilative behavior continues until a peak shear strength is mobilized. At the peak a very sharp yield point is evident and then the behavior becomes contractive. It can be seen that there is good agreement between cyclic tests during this final contractive phase. The behavior continues almost linearly and the stress paths meet the standard DSS test stress path near the end of testing.

#### 6.2.4.4 Cyclic Behavior

The previous two sections show that the behavior of the material deviates significantly with an increasing number of shear cycles. The material exhibits an increase in peak shear strength and ductility with an increase in shear phases. One possible explanation for the increase in strength is the increase in density with each phase. Consolidation takes place during each cycle, reducing the void ratio and increasing the density. Figure 6-32 shows the  $e$ - $\log \sigma'_v$  behavior for two of the specimens. It can be seen that the void ratio decreases with each phase of shearing. At shear phase one the void ratio is approximately 0.69 and lies on the virgin consolidation line, it reduces to about 0.65 in phase 2, before finally reaching a void ratio of about 0.62 for phase 3. The figure shows that the steps in void ratio are about equal with each shearing phase with a drop of 0.04 between phase 1 and 2 and a further reduction of 0.03 between phase 2 and 3. The DSS compression curve demonstrates that a much greater stress would be required to achieve the same void ratios as in shear phase 2 and 3 using consolidation alone. The stress required to achieve these void ratios can be referred to as the “effective” consolidation stress and it was found to be equal to 1130 kPa for shear phase 2 and 1771 kPa for shear phase 3.

Figure 6-33 shows the investigation between the undrained strength ratio and total density at the end of consolidation for all NC and cyclic  $CK_0$ DSS specimens. The density and undrained strength ratio at each phase of shearing in the cyclic tests are included in the figure. It can be seen that there is a gradual increase in shear strength with an increase in density for NC specimens. However, the cyclic specimens show much greater strengths at similar densities. The results show that a higher density will increase the undrained strength.

Figure 6-34 presents the shear strain at failure versus total density at the end of consolidation for the same test group. It is normal to expect an increase in brittle behavior with an increase in density. However, it can be seen in the figure that strain at failure increases with an increase in total density for all NC  $CK_0$ DSS specimens. Like Figure 6-33, the cyclic specimens do not fit the standard NC trend. The strain at failure increases significantly with increasing shear phases.

Figure 6-35 presents the undrained strength ratio versus vertical consolidation stress. The figure normalizes shear phases 2 and 3 by the vertical consolidation stress and the “effective” consolidation stress (as found in Figure 6-32). Normalizing by the “effective” consolidation stress essentially removes the effects of densification and allows an investigation into the change in soil fabric from the shearing cycles. It can be seen, if the results are adjusted for density, the strength is lower than the first shear phase. Therefore, the first shear caused densification which increases strength but the shear effects weaken the strength. The combined effect gives very low but nearly independent normalized strength.

## **6.3 ISOTROPICALLY CONSOLIDATED UNDRAINED TRIAXIAL COMPRESSION (CIUC) TESTS (SERIES A)**

### **6.3.1 Introduction**

This section presents results and behavior from isotropically consolidated undrained triaxial compression (CIUC) tests. As mentioned in the introduction to this chapter, 17 CIUC tests were performed but due to experimental loss, only 11 will be presented in this section. This group of tests is known as the Series A testing program. Series B will follow in the next section when the  $K_0$  consolidated triaxial tests are presented.

The CIUC testing program involved testing NC specimens from vertical consolidation effective stresses ranging from 100 to 900 kPa. The specimens were all manually isotropically consolidated and the undrained shearing was conducted in a load frame at a constant rate of strain of 10%/hour. All specimens were prepared to an initial setup dry density of  $1.5 \text{ g/cm}^3$  for the purposes of this investigation.

Table 6-4 lists the test number and type, the preshear conditions, and the stress-strain-strength parameters for each specimen. Note that the stress-strain-strength properties are presented using various failure criteria. Section 3.5.2 presented various failure criteria from the work of Brandon *et al.* (2006). The CIUC results presented in this table were analyzed on their criteria. After assessment, it was decided that the best five failure criteria are:- 1) At peak shear stress, 2) at 12% limiting strain, 3) at the peak principle stress ratio, 4) at the peak excess pore

pressure, and 5) at the inflection point where the material behavior changes from contractive to dilative behavior. The exact locations of these failure points will be shown in detail in Section 6.3.3. For some tests, it was not possible to get values for all the failure criteria and hence, there are parts left blank in the table.

### 6.3.2 Shear Stress-Strain Behavior

Figure 6-36 shows the shear-strain behavior ( $q = (\sigma_1 - \sigma_3)/2$  versus  $\epsilon_a$ ) for the CIUC tests. The figure shows that the yield point occurs at small strains (<1%). The results show that the behavior changes depending on the consolidation effective stress. The tests at low stresses ( $\sigma'_{vc} = 100$  kPa) have a peak undrained shear strength. After mobilization of the peak, strain softening occurs which plateaus with an increase in strain. Tests at the low to medium range of stress ( $\sigma'_{vc} = 200 - 400$  kPa) have a well defined yield point which is followed by strain softening. The stress-strain curves then go through a quasi steady state condition before the behavior becomes dilative again, with a further increase in undrained shear strength. In the case of the specimens consolidated to a vertical effective stress of 200 kPa, the dilative behavior at the end of shearing is not significant enough to increase the undrained shear strength back to the peak value. However, in the case of the specimens consolidated to a vertical effective stress of 400 kPa, the dilative behavior at the end provides shear strength values higher than the ones obtained at the yield point. Tests to the mid and high range of stress ( $\sigma'_{vc} = 600-900$  kPa) show no strain softening after the yield point and the shear strength increases with strain due to dilation.

Figures 6-37, 6-38, and 6-39 show the corresponding normalized shear stress-strain behavior ( $q/\sigma'_{vc}$  versus  $\epsilon_a$ ), with axial strain shown on linear (large strain), linear (small strains) and logarithmic scales, respectively. Again, these figures illustrate that the preshear consolidation stress level has a pronounced effect on the behavior. The figures show that there is good agreement and repeatability in behavior until the initial yield point. There is a slight increase in ductility with an increase in stress level (most apparent in Figure 6-37). However, it is the behavior after the initial yield that is affected by consolidation stress level. Contractive, quasi steady state, and ductile behavior are all displayed and they are dependent on the consolidation stress level.

### 6.3.3 Effective Stress Behavior

Figure 6-40 shows the effective stress paths of two tests using the MIT stress space ( $q = (\sigma_1 - \sigma_3)/2$ ) versus  $p' = (\sigma'_1 + \sigma'_3)/2$ ). The figure shows the variation in behavior between tests consolidated to low vertical effective stresses ( $\sigma'_{vc} \approx 200$  kPa) and tests at higher consolidation stresses ( $\sigma'_{vc} \approx 900$  kPa). The behavior changes significantly with stress level. It can be seen at low vertical consolidation effective stresses, contractive behavior occurs over the majority of the test with the mean stress,  $p'$ , decreasing. Near the end of the test, at large axial strains, there is a slight gain in shear strength and an increase in  $p'$ . The figure demonstrates all the failure criteria presented in Table 6-4. For tests at low consolidation effective stresses, there is a well defined peak shear strength. Even with some dilation near the end of testing, it is not sufficient enough to remobilize the shear strength back to the peak level. The inflection point can be seen clearly in the high consolidation effective stress test. The stress path first dilates slightly with an increase in the mean stress, it then goes through a contractive phase before the inflection point is obtained at the change between contractive and dilative behavior. The material then stays in its final dilative phase. The amount of contraction decreases with increasing consolidation effective stress. The typical shear strengths using the limiting strain at 12% criterion are shown for both tests. The figure highlights the problem with this criterion. The shear strength at 12% axial strain can be in a contractive phase in low stress tests while it can be in a dilative phase during high stress tests. This variation in behavior produces a large range in shear strength values.

Figure 6-41 shows the effective stress paths from all CIUC tests in the MIT stress space. The figure shows the variation in behavior over the range of consolidation effective stresses from 100 to 900 kPa. The material gradually becomes less contractive and more dilative with increasing stress level. The corresponding normalized effective stress paths ( $q/\sigma'_{vc}$  versus  $p'/\sigma'_{vc}$ ) are shown in Figure 6-42. In general, it can be seen that all specimens produced a small amount of dilative behavior at the beginning of the test, followed by a contractive phase. The mobilization of the inflection point is dependent on the vertical consolidation effective stress. The inflection point will occur at lower strains in tests with a higher consolidation effective stress. The behavior after the inflection point shows reasonable agreement. Much better agreement would be expected if the triaxial device had a larger strain capacity. The device is

limited to a maximum axial strain of about 15%. It is clear that the critical state value has not been mobilized in some tests using this strain.

The figure shows the difficulty in determining the undrained strength ratio ( $S_u/\sigma'_{vc}$ ) for material of this type. An investigation into this problem will be presented in Section 6.3.5.

Figure 6-43 shows the principle stress ratio ( $q/p'$ ) versus axial strain. The tests at low consolidation effective stresses ( $\sigma'_{vc} = 100$  kPa) have been removed from the figure to increase clarity. There was also some unusual pore pressure behavior in these tests at higher strains. Therefore, the tests were deemed unreliable for the purposes of this figure. It can be seen there is good repeatability during the initial phase of the test and then there is a slight deviation in behavior. There is a well defined yield point in all tests and then the principle stress ratio increases slowly with an increase in strain. All tests, except one, show a peak principle stress ratio followed by very little strain softening. The peak principle stress ratio is also known as the point of maximum stress obliquity and it is considered one of the failure criteria in Table 6-4.

The corresponding friction angles assuming zero cohesion are presented in Figure 6-44. It can be seen that the friction angle is highest at the peak principle stress ratio or maximum obliquity. The results show that the secant friction angle at maximum obliquity ranges from  $\phi' = 34^\circ$  to  $\phi' = 39^\circ$ . However, it can be seen that with an increase in axial strain the curves begin to move towards a constant friction angle of  $\phi = 35^\circ$ . Section 6.3.5 provides a more detailed analysis of the friction angles obtained during CIUC triaxial testing.

Figure 6-45 shows the excess pore pressures ( $u_e = \Delta u - \Delta \sigma_3$ ) generated during shear normalized to the vertical consolidation stress ( $\sigma'_{vc}$ ) for the CIUC triaxial tests. The results illustrate that the normalized excess pore pressure increases continuously throughout shear but then begins to level off with an increase in axial strain. The normalized excess pore pressure reaches a peak value followed by a reduction in excess pore pressure during the final phase of the test. The magnitude of excess pore pressure decreases with increasing vertical consolidation effective stresses. The normalized excess pore pressures range from 0.91 for the tests at  $\sigma'_{vc} = 200$  kPa to 0.62 for the tests consolidated to  $\sigma'_{vc} = 900$  kPa. The reduction in excess pore pressure after the peak is also more pronounced in the tests with higher vertical consolidation effective stresses. The reduction is directly proportional to the amount of dilation experienced in



the specimen. The peak normalized excess pore pressures found in this figure were used as one of the failure criteria in Table 6-4. Essentially, the undrained strength ratios generated by the peak excess pore pressure failure criterion will coincide very close to the point of inflection failure criterion because the behavior is changing from contractive to dilative in both cases.

It is also possible to plot the shear induced pore pressures ( $u_s = \Delta u - \Delta \sigma_{oct}$ , where  $\sigma_{oct} = (\sigma_1 + 2\sigma_3)/3$ ). The method isolates the pore pressure changes due to shear stress alone, removing the effect of the total stress path. Figure 6-46 shows the shear induced pore pressures normalized to the vertical consolidation stress versus axial strain. As with the normalized excess pore pressures, the positive pore pressures generated throughout shearing up to the peak values indicate the contractive behavior. After the peak, the reduction in the normalized shear induced pore pressures is a result of dilation. Similar to the normalized excess pore pressures, the normalized shear induced pore pressures are suppressed as stress level increases. However, the magnitude of the shear induced pore pressures are less than the excess pore pressures. The normalized shear induced pore pressures range from 0.78 at low stresses to 0.37 at high stress, which is a significant reduction to the values stated for the normalized excess pore pressures.

The Skempton parameter  $A (= (\Delta u - \Delta \sigma_3) / (\Delta \sigma_1 - \Delta \sigma_3))$  versus stress level is shown in Figure 6-47. The results show similar observations as before. The pore pressures generated are larger at lower stresses. The peak  $A$  parameter value ( $A_f$ ) decreases with an increase in stress level from about 1.98 at low stresses to about 0.87 at high stresses. It can be also seen that the axial strain at the peak  $A$  parameter decreases with an increase in stress. The axial strain at  $A_f$  is approximately 7% at low stresses to 1.6% at high stresses.

#### 6.3.4 Stiffness

Figure 6-48 shows the undrained secant Young's modulus normalized to the vertical consolidation stress ( $E_u / \sigma'_{vc}$ ) versus axial strain (on a log-log scale) for the CIUC triaxial tests. The results show good agreement and repeatability. In general, the behavior has slightly rounded curves displaying no yield point. Like the DSS results, there appears to be little consolidation stress dependence. Most values start at a normalized modulus of about 300 and then decrease steadily with strain.

Figure 6-49 shows the normalized undrained modulus versus consolidation stress at strain levels of 0.05, 0.1, and 1%. The figure shows that modulus is unaffected by stress level after 1% strain. The modulus values at strains of 0.05 and 0.1 % are very close to each other. The results show a clear trend of decreasing modulus with increasing stress level at small strains.

### **6.3.5 Summary of behavior**

This section provides a summary of the results obtained from the CIUC triaxial testing program. The five failure criteria, discussed earlier in this section, have been analyzed and the findings are presented.

Figure 6-50 shows the normalized undrained shear strength versus stress level for the CIUC tests using the various failure criteria. The results show, in all criteria, that the undrained strength ratio increases with increasing stress level. It can be seen that there is a large deviation in the undrained strength ratio using the peak principle stress ratio and the 12% limiting strain criteria. High normalized shear strengths are found using these criteria for consolidation effective stress levels greater than 600 kPa. The large increase in the undrained strength ratio with an increase in stress level is directly related to the degree of dilation for these criteria. It should be noted that the values obtained using the peak principle stress ratio and the 12% limiting strain criteria are very large when compared with typical clay behavior.

The peak excess pore pressure and the inflection point criteria show less deviation with increasing stress level. As mentioned in Section 6.3.3, the two criteria were expected to produce similar results because the inflection point is approximately at the peak pore pressure location. Out of the two, the peak excess pore pressure criterion is the most consistent. There is a gradual increase in the undrained strength ratio with an increase in stress level. However, this criterion is too conservative at consolidation effective stresses less than 200 kPa. It can be seen that the peak shear stress criterion is more suitable at this stress level with higher values obtained.

Figure 6-51 shows the variation in friction angle with stress level using the different failure criteria. There is a consistent trend, for all criteria, that the friction angle decreases with increasing stress level suggesting a curved failure envelope or cohesion intercept. The inflection point and the peak excess pore pressure criteria are the most conservative and are probably slightly low of the actual friction angle value. As expected the peak principle stress ratio criterion

produces the highest friction angles. The friction angle at the point of maximum obliquity ranges from  $\phi = 39^\circ$  at low stresses to  $\phi = 34^\circ$  at higher stresses. The axial strain at 12% failure criterion produces the most realistic friction angle values with less deviation with stress level. All values range between  $\phi = 34^\circ$  and  $\phi = 38^\circ$ . However, as discussed in Section 6.3.3, if a greater axial strain value was used as the failure criterion, the friction angle would likely be more consistent with a value of  $\phi = 35^\circ$ .

The axial strain at failure using the various failure criteria versus stress level are presented in Figure 6-52. The results show that the peak shear stress criterion produces strains at failure much lower than the other techniques. All failures occur at less than 1.2% axial strain using the peak shear stress criterion. However, the method is only suitable for tests up to a consolidation stress of 400 kPa. The peak principle stress ratio criterion produces a lot of scatter with no trend between stress level and strain at failure. Again, the inflection point and the peak excess pore pressure criteria produce similar results. It can be seen that strain at failure reduces with increasing stress level for both methods. The two methods are related to the degree of dilation with stress level. Higher consolidation stresses will produce more dilation and a decrease in the axial strain at failure.

## **6.4 $K_0$ - CONSOLIDATED UNDRAINED TRIAXIAL COMPRESSION (CK<sub>0</sub>UC) TESTS (SERIES B)**

### **6.4.1 Introduction**

This section presents results from  $K_0$ -consolidated undrained triaxial compression (CK<sub>0</sub>UC) tests. Six tests were sheared at a constant rate of 2%/hour after  $K_0$ -consolidation to vertical consolidation effective stresses ranging from 200 to 900 kPa. Of these, two tests experienced experimental errors and hence, are not presented. As discussed in the previous section, this phase of the triaxial testing program is known as the Series B tests.

All specimens in this study were normally consolidated using automated  $K_0$  control. Table 6-5 presents the test number and type, the preshear conditions, and the stress-strain-strength parameters for each specimen. As in Table 6-4 for the CIUC tests, five failure criteria are used to present the material properties at various stages during the test. Similar to the CIUC

results, the stress-strain properties are first presented in this section, followed by the effective stress path information. Stiffness parameters are then described before the final summary section using the various failure criteria.

#### 6.4.2 Shear Stress-Strain Behavior

Figure 6-53 shows the stress-strain behavior ( $q = (\sigma_1 - \sigma_3)/2$  versus  $\epsilon_a$ ) for the  $CK_0UC$  tests. The results show that the peak shear stress is mobilized at small strains ( $\epsilon_a < 0.5\%$ ). The peak shear stress is followed by strain softening in all cases. Depending on the vertical consolidation effective stress, the material will either go into a quasi steady state condition before dilating and regaining some shear strength or the post peak softening will plateau with an increase in strain. It can be seen that specimens with a higher vertical consolidation effective stress have a greater tendency to dilate towards the end of shearing.

Figure 6-54, 6-55, and 6-56 show the normalized shear stress-strain behavior ( $q/\sigma'_{vc}$  versus  $\epsilon_a$ ) versus axial strain on a linear scale with large strain, a linear scale with small strains, and logarithmic scales. These figures demonstrate that the preshear consolidation stress level has a pronounced effect on the normalized strength. The peak undrained shear strength ( $USR = s_u/\sigma'_{vc}$ ) increases with increasing vertical consolidation stress level. A detailed review of the USR with stress level will be presented in Section 6.4.5.

The shear stress-strain data (Figures 6-54, 6-55, and 6-56) illustrate that there is no relation between stress level and ductility before the peak shear stress. All tests yield at approximately 0.3% axial strain. Figure 6-54 demonstrates the effects of consolidation stress level on the post peak portion of the stress-strain. All specimens go through strain softening after the yield point. However, with an increasing vertical consolidation effective stress the softening becomes more suppressed. Tests consolidated to higher vertical consolidation stresses ( $\sigma'_{vc} > 400$  kPa) experience dilation with an increase in strain. At high strains the undrained strength ratio will exceed the shear stress at the yield point. The results show that the degree of dilation increases with increasing stress level.

### 6.4.3 Effective Stress Behavior

Figure 6-57 shows the effective stress paths using the MIT stress space ( $q = (\sigma_1 - \sigma_3)/2$  versus  $p' = (\sigma'_1 + \sigma'_3)/2$ ) from the  $CK_0UC$  triaxial tests. The stress paths start from the  $K_0$ -consolidation point and rise to the peak strength. Contraction then occurs with decreasing mean stress. Tests with higher vertical consolidation effective stresses experience dilation towards the end of testing as shown in the figure by the inflection point and the increase in mean effective stress.

Figure 6-58 shows the corresponding normalized effective stress paths ( $q/\sigma'_{vc}$  versus  $p'/\sigma'_{vc}$ ). All tests show a small dilative phase with an increase in the mean effective stress until the peak shear stress is mobilized. The mobilization of the peak shear strength is followed by contractive behavior from the increase in the excess pore pressures. Again, the inflection point and the dilative behavior can be seen in the tests consolidated past a vertical consolidation effective stress of 550 kPa. The dilative phase of these tests can be associated with a reduction in excess pore pressures. Up until the inflection point, the tests generally show good agreement, the shape of the stress paths and the behavior is similar.

The principle stress ratio versus axial strain ( $q/p'$  versus  $\epsilon_a$ ) is presented in Figure 6-59. The results show constant obliquity after 8% axial strain. The principle stress ratio increases gradually with an increase in axial strain. After an axial strain of approximately 4%, the increase begins to plateau. At 6% axial strain, it can be seen that the principle stress ratio is constant with an increase in strain. The results show that the critical state value can be obtained with axial strains less than 10% in  $CK_0UC$  tests and that the stress obliquity is constant at high axial strains.

The corresponding friction angle versus axial strain is shown in Figure 6-60. Again, after an axial strain of approximately 6% the behavior becomes almost constant. The friction angles range from  $\phi' = 30$  to  $\phi' = 33^\circ$  along the failure envelope. The results show that there is a correlation between friction angle and vertical consolidation effective stress. The friction angle increases with increasing stress level. A further study of this relationship will be presented in Section 6.4.5.

Figure 6-61 shows the excess pore pressure generated during undrained shear normalized to the vertical effective consolidation stress ( $\sigma'_{vc}$ ). The results demonstrate that the normalized

excess pore pressure increases continuously throughout shear before leveling off. Increasing stress levels suppress the magnitude of normalized excess pore pressures with a significant drop in excess pore pressures between the high pressure test at  $\sigma'_{vc} = 830$  kPa and the low pressure test at  $\sigma'_{vc} = 186$  kPa. The results highlight the dilative behavior of the material at higher strains due to the drop in normalized excess pore pressures after the peak point. The drop in normalized excess pore pressures is more pronounced with an increase in stress level.

The corresponding normalized shear induced pore pressures versus axial strain are presented in Figure 6-62. The plot essentially removes the effect of the starting  $K_0$  value. The results show a similar trend to that described for the normalized excess pore pressures. Increasing stress levels suppress the normalized shear induced pore pressures and the post peak normalized shear induced pore pressure decrease is more pronounced with an increase in stress level. It can be seen there is good agreement between excess and shear induced pore pressure with Figure 6-61 and 6-62 displaying similar values.

#### **6.4.4 Stiffness**

Figure 6-63 shows the undrained secant Young's modulus normalized to the vertical consolidation effective stress ( $E_u/\sigma'_{vc}$ ) versus axial strain (on a log-log scale) for the  $CK_0UC$  triaxial tests. The results show good agreement and repeatability in the early stages of the tests with a slight deviation in behavior towards the end. Generally, the behavior is slightly rounded with the modulus constantly decreasing.

Figure 6-64 shows the normalized undrained modulus versus stress level at axial strains of 0.05, 0.1, and 1%. The results show that modulus at small strains is affected by stress level. A lower modulus is found with increasing stress level. At higher strain levels, there is almost a constant modulus with increasing stress level.

#### **6.4.5 Summary of behavior**

This section provides a summary of the results obtained from the  $CK_0UC$  triaxial experimental program. Similar to the CIUC tests, the five failure criteria presented in Table 6-5 will be used for this section.

Figure 6-65 shows the normalized undrained shear strength versus stress level for the  $CK_0UC$  triaxial tests using the various failure criteria. The results show that the undrained strength ratio increases with increasing stress level. The peak shear stress criterion shows the least deviation with increasing stress level and the most reasonable values. The undrained strength ratio increases from 0.261 at low stresses to 0.308 at high stresses. The remaining four criteria show a large deviation in shear strength with increasing stress level. The four criteria produce similar results at each stress level; however, the peak excess pore pressure and inflection point criteria show the most consistency with a linear increase in the undrained strength ratio with increasing stress level. The results show that over this stress range for  $CK_0UC$  tests the peak shear stress failure criterion is the most appropriate. All other techniques produce undrained shear strengths that are too low or too conservative.

Figure 6-66 shows the friction angle versus stress level using the five failure criteria for the  $CK_0UC$  triaxial tests. As expected, the results show that the friction angles at the peak shear stress,  $\phi_p$ , are much lower than the friction angles using the other failure criteria. The other failure criteria are located close to or on the failure envelope; therefore, higher friction angles are expected. The peak friction angle increases from  $\phi_p = 21^\circ$  at low stresses to  $\phi_p = 24^\circ$  at high stresses. A similar increase in friction angle with an increase in stress level can be seen using the other failure criteria. There is excellent agreement and repeatability using all other failure criteria. The friction angle ranges from  $\phi = 30^\circ$  at low stresses to  $\phi = 33^\circ$  at high stresses. The good repeatability between failure criteria is a result of the constant principle stress ratio at higher strains and the sharp inflection point in the stress path where the behavior turns from contractive to dilative.

The ductility of the material before and after the peak shear stress was briefly discussed in Section 6.4.2. Figure 6-67 shows the axial strain at failure ( $\epsilon_f$ ) versus stress level. The results show very consistent behavior for axial strain at peak shear. All values are constant with increasing stress level. There is a larger deviation in behavior using the other failure criteria. However, in all cases, it can be seen that there is no relation between axial strain at failure and stress level. Peak shear occurs at very small strains compared to the other devices. The peak excess pore pressure criterion provides the most consistent form of analysis if the peak shear stress criterion is not considered.

## 6.5 SHEAR BEHAVIOR SUMMARY

### 6.5.1 Introduction

This section provides a summary and comparison of the results for DSS, CIUC, and CK<sub>0</sub>UC triaxial tests. The shear stress-strain curves and effective stress paths will be compared for the triaxial tests only. The DSS device shears under different conditions producing stress-strain curves and effective stress paths that are different than the triaxial device. However, the DSS behavior will be included in the final part of this section when the undrained shear strength ratio, friction angles, and axial strain versus stress level are analyzed.

### 6.5.2 Triaxial comparison – CIUC versus CK<sub>0</sub>UC

#### 6.5.2.1 Shear Stress-Strain Behavior

Figure 6-68 shows the shear stress-strain behavior for the CIUC and CK<sub>0</sub>UC triaxial tests (CIUC marked in blue and CK<sub>0</sub>UC marked in red). It should be noted, at equal stress levels, the void ratios for both CIUC and CK<sub>0</sub>UC triaxial tests are very similar at the end of consolidation. Therefore, the investigation presents the effects of a different consolidation method rather than a different density. The results show that the peak undrained shear strength ( $s_u$ ) or the initial yield point is lower for the CK<sub>0</sub>UC for tests at a similar stress level. It can also be seen that the CIUC behavior is more ductile than the CK<sub>0</sub>UC counterparts. The CK<sub>0</sub>UC tests all mobilize their peak shear strength at very small strain levels ( $\epsilon_a < 0.5\%$ ) with constant behavior with an increase stress level. The CIUC behavior is much more ductile with an increase in ductility with an increase in stress level.

The most striking difference in behavior can be seen after the initial yield point. The stress-strain behavior is similar between the two test types up to a vertical consolidation effective stress of 400 kPa. The specimens strain-soften after the peak shear stress is mobilized. The softening plateaus with an increase in axial strain until a quasi steady state condition is reached. Finally, there is a slight increase in shear strength due to dilation. At higher consolidation stress levels, large deviations in behavior are apparent. Generally, the CK<sub>0</sub>UC specimens have a similar behavior with an increase in stress level. The behavior becomes more dilative towards the end of the test with an increase in stress level but all tests exhibit strain softening to some degree. The



CIUC tests at higher stress levels display no strain softening and the behavior is much more dilative than the  $CK_0UC$  tests.

Figure 6-69 shows the normalized shear stress-strain behavior for the CIUC and  $CK_0UC$  triaxial tests. Again, the results show that the CIUC tests have greater ductility before the yield point is mobilized and the subsequent dilation is much more pronounced. It can be seen that the undrained strength ratio ( $s_u/\sigma'_{vc}$ ) is higher for the CIUC tests. A further study of this trend will be presented in Section 6.5.2.3. Figure 6-70 presents the shear stress normalized by the mean consolidation effective stress ( $p'_c = ((\sigma'_{vc} + \sigma'_{hc})/2)$ ) versus axial strain. The results show that the  $CK_0UC$  triaxial tests will produce a higher undrained strength ratio if the mean consolidation effective stress is used to normalize the data. Similar results will be produced if the shear stress was normalized by the octahedral stress,  $\sigma'_{oct}$ .

#### 6.5.2.2 Effective Stress Behavior

Figure 6-71 shows the effective stress paths for the CIUC and  $CK_0UC$  triaxial tests. The results show that the shape of the CIUC and  $CK_0UC$  stress paths are different. However, this behavior is expected due to the different starting shear conditions. The stress path shape is consistent for the  $CK_0UC$  tests with an increase in stress level while the shape of the CIUC stress path changes with an increase in stress level. The behavior is more dilative in the CIUC tests at higher stress levels, highlighting a greater reduction in excess pore pressures. Furthermore, in the  $CK_0UC$  tests that show dilative behavior after contraction, the inflection point is much sharper than the CIUC counterpart.

Figure 6-72 shows the corresponding normalized effective stress paths. The figure shows the deviation in stress path shape and behavior between test types. The interpreted failure envelope has been added to this figure. It can be seen that the CIUC tests consolidated to low effective stresses deviate from the failure envelope. The discrepancy is most likely due to the difficulty with getting accurate results at low stresses. In the low stress tests, the excess pore pressures increase dramatically during shear and the effective stress starts to move towards zero. Any discrepancies in the measuring devices or data reduction are magnified as a result. The deviation off the failure envelope in the low stress tests is most likely due to a measuring device error.

### 6.5.3 DSS - CIUC – CK<sub>0</sub>UC Summary

#### 6.5.3.1 Undrained Strength Ratio

Figure 6-73 shows the undrained strength ratio (USR) versus stress level for DSS, CIUC, and CK<sub>0</sub>UC tests. The peak shear stress criterion was used to derive the results in this figure except for the CIUC tests. The CIUC values are a combination of the peak shear stress criterion at low stresses and the peak excess pore pressure criterion at higher stresses. The results show in all cases that the undrained strength ratio increases with increasing stress level. The DSS undrained strength ratio values are much lower than the triaxial results. The USR ranges from 0.137 at low stresses to 0.183 at high stresses. It can be seen that the triaxial test results show good agreement, particularly at vertical consolidation effective stresses up to 400 kPa. After this stress level, the deviation begins to increase with the CIUC tests displaying a more pronounced increase in strength with increasing stress level. The undrained strength ratio ranges from about 0.27 at low stresses for the two test types to 0.31 for the CK<sub>0</sub>UC and 0.39 for the CIUC at higher stresses. The greater undrained strength ratio for the CIUC tests at higher stresses is related to the greater dilation experienced in these tests.

In summary, the CIUC and CK<sub>0</sub>UC triaxial tests produce similar undrained strength ratios at low stresses with the CIUC results slightly higher with an increase in stress level. The triaxial undrained strength ratio is significantly higher to that found in the DSS tests with the difference almost double the DSS value.

#### 6.5.3.2 Friction Angle and Arctan $\tau_h/\sigma'_v$

For the purposes of this section, the arctan  $\tau_h/\sigma'_v$  ( $\psi'$ ) values from the DSS device will be presented with the friction angles obtained in the triaxial devices. It will be assumed that the arctan  $\tau_h/\sigma'_v$  ( $\psi'$ ) value is approximately equal to the true friction angle ( $\phi'$ ).

The friction angles ( $\phi'$ ) and arctan  $\tau_h/\sigma'_v$  ( $\psi'$ ) values found at the peak shear stress are presented in Figure 6-74. Similar to the undrained strength ratio results, the DSS device produces the lowest values. The peak arctan  $\tau_h/\sigma'_v$  angle ( $\psi'_p$ ) ranges from  $\psi'_p = 14^\circ$  at low stresses to  $\psi'_p = 20^\circ$  at higher stresses. All test types show that the peak friction angle increases with increasing

stress level at a uniform rate. The increase in friction angle with increasing stress level is directly related to the higher undrained strength ratio with increasing stress level. Therefore, the CIUC tests produce slightly higher peak friction angles than the  $CK_0UC$  tests. The stress level range is small for the CIUC tests ( $\sigma'_{vc} = 100 - 400$  kPa) because there is no well defined peak shear stress at higher stresses and hence, the friction angle cannot be determined. The peak friction angle ranges from  $\phi'_p = 22^\circ$  at low stresses to  $\phi'_p = 24^\circ$  at higher stresses for the  $CK_0UC$  tests compared with a range from  $\phi'_p = 24^\circ$  at low stresses to  $\phi'_p = 26^\circ$  at higher stresses for the CIUC tests.

Figure 6-75 shows the friction angle versus stress level using the limiting strain criterion. A 30% limiting strain was used in the DSS tests while 12% was selected for the triaxial tests. The figure shows contrasting trends between friction angle and stress level. The DSS and  $CK_0UC$  tests show an increase in friction angle with an increase in stress level. However, in the CIUC triaxial tests the friction angle decreases with stress level. The best fit curves for each data set have been added to increase clarity. The results show that the largest deviation in friction angle is at low stresses. The friction angle ranges from  $\psi' = 22^\circ$  for the DSS tests to  $\phi' = 39^\circ$  for the CIUC tests at low stresses. As mentioned in Section 6.5.3.1, there is difficulty measuring parameters as the effective stress decreases during shear. Figure 6-76 presents the friction angles versus the mean effective stress. The results show that at lower stresses smaller friction angles will be recorded. Furthermore, the results show that the accuracy of the DSS device diminishes with a reduction in stress level. As a consequence, the low friction angles at low stress levels might not be correct. Therefore, at low stress levels the  $CK_0UC$  results provide the most accurate information.

The results show much better agreement between test types with an increase in stress level. At the maximum triaxial stress level ( $\sigma'_{vc} \approx 900$  kPa) it can be seen that the friction angle is about  $\phi = 33^\circ$  for both the CIUC and  $CK_0UC$  tests. The best fit curve for the DSS tests produces a slightly lower friction angle of  $\psi' = 31^\circ$  at the same stress level. Both the DSS and the  $CK_0UC$  tests show a plateau in the friction angle with increasing stress level. The DSS tests produce a friction angle of  $\psi' = 35^\circ$  at high stress levels. However, based on the results, a friction angle of  $\phi' = 34^\circ$  at high stress levels is more conservative for DSS and  $CK_0UC$  tests. The CIUC tests show a constant decrease in friction angle with increasing stress level. However, based on

the two other test types, it is expected that this decrease will plateau with a further increase in stress level.

In summary, the  $CK_0UC$  tests produce the most consistent results with an increase in stress level. A friction angle  $\phi' = 31^\circ$  can be expected at low stress levels and this will increase to a friction angle  $\phi = 34^\circ$  at high stress levels.

#### 6.5.3.3 Axial strain at failure

Figure 6-77 shows the axial strain at failure versus stress level for DSS, CIUC, and  $CK_0UC$  tests. The CIUC and  $CK_0UC$  triaxial tests show the axial strain at failure using the peak shear stress and the peak excess pore pressure failure criteria. The results show that the axial strain at failure using the peak shear stress criterion is very similar for both the DSS and CIUC tests. There is an increase in ductility with stress level producing axial strains at failure that range from 0.6% at low stresses to 3.7% at high stresses. It can be seen that the axial strains at failure are lower for the  $CK_0UC$  triaxial tests using the peak shear stress criterion and the axial strain at failure is constant with an increase in stress level. The axial strains at failure are only about 0.3% for the  $CK_0UC$  triaxial tests.

The peak excess pore pressure criterion produces greater axial strain values and there is reasonable agreement between the CIUC and  $CK_0UC$  triaxial tests. The axial strain at failure is greater than 8% at low stresses and decreases with an increase in stress level.

In summary, the material is brittle with a peak shear stress mobilized at axial strains less than 3.7% in all test types.

#### 6.5.3.4 Stiffness

Figure 6-78 shows the undrained secant Young's modulus normalized to the vertical consolidation effective stress versus stress level. The results show some scatter; however, there are a few observations that can be taken from the data. The CIUC triaxial tests produce higher modulus values at all strain levels than the DSS and CIUC tests. Generally, the normalized

modulus is above 300 at low strains and around 60 at 1% axial strain. The DSS tests have a normalized modulus between 150 and 200 at low strains with a drop to about 45 at 1% shear strain. Out the three test types, the  $CK_0UC$  tests show the lowest normalized undrained modulus values. The normalized modulus is about 150 at low strains but the reduction in modulus with an increase in strain is much more pronounced than the other test types. The normalized undrained modulus at 1% axial strain is about 7. When the results are analyzed as a whole group, at low strains there is a drop in the normalized modulus with an increase in the stress level. However, as the magnitude of strain increases the modulus becomes constant with increasing stress level.

Spec. Location		Index Tests			Initial Conditions		Lab Consolidation					At Max Stress			At Final Point			E <sub>u</sub> /σ' <sub>vc</sub> : @		
Test No.	Depth	LL	w <sub>n</sub>	2% <sub>μm</sub>	W <sub>n</sub> (%)	e <sub>i</sub>	CR		σ' <sub>vm</sub>	σ' <sub>vc</sub>	w <sub>c</sub>	γ	τ <sub>h</sub> /σ' <sub>vc</sub>	τ <sub>h</sub> /σ' <sub>v</sub>		τ <sub>h</sub> /σ' <sub>vc</sub>	τ <sub>h</sub> /σ' <sub>v</sub>	γ =	Δτ <sub>h</sub> =	
Sample	Loc	PL			γ <sub>t</sub>	S <sub>i</sub> (%)		δε <sub>a</sub> /δt	ε <sub>a</sub>	ε <sub>a</sub>	e <sub>c</sub>	δγ/δt	σ' <sub>v</sub> /σ' <sub>vc</sub>	ψ'		σ' <sub>v</sub> /σ' <sub>vc</sub>	ψ'	0.02	30%	
		PI				G <sub>s</sub>	RR	(%/hr)	ε <sub>a</sub>	ε <sub>a</sub>	OCR	δγ/δt	σ' <sub>v</sub> /σ' <sub>vc</sub>	ψ'		σ' <sub>v</sub> /σ' <sub>vc</sub>	ψ'	0.1	50%	
DSS788	2-5m	25.77	25.0	10.0	8.33	1.02	0.06		593	593	23.99	1.83	0.153	0.274						
		18.24				22.23		1			0.71				30.0			258	142	
Series 1	Town	7.53			1.461	2.72	N/A		15.2	15.2	1.00	4.62	0.558	16.1		0.067	26.6	144	107	
DSS790	2-5m	25.77	25.0	10.0	8.01	0.99	0.07		1182	1182	23.66	2.47	0.171	0.310						
		18.24				22.16		1			0.64				30.0			217	118	
Series 1	Town	7.53			1.482	2.72	N/A		17.24	17.24	1.00	4.7	0.551	18.4		0.085	32.7	127	91	
DSS791	2-5m	25.77	25.0	10.0	8.65	0.97	0.07		1177	1177	22.45	2.58	0.168	0.308						
		18.24				24.33		1			0.62				30.0			217	105	
Series 1	Town	7.53			1.503	2.72	N/A		17.49	17.49	1.00	4.9	0.546	18.2		0.078	32.4	117	82	
DSS792	2-5m	25.77	25.0	10.0	8.52	0.97	0.05		197	197	29.53	0.88	0.130	0.215						
		18.24				23.86		1			0.73				30.0			265	213	
Series 1	Town	7.53			1.499	2.72	N/A		12.13	12.13	1.00	4.6	0.607	12.5		0.083	19.3	187	170	
DSS793	2-5m	25.77	25.0	10.0	8.36	0.94	0.05		197	197	22.73	0.96	0.133	0.229						
		18.24				24.15		1			0.70				30.0			235	208	
Series 1	Town	7.53			1.519	2.72	N/A		12.65	12.65	1.00	4.7	0.583	13.4		0.074	25.0	174	166	
DSS794	2-5m	25.77	25.0	10.0	7.85	0.94	0.06		628	628	23.28	1.88	0.154	0.283						
		18.24				22.79		1			0.66				30.0			272	105	
Series 1	Town	7.53			1.516	2.72	N/A		14.58	14.58	1.00	4.8	0.542	16.7		0.077	29.6	105	94	
DSS795	2-5m	25.77	25.0	10.0	7.99	0.92	0.08		1765	1765	22.67	3.69	0.179	0.335						
		18.24				23.73		1			0.57				30.0			114	83	
Series 1	Town	7.53			1.534	2.72	N/A		18.02	18.02	1.00	5.1	0.535	19.9		0.095	35.2	97	67	
DSS796	2-5m	25.77	25.0	10.0	7.77	0.92	0.08		1765	1765	23.40	3.71	0.182	0.338						
		18.24				23.0		1			0.59				30.0			104	86	
Series 1	Town	7.53			1.529	2.72	N/A		17.13	17.13	1.00	5.0	0.538	20.2		0.110	34.9	97	68	

Table 6-1: Summary of CK<sub>0</sub>DSS (NC) tests (a) stresses in kPa, b) water content and strain in %, c) density in g/cm<sup>3</sup>, d) time in hours, e) wc = water content determined at end of test)

Spec. Location		Index Tests			Initial Conditions		Lab Consolidation					At Max Stress			At Final Point			E <sub>v</sub> /σ' <sub>vc</sub> : @	
Test No.	Depth	LL	w <sub>n</sub>	2%μm	W <sub>n</sub> (%)	e <sub>i</sub>	CR		σ' <sub>vm</sub>	σ' <sub>vc</sub>	w <sub>c</sub>	γ	τ <sub>h</sub> /σ' <sub>vc</sub>	τ <sub>h</sub> /σ' <sub>v</sub>		τ <sub>h</sub> /σ' <sub>vc</sub>	τ <sub>h</sub> /σ' <sub>v</sub>	γ =	Δτ <sub>h</sub> =
Sample	Loc	PL				S <sub>i</sub> (%)		δε <sub>a</sub> /δt	ε <sub>a</sub>	ε <sub>a</sub>	e <sub>c</sub>	δγ/δt	σ' <sub>v</sub> /σ' <sub>vc</sub>	ψ'		σ' <sub>v</sub> /σ' <sub>vc</sub>	ψ'	0.02	30%
		PI			γ <sub>t</sub>	G <sub>s</sub>	RR	(%/hr)	ε <sub>a</sub>	ε <sub>a</sub>	OCR							0.1	50%
DSS807	2-5m	25.77	25.0	10.0	3.4	0.82	0.05		592	592	24.21	1.47	0.161	0.289		0.047	0.518		
		18.24				11.32		1			0.65				30.0			165	155
Series 1	Town	7.53			1.549	2.72	N/A		9.2	9.2	1.00	4.4	0.557	17.0		0.090	32.7	152	123
DSS809	2-5m	25.77	25.0	10.0	5.06	0.86	0.06		593	593	23.86	1.77	0.166	0.295		0.037	0.468		
		18.24				16.07		1			0.57				30.0			185	145
Series 1	Town	7.53			1.541	2.72	N/A		15.39	15.39	1.00	4.8	0.563	17.4		0.078	29.0	145	114
DSS810	2-5m	25.77	25.0	10.0	8.83	1.04	0.06		597	597	22.66	9.52	0.267	0.48		0.081	0.515		
		18.24				23.19		1			0.73				30.0			---	---
Series 1	Town	7.53			1.455	2.72	N/A		15.30	15.30	1.00	4.5	0.555	29.8		0.157	32.4	---	---
DSS811	2-5m	25.77	25.0	10.0	9.66	1.04	0.06		591	591	---	11.39	0.284	0.510		0.064	0.563		
		18.24				25.21		1			0.69				30.0			---	---
Series 1	Town	7.53			1.462	2.72	N/A		17.47	17.47	1.00	4.7	0.557	32.1		0.113	36.1	---	---
DSS815	2-5m	25.77	25.0	10.0	7.84	0.95	0.06		590	590	23.03	9.00	0.301	0.497		0.065	0.473		
		18.24				22.47		1			0.69				30.0			---	---
Series 1	Town	7.53			1.506	2.72	N/A		13.41	13.41	1.00	4.8	0.606	31.0		0.138	29.3	---	---

Table 6-2: Summary of CK<sub>0</sub>DSS NC and cyclic tests

(a) stresses in kPa, b) water content and strain in %, c) density in g/cm<sup>3</sup>, d) time in hours, e) w<sub>c</sub> = water content determined at end of test)

Spec. Location		Index Tests			Initial Conditions		Lab Consolidation					At Max Stress			At Final Point			$E_u/\sigma'_{vc}$ : @	
Test No.	Depth	LL	$w_n$	2% $\mu$ m	$W_n(\%)$	$e_i$	CR		$\sigma'_{vm}$	$\sigma'_{vc}$	$w_c$	$\gamma$	$\tau_h/\sigma'_{vc}$	$\tau_h/\sigma'_v$		$\tau_h/\sigma'_{vc}$	$\tau_h/\sigma'_v$	$\gamma =$	$\Delta\tau_h =$
Sample	Loc	PL			$\gamma_t$	$S_i (\%)$	RR	$\delta\varepsilon_a/\delta t$ (%/hr)	$\varepsilon_a$	$\varepsilon_a$	$e_c$	$\delta\gamma/\delta t$	$\sigma'_v/\sigma'_{vc}$	$\psi'$	$\gamma$	$\sigma'_v/\sigma'_{vc}$	$\psi'$	0.02	30%
		PI				$G_s$			$\varepsilon_a$	$\varepsilon_a$	OCR							0.1	50%
DSS798	2-5m	25.77	25.0	10.0	8.15	0.92	0.07		1188	595	23.32	2.33	0.298	0.332		0.073	0.531		
		18.24				24.14		1			0.62				30.0			234	193
Series 1	Town	7.53			1.534	2.72	0.01		16.0	15.8	2.00	4.9	0.899	19.8		0.137	33.7	209	163
DSS799	5m	25.77	25.0	10.0	8.06	0.93	0.08		1178	591	24.1	2.37	0.300	0.336		0.071	0.561		
		18.24				23.63		1			0.61				30.0			178	176
Series 1	Town	7.53			1.526	2.72	0.01		16.6	16.4	2.00	5.0	0.893	20.0		0.127	36.0	176	158
DSS800	5m	25.77	25.0	10.0	7.94	0.90	0.09		1766	591	23.2	3.78	0.433	0.398		0.127	0.570		
		18.24				24.11		1			0.61				30.0			202	187
Series 1	Town	7.53			1.55	2.72	0.01		15.8	15.3	3.00	5.0	1.088	24.1		0.222	36.7	201	161
DSS801	5m	25.77	25.0	10.0	9.97	0.94	0.09		1766	591	23.22	3.58	0.414	0.390		0.100	0.557		
		18.24				29.02		1			0.60				30.0			195	178
Series 1	Town	7.53			1.547	2.72	0.01		17.6	17.2	3.00	5.1	1.061	23.6		0.180	35.7	195	156
DSS806	5m	25.77	25.0	10.0	7.88	0.91	0.08		1770	444	21.95	3.42	0.501	0.394		0.112	0.497		
		18.24				23.73		1			0.62				30.0			234	216
Series 1	Town	7.53				2.72	0.01		15.7	15.2	4.00	5.0	1.273	23.8		0.224	31.1	233	182
DSS808	5m	25.77	25.0	10.0	7.8	0.90	0.08		1771	446	22.89	3.49	0.524	0.405		0.164	0.555		
		18.24				23.5		1			0.60				30.0			241	204
Series 1	Town	7.53				2.72	0.01		16.44	15.92	4.00	5.0	1.295	24.5		0.295	35.5	233	175

Table 6-3: Summary of CK<sub>0</sub>DSS OC tests (a) stresses in kPa, b) water content and strain in %, c) density in g/cm<sup>3</sup>, d) time in hours, e) wc = water content determined at end of test)



Test No.	Initial Conditions $\sigma'_{vc}$ (kPa) $e_c$	At Peak Shear Stress				At 12% Axial Strain, ( $\epsilon_a$ )				At Pk. Principle Stress Ratio, (q/p')				At Pk. Excess Pore Pressure, ( $\delta U_{max}$ )				Inflection Point			
		$\epsilon_a$ (%)	q/ $\sigma'_{vc}$	p'/ $\sigma'_{vc}$	$\phi'_p$ (Deg)	$\epsilon_a$ (%)	q/ $\sigma'_{vc}$	p'/ $\sigma'_{vc}$	$\phi'$ (Deg)	$\epsilon_a$ (%)	q/ $\sigma'_{vc}$	p'/ $\sigma'_{vc}$	$\phi'$ (Deg)	$\epsilon_a$ (%)	q/ $\sigma'_{vc}$	p'/ $\sigma'_{vc}$	$\phi'$ (Deg)	$\epsilon_a$ (%)	q/ $\sigma'_{vc}$	p'/ $\sigma'_{vc}$	$\phi'$ (Deg)
TX920	97	0.588	0.256	0.640	23.59	--	--	--	--	--	--	--	--	--	--	--	--	--	--	--	--
CIUC	0.64																				
TX921	98	0.492	0.260	0.669	22.92	--	--	--	--	--	--	--	--	--	--	--	--	--	--	--	--
CIUC	0.64																				
TX922	98	0.556	0.269	0.672	23.59	--	--	--	--	--	--	--	--	--	--	--	--	--	--	--	--
CIUC	0.63																				
TX945	198	0.812	0.295	0.668	26.19	--	--	--	--	--	--	--	--	--	--	--	--	--	--	--	--
CIUC	0.62																				
TX970	399	1.268	0.313	0.753	24.61	12	0.285	0.481	36.3	12.630	0.291	0.489	36.5	10.831	0.277	0.472	36.0	8.813	0.272	0.469	35.5
CIUC	0.62																				
TX972	589	--	--	--	--	12	0.430	0.720	36.6	8.946	0.392	0.650	37.1	6.234	0.362	0.608	36.5	5.187	0.353	0.602	35.9
CIUC	0.62																				
TX989	198	0.971	0.272	0.632	25.46	12	0.248	0.400	38.4	8.935	0.232	0.371	38.7	8.365	0.229	0.366	38.6	7.095	0.222	0.361	38.1
CIUC	0.62																				
TX994	391	--	--	--	--	12	0.344	0.557	38.2	8.527	0.312	0.496	39.0	6.374	0.295	0.472	38.7	4.961	0.288	0.468	37.9
CIUC	0.62																				
TX997	590	--	--	--	--	12	0.542	0.922	36.0	9.564	0.479	0.808	36.4	4.367	0.356	0.621	35.0	3.175	0.335	0.608	33.4
CIUC	0.61																				
TX1000	886	--	--	--	--	12	0.602	1.067	34.3	10.687	0.564	0.997	34.4	4.092	0.380	0.709	32.4	2.811	0.349	0.691	30.4
CIUC	0.59																				
TX1003	893	--	--	--	--	6	0.485	0.884	33.3	6.033	0.486	0.886	33.3	3.491	0.394	0.762	31.1	2.188	0.351	0.737	28.5
CIUC	0.6																				

Table 6-4: Summary of CIUC triaxial tests

Test No.	Conditions	At Peak Shear Stress				At 12% Axial Strain, ( $\epsilon_a$ )				At Pk. Principle Stress Ratio, (q/p')				At Pk. Excess Pore Pressure, ( $\delta U_{max}$ )				Inflection Point			
		$\sigma'_{vc}$ (kPa) $e_c$ $K_0$	$\epsilon_a$ (%)	q/ $\sigma'_{vc}$	p'/ $\sigma'_{vc}$	$\phi'_p$ (Deg)	$\epsilon_a$ (%)	q/ $\sigma'_{vc}$	p'/ $\sigma'_{vc}$	$\phi'$ (Deg)	$\epsilon_a$ (%)	q/ $\sigma'_{vc}$	p'/ $\sigma'_{vc}$	$\phi'$ (Deg)	$\epsilon_a$ (%)	q/ $\sigma'_{vc}$	p'/ $\sigma'_{vc}$	$\phi'$ (Deg)	$\epsilon_a$ (%)	q/ $\sigma'_{vc}$	p'/ $\sigma'_{vc}$
TX1013 CK <sub>0</sub> UC	557 0.62 0.59	0.341	0.297	0.749	23.4	12	0.291	0.532	33.1	11.641	0.285	0.522	33.1	6.650	0.255	0.473	32.7	6.032	0.254	0.472	32.6
TX1018 CK <sub>0</sub> UC	363 0.64 0.55	0.285	0.297	0.727	24.1	12	0.208	0.400	31.3	8.349	0.209	0.396	31.9	8.823	0.207	0.394	31.7	9.989	0.204	0.391	31.4
TX1019 CK <sub>0</sub> UC	186 0.64 0.64	0.264	0.261	0.744	20.6	12	0.181	0.358	30.5	10.153	0.175	0.344	30.6	8.266	0.171	0.338	30.4	7.415	0.170	0.338	30.3
TX1021 CK <sub>0</sub> UC	830 0.62 0.57	0.386	0.307	0.749	24.2	12	0.303	0.561	32.8	9.019	0.290	0.535	32.9	6.628	0.281	0.521	32.7	5.901	0.280	0.520	32.5

Table 6-5: Summary of CK<sub>0</sub>UC triaxial tests

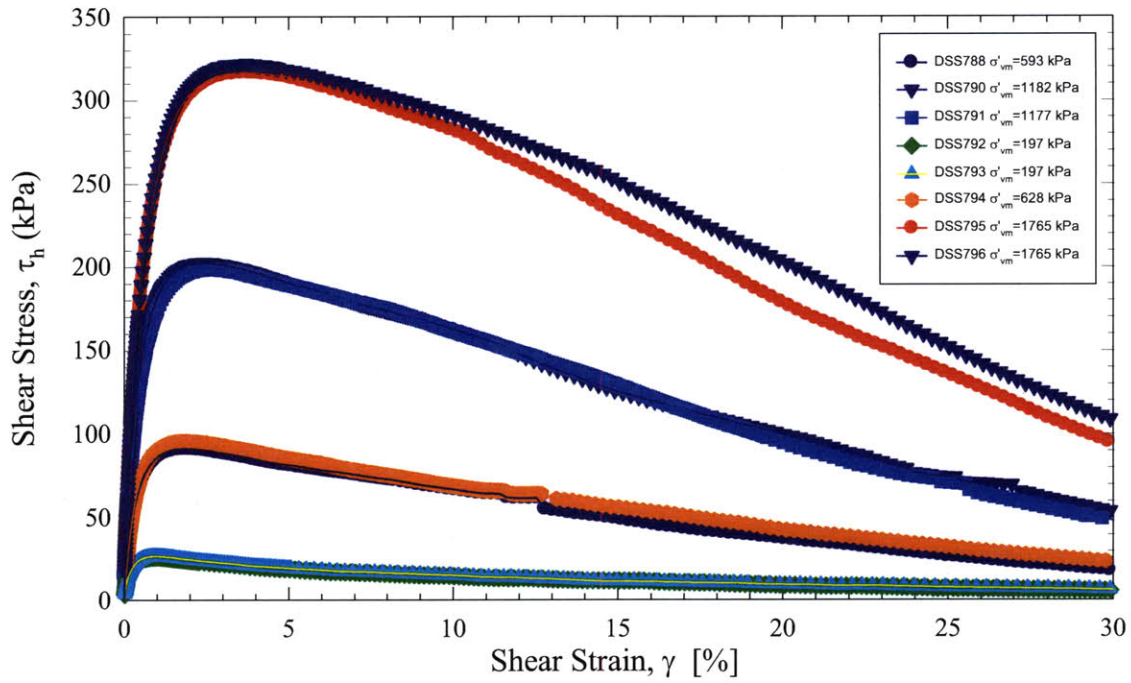


Figure 6-1: Stress-Strain curves from NC CK<sub>0</sub>DSS tests

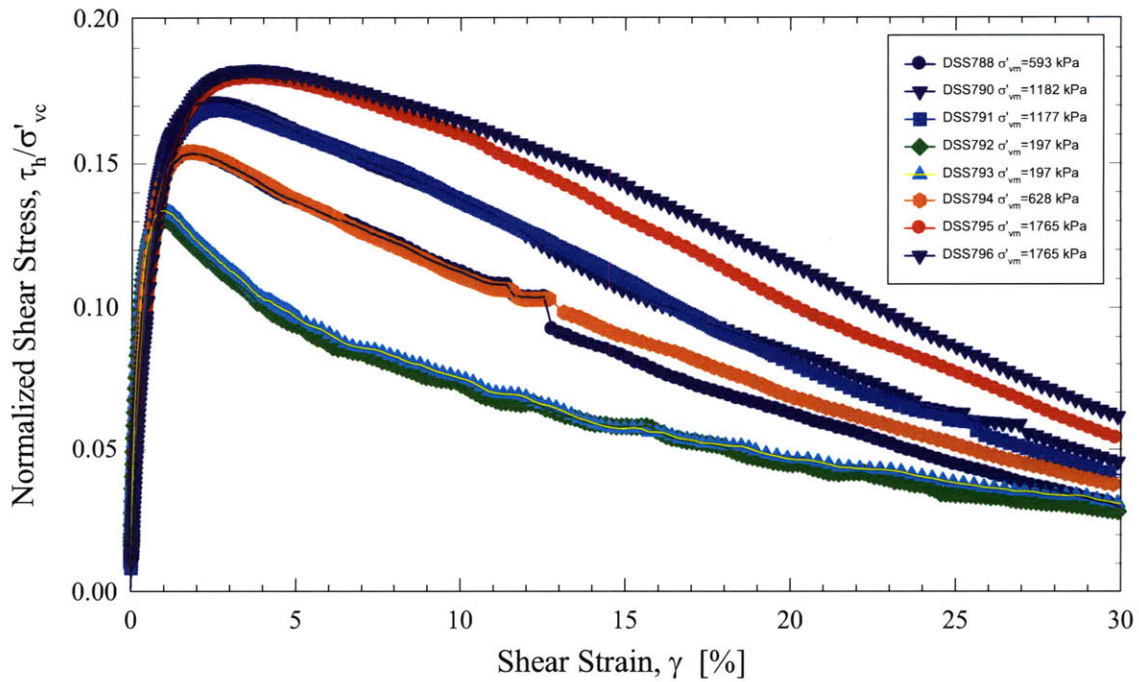


Figure 6-2: Normalized stress-strain curves from NC CK<sub>0</sub>DSS tests

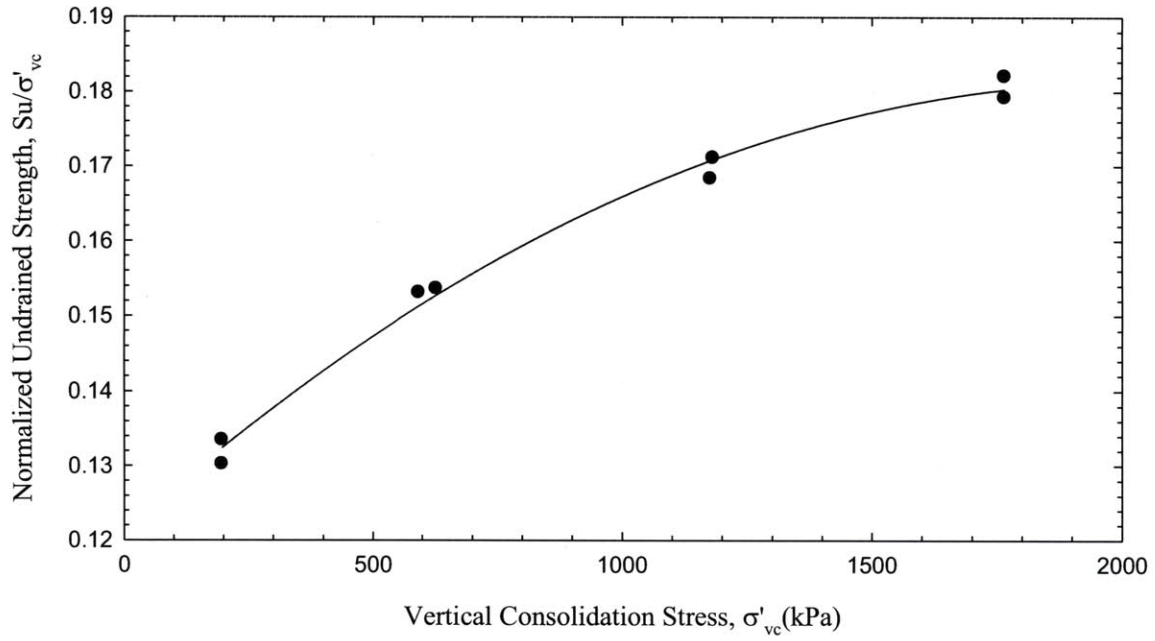


Figure 6-3: Normalized undrained shear strength versus stress level from NC  $CK_0$ DSS tests

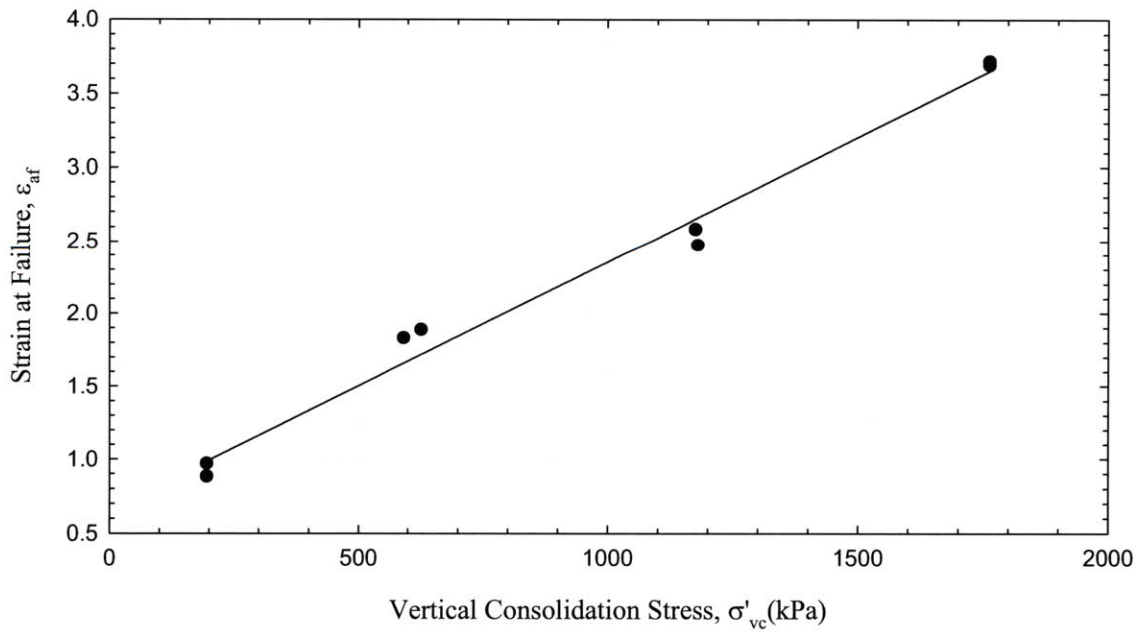


Figure 6-4: Strain at failure versus stress level from NC  $CK_0$ DSS tests

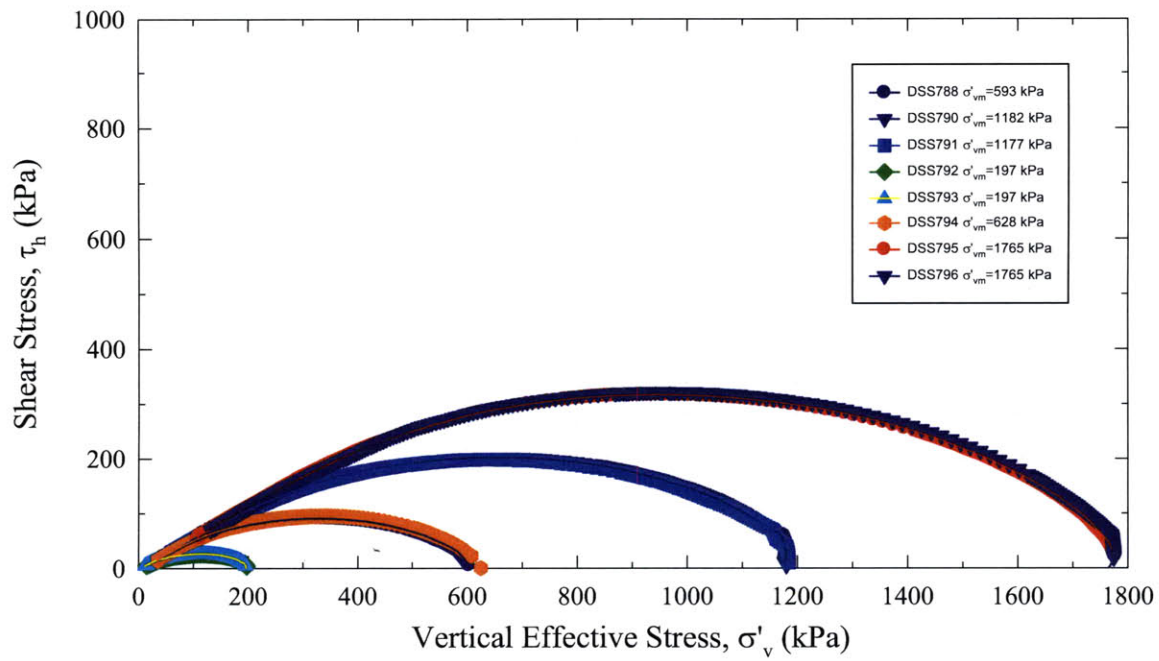


Figure 6-5: Effective stress paths from NC CK<sub>0</sub>DSS tests

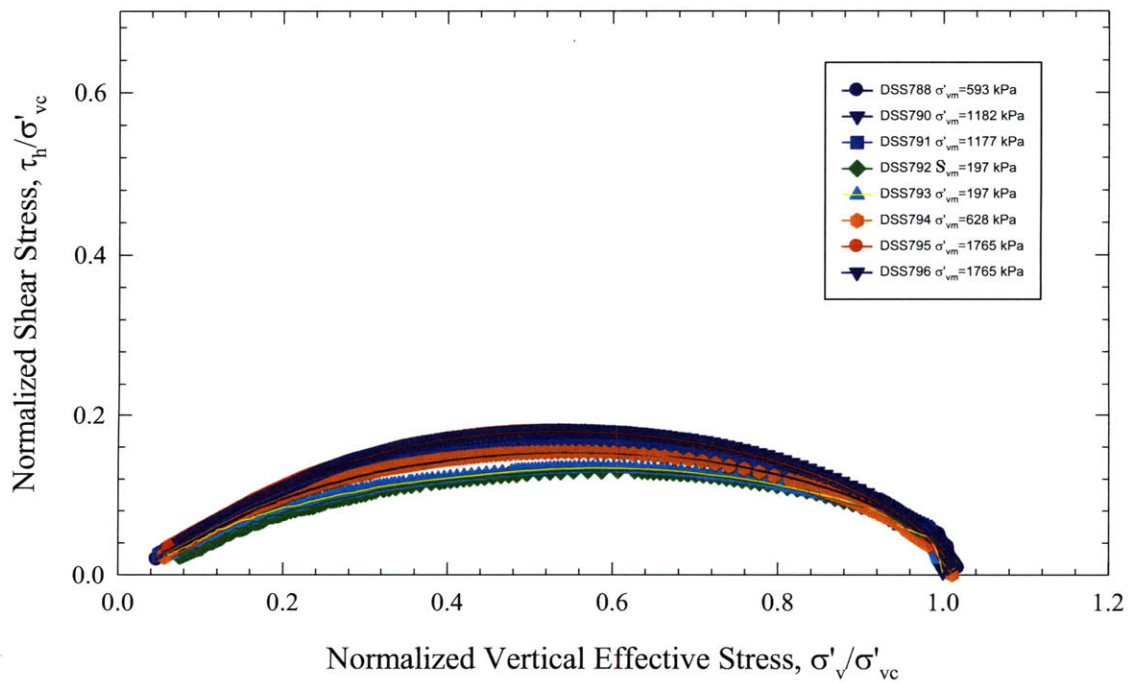


Figure 6-6: Normalized effective stress paths from NC CK<sub>0</sub>DSS tests

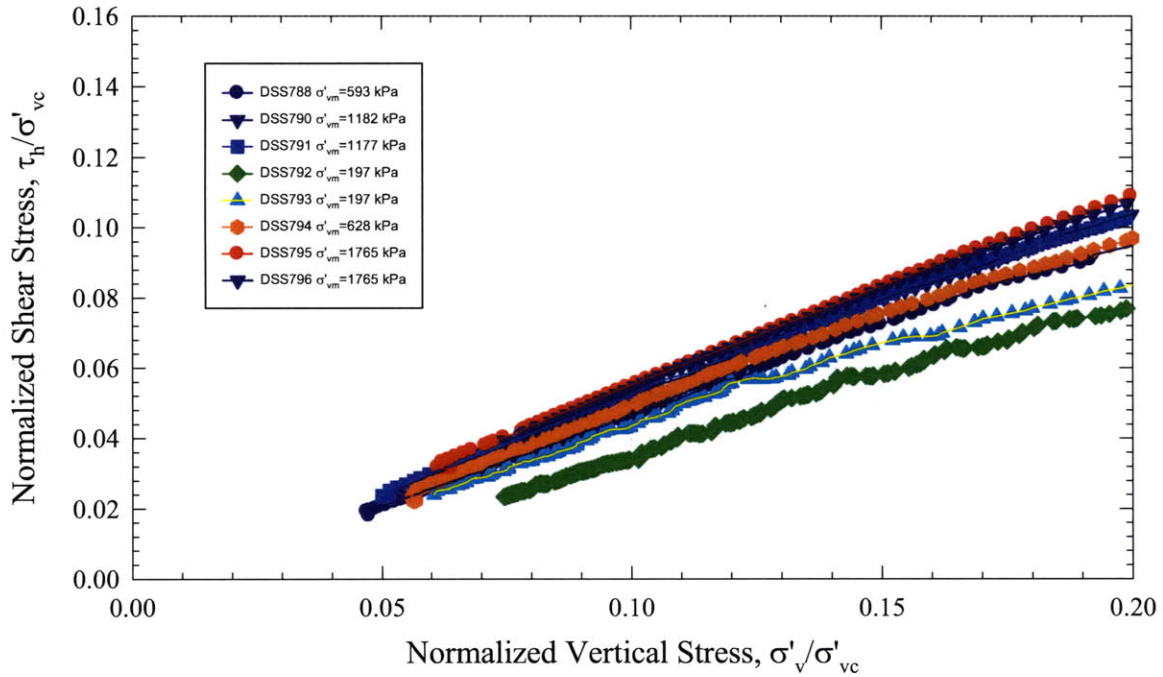


Figure 6-7: Normalized effective stress paths (close up view) from NC CK<sub>0</sub>DSS tests

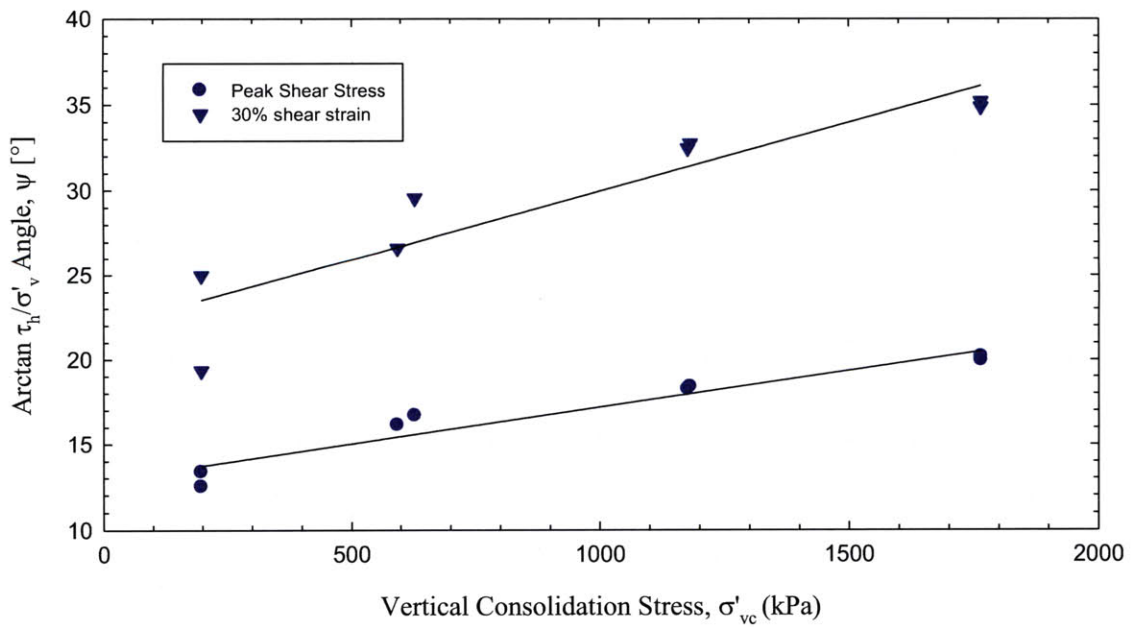


Figure 6-8: Friction angle at peak and end of shear strain versus stress level from NC CK<sub>0</sub>DSS tests

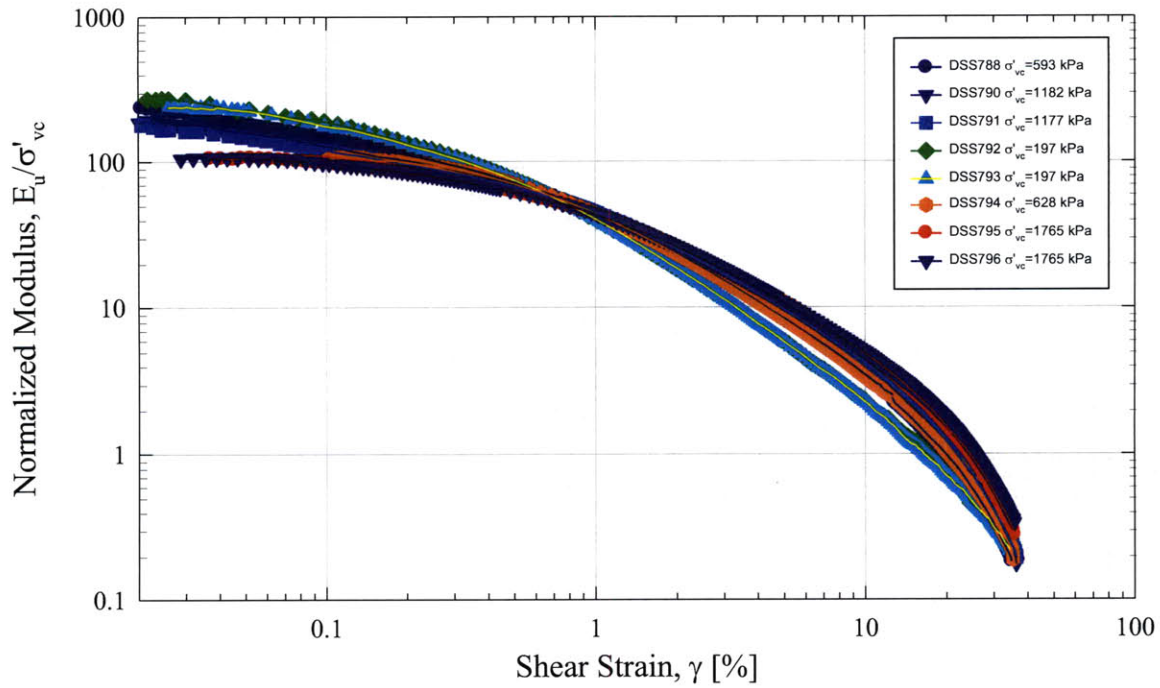


Figure 6-9: Normalized undrained secant modulus versus shear strain from NC CK<sub>0</sub>DSS tests

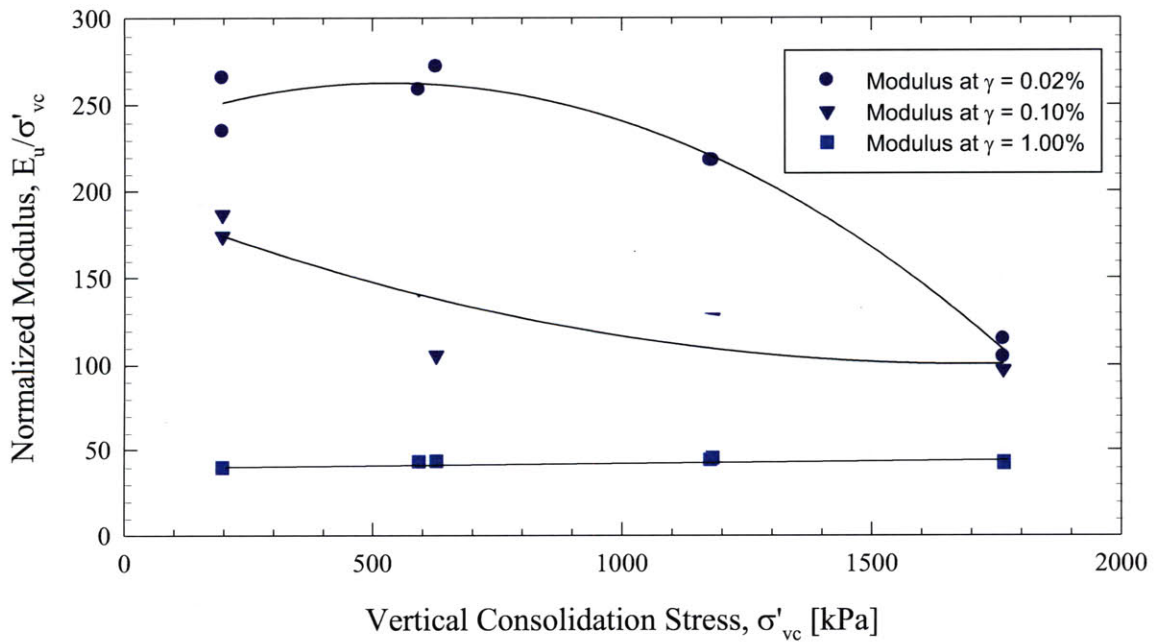


Figure 6-10: Normalized undrained secant modulus versus stress level from NC CK<sub>0</sub>DSS tests

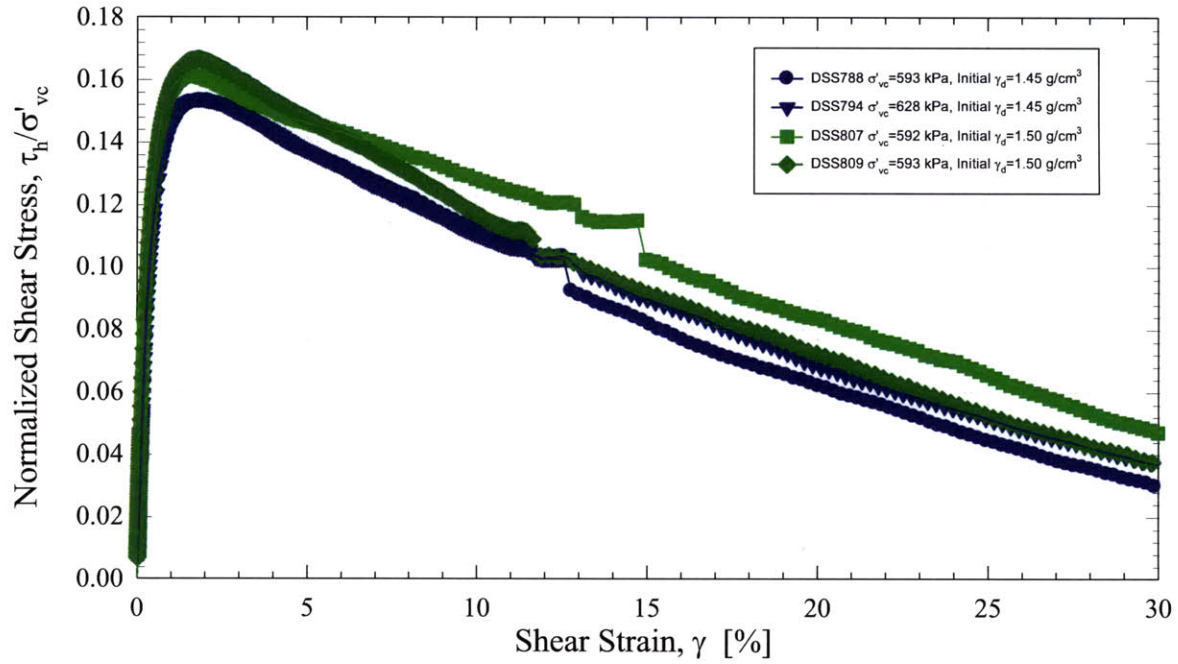


Figure 6-11: Normalized stress-strain curves from NC CK<sub>0</sub>DSS tests of different initial density

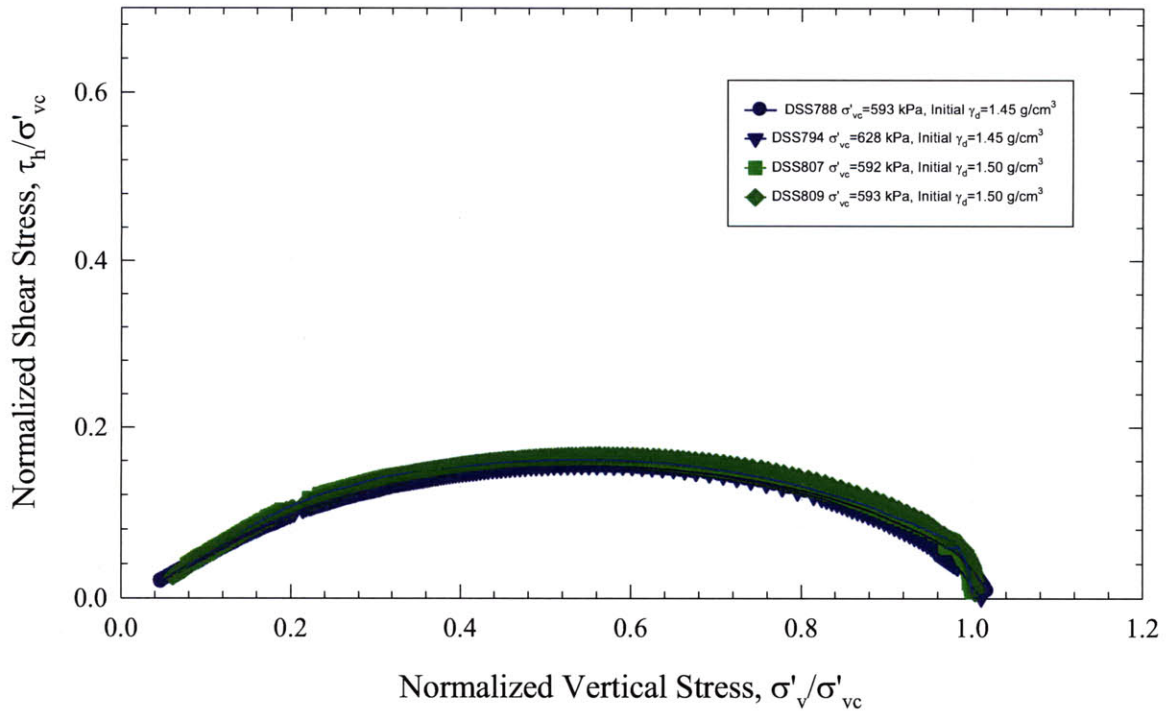


Figure 6-12: Normalized effective stress paths from NC CK<sub>0</sub>DSS tests of different initial density



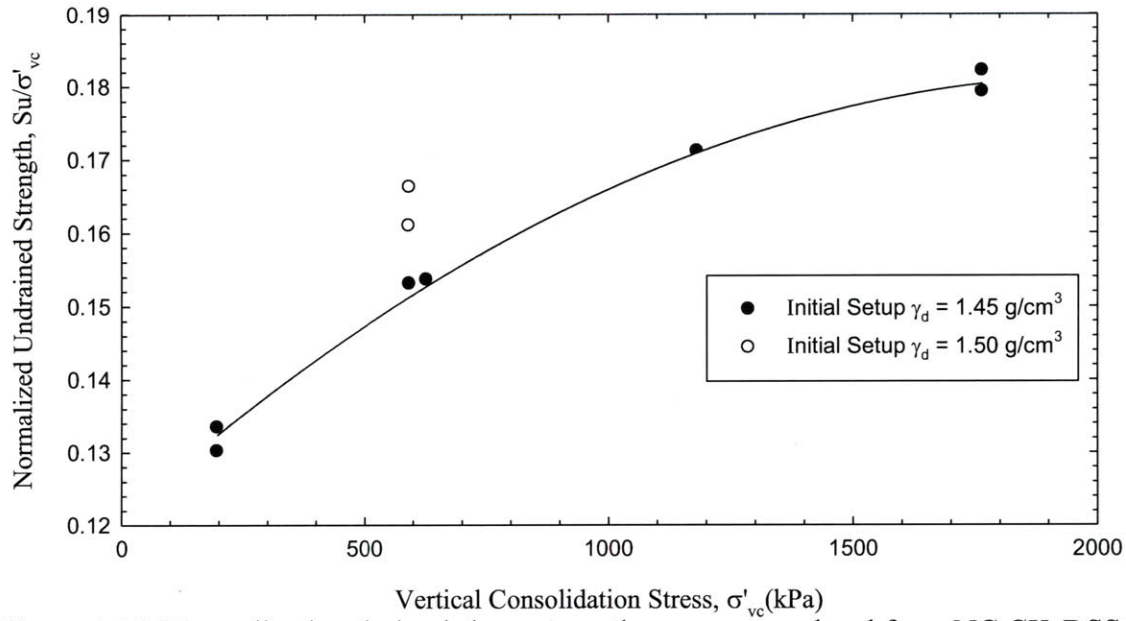


Figure 6-13: Normalized undrained shear strength versus stress level from NC CK<sub>0</sub>DSS tests with different initial setup densities

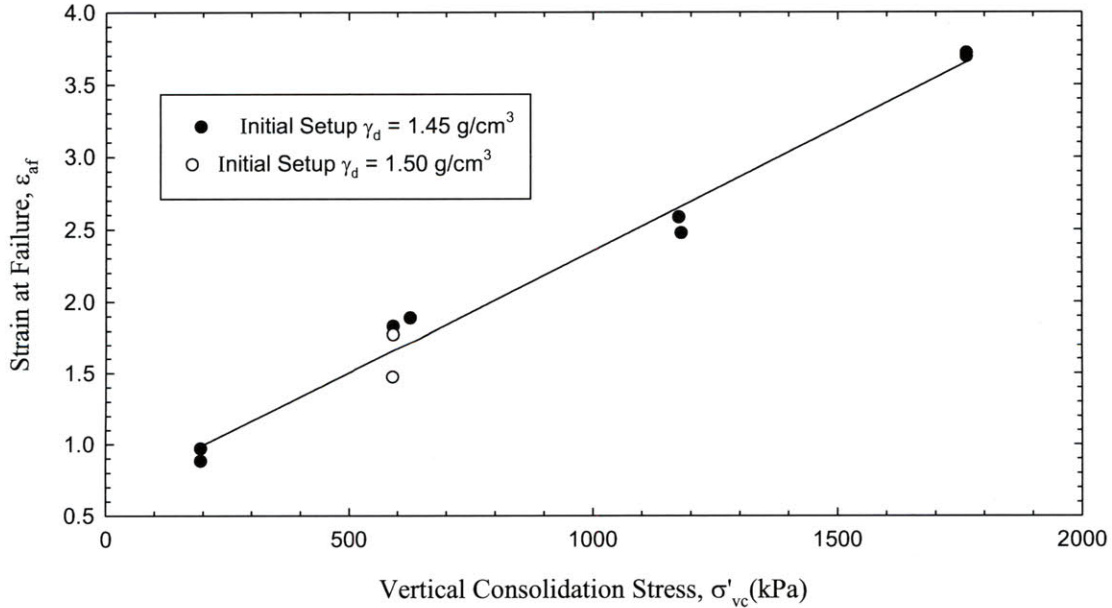


Figure 6-14: Strain at failure versus stress level from NC CK<sub>0</sub>DSS tests with different initial setup densities

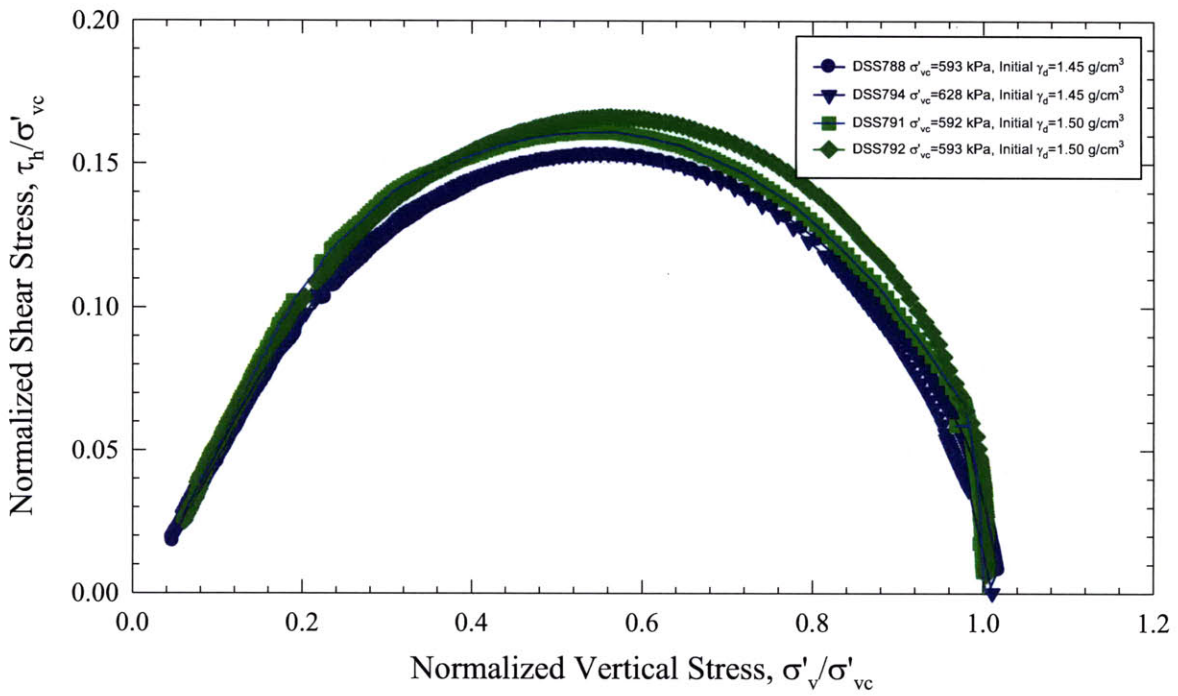


Figure 6-15: Normalized effective stress paths (close up view) from NC CK<sub>0</sub>DSS tests of different initial density

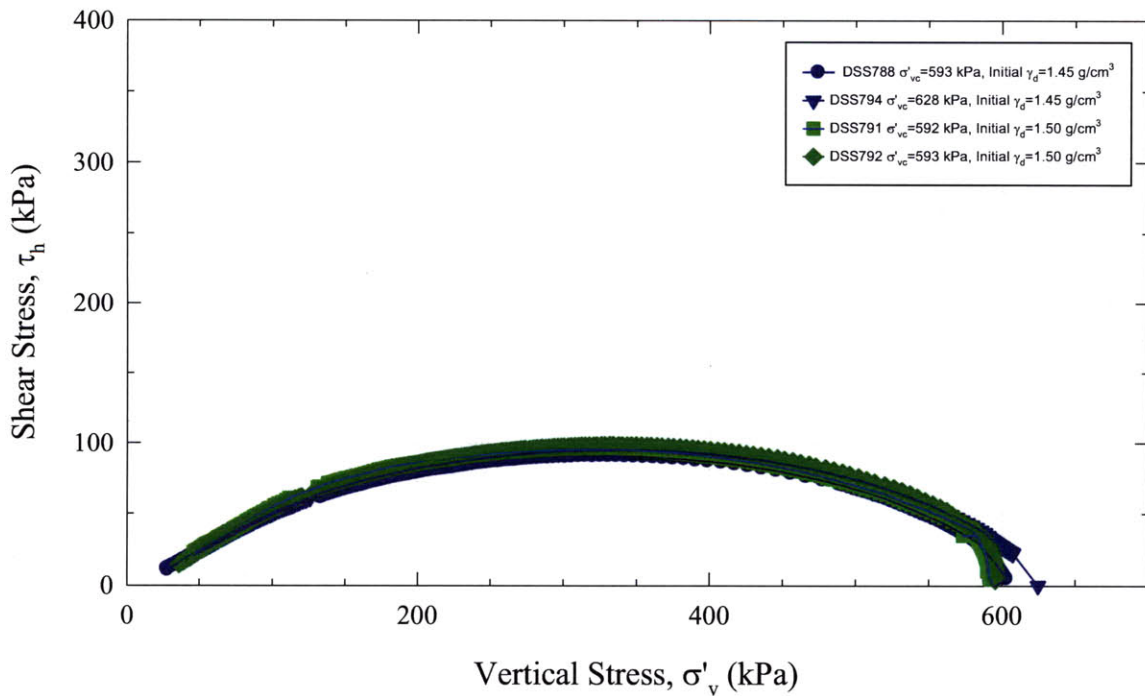


Figure 6-16: Effective stress paths for NC CK<sub>0</sub>DSS tests of different initial density

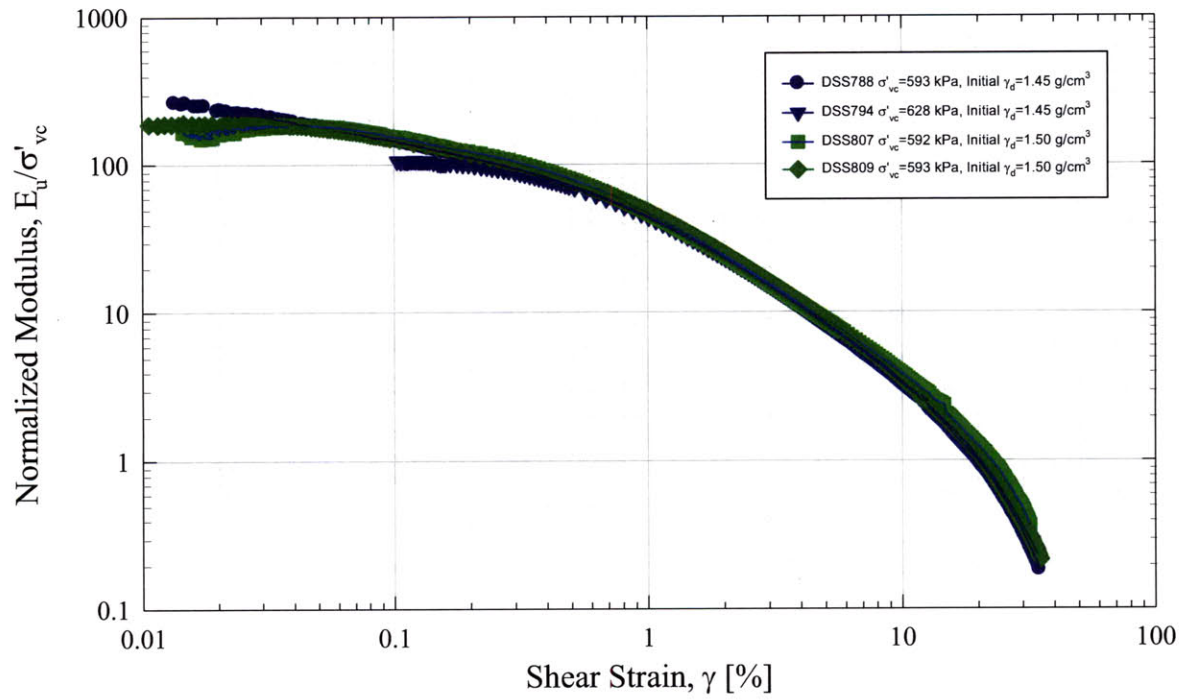


Figure 6-17: Normalized undrained secant modulus versus shear strain from NC  $CK_0$ DSS tests of different initial density

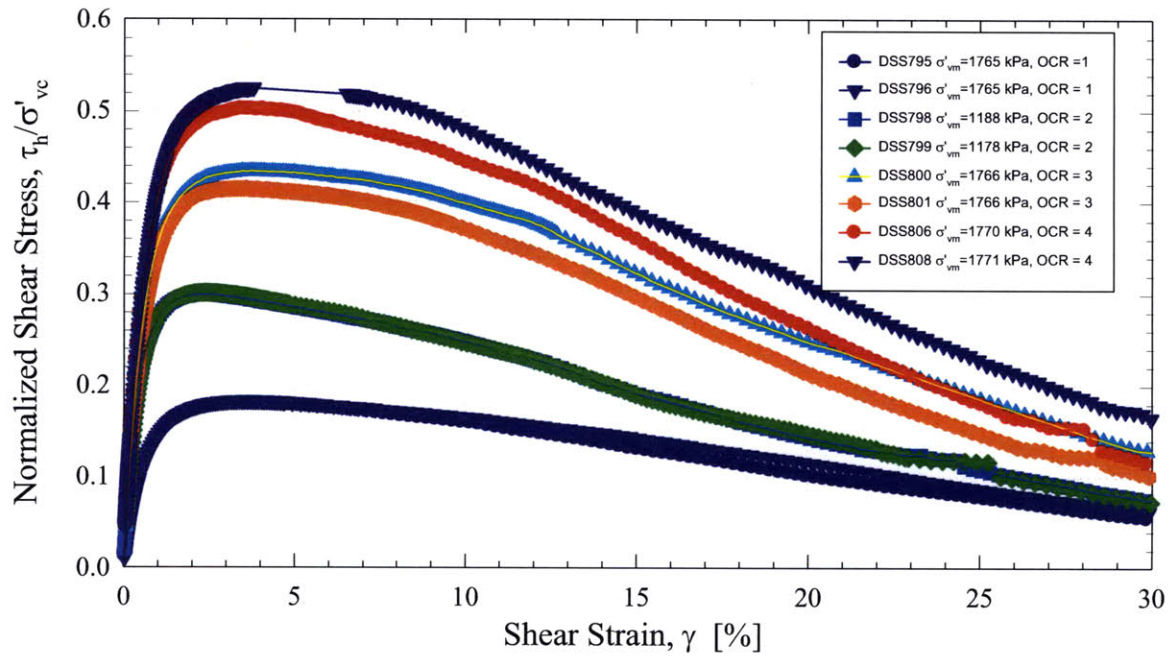


Figure 6-18: Normalized stress-strain curves from OCR=1, 2, 3, and 4 CK<sub>0</sub>DSS tests (normalized to the vertical consolidation stress,  $\sigma'_{\text{vc}}$ )

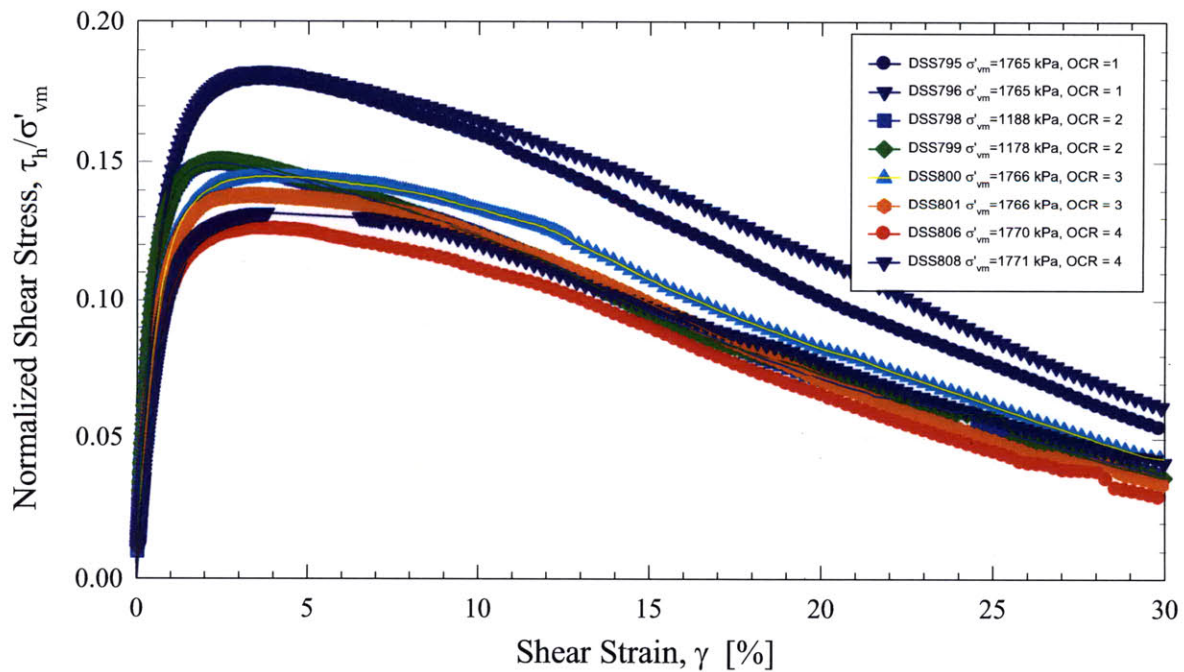


Figure 6-19: Normalized stress-strain curves from OCR=1, 2, 3, and 4 CK<sub>0</sub>DSS tests (normalized to the maximum vertical consolidation stress,  $\sigma'_{\text{vm}}$ )

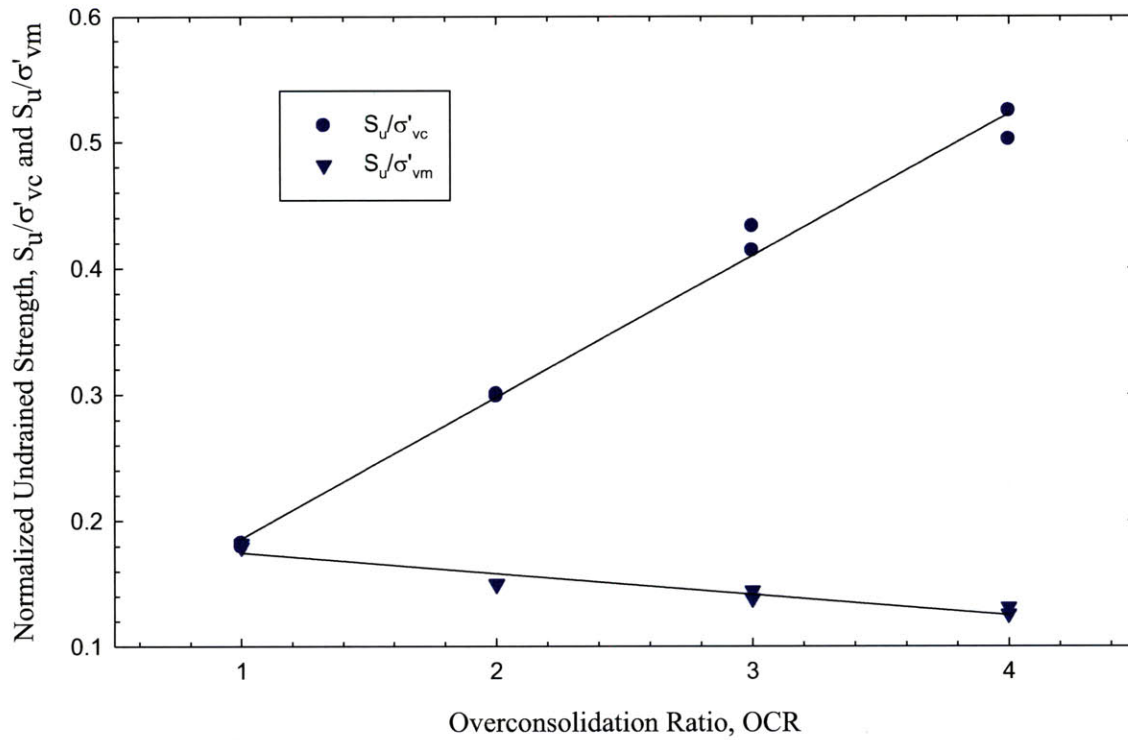


Figure 6-20: Normalized Undrained Shear strength variations with OCR from  $CK_0$ DSS tests

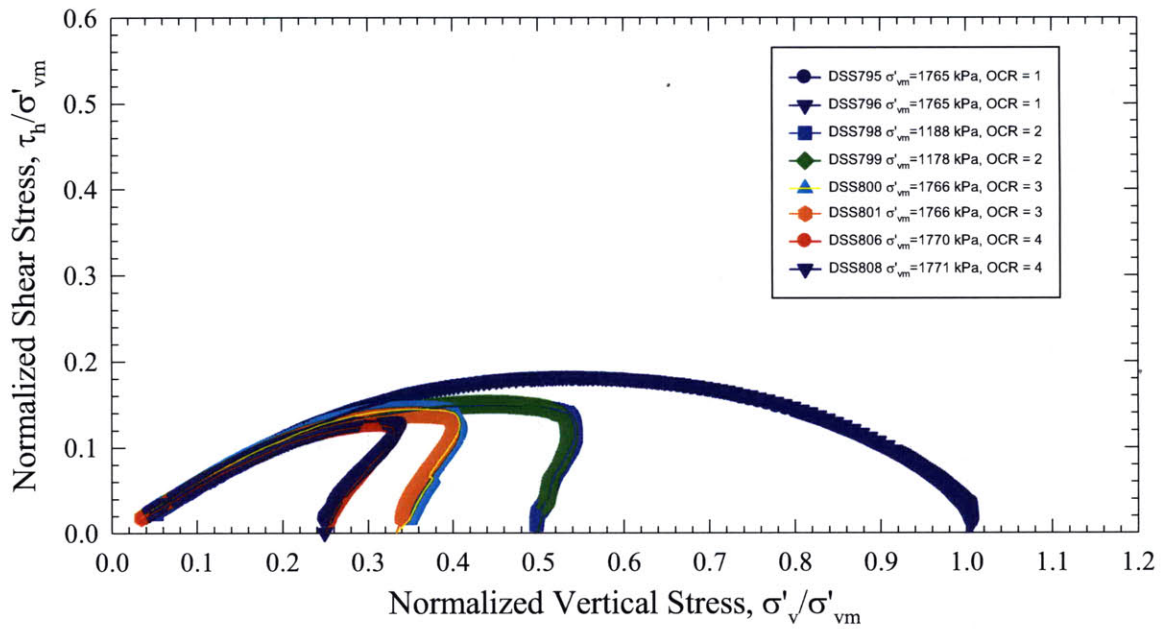


Figure 6-21: Normalized effective stress paths from OCR = 1, 2, 3, and 4  $CK_0$ DSS tests (normalized to the maximum vertical consolidation stress,  $\sigma'_{vm}$ )

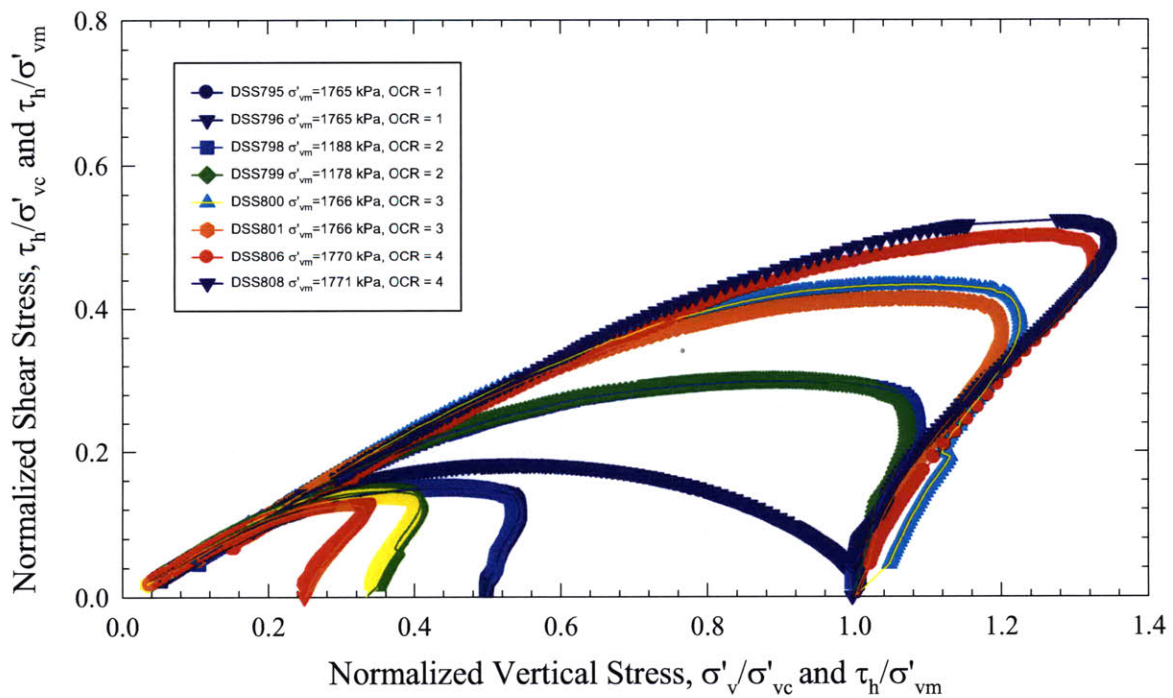


Figure 6-22: Normalized effective stress paths from OCR = 1, 2, 3, and 4  $CK_0$ DSS tests (normalized to the vertical consolidation stress,  $\sigma'_{vc}$ )

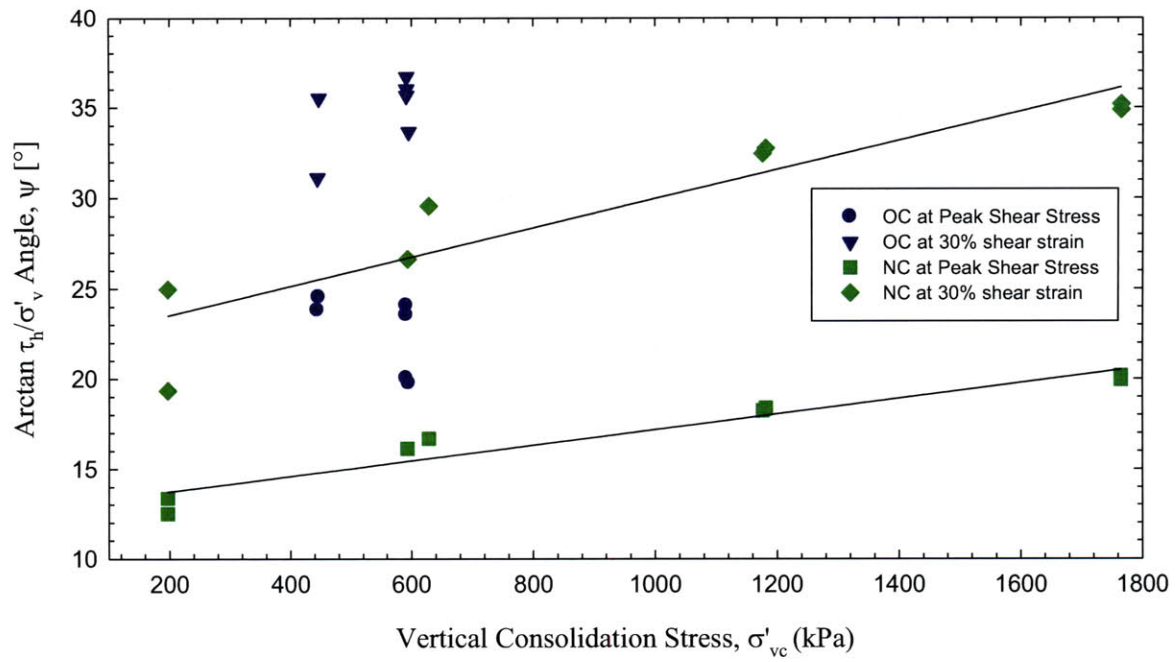


Figure 6-23: Friction angle versus vertical consolidation effective stress from OCR = 1, 2, 3, and 4 CK<sub>0</sub>DSS tests

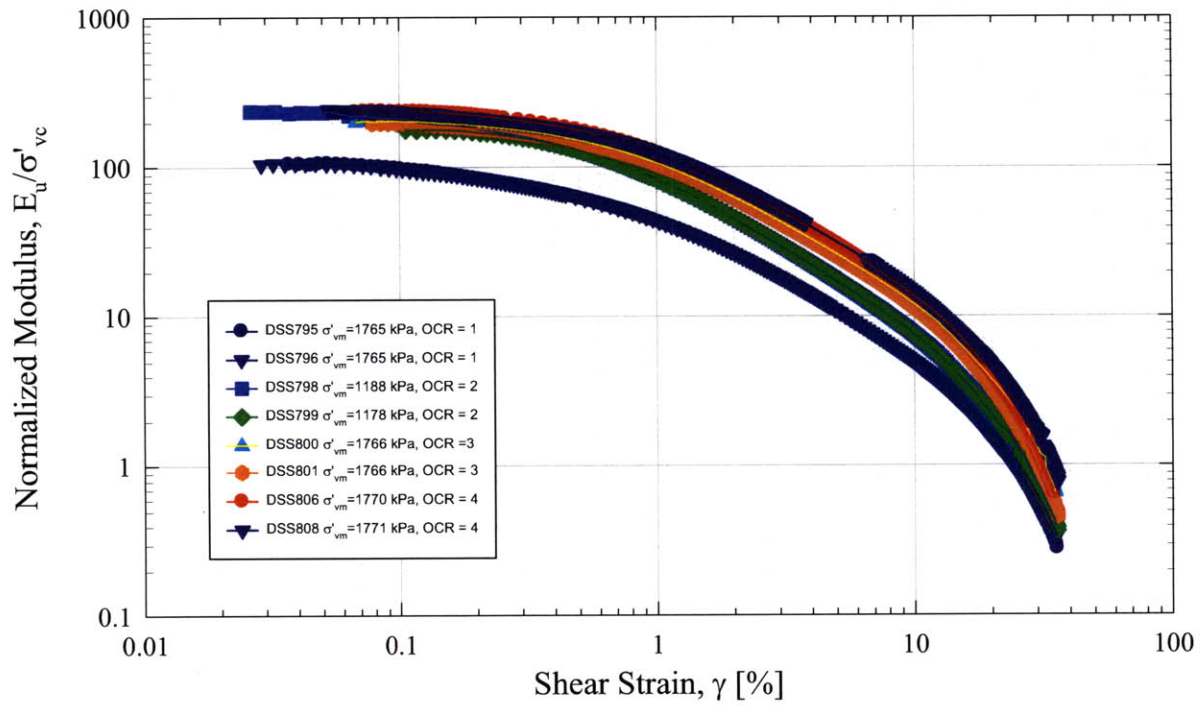


Figure 6-24: Normalized undrained secant modulus ( $E_u/\sigma'_{vc}$ ) versus shear strain from OCR = 1, 2, 3, and 4 CK<sub>0</sub>DSS tests

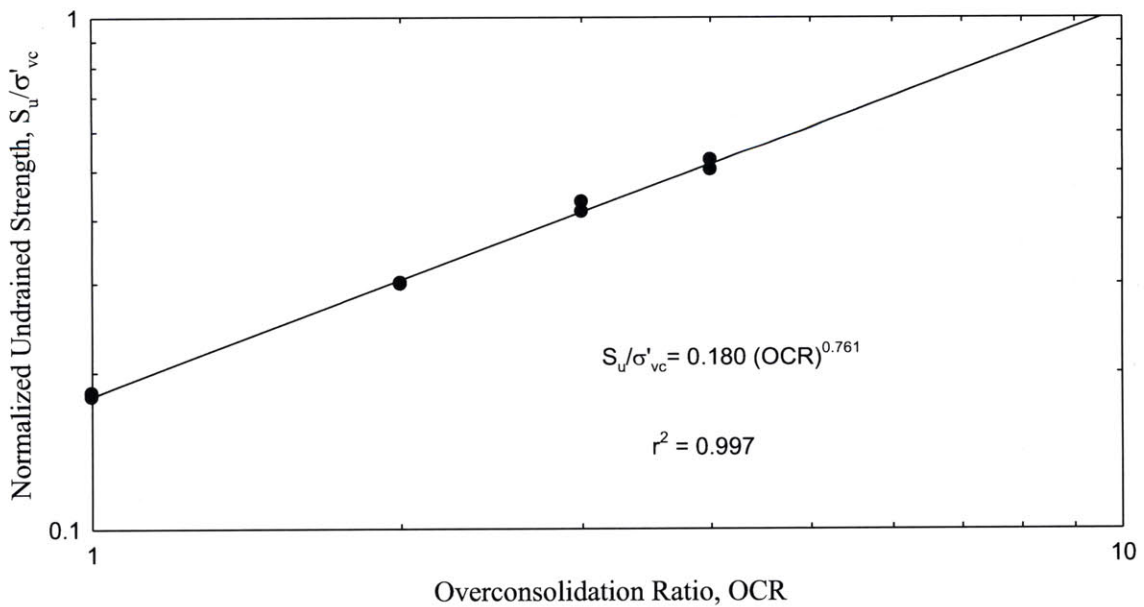


Figure 6-25: Normalized undrained strength versus OCR from CK<sub>0</sub>DSS tests



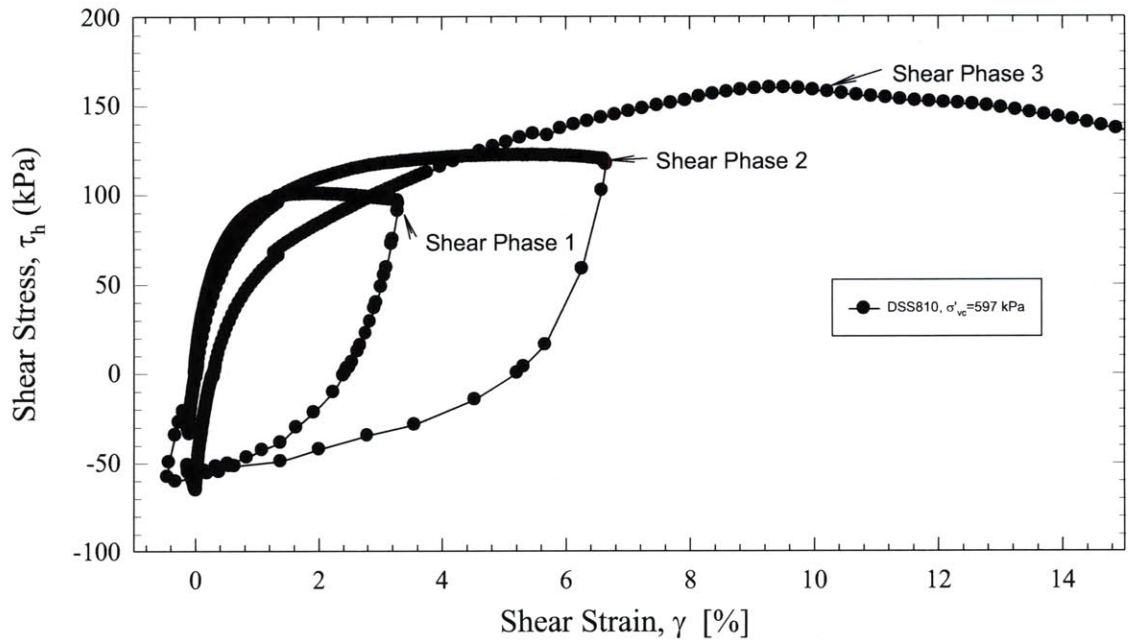


Figure 6-26: Shear stress versus strain from a typical cyclic  $CK_0$ DSS test

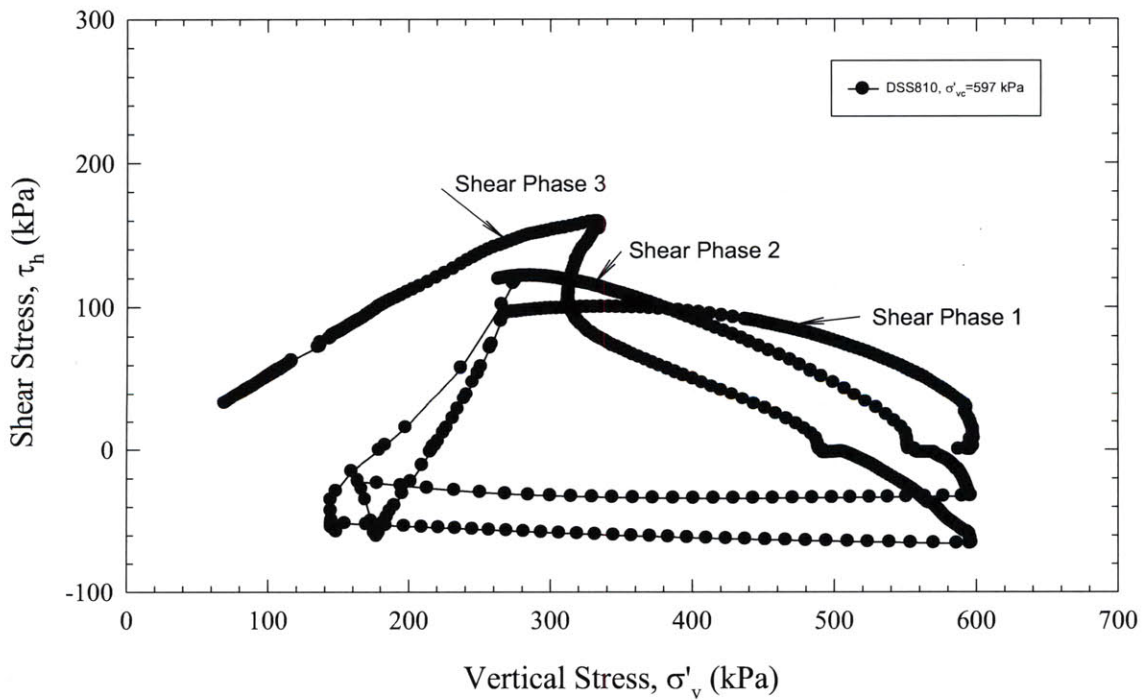


Figure 6-27: Effective stress path from a typical cyclic  $CK_0$ DSS test

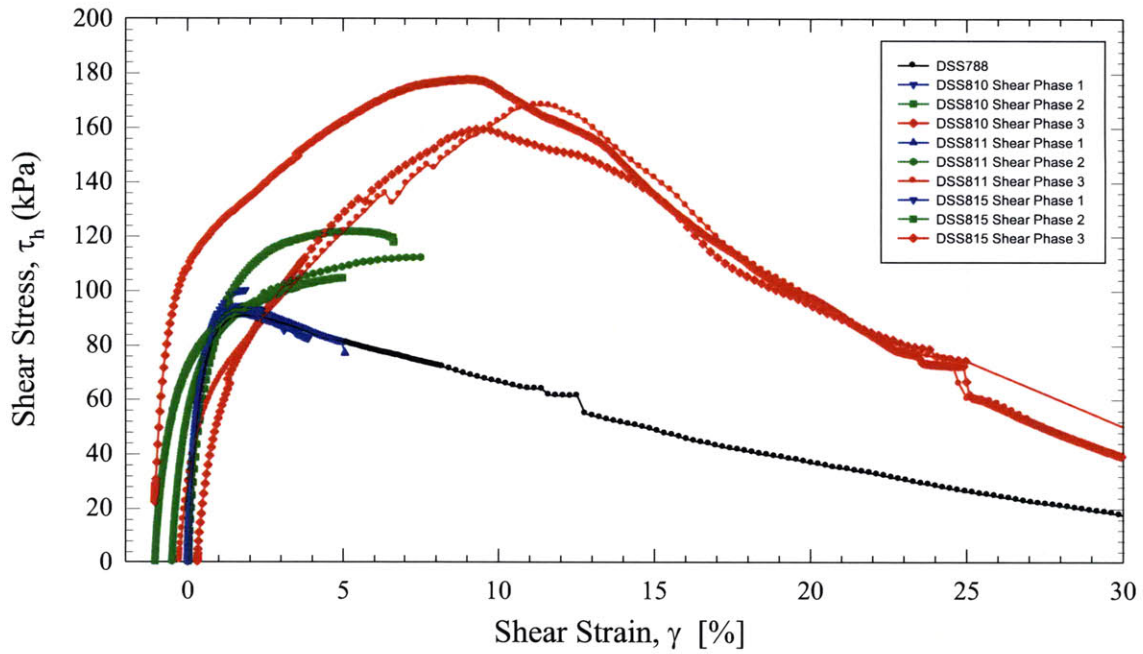


Figure 6-28: Stress-Strain curves from Cyclic  $CK_0$ DSS tests (standard NC  $CK_0$ DSS included for comparison)

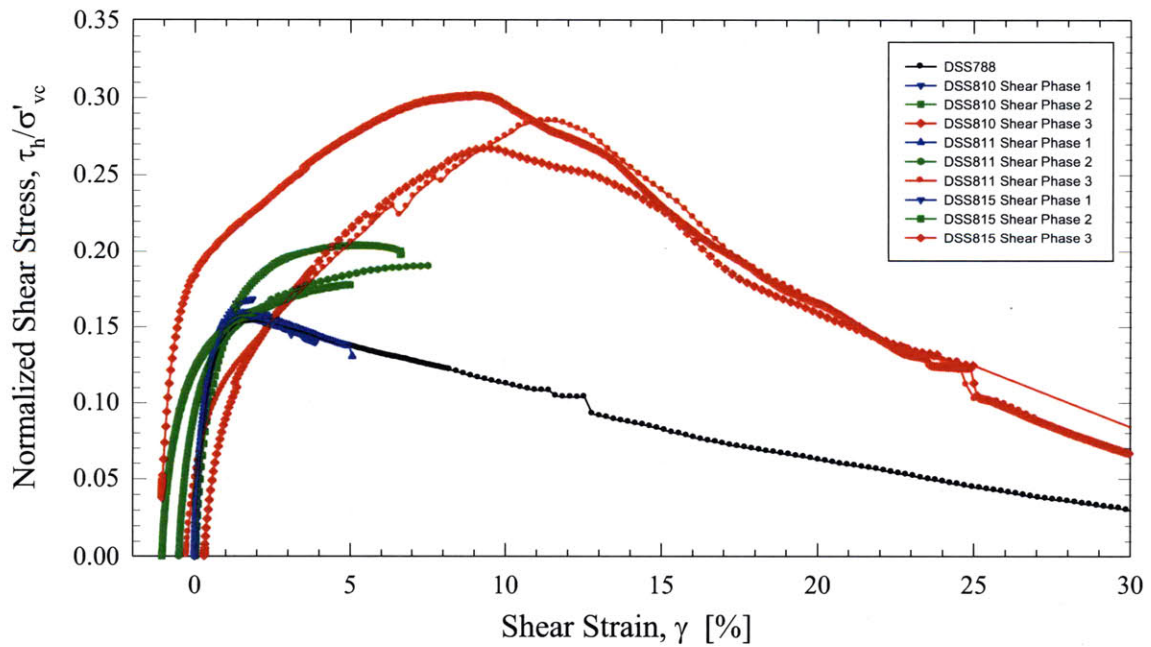


Figure 6-29: Normalized Stress-Strain curves from Cyclic  $CK_0$ DSS tests (standard NC  $CK_0$ DSS included for comparison)

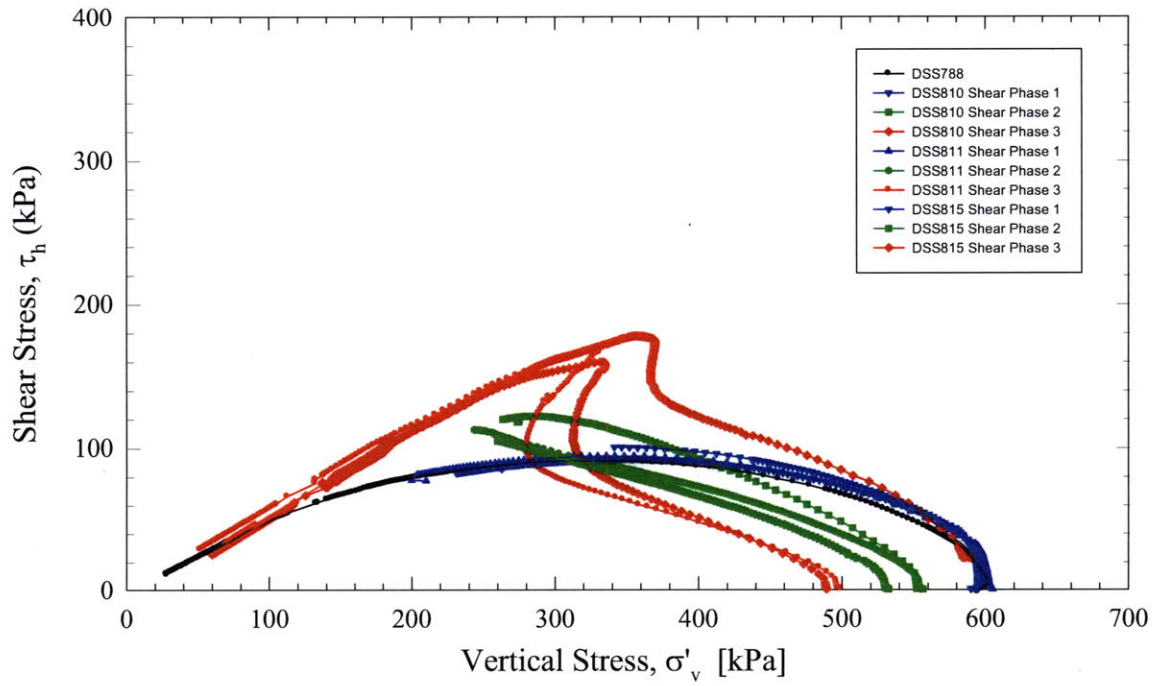


Figure 6-30: Effective stress paths from cyclic  $CK_0$ DSS tests

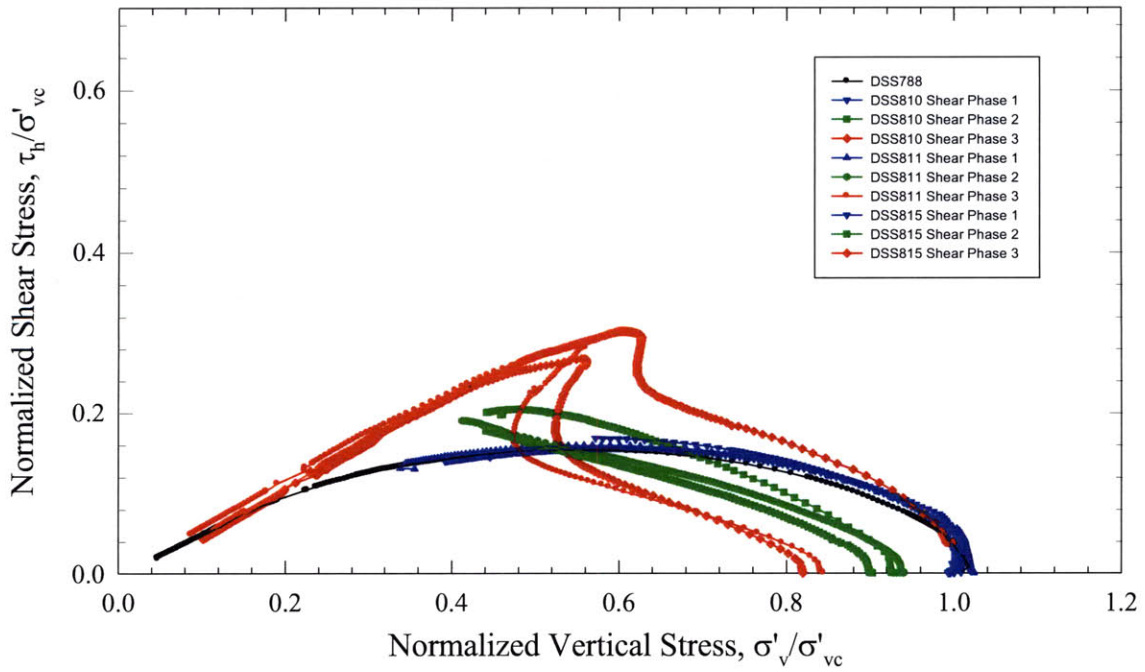


Figure 6-31: Normalized effective stress paths from cyclic  $CK_0$ DSS tests

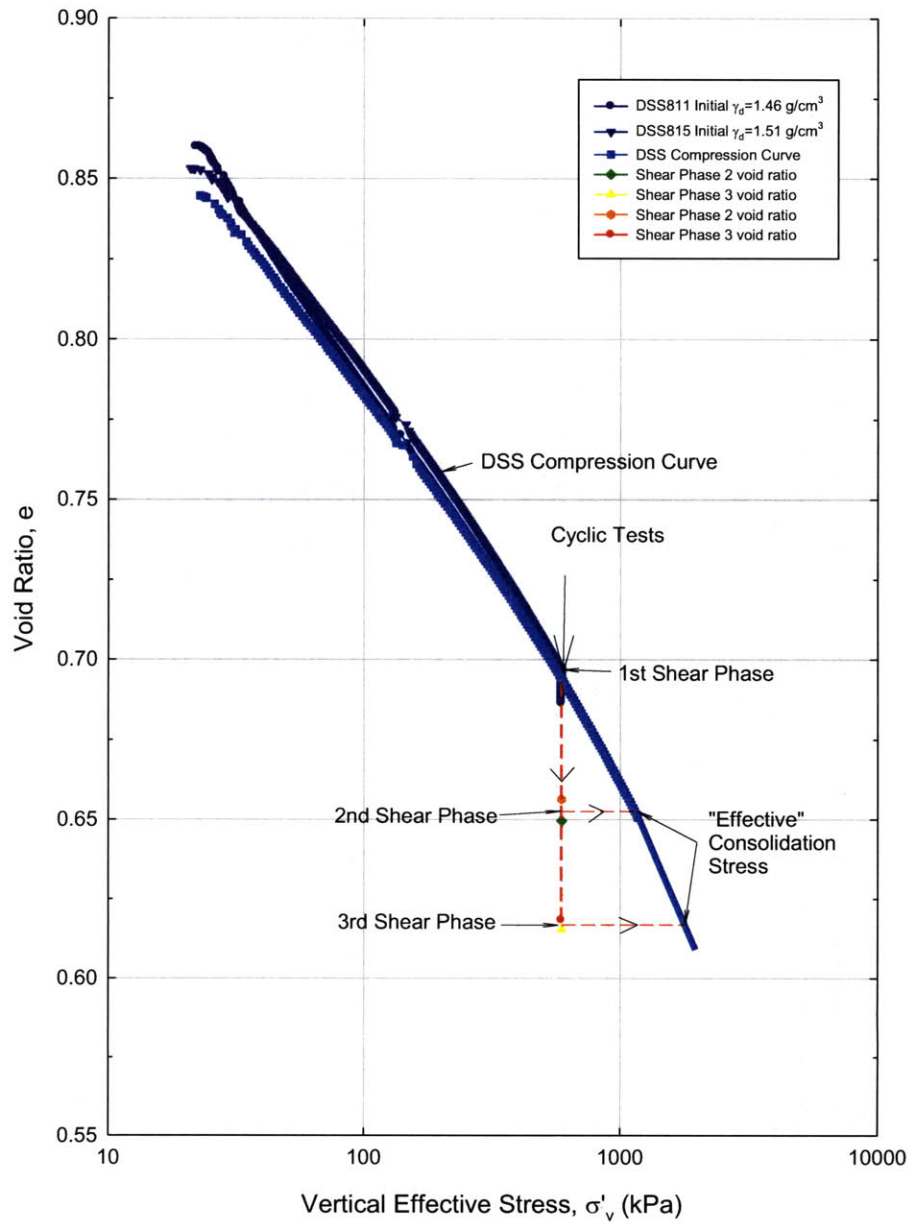


Figure 6-32: Compression behavior in  $e$ - $\log \sigma'_v$  space from cyclic  $CK_0$ DSS tests

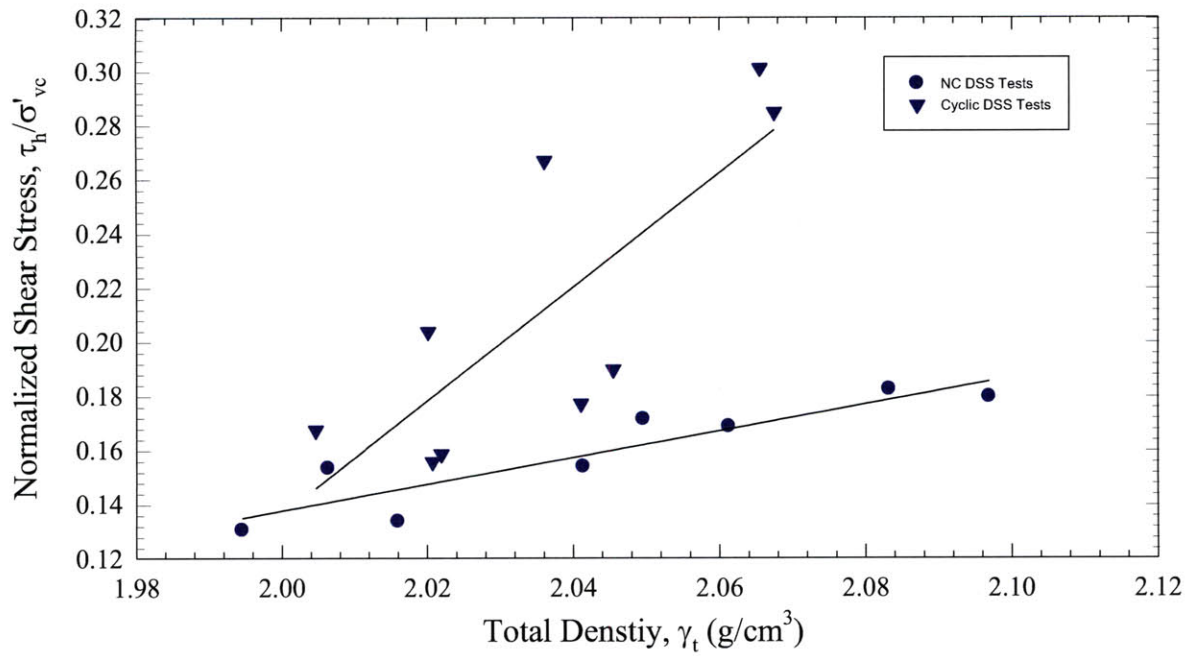


Figure 6-33: Normalized shear strength versus total density from NC and cyclic CK<sub>0</sub>DSS tests

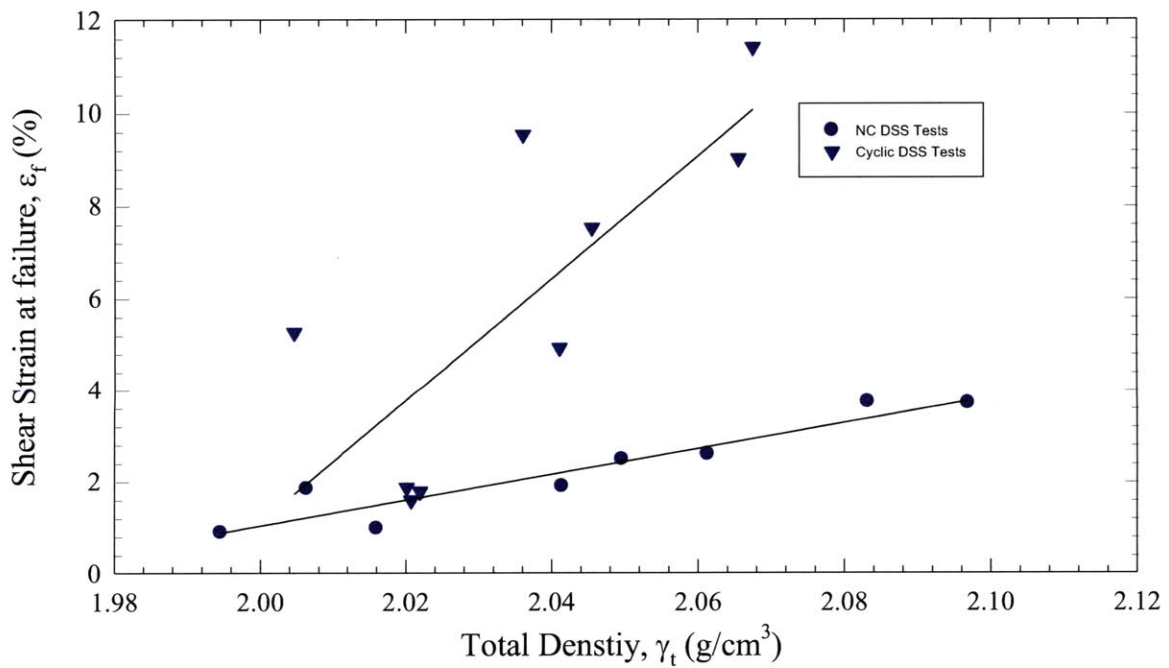


Figure 6-34: Shear strain at failure versus total density from all NC and cyclic CK<sub>0</sub>DSS tests

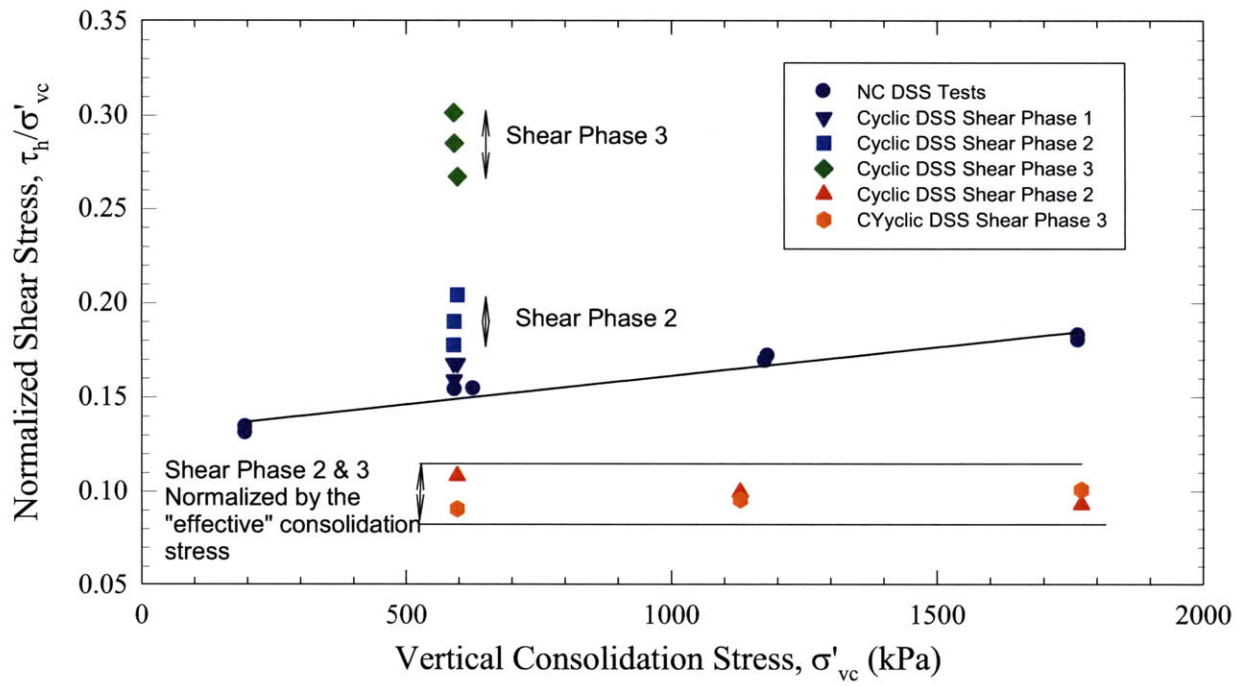


Figure 6-35: Undrained strength ratio versus vertical consolidation stress for NC and cyclic  $CK_0$ DSS tests

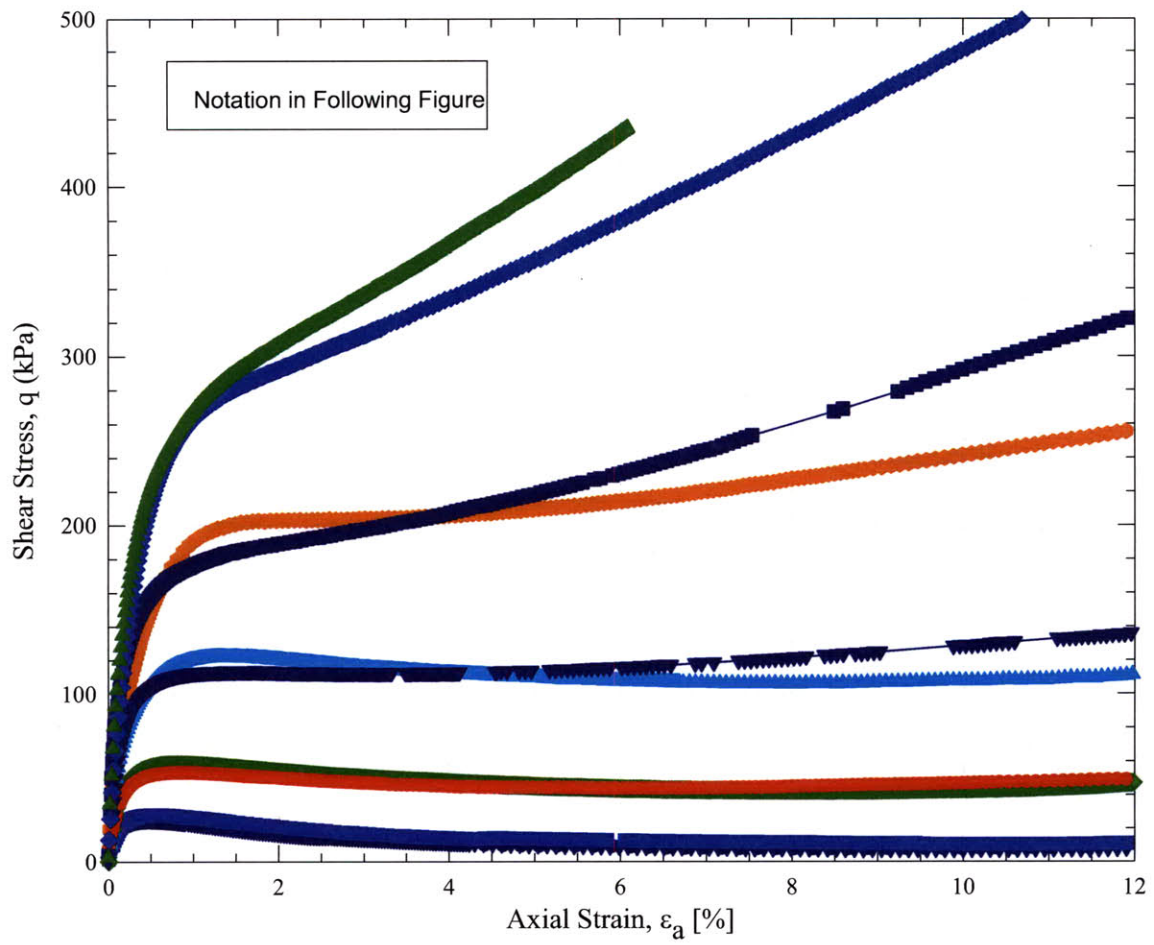


Figure 6-36: Stress-strain curves from CIUC triaxial tests

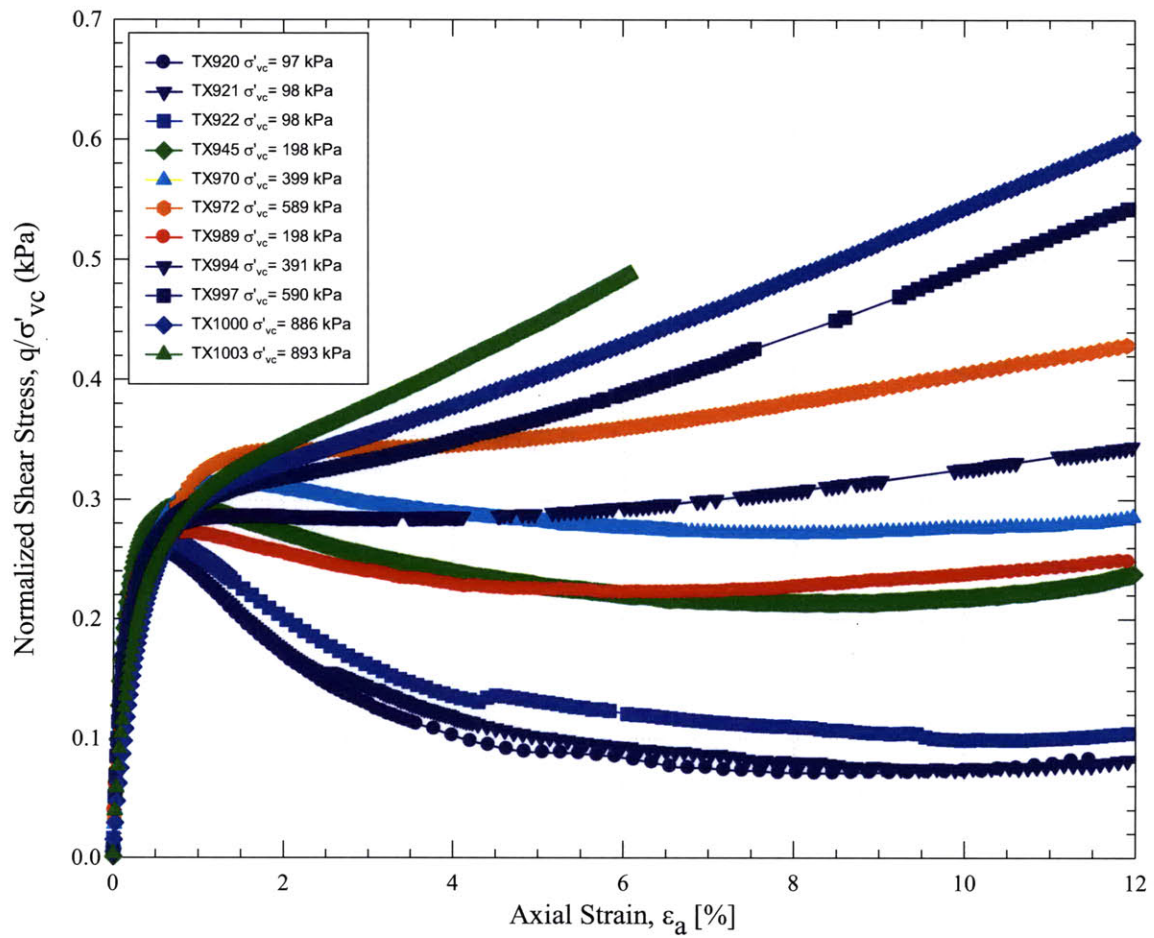


Figure 6-37: Normalized stress-strain curves from CIUC triaxial tests



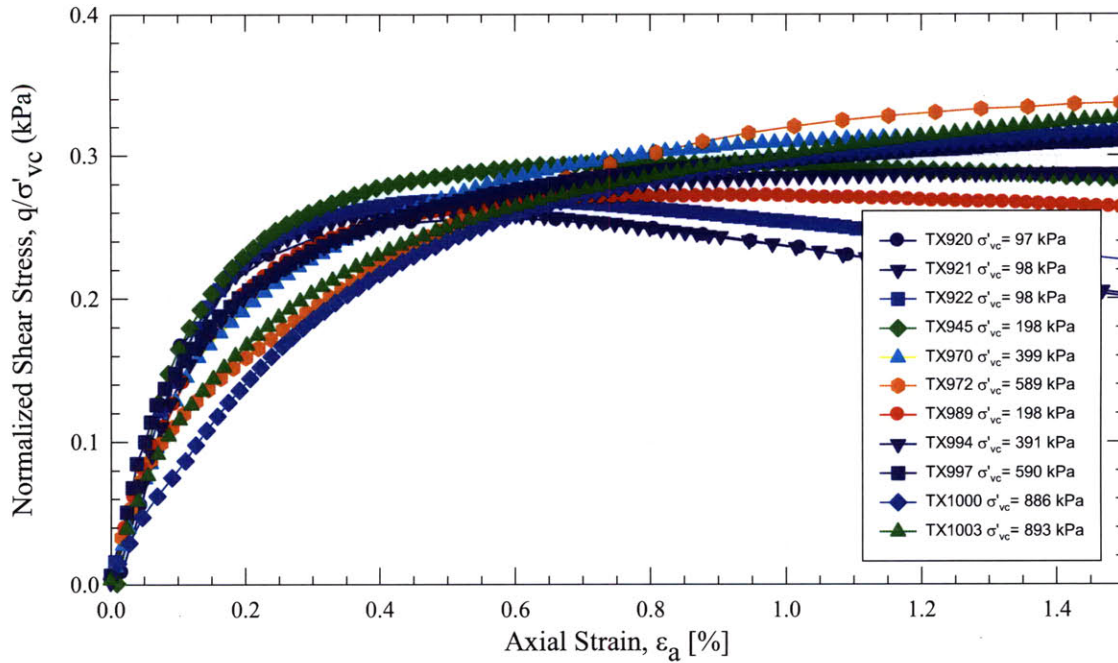


Figure 6-38: Normalized stress-strain curves (small strains) from CIUC triaxial tests

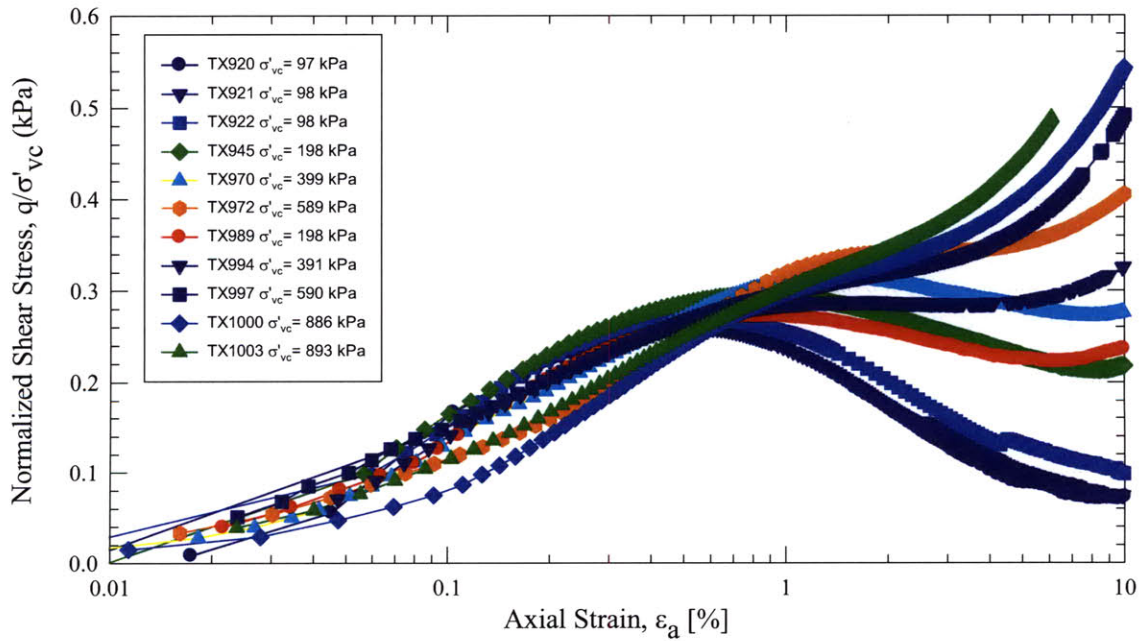


Figure 6-39: Normalized stress- (log) strain curves from CIUC triaxial tests

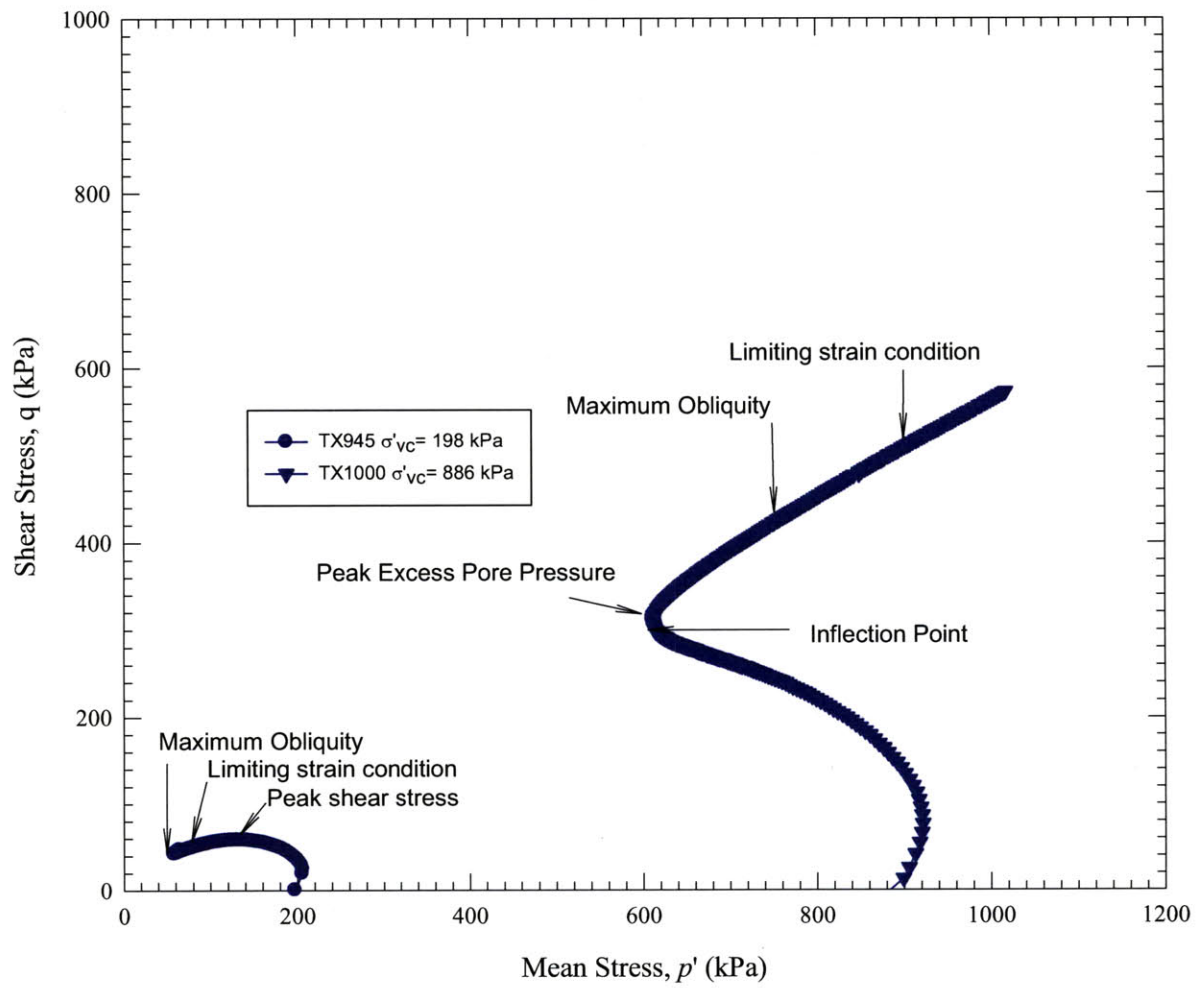


Figure 6-40: Effective stress paths from CIUC triaxial tests showing the failure criteria used this research

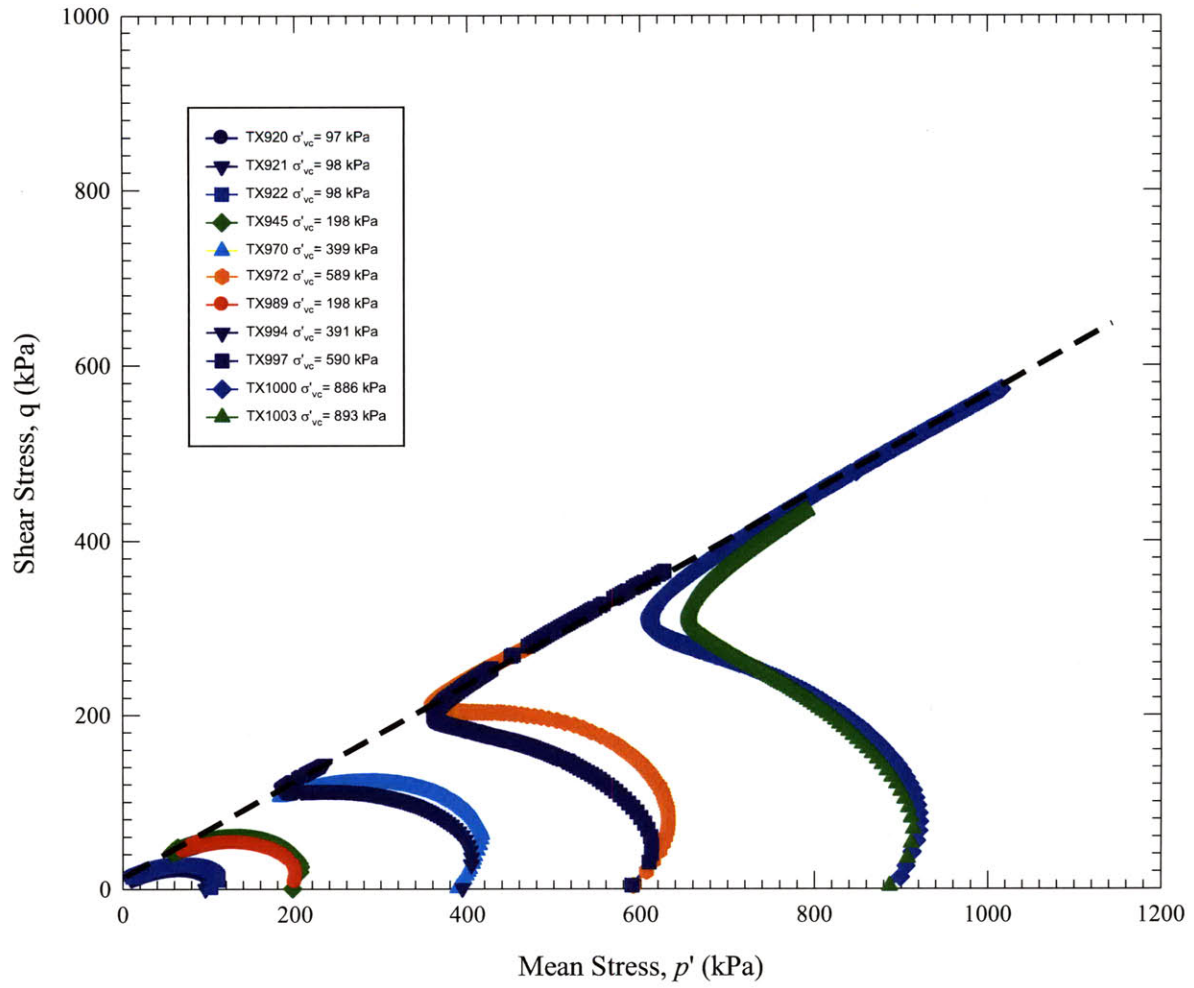


Figure 6-41: Effective stress paths from CIUC triaxial tests

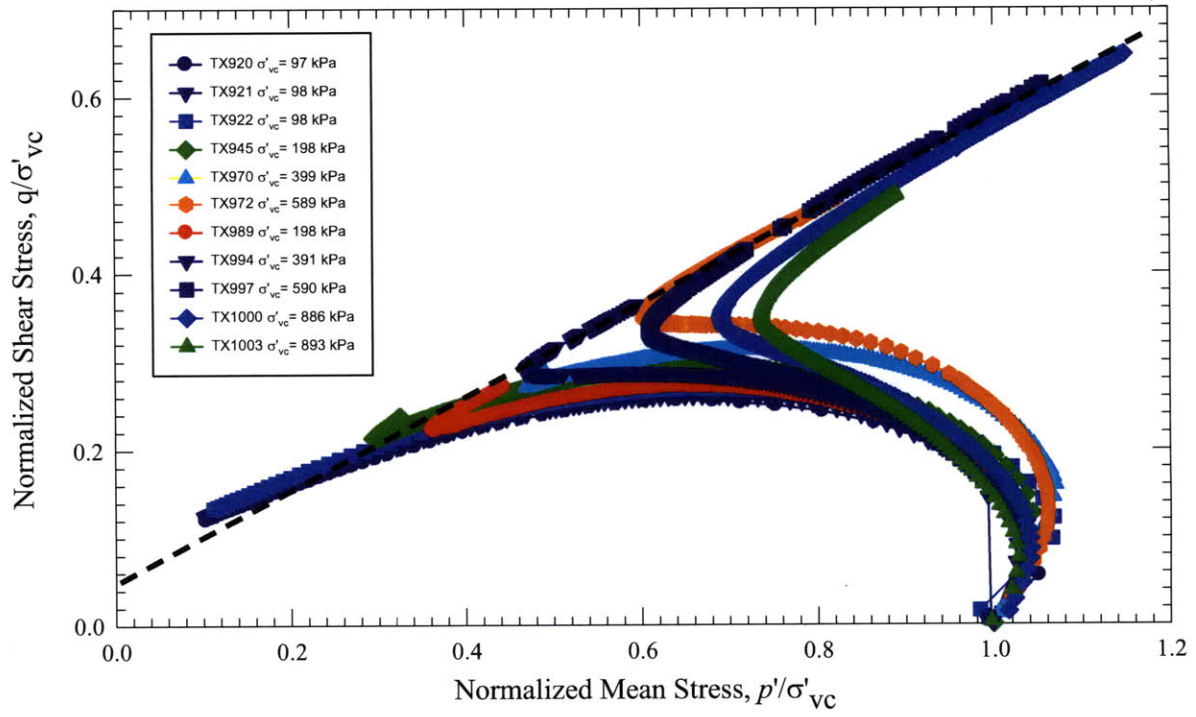


Figure 6-42: Normalized effective stress paths from CIUC triaxial tests

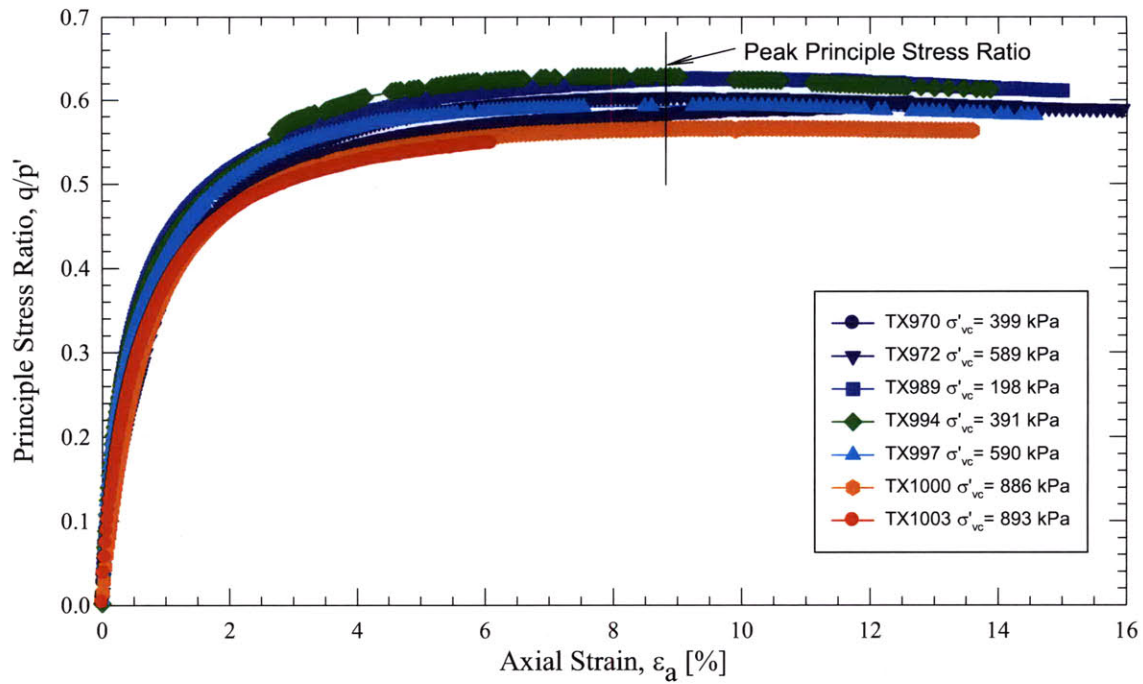


Figure 6-43: Principle stress ratio versus axial strain from CIUC triaxial tests

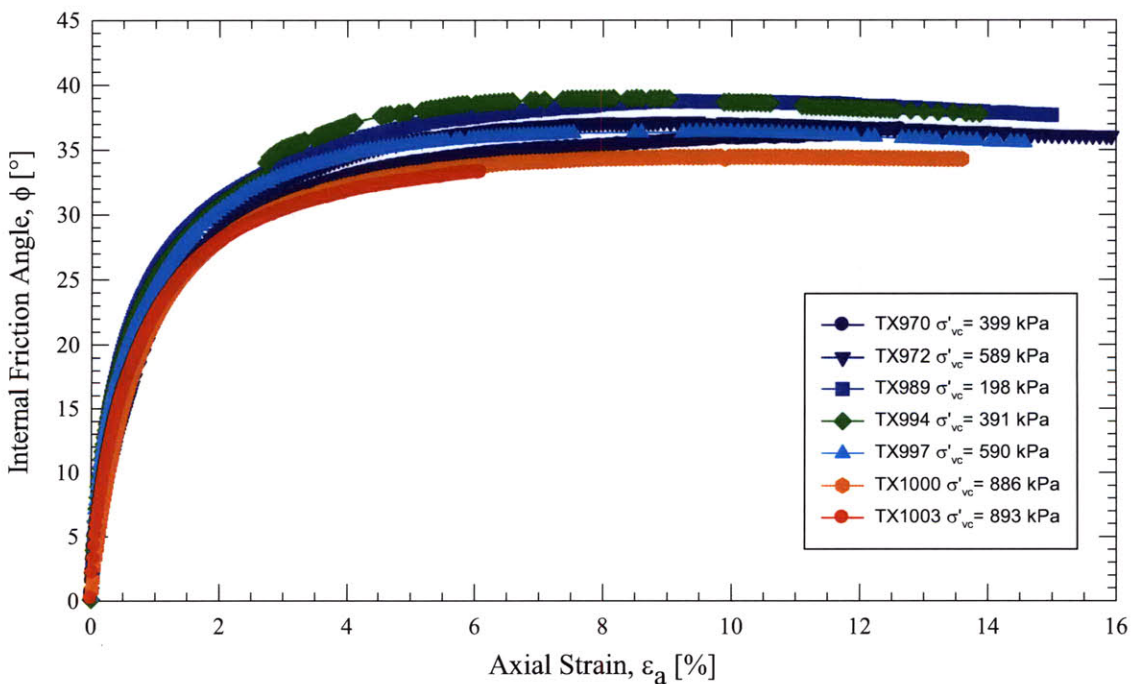


Figure 6-44: Friction angle versus axial strain from CIUC triaxial tests

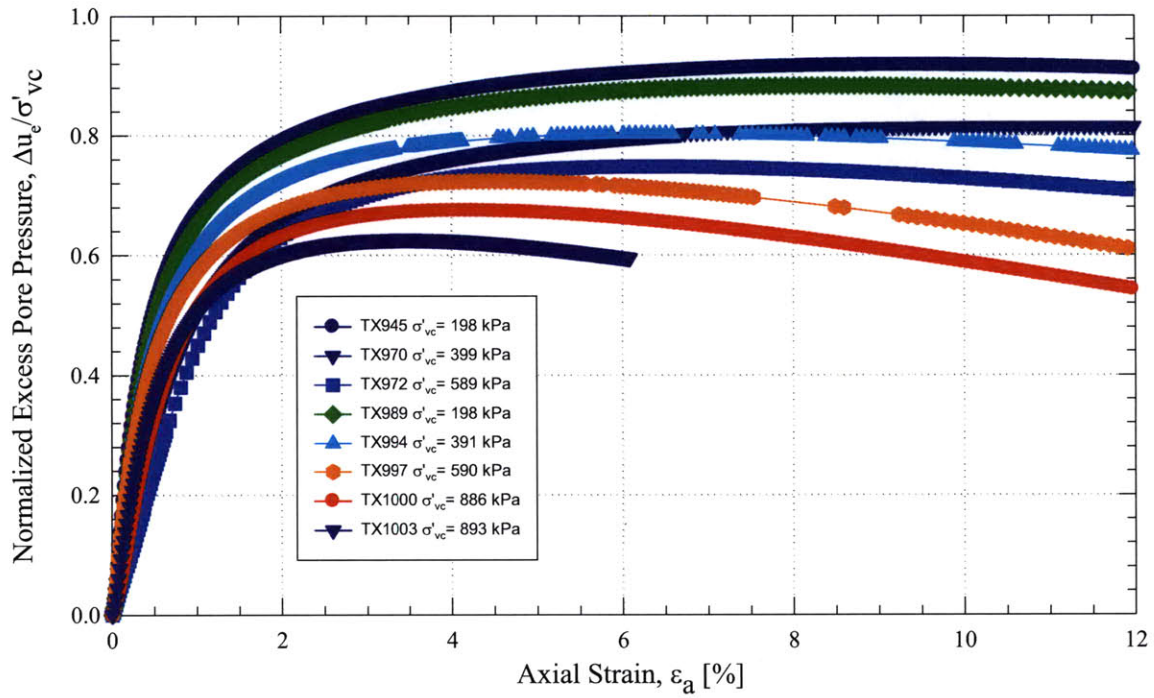


Figure 6-45: Normalized excess pore pressure versus strain from CIUC triaxial tests

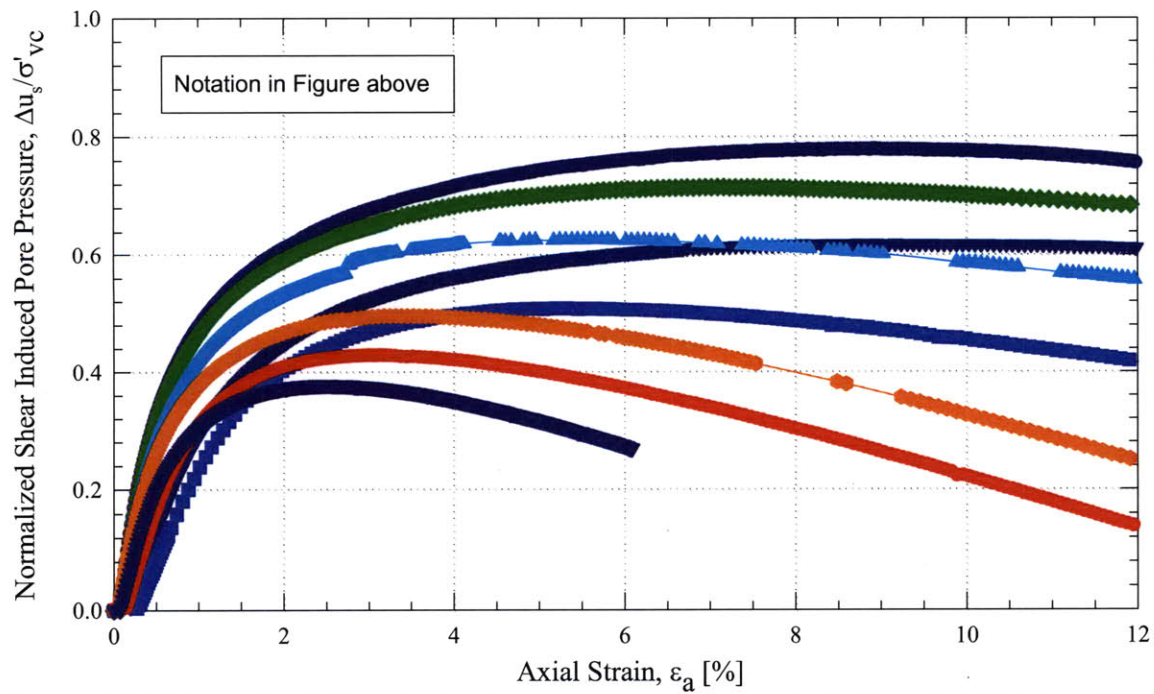


Figure 6-46: Normalized shear induced pore pressure versus strain from CIUC triaxial tests

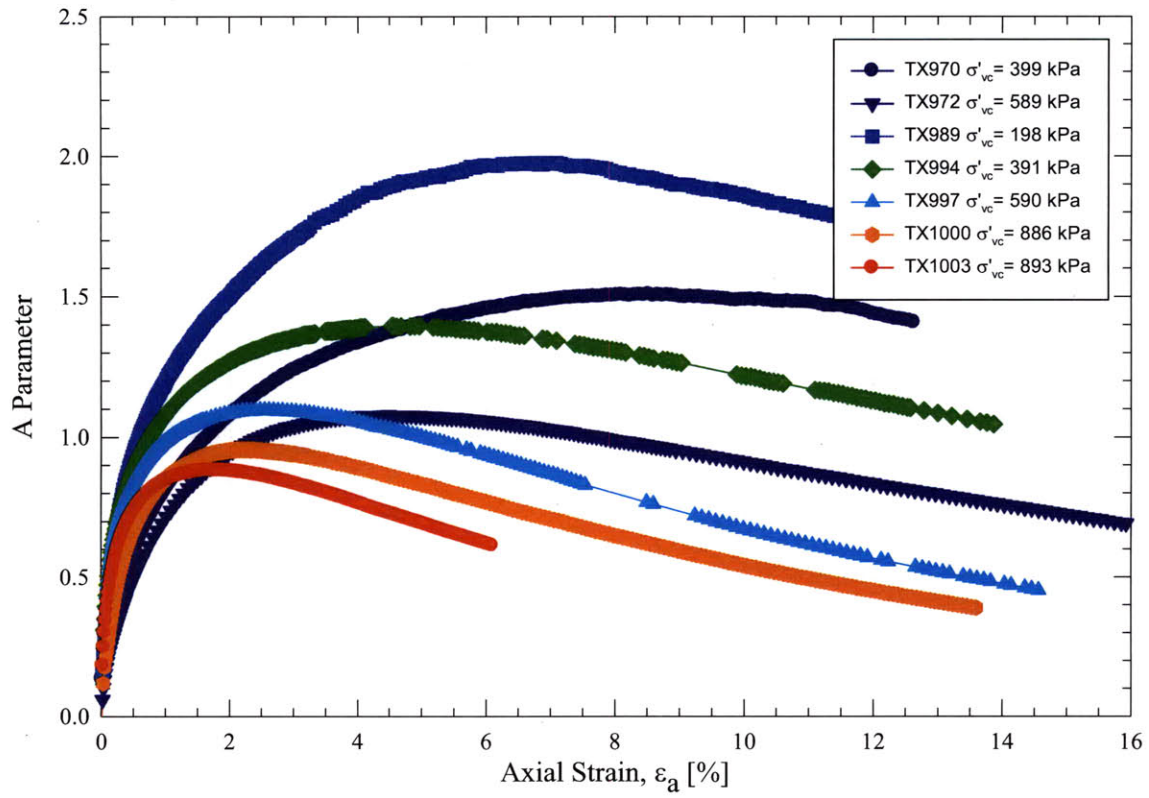


Figure 6-47: Skempton A parameter versus strain from CIUC triaxial tests

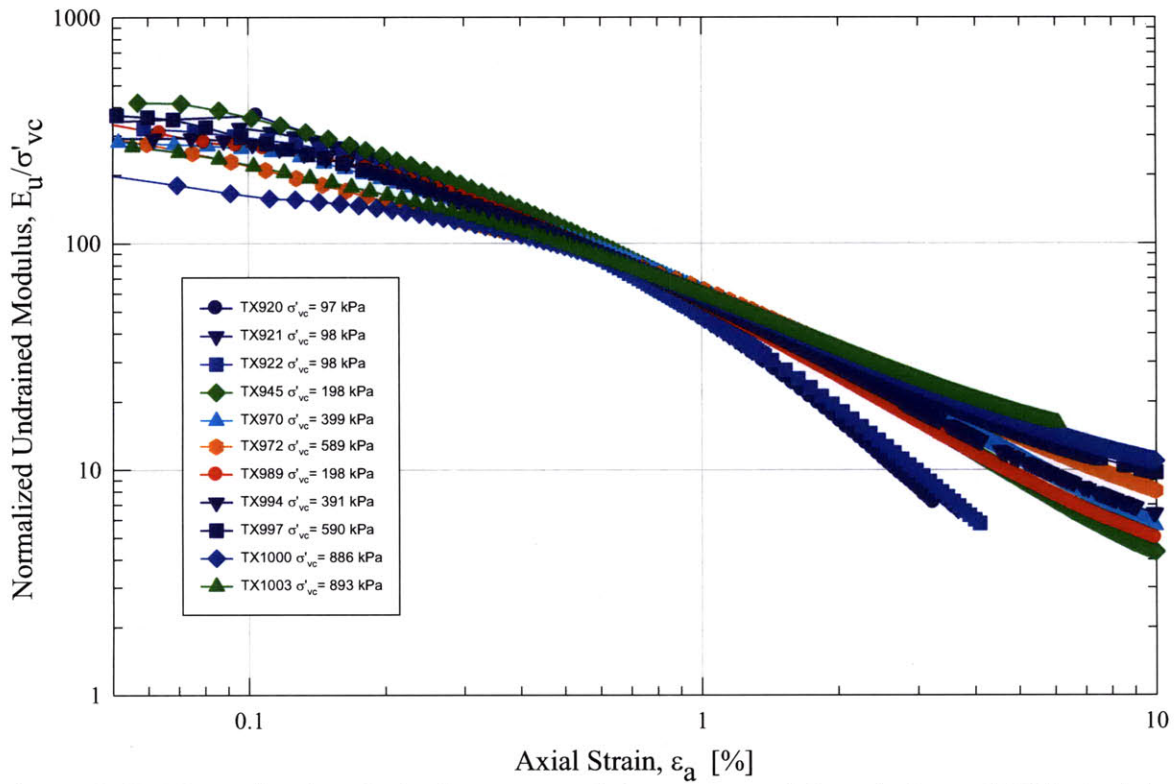


Figure 6-48: Normalized undrained secant modulus versus axial strain from CIUC triaxial tests

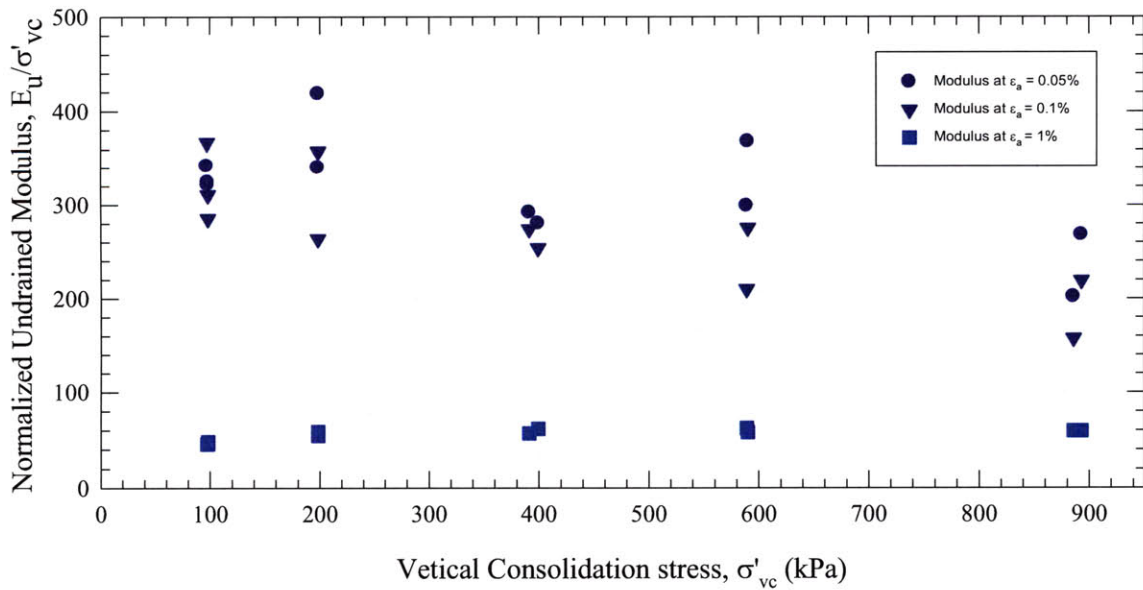


Figure 6-49: Normalized undrained secant modulus versus stress level from CIUC triaxial tests



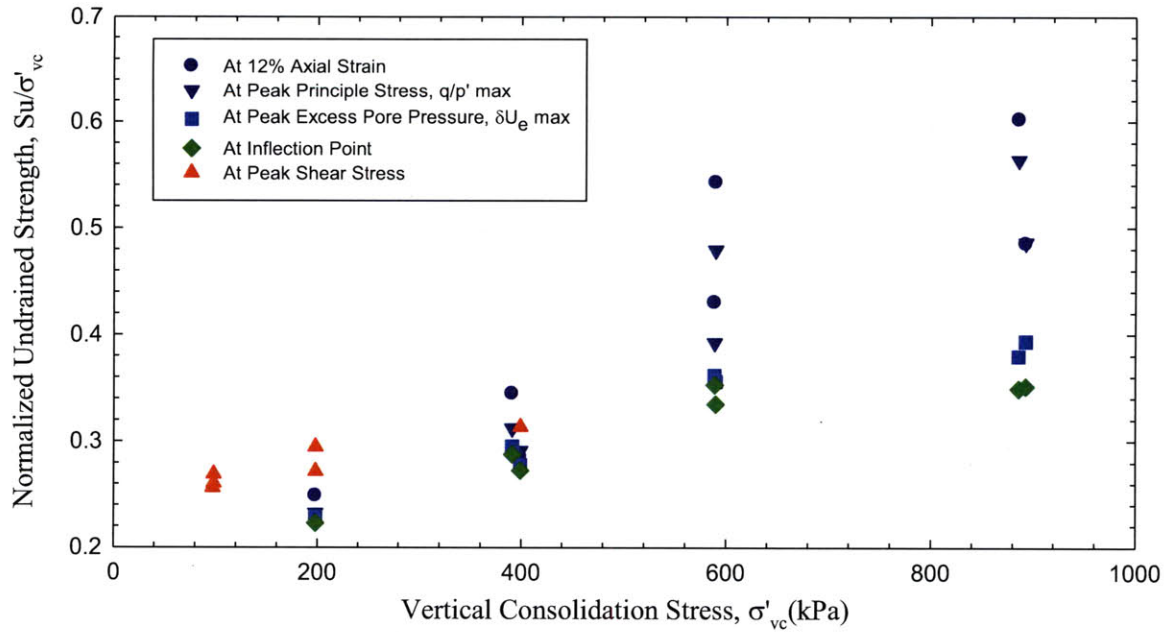


Figure 6-50: Normalized undrained shear strength versus stress level from CIUC triaxial tests

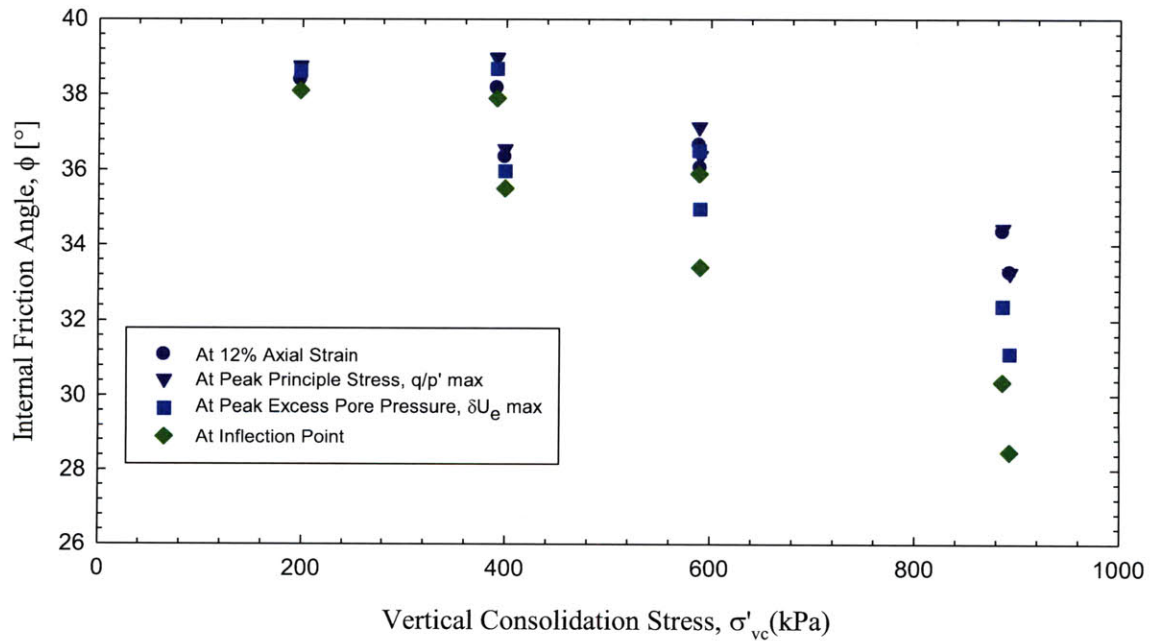


Figure 6-51: Friction angle versus stress level from CIUC triaxial tests

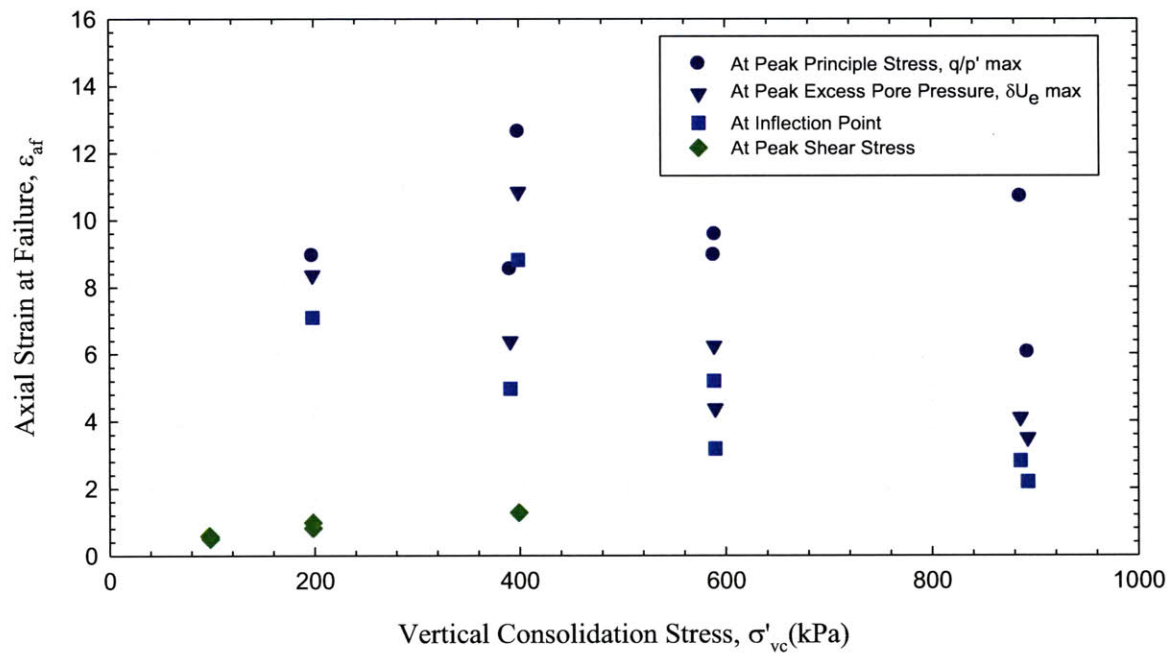


Figure 6-52: Strain at failure versus stress level from CIUC triaxial tests

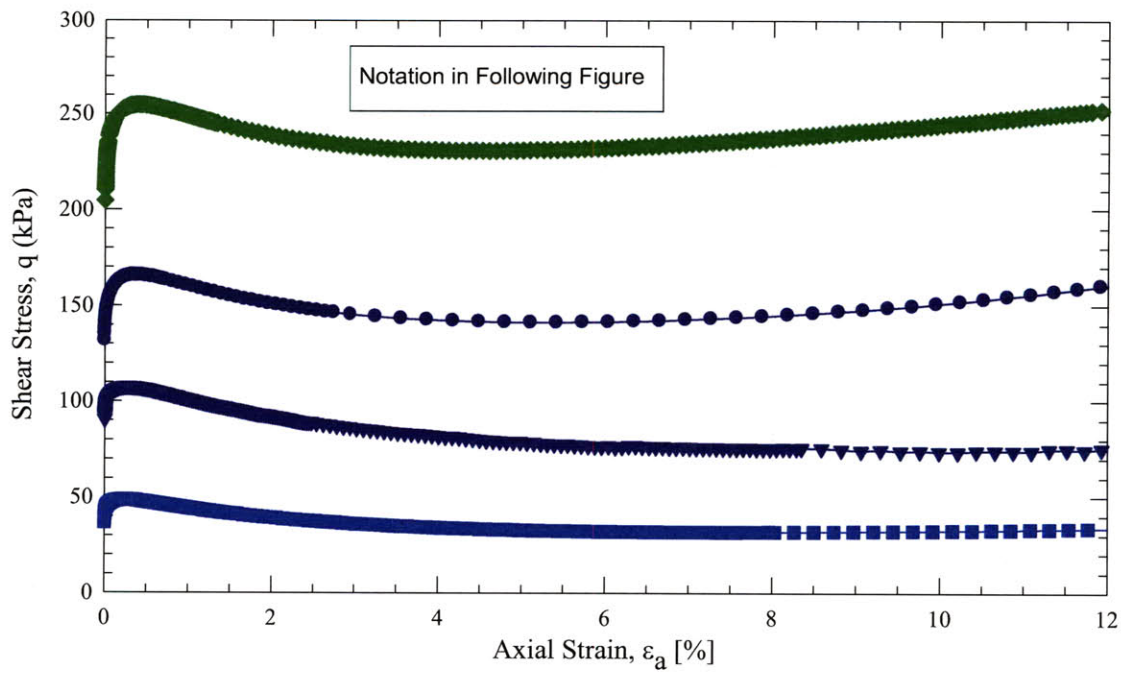


Figure 6-53: Stress-strain curves from CK<sub>0</sub>UC triaxial tests

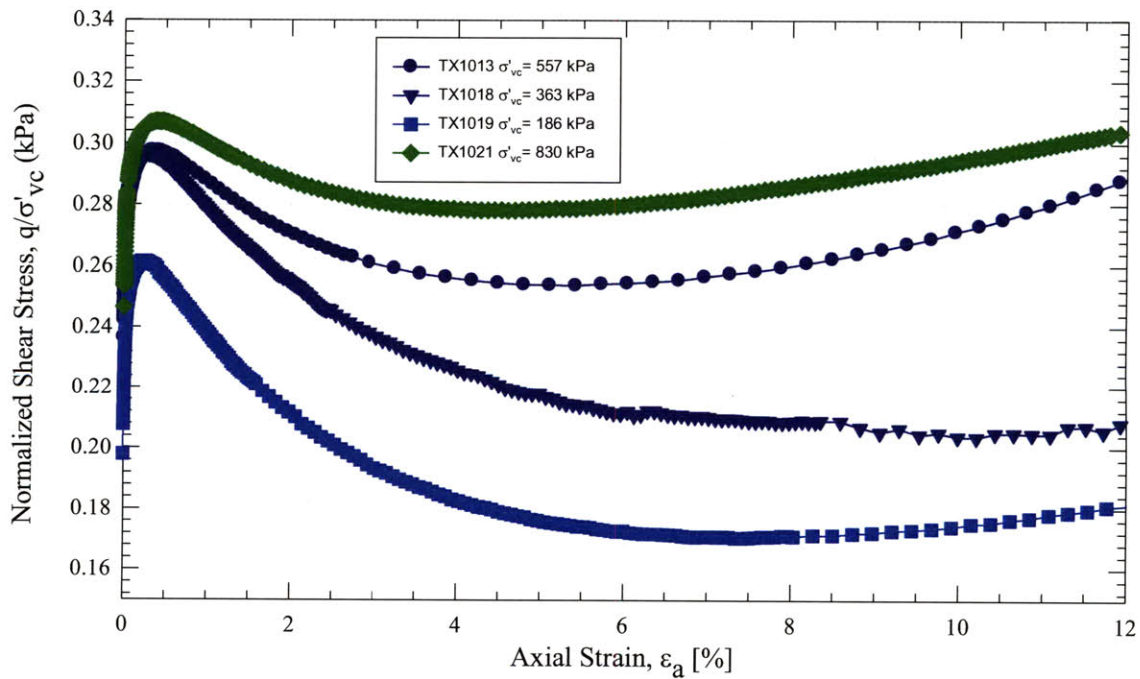


Figure 6-54: Normalized stress-strain curves from CK<sub>0</sub>UC triaxial tests

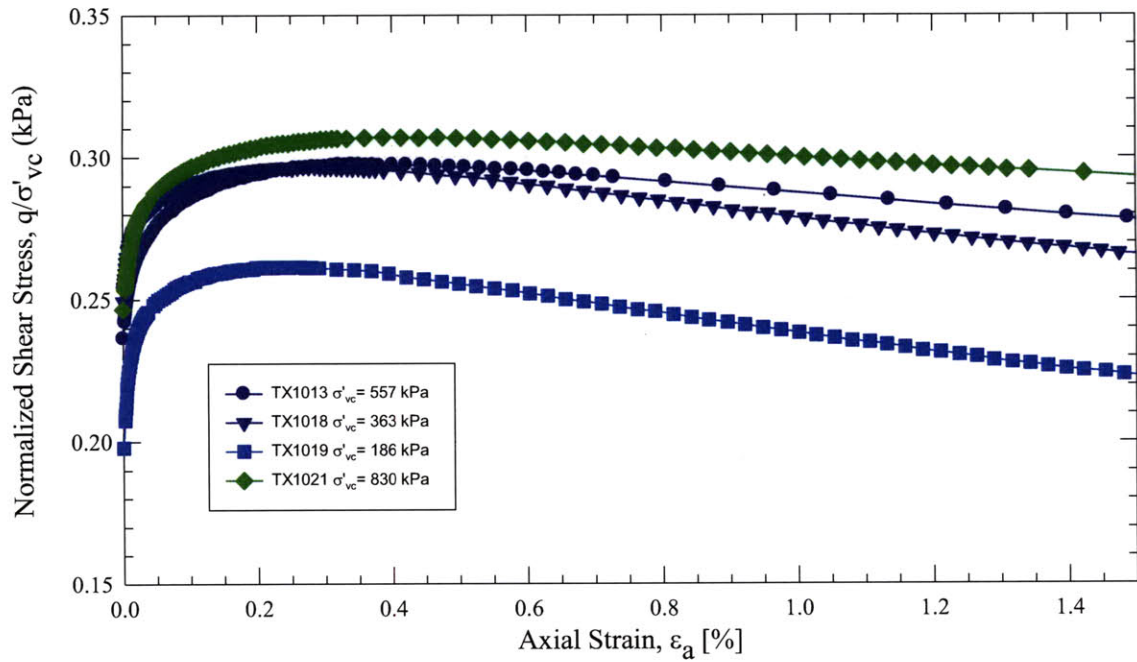


Figure 6-55: Normalized stress-strain curves (small strain) from CK<sub>0</sub>UC triaxial tests

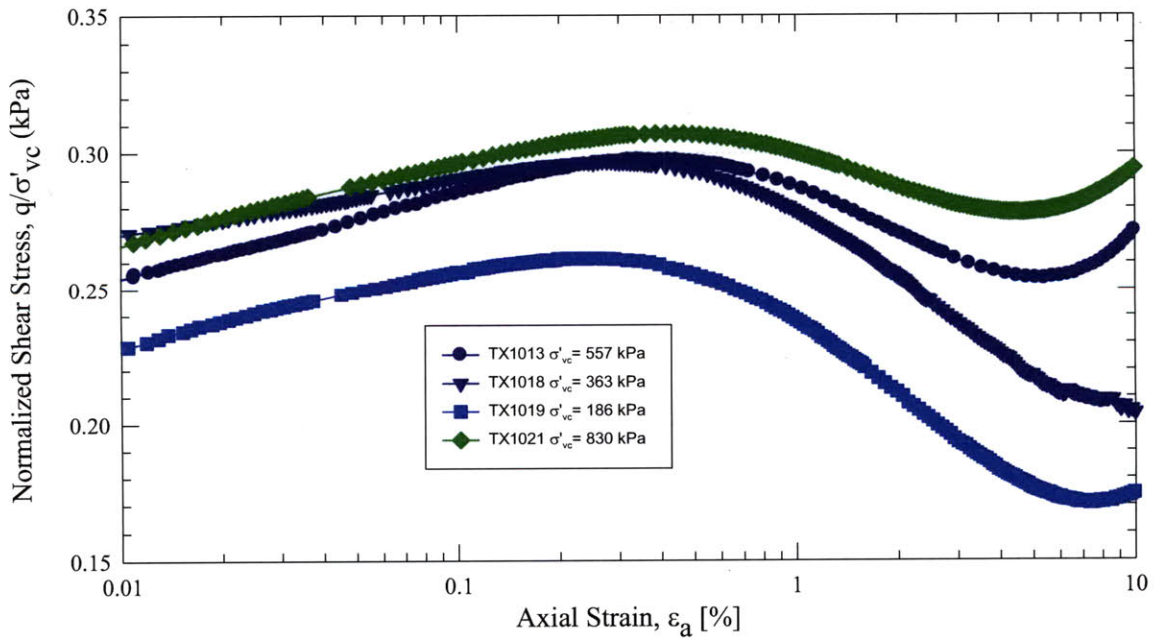


Figure 6-56: Normalized stress (log) - strain curve from CK<sub>0</sub>UC triaxial tests

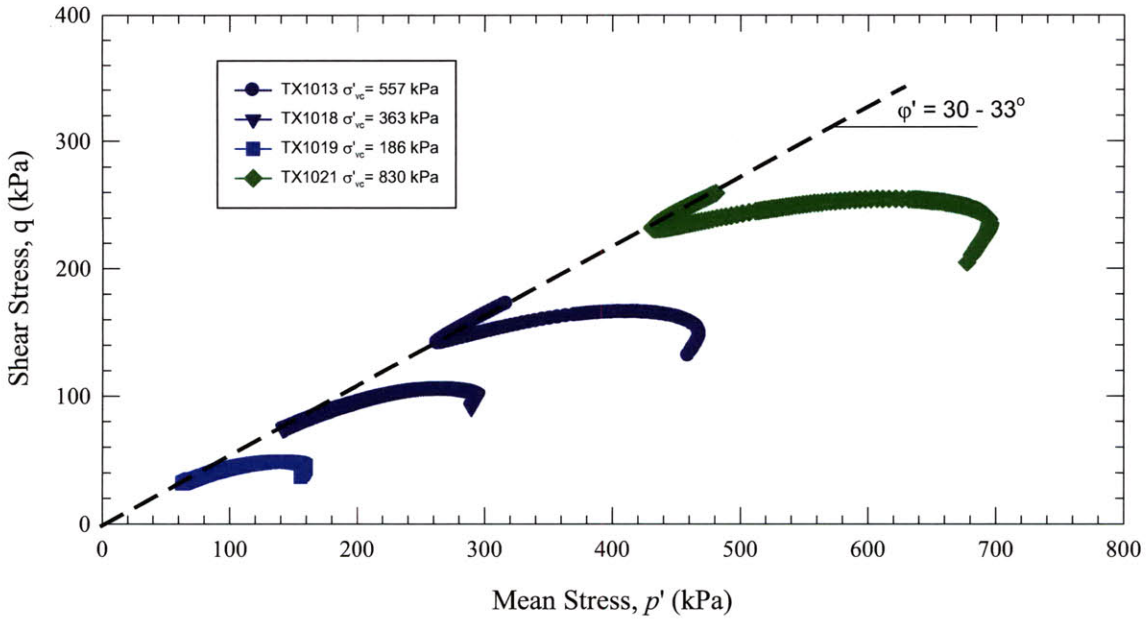


Figure 6-57: Effective stress paths from CK<sub>0</sub>UC triaxial tests

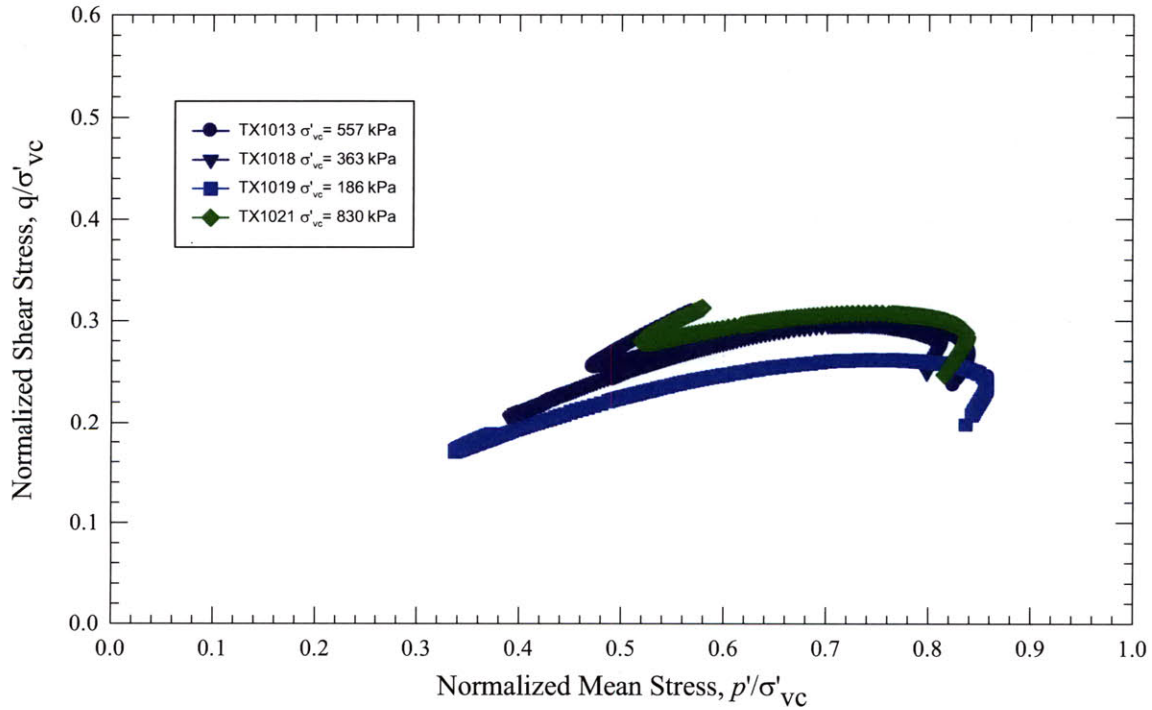


Figure 6-58: Normalized effective stress paths from CK<sub>0</sub>UC triaxial tests

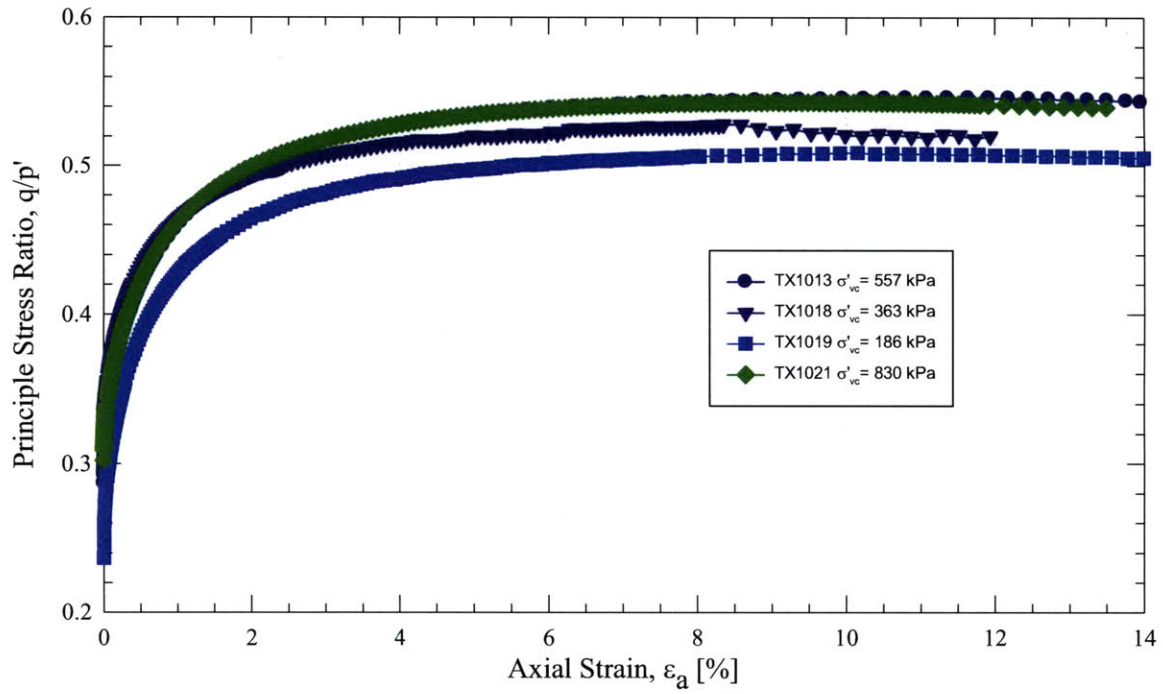


Figure 6-59: Principle stress ratio versus axial strain from  $CK_0UC$  triaxial tests

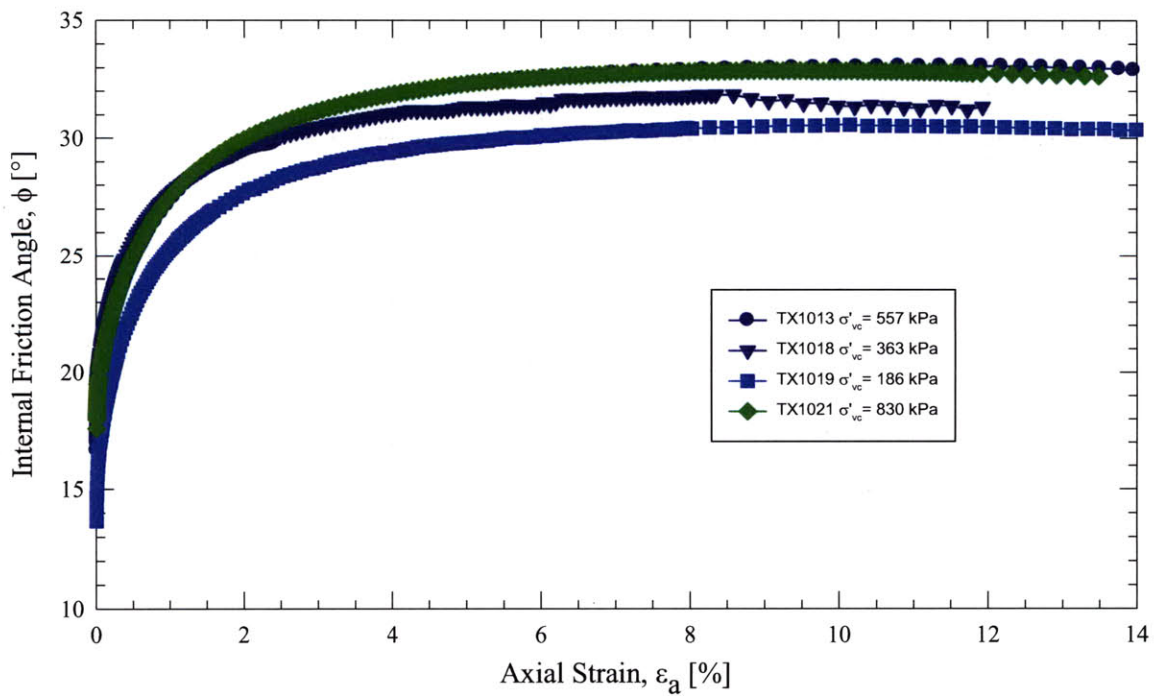


Figure 6-60: Friction angle versus axial strain from  $CK_0UC$  triaxial tests

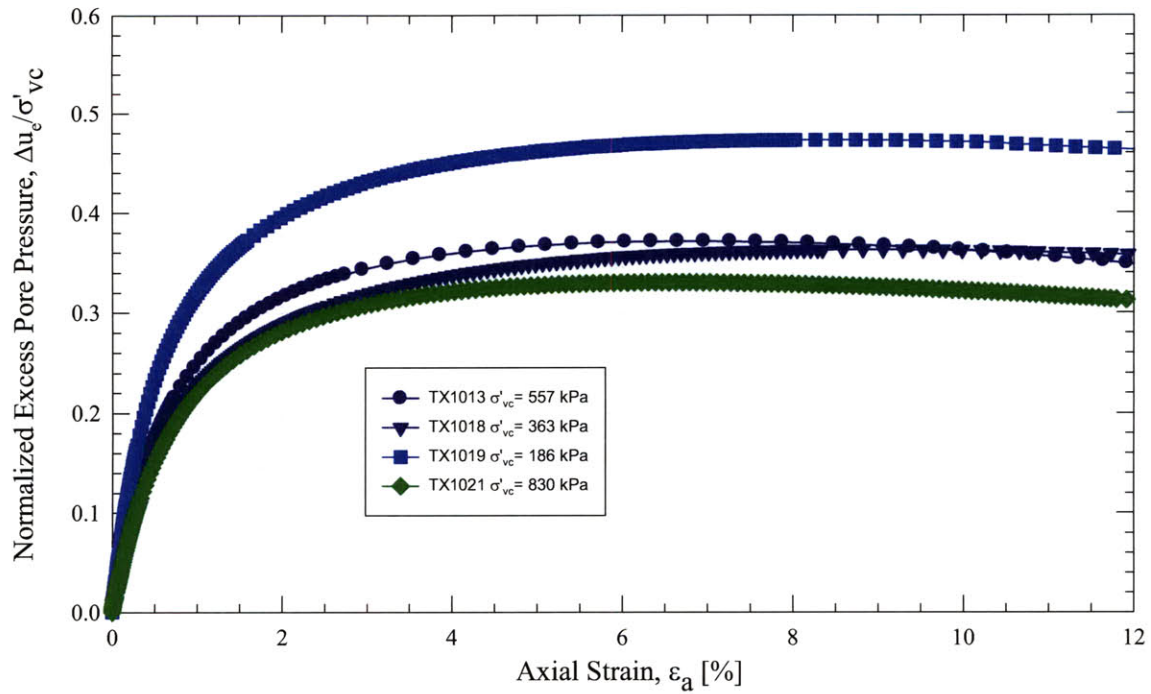


Figure 6-61: Normalized excess pore pressures versus strain from CK<sub>0</sub>UC triaxial tests

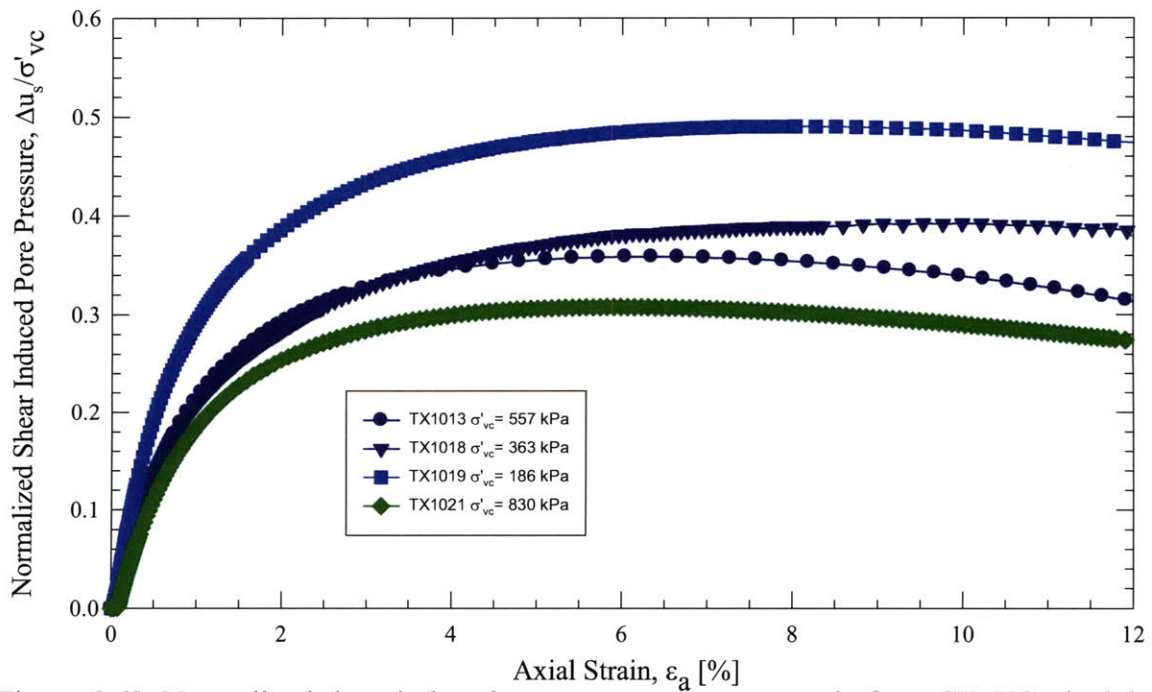


Figure 6-62: Normalized shear induced pore pressures versus strain from CK<sub>0</sub>UC triaxial tests

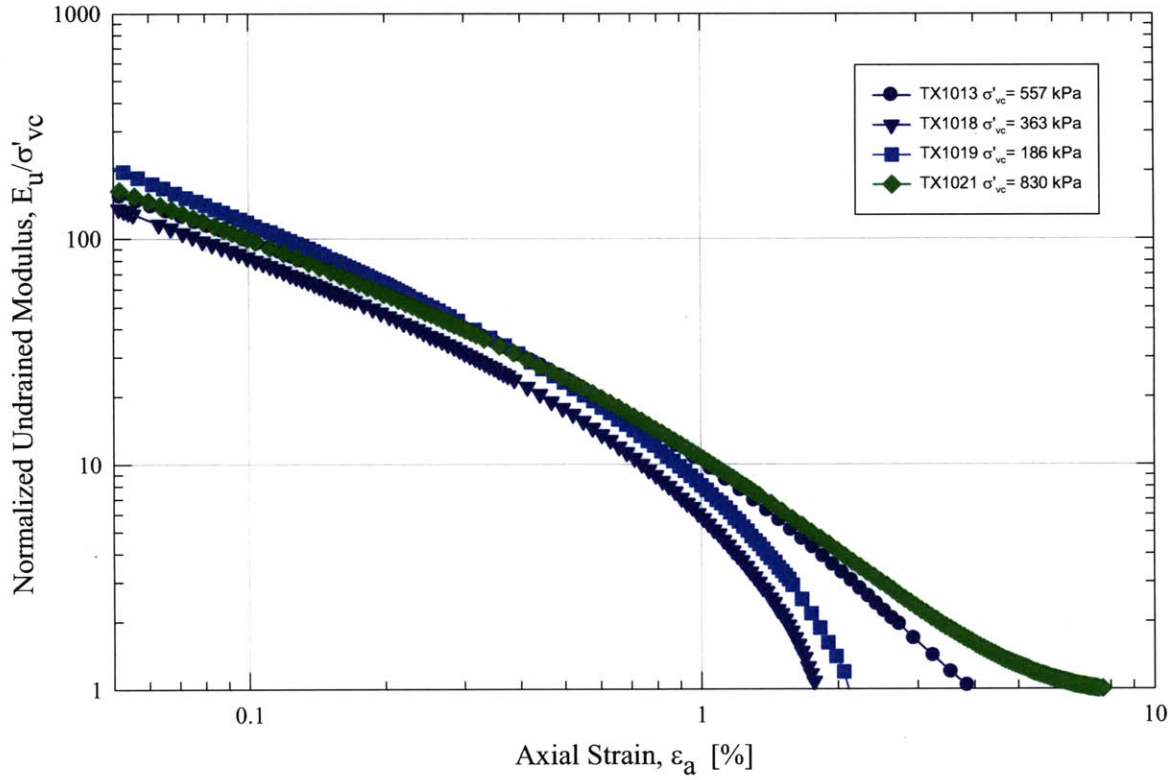


Figure 6-63: Normalized undrained secant modulus versus axial strain from CK<sub>0</sub>UC triaxial tests

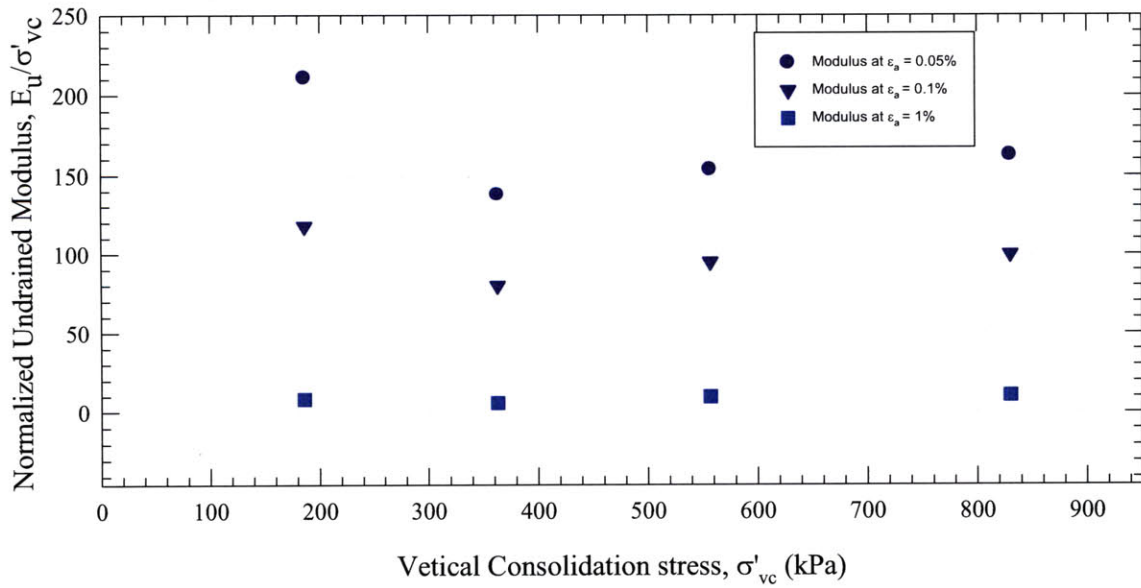


Figure 6-64: Normalized undrained secant modulus versus stress level from CK<sub>0</sub>UC triaxial tests



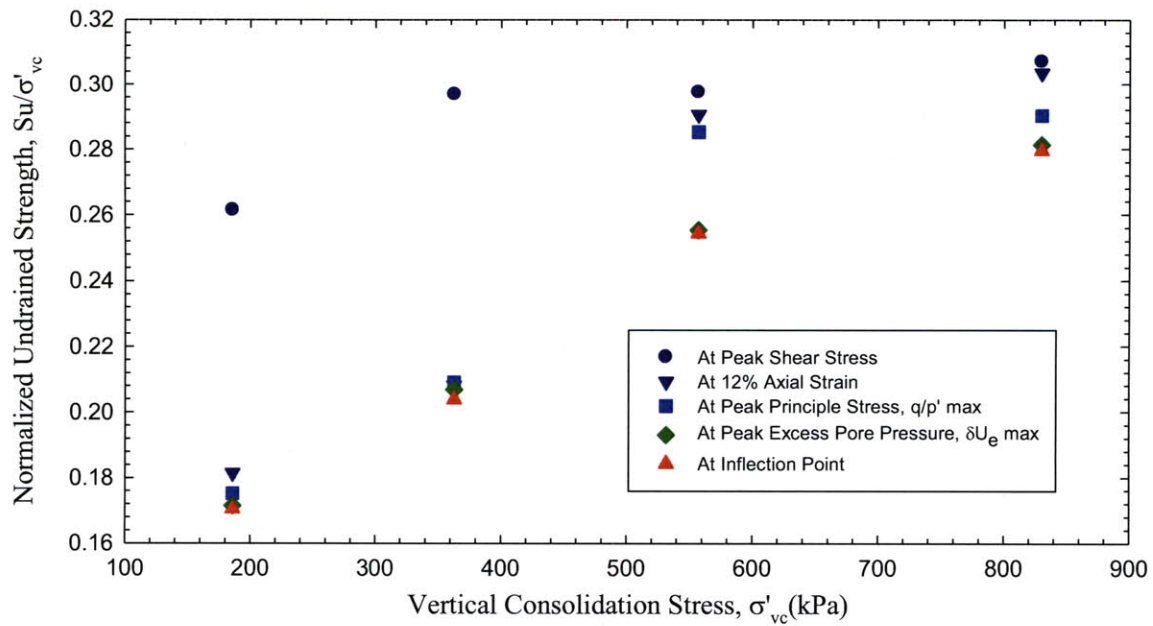


Figure 6-65: Normalized undrained strength versus stress level from CK<sub>0</sub>UC triaxial tests

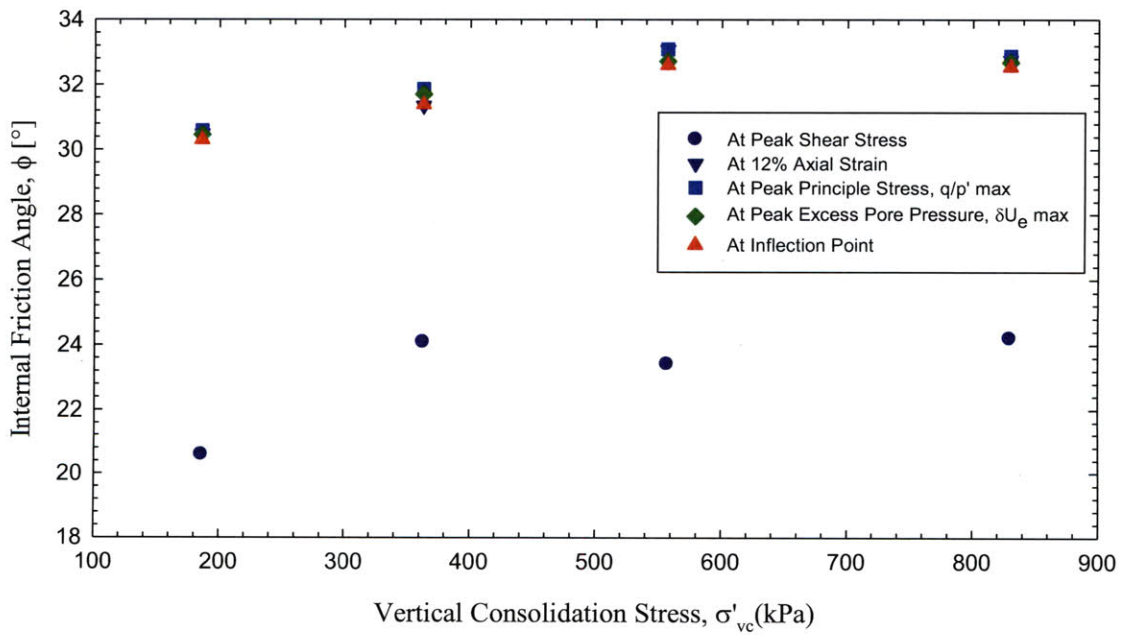


Figure 6-66: Friction angle versus stress level from CK<sub>0</sub>UC triaxial tests

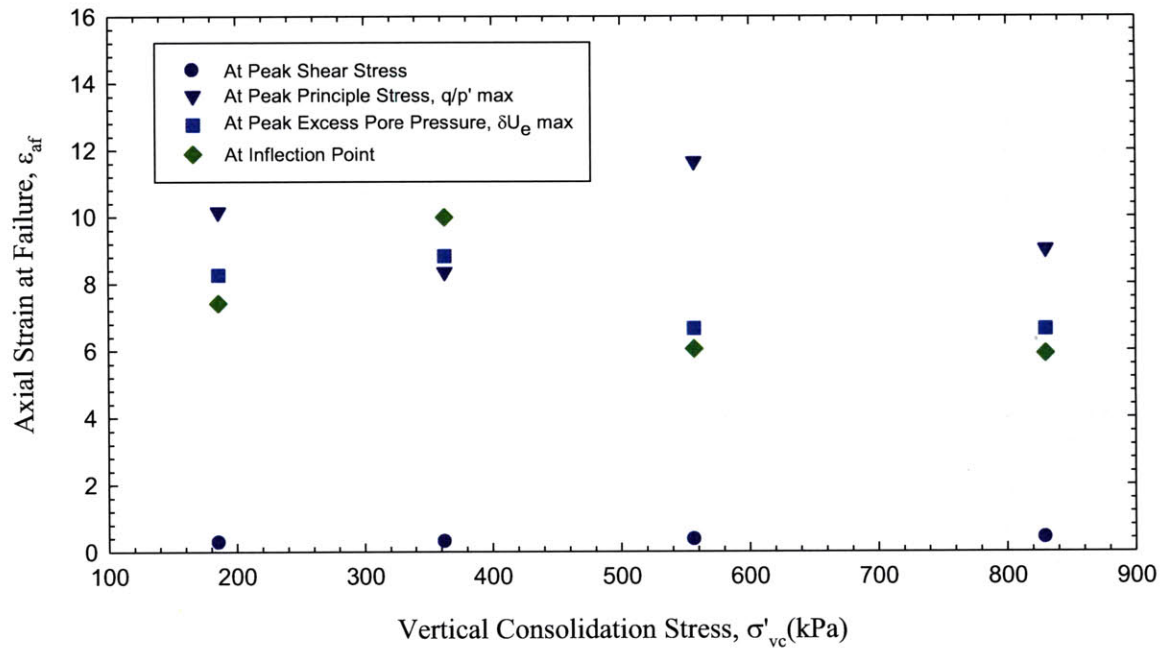


Figure 6-67: Axial strain at failure versus stress level from  $CK_0UC$  triaxial tests

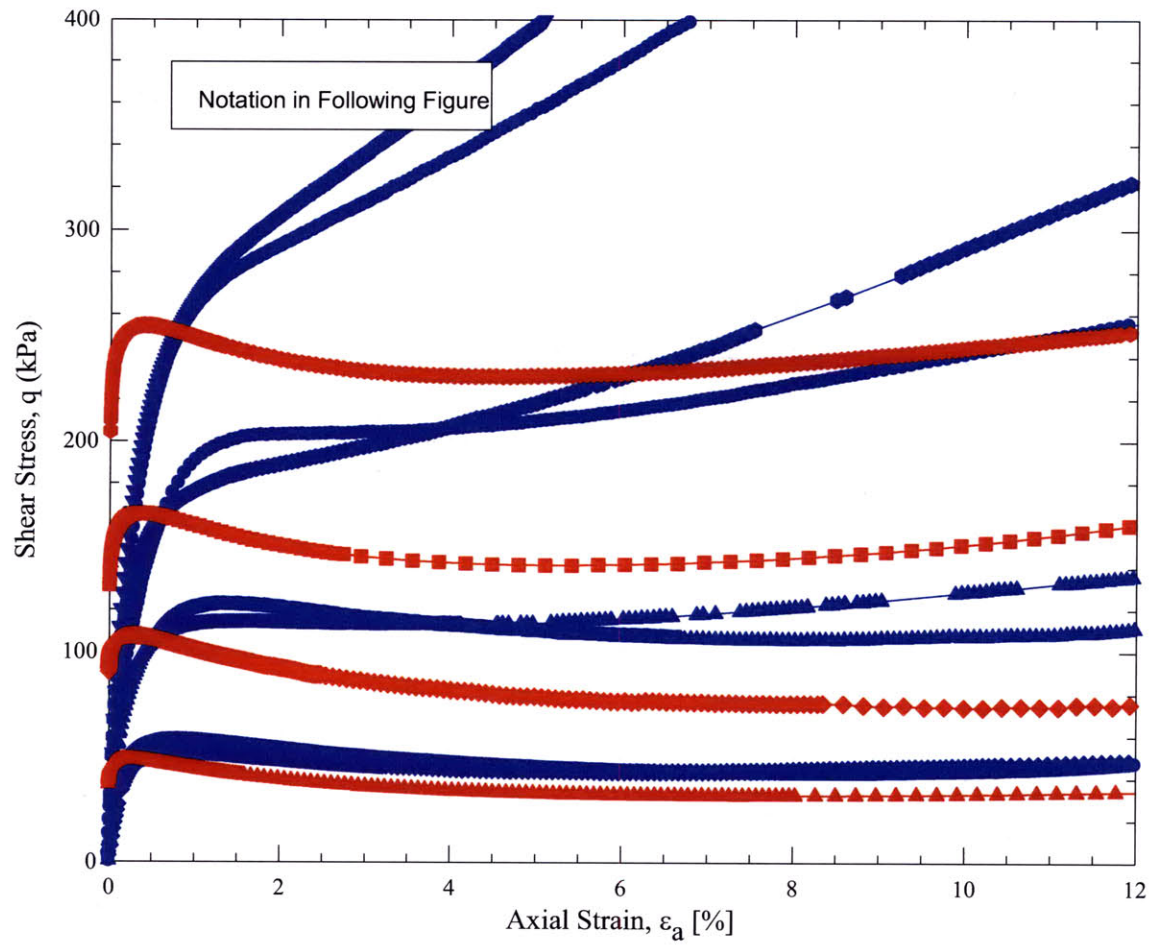


Figure 6-68: Stress-strain curves from CIUC and CK<sub>0</sub>UC triaxial tests

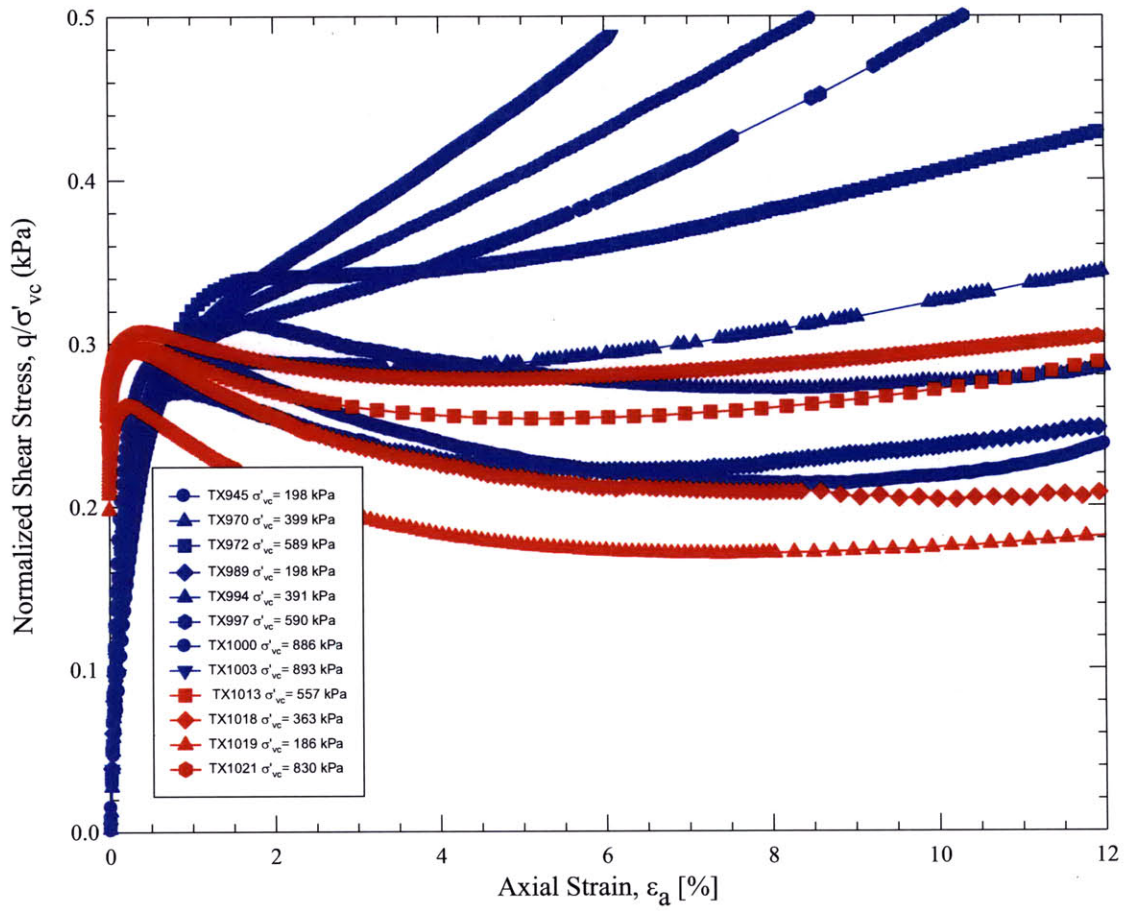


Figure 6-69: Normalized stress-strain curves from CIUC and  $CK_0$ UC triaxial tests

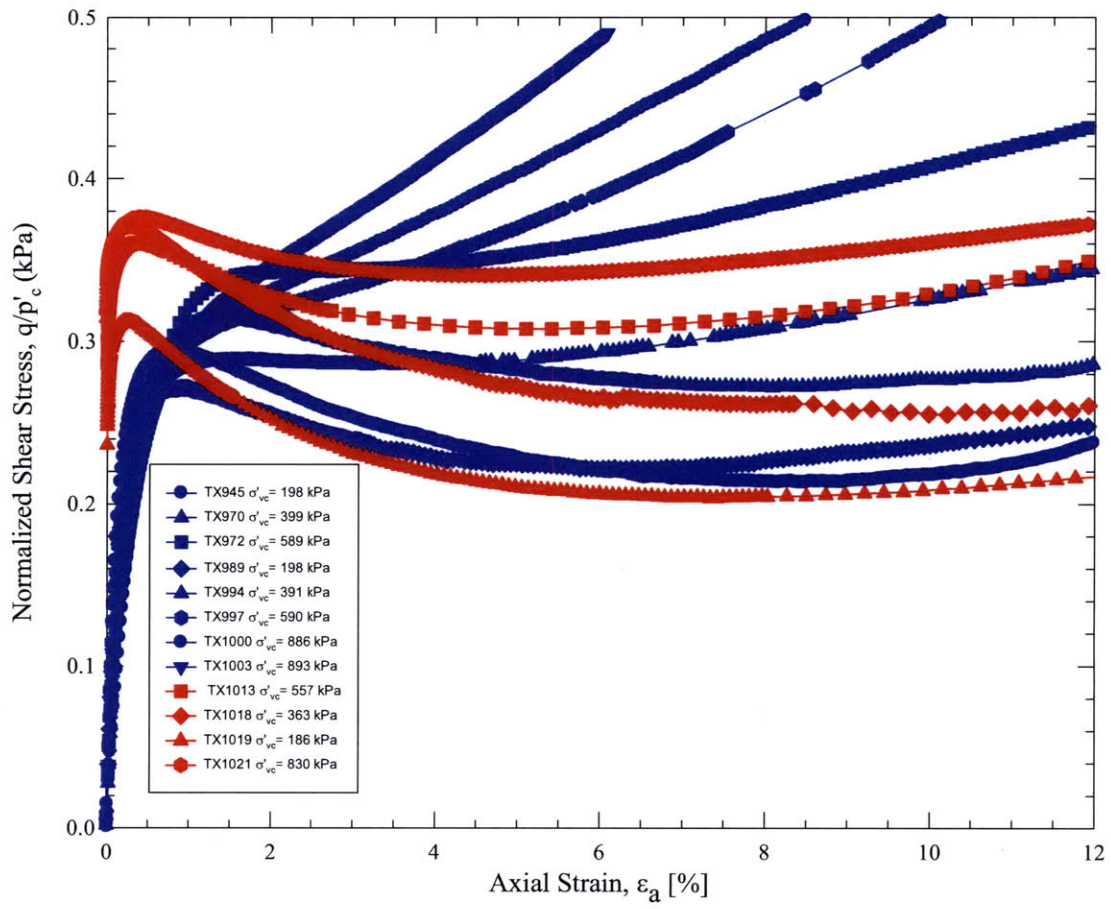


Figure 6-70: Normalized stress-strain curves from CIUC and CK<sub>0</sub>UC triaxial tests (Normalized by mean consolidation effective stress)

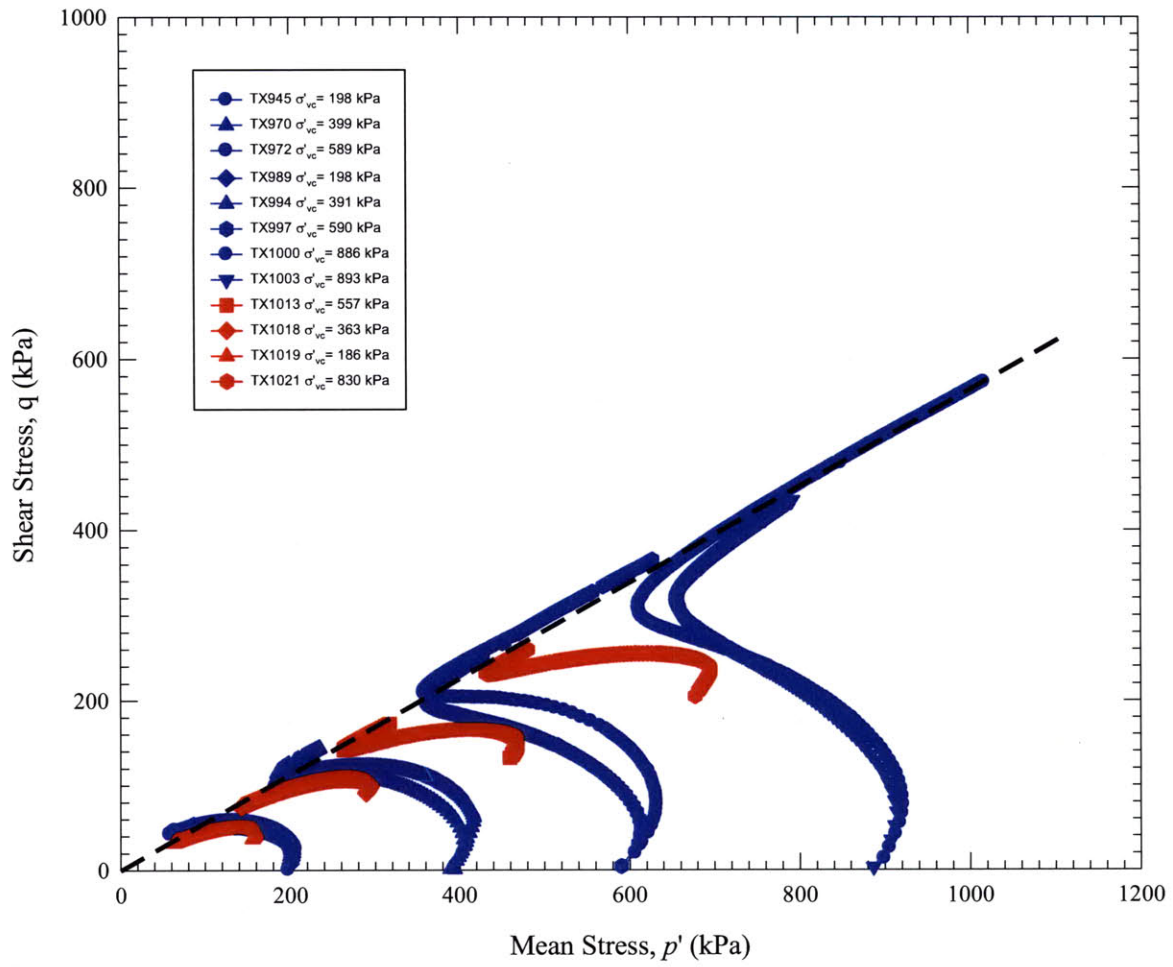


Figure 6-71: Effective stress paths from CIUC and  $CK_0$ UC triaxial tests

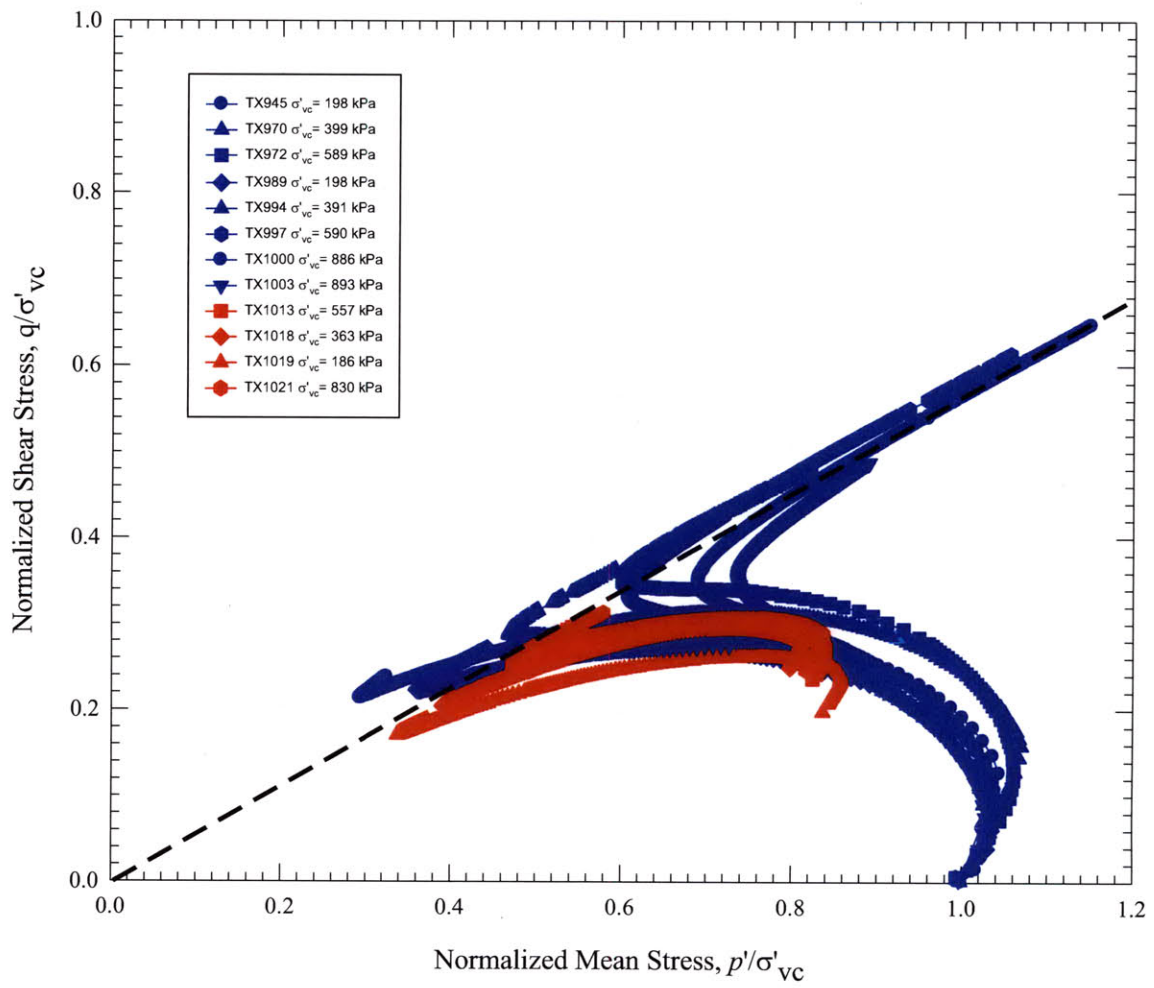


Figure 6-72: Normalized effective stress paths from CIUC and CK<sub>0</sub>UC triaxial tests

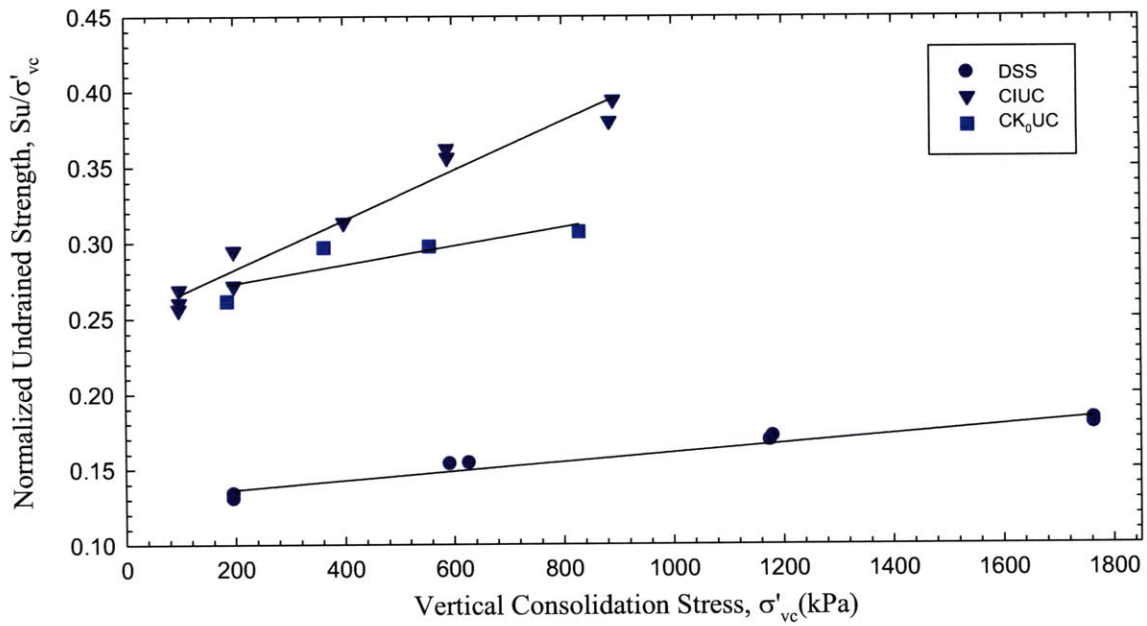


Figure 6-73: Normalized undrained strength versus stress level from DSS, CIUC, and CK<sub>0</sub>UC tests

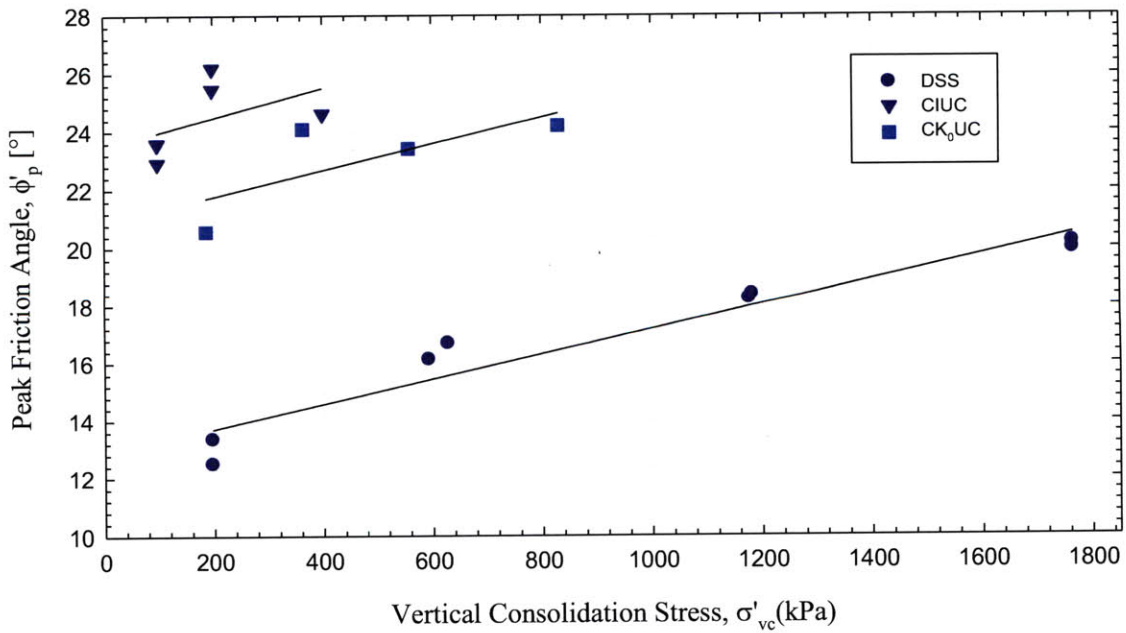


Figure 6-74: Peak friction angle versus stress level from DSS, CIUC, and CK<sub>0</sub>UC tests



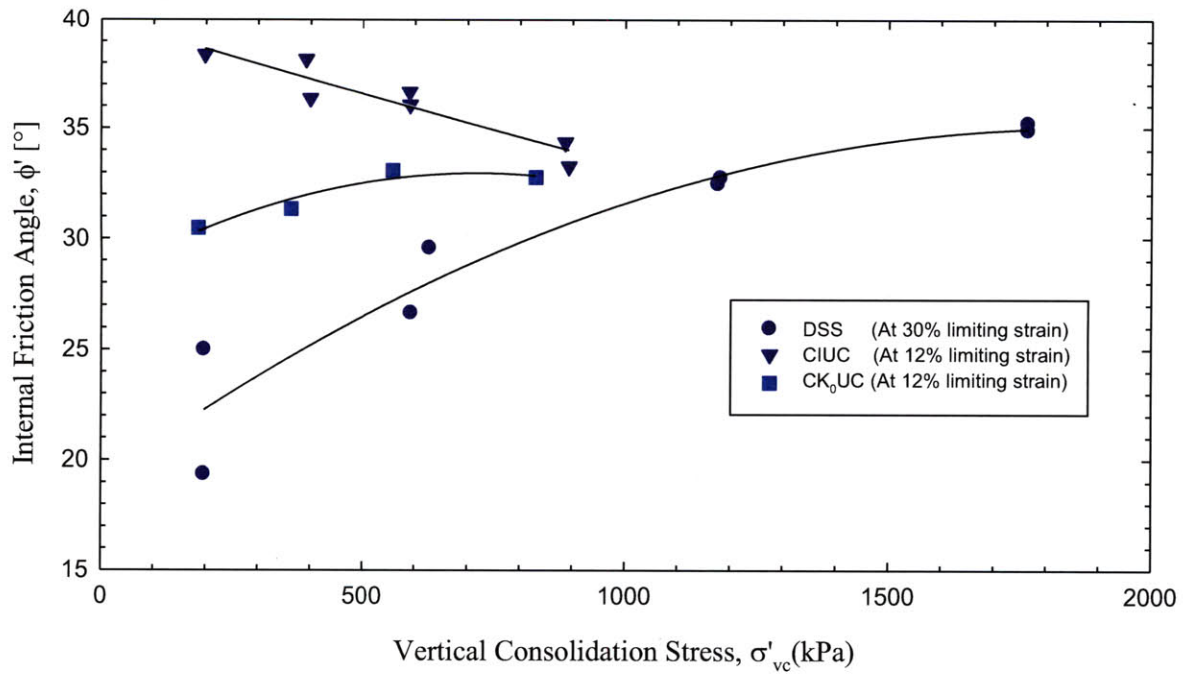


Figure 6-75: Friction angle versus consolidation stress level for DSS, CIUC, and CK<sub>0</sub>UC tests

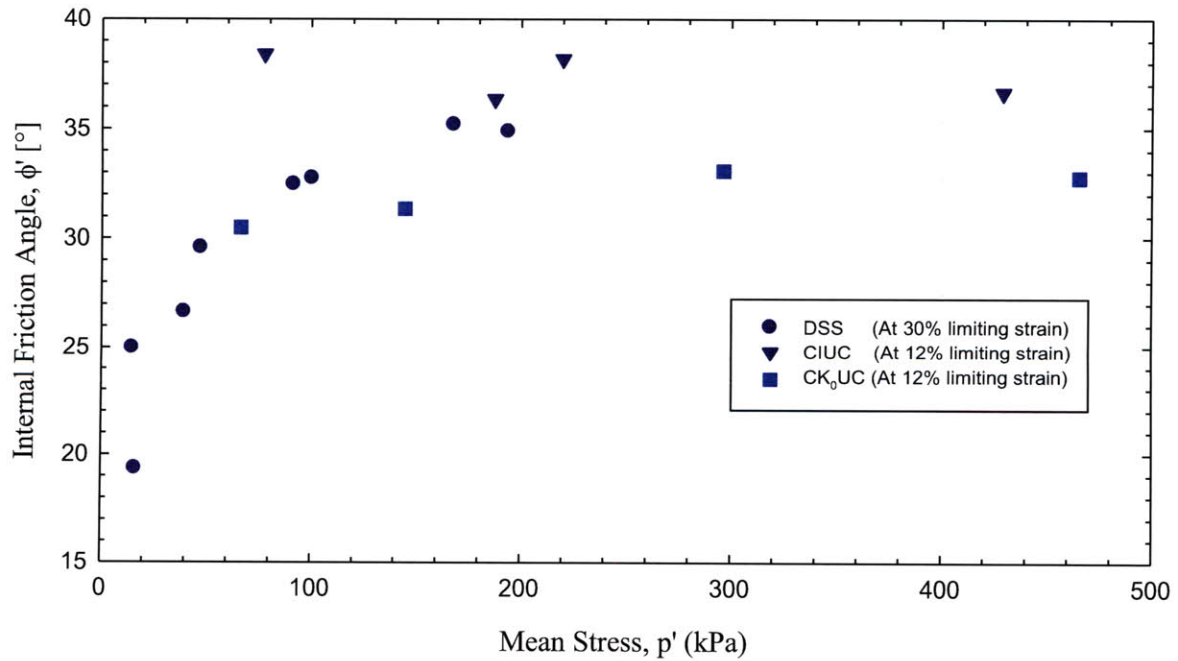


Figure 6-76: Friction angle versus mean effective stress for DSS, CIUC, and CK<sub>0</sub>UC tests

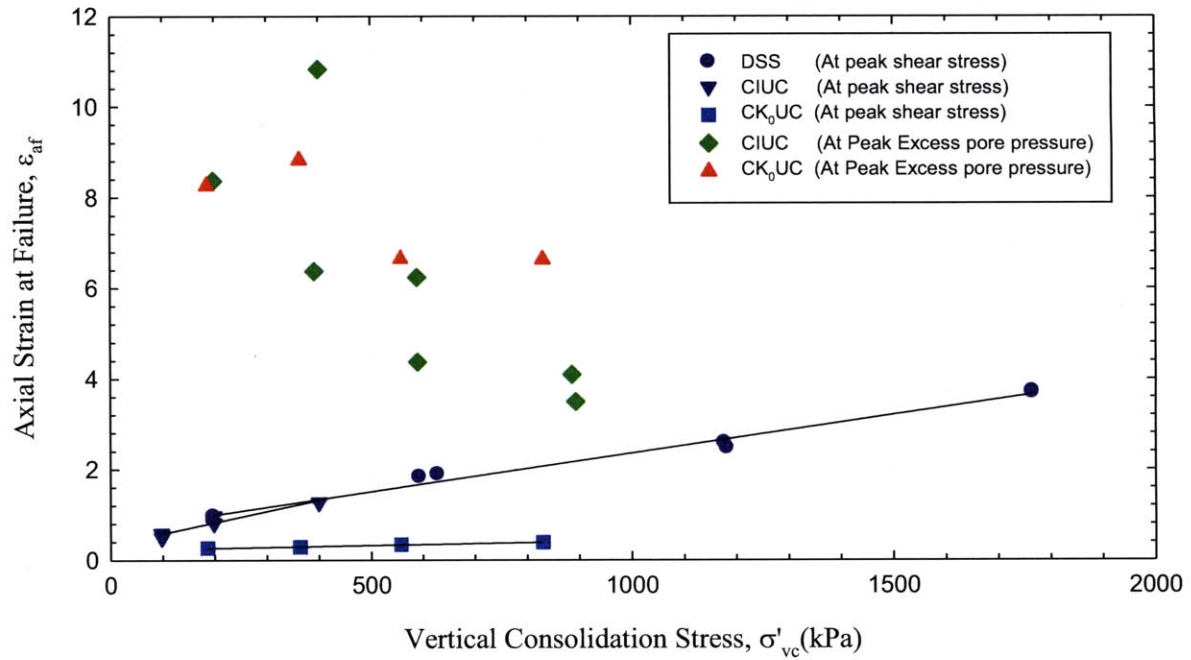


Figure 6-77: Axial strain at failure versus stress level for DSS, CIUC, and CK<sub>0</sub>UC tests

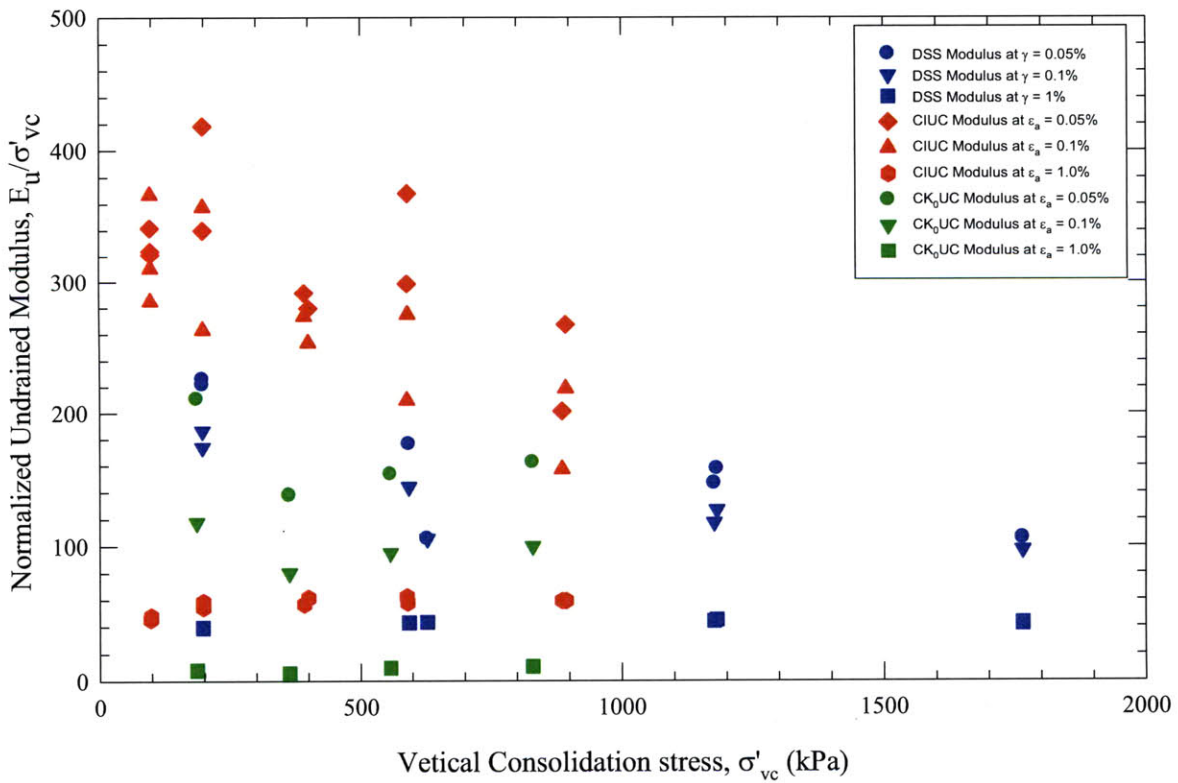


Figure 6-78: Normalized undrained secant modulus versus stress level from DSS, CIUC, and CK<sub>0</sub>UC tests

# **7 SUMMARY, CONCLUSIONS, AND RECOMMENDATIONS**

## **7.1 OVERVIEW**

During a major upgrade of the wastewater infrastructure in Skibbereen, Co. Cork, Ireland, there were many challenges during construction. The difficulties were associated with the soft silt ground conditions. The soil was sensitive and highly susceptible to liquefaction, producing poor ground bearing conditions for pipes and structures. The silt was difficult to dewater and “quick” conditions could easily occur. The material densified through vibration, creating ground settlement and damage to existing structures.

The original site investigation for the project failed to identify the engineering properties of the material. This was due to the difficulty in conducting both field and laboratory tests on the material. In general, the field results showed poor ground properties. Generally, standard penetration test results were less than 10 in the silt deposits and field vane testing produced shear strengths that ranged between 2 and 30 kPa. Due to the large deviation in the field vane results, the existing piezocone data could not be accurately calibrated to the site conditions. Original laboratory testing was extremely limited. No attempt was made to define the engineering properties and the index property testing produced results with many discrepancies.

The difficulties encountered during the project developed the need for further information and knowledge. A second site investigation during the construction project also failed to identify the engineering properties of the material. Consequently, the tube and bulk samples sourced during this secondary phase of site investigation were transported to MIT geotechnical laboratory for the purpose of this research.

A comprehensive literature review showed that extensive research has been conducted on clay and sand soils. In contrast, very little information exists on the engineering properties of silt. There are several reasons for this trend and they are primarily related to difficulties in sampling and subsequent test preparation. Low plasticity silts are very easily disturbed during sampling and preparing silt specimens for testing without disturbance is difficult.

Of those who have studied the properties of low plasticity silts, there are many contrasting views, opinions, and results. Various sampling, testing, and reconstitution procedures have been documented with no one preferred method emerging. The results and behavior found among researchers also show large deviations.

Therefore, reliable testing information was needed to understand the behavior seen in the field and to help explain some of the problems encountered during construction. The silt deposits found in Skibbereen are not localized to that area only. Throughout the south and west coast of Ireland, low plasticity silts are reported in many locations. However, the properties are relatively unknown. For future construction projects it was important to understand the behavior and determine the engineering properties before construction work commences to limit the possibility of construction difficulties. The information found in the research will help update the existing knowledge on low plasticity silts.

## **7.2 SUMMARY OF WORK UNDERTAKEN AT MIT**

This research comprised a detailed laboratory investigation of the behavior and properties of the low plasticity silt obtained from the Skibbereen site. The scope of the work was broken down into a very simple and logical process.

A detailed study of the existing literature was first conducted which highlighted the difficulties associated with this type of material. There are many contrasting views on the best methods for sampling, test preparation, reconstitution, and testing. The literature also shows a variation in the behavior and properties between researchers.

Both tube and bulk samples were transported to MIT for testing. The bulk samples were sorted and evaluated based on color, moisture content, particle size, and slake test performance before being processed into a homogeneous testing material. A determination into the feasibility of testing the tube samples found that the material was extremely disturbed. The disturbance was likely due to a combination of the transportation of the material to MIT and the difficulty of obtaining intact samples from the ground.

Two reconstitution methods were utilized in the research. The re-sedimentation procedure was first evaluated. The material is stable throughout the incremental loading

sequence. However, during extrusion from the consolidometer the material loses this stability. It will flow out of the consolidometer unless it is partially dried before extrusion. In the case of the partially dried specimens that were successfully extruded, it was found that the material is impossible to trim for test preparation. Upon contact with any trimming tool, excess water is drawn to the point of contact and the structure and shape of the specimen begins to collapse. Therefore, the research concentrated predominantly on undercompacted reconstituted specimens. The method provided a simple way of producing repeatable test specimens. However, saturating the specimens after the initial preparation is difficult with this method. The specimens tend to contract during the saturation process which can cause stability issues and unknown volumetric strains.

The experimental portion of this research can be divided between index property and engineering property testing. The index properties were first conducted to give an understanding of the material in this research. The specific gravity, Atterberg limits, grain size distribution, salt concentration, and organic content were all evaluated. The final stage of the index property testing program involved the use of a scanning electron microscope for imaging analysis and X-ray diffraction for mineralogy information.

The engineering properties were characterized by an extensive experimental testing program. In total, 17 constant rate of strain (CRS) tests were attempted to characterize the compression behavior of the material. Many tests experienced experimental problems due to the unknown testing method for the material at that time and hence, were not reported. The specimens were consolidated to stresses of approximately 15 MPa and the compression curves generally had two unload-reload cycles to provide the swelling and recompression ratio information. The hydraulic conductivity was evaluated in a modified CRS device. Specimens were consolidated to vertical effective stresses ranging from 200 to 2500 kPa. A hydraulic gradient was then applied across the specimen and the flow was recorded so the hydraulic conductivity could be calculated.

The shear strength testing program was broken into three different testing devices.  $K_0$ -consolidated direct simple shear ( $CK_0$ DSS) tests were followed by isotropically consolidated undrained compression (CIUC) tests in a manual triaxial device. The final phase of the shear testing program involved  $K_0$ -consolidated undrained compression ( $CK_0$ UC) tests in an automated

triaxial device. Normally consolidated and over consolidated tests were conducted in the DSS device. The overconsolidated specimens provided the SHANSEP parameters. The final phase of the DSS testing program involved cyclic shear tests to determine the change in shear strength and density with each shear phase. The CIUC and  $CK_0UC$  triaxial tests were only conducted on normally consolidated specimens over a vertical effective stress range from 100 to 900 kPa. The specimens were prepared to an initial setup dry density of  $1.5 \text{ g/cm}^3$  to ensure uniform testing conditions. The shear strength testing program provided the stress-strain-strength, pore pressure, undrained secant Young's modulus, and friction angle information to fully characterize the material.

### **7.3 RESULTS AND CONCLUSIONS**

An extensive experimental testing program was undertaken to fully characterize the material. After identification of the index properties, the testing program made use of the CRS, hydraulic conductivity, DSS, and the triaxial device to provide the engineering parameters. There were many other unknowns about the material before this research. The possibility of successful laboratory testing and the correct testing procedures were relatively unknown. The results, outcomes, and conclusions are included in this section.

#### **7.3.1 Feasibility of testing intact tube samples**

The tube samples transported to MIT were very disturbed and could not be used for intact testing. There are two reasons for the possible cause of this disturbance, 1) the long transportation distance caused segregation in the sample from vibrations, and 2) the material was disturbed during the sampling process. It is likely that a combination of both is the cause. However, from the behavior observed during this research, even if the transportation distance was low and better quality sampling methods were used, alteration of the structure would be likely. The material is extremely sensitive to vibration; a short distance journey from the field to the lab will segregate the material, disturbing it significantly. The material also does not have enough cohesion or a hydraulic conductivity low enough to allow extrusion from the tube. The

material will not sustain a negative pore pressure to allow trimming or test preparation. Some researches argue that low plasticity silt can be extruded directly from the sampling tube into the testing device. However, this method would be extremely difficult for this material. The structure of the material collapses instantly once it is released from the confinements of a tube. The transfer of the material from the tube to the testing device would likely cause some degree of disturbance. Therefore, it is not possible to conduct tests on material of this type without disturbance and an expensive intact sampling program is a waste of financial resources.

### **7.3.2 Development of a successful reconstitution procedure for the material**

Resedimentation was first adopted as a possible reconstitution technique for the material. However, many problems emerged during the extrusion from consolidometer to test set up phase. The structure of the material is unstable after extrusion. Again, the cohesion is too low and the hydraulic conductivity is too high to allow specimen trimming and test setup. The results from four CRS tests showed a large deviation in behavior, indicating that material had been disturbed to various degrees of severity. Therefore, resedimentation in a consolidometer is not an option for this material.

Two methods in the literature that show potential are resedimentation directly into the testing device and a wet pluviation technique. Resedimentation directly into the CRS device was conducted during this research. The tests show that the method is possible; however, there are many difficulties associated with this technique. The specimen needs to be incrementally loaded until it reaches a stable condition for testing. The incremental loading sequence is difficult to apply in the more complicated testing devices such as the triaxial device. It is also difficult to measure the strain during this incremental loading sequence. Therefore, the starting conditions for the material are generally unknown and a back calculation procedure is required from the end of testing conditions which is not ideal. It is also extremely difficult to produce repeatable specimens. The slurry is prepared in a bowl/container/tare and transferred to the device mold. It is inevitable that a percentage of the slurry will be lost either through the transfer process or through the material sticking to the bowl, funnel, and spatulas. The percentage transferred and lost during each test setup is very difficult to replicate and it highlights a significant problem

with the technique. The wet pluviation technique was not attempted during this research. The exact procedure has not been well defined by any researcher and it is thought that the method will suffer from some of the problems by resedimentation directly into the device technique. There is also the concern of segregation occurring during pluviation which would result in a non uniform specimen. However, if a successful test preparation procedure can be defined, it will possibly best represent the field soil fabric.

The undercompaction technique was utilized extensively throughout this experimental program. The method has many advantages over other techniques. The specimens are easily prepared to a desired density and void ratio. The initial density can be varied easily and the method produces repeatable and uniform specimens. The procedure is very methodical, reducing the possibility of deviation in results between different researchers. However, there are also negatives with this method, the biggest being the saturation procedure after the initial setup. The specimen structure collapses during saturation causing contraction and a reduction in volume. The reduction in volume is difficult to measure, particularly in the triaxial device where there are both vertical and horizontal confining stresses applied to the specimen. The strain magnitude during saturation is also related to the stress level applied. It is also not known if the specimens produced by the undercompaction method replicate the field fabric and it is possible that there are minor deviations in lab and field soil fabric. However, this is an issue for all reconstitution techniques. Despite the negatives for the undercompaction method, the positives far outweigh the other reconstitution techniques. Therefore, for material of this type, undercompaction is the best reconstitution method.

### **7.3.3 Development of successful testing preparation procedures**

The previous section described some of the reconstitution alternatives to undercompaction and the reasons behind the selection of the undercompaction technique for reconstitution. This section describes the successful use of the undercompaction technique for low plasticity silts.

Before this experimental program the use of the undercompaction technique for low plasticity silts was unknown. The optimum initial density, optimum initial water content, number



of compaction layers, the percentage of undercompaction, and the saturation techniques all had to be determined.

The research has found that an initial dry density of  $1.5 \text{ g/cm}^3$  with an initial water content of 3% is optimum for this material type. To ensure a uniform density throughout the specimen, zero percent undercompaction should be used. The number of compaction layers depends on the test type. No undercompacted layer should be greater than 10mm in height. The constant rate of strain, hydraulic conductivity, and direct simple shear devices should have a minimum of three layers and the triaxial specimens should have a minimum of seven layers.

The saturation procedures are similar for each test type. A confinement stress must be placed on the specimen before the saturation process to ensure stability. A gravity head of water is then applied through the base of the specimen with flow allowed through the top. Saturation should be overnight or for a minimum 12 hour period before the tests are run in the conventional manner.

#### **7.3.4 Index properties**

A comprehensive index property testing program was undertaken for this research. Before processing the material, slake tests were conducted on the partially dried bulk material. The material did not disperse after a 24 hour period in distilled water. The results are expected for clays that have true cohesion. However, for low plasticity silts the behavior is very unusual. The results show that there is some unusual type of bonding mechanism in the material that cannot be reproduced once the material has been fully dried.

The Atterberg limit tests found a liquid limit and plastic limit of 25.77 and 18.24%, producing a plasticity index equal to 7.53%. The results put the material in the CL-ML box on the Casagrande Plasticity Chart, as shown in Figure 5-3. This box is well known as an area that can produce unexpected soil behavior. The specific gravity was found to equal 2.724 and the hydrometer analysis found a well graded silt with a 10% clay and 2% sand content. The salt concentration analysis presented in Section 5.2.4 found a very low salt content. The material has likely been leached of salt from the marine environment conditions in which it was deposited.

The scanning electron microscope produced excellent images, as shown in Figure 5-4. The angular, jagged, plate like particles can be used to interpret some of the behavior observed. The low void ratios found in consolidation results are probably a result of parallel plate like orientations. The flat and jagged particles add to the difficulty of trimming the specimens. The particle shape could also be responsible for the material bending around the fall cone in the liquid limit tests.

The X-ray diffraction results show that quartz is the predominant mineral with 76% of the total composition. The clay minerals, made up of 6.8% illite and 8.8% chlorite must be responsible for some of the unusual behavior observed during this experiment investigation. The clay content is just high enough to produce behavior that is neither purely granular nor cohesive.

### **7.3.5 Engineering Properties**

#### **7.3.5.1 Introduction**

Chapter 5 presented the consolidation results from 10 CRS consolidation tests, 19  $K_0$ -consolidated direct simple shear ( $CK_0$ DSS) tests, 11 isotropically consolidated undrained triaxial compression (CIUC) tests, and 4  $K_0$ -consolidated undrained triaxial compression ( $CK_0$ UC) tests together with hydraulic conductivity results. Chapter 6 presented the corresponding shear properties and behavior for the direct simple shear and triaxial tests. The results and conclusions of the testing program are presented here.

#### **7.3.5.2 Consolidation behavior**

The compression and consolidation properties were obtained from CRS tests as well as the consolidation phase of each  $CK_0$ DSS, CIUC, and  $CK_0$ UC triaxial tests. In general, the repeatability for each test type was good. The CRS tests have a slightly rounded compression curve and there is no apparent preconsolidation pressure. The slope of the virgin consolidation line increases with stress level and a maximum compression ratio can be found at the greatest stress for all resedimentation methods. The compression curves converge at high stress levels regardless of the initial density. A deviation was found in behavior between the undercompacted and resedimented specimens, the results highlight that different reconstitution methods could

produce different behavior. In general, the compression ratio, swelling ratio, and recompression ratio show good agreement for the CRS device. A similar trend was found in the DSS results. The compression curves are slightly rounded, show no preconsolidation pressure, and the compression ratio increases with stress level. The void ratio and strain after saturation deviate slightly from each other and the stress levels are not great enough for them to converge during consolidation. Due to the manual incremental consolidation procedure and lower stress range ( $\sigma'_{vc} = 100 - 900$  kPa), the CIUC triaxial tests produce the poorest quality consolidation results. However, the same general trends were found as the CRS and DSS tests. The  $CK_0UC$  triaxial tests keep to the overall trend, the compression curves are slightly rounded with an increasing compression ratio with stress level. Figure 5-33 shows that compression ratio increases with an increase in stress level. Therefore, the void ratio and stress level have a strong effect on the compression ratio. Generally, the recompression ratio is constant with an increase in stress level.

When the various test types are analyzed together there is a deviation in the starting points of the compression curves. The deviation is due to the confining stress during saturation and the boundary condition. As shown in Figure 5-36, the triaxial compression curves start below the CRS range. The vertical effective consolidation stress was equal to 3, 20, and 40 kPa for the CRS, DSS, and triaxial devices during saturation. The stress level applied is the minimum needed for specimen stability during saturation in each respective apparatus. A subsequent investigation into stress level effects on the void ratio during saturation in the CRS device showed that void ratios after saturation equal those found in the DSS device if the same confinement stress is used. (Proving this weekend)

The coefficient of earth pressure at rest ( $K_0$ ) was obtained from feedback-controlled consolidation in the  $CK_0UC$  triaxial tests. The results showed the  $K_0$  decreases rapidly during initial loading and then the rate of  $K_0$  decrease slows with a further increase in stress. However, there is no plateau or constant value and the results show that higher stresses would produce lower  $K_0$  results. The unusual  $K_0$  behavior is also illustrated in Figure 5-34, where the effective stress paths are perfectly linear. Typically there is non-linearity in the stress paths, particularly in the early stages of  $K_0$ -consolidation. Some of the unusual behavior can be associated to the uncertain volume change from the saturation. Volumetric strain was assumed to equal axial strain at the beginning of  $K_0$ -consolidation. However, back calculation from final specimen

conditions showed that the volumetric strain is greater than axial strain. Therefore, the specimens were consolidated slightly off the  $K_0$  path. The consolidated earth pressure at rest value  $K_c$  was found to range between 0.55 and 0.59.

#### 7.3.5.3 Hydraulic Conductivity

The hydraulic conductivity ( $k$ ) and coefficient of consolidation ( $c_v$ ) could not be interpreted from the CRS tests using the standard linear theory. It requires very high strain rates in this material to produce sufficient excess pore pressure measurements to evaluate hydraulic conductivity and the coefficient of consolidation. Therefore, constant head hydraulic conductivity tests were conducted in a modified CRS device. The results were presented in Figure 5-37. Hydraulic conductivity ranges from  $1.03 \times 10^{-5}$  to  $3.77 \times 10^{-6}$  cm/sec over a void ratio range from 0.67 to 0.56. The results produce a  $c_v$  that ranges from 0.106 to 0.198 cm<sup>2</sup>/sec. The hydraulic conductivity and coefficient of consolidation are greater than those found in typical clay deposits (Boston Clue Clay,  $k_v = 1 \times 10^{-7}$  at  $e = 1.1$  to  $3 \times 10^{-9}$  at  $e = 0.53$ ,  $c_v = 15 \times 10^{-4}$  cm<sup>2</sup>/sec at  $\sigma'_{vc} = 200$  kPa (Abdulhadi, 2009)). However, they are around two orders of magnitude lower than typical sands. The hydraulic conductivity is just low enough to allow the development of excess pore pressures and undrained shear conditions. The failures seen in the field are clearly undrained due to the liquefaction and flow upon failure.

#### 7.3.5.4 Direct Simple Shear Behavior

An extensive direct simple shear testing program was undertaken in which normally consolidated (NC) and overconsolidated (OC) specimens were sheared at a constant strain rate of 5 percent per hour. The specimens were first  $K_0$ -consolidated to vertical consolidation effective stresses,  $\sigma'_{vc} = 200$  to 1800 kPa. The final phase of the DSS testing program involved cyclically shearing three specimens. The tests were prepared and consolidated in the same manner as the NC specimens. However, the cyclic specimens were sheared three times with vertical consolidation back to the original value between each phase of shearing.

In general, the normally consolidated specimens showed contractive behavior. Figure 6-1 to 6-7 displayed the stress-strain-strength and effective stress behavior. The curves are characterized by a peak followed by post peak softening. The undrained strength ratio ( $USR = s_u/\sigma'_{vc}$ ) is in a typical range for fine grained soils but increases with an increase in stress level.

This behavior is very unusual and has not been documented before in literature. The ductility of the material also increases with an increase in stress level. The magnitude of strain softening after the peak shear strength decreases with an increase in stress level, showing that the material is less contractive with higher stresses. Figure 6-9 and 6-10 demonstrated the undrained secant Young's modulus behavior. The results show that the normalized modulus is slightly affected by stress level. At low shear strains the normalized modulus is lower with an increase in stress level. However, at shear strains of 1% greater, there is no stress level dependence.

The shear behavior of specimens prepared with a different initial density and water content was also investigated. It was found that a higher initial density produces a slightly greater undrained strength ratio. However, there is no deviation in behavior besides this slight increase in strength.

Specimens with an over consolidation ratio (OCR) = 2, 3, and 4 were tested to compare behavior with the normally consolidated specimens. The shear stress-strain behavior demonstrated that the peak value of stress normalized to the maximum vertical stress decreases with an increase in OCR. However, the shear strength normalized to the vertical consolidation stress increases with OCR. The results show that the strain at peak shear stress ( $\gamma_f$ ) is unaffected by OCR which is very unusual behavior. The effective stress paths show a significant variation in behavior between NC and OC specimens. In contrast to the contractive behavior throughout the NC stress path, the OC specimens display dilative behavior during the initial phase of testing. The dilative behavior continues until the peak shear stress is mobilized and then the shear behavior becomes contractive. The dilative behavior is more pronounced in specimens with a higher OCR. The results show there is no correlation between OCR and normalized modulus. Therefore, OC specimens will produce modulus values similar to NC specimens.

The SHANSEP design method was successfully fitted to the results, as shown in Figure 6-25. The S parameter and m parameter are equal to 0.18 and 0.761 for the same maximum stress level.

The cyclic CK<sub>0</sub>DSS tests produced the most interesting behavior. The results show a dramatic increase in the peak undrained shear strength with each shear phase, as shown in Figure 6-28 and 6-29. The material also becomes much more ductile. The effective stress paths show a

pronounced difference in behavior with increasing shear phases. The behavior changes from very contractive in shear phase 1 to dilative in shear phase 3 (Figure 6-30 and 6-31). The dilative behavior continues with an increase in vertical stress until the peak shear stress is mobilized. The increase in strength is due to an increase in density with each shear phase. The findings indicate a possible way to improve the ground conditions in the field environment. Dynamic compaction or vibration techniques will shear the ground resulting in higher densities and greater strengths. However, this method would only be suitable for green field locations, due to the ensuing ground settlement that would occur.

#### 7.3.5.5 Undrained Triaxial Compression

The CIUC and  $CK_0$ UC triaxial tests investigated the effect of consolidation stress level in the range  $\sigma'_{vc} = 100 - 500$  kPa. The shear stress-strain behavior demonstrated that as stress level increases, the normalized strength increases. Again, this is very unusual behavior and it has not appeared in any literature. The CIUC behavior is much more ductile than the  $CK_0$ UC behavior. In the CIUC tests, the peak shear stress is mobilized at greater strains and the ductility increases with stress level, while the  $CK_0$ UC tests reach peak shear stress at low strains ( $\epsilon_a < 0.5\%$ ) with no deviation with stress level. The CIUC behavior is very unusual. Generally for sands, dilation will occur at low stress levels with contraction at high stress levels. However, the results in this research show the opposite behavior. The behavior goes from fully contractive at low stresses to almost completely dilative at high stresses. The  $CK_0$ UC tests show similar behavior but it is not as pronounced. All specimens strain soften to some extent; however, the degree of strain softening reduces with stress level and specimens at higher stresses experience dilation after this phase. The effective stress paths again highlight the deviation in behavior with stress level. The stress path shape is consistent for  $CK_0$ UC tests with an increase in stress level while the shape of the CIUC stress path changes with an increase in stress level. The behavior reflects a greater reduction in pore pressures towards the end of the CIUC tests.

The undrained strength, modulus, friction angle, and strain at failure results for the undrained triaxial compression tests are summarized with the DSS device in the following section.

### 7.3.5.6 Shear behavior

The undrained strength ratio (USR) versus stress level for all tests is presented in Figure 6-73. The results illustrate the trend of increasing shear strength with an increase in stress level. In the case of dilative behavior like those found in the high stress CIUC tests, the undrained strength ratio is best defined using the excess pore pressure criterion. In all other cases, the peak shear stress criterion is the preferred method. The CIUC and  $CK_0UC$  triaxial tests produce similar undrained strength ratios at low stresses. The CIUC results are slightly higher with an increase in stress level due to the more pronounced dilative behavior. The triaxial undrained strength ratio is higher to that found in the DSS tests. This behavior is expected; however the difference found is almost double the DSS value, indicating that the material exhibits strong anisotropy.

The friction angles found at the peak shear stress in all tests are shown in Figure 6-74. All test types show that the peak friction angle increases with increasing stress level at a uniform rate. The increase can be directly related to the increase in the undrained strength ratio with increasing stress level. Therefore, the CIUC tests produce the highest peak friction angles, followed by the  $CK_0UC$  tests. The peak  $\arctan \tau_h/\sigma'_v$  ( $\psi_p$ ) values for the DSS device range from  $\psi'_p = 14^\circ$  at low stresses to  $\psi'_p = 20^\circ$  at higher stresses. They are lower than the friction angles in the triaxial tests. The peak friction angles in the triaxial tests can be considered to be of greater accuracy and will range between  $\phi'_p = 22^\circ$  at low stresses to  $\phi'_p = 26^\circ$  at higher stresses.

The friction angle versus stress level using the limiting strain criterion is presented in Figure 6-75 and 6-76. There is a large deviation in the friction angles at lower stress levels which diminishes with an increase in stress level. The high friction angles found in the CIUC tests at low stresses are a result of small testing measurement discrepancies. The actual friction angle is most likely a few degrees lower. The DSS device produces low  $\psi'$  values at low stresses. It is unknown how close this value is to the actual friction angle. Therefore, the  $CK_0UC$  triaxial device produces the most consistent friction angles. A friction angle  $\phi' = 31^\circ$  can be expected at low stresses and this will increase to a friction angle  $\phi' = 34^\circ$  at high stress levels.

The axial strain at failure versus stress level is presented in Figure 6-77. Using the peak shear strength criterion, the CIUC and DSS tests have very similar behavior. The material

becomes more ductile with an increase in stress level, the strain at failure increases from 0.6% at low stresses to 3.7% at high stresses. The CK<sub>0</sub>UC triaxial tests produce much lower strains at failure. The strain at failure is about 0.3% with constant values at all stress level. The other failure criteria produce greater strain values and there is reasonable agreement between CIUC and CK<sub>0</sub>UC triaxial tests.

The undrained secant Young's modulus normalized to the vertical consolidation effective stress versus stress level for all test types was analyzed in Figure 6-78. The CIUC tests produce higher modulus values at all strain levels than the DSS and CK<sub>0</sub>UC tests. Generally, the maximum CIUC normalized modulus is above 300 and the normalized modulus is around 60 at 1% axial strain. The DSS maximum modulus is between 150 and 200 at low strains with a drop to 45 at 1% shear strain. The CK<sub>0</sub>UC triaxial tests produce the lowest values. The maximum normalized modulus is about 150 at low strains but the reduction in modulus with an increase in strain is more pronounced than the other test types. In general, at low strains the modulus decreases with an increase in stress level. However, at higher strains the modulus is constant with an increase in stress level.

## **7.4 RECOMMENDATIONS FOR FUTURE RESEARCH**

Despite the extensive testing program that was undertaken in this research, there are still many unknowns about the material. There is a shortage of quality experimental data and literature on material of this type. As a result, many properties remain unknown and further experimental work is required to develop them. Recommendations for future research are discussed in the following sections.

### **7.4.1 Triaxial Testing**

The triaxial test series presented in this study included isotropic and K<sub>0</sub> consolidated undrained compression tests on normally consolidated specimens for vertical effective stresses,  $\sigma'_{vc} = 100$  to 900 kPa. Further CIUC and CK<sub>0</sub>UC tests are required to higher stresses to investigate the effects on the stress-strain-strength behavior. At present it is unknown if the dilative behavior will continue to increase with an increase in stress level or get to a condition where the behavior becomes constant. It is also unknown if the shear strength will continue to increase with an increase in stress level. Higher stress triaxial tests will provide this data base.



The volumetric strain assumption at the beginning of  $K_0$ -consolidation needs to be investigated. The volumetric strain was assumed to equal the axial strain before  $K_0$ -consolidation in this research. This assumption is normal for clays because they experience very low strains during saturation. The void ratios calculated from the final water content found a deviation between volumetric strain and axial strain at the end of saturation for this material. Therefore, it is likely that the stress path and  $K_0$  behavior have deviated slightly from the true value. Further testing is required using different initial volumetric strain assumptions to evaluate the stress path and  $K_0$  behavior.

Triaxial tests on overconsolidated specimens are needed to compare the stress-strain-strength behavior with the normally consolidated results in this research. The testing would also allow the development of the SHANSEP parameters in triaxial compression. At present, only the DSS SHANSEP parameters have been found for one max stress level. A further investigation is needed to produce SHANSEP parameters for at least 3 maximum stress levels.

Triaxial extension tests are needed to provide stress-strain-strength behavior in the extension mode of shearing. The testing should be carried out over a range of consolidation stresses. Once complete, there would be good data for all failure mechanisms in the field.

#### **7.4.2 Reconstitution Technique**

This research found that undercompaction was, by far, the most suitable and consistent reconstitution technique for this material. However, the CRS slurry resedimentation technique results show that there are deviations in behavior between reconstitution techniques. The literature shows that the stress-strain-strength behavior can deviate significantly between different reconstitution techniques and intact samples. A thorough investigation is therefore needed to investigate the stress-strain-strength behavior using different reconstitution techniques. The investigation is needed to prove the validity of the behavior seen in the literature.

#### **7.4.3 Susceptibility to Liquefaction**

The behavior demonstrated in the field and lab show that the material can liquefy easily. A gain in excess pore pressures through vibration transforms the material from a stable condition into a viscous fluid. Specimens consolidated to stresses as high as 15 MPa will lose their

structure and turn to a fluid like substance after a few blows. The Casagrande liquid limit method is not possible due to the tapping motion. The groove will close after two or three blows at any water content. Liquefaction is one of the factors in the structural damage caused during the construction. The construction vibrations were enough to liquefy the ground in some situations resulting in the ground settlement.

Therefore, the susceptibility of the material to liquefaction needs to be investigated. A series of cyclic liquefaction tests need to be performed in the laboratory to determine these properties.

#### **7.4.4 Ground Treatment**

Chapter 2 described some of the ground treatment techniques that were used during the waste water construction project. They all involved the use of Portland cement in either a mixing or injection process. In general, tunneling control was slightly better in ground that was pretreated with cement using the horizontal direction drilling machine. However, in the case of the curved drive, presented in Chapter 2, the ground mixing with cement showed no benefits and it is possible that the grout pressures used during this process caused localized liquefaction and some of the structural damage was associated to this process rather than the tunnel boring machine action. Therefore, two questions still remain unanswered. The effectiveness of the cement treatment is unknown and if the project had to be constructed again, what is the most suitable ground treatment technique.

A thorough laboratory investigation is needed to identify the benefits, if any, of using Portland cement as a treatment technique in this type of ground. It is possible that the materials property and behavior will change dramatically after the addition of cement. The study should also involve the best application procedure for this treatment in a field environment. There are also many other treatment techniques and products available. This study has found that dynamic vibration will densify the material producing higher shear strengths and greater ductility and is a possible solution to ground treatment. However, the technique is only suitable for green field sites due to the ground settlement which will occur. The applicability of all other treatment techniques and additives for this type of material needs to be investigated in the laboratory.

## REFERENCES

- Abdulhadi, N.O. (2009), "*An Experimental Investigation into the Stress-Dependent Mechanical Behavior of Cohesive Soil with Application to Wellbore Stability*", ScD Thesis, MIT, Cambridge, MA.
- Anderson, G.R. (1991), "*Physical Mechanisms Controlling the Strength and Deformation Behavior of Frozen Sand*", ScD Thesis, MIT, Cambridge, MA.
- ASTM D2974 – 07a Standard Test Methods Standard Test Methods for Moisture, Ash, and Organic Matter of Peat and Other Organic Soils
- ASTM D4318 - 10 Standard Test Methods for Liquid Limit, Plastic Limit, and Plasticity Index of Soils
- ASTM D4767 - 04 Standard Test Method for Consolidated Undrained Triaxial Compression Test for Cohesive Soils
- Baxter, C.D.P, Bradshaw, A.S., Green, R.A., and Wang, J.H. (2008), "*Correlation between Cyclic Resistance and Shear-Wave Velocity for Providence Silts*", Journal of Geotechnical and Geoenvironmental Engineering, ASCE, January.
- Biscontin, G., Cola, S., Pestana, J.M., and Simonini, P. (2007), "*Unified Compression Model for Venice Lagoon Natural Silts*", Journal of Geotechnical and Geoenvironmental Engineering, August.
- Bjerrum, L., (1973), "*Problems of Soil Mechanics and Construction on Soft Clays*", State of the art report to session IV, 8<sup>th</sup> International conference on soil mechanics and foundation engineering, Moscow.
- Burland, J.B., (1990) "*On the compressibility and shear strength of natural clays*", Geotechnique, Vol 40., No.3, pp 319 – 378.
- Borgesson, L. (1981), "*Shear Strength of Inorganic Silty Soils*", Proceedings of the International Conference on Soil Mechanics and Foundation Engineering, Volume 1, P567 – 572.

- Boulanger, R. W. and Idriss, I. M. (2006), "*Liquefaction Susceptibility Criteria for Silts and Clays*", Journal of Geotechnical and Geoenvironmental Engineering, ASCE, November.
- Bradshaw, A.S., Miller, H.J., and Baxter, C.D.P. (2007), "*A Case Study of Construction-Related Ground Movements in Providence Silt*", Field Measurements in Geomechanics, ASCE.
- Brandon, T.L., Rose, A.T., and Duncan, J.M. (2006), "*Drained and Undrained Strength Interpretation for Low Plasticity Silts*", Journal of Geotechnical and Geoenvironmental Engineering, ASCE, February.
- Cauble, D.F. (1996) "*An Experimental Investigation of the Behavior of a Model Suction Caisson in a Cohesive Soil*", PhD Thesis, MIT, Cambridge, MIT
- Charlesworth, J.K., (1953), "*The Geology of Ireland; An Introduction*", Oliver and Boyd, Edinburgh.
- Chillarige, A.R.V., Robertson, P.K., Morgenstern, N.R., and Christian, H. (1997) "*Evaluation of the in situ state of Fraser River Sand*", Canadian Geotechnical Journal, 34: 510–519.
- Christ, M. and Kim, Y.C. (2009), "*Experimental Study on the Physical-Mechanical Properties of Frozen Silt*", Korean Society of Civil Engineers, March
- Chu, J., Leong, W.K., and Loke, W.L. (2003), "*Discussion of Defining an appropriate steady state line for Merriespruit gold tailings*", Canadian Geotechnical Journal, 40: 484–486.
- Cronin Millar Consulting Engineers, (2007), "*River Ilen and Caol Stream Redevelopment Project – Feasibility Study (Phase 1)*", The Mews, Copperfields, Cobh, Co. Cork, Ireland
- Duffy, M.J. and Devoy, R.J.N (1999), "*Contemporary process controls on the evolution of sedimentary coasts under low to high energy regimes: western Ireland*", Geologie en Mijnbouw 77: 333-349.
- Fleming, L.N. and Duncan, J.M. (1990), "*Stress-Deformation Characteristics of Alaskan Silt*", Journal of Geotechnical Engineering, Vol. 116, March.
- Fourie, A.B. and Papageorgiou, G. (2001), "*Defining an appropriate steady state line for Merriespruit gold tailings*" Canadian Geotechnical Journal, 38: 695-706.

Fourie, A.B. and Papageorgiou, G. (2003), *Reply to the discussion by J. Chu, W.K. Leong, and W.L. Loke on "Defining an appropriate steady state line for Merriespruit gold tailings"*, Canadian Geotechnical Journal, 40: 487-488.

Freeman, T.W. (1972), *Ireland a general and regional geography*, Tayler and Francis, London.

Germaine, J.T. (1982), *Development of the Directional Shear Cell for Measuring Cross-Anisotropic Clay Properties*, ScD Thesis, MIT, Cambridge, MA.

Germaine, J.T. and Germaine, A.V. (2009) *Geotechnical Laboratory Measurements for Engineers*, John Wiley and Sons, Inc.

Guo, T. and Prakash, S. (1999), *"Liquifaction of Silts and Silt Clay Mixtures"*, Journal of Geotechnical and Geoenvironmental Engineering, August.

Hoeg, K. and Dyvik, R. (1999), *"Comparison of tests on undisturbed and reconstituted silt and silty sand"*, Norwegian Geotechnical Institute, Oslo, Norway.

Hoeg, K., Dyvik, R., and Sandbaekken, G. (2000), *"Strength of Undisturbed versus Reconstituted Silt and Silty Sand Specimens"*, Journal of Geotechnical and Geoenvironmental Engineering, July.

Holland, C.H., and Sanders, T., (2009) *"The Geology of Ireland"*, Dunedin Academic, Edinburgh.

Holland, C.H., (1981), *"A geology of Ireland"*, J. Wiley, New York.

Hyde, A. F., Higuchi, T., and Yasuhara, K. (2006), *"Liquefaction, Cyclic Mobility, and Failure of Silt"*, Journal of Geotechnical and Geoenvironmental Engineering, ASCE, June.

Hyde, A. F., Higuchi, T., and Yasuhara, K. (2007), *"Postcyclic Recompression, Stiffness, and Consolidated Cyclic Strength of Silt"*, Journal of Geotechnical and Geoenvironmental Engineering, ASCE, April.

Izadi, A.M., Luna, R., and Stephenson, W. (2008), *"Liquefaction Behavior of Mississippi River Silts"*, Geotechnical Earthquake Engineering and Soil Dynamics, ASCE.

Kuerbis, R., Negussey, D., and Vaid, Y.P. (1988), *“Effect of gradation and fines content on the undrained response of sand in Hydraulic fill structures”*, Edited by D.J.A. Van Zyl and S.G. Vick., American Society of Civil Engineers, Geotechnical Special Publication 21, pp. 330–345.

Ladd, R.S. (1977), *“Specimen Preparation and Cyclic Stability of Sands”*, Journal of the Geotechnical Engineering Division, ASCE, 103(6), June

Ladd, C.C., and Foott, R. (1974), *“New design procedures for stability of soft clays”*, Journal of Geotechnical Engineering Division, ASCE, 100(7), 763-786.

Ladd, C. C., and Varallyay, J. (1965), *“The Influence of Stress Systems on the Behavior of Saturated Clays during Undrained Shear”*, Research report R65-11, Soil Publication No.177, Department of Civil Engineering, Cambridge, MA.

Ladd, C.C., Weaver, J.S., Germaine, J.T., and Sauls, D.P. (1985), *“Strength-Deformation Properties of Arctic Silt”*, Civil Engineering in the Arctic Offshore, Proceedings of the Conference Arctic '85, ASCE.

Leroueil, S. and Vaughan, P.R. (1990) *“The general and congruent effects of structure in natural soils and weak rocks”*, Geotechnique, Vol. 40, No.3, pp. 467-488

Lin, G. and Yang, W. (2006), *“Characteristics of Varved Clayey Silts at an LNG Terminal Site”*, GeoCongress, ASCE.

Long, M. (2007), *“Engineering Characterization of estuarine silts”*, Quarterly Journal of Engineering Geology and Hydrology, Vol 40, P 147-161.

Long, M. (2001), *“Discussion on Strength of Undisturbed versus Reconstituted Silt and Silty Specimens”*, Journal of Geotechnical and Geoenvironmental Engineering, November.

Long, M. (2006), *“Sample Disturbance effects on medium plasticity clay/silt”*, Geotechnical Engineering, 159, P 99-111.

Long, M., Gudjonsson, G., Donohue, S., and Hagberg, K. (2010), *“Engineering Characteristics of Norwegian glaciomarine silt”*, Engineering Geology, 110, P 51-65.

- Martin, R.T. (1982), "*Suggested Method of Test for Determination of Soluble Salts in Soil*", ASTM STP 476, 288-290
- Mesri, G. and Huvaj, N. (2007), "*Shear Strength Mobilized in Undrained Failure of Soft Clay and Silt Deposits*", Geo-Denver 2007: New Peaks in Geotechnics, ASCE.
- Muilis, J.P., Seed, H.B., Chan, C.K., Mitchell, J.K., and Arulanandan, K. (1977), "*Effects of sample preparation on sand liquefaction*", Journal of Geotechnical Engineering, 113(8), 827-845
- Murthy, R., Nazarian, S., and Picornell, M. (2008), "*Dynamic Properties of Naturally Cemented Silts*", Geotechnical Earthquake and Engineering and Soil Dynamics IV Congress, ASCE.
- Ortega, O.J. (1992) "*Computer Automation of the Consolidated-Undrained Direct Simple Shear Test*", SM Thesis, MIT, Cambridge, MA
- Pracht, M., and Sleeman, A.G., (2002), "*Geology of West Cork*", Geological Survey of Ireland, Department of Public Enterprise.
- Prakash, S. and Puri, K. (2003), "*Liquefaction of Silts and Silt-Clay Mixtures*", Department of Civil Engineering, University of Missouri and Department of Civil Engineering, Southern Illinois University.
- Santagata, M.C. (1998), "*Factors Affecting the Initial Stiffness and Stiffness Degradation of Cohesive Soils*", PhD Thesis, MIT, Cambridge, MA.
- Seah, T.H. (1990), "*Anisotropy of Resedimented Boston Blue Clay*", ScD Thesis, MIT, Cambridge, MA.
- Sheahan, T.C. (1988), "*Modification and Implementation of a Computer Controlled Triaxial Apparatus*", SM Thesis, MIT, Cambridge, MA.
- Sheahan, T.C. (1991), "*An Experimental Study of the Time-Dependent Undrained Shear Behavior of Resedimented Clay Using Automated Stress-Path Triaxial Equipment*", ScD Thesis, MIT, Cambridge, MA.

Sheahan, T.C. and Germaine, J.T. (1992), "*Computer Automation of Conventional Triaxial Equipment*", Geotechnical Testing Journal, 15 (4), 311-322

Skibbereen Town Council, (2009), "*Skibbereen Town Development Plan 2009-2015*", North Street, Skibbereen, Co. Cork, Ireland.

Smith, R.E. and Wahls, H.E. (1969), "*Consolidation Under Constant Rates of Strain*", Journal of Soil Mechanics and Foundations Division, ASCE, March.

Stark, T. D., Ebeling, R.M., and Vettel, J.J. (1994), "*Hyperbolic Stress-Strain Parameters for Silts*", Journal of Geotechnical Engineering, Vol. 120, No. 2, February.

Sun, S. and Xu, H. (Date Unknown), "*Determining the Shear Strength of Unsaturated Silt*", Department of Geological and Geotechnical Engineering, College of Civil Engineering, Hohai University, Xikang Road, Nanjing 210098, China and Department of Geology and Geophysics, University of Wisconsin-Madison, Madison, WI 53706, USA.

Vaid, Y.P., Chung, E.K.F., and Kuerbis, R.H. (1990), "*Stress path and steady state*", Canadian Geotechnical Journal 27: 1-7.

Vaid, Y.P. and Sivathayalan, S. (1999), "*Influence of Specimen Reconstituting Method on the Undrained Response of Sand*", Geotechnical Testing Journal, Vol. 22, P187-195.

Vaughan, P.R. (1997), "*Panel discussion: Sedimentation of tailings*", In Proceedings of the 14th International Conference on Soil Mechanics and Foundation Engineering, Hamburg, Germany.

Wang, J. L., and Vivatrat, V. (1982), "*Geotechnical properties of Alaskan OCSmarine silts*", 14th Annual Offshore Technical Conference, Houston, Texas, May.

Woodlock, N.H., and Strachan, R.A., (2000), "*Geological History of Britain and Ireland*", Blackwell science, Oxford; Malden MA.

Wijewickreme, D. and Sanin, V. (2008), "*Cyclic Shear Response of undisturbed and reconstituted low-plastic Fraser River Silt*", Geotechnical Earthquake and Engineering and Soil Dynamics IV Congress, ASCE.



Wissa, A.E.Z., Christian, J.T., Davis, E.H., and Heiberg, S. (1971), "*Consolidation at Constant Rate of Strain*", Journal of Soil Mechanics and Foundation, ASCE, Vol. 97, No. SM10, 1393-1412

Yasuhara, K., Murakami, S., Song, B.W., Yokokawa, S., and Hyde, A.F. (2003) "*Postcyclic Degradation of Strength and Stiffness for Low Plasticity Silt*", Journal of Geotechnical and Geoenvironmental Engineering, Vol. 129, No. 8, August.